Low temperature kinetics and dynamics

Lok Hin Li

Submitted in accordance with the requirements for the degree of
Doctor of Philosophy

The University of Leeds
School of Chemistry

September 2022

The candidate confirms that the work submitted is his own, except where work which has formed part of jointly authored publications has been included. The contribution of the candidate and the other authors to this work has been explicitly indicated below. The candidate confirms that appropriate credit has been given within the thesis where reference has been made to the work of others.

The work in Chapter 3 of this thesis will appear in the following to-be-published work:

“Experimental and theoretical study of the low-temperature kinetics of the reaction of CN with CH_2O and implications for interstellar environments” jointly-authored by Niclas A. West, Lok Hin Desmond Li, Tom J. Millar, Marie Van de Sande, Edward Rutter, Mark A. Blitz, Julia H. Lehman, Leen Decin, and Dwayne E. Heard.

Within this, the contribution of Lok Hin Desmond Li is on the theoretical calculations part for the CN + CH_2O reaction system, with the assistance from Dr Julia H. Lehman in the ab initio calculations and Dr Mark A. Blitz in the MESMER calculations. Laval experiments were performed by Dr Niclas A. West, Mr Edward Rutter and Dr Mark A. Blitz. Astrochemical modelling was performed by Prof Tom J. Millar, Dr Marie Van de Sande and Prof Leen Decin. Prof Dwayne E. Heard is the principal investigator and the corresponding author of this work.

Acknowledgements

The last four years have surely been eventful and challenging to me, as well as to a lot of people I believe. From the social movements back in my hometown to the lockdown due to the global pandemic, challenges have always popped up in this ever changing world. However, similar to a reaction pathway, these ups and downs make our life journeys more interesting and meaningful. I am very fortunate to have received help from many people during the course of my PhD study and I would like to take this opportunity thank all of them.

First and foremost, I would like to express my sincere gratitude to Prof Dwayne Heard for his care and support over the last four years. His patience and extensive knowledge has helped me a lot whenever I face any difficulties. I would also like to thank Dr Julia Lehman for her knowledge in electronic structure calculations and valuable advice in performing computational work. I am also very grateful to Dr Mark Blitz, who has guided me through the use of MESMER programme and given me precious suggestions in the interpretation of the results. I must also thank Nic and Kevin for providing many useful research resources as well as sharing their expertise in the experimental measurements which I have learnt a lot from it. Thanks to Tom, Diogo and Charlotte for their help with the ab initio calculations programme. Thanks to Robin for his expertise in the theoretical calculations and sharing of his work on the dimerisation reactions. Thanks to Joanna and Frankie for providing me valuable advice and research resources. I would also like to thank all the people in Heard's research group and the Dainton office. It is really nice to meet all of you and I really enjoyed during our social events. Thanks to my friends since the secondary school, Douglas and Jonathan, and Owen, who had also studied here in Leeds, for being great listeners during our occasional chats. Lastly and most importantly, I have to express my sincere gratitude to my family, my mum, dad and nan, for taking care of me unconditionally and being supportive continuously since my birth. They are undoubtedly the driving force for me to pursue my dreams without any worries.

Abstract

The focus of the research presented in this thesis is the chemical kinetics and dynamics of gas-phase neutral-neutral reactions at low temperature for systems potentially relevant to interstellar chemistry through understanding the mechanisms using theoretical approaches consisting of ab initio calculations and rate coefficient calculations. For CN + CH_2O, a pre-reaction complex was identified which allows the possibility of an indirect channel to products, with >99% HCN, <1% HNC and negligible addition products formed. Numerical fitting to experimental data suggested that the barrier height is slightly positive while the ab initio results suggested a slightly submerged barrier, where the difference is within the calculation uncertainty. The overall rate coefficient shows a V-shaped temperature trend, which is represented by piecewise modified Arrhenius expressions. For CN + CH_3SH and CN + CH_2S, the rate coefficients approach the collision limit at low temperature as the entire reaction pathways can be submerged below the energy of the reactants. Abstraction from the mercapto group is more energetically favourable for CN + CH_3SH. For CN + CH_2S, an addition pathway to eventually form HC(S)CN is probable, which shows significant contrast with CN + CH_2O. For NH_2 + CH_3CHO, formation of formamide is almost negligible. Rather, formation of CH_3CO is dominant under most conditions but depending on the pressure and temperature formation of CH_2CHO can also be the major route due to tunnelling. A pressure dependence and the V-shaped temperature dependence are observed for the rate coefficient. The dimerisation reactions, which potentially can be competing reactions during kinetics studies with the Laval apparatus, of CH_2O, CH_3CHO, $CH_3C(O)CH_3$ and NH_3 were investigated. The order of the stability of the most stable form of non-covalent dimer, starting from the one with the lowest relative energy, is $CH_3C(O)CH_3$, CH_3CHO, CH_2O, NH_3. $CH_3C(O)CH_3$ has the largest predicted fraction of dimers formed during Laval measurements followed by NH_3. The predicted fraction is similar for CH_2O and CH_3CHO but experiments suggested appreciable underestimation of the dimers formed for CH_2O.

Table of Contents

Acknowledgements i

Abstract.. ii

Table of Contents iii

Table of Figures vii

Table of Tables xxiii

List of abbreviations xxvi

Chapter 1 Introduction.. 1

1.1 Low temperature environments 1

1.1.1 Atmospheres of planets and moons 1

1.1.2 Interstellar medium 4

1.2 Theories of chemical kinetics 8

1.2.1 The rate equation 8

1.2.2 The temperature dependence of rate coefficients – the Arrhenius equation and non-Arrhenius behaviour................. 10

1.2.3 The pressure dependence of rate coefficients – the Lindemann mechanism 13

1.2.4 Collision theory, capture theory, and trajectory calculations . 16

1.2.5 Transition state theory 19

1.3 The significance of studies of gas-phase neutral-neutral reactions at low temperatures 23

1.4 Experimental techniques for low-temperature kinetic measurements – the Laval nozzle apparatus.. 30

1.4.1 Generation of the cold environment 30

1.4.2 Radical generation 34

1.4.3 Determination of rate coefficients and the product branching ratios 35

1.5 Overview of this thesis... 41

1.6 References 42

Chapter 2 Theoretical background and computational methods 51

2.1 Ab initio calculations 51

2.1.1 Theoretical chemistry backgrounds 52

2.1.1.1 Basis sets 54

2.1.1.2 Electronic structure methods 58

2.1.1.3 Level of theory selection, errors and computational expenses 65

2.1.2 Methodology for performing computations via the Gaussian programme 74

2.1.2.1 Finding stationary points 75

2.1.2.2 Characterisation of stationary points from vibrational frequencies 76

2.1.2.3 Verification of linkage between stationary points 78

2.1.2.4 Final results to be reported 80

2.2 Master equation calculations 81

2.2.1 Theoretical background 81

2.2.1.1 From Hinshelwood modification to the Rice-Ramsperger-Kassel-Marcus (RRKM) theory 81

2.2.1.2 Energy grains and density of states 83

2.2.1.3 Loose transition state 87

2.2.1.4 Tunnelling corrections 89

2.2.1.5 Master equation and collisional energy transfer 91

2.2.2 Methodology for performing computations via the MESMER programme 95

2.2.2.1 Essential components in MESMER simulations 96

2.2.2.2 Data fitting function of MESMER 100

2.3 References 101

Chapter 3 The reaction between the cyano radical (CN) and formaldehyde (CH_2O) 112

3.1 Introduction 112

3.2 Computational methods 120

3.3 Results and discussions 122

3.3.1 Results from ab initio calculations 122

3.3.2 Results from rate coefficient calculations 130

3.3.2.1 Data fitting for the optimisation of rate controlling parameters 132

3.3.2.2 Product branching and extrapolation from further simulations 138

3.4 Conclusion 140

3.5 References 141

Chapter 4 The reaction between the cyano radical (CN) and methanethiol (CH_3SH) and thioformaldehyde (CH_2S) 151

4.1 Introduction 151

4.2 Computational methods 162

4.3 Results and discussions 164
  4.3.1 Results from ab initio calculations and discussions 164
    4.3.1.1 CN + CH_3SH 164
    4.3.1.2 CN + CH_2S 169
  4.3.2 Results from rate coefficient calculations and discussions 173
    4.3.2.1 CN + CH_3SH 173
    4.3.2.2 CN + CH_2S 177
4.4 Conclusion 180
4.5 References 181

Chapter 5 The reaction between the amidogen radical (NH_2) and acetaldehyde (CH_3CHO) 191

5.1 Introduction 191
5.2 Computational methods 199
5.3 Results and discussions 201
  5.3.1 Results from ab initio calculations 201
  5.3.2 Results from rate coefficient calculations 204
    5.3.2.1 Rate coefficients 204
    5.3.2.2 Tunnelling and product branching ratios 210
    5.3.2.3 Troe fitting 219
5.4 Conclusion 223
5.5 References 224

Chapter 6 Theoretical calculations of dimerisation reactions in the context of Laval nozzle experiments 232

6.1 Introduction 232
6.2 Computational methods 238
6.3 Results and discussions 246
  6.3.1 Results from ab initio calculations 246
  6.3.2 Rate coefficient calculations 256
  6.3.3 Dimerisation under the context of the Laval nozzle experiments 263
  6.3.4 Discussion 281
6.4 Conclusion 288
6.5 References 290

Chapter 7 Conclusion and future work 310

Appendix A Supplementary information for the theoretical background and computational methods 314

Appendix B Supplementary information for the reaction between the cyano radical (CN) and formaldehyde (CH_2O) 318

Appendix C Supplementary information for the reaction between the cyano radical (CN) and methanethiol (CH_3SH) and thioformaldehyde 343

Appendix D Supplementary information for the reaction between the amidogen radical (NH_2) and acetaldehyde (CH_3CHO) 377

Appendix E Supplementary information for the theoretical calculations of dimerisation reactions in the context of Laval nozzle experiments 398

Table of Figures

Figure 1.1 The temperature variation with altitude for the Earth's atmosphere. Adapted from Rothery et al. (1). 2

Figure 1.2 A spectrum obtained with the use of the ALMA telescope by pointing towards the AGB star CW Leonis. Spectral features of SiC_2, SiS, AlF and CO can be identified. Taken from Decin et al. (8). 8

Figure 1.3 (Upper) The temperature dependence of the rate coefficients following the Arrhenius equation. (Lower) A linear plot is obtained by taking logarithm on both sides of the Arrhenius equation. 10

Figure 1.4 A schematic reaction profile with a positive energy barrier Ea. $\Delta H^{\circ}\mathrm{reaction}$ denotes the enthalpy change of the reaction. 11

Figure 1.5 The top row shows the energy profiles while the bottom row shows the corresponding temperature dependence of three different types of exothermic reactions. The left column shows a reaction with a noticeable barrier, the middle column shows a barrierless reaction while the right column shows a reaction initially forming a weakly bound complex followed by a barrier. Taken from Sims (19). 12

Figure 1.6 The pressure dependence of the rate coefficients described by the Lindemann mechanism. 14

Figure 1.7 (Left) The effective potential as a function of the separation between two attracting species for a head-on collision (solid line), and a non-head-on collision (dashed line) where a centrifugal barrier emerges. (Right) Possible trajectories for the interaction between two attracting species: when $b = 0$, a head-on collision happens indicated by the straight arrow; when $0 < b < b_{\mathrm{max}}$, a non-head-on collision happens where the incoming species spirals inwards; when $b > b_{\mathrm{max}}$, a deflection happens instead of a collision. 18

Figure 1.8 Potential energy surface for R 1.8 where the arrow denotes the reaction pathway. r_{AB} and r_{BC} denote the separation between A and B and between B and C respectively. The reaction starts with the approach of the two reactants A and BC, where r_{AB} decreases, and then after the formation of $\mathrm{ABC}\ddagger$, r_{BC} increases to form the products AB and C. 19

Figure 1.9 Measured rate coefficients for the CN + O_2 reaction versus temperature. The open circles are from data reported in Sims and Smith (21), the closed circles are from data reported in Sims et al. (22), and the line is the fitted expression as shown in E 1.46. Taken from Sims et al. (22). 25

Figure 1.10 The logarithm of the rate coefficients, log k (left), and the ratio of the rate coefficients with those at 300 K, $k(T)/k_{300\mathrm{K}}$ (right), versus temperature for reactions of the OH radical with various compounds. Taken from Heard (18). 26

Figure 1.11 Schematic potential energy surface for the reaction of OH + CH_3OH. Energies are in kJ mol^{-1}. Taken from Shannon et al. (26). C denotes the pre-reaction hydrogen-bonded complex. TS-H and TS-M are the two transition states leading respectively to the H abstraction products, CH_3O + H_2O and CH_2OH + H_2O. 27

Figure 1.12 Predicted percentage gain in the abundance of CH_3O (top) and percentage loss in the abundance of CH_3OH (bottom) versus time in the interstellar clouds of different temperatures (black: 10 K, red: 50 K, blue: 100 K) after the inclusion of the OH + CH_3OH reaction in the astronomical models. Taken from Acharyya et al. (44). 28

Figure 1.13 Rate coefficients for the C_2H + C_6H_6 reaction versus temperature in the temperature range of 50–300 K. The lines and error bars are from the fitted expression obtained from the measured results reported in Goulay and Leone (47) while the black dots are from the computed results reported in Woon (48). Taken from Woon (48). 29

Figure 1.14 Schematic diagram of a Laval nozzle apparatus, which shows the gas first flows from the convergent part, to the throat and eventually the divergent part. Adapted from Atkinson and Smith (49). 30

Figure 1.15 Schematic diagram of the pump-probe laser set-up for kinetic measurements in the Laval nozzle apparatus in the University of Leeds. Taken from Taylor et al. (51). 36

Figure 1.16 An experimental decay curve of OH radical for the reaction of OH + C_2H_4. Taken from Taylor et al. (51). 36

Figure 1.17 Bimolecular plots of the pseudo-first order OH decay rate coefficient *k’* against the concentration of the co-reagent C_2H_4 at 86 K (squares) and 69 K (circles) respectively. The slope of the bimolecular plot gives the reaction rate coefficient k_{bim}. Taken from Taylor et al. (51). 37

Figure 1.18 Temporal evolution of the decay of OH radicals (blue) and the formation of CH_3O radicals (black) in the reaction of OH + CH_3OH at 82 K, where measurements were taken with the LFP-LIF technique. Taken from Shannon et al. (26). 39

Figure 1.19 Schematic diagram of the Laval nozzle coupled with (top) the vacuum ultraviolet synchrotron ionisation quadrupole mass spectrometry (QMS) and (bottom) the time-of-flight mass spectrometry (TOF-MS) respectively. TP, MP and DP represent the pumping systems. Taken from Soorkia et al. (67). 40

Figure 1.20 Schematic diagram of the Laval nozzle coupled with the chirped pulse Fourier transform spectrometer. The reaction of interest shown here is the dissociation of C_2H_3CN into HCN/HNC + C_2H_2 with He as the bath gas. Taken from Hays et al. (69). 41

Figure 2.1 A plot of the amplitude of the 1s orbital (n = 1, l =0) represented by a Slater function (red) and a Gaussian function (green) versus the radius r. 55

Figure 2.2 Example of the formation of a contracted Gaussian function (green) from three primitives (black, red, blue). 56

Figure 2.3 A flow diagram of the key procedures involved in the exploration of the potential energy surface with ab initio methods. The italics within the brackets are the relevant keywords used in Gaussian to perform the calculations. See text for more details.. 74

Figure 2.4 Output of the optimisation calculation of CN + CH_2O van der Waals' complex using Gaussian at the M06-2X/aug-cc-pVTZ level of theory. The initial structure is shown in the top left hand corner while the optimised structure is shown in the top right hand corner. The distance between the two carbon atoms in the optimised structure: 2.746 Å. The plot shows how the electronic energy is minimised during the optimisation. 1 Hartree = 2625.5 kJ mol^{-1}. 76

Figure 2.5 Output of the frequency calculation of CN + CH_2O van der Waals' complex using Gaussian at the M06-2X/aug-cc-pVTZ level of theory. "Mode" stands for different vibrational modes of the complex; "Freq" stands for the calculated vibrational frequency in cm^{-1}; and "Infrared" stands for the corresponding predicted relative intensity on an infrared spectrum. Distance between the two carbon atoms: 2.746 Å. 77

Figure 2.6 Output of the IRC calculation of the transition state leading to the formation of HNC + HCO in the CN + CH_2O reaction using Gaussian at the M06-2X/aug-cc-pVTZ level of theory. y-axis denotes the electronic energy (ZPVE uncorrected) in Hartree, where 1 Hartree = 2625.5 kJ mol^{-1}. 78

Figure 2.7 Output of the relaxed scan investigating in the approach of CN towards the oxygen side of CH_2O using Gaussian at the M06-2X/aug-cc-pVTZ level of theory. x-axis is the distance between CN carbon and CH2O oxygen in Å, which is the scan coordinate in this example. y-axis denotes the electronic energy (ZPVE uncorrected) in Hartree, where 1 Hartree = 2625.5 kJ mol^{-1}. 79

Figure 2.8 Examples of (a) a harmonic oscillator potential, (b) an anharmonic oscillator potential and (c) a hindered rotor potential. 86

Figure 2.9 A schematic of the two transition state model with the reaction controlled by the outer transition state at large intermolecular distance and the inner transition state at the submerged barrier when the two reactants approach. Taken from Georgievskii and Klippenstein (63). 88

Figure 2.10 The wavefunction of a particle when encountering a potential barrier *V*, where *E* < *V*. For a narrow barrier, the amplitude of the wavefunction transmitted is non-zero. Taken from Pilling and Seakins (49). 90

Figure 2.11 A symmetric Eckart potential barrier with V_0 as the peak potential and 2*α* as the full width at half maximum. 90

Figure 2.12 A schematic showing the representation of the energy grained master equation for a reaction with multiple wells and transition states along the pathway. Taken from Glowacki et al. (48). 93

Figure 2.13 A Lennard-Jones potential with ε as the well depth at equilibrium distance and σ as the finite distance at which the potential intersects with the x-axis. 94

Figure 2.14 Variation of $\Delta Edown$ as a function of temperature using the parameters given in Table 2.10. 97

Figure 2.15 A summary of the methods used to formulate the transition probabilities between different energy grains in MESMER. 99

Figure 3.1 Experimental rate coefficients for the CH + CH_2O reaction versus temperature reported in previous literature. Taken from West et al. (2). 113

Figure 3.2 Zero-point vibrational energy (ZPVE) corrected potential energy surface in kJ mol^{-1} for the CH + CH_2O reaction at the CCSD(T)/aug-cc-pVTZ//BHandHLYP/aug-cc-pVDZ level. Adapted from Nguyen et al. (3). The three entrance channels, chain addition (red), cycloaddition (green) and insertion (blue) together with the lowest energy pathways (purple) leading to the two dominant product sets, H_2CCO + H and CH_3 + CO (yellow), are highlighted. 113

Figure 3.3 Rate coefficients for the OH + CH_2O reaction versus temperature reported in previous literature. Taken from Ocaña et al. (20). 114

Figure 3.4 Potential energy profile (in kJ mol^{-1}, ZPVE corrected) along the reaction coordinate for the H abstraction reaction of OH + $CH_2O \rightarrow H_2O$ + HCO at the CCSD(T)/CBS//CCSD/aug-cc-pVDZ level of theory. Taken from Machado et al. (28). The reaction starts off with the two reactants OH and CH_2O approaching to form a pre-reaction complex (PC) followed by a saddle point (SP) and eventually generates the products H_2O + HCO. 115

Figure 3.5 Previously published experimentally measured rate coefficients of the reaction CN + CH_2O against the inverse of temperature. Taken from Chang and Wang (55). The open circles are data from Yu et al. (54) while the closed circles are data from Chang and Wang (55). 118

Figure 3.6 Potential energy profile along the reaction coordinate for the direct H abstraction reaction of CN + $CH_2O \rightarrow$ HCN + HCO at the QCISD/6-31G//UHF/6-31G** level of theory. Adapted from Feng et al. (56). The y-axis is in Hartree, where 1 Hartree = 2625.5 kJ mol^{-1} where the barrier relative to the reactants is ~ 2 kJ mol^{-1}. 118**

Figure 3.7 Proposed abstraction and addition pathways for the reaction between CN and CH_2O by Tonolo et al. Taken from (57). Energy values (all in kJ mol^{-1}, ZPVE corrected) are obtained at the CCSD(T)/CBS+CV// B2PLYP/maug-cc-pVTZ-*d*H level of theory. PRC denotes the pre-reaction complex while 1C denotes the N≡C-CH_2O adduct. 120

Figure 3.8 PES of the CN + CH_2O reaction obtained at CCSD(T)/aug-cc-pVTZ//M06-2X/aug-cc-pVTZ level of theory. All energy values are in kJ mol^{-1} and with the inclusion of the scaled ZPVE. The red line indicates the only van der Waals complex VDW found in this work. The blue and green paths show the subsequent pathways from VDW leading to HCN + HCO (P1) and HNC + HCO (P2) products, respectively. 122

Figure 3.9 Optimised geometries of reactants, products, intermediates and transition states obtained at the M06-2X/aug-cc-pVTZ level of theory for the CN + CH_2O reaction. The labels correspond to those shown in Figure 3.8. 123

Figure 3.10 Potential energy curve (BHandHLYP/aug-cc-pVDZ, uncorrected for ZPVE) for the approach of CN to the oxygen of CH_2O. The scan coordinate of the relaxed scan is the distance between the carbon atom of the CN moiety and the oxygen atom of CH_2O. 125

Figure 3.11 Potential energy curve (BHandHLYP/aug-cc-pVDZ, uncorrected for ZPVE) for the approach of CN to the hydrogen of CH_2O. The scan coordinate of the relaxed scan is the distance between the carbon atom of the CN moiety and the hydrogen atom of CH_2O. 126

Figure 3.12 Potential energy curve (ZPVE corrected) calculated at the M06-2X/aug-cc-pVTZ level for the rotation of CN around CH_2O for O=C - - - N angle from 55º to 180º. Energy is relative to the sum of the energies (ZPVE corrected) of the two separate reacting species, CN and CH_2O, at the M06-2X/aug-cc-pVTZ level. 127

Figure 3.13 Potential energy curve (BHandHLYP/aug-cc-pVDZ, uncorrected for ZPVE) for the relaxed scan of the C-C separation starting from the adduct $H_2C(O)CN$ (Int3). 129

Figure 3.14 Calculated rate coefficients versus pressure at various temperatures which shows the pressure independence for the indirect H abstraction channel over a pressure of 10^{15}–10^{19} molecule cm^{-3}. 131

Figure 3.15 A simplified PES used for MESMER fitting scenarios (see Table 3.4) together with molecular structures at key stationary points. Initial van der Waals complex VDW (red) formation is followed by transition states to products, HCN + HCO (P1, blue) and HNC + HCO (P2, green) respectively. See text for details. ... 131

Figure 3.16 Rate coefficients plotted against temperature for results obtained from experiments with the Laval set-up (black squares) and reported from by Yu et al. (54) (green triangles) and Chang and Wang (55) (blue triangles), together with calculations from MESMER with different fitting scenarios listed in Table 3.4 (*Laval* + *Lit 2*: red line; *Laval*: black line; *Laval* + *Lit 1*: blue line). The x-axis is on a logarithmic scale in the inset. The extrapolation of *Laval* and *Laval* + *Lit 2* models only shows a noticeable deviation when the temperature is below 30 K. 137

Figure 3.17 Predicted product branching ratios of the CN + CH_2O reaction as a function of temperature using the parameters obtained from the *Laval* + *Lit 2* scenario (black: HCN; red: HNC). 138

Figure 4.1 Zero-point vibrational energy (ZPVE) corrected potential energy surface in kJ mol^{-1} for the OH + CH_3SH abstraction reaction. Taken from Mai et al. (42). On the right is the H abstraction at the methyl site, which involves a positive barrier TS1 after the formation of the weakly bound complex RC1, while on the left is the H abstraction at the mercapto site, which involves a submerged barrier TS2 after the formation of the weakly bound complex RC2. The energy values in black are obtained from the CCSD(T)/aug-cc-pV(T,Q)Z//M06-2X/aug-cc-pV(T+d)Z level (42), in pink are from the MCCM-CCSD(T)-CO-2m//MP2/cc-pVDZ level (39) and in blue are from the CBS-QB3 level (40). 155

Figure 4.2 ZPVE-corrected potential energy surface in kJ mol^{-1} for the OH + CH_2S reaction at the CCSD(T)/aug-cc-pVTZ//M06-2X/6-311++G(3df,3pd) level obtained by Arathala et al. Taken from (43). Two possible channels are found, namely the H abstraction channel via the positive barrier TS1 and the addition channel to form the adduct $H_2C(OH)S$ via the submerged barrier TS2, after the formation of the pre-reaction complex PRC1................................ 156

Figure 4.3 ZPVE-corrected potential energy surface in kJ mol^{-1} for the CN + CH_3SH reaction at the CCSD/6-311++G(d,p)//B3LYP/6-311++G(d,p) level obtained by Xu et al. Taken from (45). It is proposed that CH_3S + HCN can be formed via the pre-reaction complex IM1 and the submerged barrier TS1; CH_3S + HNC can be formed via the pre-reaction complex IM2 and the positive barrier TS2a; and CH_2SH + HNC can be formed via the positive barrier TS3. It is reported that CH_2SH + HCN cannot be formed directly from CN + CH_3SH and can only be formed from another reaction between CH_3S and HNC via a positive barrier TS2b..................... 157

Figure 4.4 ZPVE-corrected potential energy surface in kJ mol^{-1} for the CN + CH_3OH reaction at the CCSD(T)/aug-cc-pVTZ//M06-2X/aug-cc-pVTZ level obtained by Lucas. Adapted from (55). Four possible product channels are identified, from the lowest energy to the highest energy: HCN + CH_2OH, HCN + CH_3O, HNC + CH_2OH, HNC + CH_3O, where all involve the formation of a pre-reaction complex followed by surmounting a barrier. MESMER fitting to the experimental data suggest the further lowering of the energies of the transition states respectively leading to HCN + CH_2OH (TS2a) and HCN + CH_3O (TS1a) by ~2 kJ mol^{-1}, which will make the former one change from being positive to submerged. 160

Figure 4.5 PES of the H abstraction from the mercapto group for the CN + CH_3SH reaction obtained at the CCSD(T)/aug-cc-pVTZ//M06-2X/aug-cc-pVTZ level of theory. All energy values are in kJ mol^{-1} and are corrected with scaled ZPVE. 165

Figure 4.6 PES of the H abstraction from the methyl group for the CN + CH_3SH reaction. For all the species, the relative energies obtained at the CCSD(T)/aug-cc-pVTZ//M06-2X/aug-cc-pVTZ level are presented. For the two transition states, the relative energies obtained at the M06-2X/aug-cc-pVTZ level are also presented within the parentheses. All energy values are in kJ mol^{-1} and are corrected with scaled ZPVE. The dotted lines indicate large uncertainties in the transition states, which highlights the issues in the current calculations and will require further work. 167

Figure 4.7 Optimised geometries of reactants, products, intermediates and transition states obtained at the M06-2X/aug-cc-pVTZ level of theory for the CN + CH_3SH reaction. The labels correspond to those shown in Figure 4.5 and Figure 4.6. 168

Figure 4.8 PES of the addition channel for the CN + CH_2S reaction obtained at the CCSD(T)/aug-cc-pVTZ level of theory. All energy values are in kJ mol^{-1} and are corrected with scaled ZPVE......... 170

Figure 4.9 PES of the H abstraction channel for the CN + CH_2S reaction obtained at the CCSD(T)/aug-cc-pVTZ level of theory. All energy values are in kJ mol^{-1} and are corrected with scaled ZPVE......... 170

Figure 4.10 Optimised geometries of reactants, products, intermediates and transition states obtained at the M06-2X/aug-cc-pVTZ level of theory for the CN + CH_2S reaction. The labels correspond to those shown in Figure 4.8 and Figure 4.9. 171

Figure 4.11 Rate coefficient for the CN + CH_3SH reaction versus temperature in the range of T = 100–500 K. The black line is the results from MESMER calculations where no pressure dependence is observed in the total density range of 10^{13}–10^{21} molecule cm^{-3}. The red data point is from the experimental result reported by Decker and Macdonald (44). The orange line plotted alongside is the collision limit set by the ILT input parameters. 175

Figure 4.12 HCN fractional yield of the CN + CH_3SH reaction as a function of temperature. The black line is the results from MESMER calculations where no pressure dependence is observed in the total density range of 10^{13}–10^{21} molecule cm^{-3}. The red data point is from the experimental result reported by Decker and Macdonald (44). 176

Figure 4.13 Calculated rate coefficients for all the addition and abstraction channels of the CN + CH_2S reaction versus temperature in the range of 100–400 K. The two lines corresponding to the two abstraction channels overlap. No pressure dependence is observed in the total density range of 10^{13}–10^{17} molecule cm^{-3}. 178

Figure 5.1 Zero-point vibrational energy (ZPVE) corrected potential energy surface in kJ mol^{-1} for the CH_2O + NH_3 reaction at the CCSD(T)/6-311++G(3df,3pd)//M06-2X/6-311++G(3df,3pd) level obtained by Ali. Adapted from (15). 193

Figure 5.2 ZPVE-corrected potential energy surface in kJ mol^{-1} for the CH_2O + $[NH_4]^+$ reaction at the CCSD(T)/aug-cc-pVTZ//MP2/aug-cc-pVTZ level obtained by Redondo et al. Adapted from (16). 193

Figure 5.3 Energies (kJ mol^{-1}) obtained at the ωB97xD/aug-cc-pVTZ level by Darla and Sitha for different reaction pathways leading to formamide formation: left: NH_3 + CO; central: NH_3 + $[CO]^+$; right: $[NH_3]^+$ + CO. Adapted from (17). 194

Figure 5.4 Proposed formamide formation pathway for the reaction between NH_2 and CH_2O by Barone et al. Taken from (18). Energy values in black are the electronic energies obtained at CBS-QB3 while in green are with the inclusion of B2PLYP-D3/m-aug-cc-pVTZ ZPVE corrections. Structure labelled as 1 is the H_2N–CH_2O adduct. 195

Figure 5.5 Predicted rate coefficient of the reaction of NH_2 + CH_2O versus temperature by Barone et al. based on the potential energy surface shown in Figure 5.4. Adapted from (18). 196

Figure 5.6 Proposed pathway for the approach of NH_2 + CH_2O to form the adduct by Vazart et al. Adapted from (19). Energy values in bold are the electronic energies obtained at CCSD(T)/CBS+CV while in parentheses are with the inclusion of B2PLYP-D3/m-aug-cc-pVTZ ZPVE corrections. 196

Figure 5.7 PES of the NH_2 + CH_3CHO reaction obtained at CCSD(T)/aug-cc-pVTZ//M06-2X/aug-cc-pVTZ level of theory. All energy values are in kJ mol^{-1} and are corrected with scaled ZPVE. 201

Figure 5.8 Optimised geometries of reactants, products, intermediates and transition states obtained at the M06-2X/aug-cc-pVTZ level of theory for the NH_2 + CH_3CHO reaction. The labels correspond to those shown in Figure 5.7. 202

Figure 5.9 Calculated rate coefficients for the NH_2 + CH_3CHO reaction versus temperature in the range T = 25–400 K at various pressures. The legend denotes the number densities from 10^{13}–10^{23} molecule cm^{-3}. 204

Figure 5.10 Calculated rate coefficients for the NH_2 + CH_3CHO reaction versus pressure in the range of P = 10^{13}–10^{23} molecule cm^{-3} at various temperatures. The legend denotes the temperatures from 25 K to 400 K. 205

Figure 5.11 Rate coefficients plotted against temperature for results obtained from experiments with the Laval set-up (red circles) and reported from Hack et al. (30) (black line), together with calculations from MESMER for different total number density conditions (dark brown: 10^{16} molecule cm^{-3}; cyan: 10^{17} molecule cm^{-3}; gold: 10^{18} molecule cm^{-3}). 208

Figure 5.12 Fractional population of various relevant species of the NH_2 + CH_3CHO reaction system (red: the limiting reactant NH_2 radical; blue: the adduct Add; black: pre-reaction complex VDW1; yellow: pre-reaction complex VDW2; green: product set CH_3CO + NH_3; cyan: product set CH_2CHO + NH_3; purple: product set $NH_2C(O)CH_3$ amide + H) using a concentration of 10^{14} molecule cm^{-3} of the excess reactant CH_3CHO against time with (top) and without (bottom) tunnelling corrections at 100 K with a total density of 10^{15} molecule cm^{-3} (left) and 10^{19} molecule cm^{-3} (right) respectively. 211

Figure 5.13 Fractional population of various relevant species of the NH_2 + CH_3CHO reaction system (red: the limiting reactant NH_2 radical; blue: the adduct Add; black: pre-reaction complex VDW1; yellow: pre-reaction complex VDW2; green: product set CH_3CO + NH_3; cyan: product set CH_2CHO + NH_3; purple: product set $NH_2C(O)CH_3$ amide + H) using a concentration of 10^{14} molecule cm^{-3} of the excess reactant CH_3CHO against time with (top) and without (bottom) tunnelling corrections at 35 K with a total density of 10^{15} molecule cm^{-3} (left) and 10^{19} molecule cm^{-3} (right) respectively. 212

Figure 5.14 Bimolecular product formation rate coefficient for the direct channel of the NH_2 + CH_3CHO reaction without the inclusion of quantum mechanical tunnelling against temperature. There is no pressure dependence as all the lines coincide with each other. 213

Figure 5.15 Average lifetime of the pre-reaction complexes with (black) and without (red) tunnelling against temperature with a total pressure of 10^{19} molecule cm^{-3} and an excess reactant CH_3CHO concentration of 10^{14} molecule cm^{-3} in the temperature range of 25–400 K. 214

Figure 5.16 Percentage yields of different products of the NH_2 + CH_3CHO reaction as a function of temperature and pressure. 216

Figure 5.17 Fractional yields of different products of the NH_2 + CH_3CHO reaction as a function of temperature at P = 10^{16} molecule cm^{-3}. On the left, the y-axis is on a linear scale and the yield of $NH_2C(O)CH_3$ amide is too small to be visible on the graph. On the right, the y-axis is on a logarithmic scale. 217

Figure 5.18 Fractional yields of different products of the NH_2 + CH_3CHO reaction as a function of pressure at T = 35 K, 50 K, 70 K and 100 K respectively. The yield of $NH_2C(O)CH_3$ amide is too small to be visible on the graphs. 218

Figure 5.19 The Troe fits to the MESMER calculated rate coefficients for the NH_2 + CH_3CHO reaction at various temperatures. The markers are the MESMER calculated rate coefficients while the lines of the same colour are the Troe fits. The legend denotes the temperatures from 25 K to 400 K. 222

Figure 6.1 Structure of 1,2-dioxetane ($C_2O_2H_4$). 234

Figure 6.2 Rate of loss of CH radical against the concentration of CH_2O at different temperatures: red: 70 K; yellow: 56 K; green: 31 K, for an overall density of [Ar] = 10^{16}–10^{17} molecule cm^{-3}. The straight lines are the linear least-square fits to the data, where the data points obtained at higher concentrations of CH_2O are observed to be lying below this linear trend, which is thought to be due to the dimerisation of CH_2O. Taken from West et al. (122). 235

Figure 6.3 Rate of loss of OH radicals as a function of the concentration of $CH_3C(O)CH_3$ at 86 ± 4 K using *tu*-BuOOH as the precursor and N_2 as the bath gas with [M] = 4 × 10^{16} molecule cm^{-3}. Negative curvature is observed in the bimolecular plot at higher concentrations. Taken from Taylor (123). 236

Figure 6.4 Structure of the methanol non-covalent dimer. 238

Figure 6.5 Temperature profile within the 52 K nozzle used by Antiñolo et al. (126). Distance z is set as 0 for the exit of the nozzle. The leftmost data point corresponds to the sonic point. 241

Figure 6.6 Total number density profile in molecule cm^{-3} within the 52 K nozzle used by Antiñolo et al. (126). Distance z is set as 0 for the exit of the nozzle. The leftmost data point corresponds to the sonic point. 241

Figure 6.7 A schematic of the Laval nozzle setup to explain the convention used in this chapter. The exit of the nozzle is set to be at distance z = 0. Within the nozzle, z < 0; out in the stable flow region, z > 0. As there are only data up to the sonic point for the temperature and number density profiles, the convergent region of the Laval nozzle is ignored in this chapter. 242

Figure 6.8 Optimised geometries of monomers and non-covalent dimers of CH_2O, CH_3CHO, $CH_3C(O)CH_3$ and NH_3 obtained at the BHandHLYP/aug-cc-pVDZ level of theory. The Cartesian coordinates of the geometries can be found in the tables in Appendix E. 247

Figure 6.9 Internal rotations taken to be hindered rotor potentials during MESMER calculations for (top left) CH_2O C_s dimer, (top right) CH_3CHO C_1 dimer, (bottom left) $CH_3C(O)CH_3$ C_{2h} 1 dimer and (bottom right) NH_3 C_s dimer respectively. Relaxed scans were performed for rotation about the dihedral angle 1234 formed by the cyan atoms and the yellow arrows indicate how the rotation was done about the dihedral angle 1234. 254

Figure 6.10 Hindered rotor potentials obtained from the relaxed scans of the dihedral angles shown in Figure 6.9 for (top left) CH_2O C_s dimer, (top right) CH_3CHO C_1 dimer, (bottom left) $CH_3C(O)CH_3$ C_{2h} 1 dimer and (bottom right) NH_3 C_s dimer respectively at the BHandHLYP/aug-cc-pVDZ level of theory. The original optimised equilibrium dimer structures were set at a relative energy = 0 kJ/mol. 255

Figure 6.11 Potential energy surfaces used in MESMER for the dimerisation reactions of (from left to right) CH_2O, CH_3CHO, $CH_3C(O)CH_3$ and NH_3 respectively. 256

Figure 6.12 Calculated k_{loss} for the dimerisation reaction of CH_2O versus temperature in the range of T = 25–250 K with a total density of 10^{17} molecule cm^{-3}. Ar is used as the bath gas on the left while He is used as the bath gas on the right. Purple line (Harmonic hessian) is for the case when the DOS are calculated from the harmonic Hessian together with the scaling factor without the inclusion of the hindered rotor potential. Gold line (Harmonic hessian + 1 dihedral) is for the case when the DOS are calculated from the harmonic Hessian together with the scaling factor with the inclusion of the hindered rotor potential. Red line (Anharmonic) is for the case when the DOS are calculated from the anharmonic frequencies. 258

Figure 6.13 Calculated k_{loss} for the dimerisation reaction of CH_3CHO versus temperature in the range of T = 25–250 K with a total density of 10^{17} molecule cm^{-3}. Ar is used as the bath gas on the left while He is used as the bath gas on the right. Purple line (Harmonic hessian) is for the case when the DOS are calculated from the harmonic Hessian together with the scaling factor without the inclusion of the hindered rotor potential. Gold line (Harmonic hessian + 1 dihedral) is for the case when the DOS are calculated from the harmonic Hessian together with the scaling factor with the inclusion of the hindered rotor potential. 259

Figure 6.14 Calculated k_{loss} for the dimerisation reaction of CH_3COCH_3 versus temperature in the range of T = 25–250 K with a total density of 10^{17} molecule cm^{-3}. Ar is used as the bath gas on the left while He is used as the bath gas on the right. Purple line (Harmonic hessian) is for the case when the DOS are calculated from the harmonic Hessian together with the scaling factor without the inclusion of the hindered rotor potential. Gold line (Harmonic hessian + 1 dihedral) is for the case when the DOS are calculated from the harmonic Hessian together with the scaling factor with the inclusion of the hindered rotor potential. 260

Figure 6.15 Calculated k_{loss} for the dimerisation reaction of NH_3 versus temperature in the range of T = 25–250 K with a total density of 10^{17} molecule cm^{-3}. Ar is used as the bath gas on the left while He is used as the bath gas on the right. Purple line (Harmonic hessian) is for the case when the DOS are calculated from the harmonic Hessian together with the scaling factor without the inclusion of the hindered rotor potential. Gold line (Harmonic hessian + 1 dihedral) is for the case when the DOS are calculated from the harmonic Hessian together with the scaling factor with the inclusion of the hindered rotor potential. 260

Figure 6.16 Plots of grain rovibronic DOS of both the monomers (black) and the dimers of (top left) CH_2O, (top right) CH_3CHO, (bottom left) $CH_3C(O)CH_3$ and (bottom right) NH_3 against the grain energy. Purple points are for the case when the “Harmonic hessian” model was used for the calculation of DOS while gold points are for the case when the “Harmonic hessian + 1 dihedral” model was used. 262

Figure 6.17 Calculated k_{loss} for the monomers of (black) CH_2O, (red) CH_3CHO, (blue) $CH_3C(O)CH_3$ and (green) NH_3 within the 52 K nozzle from the sonic point to the exit of the nozzle using Ar as the bath gas. “Harmonic hessian” model was used on the left while “Harmonic hessian + 1 dihedral” model was used on the right.. 264

Figure 6.18 Lifetime of the stabilised dimers of (black) CH_2O, (red) CH_3CHO, (blue) $CH_3C(O)CH_3$ and (green) NH_3 within the 52 K nozzle from the sonic point to the exit of the nozzle using Ar as the bath gas and a monomer concentration of 2×10^{14} molecule cm^{-3} at the exit of the nozzle if there is no dimerisation. Plotted together is the travelling time of the gas flow from one data point to the subsequent data point (purple). “Harmonic hessian” model was used on the left while “Harmonic hessian + 1 dihedral” model was used on the right. 265

Figure 6.19 Calculated $f_{monomer}$ of CH_2O at different distances along the gas flow with different monomer concentrations using the “Harmonic hessian” model (left) and “Harmonic hessian + 1 dihedral” model (right) respectively using Ar as the bath gas. The values in the legend correspond to the supposed monomer concentration in molecule cm^{-3} at the exit of the 52 K nozzle and in the stable flow ($z \geq 0$) if there is no dimerisation. 267

Figure 6.20 (left) Calculated $f_{monomer}$ of CH_2O at z = 100 mm using the “Harmonic hessian” model (red) and “Harmonic hessian + 1 dihedral” model (blue) plotted against the [monomer] if there is no dimerisation. Curvature can be seen as a deviation from the $f_{monomer}$ = 1 level, the latter represents the scenario if there is no dimerisation. (right) Actual [monomer] present at z = 100 mm plotted against the [monomer] if there is no dimerisation. In addition to the calculated results, experimental data obtained at 40 K with He (green) and Ar (pink) as the bath gas are included as a comparison. Curvature can be seen as a deviation from the black line, which represents the scenario if there is no dimerisation. . 267

Figure 6.21 Calculated $f_{monomer}$ of CH_3CHO at different distances along the gas flow with different monomer concentrations using the "Harmonic hessian" model (left) and "Harmonic hessian + 1 dihedral" model (right) respectively using Ar as the bath gas. The values in the legend correspond to the supposed monomer concentration in molecule cm^{-3} at the exit of the 52 K nozzle and in the stable flow ($z \geq 0$) if there is no dimerisation. 268

Figure 6.22 (left) Calculated $f_{monomer}$ of CH_3CHO at z = 100 mm using the "Harmonic hessian" model (red) and "Harmonic hessian + 1 dihedral" model (blue) plotted against the [monomer] if there is no dimerisation. Curvature can be seen as a deviation from the $f_{monomer}$ = 1 level, which represents the scenario if there is no dimerisation. (right) Actual [monomer] present at z = 100 mm plotted against the [monomer] if there is no dimerisation. In addition to the calculated results, experimental data obtained at 25 K with Ar (green) as the bath gas are included as a comparison. Curvature can be seen as a deviation from the black line, which represents the scenario if there is no dimerisation. 269

Figure 6.23 Calculated $f_{monomer}$ of $CH_3C(O)CH_3$ at different distances along the gas flow with different monomer concentrations using the "Harmonic hessian" model (left) and "Harmonic hessian + 1 dihedral" model (right) respectively using Ar as the bath gas. The values in the legend correspond to the supposed monomer concentration in molecule cm^{-3} at the exit of the 52 K nozzle and in the stable flow ($z \geq 0$) if there is no dimerisation. 269

Figure 6.24 (left) Calculated $f_{monomer}$ of $CH_3C(O)CH_3$ at z = 100 mm using the "Harmonic hessian" model (red) and "Harmonic hessian + 1 dihedral" model (blue) plotted against the [monomer] if there is no dimerisation. Curvature can be seen as a deviation from the $f_{monomer}$ = 1 level, which represents the scenario if there is no dimerisation. (right) Actual [monomer] present at z = 100 mm plotted against the [monomer] if there is no dimerisation. In addition to the calculated results, experimental data obtained at 40 K with Ar (green) as the bath gas are included as a comparison. Curvature can be seen as a deviation from the black line, which represents the scenario if there is no dimerisation. 270

Figure 6.25 Calculated $f_{monomer}$ of NH_3 at different distances along the gas flow with different monomer concentrations using the "Harmonic hessian" model (left) and "Harmonic hessian + 1 dihedral" model (right) respectively using Ar as the bath gas. The values in the legend correspond to the supposed monomer concentration in molecule cm^{-3} at the exit of the 52 K nozzle and in the stable flow ($z \geq 0$) if there is no dimerisation. 272

Figure 6.26 (left) Calculated $f_{monomer}$ of NH_3 at z = 100 mm using the “Harmonic hessian” model (red) and “Harmonic hessian + 1 dihedral” model (blue) plotted against the [monomer] if there is no dimerisation. Curvature can be seen as a deviation from the $f_{monomer}$ = 1 level, which represents the scenario if there is no dimerisation. (right) Actual [monomer] present at z = 100 mm plotted against the [monomer] if there is no dimerisation. In addition to the calculated results, experimental data obtained at 40 K with Ar (green) as the bath gas are included as a comparison. Curvature can be seen as a deviation from the black line, which represents the scenario if there is no dimerisation. 272

Figure 6.27 (Upper left) Temperature and number density profile within the M2.25 N_2 106 K nozzle from the sonic point to the nozzle exit. (Upper right) Mach number and flow speed profile within the M2.25 N_2 106 K nozzle from the sonic point to the nozzle exit. (Lower) Calculated k_{loss} for the monomers of (black) CH_2O, (red) CH_3CHO, (blue) $CH_3C(O)CH_3$ and (green) NH_3 within the M2.25 N_2 106 K nozzle from the sonic point to nozzle exit. “Harmonic hessian” model was used on the left while “Harmonic hessian + 1 dihedral” model was used on the right. 274

Figure 6.28 Calculated $f_{monomer}$ of (upper left) CH_2O, (upper right) CH_3CHO, (lower left) $CH_3C(O)CH_3$ and (lower right) NH_3 at z = 100 mm out of the M2.25 N_2 106 K nozzle using the “Harmonic hessian” model (red) and “Harmonic hessian + 1 dihedral” model (blue) plotted against the [monomer] if there is no dimerisation. Curvature can be seen as a deviation from the $f_{monomer}$ = 1 level (black line), which represents the scenario if there is no dimerisation. 275

Figure 6.29 (Upper left) Temperature and number density profile within the M2.75 N_2 91 K nozzle from the sonic point to the nozzle exit. (Upper right) Mach number and flow speed profile within the M2.75 N_2 91 K nozzle from the sonic point to the nozzle exit. (Lower) Calculated k_{loss} for the monomers of (black) CH_2O, (red) CH_3CHO, (blue) $CH_3C(O)CH_3$ and (green) NH_3 within the M2.75 N_2 91 K nozzle from the sonic point to nozzle exit. “Harmonic hessian” model was used on the left while “Harmonic hessian + 1 dihedral” model was used on the right. 276

Figure 6.30 Calculated $f_{monomer}$ of (upper left) CH_2O, (upper right) CH_3CHO, (lower left) $CH_3C(O)CH_3$ and (lower right) NH_3 at z = 100 mm out of the M2.75 N_2 91 K nozzle using the “Harmonic hessian” model (red) and “Harmonic hessian + 1 dihedral” model (blue) plotted against the [monomer] if there is no dimerisation. Curvature can be seen as a deviation from the $f_{monomer}$ = 1 level (black line), which represents the scenario if there is no dimerisation. 277

Figure 6.31 (Upper left) Temperature and number density profile within the M3.3 N_2 85 K nozzle from the sonic point to the nozzle exit. (Upper right) Mach number and flow speed profile within the M3.3 N_2 85 K nozzle from the sonic point to the nozzle exit. (Lower) Calculated k_{loss} for the monomers of (black) CH_2O, (red) CH_3CHO, (blue) $CH_3C(O)CH_3$ and (green) NH_3 within the M3.3 N_2 85 K nozzle from the sonic point to nozzle exit. "Harmonic hessian" model was used on the left while "Harmonic hessian + 1 dihedral" model was used on the right. 278

Figure 6.32 Calculated $f_{monomer}$ of (upper left) CH_2O, (upper right) CH_3CHO, (lower left) $CH_3C(O)CH_3$ and (lower right) NH_3 at z = 100 mm out of the M3.3 N_2 85 K nozzle using the "Harmonic hessian" model (red) and "Harmonic hessian + 1 dihedral" model (blue) plotted against the [monomer] if there is no dimerisation. Curvature can be seen as a deviation from the $f_{monomer}$ = 1 level (black line), which represents the scenario if there is no dimerisation. 279

Figure 6.33 (Upper left) Temperature and number density profile within the M4 He 35 K nozzle from the sonic point to the nozzle exit. (Upper right) Mach number and flow speed profile within the M4 He 35 K nozzle from the sonic point to the nozzle exit. (Lower) Calculated k_{loss} for the monomers of (black) CH_2O, (red) CH_3CHO, (blue) $CH_3C(O)CH_3$ and (green) NH_3 within the M4 He 35 K nozzle from the sonic point to nozzle exit. "Harmonic hessian" model was used on the left while "Harmonic hessian + 1 dihedral" model was used on the right. 280

Figure 6.34 Calculated $f_{monomer}$ of (upper left) CH_2O, (upper right) CH_3CHO, (lower left) $CH_3C(O)CH_3$ and (lower right) NH_3 at z = 100 mm out of the M4 He 35 K nozzle using the "Harmonic hessian" model (red) and "Harmonic hessian + 1 dihedral" model (blue) plotted against the [monomer] if there is no dimerisation. Curvature can be seen as a deviation from the $f_{monomer}$ = 1 level (black line), which represents the scenario if there is no dimerisation. 281

Figure 6.35 Actual [monomer] present at z = 100 mm using the "Harmonic hessian" model (red) and "Harmonic hessian + 1 dihedral" model (blue) with 10 times (left) and 100 times (right) the original k_{loss} plotted against the [monomer] if there is no dimerisation. Apart from the calculated results, experimental data obtained at 40 K with He (green) and Ar (pink) as the bath gas are included as comparison. Curvature can be seen as a deviation from the $y = x$ black line, which represents the scenario if there is no dimerisation. 283

Figure 6.36 (Left) Calculated k_{loss} for the dimerisation reaction of CH_3CHO versus temperature in the range of T = 25–250 K with a total density of 10^{17} molecule cm^{-3} in Ar bath gas using the “Harmonic hessian + 1 dihedral” model when different number of dimer conformers are included in the MESMER calculations. Original: C_1 only; 3 conformers: the three lowest-energy conformers (C_1, C_2, C_i); 6 conformers: all the six conformers identified in this work (C_1, C_2, C_i, C_s, C_{2h} 1, C_{2h} 2). (Right) Ratio of k_{loss} using multiple number of conformers versus using only one conformer in the original model. 284

Figure 6.37 (Left) Calculated k_{loss} for the dimerisation reaction of CH_2O versus temperature in the range of T = 25–250 K with a total density of 10^{17} molecule cm^{-3} in Ar bath gas using the “Harmonic hessian + 1 dihedral” model when the relative energy of the dimer is artificially lowered. The legend denotes the amount of energy lowered in kJ mol^{-1}. (Right) Ratio of k_{loss} using the artificially lowered dimer energy value versus using the original energy value. 285

Figure 6.38 (Left) Calculated k_{loss} for the dimerisation reaction of CH_2O versus temperature in the range of T = 25–250 K with a total density of 10^{17} molecule cm^{-3} in Ar bath gas using the “Harmonic hessian + 1 dihedral” model when the frequency values of the dimer are artificially lowered by using a different scaling factor. The legend denotes the scaling factor used. (Right) Ratio of k_{loss} using the artificially lowered dimer frequency values versus using the original frequency values. 285

Figure 6.39 Evolution of the R vector defined as the vector between the centres-of-mass of the two reactants for the OH + CH_2O reaction. It can be seen that the two species are in “roaming state”, that is, they are trapped to rotate about each other. Taken from (167)... 287

Table of Tables

Table 1.1 Some major species detected in the atmosphere of Titan. Adapted from Cui et al. (3). 3

Table 1.2 Characteristics of different components in the interstellar medium. Adapted from Kwok (6). 5

Table 1.3 Selected molecular species identified in giant molecular clouds. Question marks denote unconfirmed detections. Taken from the Cologne Database for Molecular Spectroscopy (9). 6

Table 1.4 List of the radical-neutral reactions studied by our group at low temperature with the use of the Laval nozzle set-up...............34

Table 1.5 Possible precursors together with the required laser wavelength for the excitation λ used in selected previous studies for the generation of the required radicals in the Laval gas flow .35

Table 1.6 Characteristic excitation transition used in selected previous LIF studies for monitoring the concentration of the radicals........38

Table 2.1 Mean absolute deviation from the composite method in the calculated electronic energies of 11 glucose conformers at the HF level with different basis sets. Adapted from Cramer (1)..............66

Table 2.2 Mean absolute deviation from experiments in the calculated atomisation energies (energies required for the complete separation of all atoms in the species) of a collection of molecules and ions formed from elements in the first two rows at various levels of theory with different basis sets. Adapted from Feller and Peterson (29). 66

Table 2.3 Root mean square error compared to the CBS limit in the calculated electronic energies of the S22 set of noncovalent dimers and bimolecular complexes formed from C, N, O and H only at the B3LYP level with different basis sets. Adapted from Witte et al. (30)...67

Table 2.4 Mean absolute deviation from the full CI in the calculated electronic energies of HB, H_2O and HF at the equilibrium geometries using various methods. Adapted from Cramer (1). 69

Table 2.5 Mean absolute deviation from the W1 model in the calculated electronic energies of selected nonbonded complexes formed from elements in the first two rows at various levels of theory using the aug-cc-pVTZ basis set. Adapted from Zhao and Truhlar (35)........69

Table 2.6 Root mean square error in the calculated electronic energies of the MGCDB84 database consists of various atoms, molecules, dimers and clusters at different levels of theory. Adapted from Mardirossian and Head-Gordon (36). 69

Table 2.7 Mean absolute deviation from experiments in the calculated atomisation energies of a selected set of molecules consisting of C, N, O, F and H only at different levels of theory based on geometries optimised at different levels. Adapted from Martin (39). 71

Table 2.8 The scaling in computational cost for Hartree-Fock and post-SCF methods. Adapted from Cramer (1). 72

Table 2.9 Values of the Lennard-Jones parameters for different bath gases. Taken from Gilbert and Smith (51). 96

Table 2.10 Values used as the input parameters in MESMER for the calculations of $\Delta Edown$ between the intermediate with a given bath gas 96

Table 3.1 Barrier height for the reaction OH + $CH_2O \rightarrow HCO + H_2O$ reported in previous literature calculated at different levels of theory. Adapted from Machado et al. (28). 116

Table 3.2 Rate coefficients and experimental conditions for kinetic studies of the CN + CH_2O reaction with the Laval set-up by courtesy of Dr Niclas West and Mr Edward Rutter 132

Table 3.3 Rate coefficients of the CN + CH_2O reaction measured at room temperature and above reported in previous literature 133

Table 3.4 Fitting scenarios and optimised kinetic parameters from MESMER fitting 134

Table 3.5 Best-fitted parameters of the modified Arrhenius expression to the MESMER simulated overall rate coefficient 139

Table 4.1 Detected abundance of CH_3SH and CH_2S in selected interstellar objects 152

Table 4.2 Experimental rate coefficients of the OH + CH_3SH reaction reported in previous literature 154

Table 4.3 Parameters used to calculated $A\mathrm{ILT}\infty$ for the reaction between CN and CH_3SH 174

Table 4.4 Parameters used to calculated $A\mathrm{ILT}\infty$ for the reaction between CN and CH_2S 177

Table 5.1 Proposed H abstraction pathway for the NH_2 + CH_2O reaction and ZPVE corrected relative energies (kJ mol^{-1}) obtained at various levels by Li and Lü. Adapted from (26). 197

Table 5.2 Preliminary rate coefficients and experimental conditions for kinetic studies of the NH_2 + CH_3CHO reaction by courtesy of Dr Kevin Douglas 207

Table 5.3 The set of optimised Troe fit parameters for the MESMER calculated rate coefficients for the NH_2 + CH_3CHO reaction 222

Table 6.1 Properties of the nozzles used in the Laval experiments in our group provided by Dr Kevin Douglas 245

Table 6.2 ZPVE corrected relative energies (kJ mol^{-1}) of different structures of the CH_2O dimer 249

Table 6.3 ZPVE corrected relative energies (kJ mol^{-1}) of different structures of the CH_3CHO dimer 250

Table 6.4 ZPVE corrected relative energies (kJ mol^{-1}) of different structures of the $CH_3C(O)CH_3$ dimer 251

Table 6.5 Relative energies (kJ mol^{-1}) of different structures of the NH_3 dimer 252

Table 6.6 Rotational constants and vibrational frequencies of the species included in the MESMER calculations obtained at the BHandHLYP/aug-cc-pVDZ level of theory 253

List of abbreviations

AGB	Asymptotic giant branch
ALMA	Atacama Large Millimetre/submillimetre Array
ARC	Advanced Research Computing
ASI	Italian Space Agency
aug-cc-pVDZ	Augmented Dunning's correlation-consistent polarised valence double-zeta basis sets
aug-cc-pVTZ	Augmented Dunning's correlation-consistent polarised valence triple-zeta basis sets
B3LYP	Becke 3-parameter Lee-Yang-Parr
BHandHLYP	Becke half-and-half Lee-Yang-Parr
CBS	Complete basis set
CCSD(T)	Coupled-cluster including single and double excitations and perturbative treatment of triple excitations
CI	Configuration interaction
COM	Complex organic molecule
CRESU	Cinétique de Réaction de Ecoulement Supersonique Uniforme
DFT	Density functional theory
DNA	Deoxyribonucleic acid
DOS	Density of states
EGME	Energy grained master equation
ESA	European Space Agency
FID	Free induction decay
GGA	Generalised gradient approximation
GTO	Gaussian-type orbital
HF	Hartree-Fock
ILT	Inverse Laplacian transformation
IRC	Intrinsic reaction coordinates

ISM	Interstellar medium
KIDA	Kinetic Database for Astrochemistry
LDA	Local density approximation
LFP	Laser flash photolysis
LIF	Laser-induced fluorescence spectroscopy
M06	Minnesota 06 functional
MEP	Minimum energy path
MESMER	Master Equation Solver for Multi Energy well Reactions
mGGA	Meta-generalised gradient approximation
MP	Møller-Plesset
NASA	National Aeronautics and Space Administration
PES	Potential energy surface
PMT	Photomultiplier tube
PPCC	Particle per cubic centimetre
QMS	Quadrupole mass spectrometry
RNA	Ribonucleic acid
RRKM	Rice-Ramsperger-Kassel-Marcus
SCF	Self-consistent field
STO	Slater-type orbital
TOF-MS	Time-of-flight mass spectrometry
TST	Transition state theory
VDW	Van der Waals
VOC	Volatile organic compound
VTST	Variational transition state theory
WKB	Wentzel-Kramers-Brillouin
ZPVE	Zero-point vibrational energy

Chapter 1

Introduction

The study of chemistry essentially involves the understanding of how reactions take place. Quantitatively determining the rates of reactions and explaining the underlying mechanisms is covered in the field of chemical kinetics and dynamics. The category of interest in this thesis is gas-phase neutral-neutral reactions where their behaviour under low temperature conditions is the focus. In this chapter, some relevant examples of cold environments will be first introduced to illustrate the potential applications of this work. Theories of basic chemical kinetics will then be included to set the scene for later discussions. The motivation of the kinetics study of gas-phase neutral-neutral reactions under low temperature conditions follows next, together with a brief introduction of the Laval nozzle experiment, which is the main set-up used by our group in the School of Chemistry at the University of Leeds for the measurements of rate coefficients at low temperature. Finally, there will be an overview of the rest of the thesis, which demonstrates the use of the theoretical approaches in the study of the low temperature kinetics of various gas-phase neutral-neutral reaction systems.

1.1 Low temperature environments

While we normally reside on the Earth's surface and experience an ambient temperature, low temperature environments are not rare in the universe. These cold systems in nature can be as close as just tens of kilometres above where we are usually located at, or as far as millions of lightyears away from us.

1.1.1 Atmospheres of planets and moons

The first example of a low temperature environment to be introduced is our Earth's atmosphere. Its temperature variation with altitude is shown in Figure 1.1 and based on such variation it can be divided into four regions (1, 2). The lowermost region is the troposphere where the temperature decreases rapidly with an increasing altitude up to the tropopause located at ~15 km above the Earth's surface with the temperature at ~220 K. The uppermost region is the thermosphere where the temperature increases with altitude. In between there is the mesosphere where the temperature decreases with altitude but more slowly than that observed in the troposphere. Between the troposphere and the mesosphere, it is also distinctive for the Earth's atmosphere to have the stratosphere at ~15–50 km above the Earth's surface. The special feature for the stratosphere is that it is where the ozone O_3 layer is situated at, with a rising temperature as the altitude increases.

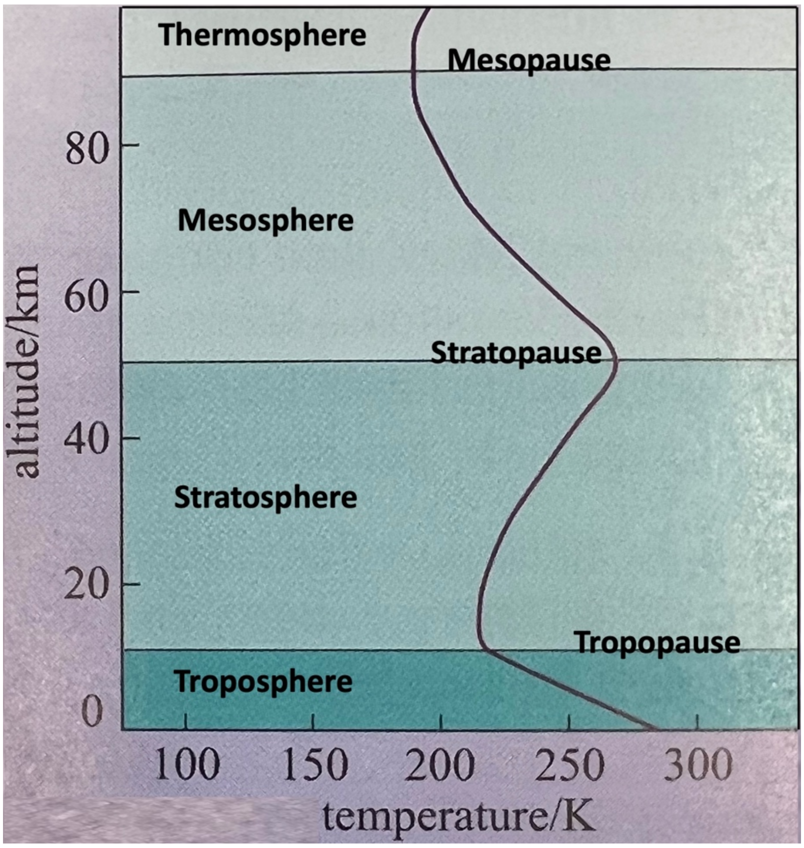

Figure 1.1 The temperature variation with altitude for the Earth's atmosphere. Adapted from Rothery et al. (1).

Considering the chemistry in the lower atmosphere, the OH radical plays a notably important role (2). The sources of atmospheric OH radicals are mainly from the reaction of water vapour with excited oxygen atoms $O(^1D)$ generated from the photolysis of ozone. The reaction of OH radical with CO and O_2 forms

HO_2 in the HOx cycle in the atmosphere. At the same time, the removal of OH radical can be done via reaction with volatile organic compounds (VOCs), a class of air pollutants, where the OH radical performs the function of a scavenger to help clean the air.

Table 1.1 Some major species detected in the atmosphere of Titan. Adapted from Cui et al. (3).

Species	**Chemical formula**
Nitrogen	N_2
Methane	CH_4
Hydrogen	H_2
Argon	Ar
Acetylene	C_2H_2
Ethylene	C_2H_4
Ethane	C_2H_6
Methylacetylene	CH_3C_2H
Propane	C_3H_8
Diacetylene	C_4H_2
Benzene	C_6H_6
Cyanoacetylene	HC_3N
Acetonitrile	CH_3CN
Cyanogen	C_2N_2
Ammonia	NH_3
Carbon dioxide	CO_2

Another noteworthy example of a low temperature environment is the atmosphere of Titan, the largest satellite of Saturn. It has a dense atmosphere which is predominantly composed of molecular nitrogen N_2 and is predicted to consist of four distinct regions (1, 3). These characteristics match the observations of our Earth today as well as the predictions of the prebiotic Earth, which makes Titan a popular study target in the research field. More information about Titan was obtained after the Cassini-Huygens mission jointly led by NASA, ESA and ASI (4), which involved the landing of the Huygens probe onto Titan's surface. It was found that the surface temperature of Titan is about 94 K and the atmospheric pressure on the surface is about 1.5 atm (1). Lakes composed of liquid hydrocarbons have been discovered on Titan's surface. While the most abundant species in Titan's atmosphere is N_2, the second most abundant is methane CH_4, which makes up of several percent in the composition of the atmosphere, and the third is molecular hydrogen H_2, which contributes several tenths of percent (1, 3). The remainder (<1%) is mainly composed of various hydrocarbons and nitrogen-bearing species as shown in Table 1.1. The interactions among these species, which can possibly lead to more complex organic compounds, formulate the diverse chemistry in this cold and rather dense environment.

1.1.2 Interstellar medium

The interstellar medium (ISM) refers to the space between stars. The sparsest regions can have number densities in the order of 10^{-3} molecule cm^{-3}, which is much less dense than the best vacuum attained on Earth, while the most dense regions can have densities up to 10^{6} molecule cm^{-3} (5-7). The interstellar medium also has a wide variety of temperature conditions, ranging from the order of 10 K to 10^{6} K (5-7). Such diverse conditions allow the existence of all states of matter and the presence of interstellar matter can be verified through its blocking, or extinction, of starlight (5, 6). The characteristics of different phases of components in the interstellar medium are presented in Table 1.2.

To discuss about the origin of this interstellar matter, it is necessary to briefly introduce the life cycle of stars. A star spends mostly of its lifetime shining as a main-sequence star, where its energy mainly comes from thermonuclear burning. Approaching the end of its lifetime, it runs out of hydrogen fuel to support the fusion process. The core shrinks while the outer layer expands and it gradually becomes an asymptotic giant branch (AGB) star. Although the subsequent series of events differ for stars of different masses, in general the core collapses under gravity and the outer gaseous shells drift away as planetary nebulae or supernova remnants (5-8). The ejected materials, which are composed of helium and other heavy elements generated from stellar nucleosynthesis, chemically enrich the interstellar medium (5-7). On the other hand, star formation can often be found at molecular hot cores with the interstellar matter acting as a source of materials for the protostars.

Table 1.2 Characteristics of different components in the interstellar medium. Adapted from Kwok (6).

Component	Typical T (K)	Typical density (molecule cm^{-3})	Ionisation fraction
Hot ionised medium	10^6	0.003	1
Warm ionised medium	10^4	>10	1
Warm neutral medium	8×10^3–10^4	0.1	0.1
Atomic cold neutral medium (diffuse clouds)	100	10–100	~10^{-3}
Molecular cold neutral medium (molecular clouds)	0–50	10^3–10^5	10^{-7}–10^{-8}
Molecular hot cores	100–300	>10^6	≤10^{-8}

The interstellar medium is dominated by the two lightest elements, H and He, but other species containing heavier elements can also be observed. Roughly 99% of the mass of the interstellar medium comes from gaseous species while around 1% is contributed by dust typically composed of elements like C, Si, Fe and O (5-7). Until now, about 270 molecular species have been detected in the molecular clouds (9), which are located at the colder regions of outer space. As shown in Table 1.3, polyatomic molecules are not rare to be detected in the interstellar medium.

Table 1.3 Selected molecular species identified in giant molecular clouds. Question marks denote unconfirmed detections. Taken from the Cologne Database for Molecular Spectroscopy (9).

Diatomic molecules	H_2, AlF, AlCl, AlO, C_2, CH, CH^+, CN, CN^-, CO, CO^+, CF^+, CP, CS, HCl, HCl^+, KCl, NH, NO, NO^+?, NS, NS^+, N_2, NaCl, OH, OH^+, O_2, PN, PO, PO^+, SO, SO^+, SH, SH^+, SiC, SiN, SiO, SiS, SiH?, HF, HD, FeO?, TiO, ArH^+, HeH^+
Triatomic molecules	C_3, C_2H, CO_2, C_2O, C_2S, CH_2, C_2N, H_3^+, HCN, HCO, HCO^+, HOC^+, HCS, HCS^+, HSC, H_2O, H_2O^+, HO_2, H_2Cl^+, H_2S, HS_2, HNC, HNO, HCP, CCP, MgCN, MgNC, NH_2, N_2H^+, N_2O, NCO, NCS, NaCN, OCS, SO_2, *c*-SiC_2, SiCN, SiNC, Si_2C, AlNC, AlOH, KCN, FeCN, CaNC, TiO_2
4-atom molecules	CH_3, *c*-C_3H, *l*-C_3H, C_3H^+, C_3N, C_3N^-, C_3O, C_3S, C_2H_2, CNCN, HCCN, $HCNH^+$, HNCO, HNCS, $HOCO^+$, H_2CO, H_2CN, H_2CS, H_3O^+, HCNO, HOCN, HSCN, H_2O_2, HCCO, HCCS, HONO, HNCN, H_2NC, $HCCS^+$, NH_3, PH_3, *c*-SiC_3, HMgNC, MgC_2H
5-atom molecules	C_5, C_4H, C_4Si, C_4S, *c*-C_3H_2, *l*-C_3H_2, CH_2CN, CH_4, C_4H^-, CH_3O, CH_3Cl, HC_3N, HC_2NC, HCOOH, H_2CHN, H_2C_2O, H_2C_2S, H_2NCN, HNC_3, H_2COH^+, HC_3O^+, HC_3S^+, HC(O)CN, HNCNH, H_2NCO^+, HC(S)CN, HC(O)SH, HCCCO, SiH_4, NH_4^+, $NCCNH^+$, NH_2OH, MgC_3N
6-atom molecules	C_5H, C_5H^+, C_5N, C_5N^-, C_5O, C_5S, C_2H_4, C_3H_3, *c*-C_3C_2H, CH_3CN, CH_3NC, CH_3OH, CH_3SH, CH_3CO^+, HC_3NH^+, $HCCNCH^+$, HCCCHO, NH_2CHO, *l*-H_2C_4, *l*-HC_4H, *l*-HC_4N, *c*-H_2C_3O, H_2C_3S, HCCCHS, H_2CCNH, HNCHCN, SiH_3CN, MgC_4H
7-atom molecules	C_6H, C_6H^-, CH_2CHCN, CH_3C_2H, *c*-C_3HCCH, *l*-H_2C_5, CH_2CHOH, CH_3CHO, CH_3NH_2, *c*-C_2H_4O, CH_3NCO, HC_5N, HC_5O, HC_4NC, $HOCH_2CN$, HCCCHNH, CH_2C_3N, MgC_5N
8-atom molecules	C_6H_2, C_7H, *l*-HC_6H, CH_3C_3N, CH_2CHCCH, $HC(O)OCH_3$, CH_3COOH, CH_2OHCHO, CH_2CHCHO, $(CHOH)_2$, CH_2CCHCN, H_2NCH_2CN, CH_3CHNH, $H_2NC(O)NH_2$, $HCCCH_2CN$, $C_2H_3NH_2$, HC_5NH^+, CH_3SiH_3, MgC_6H

9-atom molecules	C_8H, C_8H^-, C_3H_6, CH_3C_4H, $H_2CCCHCCH$, CH_3CH_2CN, $HCCCHCHCN$, H_2CCHC_3N, $(CH_3)_2O$, CH_3CH_2OH, $HOCHCHCHO$?, HC_7N, HC_7O, $CH_3C(O)NH_2$, CH_3NHCHO, CH_3CH_2SH
10-atom molecules	$c\text{-}C_6H_4$, CH_3C_5N, H_2CCCHC_3N, $CH_3CHCHCN$, $CH_3C(CN)CH_2$, CH_2CHCH_2CN, $(CH_3)_2CO$, $(CH_2OH)_2$, CH_3CH_2CHO, CH_3CHCH_2O, CH_3OCH_2OH, C_2H_5NCO, $C_2H_5NH_2$?, HC_7NH^+
11-atom molecules	$c\text{-}C_5H_6$, H_2CCCHC_4H, CH_3C_6H, HC_9N, C_2H_5OCHO, $CH_3OC(O)CH_3$, $CH_3C(O)CH_2OH$, $HOCH_2CH_2NH_2$
12-atom molecules	$c\text{-}C_6H_6$, $n\text{-}C_3H_7CN$, $i\text{-}C_3H_7CN$, $1\text{-}c\text{-}C_5H_5CN$, $2\text{-}c\text{-}C_5H_5CN$, CH_3C_7N?, $C_2H_5OCH_3$, $n\text{-}C_3H_7OH$, $i\text{-}C_3H_7OH$
>12-atom molecules	$HC_{11}N$, $c\text{-}C_6H_5CN$, $1\text{-}c\text{-}C_5H_5CCH$, $2\text{-}c\text{-}C_5H_5CCH$, $c\text{-}C_5H_4CCH_2$, $c\text{-}C_9H_8$, $1\text{-}C_{10}H_7CN$, $2\text{-}C_{10}H_7CN$, C_{60}, C_{60}^+, C_{70}

Spectroscopy is a useful technique to distinguish the species observed in the interstellar medium. Some common types of spectroscopies used in the laboratories to characterise different species include electronic spectroscopy, vibrational spectroscopy and rotational spectroscopy. These can also be used during astronomical observations, but the redshift of the spectral lines due to the Doppler effect and the expansion of the universe has to be considered for distant objects (5-7). Apart from the visible light range, there is another optical window in the radio wave range for the Earth's atmosphere where the electromagnetic radiation in this region can pass through the atmosphere without much absorption. Therefore, ground-based radio telescopes have played a significant role in astronomical observation. For example, recently the first detection of the aromatic molecule benzonitrile C_6H_5CN in the interstellar medium has been made (10) with the use of the Green Bank radio telescope in the United States (11). There has also been developments in the observational astronomy at other wavelengths. A relevant example is the Atacama Large Millimetre/submillimetre Array (ALMA) in Chile (12), which is capable of measuring signals from 0.32 mm to 8.6 mm, covering from far-infrared to radio wave region. Figure 1.2 shows an example of a spectrum obtained with the use of the ALMA telescope. The observation was targeted at the region where the

AGB star CW Leonis is located at and from the spectral lines, SiC_2, SiS, AlF and CO are suggested to be present in the ejected materials (8).

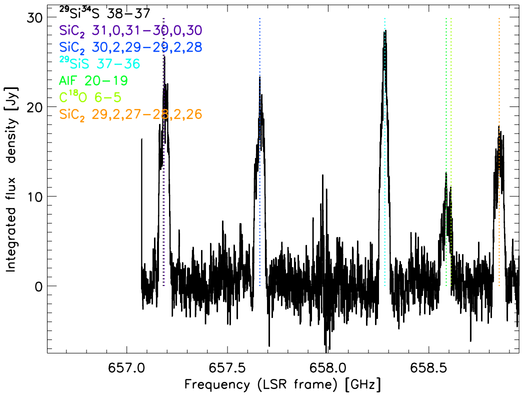

Figure 1.2 A spectrum obtained with the use of the ALMA telescope by pointing towards the AGB star CW Leonis. Spectral features of SiC_2, SiS, AlF and CO can be identified. Taken from Decin et al. (8).

1.2 Theories of chemical kinetics

1.2.1 The rate equation

Chemical kinetics is a study concerning changes over time, or known as rates, of chemical reactions (13-15). For a chemical reaction

$$a\mathrm{A} + b\mathrm{B} \rightarrow c\mathrm{C} + d\mathrm{D} \qquad \text{R 1.1}$$

where *a* moles of reactant A react with *b* moles of reactant B giving *c* moles of product C and *d* moles of product D, the reaction rate *r* can be defined as the consumption rate of the reactants:

$$r = -\frac{1}{a}\frac{d[\mathrm{A}]}{dt} = -\frac{1}{b}\frac{d[\mathrm{B}]}{dt} \qquad \text{E 1.1}$$

or as the formation rate of the products:

$$r = \frac{1}{c}\frac{d[\mathrm{C}]}{dt} = \frac{1}{d}\frac{d[\mathrm{D}]}{dt} \qquad \text{E 1.2}$$

where $[\mathrm{X}]$ is the concentration of species X. In general, a rate law, which expresses the reaction rate as a function of the concentrations with the introduction of rate coefficient *k*, can be written as follows:

$$r = k[\mathrm{A}]^{\alpha}[\mathrm{B}]^{\beta} \tag{E 1.3}$$

where α and β are the orders of the reaction with respect to species A and B which are obtained from experiments. The sum of α and β is the overall order of the reaction.

Another concept relevant to elementary reaction is molecularity, which refers to the number of reactants involved in an elementary reaction step. In this thesis, the types of reactions mainly to be dealt with are unimolecular reactions

$$\mathrm{A} \rightarrow \mathrm{products} \tag{R 1.2}$$

and bimolecular reactions

$$\mathrm{A} + \mathrm{B} \rightarrow \mathrm{products} \tag{R 1.3}$$

The respective rate equations with respect to the concentration of species A will then be (13-15):

$$\frac{d[\mathrm{A}]}{dt} = -k_{\mathrm{uni}}[\mathrm{A}] \tag{E 1.4}$$

$$\frac{d[\mathrm{A}]}{dt} = -k_{\mathrm{bim}}[\mathrm{A}][\mathrm{B}] \tag{E 1.5}$$

For the case of unimolecular (first-order) reactions, the integrated form of E 1.4 gives the following:

$$[\mathrm{A}] = [\mathrm{A}]_0 e^{-k_{\mathrm{uni}} t} \tag{E 1.6}$$

where $[\mathrm{A}]_0$ is the initial concentration of species A. With this form, the rate coefficient can then be obtained by tracing properties that are relative to $[\mathrm{A}]$ at different time *t*. For the case of bimolecular reactions, this integration cannot be done when species A and B are different with $[\mathrm{B}]$ also varying with *t*. However, if species A is the limiting reactant while species B is the excess reactant with $[\mathrm{B}]$ staying almost constant throughout the reaction, then the reaction can be considered as a pseudo-first order reaction, represented by:

$$[\mathrm{A}] = [\mathrm{A}]_0 e^{-k' t} \tag{E 1.7}$$

where $k' = k_{\mathrm{bim}}[\mathrm{B}]$.

1.2.2 The temperature dependence of rate coefficients – the Arrhenius equation and non-Arrhenius behaviour

Experimentally, the rate coefficient *k* is found to be strongly dependent on temperature *T*. In 1889, Svante Arrhenius, based on a wide range of reactions, summarised the experimental observations into a relationship, now famously known as the Arrhenius equation (16):

$$k = Ae^{-\frac{E_a}{RT}} \qquad \text{E 1.8}$$

where *A* is the pre-exponential factor, E_a is the activation energy and *R* is the universal gas constant. Taking natural logarithms of both sides and rearranging the terms gives:

$$\ln k = -\frac{E_a}{R}\frac{1}{T} + \ln A \qquad \text{E 1.9}$$

and so for reactions following the Arrhenius relationship, plotting ln *k* against 1/*T* results in a straight line as shown in Figure 1.3.

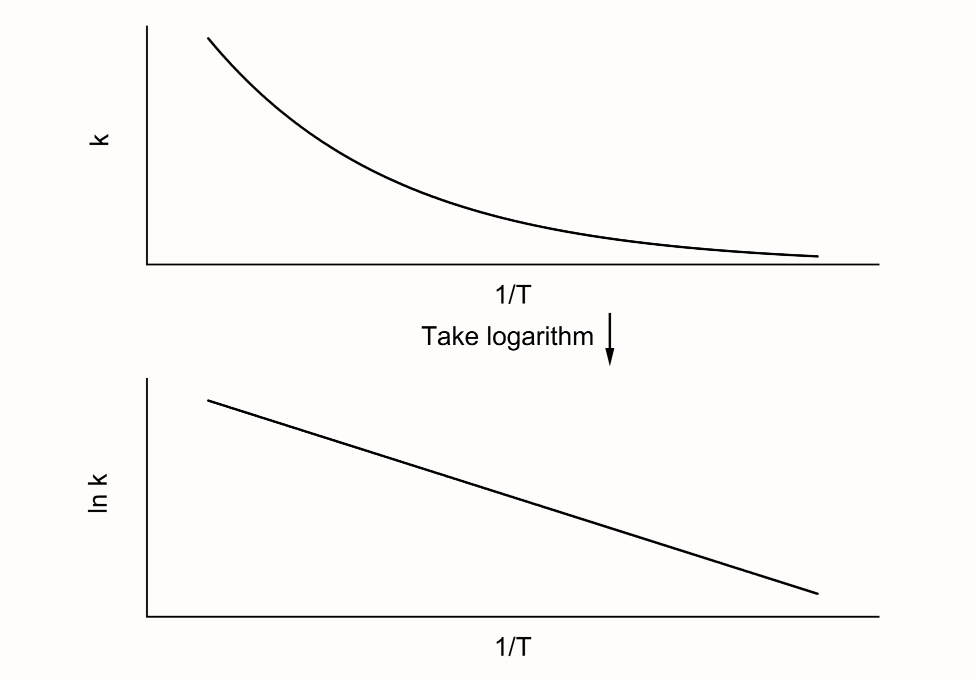

Figure 1.3 (Upper) The temperature dependence of the rate coefficients following the Arrhenius equation. (Lower) A linear plot is obtained by taking logarithm on both sides of the Arrhenius equation.

An important quantity to note here is E_a. Taken as a positive value, E_a can be treated as the amount of energy required for the reactants to initiate the reaction (13-17). A schematic energy profile for such reaction is shown in Figure 1.4. As temperature is a measure of the average kinetic energy, at higher temperature, more reagents possess enough energy to overcome the positive barrier and react to give the products, leading to an increase in the reaction rate.

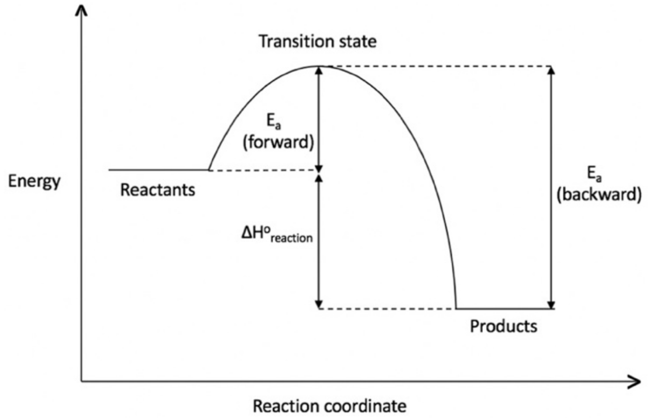

Figure 1.4 A schematic reaction profile with a positive energy barrier E_a. $\Delta H^{\circ}_{\text{reaction}}$ denotes the enthalpy change of the reaction.

Although the Arrhenius equation helps explain the temperature dependence of *k* for many reactions, exceptions are not uncommon (13-15, 18). One of the causes for the deviation from the Arrhenius equation is due to the pre-exponential factor *A*. Instead of being merely just a constant, *A* actually depends on the temperature, where a further breakdown of *A* will be covered in later discussions. Another potential cause for such deviation is the occurrence of quantum mechanical tunnelling. Considering from a classical point of view, the reacting species have to possess enough energy to surmount the barrier to form the products. However, according to the theory of quantum mechanics, a particle, described by its wavefunction ψ, can penetrate into the classically forbidden region. Given a narrow enough barrier along the reaction coordinate, the transmission from the reactants to the products is possible even when the energy of the reactants is below that of the barrier. This makes the actual reaction rate faster than that predicted from the Arrhenius equation, particularly at lower temperature where fewer reactants have enough energy to surmount the barrier.

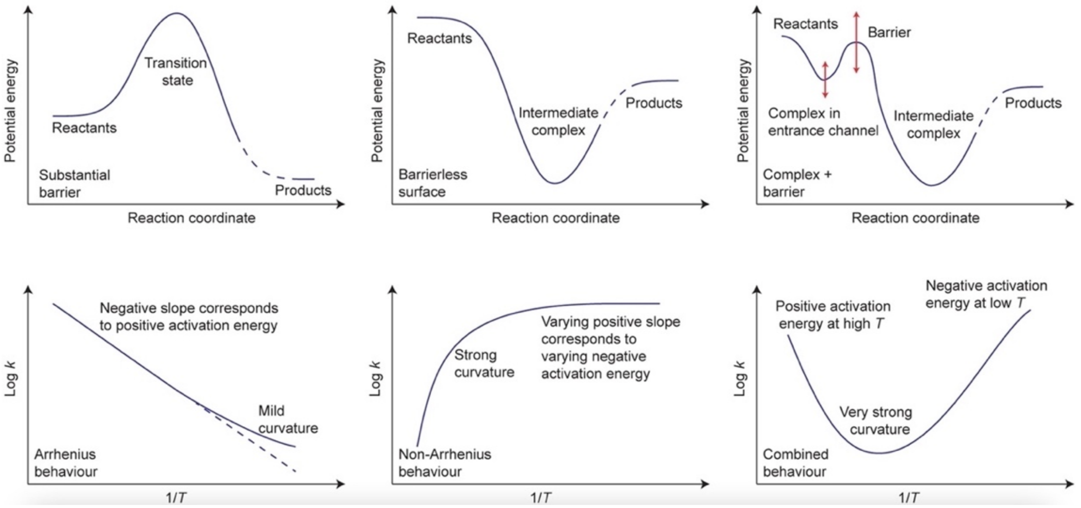

Figure 1.5 The top row shows the energy profiles while the bottom row shows the corresponding temperature dependence of three different types of exothermic reactions. The left column shows a reaction with a noticeable barrier, the middle column shows a barrierless reaction while the right column shows a reaction initially forming a weakly bound complex followed by a barrier. Taken from Sims (19).

Another reason leading to the observation of non-Arrhenius behaviour lies fundamentally on the fact that the reaction involved cannot be represented by simply surmounting a positive energy barrier. Ian Sims (19) summarised three types of exothermic reactions, as presented in Figure 1.5. The left column of Figure 1.5 shows a similar energy profile as Figure 1.4, where the temperature dependence of the reaction rate coefficient in general follows the Arrhenius behaviour, except the mild curvature at the low temperature range possibly due to the aforementioned tunnelling effect. The middle column of Figure 1.5 shows a barrierless reaction, where the potential curve falls into a deep well right after the entry of the channel without surmounting any barrier. Such a potential well can be observed when the attractive long-range forces between the reactants dominate during the reaction and these attractive interactions contributed from the London dispersion forces follow the $\frac{1}{r^6}$ relationship (14, 19, 20), where r is the separation between the two species. These reactions instead show a negative temperature dependence and possible examples include ion-molecule reactions like $CH_4 + O_2^+$ (20), radical-radical reactions like CN + O_2 (21-23) and the recombination of iodine atoms I through forming a complex IM with a third body M (14). The right column of Figure 1.5 shows a reaction with a more complicated energy profile. The reaction path starts off with the formation of a loosely bound complex, also known as the van der Waals complex or entrance channel complex, followed by a barrier which can be of higher energy than the reactants, or lower, where in such a case it is known as a submerged barrier. The resultant temperature dependence will be a combination of the two aforementioned cases. In the high-temperature regime, the temperature dependence is controlled by the barrier while in the low-temperature regime, an inverse temperature dependence is observed as the rate determining step becomes the initial complex formation step (19), where possible examples include CN + C_2H_6 (24, 25) and OH + CH_3OH (26-30).

1.2.3 The pressure dependence of rate coefficients – the Lindemann mechanism

Apart from displaying a temperature dependence, it is also possible for the rate coefficients of some reactions to demonstrate a pressure dependence. Frederick Lindemann (31) proposed the following mechanism, which was initially in an attempt to explain the pressure dependence observed for the unimolecular dissociation reaction, instead of just one single step as represented in R 1.2

$$\mathrm{A} + \mathrm{M} \underset{k_{-1}}{\overset{k_1}{\rightleftharpoons}} \mathrm{A}^* + \mathrm{M} \qquad \text{R 1.4}$$

$$\mathrm{A}^* \xrightarrow{k_2} \mathrm{products} \qquad \text{R 1.5}$$

The reacting molecule A is excited to form the energised molecule A^* through the collision with another molecule M that exists in the system, which can be another A molecule or a bath gas molecule. A^* can either be deactivated by collision with M or react to form the products. As A^* is a transient species, by applying the steady-state approximation:

$$\frac{d[\mathrm{A}^*]}{dt} = k_1[\mathrm{A}][\mathrm{M}] - k_{-1}[\mathrm{A}^*][\mathrm{M}] - k_2[\mathrm{A}^*] = 0 \qquad \text{E 1.10}$$

$$[\mathrm{A}^*] = \frac{k_1[\mathrm{A}][\mathrm{M}]}{k_{-1}[\mathrm{M}]+k_2} \qquad \text{E 1.11}$$

The overall unimolecular rate coefficient k_{uni} for the reaction is given by:

$$\frac{d[\mathrm{products}]}{dt} = k_{\mathrm{uni}}[\mathrm{A}] = k_2[\mathrm{A}^*] \qquad \text{E 1.12}$$

$$k_{\mathrm{uni}} = \frac{k_1 k_2[\mathrm{M}]}{k_{-1}[\mathrm{M}]+k_2} \qquad \text{E 1.13}$$

which is dependent on the pressure, or the total number density. At the high pressure limit k_∞, $k_{-1}[\mathrm{M}] \gg k_2$, so:

$$k_\infty \approx \frac{k_1 k_2[\mathrm{M}]}{k_{-1}[\mathrm{M}]} = \frac{k_1 k_2}{k_{-1}} \qquad \text{E 1.14}$$

which is pressure independent, while at the low pressure limit k_0, $k_{-1}[\mathrm{M}] \ll k_2$, thus:

$$k_0 \approx \frac{k_1 k_2[\mathrm{M}]}{k_2} = k_1[\mathrm{M}] \qquad \text{E 1.15}$$

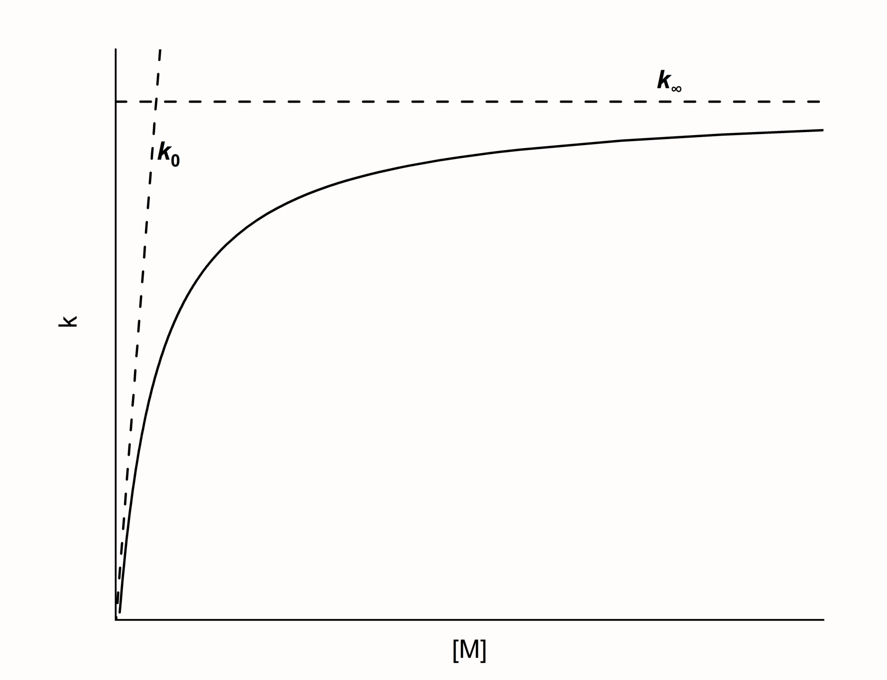

Figure 1.6 The pressure dependence of the rate coefficients described by the Lindemann mechanism.

E 1.13 can then be rewritten as the following:

$$k_{\mathrm{uni}} = \frac{\frac{k_1}{k_{-1}} k_1 k_2 [\mathrm{M}]}{k_1[\mathrm{M}] + \frac{k_1 k_2}{k_{-1}}} = \frac{k_\infty k_1 [\mathrm{M}]}{k_1[\mathrm{M}] + k_\infty} = \frac{k_\infty}{1 + \frac{k_\infty}{k_1[\mathrm{M}]}} \qquad \text{E 1.16}$$

where plots of the overall rate coefficients against $[\mathrm{M}]$ similar to that in Figure 1.6 can then be drawn. At high $[\mathrm{M}]$, k approaches k_∞, while at low $[\mathrm{M}]$, k approaches k_0, with the curvature in between known as the fall-off region.

Similarly, the Lindemann mechanism can be adapted for the bimolecular association reaction, which can be considered as the reverse process of the unimolecular dissociation, as the following

$$\mathrm{A} + \mathrm{B} \underset{k_2}{\overset{k_{-2}}{\rightleftharpoons}} \mathrm{AB}^* \qquad \text{R 1.6}$$

$$\mathrm{AB}^* + \mathrm{M} \xrightarrow{k_{-1}} \mathrm{AB} + \mathrm{M} \qquad \text{R 1.7}$$

Again using the steady-state approximation:

$$\frac{d[\mathrm{AB}^*]}{dt} = k_{-2}[\mathrm{A}][\mathrm{B}] - k_2[\mathrm{AB}^*] - k_{-1}[\mathrm{AB}^*][\mathrm{M}] = 0 \qquad \text{E 1.17}$$

$$[\mathrm{AB}^*] = \frac{k_{-2}[\mathrm{A}][\mathrm{B}]}{k_2 + k_{-1}[\mathrm{M}]} \qquad \text{E 1.18}$$

The overall bimolecular rate coefficient k_{bim} for the reaction is given by:

$$\frac{d[\mathrm{AB}]}{dt} = k_{\mathrm{bim}}[\mathrm{A}][\mathrm{B}] = k_{-1}[\mathrm{AB}^*][\mathrm{M}] \qquad \text{E 1.19}$$

$$k_{\mathrm{bim}} = \frac{k_{-2} k_{-1}[\mathrm{M}]}{k_2 + k_{-1}[\mathrm{M}]} \qquad \text{E 1.20}$$

At the high pressure limit k_∞, $k_{-1}[\mathrm{M}] \gg k_2$, so:

$$k_\infty \approx \frac{k_{-2} k_{-1}[\mathrm{M}]}{k_{-1}[\mathrm{M}]} = k_{-2} \qquad \text{E 1.21}$$

while at the low pressure limit k_0, $k_{-1}[\mathrm{M}] \ll k_2$, thus:

$$k_0 \approx \frac{k_{-2} k_{-1}[\mathrm{M}]}{k_2} \qquad \text{E 1.22}$$

1.2.4 Collision theory, capture theory, and trajectory calculations

Collision theory is one of the theoretical methods to examine the reaction rate simply by taking the assumption that the molecules are hard spheres (13-15, 32, 33). This means the reacting species are not penetrable and they can only interact when they are in contact. Consider again the reactants A and B, the rate for the reaction between them depends on their collision frequency and the probability that a collision can lead to a reaction.

The collision frequency depends on the relative collision velocity, the contact area and the number of molecules of the respective reactants per unit volume (13-15, 32, 33). For species possessing a Maxwell-Boltzmann distribution of velocities, the mean relative collision velocity v is given by:

$$v = \sqrt{\frac{8k_BT}{\pi\mu}} \qquad \text{E 1.23}$$

where k_B is the Boltzmann constant, T is the temperature and μ is the reduced mass of molecules A and B. For a collision to occur, the centres of the two molecules have to be within an area known as the collision cross section σ, which is given by:

$$\sigma = \pi b_{\mathrm{max}}^2 \qquad \text{E 1.24}$$

where b_{max} is the maximum impact parameter, or in other words the initial perpendicular separation of the paths of the two colliding bodies, that can result in a collision. Under the rigid sphere assumption, b_{max} is the sum of the radii of molecules A and B ($r_{\mathrm{A}} + r_{\mathrm{B}}$). For collisions that can succeed to form products, the colliding species have to possess enough energy along their line of centres to surmount the activation barrier E_a. Therefore, the probability for a collision that can result in a reaction depends on the fraction of molecules possessing energy greater that E_a, which is $e^{-\frac{E_a}{RT}}$. Combining these factors, the rate coefficient is then given by (13-15, 32, 33):

$$k = \sqrt{\frac{8k_BT}{\pi\mu}}\pi(r_{\mathrm{A}} + r_{\mathrm{B}})^2 e^{-\frac{E_a}{RT}} \qquad \text{E 1.25}$$

where apart from $e^{-\frac{E_a}{RT}}$, the $\sqrt{\frac{8k_BT}{\pi\mu}}$ part also depends on the temperature. However, the predicted values from the simple collision theory are of limited accuracy because it neglects the intermolecular forces between the molecules and whether the molecules are in the proper orientation for reactions to occur. Thus, to correct for the differences between the predicted and experimental values, typically the steric factor is ρ also introduced into the expression (13-15).

On the other hand, for barrierless processes, capture theory is a better predictive tool instead as the reaction is dominated by the long-range attractive forces rather than having a barrier. The initial model attempted to describe the case of ion-molecule reactions (34-36), which involves the use of an interaction potential V to represent the long-range attractive forces:

$$V_r = \sum_n -\frac{C_n}{r^n} \qquad \text{E 1.26}$$

where the coefficient C_n and the exponential n depend on the nature of the intermolecular forces present with r being the intermolecular separation. Apart from the radial component, if the encounter between the two reacting species is not head-on, then the angular component is also important. By including the following potential to account for the relative orbital motion:

$$V = \frac{L^2}{2\mu r^2} \qquad \text{E 1.27}$$

where μ is the reduced mass and L is the angular momentum given by:

$$L = \mu v b \qquad \text{E 1.28}$$

where v is the relative velocity and b is the impact parameter, the effective potential of the pathway becomes (34-36):

$$V_{\text{eff}} = \frac{L^2}{2\mu r^2} - \sum_n \frac{C_n}{r^n} = \frac{1}{2}\mu v^2\left(\frac{b^2}{r^2}\right) - \sum_n \frac{C_n}{r^n} = \frac{Eb^2}{r^2} - \sum_n \frac{C_n}{r^n} \qquad \text{E 1.29}$$

where E is the collision energy. While the latter terms in the effective potential are attractive, the first term is repulsive, resulting in a small centrifugal barrier as shown in Figure 1.7. Assuming that the reaction will occur if and only if the collision energy is equal to or greater than the maximum in the effective potential, the rate coefficient can be determined by an integration of the reaction cross section, given by E 1.24 using b_{max}, over the velocities (34-36). b_{max} is defined as such that the collision energy is equal to the maximum in the effective potential, so it can be solved using E 1.29 after locating the corresponding r for the maximum in the effective potential via a differentiation of E 1.29. The accuracy of the capture theory lies largely on the evaluation of the potential contributed from different intermolecular forces $-\frac{C_n}{r^n}$, and for the adaptation to neutral-neutral reactions, different models (36-38) have been reported to accommodate the different nature of the intermolecular forces involved.

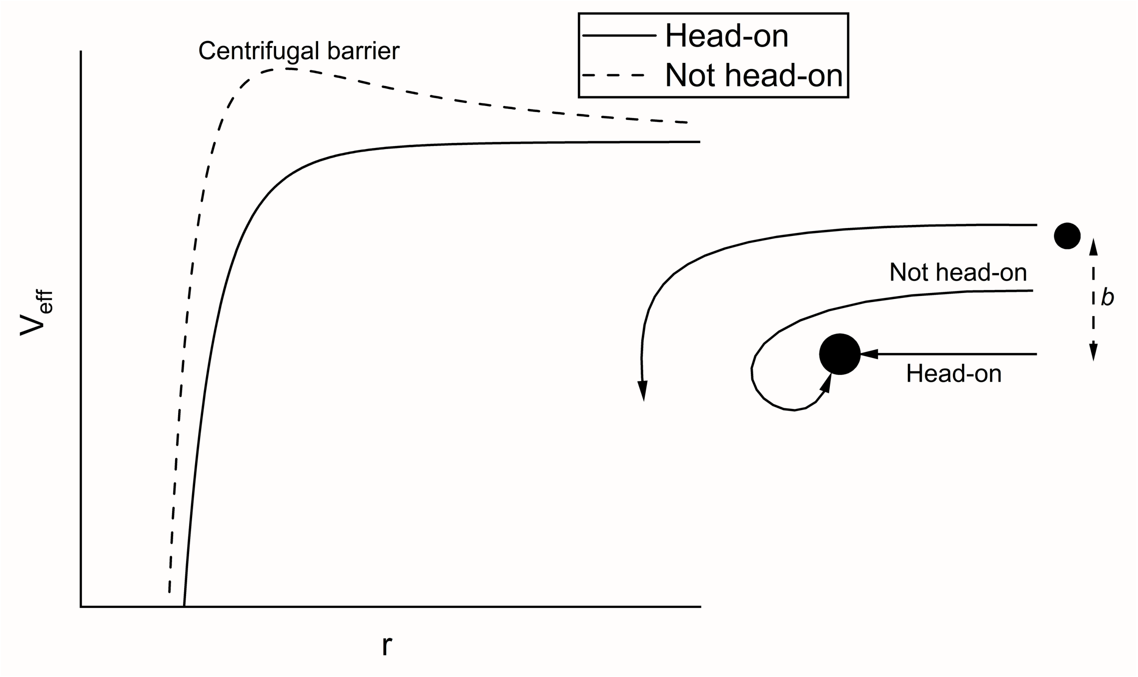

Figure 1.7 (Left) The effective potential as a function of the separation between two attracting species for a head-on collision (solid line), and a non-head-on collision (dashed line) where a centrifugal barrier emerges. (Right) Possible trajectories for the interaction between two attracting species: when *b* = 0, a head-on collision happens indicated by the straight arrow; when 0 < *b* < *b*$_{\text{max}}$, a non-head-on collision happens where the incoming species spirals inwards; when *b* > *b*$_{\text{max}}$, a deflection happens instead of a collision.

Trajectory calculations can also be done, while the actual computations are out of the scope of this work, to illustrate the dynamics of the reaction system given the potential surface if the coordinate system of the centre-of-mass frame is known (14, 39). Briefly, the calculations concern the Hamiltonian $\mathcal{H}$ of the system, which is given by:

$$\mathcal{H} = \mathcal{T} + \mathcal{V} \qquad \text{E 1.30}$$

where $\mathcal{T}$ and $\mathcal{V}$ are the kinetic and potential energies respectively. By the conservation of angular momentum and the total energy, the time-dependent coordinates of the individual atoms and the energy distribution are worked out. This process has to be repeated for a statistically significant quantity of trajectories with a set of randomised geometric collision parameters in order to figure out a representative picture of the reactive probability, the scattering pattern and the reaction mechanism.

1.2.5 Transition state theory

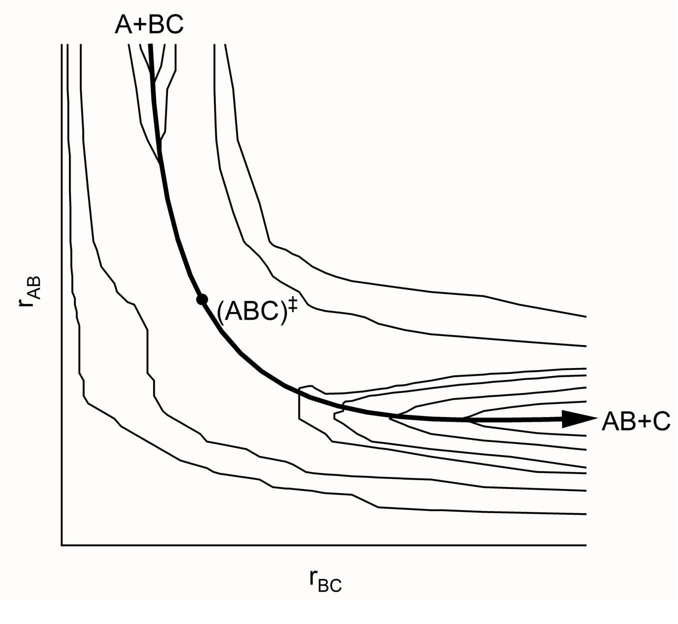

Figure 1.8 Potential energy surface for R 1.8 where the arrow denotes the reaction pathway. r_{AB} and r_{BC} denote the separation between A and B and between B and C respectively. The reaction starts with the approach of the two reactants A and BC, where r_{AB} decreases, and then after the formation of $(\mathrm{ABC})^{\ddagger}$, r_{BC} increases to form the products AB and C.

Transition state theory (TST) is a theoretical method that examines reaction rate and helps rationalise the Arrhenius equation from a statistical viewpoint. It is postulated that the reaction from the reactants to the products proceeds through a transient transition state, where an equilibrium exists between the reactants and the transition state, and once the system has passed the transition state it will continue to form the products without turning back (13-15, 40). In other words, the reaction can be represented as

$$\mathrm{A} + \mathrm{BC} \underset{k_{-1}}{\overset{k_1}{\rightleftharpoons}} (\mathrm{ABC})^{\ddagger} \overset{k_2}{\rightarrow} \mathrm{AB} + \mathrm{C} \qquad \text{R 1.8}$$

where the reactants A and BC form the products AB and C through a transition state $(\mathrm{ABC})^{\ddagger}$ with energy $\Delta E^{\ddagger}$ above the reactants. k_1 and k_{-1} are the rate coefficients for the forward and backward reactions of the formation of $(\mathrm{ABC})^{\ddagger}$ while k_2 is the rate coefficient for the formation of the products AB and C from $(\mathrm{ABC})^{\ddagger}$. Figure 1.8 is an example of the contour map of the potential energy surface (PES), which is generated by mapping the potential energy as a function of different geometric parameters, for R 1.8 and Figure 1.4 will then be the energy curve cutting the surface along the reaction path. $(\mathrm{ABC})^{\ddagger}$ is the bottleneck of the reaction path (13-15, 40), a priori taken as the saddle point on the PES for the convenience of locating it by quantum chemical software, where the negative curvature is along the reaction path. The rate equation of the overall reaction is given by:

$$\frac{d[\mathrm{products}]}{dt} = k[\mathrm{A}][\mathrm{BC}] \qquad \text{E 1.31}$$

and with the transition state theory the following can also be written:

$$\frac{d[\mathrm{products}]}{dt} = k_2[(\mathrm{ABC})^{\ddagger}] \qquad \text{E 1.32}$$

Combining E 1.31 and E 1.32 and rearranging the terms give the Eyring equation:

$$k = k_2 \frac{[(\mathrm{ABC})^{\ddagger}]}{[\mathrm{A}][\mathrm{BC}]} = k_2 K^{\ddagger} \qquad \text{E 1.33}$$

where $K^{\ddagger}$ is the equilibrium constant between the reactants and the transition state (13-15, 40).

According to the theory of statistical mechanics, $K^{\ddagger}$ can be expressed in terms of the molar partition functions q of the respective species (13-15, 40):

$$K^{\ddagger} = \frac{[(\mathrm{ABC})^{\ddagger}]}{[\mathrm{A}][\mathrm{BC}]} = \frac{q_{(\mathrm{ABC})^{\ddagger}}}{q_{\mathrm{A}}q_{\mathrm{BC}}} e^{-\frac{\Delta E^{\ddagger}}{RT}} \tag{E 1.34}$$

The partition function for a molecule q can be expressed as the product from different contributions: electronic q_{elec}, translational q_{trans}, vibrational q_{vib} and rotational q_{rot} energies, that is:

$$q = q_{\mathrm{elec}} q_{\mathrm{trans}} q_{\mathrm{vib}} q_{\mathrm{rot}} \tag{E 1.35}$$

The electronic partition function q_{elec} is given by:

$$q_{\mathrm{elec}} = \sum_i g_i \, e^{-\frac{E_i}{k_B T}} \tag{E 1.36}$$

where k_B is the Boltzmann constant, g_i is the degeneracy of the level i and E_i is the energy difference from the ground state to the level i. The translational partition function q_{trans} is given by:

$$q_{\mathrm{trans}} = \frac{V\left(\sqrt{2\pi m k_B T}\right)^3}{h^3} \tag{E 1.37}$$

for a molecule of mass m in a container of volume V with h being the Planck constant. The vibrational partition function q_{vib} is given by:

$$q_{\mathrm{vib}} = \prod_i \frac{1}{1 - e^{-\frac{h\nu_i}{k_B T}}} \tag{E 1.38}$$

where ν_i is the vibrational frequency of the i-th vibrational mode. The rotational partition function q_{rot} for linear rotors is given by:

$$q_{\mathrm{rot}} = \frac{1}{\sigma} \frac{8\pi^2 k_B T}{h^2} I \tag{E 1.39}$$

where I is the moment of inertia and σ is the symmetry number, while for non-linear rotors is given by:

$$q_{\mathrm{rot}} = \frac{1}{\sigma} \sqrt{\left(\frac{8\pi^2 k_B T}{h^2}\right)^3 \pi I_a I_b I_c} \tag{E 1.40}$$

where I_a, I_b and I_c are the moments of inertia about the principal axes.

Upon the formation of the transition state, there is a special nonequilibrium vibration $\nu^{\ddagger}$, which has an imaginary frequency and corresponds to a movement along the reaction coordinate. Transition state theory assumes that this vibrational mode can be separated from other contributions (13-15, 40), of which the partition function contributed from this vibrational mode $q_{\mathrm{vib}}{}'$ is given by:

$$q_{\mathrm{vib}}{}' = \lim_{\nu^{\ddagger}\to 0} \frac{1}{1-e^{-\frac{h\nu^{\ddagger}}{k_B T}}} \approx \frac{k_B T}{h\nu^{\ddagger}} \qquad \text{E 1.41}$$

It is valid to take the limit as that particular vibration corresponds to the motion leading to the dissociation of the activated complex, that is, the force constant and $\nu^{\ddagger}$ are much lower than those for the other ordinary vibrations. The equilibrium constant becomes:

$$K^{\ddagger} = \frac{q_{\mathrm{vib}}{}'\bar{q}_{(\mathrm{ABC})^{\ddagger}}}{q_{\mathrm{A}}q_{\mathrm{BC}}} e^{-\frac{\Delta E^{\ddagger}}{RT}} = \frac{k_B T}{h\nu^{\ddagger}} \frac{\bar{q}_{(\mathrm{ABC})^{\ddagger}}}{q_{\mathrm{A}}q_{\mathrm{BC}}} e^{-\frac{\Delta E^{\ddagger}}{RT}} \qquad \text{E 1.42}$$

where $\bar{q}_{(\mathrm{ABC})^{\ddagger}}$ is the partition function of $(\mathrm{ABC})^{\ddagger}$ without the contribution from $\nu^{\ddagger}$. On the other hand, $\nu^{\ddagger}$ is responsible for converting $(\mathrm{ABC})^{\ddagger}$ to the products, so the rate coefficient of product formation from the transition state k_2 is proportional to $\nu^{\ddagger}$, which means:

$$k_2 = \kappa \nu^{\ddagger} \qquad \text{E 1.43}$$

where κ is the transmission factor. Substituting E 1.42 and E 1.43 into E 1.33 gives (13-15, 40):

$$k = \kappa \nu^{\ddagger} \frac{k_B T}{h\nu^{\ddagger}} \frac{\bar{q}_{(\mathrm{ABC})^{\ddagger}}}{q_{\mathrm{A}}q_{\mathrm{BC}}} e^{-\frac{\Delta E^{\ddagger}}{RT}} = \kappa \frac{k_B T}{h} \frac{\bar{q}_{(\mathrm{ABC})^{\ddagger}}}{q_{\mathrm{A}}q_{\mathrm{BC}}} e^{-\frac{\Delta E^{\ddagger}}{RT}} \qquad \text{E 1.44}$$

which is in a comparable form with the Arrhenius equation E 1.8, where the pre-exponential factor is now in the form of $\kappa \frac{k_B T}{h} \frac{\bar{q}_{(\mathrm{ABC})^{\ddagger}}}{q_{\mathrm{A}}q_{\mathrm{BC}}}$. Apart from the T explicitly in $\frac{k_B T}{h}$, all the partition functions q also depend on the temperature.

From a thermodynamic perspective, E 1.44 can be rewritten as (13-15):

$$k = \kappa \frac{k_B T}{h} \bar{K}^{\ddagger} \qquad \text{E 1.45}$$

where $\overline{K}^{\ddagger}$ is the equilibrium constant for the formation of the transition state with the removal of one degree of freedom. From the van't Hoff equation, the standard Gibbs free energy of activation $\Delta G^{\ddagger\circ}$ can be expressed in terms of the equilibrium constant by:

$$\Delta G^{\ddagger\circ} = -RT \ln \overline{K}^{\ddagger} \qquad \text{E 1.46}$$

The Gibbs free energy can also be expressed in terms of the enthalpy and the entropy by:

$$\Delta G^{\ddagger\circ} = \Delta H^{\ddagger\circ} - T\Delta S^{\ddagger\circ} \qquad \text{E 1.47}$$

Therefore, E 1.45 becomes (13-15):

$$k = \kappa \frac{k_B T}{h} e^{-\frac{\Delta G^{\ddagger\circ}}{RT}} = \kappa \frac{k_B T}{h} e^{\frac{\Delta S^{\ddagger\circ}}{R}} e^{-\frac{\Delta H^{\ddagger\circ}}{RT}} \qquad \text{E 1.48}$$

The activation energy E_a is defined by:

$$\frac{d \ln k}{dT} = \frac{E_a}{RT^2} \qquad \text{E 1.49}$$

By assuming the ideal gas law, the activation energy can be expressed in terms of the enthalpy by:

$$E_a = \Delta H^{\ddagger\circ} + (1 - \Delta n^{\ddagger})RT \qquad \text{E 1.50}$$

Thus, E 1.48 becomes (13-15):

$$k = \kappa \frac{k_B T}{h} e^{(1-\Delta n^{\ddagger})} e^{\frac{\Delta S^{\ddagger\circ}}{R}} e^{-\frac{E_a}{RT}} \qquad \text{E 1.51}$$

where $\Delta n^{\ddagger}$ is the change in the number of moles upon the formation of the transition state from the reactants. For unimolecular reactions, $\Delta n^{\ddagger}$ is 0, while for bimolecular reactions, $\Delta n^{\ddagger}$ is –1.

1.3 The significance of studies of gas-phase neutral-neutral reactions at low temperatures

As suggested in Section 1.1.2, many molecular species have been observed in the cold region of the interstellar medium. At such low temperatures, for reactions with activation barriers that follow the Arrhenius equation as shown in Section 1.2.2, their reaction rates are extremely small to be responsible for the synthesis of the numerous molecules being detected. Instead, reactions that can proceed quickly even at low temperature, where very often show deviation from the Arrhenius equation, will be the promising candidates to be considered. Kinetic data of the reactions relevant to the astrochemical studies are catalogued into databases such as UMIST (41) and KIDA (42), where there are well-studied rate coefficient values for some reactions but also approximated predictions for some of the others.

In the beginning, the category of ion-neutral reactions, which are expected to be barrierless and with large rate coefficients at low temperature, have been the focus of the studies in the interstellar chemistry. As shown in Table 1.2, neutral species rather than ions dominate in the cold region in the interstellar medium. Therefore, it is suggested that a general scheme for molecular synthesis proceeds in the following way: the neutral species are first ionised by photons to form ions and then the ion-neutral reaction takes place, after the completion of the reaction the products should become charge-neutral quickly (7). As hydrogen is the most abundant element in the universe, it is believed that the interstellar chemistry starts with the ionisation of H_2 by cosmic rays to form H_2^+, which can quickly react with another H_2 to form H_3^+, where H_3^+ can then react with other neutral species X to form other ions (43-46).

$$\mathrm{H_2 + cosmic\ ray \rightarrow H_2^+ + e^-} \qquad \text{R 1.9}$$

$$\mathrm{H_2^+ + H_2 \rightarrow H_3^+ + H} \qquad \text{R 1.10}$$

$$\mathrm{H_3^+ + X \rightarrow H_2 + HX^+} \qquad \text{R 1.11}$$

For instance, X can be O, which will form OH^+ and can subsequently form H_3O^+ by reacting with H_2; or X can be C, which can eventually form various hydrocarbon species after further reactions.

Another category of reactions that are thought to be able to proceed quickly at low temperature involve the participation of dust particles. These particles can be derived from SiO or TiO and for dust particles surrounded by an icy mantle, they provide a catalytic surface for chemical reactions. Reactions that can be catalysed by these surfaces include the formation of H_2 from two H atoms as well as the synthesis of various organic compounds with the use of adsorbed CO (7).

For gas-phase neutral-neutral reactions, originally they were thought to be insignificant in the interstellar medium because the existence of an appreciable barrier essentially stops the reactions between stable species at low temperature. Nonetheless, reactions involving radicals can still proceed quickly under low temperature conditions as it is not necessary for the reactions to proceed by surmounting a barrier (45). The first neutral-neutral reaction being studied experimentally at temperature below 100 K (21, 22) involves two radicals: CN and O_2, and the measured rate coefficients show a negative temperature dependence as shown in Figure 1.9, following an expression of:

$$k = (2.4 \pm 0.1) \times 10^{-11} \left(\frac{T}{298}\right)^{-(0.60 \pm 0.05)} \ \mathrm{cm^3\ molecule^{-1}\ s^{-1}} \qquad \text{E 1.52}$$

in the temperature range of 26–761 K.

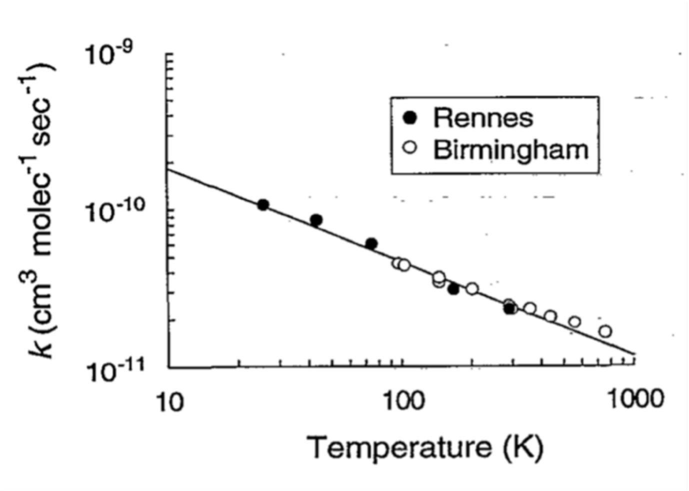

Figure 1.9 Measured rate coefficients for the CN + O_2 reaction versus temperature. The open circles are from data reported in Sims and Smith (21), the closed circles are from data reported in Sims et al. (22), and the line is the fitted expression as shown in E 1.46. Taken from Sims et al. (22).

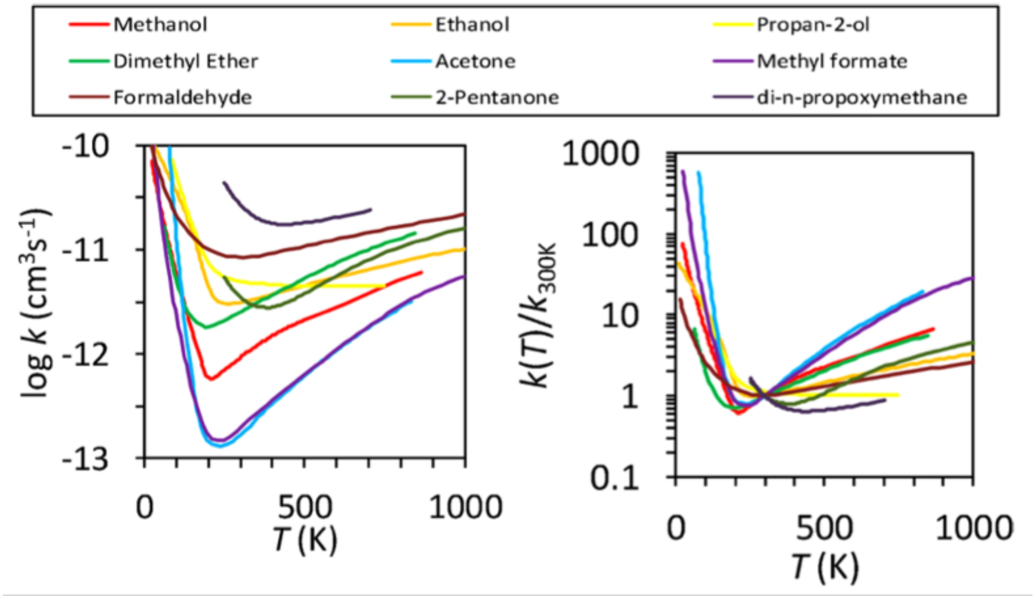

Figure 1.10 The logarithm of the rate coefficients, log *k* (left), and the ratio of the rate coefficients with those at 300 K, $k(T)/k_{300K}$ (right), versus temperature for reactions of the OH radical with various compounds. Taken from Heard (18).

Following the promising results obtained from the radical-radical reactions, increasingly further research has also shed light on the evaluation of the rate coefficients of radical-neutral reactions under low temperature conditions. One particular category that is highlighted here is the reactions of the OH radical with complex organic molecules (COMs) generally composed of at least 6 atoms containing carbon. It is believed that the reactions involving these COMs, including both their formation and destruction, are important to the generation of prebiotic precursors in the interstellar medium (18). As reported in Figure 1.10, many reactions involving the OH radical with COMs show a V-shaped temperature dependence trend similar to that shown in the right column of Figure 1.5.

A notable example is the reaction between OH radical with methanol CH_3OH (26), where a schematic potential energy surface for the reaction is shown in Figure 1.11. At high temperature, the reactants have enough energy to surmount the transition state and eventually generate the products, leading to the Arrhenius relationship observed for the rate coefficient. On the other hand, OH and CH_3OH can form a hydrogen-bonded complex through a barrierless reaction before the reaction path reaches the barrier. At low temperature, while fewer reactants possess enough energy to surmount the barrier, tunnelling to form the H abstraction products from the complex is suggested to be facile because the lifetime of the complex becomes sufficiently long that the probability of tunnelling increases. As a result, a much larger rate coefficient value is obtained at low temperature because the dissociation of the complex becomes less favourable (26). At high temperature, the dominant products are found to be $CH_2OH + H_2O$ due to a lower barrier as shown in Figure 1.11. However, at low temperature, the dominant products become $CH_3O + H_2O$, as the barrier is suggested to be narrower as the imaginary frequency is larger (26) which turns out to be the vital factor in determining the product branching ratio when the reaction relies on tunnelling to proceed. Further details on quantum mechanical tunnelling will be covered in the next chapter.

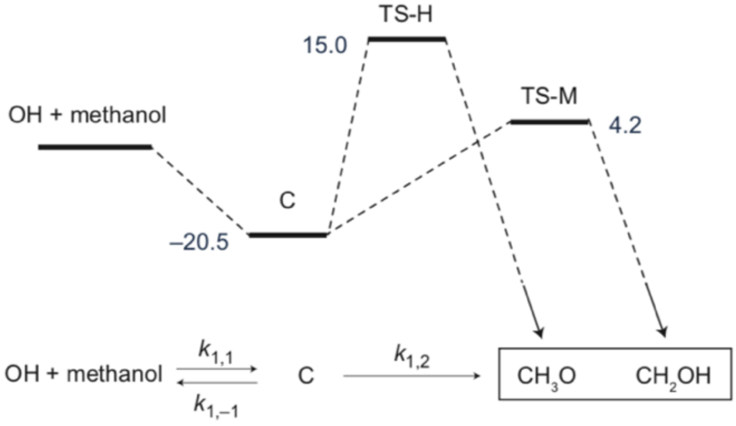

Figure 1.11 Schematic potential energy surface for the reaction of OH + CH_3OH. Energies are in kJ mol^{-1}. Taken from Shannon et al. (26). C denotes the pre-reaction hydrogen-bonded complex. TS-H and TS-M are the two transition states leading respectively to the H abstraction products, $CH_3O + H_2O$ and $CH_2OH + H_2O$.

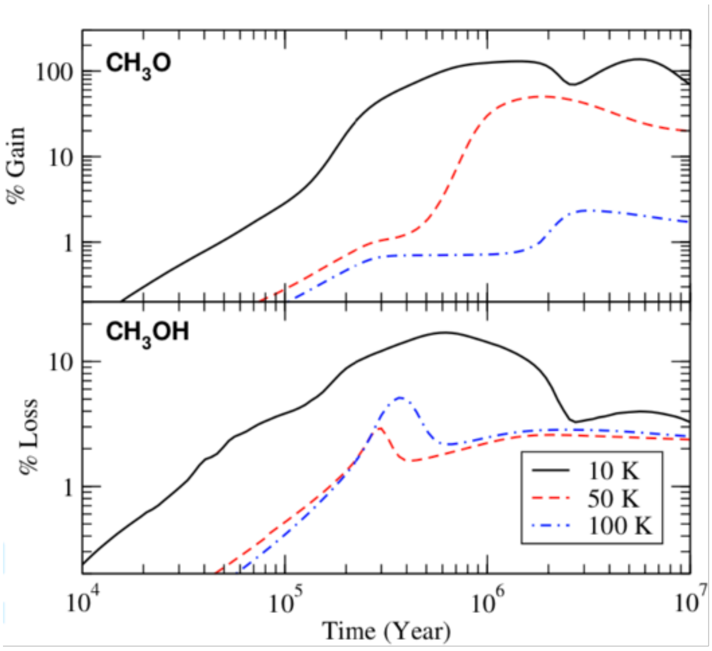

Figure 1.12 Predicted percentage gain in the abundance of CH_3O (top) and percentage loss in the abundance of CH_3OH (bottom) versus time in the interstellar clouds of different temperatures (black: 10 K, red: 50 K, blue: 100 K) after the inclusion of the OH + CH_3OH reaction in the astronomical models. Taken from Acharyya et al. (44).

Both the reactants and the products for the OH + CH_3OH reaction are species that have been detected in the ISM and the aforementioned findings for the OH + CH_3OH reaction have provided new insights in the interstellar chemistry. By applying the results in the astronomical models as shown in Figure 1.12 (44), it can contribute up to a further 10% loss in CH_3OH and 100% gain in CH_3O than previously predicted in the interstellar clouds of 10 K over a timescale of 10^6 years.

Other than the OH radical, there has also been research work involving other radicals, including but not limited to CN, CH, C_2H and NH (45). Both the experimental approaches and the theoretical approaches have successfully provided valuable results in the kinetic studies of the radical-neutral reactions. One more example to be shown here in Figure 1.13 is the C_2H + C_6H_6 reaction (47, 48). Measurements have been carried out in the temperature range of 105–298 K to obtain the following fitted expression for the rate coefficient:

$$k = (3.28 \pm 1.0) \times 10^{-10} \left(\frac{T}{298}\right)^{-(0.18 \pm 0.18)} \text{ cm}^3 \text{ molecule}^{-1} \text{ s}^{-1} \qquad \text{E 1.53}$$

while computations have been performed using the master equation method, which will be covered in Chapter 2 in this thesis, to obtain the rate coefficients in the temperature range of 50–300 K. The calculated rate coefficients are within the predicted range from the experiments, which demonstrates the complementarity of both approaches in the exploration of low temperature reaction kinetics.

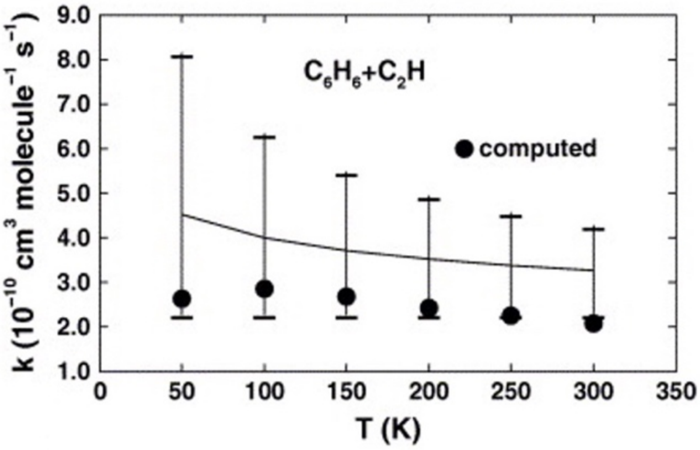

Figure 1.13 Rate coefficients for the C_2H + C_6H_6 reaction versus temperature in the temperature range of 50–300 K. The lines and error bars are from the fitted expression obtained from the measured results reported in Goulay and Leone (47) while the black dots are from the computed results reported in Woon (48). Taken from Woon (48).

Results from the previous literature presented in this section demonstrate that it is not rare for radical-neutral reactions to display non-Arrhenius behaviour, where many of the reactants involved can be found in the ISM. Thus, the contribution of radical-neutral reactions in such cold environment can possibly be more significant than previously expected and further research, both experimentally and theoretically, on the reaction mechanism of different radical-neutral reaction systems should be done.

1.4 Experimental techniques for low-temperature kinetic measurements – the Laval nozzle apparatus

Although this thesis focusses on the theoretical work done on the studies of the low temperature kinetic behaviour of molecular species identified in outer space, the experimental approach will also be briefly discussed here. Various reactions have been carried out under a cold environment by our group at the University of Leeds, with the use of the Laval nozzle set-up to mimic the conditions in the interstellar medium.

1.4.1 Generation of the cold environment

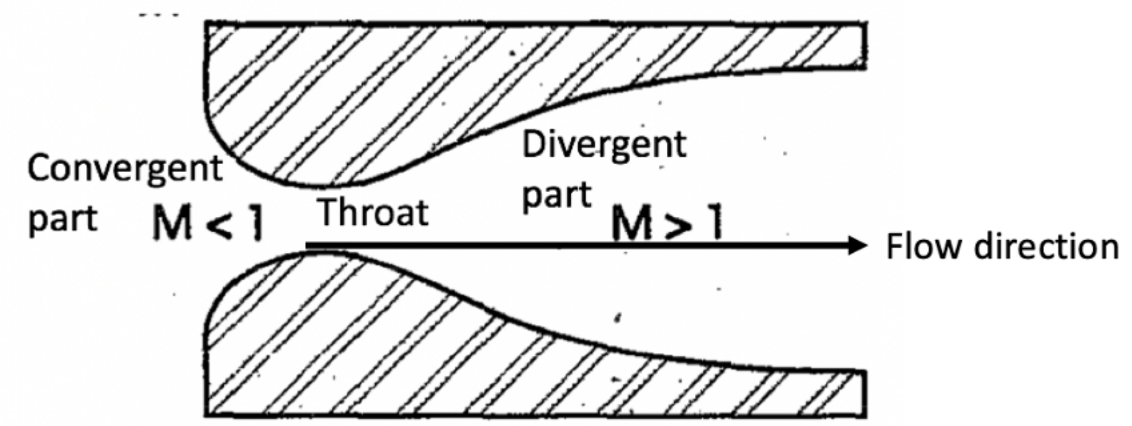

Figure 1.14 Schematic diagram of a Laval nozzle apparatus, which shows the gas first flows from the convergent part, to the throat and eventually the divergent part. Adapted from Atkinson and Smith (49).

The CRESU (Cinétique de Réaction de Ecoulement Supersonique Uniforme) method is one of the most successful methods for the study of low temperature reactions, which involves the use of an apparatus called a Laval nozzle. A Laval nozzle is a tube with a specially designed convergent-divergent shape, where the converging section is asymmetric with the diverging section as shown in Figure 1.14. It was first developed by Gustaf de Laval in the 19th century and originally applied in supersonic wind tunnels to generate a uniform flow with the greatest possible cross-sectional area out of the exit (45, 46, 49). Prior the entry of the nozzle, a mixture of gas is prepared in the stagnation region. Then the high-pressure gas is fed to the inlet of the nozzle and it starts to accelerate when it propagates through the converging part. After flowing through the narrowest part known as throat, the gas reaches the diverging part and expands into a collimated isentropic flow (7, 18, 45, 46, 49-51).

The Mach number M, which is dimensionless and defined as the flow speed over the local speed of sound, is a useful parameter to describe the velocity of the gas flow:

$$M = \frac{v_{\text{flow}}}{v_{\text{sound}}} \qquad \text{E 1.54}$$

where the speed of sound v_{sound} depends on the properties of the medium it is travelling such as the type of carrier gas used and the temperature, and is given by:

$$v_{\text{sound}} = \sqrt{\gamma R T} \qquad \text{E 1.55}$$

where R is the universal gas constant and γ is the ratio of the heat capacities of the carrier gas $\frac{C_p}{C_v}$. The Mach number is smaller than 1 in the converging section and the flow is subsonic; the Mach number is equal to 1 at the throat; and further increases to greater than 1 in the diverging section where the flow is supersonic (49). For instance, the nozzles used by our group in the University of Leeds can accelerate the gas to between Mach 2.49 and 5 (52).

Coupled with a reduction in pressure after passing the throat is a cooling of the gas. Due to a high gas density, frequent collisions among the molecules occur and thermal equilibrium can be achieved in the flow. The resulting flow, typically within a vacuum chamber, is axisymmetric and maintains a constant temperature, density and velocity over some decimetres (46, 49-52). Apart from the type of carrier gas, the temperature and the Mach number of the flow generated are governed by geometric factors such as radius, length and curvature of the Laval nozzle, with the relationship between the Mach number and the properties of the flow summarised by the following equations (46, 49-51):

$$\frac{P_i}{P_0} = \left[\frac{(\gamma+1)M^2}{(\gamma+1)M^2+2}\right]^{\frac{\gamma}{\gamma-1}} \left(\frac{\gamma+1}{2\gamma M^2-\gamma+1}\right)^{\frac{1}{\gamma-1}} \quad \text{E 1.56}$$

$$\frac{T_0}{T} = 1 + \frac{\gamma-1}{2}M^2 \quad \text{E 1.57}$$

$$\frac{P_0}{P} = \left(1 + \frac{\gamma-1}{2}M^2\right)^{\frac{\gamma}{\gamma-1}} \quad \text{E 1.58}$$

$$\frac{n_0}{n} = \left(1 + \frac{\gamma-1}{2}M^2\right)^{\frac{1}{\gamma-1}} \quad \text{E 1.59}$$

where P_i is the impact pressure in the expanded gas flow measured by a small duct known as the Pitot tube, T_0, P_0 and n_0 are the temperature, pressure and number density in the stagnation region before the expansion and T, P and n are the corresponding parameters in the resulting static supersonic flow respectively.

It is favourable to use the Laval nozzle technique over other methods in the kinetic studies at the range of about or below 100 K because of the following advantages. First, there is no significant condensation problem at the walls, of which its emergence alters the actual partial pressures of the gaseous species in the flow, hindering the accurate determination of rate coefficients for gas-phase reactions. In contrast, for measurements taken within a static cell or a flow tube, the cold condition is generated by applying cryogens in the outer jacket that surrounds the reaction chamber. The gas species inside the chamber will condense at the walls if their partial pressures are higher than the vapour pressures at the wall temperature and the effectiveness of cooling depends on the nature of the cryogens used, for instance, liquid nitrogen N_2 can only be used to cool down to 77 K while liquid helium He can be down to 18 K or less (18, 53, 54). These factors restrict the maximum concentration of the gas reactants, the choice of gas reactants and the minimum workable temperature for measurements, but the Laval nozzle is free from these problems due to the fast expansion process and the lack of walls. However, the formation of oligomers, for example, dimers, of the reactants is still a concern in the Laval set-up because the rate for the oligomers undergoing the reaction can be different to that for the monomers, and this will be discussed in Chapter 6 in this thesis. Another advantage for the Laval set-up is the production of a thermally equilibrated flow, which makes kinetics measurements possible. This is in contrast to the free jet expansion method, where instead of using a specially shaped Laval nozzle to control the expansion, a pinhole of ~0.05 cm in diameter is used such that the outcoming jet can flow freely. Molecules have to undergo numerous collisions in the high pressure region, which convert the random internal energy into directed translational energy, before passing the pinhole into the low pressure region and the resulting jet is cooled due to the limited span of the molecular speed distribution. However, the outcoming flow possess a significant gradient in terms of temperature and density where thermal equilibrium, which is necessary for kinetic studies, can hardly be confirmed (7, 18, 53, 54).

Nevertheless, the CRESU method still has disadvantages. For a continuous CRESU apparatus, a large gas flow rate, normally 50 dm^3 min^{-1}, is essential to sustain an extremely cold supersonic flow, which can only be accomplished with the use of huge pumping systems that can attain about 30,000 m^3 h^{-1} in terms of the pumping speeds (45, 46, 54). A solution to relax the pumping system requirement, as well as reduce the cost and space involved, is the use of a pulsed Laval nozzle system, where the flow of gas is controlled by pulsed valves or a rotating disk, but the trade-off is the lowest possible temperature achieved in the flow (18, 45, 46, 51, 54). The current record set by the continuous flow is 5.8 ± 0.8 K (55) while the pulsed flow is 11.7 ± 0.7 K (30). For the pulsed Laval system at the University of Leeds, it is capable for kinetic measurements in the temperature range of 24–148 K (46).

A list of the radical-neutral reactions studied with the Laval nozzle method by our group and published is shown in Table 1.4 while a more complete list of the reactions studied with the Laval experiment by different research groups around the world can be found in Cooke and Sims (45) and Rowe et al. (46).

Table 1.4 List of the radical-neutral reactions studied by our group at low temperature with the use of the Laval nozzle set-up

Radical	Co-reagent	Reference
OH	C_2H_2	(51, 54, 56)
	C_2H_4	(51, 54)
	C_3H_4	(51, 54)
	C_6H_6	(54)
	$CH_3C(O)CH_3$	(54, 56-59)
	$CH_3C(O)CH_2CH_3$	(54, 57)
	CH_3OCH_3	(56-59)
	CH_3OH	(26, 27, 56, 59)
	CH_3CH_2OH	(59, 60)
	$CH_3CH(OH)CH_3$	(60)
	NH_3	(56, 59)
CH_3O	NO	(59)
C_2H_5O	NO	(59)
CH	CH_2O	(52)
NH_2	CH_2O	(61)
CN	CH_2O	To be submitted

1.4.2 Radical generation

During the study of radical-neutral reactions, many of the radicals have to be produced in situ due to their reactive nature, which then requires the selection of a suitable precursor to generate the radical species. Before entering the Laval nozzle, the precursor, the co-reagent, which is in excess, and the carrier gas are mixed in the gas reservoir to form a diluted (around or less than 1%) mixture. An ideal carrier gas has to be inert, and the common choices are nitrogen N_2, argon Ar and helium He. Laser flash photolysis (LFP) is a usual technique to excite the precursor to form the radicals with a pump laser, which is often an excimer laser, directing antiparallel or parallel to the gas flow in the experimental set-up. A selected list of candidates of precursors used in previous studies is presented in Table 1.5.

Table 1.5 Possible precursors together with the required laser wavelength for the excitation λ used in selected previous studies for the generation of the required radicals in the Laval gas flow

Radical	Precursor	Reference
OH	H_2O_2 (λ = 193, 248, 266 nm)	(28, 30)
	$(CH_3)_3COOH$ (λ = 248 nm)	(26, 30, 51, 57, 58, 60)
	$CH_3C(O)CH_3$ (λ = 248 nm) followed by $CH_3CO + O_2$	(58)
	$O(^1D) + H_2$	(26, 27)
CH_3O	CH_3ONO (λ = 248 nm)	(59)
C_2H_5O	C_2H_5ONO (λ = 248 nm)	(59)
CH	$CHBr_3$ (λ = 248, 266 nm)	(52)
NH_2	NH_3 (λ = 213 nm)	(61)
CN	NCNO (λ = 532, 583 nm)	(21, 22, 24)
	ICN (λ = 266 nm)	(62)
C_2H	C_2H_2 (λ = 193 nm)	(47, 63-67)
	CF_3C_2H (λ = 193 nm)	(47)

1.4.3 Determination of rate coefficients and the product branching ratios

The method used to measure the reaction rate coefficients depends on the nature of the species under study. One of the popular options is laser-induced fluorescence spectroscopy (LIF), which involves the use of a second (probe) laser. In practice, the probe laser is pointed in a direction crossing the gas beam and pump laser perpendicularly or in a counter-propagating direction. The probe laser excites one of the species in the reacting system, typically the radical reactant, such that it subsequently undergoes fluorescence. The fluorescence signal is focused by optics and collected by a sensitive light detecting device such as photomultiplier tube (PMT), located at a direction normal to both the gas flow and the probe laser as shown in Figure 1.15, and to prevent scattered light, an interference filter is also used. The fluorescence collected provides information regarding the relative concentration of the species monitored.

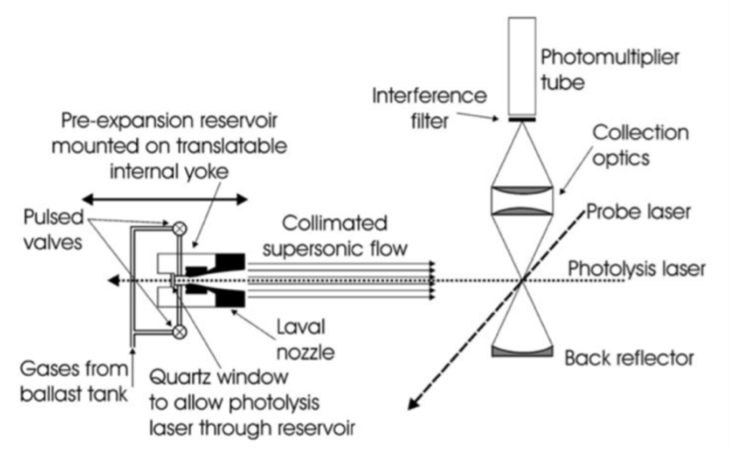

Figure 1.15 Schematic diagram of the pump-probe laser set-up for kinetic measurements in the Laval nozzle apparatus in the University of Leeds. Taken from Taylor et al. (51).

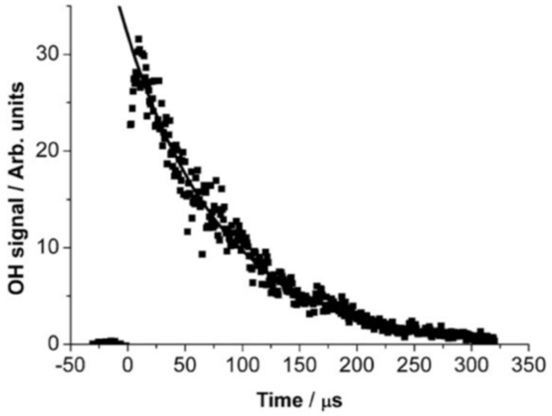

Figure 1.16 An experimental decay curve of OH radical for the reaction of OH + C_2H_4. Taken from Taylor et al. (51).

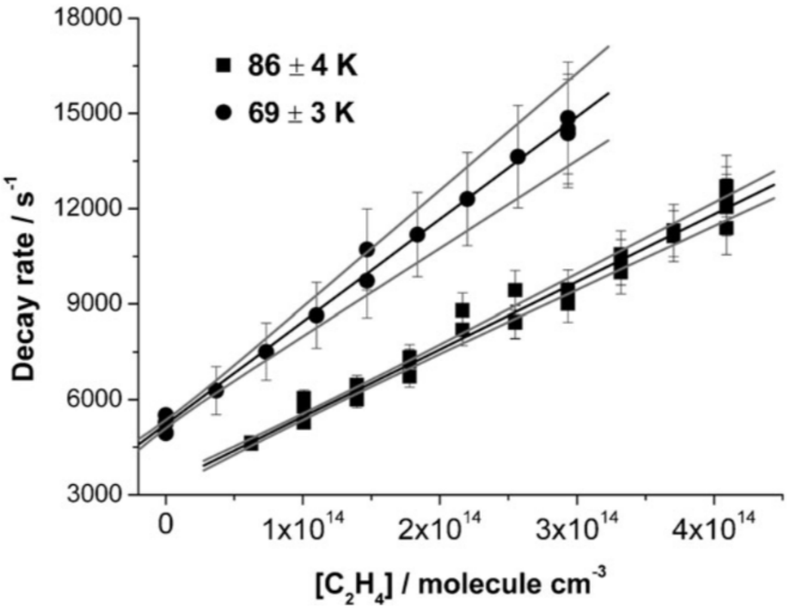

Figure 1.17 Bimolecular plots of the pseudo-first order OH decay rate coefficient *k'* against the concentration of the co-reagent C_2H_4 at 86 K (squares) and 69 K (circles) respectively. The slope of the bimolecular plot gives the reaction rate coefficient k_{bim}. Taken from Taylor et al. (51).

By changing the time delay between the pump laser and the probe laser, the temporal profile of the concentration of the radical can be obtained. For instance, a typical OH radical decay profile is shown in Figure 1.16. The rate equation for such decay can be represented by:

$$\frac{d[\text{radical}]}{dt} = -k_{\text{bim}}[\text{radical}][\text{co-reagent}] \qquad \text{E 1.60}$$

If the co-reagent is in excess, by applying the pseudo-first order conditions where $[\text{co-reagent}] \gg [\text{radical}]$ with $[\text{co-reagent}]$ being constant, E 1.60 can be converted to E 1.61 similar to the conversion from E 1.5 to E 1.7:

$$[\text{radical}] = [\text{radical}]_0 e^{-k_{\text{bim}}[\text{co-reagent}]t} = [\text{radical}]_0 e^{-k't} \qquad \text{E 1.61}$$

where $k' = k_{\text{bim}}[\text{co-reagent}]$ and $[\text{radical}]_0$ is the initial concentration of the radical. The decay curve for a particular $[\text{co-reagent}]$ at a particular temperature as shown in Figure 1.16 can then be fitted to the exponential expression E 1.61 to obtain k'. By repeating the experiments at different $[\text{co-reagent}]$, a plot of k' against $[\text{co-reagent}]$ as shown in Figure 1.17, known as a bimolecular or second order plot, can be generated. The slope of such plot gives the bimolecular rate coefficient k_{bim} at the particular temperature where measurements are taken.

Radicals that can be monitored using LIF include OH, CH and CN, and their characteristic excitation transitions used in previous studies are presented in Table 1.6.

Table 1.6 Characteristic excitation transition used in selected previous LIF studies for monitoring the concentration of the radicals

Radical	Characteristic excitation transition	Wavelength (nm)	Reference
OH	$A^2\Sigma^+$-$X^2\Pi_i$ (0,0), (1,0)	282, 308	(26-28, 30, 51, 57, 58, 60)
CH	$B^2\Sigma$-$X^2\Pi$ (1,0)	364	(52)
NH_2	A^2A_1-X^2B_1	598	(61)
CN	$B^2\Sigma^+$-$X^2\Sigma^+$ (0,0), (1,0)	388, 420	(21, 22, 24, 62)
CH_3O	A^2A_1-X^2E (0,0), (1,0)	297, 310	(26, 59)
C_2H_5O	A^2A_1-X^2A'' (3,0)	323	(59)

Instead of monitoring the radical reactant species, depending on the properties of the products, occasionally the products can be identified and monitored by LIF. For instance, the reaction between OH and CH_3OH can give CH_3O as one of the products, which has a characteristic A^2A_1-X^2E transition at 297 nm, making the product possible to be monitored with the fluorescence intensity (26) as shown in Figure 1.18, where studying the kinetics of the production of CH_3O led to the same rate coefficient as for monitoring the OH reactant.

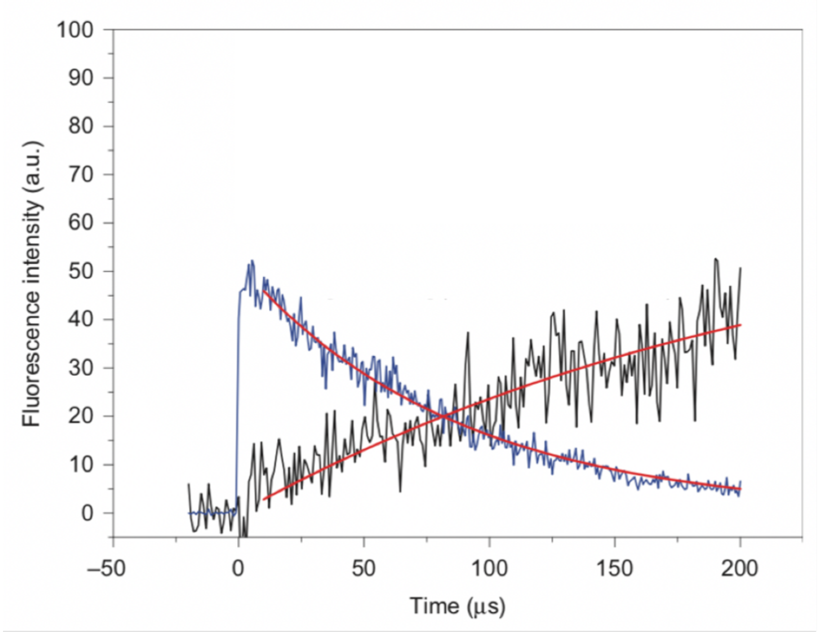

Figure 1.18 Temporal evolution of the decay of OH radicals (blue) and the formation of CH_3O radicals (black) in the reaction of OH + CH_3OH at 82 K, where measurements were taken with the LFP-LIF technique. Taken from Shannon et al. (26).

Apart from LIF, other techniques have also been used to determine rate coefficients by ourselves and other groups with the Laval nozzle set-up. One of the methods is to monitor the chemiluminescence, where photon emission is induced by a chemical reaction rather than being excited by a laser as for LIF. This method has been successfully applied for reactions involving the C_2H radical (47, 63-65), where measurements of the decay of C_2H are achieved by the inclusion of a trace amount of O_2 in the gas flow because C_2H can react with O_2 to give CH $A^2\Delta$-$X^2\Pi$ chemiluminescence at 430 nm.

Another technique that has been previously reported to be incorporated with the Laval nozzle is mass spectrometry, which is useful in the identification of products. The relevant experimental set-up, which is shown in Figure 1.19, has been applied in the studies of the reactions between C_2H with C_2H_2 and C_4H_6 (66, 67). After the gas mixture passes through the Laval nozzle, a cooled collimated beam of gas flow is formed and at the end of the flow, either a skimmer or an airfoil is used to sample the beam. The next compartment the flow enters is the ionisation chamber, where the photoionisation of the reacted gas can be achieved either by a laser (66) or a vacuum ultraviolet synchrotron (67). The ionised fragments or parent species ions then move towards a detector, where a mass spectrum can be recorded either by the time-of-flight mass spectrometry (TOF-MS) or the quadrupole mass spectrometry (QMS).

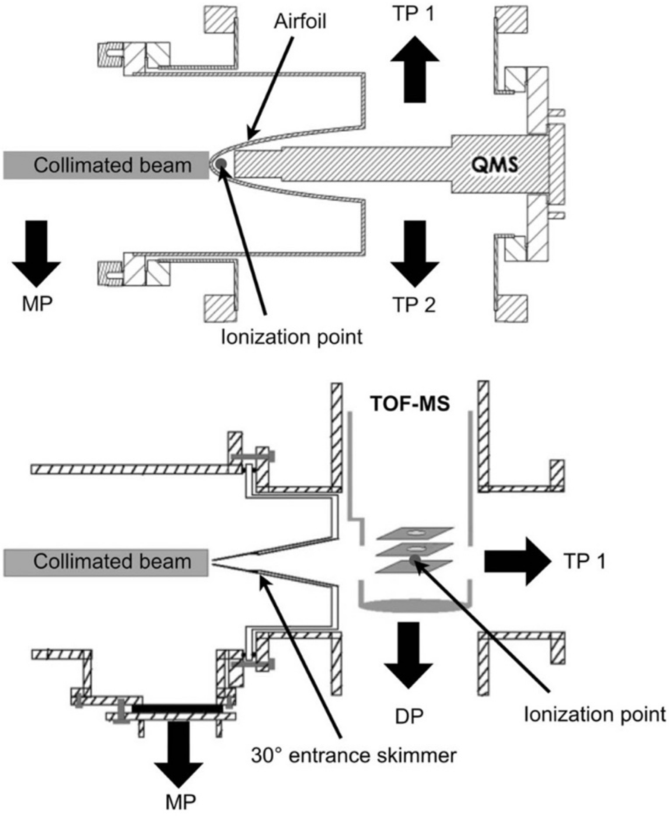

Figure 1.19 Schematic diagram of the Laval nozzle coupled with (top) the vacuum ultraviolet synchrotron ionisation quadrupole mass spectrometry (QMS) and (bottom) the time-of-flight mass spectrometry (TOF-MS) respectively. TP, MP and DP represent the pumping systems. Taken from Soorkia et al. (67).

More recently, a chirped pulse Fourier transform millimetre wave spectrometer coupled with the Laval nozzle apparatus has been developed (68, 69), where the schematic of the set-up is shown in Figure 1.20. A pair of transmitter and receiver are located downstream from the nozzle exit, where the transmitter generates chirped pulses of millimetre-wave radiation to excite the products while the signals of the subsequent free induction decay (FID) of the excited species are recorded by the receiver. Successful detections of OCS (68), HCN and HNC (69) among the product species in the gas flow have been reported with the use of this experimental set-up.

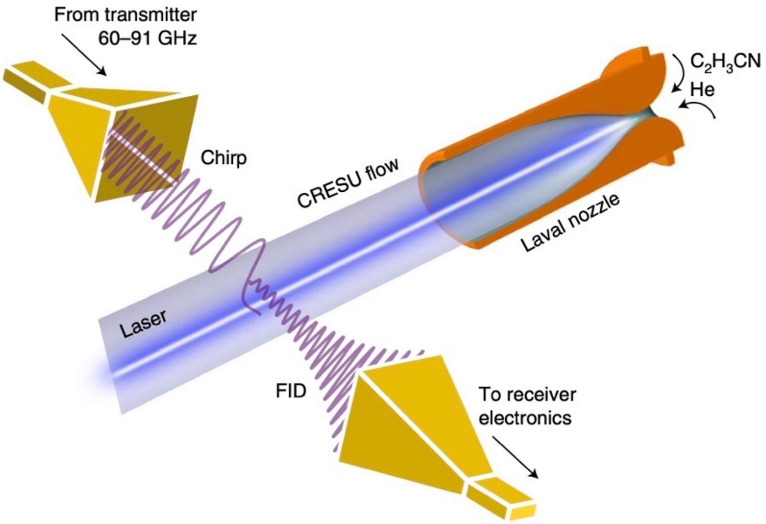

Figure 1.20 Schematic diagram of the Laval nozzle coupled with the chirped pulse Fourier transform spectrometer. The reaction of interest shown here is the dissociation of C_2H_3CN into HCN/HNC + C_2H_2 with He as the bath gas. Taken from Hays et al. (69).

1.5 Overview of this thesis

This chapter has provided a general background to the studies of the low temperature kinetics and dynamics, from a brief introduction of examples of low temperature environments to some relevant kinetic theories. The importance of gas-phase neutral-neutral reactions under low temperature conditions, which is a major incentive in this research project, has been illustrated followed by an overview of the Laval nozzle experiments typically used to enable low temperature kinetic measurements.

The remainder of this thesis will cover the kinetic studies on various reaction systems using theoretical approaches. Chapter 2 will give a detailed description of the computational methods, from the calculations for obtaining the potential energy surfaces to the reaction rate coefficients. Chapter 3 will focus on the reaction between CN and CH_2O, where experimental results are available from our group for comparison with theoretical calculations in order to examine the accuracy of the computations performed. Together with the rate coefficients and product branching ratios, an interpretation of the reaction mechanism will also be provided. Chapter 4 will contain the discussion on the reactions of CN with CH_3SH and CH_2S, with the aim to compare the reactions involving the sulphur-bearing species with those involving the isovalent oxygen-bearing analogues, CN + CH_3OH and CN + CH_2O, where the latter one is elucidated in further detail in Chapter 3. Chapter 5 will be concerned with the reaction between NH_2 and CH_3CHO. Again, the possible reaction channels are identified and the rate coefficients and product branching ratios are calculated. Chapter 6 will be dedicated to the study of dimerisation reactions. The formation of non-covalent dimers of CH_2O, CH_3CHO, $CH_3C(O)CH_3$ and NH_3, which are some of the reagents being used for the Laval experiments by our group, has been investigated in order to estimate their effect in the gas flow when kinetic measurements are being taken. Finally, Chapter 7 will give a summary of the conclusions drawn from the research work presented in this thesis as well as discuss some possible future research directions based on the findings obtained.

1.6 References

1. Rothery, D.A., McBride, N., Gilmour, I. and Bland, P.A. *An introduction to the solar system.* Revised edition / edited by David A. Rothery, Neil McBride and Iain Gilmour ; authors, Philip A. Bland [and others]. ed. Cambridge: Cambridge University Press, 2011.

2. Wayne, R.P. *Chemistry of atmospheres : an introduction to the chemistry of the atmospheres of Earth, the planets, and their satellites.* Third edition. ed. Oxford: Oxford University Press, 2000.

3. Cui, J., Yelle, R.V., Vuitton, V., Waite, J.H., Kasprzak, W.T., Gell, D.A., Niemann, H.B., Müller-Wodarg, I.C.F., Borggren, N., Fletcher, G.G., Patrick, E.L., Raaen, E. and Magee, B.A. Analysis of Titan's neutral upper atmosphere from Cassini Ion Neutral Mass Spectrometer measurements. *Icarus.* 2009, **200**(2), pp.581-615.

4. *European Space Agency.* [Online]. [Accessed 30/07/2019]. Available from: https://www.esa.int/Our_Activities/Space_Science/Cassini-Huygens/Cassini-Huygens_mission_facts

5. Tielens, A.G.G.M. *The physics and chemistry of the interstellar medium.* Repr. with corr. ed. Cambridge; New York: Cambridge University Press, 2006.

6. Kwok, S. *Physics and chemistry of the interstellar medium.* University Science Books, 2007.

7. Vallance, C. *Astrochemistry: from the Big Bang to the present day.* London: World Scientific Publishing, 2017.

8. Decin, L., Richards, A.M.S., Neufeld, D., Steffen, W., Melnick, G. and Lombaert, R. ALMA data suggest the presence of spiral structure in the inner wind of CW Leonis. *Astronomy & Astrophysics.* 2015, **574**, p.A5.

9. *The Cologne Database for Molecular Spectroscopy - Molecules in Space.* [Online]. [Accessed 21/09/2022]. Available from: https://cdms.astro.uni-koeln.de/classic/molecules

10. McGuire, B.A., Burkhardt, A.M., Kalenskii, S., Shingledecker, C.N., Remijan, A.J., Herbst, E. and McCarthy, M.C. Detection of the aromatic molecule benzonitrile (c-C_6H_5CN) in the interstellar medium. *Science.* 2018, **359**(6372), p.202.

11. *Green Bank Telescope.* [Online]. [Accessed 30/07/2019]. Available from: https://greenbankobservatory.org/science/telescopes/gbt/

12. *The Atacama Large Millimeter/submillimeter Array Observatory.* [Online]. [Accessed 30/07/2019]. Available from: https://www.almaobservatory.org/en/home/

13. Pilling, M.J. and Seakins, P.W. *Reaction kinetics.* Oxford: Oxford University Press, 1995.

14. Steinfeld, J.I., Francisco, J.S. and Hase, W.L. *Chemical kinetics and dynamics.* 2nd ed. Upper Saddle River, N.J: Prentice Hall, 1998.

15. Atkins, P.W. and De Paula, J. *Atkins' Physical chemistry.* 9th ed. Oxford: Oxford University Press, 2010.

16. Arrhenius, S. *Über die Reaktionsgeschwindigkeit bei der Inversion von Rohrzucker durch Säuren*. Zeitschrift für Physikalische Chemie. 1889, 4U, p.226. [Accessed 22/02/2019]. Available from: http://pubs.rsc.org/en/content/articlepdf/2014/cp/c3cp54664k

17. Laidler, K.J. The development of the Arrhenius equation. *Journal of Chemical Education.* 1984, **61**(6), p.494.

18. Heard, D.E. Rapid Acceleration of Hydrogen Atom Abstraction Reactions of OH at Very Low Temperatures through Weakly Bound Complexes and Tunneling. *Accounts of Chemical Research.* 2018, **51**(11), pp.2620-2627.

19. Sims, I.R. Tunnelling in space. *Nature Chemistry.* 2013, **5**, p.734.

20. Smith, I.W.M. Neutral/neutral reactions without barriers: comparisons with ion/molecule systems and their possible role in the chemistry of interstellar clouds. *International Journal of Mass Spectrometry and Ion Processes.* 1995, **149-150**, pp.231-249.

21. Sims, I.R. and Smith, I.W.M. Rate constants for the radical-radical reaction between CN and O_2 at temperatures down to 99 K. *Chemical Physics Letters.* 1988, **151**(6), pp.481-484.

22. Sims, I.R., Queffelec, J.L., Defrance, A., Rebrion-Rowe, C., Travers, D., Rowe, B.R. and Smith, I.W.M. Ultra-low temperature kinetics of neutral–neutral reactions: The reaction $CN+O_2$ down to 26 K. *The Journal of Chemical Physics.* 1992, **97**(11), pp.8798-8800.

23. Klippenstein, S.J. and Kim, Y.W. Variational statistical study of the $CN+O_2$ reaction employing ab initio determined properties for the transition state. *The Journal of Chemical Physics.* 1993, **99**(8), pp.5790-5799.

24. Sims, I.R., Queffelec, J.-L., Travers, D., Rowe, B.R., Herbert, L.B., Karthäuser, J. and Smith, I.W.M. Rate constants for the reactions of CN with hydrocarbons at low and ultra-low temperatures. *Chemical Physics Letters.* 1993, **211**(4), pp.461-468.

25. Georgievskii, Y. and Klippenstein, S.J. Strange Kinetics of the C_2H_6 + CN Reaction Explained. *The Journal of Physical Chemistry A.* 2007, **111**(19), pp.3802-3811.

26. Shannon, R.J., Blitz, M.A., Goddard, A. and Heard, D.E. Accelerated chemistry in the reaction between the hydroxyl radical and methanol at interstellar temperatures facilitated by tunnelling. *Nature Chemistry.* 2013, **5**(9), pp.745-749.

27. Gómez Martín, J.C., Caravan, R.L., Blitz, M.A., Heard, D.E. and Plane, J.M.C. Low Temperature Kinetics of the CH_3OH + OH Reaction. *The Journal of Physical Chemistry A.* 2014, **118**(15), pp.2693-2701.

28. Antiñolo, M., Agúndez, M., Jiménez, E., Ballesteros, B., Canosa, A., Dib, G.E., Albaladejo, J. and Cernicharo, J. Reactivity of OH and CH_3OH between 22 and 64 K: modeling the gas phase production of CH_3O in Barnard 1b. *The Astrophysical Journal.* 2016, **823**(1), p.25.

29. Roncero, O., Zanchet, A. and Aguado, A. Low temperature reaction dynamics for CH_3OH + OH collisions on a new full dimensional potential energy surface. *Physical Chemistry Chemical Physics.* 2018, **20**(40), pp.25951-25958.

30. Ocaña, A.J., Blázquez, S., Potapov, A., Ballesteros, B., Canosa, A., Antiñolo, M., Vereecken, L., Albaladejo, J. and Jiménez, E. Gas-phase reactivity of CH_3OH toward OH at interstellar temperatures (11.7–177.5 K): experimental and theoretical study. *Physical Chemistry Chemical Physics.* 2019, **21**(13), pp.6942-6957.

31. Lindemann, F.A., Arrhenius, S., Langmuir, I., Dhar, N.R., Perrin, J. and McC. Lewis, W.C. Discussion on “the radiation theory of chemical action”. *Transactions of the Faraday Society.* 1922, **17**(0), pp.598-606.

32. Trautz, M. Das Gesetz der Reaktionsgeschwindigkeit und der Gleichgewichte in Gasen. Bestätigung der Additivität von Cv-3/2R. Neue Bestimmung der Integrationskonstanten und der Moleküldurchmesser. *Zeitschrift für anorganische und allgemeine Chemie.* 1916, **96**(1), pp.1-28.

33. Lewis, W.C.M. XLI.—Studies in catalysis. Part IX. The calculation in absolute measure of velocity constants and equilibrium constants in gaseous systems. *Journal of the Chemical Society, Transactions.* 1918, **113**(0), pp.471-492.

34. Gioumousis, G. and Stevenson, D.P. Reactions of Gaseous Molecule Ions with Gaseous Molecules. V. Theory. *The Journal of Chemical Physics.* 1958, **29**(2), pp.294-299.

35. Su, T. and Chesnavich, W.J. Parametrization of the ion–polar molecule collision rate constant by trajectory calculations. *The Journal of Chemical Physics.* 1982, **76**(10), pp.5183-5185.

36. Tsikritea, A., Diprose, J.A., Softley, T.P. and Heazlewood, B.R. Capture theory models: An overview of their development, experimental verification, and applications to ion–molecule reactions. *The Journal of Chemical Physics.* 2022, **157**(6), p.060901.

37. Stoecklin, T., Dateo, C.E. and Clary, D.C. Rate constant calculations on fast diatom–diatom reactions. *Journal of the Chemical Society, Faraday Transactions.* 1991, **87**(11), pp.1667-1679.

38. Auzinsh, M., Dashevskaya, E.I., Litvin, I., Nikitin, E.E. and Troe, J. Mutual Capture of Dipolar Molecules at Low and Very Low Energies. II. Numerical Study. *The Journal of Physical Chemistry A.* 2011, **115**(20), pp.5027-5037.

39. Levine, R.D. *Molecular reaction dynamics.* Cambridge: Cambridge University Press, 2005.

40. Eyring, H. The Activated Complex in Chemical Reactions. *The Journal of Chemical Physics.* 1935, **3**(2), pp.107-115.

41. McElroy, D., Walsh, C., Markwick, A.J., Cordiner, M.A., Smith, K. and Millar, T.J.J.A. The UMIST database for astrochemistry 2012. *Astronomy & Astrophysics.* 2013, **550**, p.A36.

42. Agúndez, M. and Wakelam, V. Chemistry of Dark Clouds: Databases, Networks, and Models. *Chemical Reviews.* 2013, **113**(12), pp.8710-8737.

43. Herbst, E. and Klemperer, W. The Formation and Depletion of Molecules in Dense Interstellar Clouds. *Astrophysical Journal.* 1973, **185**, pp.505-534.

44. Acharyya, K., Herbst, E., Caravan, R.L., Shannon, R.J., Blitz, M.A. and Heard, D.E. The importance of OH radical-neutral low temperature tunnelling reactions in interstellar clouds using a new model. *Molecular Physics.* 2015, **113**(15-16), pp.2243-2254.

45. Cooke, I.R. and Sims, I.R. Experimental Studies of Gas-Phase Reactivity in Relation to Complex Organic Molecules in Star-Forming Regions. *ACS Earth and Space Chemistry.* 2019, **3**(7), pp.1109-1134.

46. Rowe, B.R., Canosa, A. and Heard, D.E. *Uniform supersonic flows in chemical physics : chemistry close to absolute zero studied using the CRESU method.* New Jersey: World Scientific, 2022.

47. Goulay, F. and Leone, S.R. Low-Temperature Rate Coefficients for the Reaction of Ethynyl Radical (C_2H) with Benzene. *The Journal of Physical Chemistry A.* 2006, **110**(5), pp.1875-1880.

48. Woon, D.E. Modeling chemical growth processes in Titan’s atmosphere: 1. Theoretical rates for reactions between benzene and the ethynyl (C_2H) and cyano (CN) radicals at low temperature and pressure. *Chemical Physics.* 2006, **331**(1), pp.67-76.

49. Atkinson, D.B. and Smith, M.A. Design and characterization of pulsed uniform supersonic expansions for chemical applications. *Review of Scientific Instruments.* 1995, **66**(9), pp.4434-4446.

50. Potapov, A., Canosa, A., Jimenez, E. and Rowe, B. Uniform Supersonic Chemical Reactors: 30 Years of Astrochemical History and Future Challenges. *Angewandte Chemie-International Edition.* 2017, **56**(30), pp.8618-8640.

51. Taylor, S.E., Goddard, A., Blitz, M.A., Cleary, P.A. and Heard, D.E. Pulsed Laval nozzle study of the kinetics of OH with unsaturated hydrocarbons at very low temperatures. *Physical Chemistry Chemical Physics.* 2008, **10**(3), pp.422-437.

52. West, N.A., Millar, T.J., Van de Sande, M., Rutter, E., Blitz, M.A., Decin, L. and Heard, D.E. Measurements of Low Temperature Rate Coefficients for the Reaction of CH with CH_2O and Application to Dark Cloud and AGB Stellar Wind Models. *The Astrophysical Journal.* 2019, **885**(2), p.134.

53. Sims, I.R. and Smith, I.W.M. Gas-Phase Reactions and Energy Transfer at Very Low Temperatures. *Annual Review of Physical Chemistry.* 1995, **46**(1), pp.109-138.

54. Taylor, S.E. *Reaction kinetics at very low temperatures measured using a pulsed Laval nozzle system*. Dissertation/Thesis thesis, University of Leeds, 2007.

55. Berteloite, C., Lara, M., Bergeat, A., Le Picard, S.D., Dayou, F., Hickson, K.M., Canosa, A., Naulin, C., Launay, J.-M., Sims, I.R. and Costes, M. Kinetics and Dynamics of the $S(^1D_2) + H_2 \text{->} SH + H$ Reaction at Very Low Temperatures and Collision Energies. *Physical Review Letters.* 2010, **105**(20), p.203201.

56. Shannon, R.J. *Experimental and computational studies of hydroxyl radical kinetics at very low temperatures*. Dissertation/Thesis thesis, University of Leeds, 2012.

57. Shannon, R.J., Taylor, S., Goddard, A., Blitz, M.A. and Heard, D.E. Observation of a large negative temperature dependence for rate coefficients of reactions of OH with oxygenated volatile organic compounds studied at 86-112 K. *Physical Chemistry Chemical Physics.* 2010, **12**(41), pp.13511-13514.

58. Shannon, R.J., Caravan, R.L., Blitz, M.A. and Heard, D.E. A combined experimental and theoretical study of reactions between the hydroxyl radical and oxygenated hydrocarbons relevant to astrochemical environments. *Physical Chemistry Chemical Physics.* 2014, **16**(8), pp.3466-3478.

59. Caravan, R.L. *Low temperature kinetic studies using a pulsed laval nozzle apparatus*. Dissertation/Thesis thesis, University of Leeds, 2015.

60. Caravan, R.L., Shannon, R.J., Lewis, T., Blitz, M.A. and Heard, D.E. Measurements of Rate Coefficients for Reactions of OH with Ethanol and Propan-2-ol at Very Low Temperatures. *Journal of Physical Chemistry A.* 2015, **119**(28), pp.7130-7137.

61. Douglas, K.M., Lucas, D.I., Walsh, C., West, N.A., Blitz, M.A. and Heard, D.E. The Gas-phase Reaction of NH_2 with Formaldehyde (CH_2O) is not a Source of Formamide (NH_2CHO) in Interstellar Environments. *The Astrophysical Journal Letters.* 2022, **937**(1), p.L16.

62. Morales, S.B., Le Picard, S.D., Canosa, A. and Sims, I.R. Experimental measurements of low temperature rate coefficients for neutral–neutral reactions of interest for atmospheric chemistry of Titan, Pluto and Triton: Reactions of the CN radical. *Faraday Discussions.* 2010, **147**(0), pp.155-171.

63. Vakhtin, A.B., Heard, D.E., Smith, I.W.M. and Leone, S.R. Kinetics of C_2H radical reactions with ethene, propene and 1-butene measured in a pulsed Laval nozzle apparatus at T=103 and 296 K. *Chemical Physics Letters.* 2001, **348**(1), pp.21-26.

64. Nizamov, B. and Leone, S.R. Kinetics of C_2H Reactions with Hydrocarbons and Nitriles in the 104−296 K Temperature Range. *The Journal of Physical Chemistry A.* 2004, **108**(10), pp.1746-1752.

65. Nizamov, B. and Leone, S.R. Rate Coefficients and Kinetic Isotope Effect for the C_2H Reactions with NH_3 and ND_3 in the 104−294 K Temperature Range. *The Journal of Physical Chemistry A.* 2004, **108**(17), pp.3766-3771.

66. Lee, S., Hoobler, R.J. and Leone, S.R. A pulsed Laval nozzle apparatus with laser ionization mass spectroscopy for direct measurements of rate coefficients at low temperatures with condensable gases. *Review of Scientific Instruments.* 2000, **71**(4), pp.1816-1823.

67. Soorkia, S., Liu, C.-L., Savee, J.D., Ferrell, S.J., Leone, S.R. and Wilson, K.R. Airfoil sampling of a pulsed Laval beam with tunable vacuum ultraviolet synchrotron ionization quadrupole mass spectrometry: Application to low-temperature kinetics and product detection. *Review of Scientific Instruments.* 2011, **82**(12), p.124102.

68. Hays, B.M., Guillaume, T., Hearne, T.S., Cooke, I.R., Gupta, D., Abdelkader Khedaoui, O., Le Picard, S.D. and Sims, I.R. Design and performance of an E-band chirped pulse spectrometer for kinetics applications: OCS – He pressure broadening. *Journal of Quantitative Spectroscopy and Radiative Transfer.* 2020, **250**, p.107001.

69. Hays, B.M., Gupta, D., Guillaume, T., Abdelkader Khedaoui, O., Cooke, I.R., Thibault, F., Lique, F. and Sims, I.R. Collisional excitation of HNC by He found to be stronger than for structural isomer HCN in experiments at the low temperatures of interstellar space. *Nature Chemistry.* 2022, **14**(7), pp.811-815.

Chapter 2

Theoretical background and computational methods

In this work, theoretical approaches are applied to the study of the chemical kinetics of various chemical systems. The significance of computational work in studying chemical reactions can be illustrated in two key points. First, results obtained from calculations can be compared with those from experiments and the interpretation of the results can also help rationalise the reaction mechanism. Second, computational work can overcome restrictions encountered in doing experimental measurements. For example, simulations based on a reasonable computational model can extrapolate to conditions, such as temperature and pressure, beyond the experimental limit or help predict the product branching ratio when the monitoring of product yields can be difficult.

The theoretical approach used here involves two main parts: performing ab initio or density functional theory (DFT) electronic structure calculations to obtain characteristics (stationary points, linkages) of the potential energy surface (PES) of the reaction; and then solving the master equation that uses the ab initio calculation results as the initial input to obtain the reaction rate coefficients. This chapter will give a brief overview of the theoretical background of aspects of computational chemistry and master equation simulations, followed by the actual computational programmes and procedures applied for these two parts of the methodology employed in this thesis.

2.1 Ab initio calculations

As discussed in Chapter 1, a reaction can be considered as a movement along a pathway on a PES. Before moving onto the calculation of reaction rate coefficients for certain pathways, a detailed PES of the system has to be obtained first by electronic structure calculations. In particular, the stationary points and how they are connected on the PES are needed in order to understand how the reaction progresses. This section will first introduce the theories involved in electronic structure calculations, including basis sets, approximation methods and errors, and then move on to the details of the calculations performed. Examples from this work will be used to illustrate the application of aspects of the methods used.

2.1.1 Theoretical chemistry backgrounds

Electronic structure theory calculations of molecules attempt to solve the Schrödinger equation (1-4). For atoms arranged in a certain configuration in 3-D space, the time-dependent Schrödinger equation is given by (5):

$$\left[-\frac{\hbar^2}{2m}\nabla^2 + V(\boldsymbol{r})\right]\Psi(\boldsymbol{r},t) = i\hbar\frac{\partial}{\partial t}\Psi(\boldsymbol{r},t) \qquad \text{E 2.1}$$

$$\widehat{\mathcal{H}}\Psi(\boldsymbol{r},t) = i\hbar\frac{\partial}{\partial t}\Psi(\boldsymbol{r},t) \qquad \text{E 2.2}$$

where $\hbar = \frac{h}{2\pi}$ with h being the Planck constant, m is the mass and Ψ is the time-dependent wavefunction for some position vector $\boldsymbol{r}$. Ψ is the probability amplitude such that its absolute square $|\Psi|^2$, given by the product of Ψ and its complex conjugate, gives the probability of finding the particle at the given position and time. $\widehat{\mathcal{H}}$ is the time-dependent Hamiltonian operator concerning the total energy of the system, which consists of the potential energy operator $V(\boldsymbol{r})$ and the kinetic energy operator $-\frac{\hbar^2}{2m}\nabla^2$ where ∇^2 is the Laplacian operator defined as the divergence of the gradient of a function. For a conservative system with the energy, E, being constant:

$$\Psi(\boldsymbol{r},t) = \psi(\boldsymbol{r})e^{-\frac{iEt}{\hbar}} \qquad \text{E 2.3}$$

and so the time-independent Schrödinger equation can be written as:

$$\left[-\frac{\hbar^2}{2m}\nabla^2 + V(\boldsymbol{r})\right]\psi(\boldsymbol{r}) = E\psi(\boldsymbol{r}) \qquad \text{E 2.4}$$

$$\widehat{H}\psi(\boldsymbol{r}) = E\psi(\boldsymbol{r}) \qquad \text{E 2.5}$$

The time-independent Schrödinger equation is an eigenvalue equation, where the time-independent Hamiltonian operator $\widehat{H}$ operates on the time-independent wavefunction ψ, which is the eigenvector, yielding the energy E, which is the eigenvalue, multiplied by the original wavefunction. The Hamiltonian is given by:

$$\widehat{H} = -\frac{\hbar^2}{2m_k}\sum_k \nabla_k^2 - \frac{\hbar^2}{2m_e}\sum_i \nabla_i^2 + \frac{1}{2}\sum_{k\neq l}\frac{Z_k Z_l e^2}{r_{kl}} + \frac{1}{2}\sum_{i\neq j}\frac{e^2}{r_{ij}} - \sum_i\sum_k\frac{Z_k e^2}{r_{ik}} \qquad \text{E 2.6}$$

where m_k is the mass for nucleus k, m_e is the electron mass, Z is the charge, e is the elementary charge and r is the distance. The subscripts i and j are for the electrons while the subscripts k and l are for the nuclei. The first two terms correspond to the kinetic energy of the nuclei and electrons respectively while the last three terms correspond to the Coulombic nucleus-nucleus repulsion, electron-electron repulsion and electron-nucleus attraction respectively. By applying the Born-Oppenheimer approximation (6), which is based on the fact that the mass of nucleus is much larger than that of the electron and so the nucleus is almost fixed during the motion of the electron, the nuclear part ψ_n and electronic part ψ_e of the wavefunction ψ can be treated as separable and the term corresponding to the kinetic energy of the nuclei can be removed, so considering ψ_e:

$$(\widehat{H_e} + \frac{1}{2}\sum_{k \neq l} \frac{Z_k Z_l e^2}{r_{kl}})\psi_e(\vec{r}) = E_e \psi_e(\vec{r}) \qquad \text{E 2.7}$$

where $\frac{1}{2}\sum_{k \neq l} \frac{Z_k Z_l e^2}{r_{kl}}$ is some constant and the electronic part of the Hamiltonian $\widehat{H_e}$ is given by (1-4):

$$\widehat{H_e} = -\frac{\hbar^2}{2m_e}\sum_i \nabla_i^2 - \sum_i \sum_k \frac{Z_k e^2}{r_{ik}} + \frac{1}{2}\sum_{i \neq j} \frac{e^2}{r_{ij}} \qquad \text{E 2.8}$$

For atomic species, the Schrödinger equation can only be solved exactly for the hydrogenic atom, that is, atom or ion consisting of a positively charged core and a single valence electron, for example H and He^+, because the difficulty rises rapidly for multi-electron systems. The source of the rising complexity lies in the electron-electron interaction term $+\frac{1}{2}\sum_{i \neq j} \frac{e^2}{r_{ij}}$, which depends on the distance between two electrons r_{ij} (1-4). That is to say, the motions of all the electrons are not independent of all of the others and there exists correlation between them, so approximations have to been made for this electron-electron term during actual computations for different molecular species. Depending on the accuracy required and the computational cost, different levels of theory, which consists of the method and the basis set, are selected. The method specifies how the Schrödinger equation is approximated, while the basis set indicates the granularity with which the wavefunction is described.

2.1.1.1 Basis sets

During calculations, it is useful to represent the molecular orbitals ψ as certain mathematical functions, where it is common to consider the molecular orbital as a linear combination of N atomic orbitals χ_i:

$$\psi = \sum_{i=1}^{N} c_i \chi_i \qquad \text{E 2.9}$$

An initial approximation of the mathematical form of the wavefunctions χ_i, known as the basis set, has to be supplied in order to start the calculations. The variational principle states that the true wavefunction with the set of optimised parameters gives the lowest energy. In other words, the energy from using the estimated wavefunction E_ψ is always greater than or equal to that of the real energy of the system E_o, which would come from using the true (unknown) molecular wavefunction:

$$E_\psi \geq E_o \qquad \text{E 2.10}$$

With this principle, the coefficients c_i in the initial estimate keep being refined until the set of optimised coefficients are reached (1-4). This lowest limit can be attained if the basis set used is complete and with an infinite number of functions, which is not feasible for the computation of multi-electron systems.

The selection of the functional form of the wavefunction is important for both computational expense and accuracy of the calculations. John Slater (7) introduced the following function in spherical coordinates (r, θ, φ) to represent the wavefunction of an atomic orbital χ, which is now known as the Slater-type orbital (STO):

$$\chi_{\zeta,n,l,m}(r, \theta, \varphi) = N Y_{l,m}(\theta, \varphi) r^{n-1} e^{-\zeta r} \qquad \text{E 2.11}$$

where N is the normalisation constant to normalise the probability, $Y_{l,m}$ are the spherical harmonic functions and ζ (zeta) is a positive parameter known as the orbital exponent. n, l, m are the set of quantum numbers that describe the electron, with n being the principal quantum number that describes the energy level, l being the azimuthal quantum number that describes the orbital angular momentum and m being the magnetic quantum number that describes the projection of the orbital angular momentum along a unique axis. STO can be expensive to compute, so instead, a Gaussian-type orbital (GTO), which is given by:

$$\chi_{\zeta,n,l,m}(r,\theta,\varphi) = NY_{l,m}(\theta,\varphi)r^{2n-2-l}e^{-\zeta r^2} \qquad \text{E 2.12}$$

is more favourable in computation despite the slight loss in accuracy. (1-4). An example of the 1s orbital (principal quantum number n = 1, azimuthal quantum number l = 0) represented by the STO and GTO is shown in Figure 2.1.

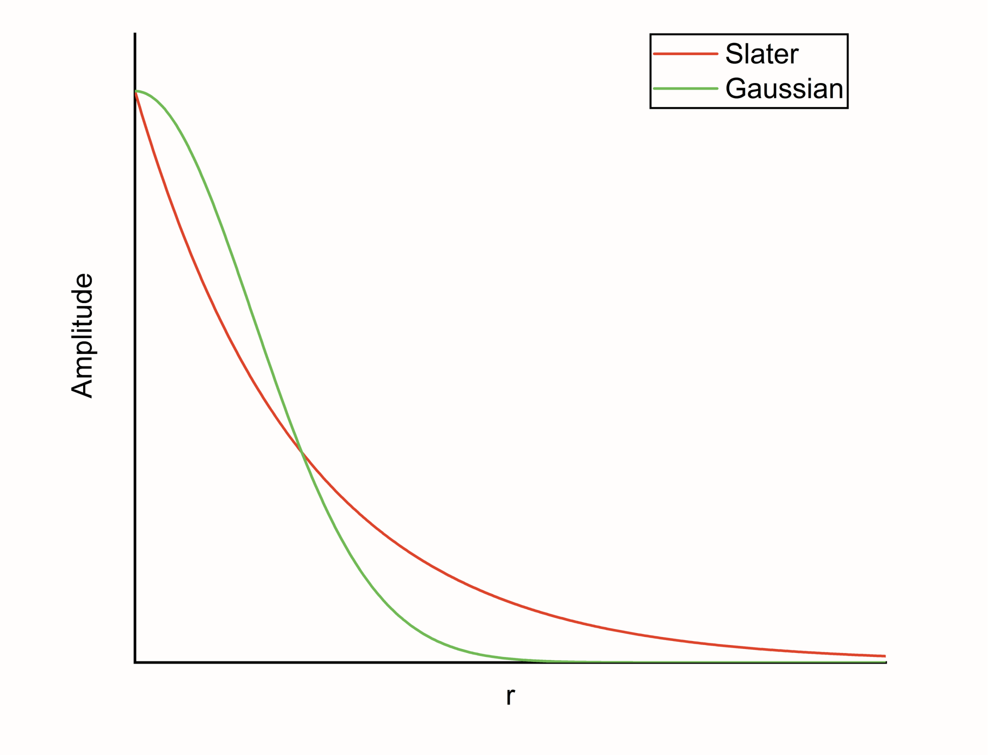

Figure 2.1 A plot of the amplitude of the 1s orbital (*n* = 1, *l* =0) represented by a Slater function (red) and a Gaussian function (green) versus the radius *r*.

In order to improve the accuracy in the representation of the orbitals, more GTOs have to be included in the calculations but this will increase the number of unknown coefficients c_i. Thus, a typical approach to balance between accuracy and computational expense is to group a few, let us say M, GTOs, where these individual GTO components are known as primitives, g, together as a linear combination to form something called contracted Gaussian functions χ_{contract}:

$$\chi_{\text{contract}} = \sum_{j=1}^{M} d_j g_j \qquad \text{E 2.13}$$

with a fixed contraction coefficient d. Figure 2.2 shows an example of a contracted Gaussian function formed from three primitives. The computations of the molecular orbitals will then be working with the linear combination of the contracted Gaussians:

$$\psi = \sum_{i=1}^{N} c_i' \chi_{\text{contract},i} \qquad \text{E 2.14}$$

With this approach the number of unknown coefficients having to be dealt with becomes the number of contracted Gaussians rather than the number of primitives (1-4).

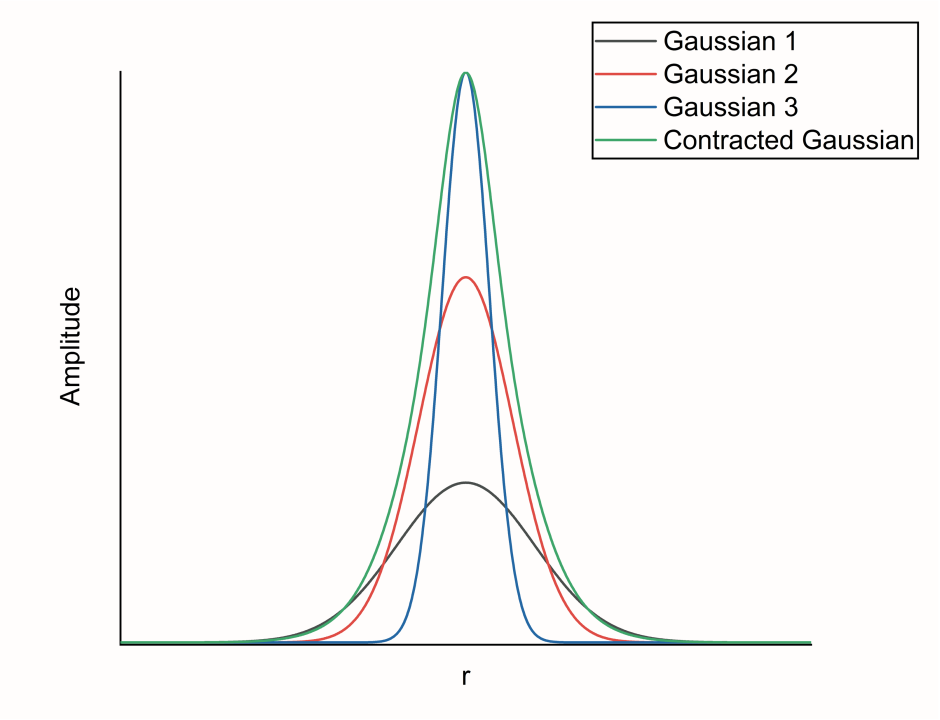

Figure 2.2 Example of the formation of a contracted Gaussian function (green) from three primitives (black, red, blue).

A minimal basis set can be constructed by representing each orbital with one contracted function, for example, the STO-*n*G basis set where each orbital is represented by a single STO-like contracted Gaussian formed from *n* primitives (8). However, there is significant discrepancy between such formalism with the actual orbital, in particular for the valence shell. Improvement can be made by representing an orbital with more sets of basis functions (1-4), for instance, a double-zeta(ζ) basis set or a triple-zeta(ζ) basis set meaning the valence orbitals are represented by two or three separate linear combinations respectively. To account for cases where the electron is far away from the nucleus, for example lone pair electrons or electrons in anions, diffuse functions should be included (1-4). This process is also known as augmentation, where diffuse functions are of the same form as the functions already included but more extended to cover the more distant portion of the orbital. To account for the distortion of orbitals by the surrounding environment, flexibility in the shape of the orbital can be provided by the inclusion of polarised functions, which are functions of a higher angular momentum l than those that describe the valence orbitals (1-4).

One of the categories of basis sets are the Pople basis sets (9, 10) and they are normally named as *A*-*BC*G for some numbers *A*, *B* and *C*. Some examples include 3-21G, 6-31G(d), 6-31+G(d,p) and 6-311++G(3df,2p). Their names can be understood in the following way. For the core orbitals, they are represented by one contracted Gaussian, with the number before the hyphen indicating the number of primitives included. The numbers after the hyphen give information about the number of primitives used to represent the valence orbitals. Two digits after the hyphen indicate a double-zeta basis set while three indicate a triple-zeta basis set, where each digit corresponds to the number of primitives in each of the linear combinations. A single '+' means the inclusion of additional diffuse functions for non-hydrogen atoms while '++' means the inclusion of additional diffuse functions for all atoms. The last part with the brackets indicate the inclusion of polarised functions, where the numbers and letters before the comma are for non-hydrogen atoms while after the comma are for hydrogen atoms. Thus, '(3df,2p)' means 3 sets of d-functions and 1 set of f-functions are added to non-hydrogen atoms while 2 sets of p-functions are added to hydrogen atoms. Some literature may use asterisks to indicate the inclusion of polarised functions, where '*' is equivalent to (d) meaning 1 additional set of d-function for non-hydrogen atoms while '**' is equivalent to (d,p).

Another category of basis sets are the Dunning's correlation-consistent (cc) basis sets (11-13), which are designed to account for electron correlation and be capable to be extrapolated to the complete basis set (CBS) limit. For cc basis sets, comparable amounts of improvement for the electron correlation energy are made when successful functions of higher angular momentum are included. Some examples include cc-pVDZ, aug-cc-pVTZ and jul-cc-pVQZ. For the nomenclature, they contain the 'cc-p' part, of which 'cc' indicates that they belong to the correlation-consistent basis sets while 'p' stands for polarised, meaning successively larger polarised functions are by default added upon using this category of basis sets. Orbital representations by multiple sets of basis functions are indicated by the suffix. Typically they are included in the name in the form of V*N*Z, where 'V' stands for valence while 'Z' stands for zeta, meaning each of the valence orbitals is represented by multiple (*N*) linear combinations, where *N* = D, T, Q, 5, … corresponds to double-, triple-, quadruple-, quintuple-, …, zeta basis sets respectively. The inclusion of diffuse functions, or in other words, augmentation, is indicated by the prefix. Full augmentation, meaning the inclusion of diffuse functions for orbitals of every atom and every level of angular momentum, is denoted by 'aug'. Partial augmentation can be denoted by the calendar basis set naming scheme (14), that is, 'jul', 'jun', 'may', 'apr', etc. Diffuse functions on hydrogen atoms are removed when 'aug' is replaced by 'jul'. Diffuse functions on the occupied orbitals with the highest angular momentum of the heavier atoms are removed when 'jul' is replaced by 'jun' and this deletion successively progresses to orbitals with lower angular momentum when moving to a previous calendar month.

2.1.1.2 Electronic structure methods

With basis sets providing a means to describe the wavefunction, the next thing to consider is the calculation method to solve the Schrödinger equation. As mentioned in the previous section, approximation methods are required for the electron correlation term and they can be classified in terms of the approach. For semi-empirical methods, the Schrödinger equation is simplified based on parameters obtained from experimental data (1-4). In contrast, ab initio methods, which will be explained in detail in the following, imply derivations from first principles and without empirical data, so the input will only be fundamental constants (1-4). Another type of method is based on Density Functional Theory (DFT), which considers the electron correlation through a functional of the electron probability density (1-4) rather than individual wavefunctions.

The simplest form of ab initio method is the Hartree-Fock method, also known as the mean-field method or self-consistent field (SCF) method, where the Fock operator f is involved. The Fock operator has a comparable form as the Hamiltonian operator shown in E 2.8 and acts on a molecular orbital, which is a collection of electronic wavefunctions. In the Fock operator, for the electron-electron interaction, instead of considering each electron-electron pair, it is treated as an interaction with a potential V^{HF} averaged over a given distribution of the other electrons in the system $[j]$ (1-4, 15):

$$f_i = -\frac{1}{2}\nabla_i^2 - \sum_k^{\mathrm{nuclei}} \frac{Z_k}{r_{ik}} + V_i^{\mathrm{HF}}[j] \qquad \text{E 2.15}$$

The calculations proceed by solving the secular equation:

$$\det|\boldsymbol{F} - \boldsymbol{\varepsilon S}| = 0 \qquad \text{E 2.16}$$

where $\boldsymbol{F}$ is the Fock matrix with elements given by:

$$F_{ij} = \int \psi_i^* f \psi_j \qquad \text{E 2.17}$$

$\boldsymbol{S}$ is the overlap matrix with elements given by:

$$S_{ij} = \int \psi_i^* \psi_j \qquad \text{E 2.18}$$

and $\boldsymbol{\varepsilon}$ is the diagonal matrix of the energies. A guess wavefunction expressed as a linear combination of basis set functions is provided as a starting point for the computation of $V^{\mathrm{HF}}[j]$. A new molecular orbital wavefunction is generated after solving in each iteration and it is then substituted back into E 2.16 (1-4, 15). After several iterations, ideally, convergence is reached.

It is also worthwhile to briefly mention about how to handle the electron spin in the computation process. For a restricted (R) calculation, the orbitals used are all doubly occupied, each accommodating two electrons of opposite spin (one with spin quantum number m_s +1/2 and the other with –1/2) (2-4). Thus, it is not suitable for species with unpaired electrons, for instance radicals. There are two ways to accommodate situations with unpaired electrons. For a restricted open-shell (RO) calculation, all electrons are forced to occupy doubly occupied orbitals except for those in open-shell orbitals while for an unrestricted (U) calculation, this restriction is lifted. The unrestricted formalism was chosen for the calculations done in this work.

As the Hartree-Fock method considers the average effect only, the exact electron-electron interaction is poorly represented. The Hartree-Fock method only takes into account of the exchange interaction arising from the Pauli exclusion principle which states that no two identical electrons can have the same set of quantum numbers (principal quantum number, azimuthal quantum number, magnetic quantum number and spin quantum number). The difference between the actual energy value and the value obtained from the Hartree-Fock method using a complete basis set is known as the electron correlation energy. The aim to improve upon the Hartree-Fock results with a better description of the electron correlation led to the invention of a range of post-SCF methods (1-4). These methods include the configuration interaction (CI) calculation (16, 17), Møller-Plesset (MP) many-body perturbation theory (18) and the coupled-cluster (CC) method (19).

For the CI method, the wavefunction ψ is represented as a linear combination of orbitals:

$$\psi = c_0\psi^{\mathrm{HF}} + c_1\psi_1 + c_2\psi_2 + \cdots \qquad \text{E 2.19}$$

where the leading term, which is the dominant one, contains the Hartree-Fock wavefunction ψ^{HF}. The wavefunctions in the subsequent terms are formed by exciting electrons from occupied orbitals to virtual orbitals and a full CI calculation means all possible excitations are considered (1-4, 16). Due to the constraint of computational resources, the excitations considered are often truncated. For example, if single excitations (denoted by S) are considered, a $\sum_{a,p} c_a^p \psi_a^p$ term will be included and if double excitations (denoted by D) are considered, a $\sum_{\substack{a<b \\ p<q}} c_{ab}^{pq} \psi_{ab}^{pq}$ term will be included, where a, b are occupied orbitals while p, q are virtual orbitals (1-4, 16). Thus, CISD means the configuration interaction with single and double excitations. An improvement on the CI method is the quadratically convergent configuration interaction (QCI) theory. It is derived from the CI method by including more higher order terms and the resulting expression is found to be similar to that from the CC method except omitting some terms which are computationally expensive (1, 2, 20, 21).

For MP perturbation theory, it refines the description of the effect of electron correlation of the Hartree-Fock wavefunction ψ^{HF} by considering perturbation terms (1-4, 18). The electronic Hamiltonian is considered as:

$$\widehat{H} = \widehat{H^{(0)}} + \lambda \widehat{H^{(1)}} + \lambda^2 \widehat{H^{(2)}} + \cdots \qquad \text{E 2.20}$$

where $\widehat{H^{(0)}}$ is the Hartree-Fock Hamiltonian and the latter terms are the perturbation terms with some arbitrary parameter λ. The ground-state wavefunction is given by:

$$\psi_0 = \psi_0^{(0)} + \lambda \psi_0^{(1)} + \lambda^2 \psi_0^{(2)} + \cdots \qquad \text{E 2.21}$$

and the energy is given by:

$$E_0 = E_0^{(0)} + \lambda E_0^{(1)} + \lambda^2 E_0^{(2)} + \cdots \qquad \text{E 2.22}$$

The first-order correction to the energy $E_0^{(1)}$ will then be the expectation value of $\widehat{H^{(1)}}$:

$$E_0^{(1)} = \int \psi_0^* \widehat{H^{(1)}} \psi_0 \qquad \text{E 2.23}$$

and the second-order correction to the energy $E_0^{(2)}$ will be given by (1-4, 18):

$$E_0^{(2)} = \sum_{j \neq 0} \frac{\int \psi_j^* \widehat{H^{(1)}} \psi_0 \int \psi_0^* \widehat{H^{(1)}} \psi_j}{E_0^{(0)} - E_j^{(0)}} \qquad \text{E 2.24}$$

These series of MP methods are named as MPn, where n is the order of perturbation terms included, for instance MP2 refers to the summation up to the $E_0^{(2)}$ term while MP4 refers to the summation up to the $E_0^{(4)}$ term.

For the CC method, the exact wavefunction ψ is related to that calculated from the Hartree-Fock method ψ^{HF} with the cluster operator C (1-4, 19) by:

$$\psi = e^{C}\psi^{\mathrm{HF}} \tag{E 2.25}$$

where C is a summation of i-electron excitation operator C_i:

$$C = C_1 + C_2 + \cdots + C_N \tag{E 2.26}$$

The naming of the CC series of methods depend on the C_i included, where S denotes singular (C_1), D denotes double (C_2), T denotes triple (C_3) and so on (1-4, 19). Thus, CCSDT means C is given by the sum of C_1, C_2 and C_3 in the computation process, that is, coupled-cluster including the exact single, double and triple excitations (and approximations of the higher-order ones). It is also important to note the difference between CCSDT and CCSD(T), where the pair of brackets indicate that the contribution from the term inside is calculated with many-body perturbation theory (1, 2). Therefore, CCSD(T) means coupled-cluster including single and double excitations and perturbative treatment of triple excitations.

Instead of using the wavefunction approaches for the methods discussed above, DFT takes into account of the spatial distribution of electron density $\rho(\boldsymbol{r})$ where, physically speaking, an integration of the electron density gives the position-dependent number of electrons. Hohenberg and Kohn (22) demonstrated that instead of considering each individual configuration of the wavefunction, the ground-state energy of a molecule E can also be expressed as a functional of the ground-state electron density function ρ:

$$E[\rho] = T[\rho] + \int \rho(\boldsymbol{r})\, v(\boldsymbol{r}) d\boldsymbol{r} + V_{\mathrm{ee}}[\rho] \tag{E 2.27}$$

where $T[\rho]$ is the kinetic energy term, $\int \rho(\boldsymbol{r})\, v(\boldsymbol{r}) d\boldsymbol{r}$ is the term corresponding to the electron-nuclei potential energy, of which the interaction between electrons and nuclei is expressed as an external potential $v(\boldsymbol{r})$, and $V_{\mathrm{ee}}[\rho]$ is the electron-electron potential energy term, which can be expressed as the sum of the classical Coulombic part $J[\rho]$ and the quantum mechanical correction part (1-4, 22). Similar to the wavefunction, the variational principle also applies to the electron density. The essence of the energy calculation using DFT is to mimic the actual scenario containing interacting electrons with a reference system, named as “ref” for the time being, with identical electron density ρ but containing non-interacting electrons represented by one-electron Kohn-Sham orbitals ψ^{KS} (23). The energy can then be written as:

$$E[\rho] = T[\rho] + \int \rho(\boldsymbol{r})\, v(\boldsymbol{r}) d\boldsymbol{r} + V_{\mathrm{ee}}[\rho] \qquad \text{E 2.28}$$

$$= T_{\mathrm{ref}}[\rho] - T_{\mathrm{ref}}[\rho] + T[\rho] + \int \rho(\boldsymbol{r})\, v(\boldsymbol{r}) d\boldsymbol{r} + J[\rho] - J[\rho] + V_{\mathrm{ee}}[\rho]$$

$$= T_{\mathrm{ref}}[\rho] + \int \rho(\boldsymbol{r})\, v(\boldsymbol{r}) d\boldsymbol{r} + J[\rho] + E_{\mathrm{XC}}[\rho]$$

where the exchange-correlation energy $E_{\mathrm{XC}}[\rho]$ which is contributed from the remainder of interelectronic interaction is given by:

$$E_{\mathrm{XC}}[\rho] = T[\rho] + V_{\mathrm{ee}}[\rho] - (T_{\mathrm{ref}}[\rho] + J[\rho]) \qquad \text{E 2.29}$$

The exchange-correlation energy functional $E_{\mathrm{XC}}[\rho]$ can also be expressed as a sum of the exchange functional $E_{\mathrm{X}}[\rho]$ and the correlation functional $E_{\mathrm{C}}[\rho]$. A Schrödinger-like equation, now known as the Kohn-Sham equation (1-4, 23, 24), can be set up as follows:

$$h_i^{\mathrm{KS}} \psi^{\mathrm{KS}}(i) = \varepsilon^{\mathrm{KS}} \psi^{\mathrm{KS}}(i) \qquad \text{E 2.30}$$

where the Kohn-Sham Hamiltonian h_i^{KS} is given by:

$$h_i^{\mathrm{KS}} = -\frac{\hbar^2}{2m_e}\nabla_i^2 + \int \frac{e^2 \rho(\boldsymbol{r}_k)}{|\boldsymbol{r}_i - \boldsymbol{r}_k|} d\boldsymbol{r}_k + v(\boldsymbol{r}_i) + v_{\mathrm{XC}}(\boldsymbol{r}_i) \qquad \text{E 2.31}$$

with each of the four terms corresponds to the four terms in E 2.28, namely kinetic energy, electron-nuclei potential energy, classical electron-electron potential energy and exchange-correlation potential energy respectively. The complexity again lies on the last term $v_{\mathrm{XC}}(\boldsymbol{r}_i)$, which leads to the development of different DFT methods to approximate this exchange-correlation potential (1-4). The simplest form to approximate the exchange-correlation term is the local density approximation (LDA), where $E_{\mathrm{XC}}^{\mathrm{LDA}}$ is solely given by a function f on the electron density ρ:

$$E_{\mathrm{XC}}^{\mathrm{LDA}}[\rho] = \int f(\rho(\boldsymbol{r}))\, d\boldsymbol{r} \qquad \text{E 2.32}$$

Improvements on the approximation scheme can be done by also considering the dependence on the gradient ∇ of the electron density, leading to the generalised gradient approximation (GGA) method:

$$E_{\mathrm{XC}}^{\mathrm{GGA}}[\rho] = \int f\big(\rho(\boldsymbol{r}), \nabla\rho(\boldsymbol{r})\big)\, d\boldsymbol{r} \qquad \text{E 2.33}$$

Further extensions give the meta-generalised gradient approximation (mGGA), which includes the contribution from the Laplacian ∇^2 of the electron density as well as the kinetic energy density τ:

$$E_{\mathrm{XC}}^{\mathrm{mGGA}}[\rho] = \int f\big(\rho(\boldsymbol{r}), \nabla\rho(\boldsymbol{r}), \nabla^2\rho(\boldsymbol{r}), \tau(\boldsymbol{r})\big)\, d\boldsymbol{r} \qquad \text{E 2.34}$$

Apart from the traditional functionals, hybrid functionals have also been developed, where the exchange-correlation is a linear combination of a mixture of Hartree-Fock exchange $E_{\mathrm{X}}^{\mathrm{HF}}$ and density functional exchange-correlation. Different hybrid functionals have been designed by altering the exchange-correlation components included and their respective weightings. Some examples of hybrid functional methods include B3LYP (Becke 3-parameter Lee-Yang-Parr) (25), where the exchange-correlation functional is defined as:

$$E_{\mathrm{XC}}^{\mathrm{B3LYP}} = 0.2E_{\mathrm{X}}^{\mathrm{HF}} + 0.8E_{\mathrm{X}}^{\mathrm{LSDA}} + 0.72\Delta E_{\mathrm{X}}^{\mathrm{Becke88}} + 0.19E_{\mathrm{C}}^{\mathrm{VWN}} + 0.81E_{\mathrm{C}}^{\mathrm{LYP}} \qquad \text{E 2.35}$$

and BHandHLYP (Becke half-and-half Lee-Yang-Parr) (26), where the exchange-correlation functional is defined as:

$$E_{\mathrm{XC}}^{\mathrm{BH\&HLYP}} = 0.5E_{\mathrm{X}}^{\mathrm{HF}} + 0.5E_{\mathrm{X}}^{\mathrm{LSDA}} + 0.5\Delta E_{\mathrm{X}}^{\mathrm{Becke88}} + E_{\mathrm{C}}^{\mathrm{LYP}} \qquad \text{E 2.36}$$

More complicated hybrid functionals which aim to improve the accuracy have later been developed, such as the series of Minnesota functionals. An example that is used in this work is M06-2X (27) released in 2006 with a doubling of the Hartree-Fock exchange contribution, which consists of 32 fitted parameters apart from $0.54E_{\mathrm{X}}^{\mathrm{HF}}$ component.

For systems at low velocities compared with the speed of light c, the laws of Newtonian mechanics apply. However, when the velocity becomes comparable with the speed of light, the effect of relativity has to be considered. One consequence from the effect of relativity is that the relativistic mass m_{rel} of an electron is now given by:

$$m_{\mathrm{rel}} = \frac{m_e}{\sqrt{1 - \frac{v_e^2}{c^2}}} \qquad \text{E 2.37}$$

where m_e is the rest mass of electron and v_e is the velocity. Consider the Schrödinger equation in E 2.1, the Hamiltonian operator depends on the momentum and mass, which means modifications to the Hamiltonian operator are required in order to correct for the relativistic effect (1, 2, 28). According to the Bohr model of a hydrogenic atom, the following relationship holds:

$$\frac{v_e}{c} = \frac{Z\alpha}{n} \qquad \text{E 2.38}$$

where Z is the atomic number, n is the principal quantum number and α is the Sommerfeld's fine-structure constant. Thus, given a larger Z, the velocity of an electron in an orbital of a heavier atom is higher than that in the same orbital of a lighter atom and relativistic effect is more significant in heavier atoms. It is suggested that the substantial relativistic effect have to be taken into account of during the calculations for atoms beyond the first three rows of the Periodic Table (Z > 36) (1, 2, 28). In this work, as the heaviest atom considered is sulphur, which has an atomic number of 16, together with the constraint of computational resources, only non-relativistic calculations have been performed. Error due to the relativistic effect for the results presented in this work is expected to be larger for the sulphur-bearing species than other species containing lighter atoms. Relativistic calculations should reduce this error and provide more accurate results but the actual details of such computations are beyond the scope of this thesis.

2.1.1.3 Level of theory selection, errors and computational expenses

As suggested in previous sections, approximations are needed in order to make the computations feasible. Errors are involved following the application of approximations, which can undermine the accuracy of the results. However, the hardware available poses a limit on the computational resources, including time and memory. Therefore, it is important to strike a balance between accuracy and computational costs when choosing the level of theory for calculations.

Table 2.1 Mean absolute deviation from the composite method in the calculated electronic energies of 11 glucose conformers at the HF level with different basis sets. Adapted from Cramer (1).

Basis set	Mean absolute deviation (kJ mol^{-1})
STO-3G	4.6
3-21G	8.4
6-31G(d)	0.8
cc-pVDZ	0.4

Table 2.2 Mean absolute deviation from experiments in the calculated atomisation energies (energies required for the complete separation of all atoms in the species) of a collection of molecules and ions formed from elements in the first two rows at various levels of theory with different basis sets. Adapted from Feller and Peterson (29).

Method	Basis set	Mean absolute deviation (kJ mol^{-1})
HF	aug-cc-pVDZ	355
HF	aug-cc-pVTZ	276
HF	aug-cc-pVQZ	255
CCSD	aug-cc-pVDZ	88
CCSD	aug-cc-pVTZ	46
CCSD	aug-cc-pVQZ	29
CCSD(T)	aug-cc-pVDZ	75
CCSD(T)	aug-cc-pVTZ	21
CCSD(T)	aug-cc-pVQZ	8

Table 2.3 Root mean square error compared to the CBS limit in the calculated electronic energies of the S22 set of noncovalent dimers and bimolecular complexes formed from C, N, O and H only at the B3LYP level with different basis sets. Adapted from Witte et al. (30).

Basis set	Root mean square error (kJ mol^{-1})
6-31G(d)	11.42
cc-pVDZ	7.15
6-31++G(d,p)	3.14
6-311++G(d,p)	2.93
aug-cc-pVDZ	3.14
cc-pVTZ	4.14
6-311++G(3df,3pd)	2.09
aug-cc-pVTZ	0.88

A source of error is from the basis sets selected. A complete infinite basis set can represent any orbital exactly and the use of a finite basis set gives rise to the basis set truncation error. Choosing a basis set that can minimise the error within the computational constraints depends on the species being studied. For instance, it is straightforward that polarised functions should be included in the basis sets for species with significant polarizability, and diffuse functions should be included for hydrogen bonding, anions, lone pair electrons and reacting intermediates due to an increased separation between the electron and the nucleus. In this work, the species involved include radicals, small organic molecules, transition states and intermediates formed from their abstraction, addition and isomerisation reactions, van der Waals complexes, and dimers, which all consist of non-metallic elements in the first two rows of the Periodic Table. Presented below are results from some previous benchmark studies on the errors in the calculated energies of some comparable species. Table 2.1 shows the calculations for glucose conformers ($C_6H_{12}O_6$) (1) where small basis sets (STO-3G, 3-21G) give a bigger error than large basis sets with the inclusion of polarised functions (6-31G(d), cc-PVDZ, cc-pVTZ). A similar trend, where a larger basis set performs better, can also be seen for the calculations on a wide collections of small molecules and ions made of elements in the first two rows (29), as shown in Table 2.2. Table 2.3 shows the results for the S22 dataset (30) which consists of 22 noncovalent dimers and complexes of small- and medium-sized molecules containing only C, N, O and H. It is observed that basis set augmentation is effective in reducing the error and improving the accuracy in the energy calculations for these complexes with intermolecular noncovalent interactions.

During the calculations for weakly bound complexes, for example a noncovalent dimer, which will be the main focus in Chapter 6, the use of finite basis sets can give rise to a basis set superposition error (1-4). The interaction energy can be computed from the energy difference between the dimer and the sum of the two separated monomers. With the same finite basis set, when calculating the energies for the individual monomers, the orbitals are described by basis functions centred on atoms of the separated monomer only. However, when calculating for the whole dimer, the orbitals are described by basis functions centred on all the atoms, and the resulting overlapping in effect enlarges the actual basis set representing the complex compared with that of the individual components. This will erroneously lower the calculated energy of the dimer relative to the two separated monomers. One approach to correct this error is to use the counterpoise method (1-4). During the calculations for the individual monomer, apart from the basis functions centred on atoms of that component, basis functions of ghost atoms of the other component are added such that the actual basis set is mixed in the same way as that for the whole complex. Another way to overcome this error is to extrapolate to the complete basis set limit. For example, a feature of the Dunning basis sets (11-13) is the possibility to extrapolate to a complete basis set from finite basis sets (31-33). Energy calculations on the same species can be performed using aug-cc-pVTZ, aug-cc-pVQZ and aug-cc-pV5Z basis sets. If the values show an asymptotic trend, formulae can be used to extrapolate to the complete basis set limit.

Table 2.4 Mean absolute deviation from the full CI in the calculated electronic energies of HB, H_2O and HF at the equilibrium geometries using various methods. Adapted from Cramer (1).

Method	Mean absolute deviation (kJ mol^{-1})
MP2	43.51
MP4	5.44
CISD	24.27
QCISD	7.11
CCSD	7.95
QCISD(T)	1.26
CCSD(T)	1.26

Table 2.5 Mean absolute deviation from the W1 model in the calculated electronic energies of selected nonbonded complexes formed from elements in the first two rows at various levels of theory using the aug-cc-pVTZ basis set. Adapted from Zhao and Truhlar (35).

Method	Mean absolute deviation (kJ mol^{-1})
MP2	1.87
B3LYP	2.81
BHandHLYP	2.30

Table 2.6 Root mean square error in the calculated electronic energies of the MGCDB84 database consists of various atoms, molecules, dimers and clusters at different levels of theory. Adapted from Mardirossian and Head-Gordon (36).

Method	Root mean square error (kJ mol^{-1})
B3LYP	12.72
M06-2X	1.38

The next thing to consider apart from the basis sets in the discussion of errors is the electronic calculation method selected. As shown in Table 2.2, the Hartree-Fock method performs rather poorly in obtaining an accurate energy value as the exact electron correlation cannot be meticulously described by a mean-field potential. The performance of different post-SCF methods, including configuration interaction, Møller-Plesset and coupled-cluster, on small species formed from elements in the first two rows are shown in Table 2.2 and Table 2.4. The general trend is that the inclusion of higher order terms reduces the error. In particular, the CCSD(T) method has a high accuracy in energy calculation and thus is commonly known as the golden standard (34). The performance of selected DFT methods are presented in Table 2.5 and Table 2.6. Table 2.5 shows the deviations from the values obtained from the W1 model, which is a composite method that includes the extrapolation to the CBS limit of a CCSD(T) calculation, core-valence electron correlation corrections and relativistic corrections (35), on a list of selected nonbonded complexes formed from elements in the first two rows where any one of the four interactions is involved: hydrogen bonding, charge transfer, dipole interactions, and weak interactions. Table 2.6 shows the results on the MGCDB84, a Main Group Chemistry DataBase constructed from 84 previously reported benchmark data-sets (36), which consists of a wide range of atoms, ions, organic molecules of various sizes, weakly bounded complexes, dimers and clusters. For B3LYP and BHandHLYP, their accuracy is comparable to that of MP2. M06-2X, which is a highly fitted hybrid functional recommended for main-group thermochemistry and kinetics (27), shows a better performance on the MGCDB84 database compared with B3LYP.

Apart from the energy calculation, the calculation method and basis set chosen also lead to an error in the geometry optimisation and frequency calculation, which involve the evaluation of the derivates of the energy values. For vibrational frequencies, actual spectra collected from experiments, although this is not possible for some intermediates, can be used to assess the deviation in the calculated values. By compiling the data for sufficient species, the offset can be known and corrected by multiplying by a scaling factor c. The equation solved in the benchmark studies to find the scaling factor for a particular level of theory is the following (37):

$$c = \frac{\Sigma(\nu_{i,\mathrm{expt}} \cdot \nu_{i,\mathrm{calc}})}{\Sigma(\nu_{i,\mathrm{calc}}{}^2)} \qquad \text{E 2.39}$$

where $\nu_{i,\mathrm{expt}}$ and $\nu_{i,\mathrm{calc}}$ are the experimental and calculated vibrational frequencies for the i-th vibrational mode respectively. Typically this scaling factor, which is based on the average of all the vibrations, lies in the range between 0.8 and 1. An example of a database compiling the scaling factors for different levels of theory is the Database of Frequency Scale Factors for Electronic Model Chemistries by the Truhlar group (38).

Table 2.7 Mean absolute deviation from experiments in the calculated atomisation energies of a selected set of molecules consisting of C, N, O, F and H only at different levels of theory based on geometries optimised at different levels. Adapted from Martin (39).

Level of theory		Mean absolute deviation (kJ mol^{-1})
Energy	**Geometry**	
CCSD(T)/cc-pVDZ	CCSD(T)/cc-pVDZ	10.84
CCSD(T)/cc-pVTZ	MP2/6-31G(d)	3.85
CCSD(T)/cc-pVTZ	CCSD(T)/cc-pVDZ	3.97
CCSD(T)/cc-pVTZ	CCSD(T)/cc-pVTZ	3.89

For geometry optimisation, errors do exist for the optimised geometric parameters, but if in the end the energies of the calculated species are what is of interested, the errors in energies contributed from the level of theory chosen for the geometry optimisation is found to be less significant than that for the energy calculation based on the optimised geometry obtained. Table 2.7 compares the contribution to the errors in energies from the method used for energy calculation with that for geometry optimisation. For the same species, starting with a geometrical structure optimised at the same level of theory, using a more accurate method for the energy calculation step can help refine the theoretical energy value. On the other hand, even when the geometry optimisation step is done with a different level of theory, the error does not differ much given using the same level of theory for the energy calculation (39). However, it is worth noting that these benchmarks are obtained from the energy minima on the PES, the situation for the transition states can be different, where potentially there can be noticeable deviation for the geometric parameters across different levels of theory.

Another aspect to consider in running calculations is the computational expense. It is obvious that using a larger basis set requires more computational resources. Typically the computational cost scales as a factor of the number of basis functions *N*, and the exponent is determined by the calculation method used. Table 2.8 lists the scaling factor of the cost for various ab initio methods. The cost for the simplest ab initio method, Hartree-Fock, scales as N^4 and other post-SCF methods vary even as a higher order of *N*. In contrast, the cost for DFT methods in general varies no worse than N^3 (1), which is a feature that makes DFT methods more favourable to be chosen for calculations.

Table 2.8 The scaling in computational cost for Hartree-Fock and post-SCF methods. Adapted from Cramer (1).

Relative scale in cost	Method
N^4	HF
N^5	MP2
N^6	CISD, CCSD, QCISD
N^7	MP4, CCSD(T), QCISD(T)
N^8	CCSDT

The nature of the calculation job also determines the computational cost. Running an optimisation calculation typically requires more computational resources than a “single-point” energy calculation at the same level of theory for the same species. While energy calculation jobs only require the evaluation of the single-point energy, for each optimisation step, the programme already needs to evaluate the energy and the derivatives. The number of steps needed in an optimisation job, as well as the computational time, also depends on how far off the initial input structure is compared with the optimised one.

Considering the ratio between performance and cost, a practical way is to run the optimisation jobs at a lower level of theory followed by refining the energy values at a higher level of theory, for example including higher-order perturbation terms or using a larger basis set. For such a calculation scheme, the naming convention in the literature for the level of theory used is *energy_method/energy_basis_set//geometry_method/geometry_basis_set* (4), where the first half refers to the level of theory used in energy calculation and the latter refers to that used in geometry optimisation which gives the structure to be based on during energy calculation.

In this thesis, geometry optimisations and frequency calculations are typically performed using the BHandHLYP/aug-cc-pVDZ and M06-2X/aug-cc-pVTZ levels of theory and then a refined energy value is obtained for the optimised structure using the CCSD(T)/aug-cc-pVTZ level of theory.

This work was undertaken on ARC3 and ARC4 (40), part of the High Performance Computing facilities at the University of Leeds, UK. ARC3 has 252 standard nodes with 24 cores and 128GB of memory each and 4 high memory nodes with 24 cores and 768GB of memory each. ARC4 has 149 standard nodes with 40 cores and 192GB of memory each and 2 high memory nodes with 40 cores and 768GB of memory each. Typically, the longest allowed computational time per calculation job requested is 48 hours.

2.1.2 Methodology for performing computations via the Gaussian programme

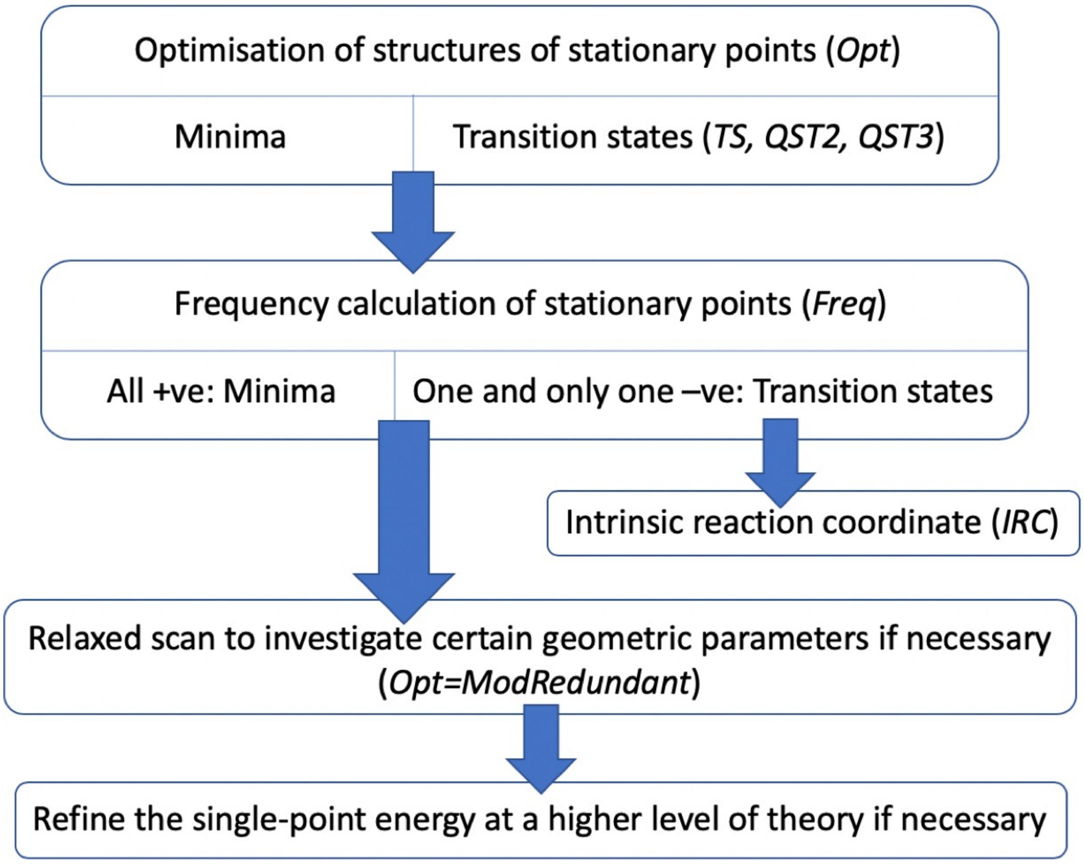

Figure 2.3 A flow diagram of the key procedures involved in the exploration of the potential energy surface with ab initio methods. The italics within the brackets are the relevant keywords used in Gaussian to perform the calculations. See text for more details.

The exploration of the potential energy surface involves optimisations of the geometrical structures of the stationary points, vibrational frequency calculations, verifications of the linkages between stationary points and energy calculations. A standard procedure performed by the author in the University of Leeds will be explained in this section and the essential steps are shown in Figure 2.3. There are many quantum chemistry programmes that can serve the purpose of performing ab initio electron structure calculations, including but not limited to, Gaussian (41), Molpro (42), GAMESS (43), MOLCAS (44), PSI (45) and Q-Chem (46). In this work, all electronic structure calculations were carried out using the Gaussian 09 programme (41), where further details for the input and output files can be found in Appendix A.

2.1.2.1 Finding stationary points

The first step of the calculations was to find and optimise the structures of the stationary points, which include reactants, products, intermediates and transition states. An approximate structure based on chemical intuition including the relative positions of the atoms present was supplied as input and optimisation was carried out by Gaussian using the Berny optimisation algorithm (47) which involves the evaluation of the analytical gradients (derivatives). The Hessian matrix containing the second-order partial derivatives, which is an estimate in the first step, keeps being updated throughout the optimisation. The derivatives of the latest step are compared with the previous step having lowest energy. The change of energy and displacement for the next projected step are used as convergence criteria of the optimisation (4). It is possible to select the tightness of the convergence criteria for the optimisation job in the Gaussian programme. Also, particularly for the calculations using DFT which involve the numerical integration of the functional, the fineness of the integration grid can be selected in the Gaussian programme. A possible option is a ‘pruned (99,590) ultrafine grid’, which will appear in later chapters. ‘Pruned grids’ are optimised to use the minimal number of points to attain a given level of accuracy and ‘(99,590)’ means the grids have 99 radial shells and 590 angular points per shell.

An example shown here below in Figure 2.4 is for the search and optimisation of a potential van der Waals’ complex in the CN + CH_2O reaction. An initial structure with a CN radical being placed near a CH_2O molecule, about 2.5 – 3 Å apart, was used in this case and the programme gradually changed the geometric parameters to attain an optimised structure.

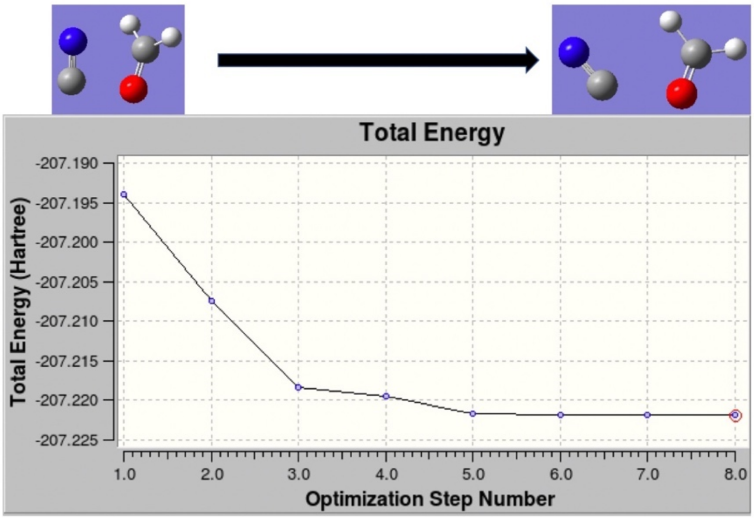

Figure 2.4 Output of the optimisation calculation of CN + CH_2O van der Waals' complex using Gaussian at the M06-2X/aug-cc-pVTZ level of theory. The initial structure is shown in the top left hand corner while the optimised structure is shown in the top right hand corner. The distance between the two carbon atoms in the optimised structure: 2.746 Å. The plot shows how the electronic energy is minimised during the optimisation. 1 Hartree = 2625.5 kJ mol^{-1}.

2.1.2.2 Characterisation of stationary points from vibrational frequencies

The subsequent procedure after obtaining the optimised structure was to characterise it by performing vibrational frequency calculations, which involves the evaluation of the second derivatives of the energy. For a minimum point on the PES, all frequency values should be positive while for a transition state, there should be one and only one imaginary vibrational frequency, of which the motion corresponds to the direction of the reaction. Going back to the example of the van der Waals complex formed in the CN + CH_2O reaction, it can be seen in Figure 2.5 that all of its frequency values are positive.

While single point energy calculations and optimisation only considered the electronic energy, calculations of vibrational frequencies helped evaluate zero-point vibrational energies (ZPVE). The ZPVE calculated from the harmonic frequencies can be generated simply using the *Freq* keyword in Gaussian. However, due to the fact that approximation methods are used in the exploration of the PES and also the actual potential well is not a perfect harmonic oscillator, there are discrepancies between the calculated harmonic frequency values, as well as ZPVE, from Gaussian with the experimental ones. To account for these errors, the calculated ZPVE was then multiplied by the scaling factor unique to the level of theory used. Gaussian also provides the *Anharmonic* option under the *Freq* keyword, where the frequency values obtained will be based on the anharmonic model rather than the harmonic oscillator, but more computational resources will be required. Further discussions on the harmonic and anharmonic oscillators will be covered in the next section on rate coefficient calculations.

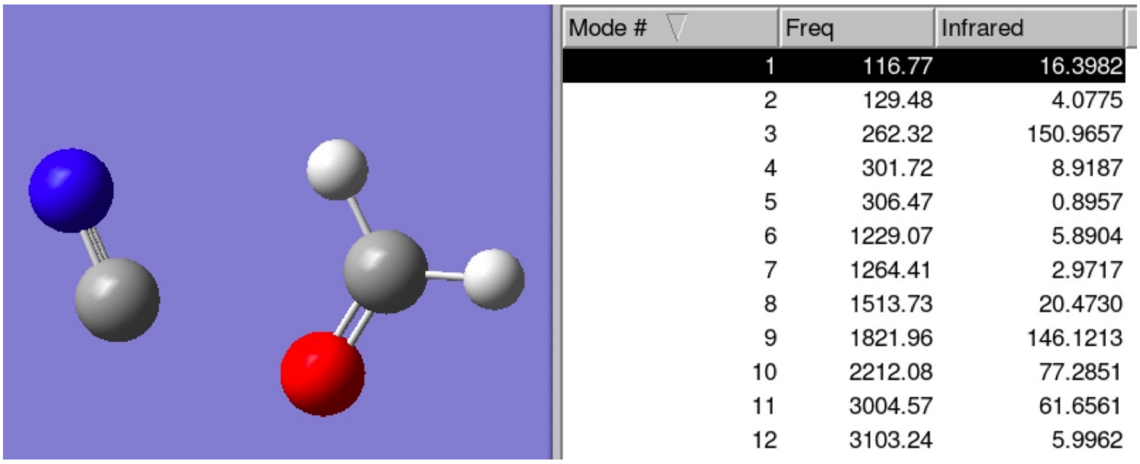

Mode #	Freq	Infrared
1	116.77	16.3982
2	129.48	4.0775
3	262.32	150.9657
4	301.72	8.9187
5	306.47	0.8957
6	1229.07	5.8904
7	1264.41	2.9717
8	1513.73	20.4730
9	1821.96	146.1213
10	2212.08	77.2851
11	3004.57	61.6561
12	3103.24	5.9962

Figure 2.5 Output of the frequency calculation of CN + CH_2O van der Waals' complex using Gaussian at the M06-2X/aug-cc-pVTZ level of theory. "Mode" stands for different vibrational modes of the complex; "Freq" stands for the calculated vibrational frequency in cm^{-1}; and "Infrared" stands for the corresponding predicted relative intensity on an infrared spectrum. Distance between the two carbon atoms: 2.746 Å.

Apart from vibrational frequency values, rotational constants can also be found in the output file.

2.1.2.3 Verification of linkage between stationary points

After the identification and classification of the stationary points, the next step is to verify the linkage between them on the PES. For transition states, intrinsic reaction coordinate (IRC) calculations were performed. The steepest-descent path on the PES from the transition state to a minimum point is known as the minimum energy path (MEP), while the IRC is the MEP in mass-weighted coordinates, which means . IRC calculations involved forward and backward tracing along the PES following the direction corresponding to the imaginary frequency such that the linkage with the respective minima was verified. As an example, Figure 2.6 illustrates the results from the IRC calculations performed upon a transition state found in the CN + CH_2O reaction, and shows that it corresponds to the transition state leading to the formation of HNC + HCO.

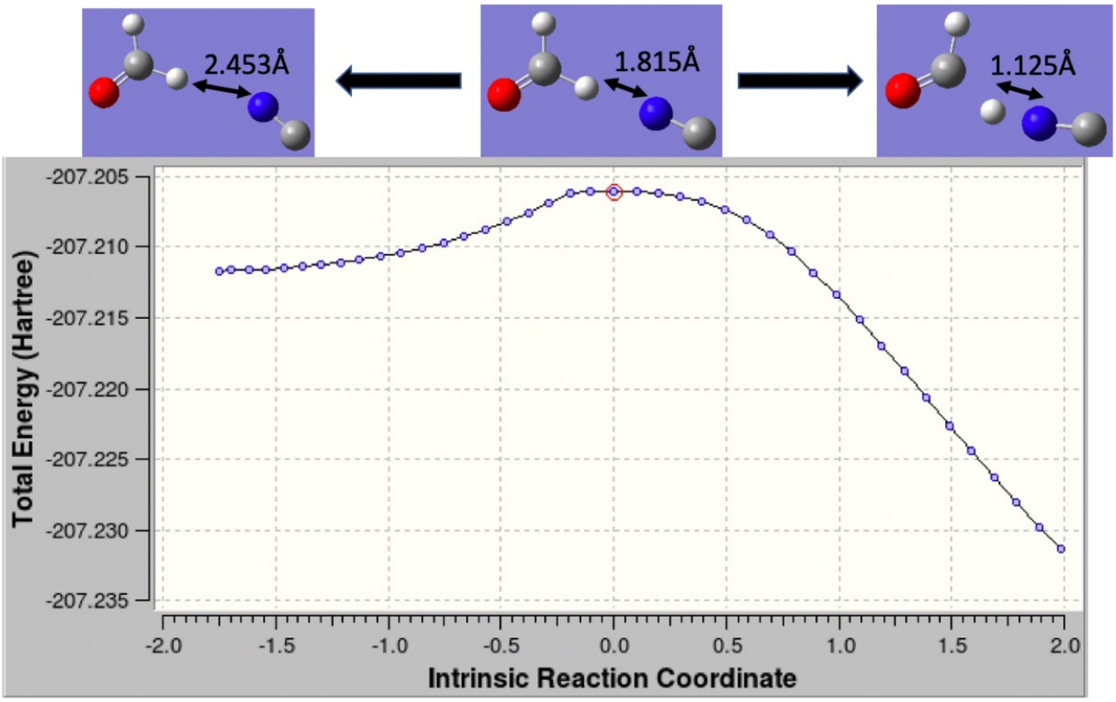

Figure 2.6 Output of the IRC calculation of the transition state leading to the formation of HNC + HCO in the CN + CH_2O reaction using Gaussian at the M06-2X/aug-cc-pVTZ level of theory. y-axis denotes the electronic energy (ZPVE uncorrected) in Hartree, where 1 Hartree = 2625.5 kJ mol^{-1}.

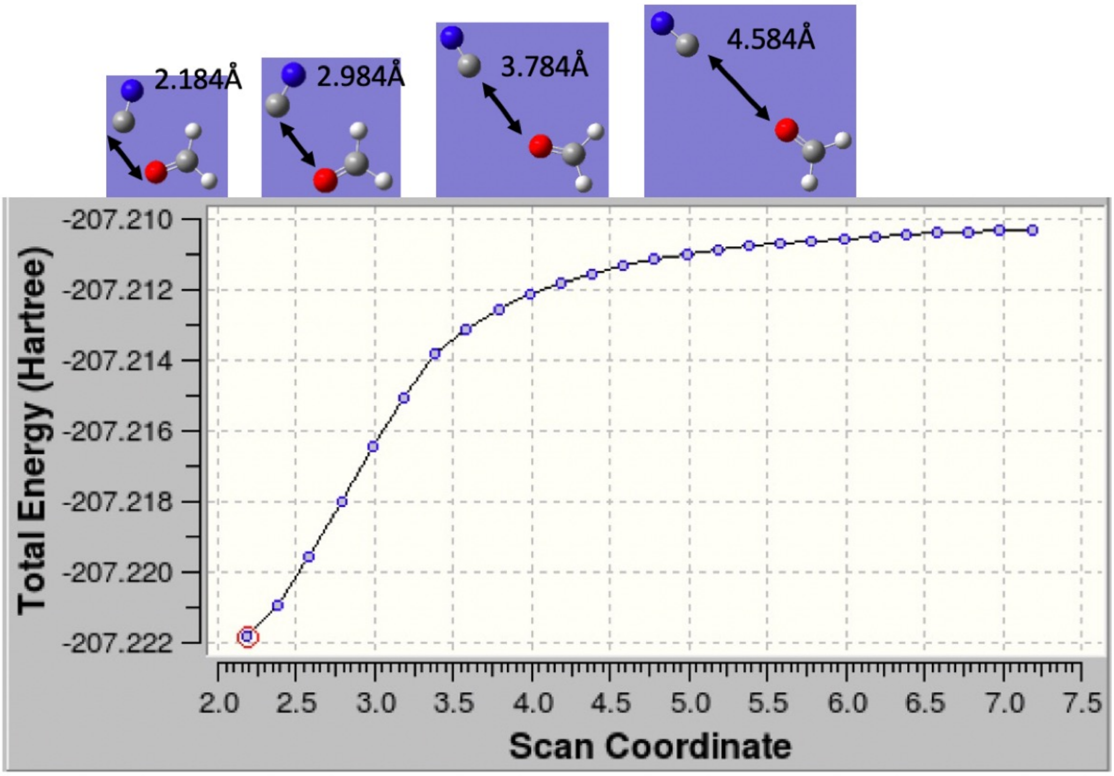

Figure 2.7 Output of the relaxed scan investigating in the approach of CN towards the oxygen side of CH_2O using Gaussian at the M06-2X/aug-cc-pVTZ level of theory. x-axis is the distance between CN carbon and CH2O oxygen in Å, which is the scan coordinate in this example. y-axis denotes the electronic energy (ZPVE uncorrected) in Hartree, where 1 Hartree = 2625.5 kJ mol^{-1}.

Another useful technique to explore the PES was to perform scans along user-defined geometric parameters, such as a bond distance, a bond angle or dihedral angle. Two types of scanning can be done with Gaussian, namely fixed and relaxed, where the difference lies on whether the other geometric parameters were allowed to be optimised while scanning along the user-defined one. The relaxed scan was chosen because it reflects how the actual molecules would travel on the PES given the assumption that the movements in the other coordinates are infinitely faster than the movement along the constrained coordinate. For instance, in order to understand how CN and CH_2O approach each other to form the van der Waals' complex, relaxed scans can be performed. Figure 2.7 shows the relaxed scan of the approach of CN towards the oxygen side of CH_2O, using the distance between CN carbon and CH_2O

oxygen as the scan coordinate. The smooth monotonic curve obtained suggests that such approach to form the van der Waals complex from the two separate reactants is barrierless.

For a relaxed scan about a dihedral angle, a potential application is to obtain the hindered rotor potential about an internal rotation, which is a more realistic descriptions of motions compared to the harmonic oscillator. A 360° relaxed scan about the dihedral angle corresponding to the internal rotation is required to generate the full hindered rotor potential. The results obtained could alter the density of the rovibrational states of the species, which will be discussed in Section 2.2 on the MESMER calculations and in Chapter 6 on dimers.

2.1.2.4 Final results to be reported

The last step is to refine the energy values at a higher level of theory based on the structures optimised at a lower level of theory. As suggested in Section 2.1.1.3, accuracy and efficiency are both considered in adopting such calculation procedure. No specific job type keyword is needed for Gaussian to perform a single-point energy calculation except the level of theory required. Apart from single-point energy, the dipole moment of the species is also reported in the energy calculation output file.

In the output files of Gaussian, the energy values are absolute and are reported in Hartree, which is the electric potential energy of the H atom in its ground state, but for easier understanding, they will be converted into relative energy and are reported as kJ mol^{-1} in the later chapters, where 1 Hartree = 2625.5 kJ mol^{-1}. Other relevant output include the geometry structures consisting of distances, angles and dihedral angles, vibrational frequencies, rotational constants, and dipole moments, which are reported in the Gaussian output in the units of angstrom, degree, cm^{-1}, GHz and Debye respectively.

2.2 Master equation calculations

After obtaining a detailed potential energy surface, rate coefficients will be calculated by the method of solving the master equation. To set up the master equation, results from the ab initio calculations discussed in the previous section, including geometric structures of the stationary points, energies, vibrational frequencies, rotational constants and reaction pathways, are required. This section will first introduce the theoretical background of reaction kinetics involved in the master equation method followed by the computational details applied in this work in the calculation of rate coefficients using the master equation solver programme MESMER (48).

2.2.1 Theoretical background

2.2.1.1 From Hinshelwood modification to the Rice-Ramsperger-Kassel-Marcus (RRKM) theory

Discussed in Section 1.2.3, the Lindemann mechanism attempted to explain the pressure dependence of the overall reaction rate coefficients. Although it can qualitatively explain the reaction mechanism, experimental measurements suggested that the Lindemann theory underestimates the values of the actual overall rate coefficients (49-52). The Lindemann theory fails in providing a quantitative description of the reaction because of the negligence of two aspects: the contribution of the internal degrees of freedom of the molecules, mainly the vibrational modes, in the rate of energisation; and the fact that the reaction can only proceed via a transition state where energy has to be localised in the particular degree of freedom leading to the products.

Considering the reaction mechanism R 1.4 and R 1.5, Cyril Hinshelwood (53) proposed that for a molecule with s degrees of freedom, the rate coefficient of activation k_1 is in the form of (49-52):

$$k_1 = \frac{Z}{(s-1)!}\left(\frac{E_0}{k_B T}\right)^{s-1} e^{-\frac{E_0}{k_B T}} \qquad \text{E 2.40}$$

where Z is the hard-sphere collision frequency and the rest is the probability for the total energy of the molecule exceeding the critical energy for reaction E_0, rather than in the form of:

$$k_1 = Ze^{-\frac{E_0}{k_B T}} \quad \text{E 2.41}$$

as predicted by the original Lindemann mechanism. The extra $\frac{1}{(s-1)!}\left(\frac{E_0}{k_B T}\right)^{s-1}$ factor, typically with $E_0 \gg k_B T$, covers the contribution of the s vibrational modes for the molecule to possess energy ≥ E_0. This is known as the Hinshelwood modification, which sheds light on the first failure of the Lindemann mechanism.

To account for the second failure of the Lindemann mechanism, Oscar Rice, Herman Ramsperger and Louis Kassel (54-56) developed the RRK theory which makes use of the microscopic energy dependent rate coefficients $k(E)$ rather than the macroscopic $k(T)$. The internal distribution of the energy within the molecule among different states is then considered. Later, Rudolph Marcus (57) refined the theory by the introduction of the differentiation between an energised molecule A^* and an activated molecule $\mathrm{A}^\ddagger$, or in other words the transition state, forming the RRKM theory. The RRKM mechanism can be represented as

$$\mathrm{A} + \mathrm{M} \xrightarrow{\delta k_1(E^* \to E^* + \delta E)} \mathrm{A}^*(E^* \to E^* + \delta E) + \mathrm{M} \quad \text{R 2.1}$$

$$\mathrm{A}^*(E^* \to E^* + \delta E) + \mathrm{M} \xrightarrow{k_{-1}} \mathrm{A} + \mathrm{M} \quad \text{R 2.2}$$

$$\mathrm{A}^*(E^* \to E^* + \delta E) \xrightarrow{k_2(E^*)} \mathrm{A}^\ddagger \quad \text{R 2.3}$$

$$\mathrm{A}^\ddagger \xrightarrow{k^\ddagger} \mathrm{P} \quad \text{R 2.4}$$

where $\delta k_1(E^* \to E^* + \delta E)$ denotes the rate to excite A to the energy range $E^* \to E^* + \delta E$. Assuming a steady state for $[\mathrm{A}^*(E^* \to E^* + \delta E)]$, the unimolecular rate coefficient k_{uni} for the energy range $E^* \to E^* + \delta E$ is given by:

$$k_{\mathrm{uni}}(E^* \to E^* + \delta E) = \frac{k_2(E^*)\delta k_1(E^* \to E^* + \delta E)/k_{-1}}{1 + k_2(E^*)/k_{-1}[\mathrm{M}]} \quad \text{E 2.42}$$

The overall rate coefficient $k_{\text{uni}}(E)$ will be obtained by integrating the expression in E 2.42 from the critical energy E_0 to E (50-52):

$$k_{\text{uni}}(E) = \int_{E_0}^{E} \frac{k_2(E^*)dk_1(E^* \to E^* + \delta E)/k_{-1}}{1 + k_2(E^*)/k_{-1}[\text{M}]} \qquad \text{E 2.43}$$

The expression for $\delta k_1(E^* \to E^* + \delta E)/k_{-1}$ can be obtained from the equilibrium constant of R 2.1 and R 2.2, which can also be represented by the partition functions Q (52):

$$\frac{\delta k_1(E^* \to E^* + \delta E)}{k_{-1}} = \frac{Q_{\text{A}^*(E^* \to E^* + \delta E)}}{Q_{\text{A}}} = \frac{\rho(E^*)}{Q_{\text{A}}} \delta E e^{-\frac{E^*}{k_B T}} \qquad \text{E 2.44}$$

while the expression for $k_2(E^*)$ is given by another equilibrium (52):

$$k_2(E^*) = \frac{1}{2} k^{\ddagger} \frac{[\text{A}^{\ddagger}]}{[\text{A}^*]} = \frac{W(E - E_0)}{h\rho(E^*)} \qquad \text{E 2.45}$$

where h is the Planck’s constant. $\rho(E^*)$ is the density of rovibrational states of the reactants and $W(E - E_0)$ is the sum of density of rovibrational states of the transition state between energy E and the critical energy E_0.

There are a few assumptions involved in the RRKM theory in order to allow the calculations of the microcanonical rate coefficients to be done (52). First, the energy transfer is rapid within the molecule compared to the timescale of reaction, such that statistical redistribution of the energy between different degrees of freedom can be swiftly achieved. Second, the equilibrium for the transition state exists such that the equations E 2.42 – E 2.45 are valid. Third, the density of rovibrational states are considered as a continuous distribution rather than being quantised.

2.2.1.2 Energy grains and density of states

The last section has shown that the energy states form the vital part of the RRKM theory, so it is worthwhile to briefly discuss about the energy states. While the calculated electronic energy values from ab initio calculations correspond to the well depths of the minima and barrier heights of saddle points, the energy states discussed above are constructed from the vibrational frequencies and rotational constants.

For vibrational energy, the harmonic oscillator approximation is commonly used for simplicity, and the energy states of that parabolic potential can be described as (3):

$$E_{\mathrm{v}} = \left(\mathrm{v} + \tfrac{1}{2}\right) h\nu \qquad \text{E 2.46}$$

with the vibrational quantum number $\mathrm{v} = 0, 1, 2, \ldots$, where h is the Planck's constant and ν is the vibrational frequency. For rotational energy, it can be expressed in terms of the rotational constants A, B, C (3), where:

$$A = \frac{h}{8\pi^2 I_A}, B = \frac{h}{8\pi^2 I_B}, C = \frac{h}{8\pi^2 I_C} \qquad \text{E 2.47}$$

with I_A, I_B, I_C being the moment of inertia along the three orthogonal axes. By applying the rigid rotor approximation, the energy for a spherical rotor ($A = B = C$) can be expressed as:

$$E_J = hBJ(J + 1) \qquad \text{E 2.48}$$

while for an oblate rotor ($A < B = C$) or a prolate rotor ($A > B = C$), the energy is:

$$E_J = hBJ(J + 1) + h(A - B)K^2 \qquad \text{E 2.49}$$

where J is the total rotational angular momentum quantum number and K is the quantum number that specifies the projection of the total angular momentum along a unique axis. For a linear rotor, K becomes zero so E 2.49 becomes E 2.48.

Energy levels generated from these two approximations do not include vibrational anharmonicity or centrifugal distortion, and so this does not represent the real scenario. For instance, when considering the actual anharmonic vibration, the vibration energies should be in the form of an infinite series (3):

$$\begin{aligned} E_{\mathrm{v}} = {} & \left(\mathrm{v} + \frac{1}{2}\right) h\nu_e - \left(\mathrm{v} + \frac{1}{2}\right)^2 h\nu_e x_e \\ & + \left(\mathrm{v} + \tfrac{1}{2}\right)^3 h\nu_e y_e - \left(\mathrm{v} + \tfrac{1}{2}\right)^4 h\nu_e z_e + \cdots \end{aligned} \qquad \text{E 2.50}$$

where the contribution from the leading term, which is of the same form as the harmonic oscillator, is dominant. The higher order terms take into account the anharmonicity, with x_e, y_e, z_e,… known as the anharmonicity constants. Cutting off at the second-order term gives the Morse potential:

$$E_{\mathrm{v}} = \left(\mathrm{v} + \tfrac{1}{2}\right) h\nu_e - \left(\mathrm{v} + \tfrac{1}{2}\right)^2 h\nu_e x_e \qquad \text{E 2.51}$$

Figure 2.8(a) shows an example of a harmonic potential, which is in the form of a parabolic well with evenly spaced vibrational states, while Figure 2.8(b) shows an example of an anharmonic potential, which is steeper in its energy gradient at short internuclear distances while trending toward an asymptotic value at long internuclear distances. At increasing energy the anharmonic potential shows a larger well width compared to the harmonic one, making the packing of the energy states closer with increasing energy until reaching the point where the bond breaks. Some vibrational modes, typically with lower frequencies, are known as hindered rotors, for instance the internal rotation of the methyl group –CH_3 about the C–C bond in a CH_3CHO molecule. It requires energy to overcome the hindrance in order to complete the whole torsional rotation cycle as shown in Figure 2.8(c). Thus, at lower energies, they behave like anharmonic oscillators and the effect again is an increase in the density of states (DOS) (58). When the energy increases way beyond this hindrance, the torsional rotation can then be considered as a free rotation instead.

During actual computations, the energy states are partitioned into energy grains of a certain size $\Delta\nu$ and the calculations will be dealing with the density of states of each energy grain. If E_{max} is the maximum energy value put under consideration, then the number of energy grains M is given by:

$$M = \frac{E_{\mathrm{max}}}{\Delta\nu} + 1 \qquad \text{E 2.52}$$

One way to calculate the DOS is the Beyer-Swinehart algorithm (48, 52, 59), where an array of M elements is used and after the direct counting process looping over all the rovibrational frequencies the elements will give the sum of the density of state up to each partitioned energy grain.

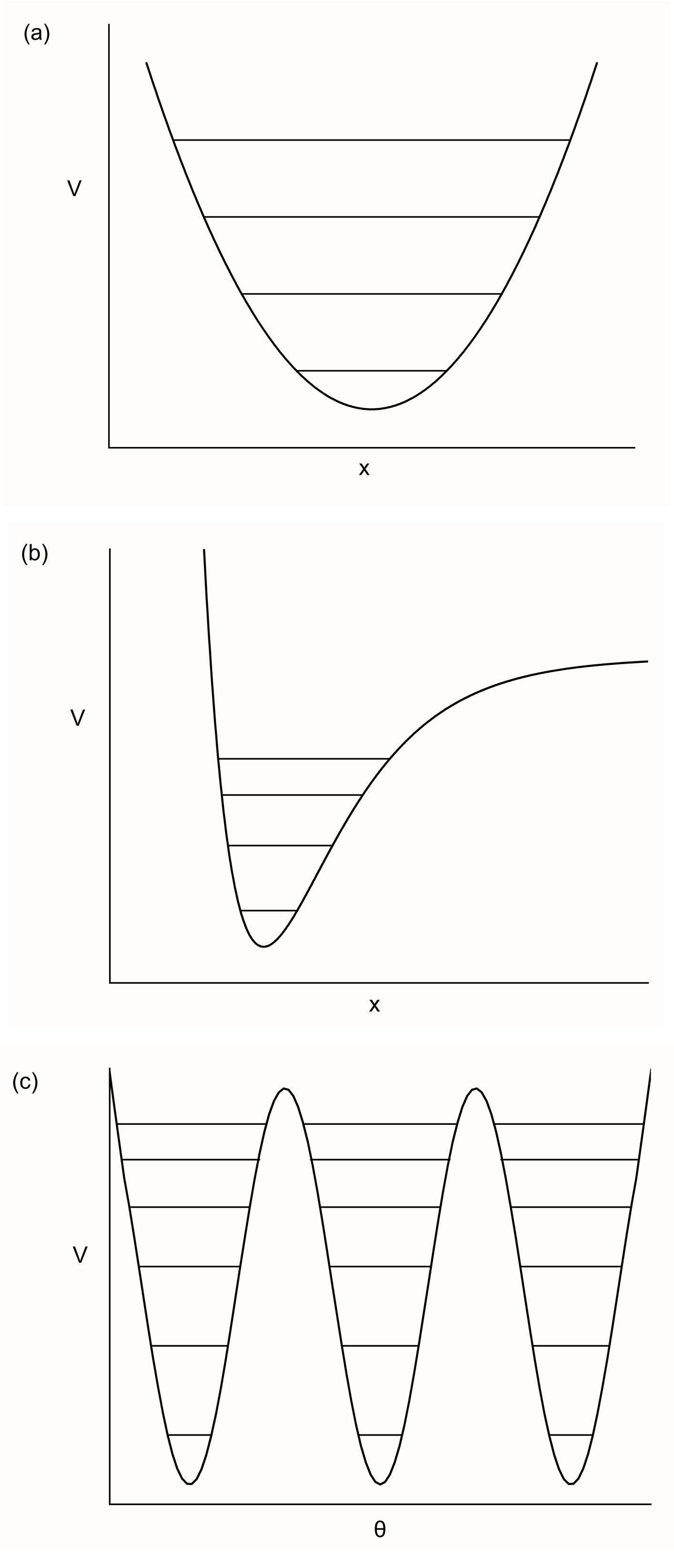

Figure 2.8 Examples of (a) a harmonic oscillator potential, (b) an anharmonic oscillator potential and (c) a hindered rotor potential.

2.2.1.3 Loose transition state

A reactive process, for example a barrierless association, can occur without a well-defined barrier as suggested in Chapter 1. One of the important assumptions of the classical transition state theory is the no-recrossing approximation, and when the transition state is tight, the saddle point can be located easily. However, if the transition state is loose, that is, the barrier is only of small energy or there is even no barrier, the saddle point is no longer easy-to-handle. The rate coefficient calculated from the classical transition state theory overestimates the actual rate coefficient substantially and can only be treated as an upper bound due to the appreciable occurrence of recrossing (49, 50, 60, 61). Taking the reaction path as the minimum energy path (MEP), which is the steepest path connecting the transition state to the reactants and products, variational transition state theory (VTST) computes the rate coefficients in the form similar to E 1.42:

$$k = \frac{k_B T}{h} \frac{q_{\mathrm{TS}}}{q_{\mathrm{reactants}}} e^{-\frac{V_{\mathrm{MEP}}}{RT}} \qquad \text{E 2.53}$$

at different dividing surfaces perpendicular to the MEP where the optimised position of the dividing surface gives the minimum recrossing and the minimum rate coefficient value (49, 50, 60, 61). The details for the actual computations using VTST are beyond the scope of this thesis.

For reactions with a more complicated energy profile similar to that shown in the right column of Figure 1.5, which involves the formation of a loosely bound complex followed by a barrier, Greenwald et al. (62) proposed the use of the two transition state model to explain the reactions. The first outer transition state is barrierless and considers the long-range interactions, while the second inner transition state lies at the location conventionally seen as the saddle point, with a schematic of the reaction potential shown in Figure 2.9. It is suggested that (62, 63) at high temperature, the inner transition state controls the reaction rate, variational calculations indicated that the outer transition state leading to the van der Waals well becomes more dominant at low enough temperature, which demonstrates the flexibility of the dominant transition state.

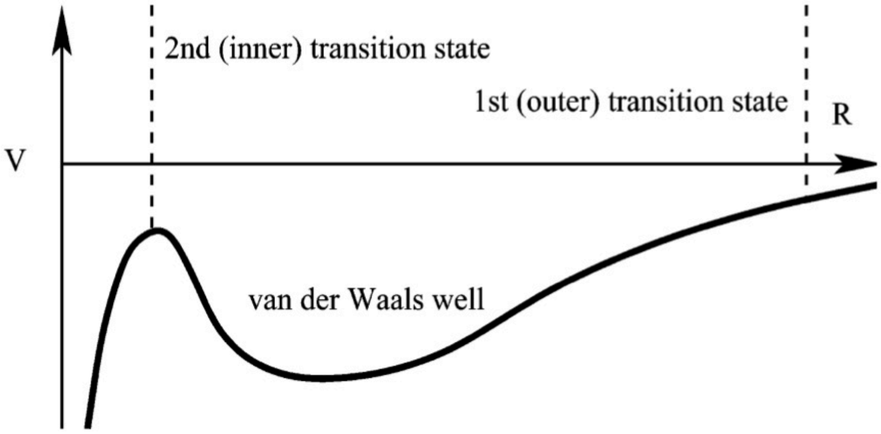

Figure 2.9 A schematic of the two transition state model with the reaction controlled by the outer transition state at large intermolecular distance and the inner transition state at the submerged barrier when the two reactants approach. Taken from Georgievskii and Klippenstein (63).

Alternatively, the barrierless entrance channels can be treated with the inverse Laplace transformation (ILT) method, which was mainly used in this work to convert between the macroscopic $k(T)$, particularly when experimental $k(T)$ is available, and the microscopic $k(E)$ (48, 50). A Laplace transform $\mathcal{L}$ is defined as the following (50):

$$F(p) = \mathcal{L}[f(t)] = \int_0^\infty e^{-pt} f(t)\, dt \qquad \text{E 2.54}$$

for some functions F and f and some parameters p and t. An inverse Laplace transform would then be:

$$\mathcal{L}^{-1}[F(p)] = f(t) \qquad \text{E 2.55}$$

It is suggested that the canonical unimolecular rate coefficient for high-pressure limit k^∞ can be expressed as (48):

$$k^\infty(\beta) = \frac{1}{Q(\beta)} \int_0^\infty k(E)\rho(E)e^{-\beta E}\, dE \qquad \text{E 2.56}$$

where Q is the partition function, ρ is the density of states and $\beta = 1/k_B T$. By rearranging the terms and comparing with E 2.54:

$$Q(\beta)k^\infty(\beta) = \int_0^\infty k(E)\rho(E)e^{-\beta E}\, dE = \mathcal{L}[k(E)\rho(E)] \qquad \text{E 2.57}$$

Thus, $k(E)$ can be obtained by performing an inverse Laplace transform on k^∞:

$$k(E)\rho(E) = \mathcal{L}^{-1}[Q(\beta)k^{\infty}(\beta)] \qquad \text{E 2.58}$$

k^{∞} can technically be any rate expression and in this work it is taken as the form of a modified Arrhenius expression (48):

$$k^{\infty}(\beta) = A_0\left(\frac{\beta_0}{\beta}\right)^n e^{-\beta E_a} \qquad \text{E 2.59}$$

where A_0, n, and E_a are the pre-exponential factor, the temperature exponent and the activation energy respectively, then:

$$k(E)\rho(E) = A_0\beta_0^n\mathcal{L}^{-1}\left[\frac{Q(\beta)}{\beta^n}e^{-\beta E_a}\right] \qquad \text{E 2.60}$$

which can effectively convert between $k(E)$ and $k(T)$ with $\rho(E)$ being the DOS.

2.2.1.4 Tunnelling corrections

Tunnelling corrections are relevant when there is a barrier to reaction. In quantum mechanics, a particle is described by its wavefunction ψ, which satisfies the Schrödinger equation. The probability of finding the particle at x is given by the absolute square of $\psi(x)$. Except for a hard wall boundary condition where the potential barrier rises to infinity, the wavefunction can penetrate into the classically forbidden region, where the total energy E is smaller than the potential energy V (3, 49, 64). For example for a rectangular barrier as shown in Figure 2.10, the wavefunction within the barrier is given by:

$$\psi(x) = Ae^{-\frac{\sqrt{2m(V-E)}}{\hbar}} \qquad \text{E 2.61}$$

where A is the normalisation constant (3, 49, 64). The wavefunction shows an exponential decay within the barrier. If the barrier is of infinite width, the amplitude of the wavefunction will eventually fall to 0. However, if the barrier is of finite width, the wavefunction can exist as non-zero values on both sides of the barrier.

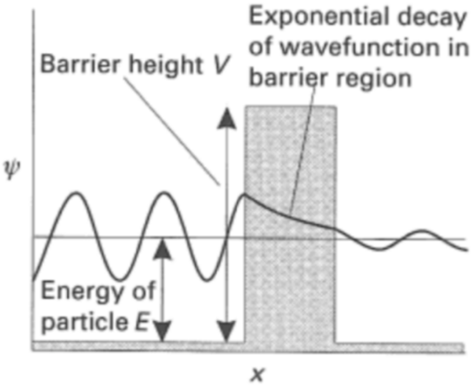

Figure 2.10 The wavefunction of a particle when encountering a potential barrier *V*, where *E* < *V*. For a narrow barrier, the amplitude of the wavefunction transmitted is non-zero. Taken from Pilling and Seakins (49).

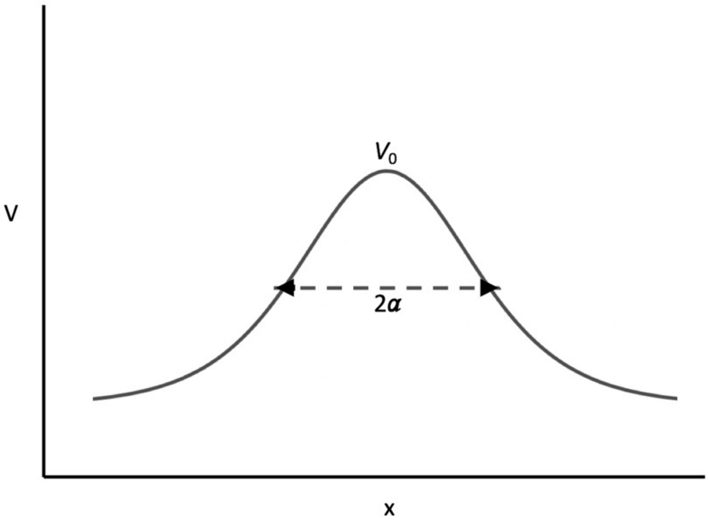

Figure 2.11 A symmetric Eckart potential barrier with V_0 as the peak potential and 2*α* as the full width at half maximum.

While a rectangular barrier is unrealistic, a better representation for a barrier on the potential energy surface for a reacting system can be the Eckart barrier (65). A special case of the Eckart barrier is shown in Figure 2.11, which is symmetric and given by the following expression (3, 48):

$$V(x) = \frac{V_0}{\cosh^2\left(\frac{x}{\alpha}\right)} \qquad \text{E 2.62}$$

where V_0 is the peak potential and 2α is the full width at half maximum. In actual practice, given that the potential energies of the reactants V_R, the products V_P and the barrier $V^\ddagger$, where $V^\ddagger > V_\mathrm{R}, V_\mathrm{P}$, together with the magnitude of the imaginary frequency ω_i are known, the barrier can be expressed as an unsymmetric Eckart potential with the transmission probability at a particular energy $T(E)$ given by (66):

$$T(E) = \frac{\sinh(a)\sinh(b)}{\sinh^2\left(\frac{a+b}{2}\right)+\cosh^2(c)} \qquad \text{E 2.63}$$

$$a = \frac{4\pi}{\hbar\omega_i}\sqrt{E + (V^\ddagger - V_\mathrm{R})}\left(\frac{1}{\sqrt{V^\ddagger - V_\mathrm{R}}} + \frac{1}{\sqrt{V^\ddagger - V_\mathrm{P}}}\right)^{-1} \qquad \text{E 2.64}$$

$$b = \frac{4\pi}{\hbar\omega_i}\sqrt{E + (V^\ddagger - V_\mathrm{P})}\left(\frac{1}{\sqrt{V^\ddagger - V_\mathrm{R}}} + \frac{1}{\sqrt{V^\ddagger - V_\mathrm{P}}}\right)^{-1} \qquad \text{E 2.65}$$

$$c = 2\pi\sqrt{\frac{(V^\ddagger - V_\mathrm{R})(V^\ddagger - V_\mathrm{P})}{(\hbar\omega_i)^2} + \frac{1}{16}} \qquad \text{E 2.66}$$

The tunnelling probability can thus be promoted by an increase of ω_i and a decrease of $V^\ddagger$.

It is understood that the effect of tunnelling can also be estimated using other methods. For instance, the Wentzel-Kramers-Brillouin (WKB) method reported by Garrett and Truhlar (67) which involves the integration of the potential along the minimum energy path. However, this would mean the requirement of the detailed knowledge of the potential energy along the path which can be computationally expensive to obtain and is not always available.

2.2.1.5 Master equation and collisional energy transfer

The master equation is a collection of differential equations which describe how a system evolves over time. By solving the master equation, phenomenological kinetic quantities of the system such as rate coefficients, species profiles and branching ratios can be determined (48). The master equation considers the probability of a particle to undergo switching between different grains. For instance, consider a particle, which can be in any of the N grains G_N. The change of its probability P to be in a particular grain G_i at time t is:

$$\frac{dP_{G_i}(t)}{dt} = \sum_{G_j(j\neq i)}^{G_N} \left(-k(G_i \rightarrow G_j)P_{G_i}(t) + k(G_j \rightarrow G_i)P_{G_j}(t)\right) \qquad \text{E 2.67}$$

where $k(G_i \rightarrow G_j)$ is the rate coefficient for the particle to switch from that particular grain G_i to another grain G_j given it is in grain G_i. The whole collection of differential equations will be obtained by considering $\frac{dP_G(t)}{dt}$ for all grains and, when extending to a real situation with many more particles in the system, it will be considered in terms of the distribution of the population of particles over the grains.

Taking Figure 2.12 as an example of a reaction system, the time evolution of the population n of an isomer i with energy E is given by the following differential equation (48):

$$\frac{dn_i(E)}{dt} = \omega \int_{E_{0i}}^{\infty} P(E|E')\, n_i(E')dE' - \omega n_i(E) \qquad \text{E 2.68}$$

$$+\sum_{i\neq j}^{M} k_{ij}(E)n_j(E) - \sum_{i\neq j}^{M} k_{ji}(E)n_i(E) - k_{Pi}(E)n_i(E)$$

$$+K_{Ri}^{\mathrm{eq}} k_{Ri}(E)\frac{\rho_i(E)e^{-\beta E}}{Q_i(\beta)} n_{\mathrm{A}}n_{\mathrm{B}} - k_{Ri}(E)n_i(E)$$

The first two terms consider the collisional population gain and loss of i with energy E, where ω and $P(E|E')$ refer to the collision frequency and the probability of transition $E' \rightarrow E$ due to collisions, which will be discussed in more detail below. The third and fourth terms consider the population gain and loss of i from and to another isomer j, where k_{ij} refers to the microcanonical rate coefficient from j to i. The fifth term considers the population loss to the products P, otherwise known as the sink. The last two terms are known as the bimolecular source terms, which consider the population gain through bimolecular association of A and B (together known as reactants R) and loss through dissociation back to the reactants. K_{Ri}^{eq} is the equilibrium constant between i and R, Q_i is the rovibrational partition function of i and $\beta = \frac{1}{k_B T}$, where k_B is the Boltzmann constant. Pseudo-first order treatment, as discussed in Section 1.2.1, can be applied to the bimolecular source terms when the deficient reactant and the excess reactant are defined.

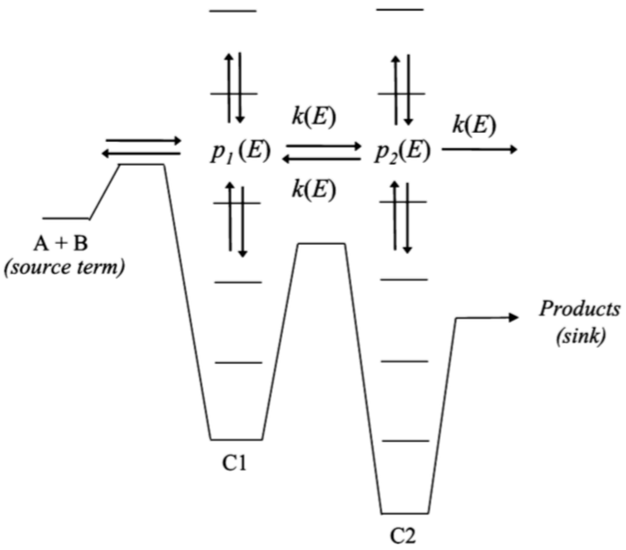

Figure 2.12 A schematic showing the representation of the energy grained master equation for a reaction with multiple wells and transition states along the pathway. Taken from Glowacki et al. (48).

When the analysis is extended further by considering other species i and other energy E, a collection of differential equations E 2.68 are obtained. This can be represented as the matrix form:

$$\frac{d}{dt}\mathbf{n} = \mathbf{Mn} \qquad \text{E 2.69}$$

where $\mathbf{n}$ is the population vector and $\mathbf{M}$ is the matrix containing the transition probabilities. E 2.69 is known as the matrix-form energy grained master equation (EGME).

The last five terms in E 2.68 take into account of the reactive processes that involve chemical changes, with the calculation for the microcanonical rate coefficients already discussed in Sections 2.2.1.1 – 2.2.1.4. The first two terms considers the upward and downward transition of the species along the energy ladder due to collisions. For these collisional energy transfer processes, two factors are considered, namely the collision frequency and the probability that a state transition resulted from a collision.

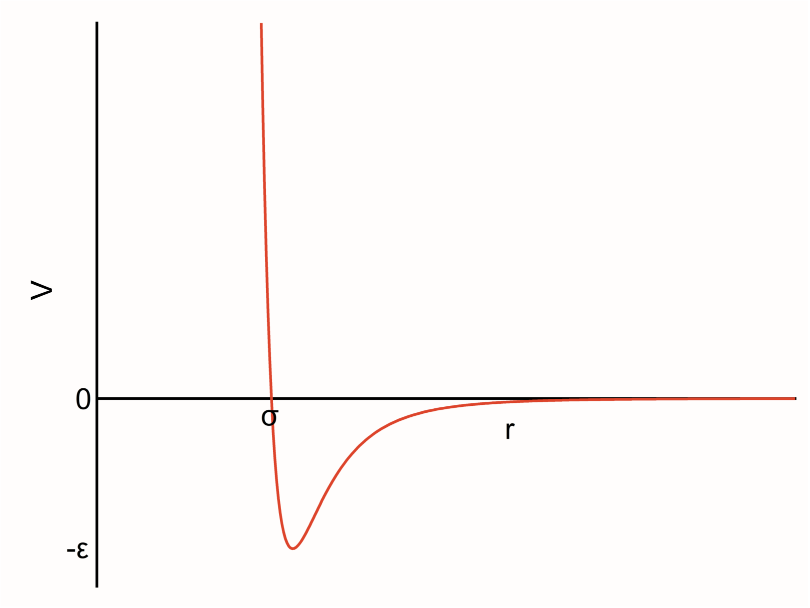

Figure 2.13 A Lennard-Jones potential with ε as the well depth at equilibrium distance and σ as the finite distance at which the potential intersects with the x-axis.

The collision theory model based on the hard sphere approximation, that is, there is no interaction between the spheres, has been discussed in Chapter 1 and such an assumption implies a step function as the intermolecular potential. A more realistic model to represent the intermolecular interaction is the Lennard-Jones potential V_{LJ} (68, 69):

$$V_{\mathrm{LJ}}(r) = 4\varepsilon\left[\left(\frac{\sigma}{r}\right)^{12} - \left(\frac{\sigma}{r}\right)^{6}\right] \qquad \text{E 2.70}$$

where r is the intermolecular distance, ε is the well depth at equilibrium distance and σ is the finite distance at which the potential intersects with the x-axis as shown in Figure 2.13. The first term is to represent the repulsive forces while the second term is for the attractive forces. The Lennard-Jones collision frequency Z_{LJ} between A and M is defined by (51, 70):

$$Z_{\mathrm{LJ}} = \sqrt{\frac{8k_BT}{\pi\mu}}\pi{\sigma_{\mathrm{AM}}}^2\Omega_{\mathrm{AM}}^{(2,2)*} \qquad \text{E 2.71}$$

where $\Omega_{\mathrm{AM}}^{(2,2)*}$ is a function of $\frac{k_BT}{\varepsilon_{\mathrm{AM}}}$ and the Lennard-Jones parameters between different species $(\sigma_{\mathrm{AM}}, \varepsilon_{\mathrm{AM}})$ can be combined from those of individual species $(\sigma_{\mathrm{AA}}, \sigma_{\mathrm{MM}}, \varepsilon_{\mathrm{AA}}\ \varepsilon_{\mathrm{MM}})$ by the following:

$$\sigma_{\mathrm{AM}} = \frac{1}{2}(\sigma_{\mathrm{AA}} + \sigma_{\mathrm{MM}}) \qquad \text{E 2.72}$$

$$\varepsilon_{\mathrm{AM}} = \sqrt{\varepsilon_{\mathrm{AA}}\varepsilon_{\mathrm{MM}}} \qquad \text{E 2.73}$$

For the collisional energy transfer probability, one of the models is the exponential-down model (51, 71), which was used in this work. The probability P of a downward transition $E \rightarrow E'$, where $E > E'$, due to collision is determined by:

$$P(E'|E) = A(E)\exp\left(-\frac{E-E\prime}{\langle\Delta E\rangle_{down}}\right) \qquad \text{E 2.74}$$

where $A(E)$ is the normalisation constant and $\langle\Delta E\rangle_{down}$ is the average energy transferred in each deactivating collision. With this formalism, collisions involving minute energy transfer are more frequent than those involving a large energy difference. The probability of an upward collision can be found by the principle of detailed balance, which means the upward collision is in equilibrium with the downward collision at equilibrium:

$$P(E'|E)f(E) = P(E|E')f(E') \qquad \text{E 2.75}$$

where $f(E)$ and $f(E')$ are the equilibrium distributions.

2.2.2 Methodology for performing computations via the MESMER programme

A master equation solver makes use of computational chemistry results to formulate and solve the master equation to provide the phenomenological kinetic quantities, such as the rate coefficients and population, of a reaction system. Some of the available master equation solver packages include Multiwell (72, 73) and MESS (Master Equation System Solver) (74) software. In this work, all of the master equation calculations were performed using the MESMER (Master Equation Solver for Multi Energy well Reactions) (48) programme. With the stationary points of the PES being known, MESMER solves the energy-grained master equation to give the rate coefficients, species-time profiles and branching ratios. This section will introduce some essential components in MESMER calculations and also the unique data fitting feature of MESMER, while further details can be found in Appendix A.

2.2.2.1 Essential components in MESMER simulations

First, the properties of species present in the system under consideration, including the reactants, the products, the intermediates, the transition states and the bath gases have to be specified for MESMER calculations. Gaussian results including the geometric structures (in particular the symmetry number), the energy values, all the vibrational frequencies (both real and imaginary) or the Hessian, the scaling factor and the rotational constants are provided as the input. The DOS is calculated from the vibrational frequencies using the harmonic oscillator approximation, unless the details for the anharmonicity are provided, and from the rotational constants using the rigid rotor approximation. The hindered rotor potential option is also available in MESMER. Other properties required for the calculations include the molecular weight and the spin multiplicity.

Table 2.9 Values of the Lennard-Jones parameters for different bath gases. Taken from Gilbert and Smith (51).

Bath gas	ε (K)	σ (Å)
He	10	2.55
Ar	114	3.47
N_2	48	3.9

Table 2.10 Values used as the input parameters in MESMER for the calculations of $\langle \Delta E \rangle_{down}$ between the intermediate with a given bath gas

Bath gas	$\langle \Delta E \rangle_{down,ref}$ (cm^{-1})	n
He	100	1
Ar	200	0.5
N_2	250	0.25

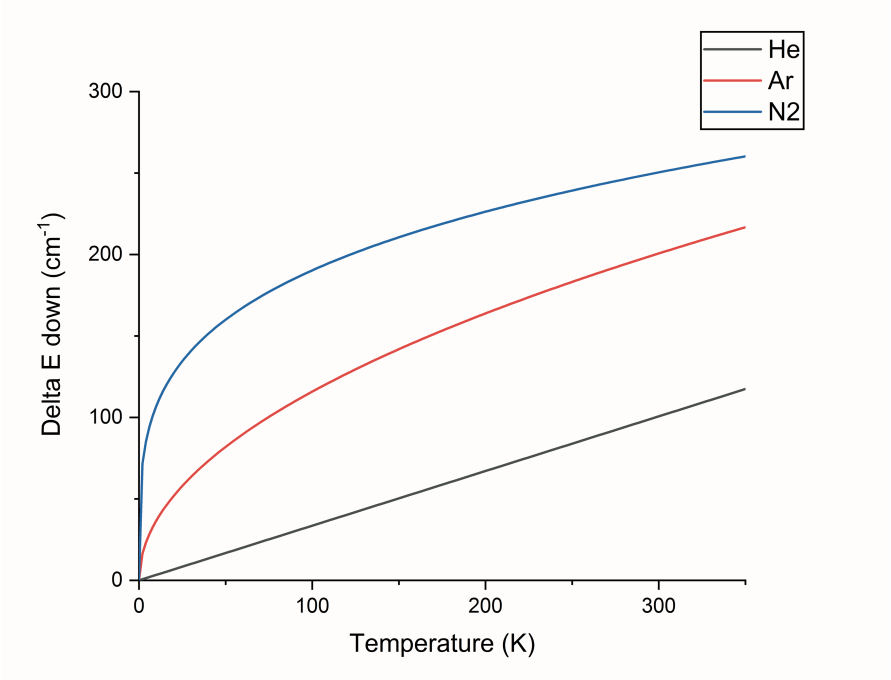

Figure 2.14 Variation of $\langle \Delta E \rangle_{down}$ as a function of temperature using the parameters given in Table 2.10.

To model the pressure dependence of the reaction, the Lennard-Jones ε and σ parameters for the bath gases and intermediates, and the collisional transferred energy $\langle \Delta E \rangle_{down}$ for the intermediates with different bath gases will be needed. Experimental values of the Lennard-Jones parameters for the bath gases reported by Gilbert and Smith (51), which is listed here in Table 2.9, are used. For the intermediates, experimental data for the Lennard-Jones parameters are not available and so they are left out in the MESMER input file. Instead, MESMER will estimate the parameters using the model reported by Jasper (75) which is based on the functional group and the number of non-hydrogen atoms present. For the $\langle \Delta E \rangle_{down}$ as mentioned in Section 2.2.1.5, in MESMER, the temperature dependent $\langle \Delta E \rangle_{down}$ is modelled as:

$$\langle \Delta E \rangle_{down} = \langle \Delta E \rangle_{down,ref} \left(\frac{T}{298\ \mathrm{K}} \right)^{n} \qquad \text{E 2.76}$$

where $\langle \Delta E \rangle_{down,ref}$ and n are the input parameters. In general, a $\langle \Delta E \rangle_{down}$ value of ~100 cm^{-1} can be considered as weak colliders while ~1000 cm^{-1} or above are strong colliders, with the inert gases typically near the lower end of this range (76). It is assumed here that for a given bath gas, the values of $\langle \Delta E \rangle_{down,ref}$ and n for the collision with any intermediates are the same. Table

2.10 lists out the empirical values of $\langle \Delta E \rangle_{down,ref}$ and n used for the collision of the intermediates with three different bath gases, namely He, Ar and N_2, in MESMER calculations with Figure 2.14 showing the plot of $\langle \Delta E \rangle_{down}$ as a function of temperature. It is important to note that there is appreciable uncertainty in the energy transfer values, while the ordering assigned here (collision with He < collision with Ar < collision with N_2) is correct, the actual $\langle \Delta E \rangle_{down}$ values can vary considerably as a function temperature due to the uncertainties in the empirical values of $\langle \Delta E \rangle_{down,ref}$ and n for different intermediates.

The next piece of information required is the PES that shows how the stationary points are connected, which means the inclusion of all the individual elementary steps of the reaction system in the MESMER input file. The roles of the species involved in the reaction have to be specified, such as deficient reactant, excess reactant, transition state, sink for products that will be removed from the system, or modelled molecules for intermediates. For a reactive step with a well-defined barrier, the RRKM theory is applied as discussed in Section 2.2.1.1, where corrections for quantum mechanical tunnelling across the barrier can be implemented by using the Eckart barrier option as discussed in Section 2.2.1.4. For a reactive step without a well-defined barrier, microcanonical rate coefficients $k(E)$ can be calculated with the ILT method as discussed in Section 2.2.1.3 from the canonical high-pressure limit rate coefficient $k^{\infty}(T)$. In MESMER, $k^{\infty}(T)$ is represented a modified Arrhenius expression:

$$k^{\infty}(T) = A^{\infty}\left(\frac{T}{T^{\infty}}\right)^{n^{\infty}} \exp\left(-\frac{E_a^{\infty}}{RT}\right) \qquad \text{E 2.77}$$

where A^{∞} is the pre-exponential factor, n^{∞} is the modified Arrhenius factor and T^{∞} is a user-defined temperature value, which are all MESMER input parameters. The activation energy E_a^{∞} is set as 0 when the reactive process is barrierless. A sensible choice of the ILT parameters for the entrance channel will be the collision limit. An estimate of this value for neutral-neutral reactions suggested from previous work (58, 77) is a constant value of 3×10^{-10} cm^3 molecule^{-1} s^{-1}, which ignores the entropic hindrance, while a more accurate description can be obtained through the capture theory calculations as discussed in Chapter 1 or the VTST calculations as discussed earlier in this

Chapter. Figure 2.15 summarises the methods used to formulate the master equation with respective to different processes in MESMER.

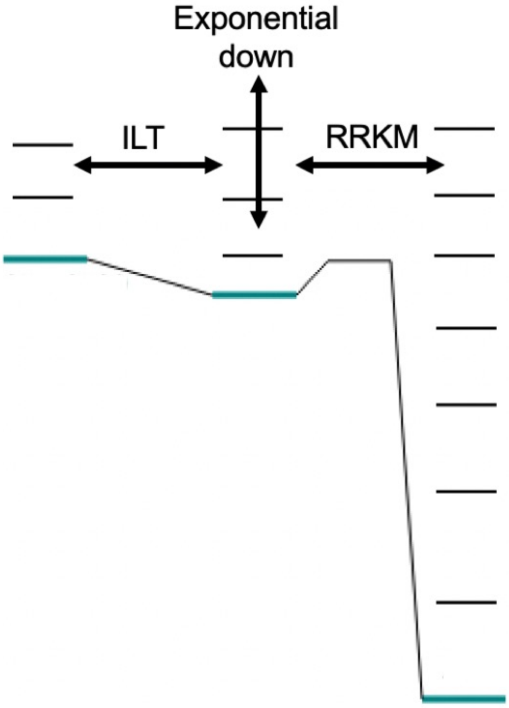

Figure 2.15 A summary of the methods used to formulate the transition probabilities between different energy grains in MESMER.

The physical conditions, including the pressure, the temperature, and the bath gas used, under which the calculation is to be run also have to be specified, together with a suitable precision and grain size. The precision determines the number of numerical digits being considered and saved during the course of calculations. In general, a higher precision is needed when the temperature is lowered so that the precision of the calculation can accommodate for the minute value of the rate for the system to get out of a potential well. For the grain size, typically 40–250 cm^{-1} can be considered as a suitable option (48), but at lower temperatures, a smaller grain size has to be used such that the amount of energy involved in an energy transfer event, for example $\langle \Delta E \rangle_{down}$, can span across a few energy grains. Higher precision and smaller grain sizes can improve the accuracy of the calculations but will raise the computational cost.

Upon solving the matrix-form energy grained master equation (EGME), MESMER obtains a number of eigenvalues as the solutions. MESMER makes use of the Bartis-Widom method (78) to assign the eigenvalues to the individual rate coefficients of the system. If there is only one reactive step in the reaction system being considered, then it will assign the smallest eigenvalue to the rate coefficient. For an actual multi-well systems with more reactive steps, the rate coefficients of the reactive steps between different species will be among the eigenvalues obtained. The assignment of the eigenvalue to an individual rate coefficient is done by assuming that the lowest eigenvalues are the chemically significant eigenvalues instead of the eigenvalues corresponding to the collision energy transfer.

2.2.2.2 Data fitting function of MESMER

Apart from running simulations by inserting the computational chemistry output parameters, ILT parameters, and collision-related parameters, a unique feature of MESMER is data fitting. When experimental data are available, the experimentally measured rate coefficient k_{expt} can be compared with the calculated rate coefficient k_{calc}, and then some of the important input parameters can be adjusted to better match the experimental data. The selection of the parameters to be fitted depends on the intended purpose. For instance, the ILT parameters can be optimised instead of using some arbitrary estimations. The computational parameters such as well depth and barrier height can also be adjusted to compensate any computational errors. The transition state imaginary frequency value can also be fitted based on the effect of tunnelling observed through the experimentally measured rate coefficients.

In order to implement the data fitting, the experimentally measured rate coefficients k_{expt} have to be provided alongside the corresponding experimental conditions including temperature, total pressure or concentration and the type of bath gas used. For weighted fitting, the uncertainties σk_{expt} for the experimental measurements are also needed. By providing a floating range for the parameters to be optimised, together with the number of fitting iterations or the tolerance for the fitting, the fitting procedure in MESMER will essentially try to minimise χ^2 (48), where:

$$\chi^2 = \sum \frac{\left(k_{\mathrm{expt}} - k_{\mathrm{calc}}\right)^2}{\sigma k_{\mathrm{expt}}{}^2} \quad \text{E 2.78}$$

The aim of this fitting procedure is to obtain an optimised set of parameters for extrapolation of the simulation to temperature and pressure conditions beyond the experimental values. This is particularly useful for the study of astrochemical reactions, where the actual environment can be of extreme conditions while the experimental conditions are limited by the apparatus.

2.3 References

1. Cramer, C.J. *Essentials of computational chemistry : theories and models.* Chichester: Wiley, 2002.

2. Jensen, F. *Introduction to computational chemistry.* Second edition. ed. Chichester: Wiley, 2007.

3. Atkins, P.W. and Friedman, R. *Molecular quantum mechanics.* 5th ed. Oxford: Oxford University Press, 2011.

4. Foresman, J.B. and Frisch, *Æ. Exploring Chemistry with Electronic Structure Methods.* 3rd ed. USA: Gaussian, 2015.

5. Schrödinger, E. An Undulatory Theory of the Mechanics of Atoms and Molecules. *Physical Review.* 1926, **28**(6), pp.1049-1070.

6. Born, M. and Oppenheimer, R. Zur Quantentheorie der Molekeln. *Annalen der Physik.* 1927, **389**(20), pp.457-484.

7. Slater, J.C. Atomic Shielding Constants. *Physical Review.* 1930, **36**(1), pp.57-64.

8. Hehre, W.J., Stewart, R.F. and Pople, J.A. Self-Consistent Molecular-Orbital Methods. I. Use of Gaussian Expansions of Slater-Type Atomic Orbitals. *The Journal of Chemical Physics.* 1969, **51**(6), pp.2657-2664.

9. Ditchfield, R., Hehre, W.J. and Pople, J.A. Self-Consistent Molecular-Orbital Methods. IX. An Extended Gaussian-Type Basis for Molecular-Orbital Studies of Organic Molecules. *The Journal of Chemical Physics.* 1971, **54**(2), pp.724-728.

10. Clark, T., Chandrasekhar, J., Spitznagel, G.W. and Schleyer, P.V.R. Efficient diffuse function-augmented basis sets for anion calculations. III. The 3-21+G basis set for first-row elements, Li–F. *Journal of Computational Chemistry.* 1983, **4**(3), pp.294-301.

11. Dunning, T.H. Gaussian basis sets for use in correlated molecular calculations. I. The atoms boron through neon and hydrogen. *The Journal of Chemical Physics.* 1989, **90**(2), pp.1007-1023.

12. Kendall, R.A., Dunning, T.H. and Harrison, R.J. Electron affinities of the first-row atoms revisited. Systematic basis sets and wave functions. *The Journal of Chemical Physics.* 1992, **96**(9), pp.6796-6806.

13. Woon, D.E. and Dunning Jr., T.H. Gaussian basis sets for use in correlated molecular calculations. V. Core-valence basis sets for boron through neon. *The Journal of Chemical Physics.* 1995, **103**(11), pp.4572-4585.

14. Papajak, E., Zheng, J., Xu, X., Leverentz, H.R. and Truhlar, D.G. Perspectives on Basis Sets Beautiful: Seasonal Plantings of Diffuse Basis Functions. *Journal of Chemical Theory and Computation.* 2011, **7**(10), pp.3027-3034.

15. Hartree, D.R. The Wave Mechanics of an Atom with a Non-Coulomb Central Field. Part II. Some Results and Discussion. *Mathematical Proceedings of the Cambridge Philosophical Society.* 1928, **24**(1), pp.111-132.

16. Shavitt, I. The Method of Configuration Interaction. In: Schaefer, H.F. ed. *Methods of Electronic Structure Theory*. Boston, MA: Springer US, 1977, pp.189-275.

17. Meckler, A. Electronic Energy Levels of Molecular Oxygen. *The Journal of Chemical Physics.* 1953, **21**(10), pp.1750-1762.

18. Møller, C. and Plesset, M.S. Note on an Approximation Treatment for Many-Electron Systems. *Physical Review.* 1934, **46**(7), pp.618-622.

19. Čížek, J. On the Correlation Problem in Atomic and Molecular Systems. Calculation of Wavefunction Components in Ursell-Type Expansion Using Quantum-Field Theoretical Methods. *The Journal of Chemical Physics.* 1966, **45**(11), pp.4256-4266.

20. Pople, J.A., Head-Gordon, M. and Raghavachari, K. Quadratic configuration interaction. A general technique for determining electron correlation energies. *The Journal of Chemical Physics.* 1987, **87**(10), pp.5968-5975.

21. Hampel, C., Peterson, K.A. and Werner, H.-J. A comparison of the efficiency and accuracy of the quadratic configuration interaction (QCISD), coupled cluster (CCSD), and Brueckner coupled cluster (BCCD) methods. *Chemical Physics Letters.* 1992, **190**(1), pp.1-12.

22. Hohenberg, P. and Kohn, W. Inhomogeneous Electron Gas. *Physical Review.* 1964, **136**(3B), pp.B864-B871.

23. Kohn, W. and Sham, L.J. Self-Consistent Equations Including Exchange and Correlation Effects. *Physical Review.* 1965, **140**(4A), pp.A1133-A1138.

24. Parr, R.G. and Yang, W. *Density-functional theory of atoms and molecules.* New York; Oxford: Oxford University Press, 1989.

25. Becke, A.D. Density-functional thermochemistry. III. The role of exact exchange. *The Journal of Chemical Physics.* 1993, **98**(7), pp.5648-5652.

26. Becke, A.D. A new mixing of Hartree–Fock and local density-functional theories. *The Journal of Chemical Physics.* 1993, **98**(2), pp.1372-1377.

27. Zhao, Y. and Truhlar, D.G. The M06 suite of density functionals for main group thermochemistry, thermochemical kinetics, noncovalent interactions, excited states, and transition elements: two new functionals and systematic testing of four M06-class functionals and 12 other functionals. *Theoretical Chemistry Accounts.* 2008, **120**(1), pp.215-241.

28. Yatsimirskii, K.B. Relativistic effects in chemistry. *Theoretical and Experimental Chemistry.* 1995, **31**(3), pp.153-168.

29. Feller, D. and Peterson, K.A. An examination of intrinsic errors in electronic structure methods using the Environmental Molecular Sciences Laboratory computational results database and the Gaussian-2 set. *The Journal of Chemical Physics.* 1998, **108**(1), pp.154-176.

30. Witte, J., Neaton, J.B. and Head-Gordon, M. Push it to the limit: Characterizing the convergence of common sequences of basis sets for intermolecular interactions as described by density functional theory. *The Journal of Chemical Physics.* 2016, **144**(19), p.194306.

31. Feller, D., Peterson, K.A. and Dixon, D.A. A survey of factors contributing to accurate theoretical predictions of atomization energies and molecular structures. *The Journal of Chemical Physics.* 2008, **129**(20), p.204105.

32. Feller, D., Peterson, K.A. and Grant Hill, J. On the effectiveness of CCSD(T) complete basis set extrapolations for atomization energies. *The Journal of Chemical Physics.* 2011, **135**(4), p.044102.

33. Feller, D. Benchmarks of improved complete basis set extrapolation schemes designed for standard CCSD(T) atomization energies. *The Journal of Chemical Physics.* 2013, **138**(7), p.074103.

34. Riley, K.E., Pitoňák, M., Jurečka, P. and Hobza, P. Stabilization and Structure Calculations for Noncovalent Interactions in Extended Molecular Systems Based on Wave Function and Density Functional Theories. *Chemical Reviews.* 2010, **110**(9), pp.5023-5063.

35. Zhao, Y. and Truhlar, D.G. Benchmark Databases for Nonbonded Interactions and Their Use To Test Density Functional Theory. *Journal of Chemical Theory and Computation.* 2005, **1**(3), pp.415-432.

36. Mardirossian, N. and Head-Gordon, M. Thirty years of density functional theory in computational chemistry: an overview and extensive assessment of 200 density functionals. *Molecular Physics.* 2017, **115**(19), pp.2315-2372.

37. *NIST Computational Chemistry Comparison and Benchmark Database.* [Online]. [Accessed 29/09/2022]. Available from: http://cccbdb.nist.gov/

38. *Database of Frequency Scale Factors for Electronic Model Chemistries.* [Online]. [Accessed 27/02/2023]. Available from: https://comp.chem.umn.edu/freqscale/

39. Martin, J.M.L. On the performance of correlation consistent basis sets for the calculation of total atomization energies, geometries, and harmonic frequencies. *The Journal of Chemical Physics.* 1994, **100**(11), pp.8186-8193.

40. *Research Computing at Leeds.* [Online]. [Accessed 29/09/2022]. Available from: https://arc.leeds.ac.uk/

41. Frisch, M.J., Trucks, G.W., Schlegel, H.B., Scuseria, G.E., Robb, M.A., Cheeseman, J.R., Scalmani, G., Barone, V., Mennucci, B., Petersson, G.A., Nakatsuji, H., Caricato, M., Li, X., Hratchian, H.P., Izmaylov, A.F., Bloino, J., Zheng, G., Sonnenberg, J.L., Hada, M., Ehara, M., Toyota, K., Fukuda, R., Hasegawa, J., Ishida, M., Nakajima, T., Honda, Y., Kitao, O., Nakai, H., Vreven, T., J. A. Montgomery, J., Peralta, J.E., Ogliaro, F., Bearpark, M., Heyd, J.J., Brothers, E., Kudin, K.N., Staroverov, V.N., Keith, T., Kobayashi, R., Normand, J., Raghavachari, K., Rendell, A., Burant, J.C., Iyengar, S.S., Tomasi, J., Cossi, M., Rega, N., Millam, J.M., Klene, M., Knox, J.E., Cross, J.B., Bakken, V., Adamo, C., Jaramillo, J., Gomperts, R., Stratmann, R.E., Yazyev, O., Austin, A.J., Cammi, R., Pomelli, C., Ochterski, J.W., Martin, R.L., Morokuma, K., Zakrzewski, V.G., Voth, G.A., Salvador, P., Dannenberg, J.J., Dapprich, S., Daniels, A.D., Farkas, O., Foresman, J.B., Ortiz, J.V., Cioslowski, J. and Fox, D.J. *Gaussian 09 Revision D.01*. Wallingford CT: Gaussian, Inc. 2013.

42. Werner, H.J., Knowles, P.J., Knizia, G., Manby, F.R., Schütz, M., Celani, P., Györffy, W., Kats, D., Korona, T., Lindh, R., Mitrushenkov, A., Rauhut, G., Shamasundar, K.R., Adler, T.B., Amos, R.D., Bennie, S.J., Bernhardsson, A., Berning, A., Cooper, D.L., Deegan, M.J.O., Dobbyn, A.J., Eckert, F., Goll, E., Hampel, C., Hesselmann, A., Hetzer, G., Hrenar, T., Jansen, G., Köppl, C., Lee, S.J.R., Liu, Y., Lloyd, A.W., Ma, Q., Mata, R.A., May, A.J., McNicholas, S.J., Meyer, W., III, T.F.M., Mura, M.E., Nicklass, A., O'Neill, D.P., Palmieri, P., Peng, D., Petrenko, T., Pflüger, K., Pitzer, R., Reiher, M., Shiozaki, T., Stoll, H., Stone, A.J.,

Tarroni, R., Thorsteinsson, T., Wang, M. and Welborn, M. *MOLPRO, a package of ab initio programs*.

43. Barca, G.M.J., Bertoni, C., Carrington, L., Datta, D., De Silva, N., Deustua, J.E., Fedorov, D.G., Gour, J.R., Gunina, A.O., Guidez, E., Harville, T., Irle, S., Ivanic, J., Kowalski, K., Leang, S.S., Li, H., Li, W., Lutz, J.J., Magoulas, I., Mato, J., Mironov, V., Nakata, H., Pham, B.Q., Piecuch, P., Poole, D., Pruitt, S.R., Rendell, A.P., Roskop, L.B., Ruedenberg, K., Sattasathuchana, T., Schmidt, M.W., Shen, J., Slipchenko, L., Sosonkina, M., Sundriyal, V., Tiwari, A., Galvez Vallejo, J.L., Westheimer, B., Włoch, M., Xu, P., Zahariev, F. and Gordon, M.S. Recent developments in the general atomic and molecular electronic structure system. *The Journal of Chemical Physics.* 2020, **152**(15), p.154102.

44. Aquilante, F., Autschbach, J., Baiardi, A., Battaglia, S., Borin, V.A., Chibotaru, L.F., Conti, I., De Vico, L., Delcey, M., Fdez. Galván, I., Ferré, N., Freitag, L., Garavelli, M., Gong, X., Knecht, S., Larsson, E.D., Lindh, R., Lundberg, M., Malmqvist, P.Å., Nenov, A., Norell, J., Odelius, M., Olivucci, M., Pedersen, T.B., Pedraza-González, L., Phung, Q.M., Pierloot, K., Reiher, M., Schapiro, I., Segarra-Martí, J., Segatta, F., Seijo, L., Sen, S., Sergentu, D.-C., Stein, C.J., Ungur, L., Vacher, M., Valentini, A. and Veryazov, V. Modern quantum chemistry with [Open]Molcas. *The Journal of Chemical Physics.* 2020, **152**(21), p.214117.

45. Smith, D.G.A., Burns, L.A., Simmonett, A.C., Parrish, R.M., Schieber, M.C., Galvelis, R., Kraus, P., Kruse, H., Di Remigio, R., Alenaizan, A., James, A.M., Lehtola, S., Misiewicz, J.P., Scheurer, M., Shaw, R.A., Schriber, J.B., Xie, Y., Glick, Z.L., Sirianni, D.A., O'Brien, J.S., Waldrop, J.M., Kumar, A., Hohenstein, E.G., Pritchard, B.P., Brooks, B.R., Schaefer, H.F., Sokolov, A.Y., Patkowski, K., DePrince, A.E., Bozkaya, U., King, R.A., Evangelista, F.A., Turney, J.M., Crawford, T.D. and Sherrill, C.D. PSI4 1.4: Open-source software for high-throughput quantum chemistry. *The Journal of Chemical Physics.* 2020, **152**(18), p.184108.

46. Epifanovsky, E., Gilbert, A.T.B., Feng, X., Lee, J., Mao, Y., Mardirossian, N., Pokhilko, P., White, A.F., Coons, M.P., Dempwolff, A.L., Gan, Z., Hait, D., Horn, P.R., Jacobson, L.D., Kaliman, I., Kussmann, J., Lange, A.W., Lao, K.U., Levine, D.S., Liu, J., McKenzie, S.C., Morrison, A.F.,

Nanda, K.D., Plasser, F., Rehn, D.R., Vidal, M.L., You, Z.-Q., Zhu, Y., Alam, B., Albrecht, B.J., Aldossary, A., Alguire, E., Andersen, J.H., Athavale, V., Barton, D., Begam, K., Behn, A., Bellonzi, N., Bernard, Y.A., Berquist, E.J., Burton, H.G.A., Carreras, A., Carter-Fenk, K., Chakraborty, R., Chien, A.D., Closser, K.D., Cofer-Shabica, V., Dasgupta, S., de Wergifosse, M., Deng, J., Diedenhofen, M., Do, H., Ehlert, S., Fang, P.-T., Fatehi, S., Feng, Q., Friedhoff, T., Gayvert, J., Ge, Q., Gidofalvi, G., Goldey, M., Gomes, J., González-Espinoza, C.E., Gulania, S., Gunina, A.O., Hanson-Heine, M.W.D., Harbach, P.H.P., Hauser, A., Herbst, M.F., Hernández Vera, M., Hodecker, M., Holden, Z.C., Houck, S., Huang, X., Hui, K., Huynh, B.C., Ivanov, M., Jász, Á., Ji, H., Jiang, H., Kaduk, B., Kähler, S., Khistyaev, K., Kim, J., Kis, G., Klunzinger, P., Koczor-Benda, Z., Koh, J.H., Kosenkov, D., Koulias, L., Kowalczyk, T., Krauter, C.M., Kue, K., Kunitsa, A., Kus, T., Ladjánszki, I., Landau, A., Lawler, K.V., Lefrancois, D., Lehtola, S., Li, R.R., Li, Y.-P., Liang, J., Liebenthal, M., Lin, H.-H., Lin, Y.-S., Liu, F., Liu, K.-Y., Loipersberger, M., Luenser, A., Manjanath, A., Manohar, P., Mansoor, E., Manzer, S.F., Mao, S.-P., Marenich, A.V., Markovich, T., Mason, S., Maurer, S.A., McLaughlin, P.F., Menger, M.F.S.J., Mewes, J.-M., Mewes, S.A., Morgante, P., Mullinax, J.W., Oosterbaan, K.J., Paran, G., Paul, A.C., Paul, S.K., Pavošević, F., Pei, Z., Prager, S., Proynov, E.I., Rák, Á., Ramos-Cordoba, E., Rana, B., Rask, A.E., Rettig, A., Richard, R.M., Rob, F., Rossomme, E., Scheele, T., Scheurer, M., Schneider, M., Sergueev, N., Sharada, S.M., Skomorowski, W., Small, D.W., Stein, C.J., Su, Y.-C., Sundstrom, E.J., Tao, Z., Thirman, J., Tornai, G.J., Tsuchimochi, T., Tubman, N.M., Veccham, S.P., Vydrov, O., Wenzel, J., Witte, J., Yamada, A., Yao, K., Yeganeh, S., Yost, S.R., Zech, A., Zhang, I.Y., Zhang, X., Zhang, Y., Zuev, D., Aspuru-Guzik, A., Bell, A.T., Besley, N.A., Bravaya, K.B., Brooks, B.R., Casanova, D., Chai, J.-D., Coriani, S., Cramer, C.J., Cserey, G., DePrince, A.E., DiStasio, R.A., Dreuw, A., Dunietz, B.D., Furlani, T.R., Goddard, W.A., Hammes-Schiffer, S., Head-Gordon, T., Hehre, W.J., Hsu, C.-P., Jagau, T.-C., Jung, Y., Klamt, A., Kong, J., Lambrecht, D.S., Liang, W., Mayhall, N.J., McCurdy, C.W., Neaton, J.B., Ochsenfeld, C., Parkhill, J.A., Peverati, R., Rassolov, V.A., Shao, Y., Slipchenko, L.V., Stauch, T., Steele, R.P., Subotnik, J.E., Thom, A.J.W., Tkatchenko, A., Truhlar, D.G., Van Voorhis, T., Wesolowski, T.A., Whaley, K.B., Woodcock, H.L., Zimmerman, P.M., Faraji, S., Gill, P.M.W., Head-Gordon, M., Herbert, J.M. and Krylov, A.I. Software for the frontiers of quantum chemistry: An overview of developments in the Q-Chem 5 package. *The Journal of Chemical Physics.* 2021, **155**(8), p.084801.

47. Schlegel, H.B. Optimization of equilibrium geometries and transition structures. *Journal of Computational Chemistry.* 1982, **3**(2), pp.214-218.

48. Glowacki, D.R., Liang, C.-H., Morley, C., Pilling, M.J. and Robertson, S.H. MESMER: An Open-Source Master Equation Solver for Multi-Energy Well Reactions. *The Journal of Physical Chemistry A.* 2012, **116**(38), pp.9545-9560.

49. Pilling, M.J. and Seakins, P.W. *Reaction kinetics.* Oxford: Oxford University Press, 1995.

50. Steinfeld, J.I., Francisco, J.S. and Hase, W.L. *Chemical kinetics and dynamics.* 2nd ed. Upper Saddle River, N.J: Prentice Hall, 1998.

51. Gilbert, R.G. and Smith, S.C. *Theory of unimolecular and recombination reactions.* Oxford: Blackwell Scientific, 1990.

52. Holbrook, K.A., Pilling, M.J., Robertson, S.H. and Robinson, P.J. *Unimolecular reactions.* Second edition. ed. Chichester: Wiley, 1996.

53. Hinshelwood, C.N. and Sidgwick, N.V. On the theory of unimolecular reactions. *Proceedings of the Royal Society of London. Series A, Containing Papers of a Mathematical and Physical Character.* 1926, **113**(763), pp.230-233.

54. Rice, O.K. and Ramsperger, H.C. Theories of Unimolecular Gas Reactions at Low Pressures. *Journal of the American Chemical Society.* 1927, **49**(7), pp.1617-1629.

55. Rice, O.K. and Ramsperger, H.C. Theories of Unimolecular Gas Reactions at Low Pressures. II. *Journal of the American Chemical Society.* 1928, **50**(3), pp.617-620.

56. Kassel, L.S. Studies in Homogeneous Gas Reactions. I. *The Journal of Physical Chemistry.* 1927, **32**(2), pp.225-242.

57. Marcus, R.A. Unimolecular Dissociations and Free Radical Recombination Reactions. *The Journal of Chemical Physics.* 1952, **20**(3), pp.359-364.

58. Shannon, R.J. *Experimental and computational studies of hydroxyl radical kinetics at very low temperatures*. Dissertation/Thesis thesis, University of Leeds, 2012.

59. Beyer, T. and Swinehart, D.F. Algorithm 448: number of multiply-restricted partitions. *Communications of the Association for Computing Machinery.* 1973, **16**, p.379.

60. Truhlar, D.G. and Garrett, B.C. Variational Transition State Theory. *Annual Review of Physical Chemistry.* 1984, **35**(1), pp.159-189.

61. Weitzel, K.-M. On the distinction between tight and loose transition states in unimolecular dissociations. *Chemical Physics Letters.* 1991, **186**(6), pp.490-494.

62. Greenwald, E.E., North, S.W., Georgievskii, Y. and Klippenstein, S.J. A Two Transition State Model for Radical−Molecule Reactions: A Case Study of the Addition of OH to C_2H_4. *The Journal of Physical Chemistry A.* 2005, **109**(27), pp.6031-6044.

63. Georgievskii, Y. and Klippenstein, S.J. Strange Kinetics of the C_2H_6 + CN Reaction Explained. *The Journal of Physical Chemistry A.* 2007, **111**(19), pp.3802-3811.

64. Atkins, P.W. and De Paula, J. *Atkins' Physical chemistry.* 9th ed. Oxford: Oxford University Press, 2010.

65. Eckart, C. The Penetration of a Potential Barrier by Electrons. *Physical Review.* 1930, **35**(11), pp.1303-1309.

66. Miller, W.H. Tunneling corrections to unimolecular rate constants, with application to formaldehyde. *Journal of the American Chemical Society.* 1979, **101**(23), pp.6810-6814.

67. Garrett, B.C. and Truhlar, D.G. Semiclassical tunneling calculations. *The Journal of Physical Chemistry.* 1979, **83**(22), pp.2921-2926.

68. Jones, J.E. and Chapman, S. On the determination of molecular fields.—I. From the variation of the viscosity of a gas with temperature. *Proceedings of the Royal Society of London. Series A, Containing Papers of a Mathematical and Physical Character.* 1924, **106**(738), pp.441-462.

69. Jones, J.E. and Chapman, S. On the determination of molecular fields. —II. From the equation of state of a gas. *Proceedings of the Royal Society of London. Series A, Containing Papers of a Mathematical and Physical Character.* 1924, **106**(738), pp.463-477.

70. Troe, J. Theory of thermal unimolecular reactions at low pressures. II. Strong collision rate constants. Applications. *The Journal of Chemical Physics.* 1977, **66**(11), pp.4758-4775.

71. Troe, J. Theory of thermal unimolecular reactions at low pressures. I. Solutions of the master equation. *The Journal of Chemical Physics.* 1977, **66**(11), pp.4745-4757.

72. Barker, J.R. Multiple-Well, multiple-path unimolecular reaction systems. I. MultiWell computer program suite. *International Journal of Chemical Kinetics.* 2001, **33**(4), pp.232-245.

73. Barker, J.R. Energy transfer in master equation simulations: A new approach. *International Journal of Chemical Kinetics.* 2009, **41**(12), pp.748-763.

74. Georgievskii, Y., Miller, J.A., Burke, M.P. and Klippenstein, S.J. Reformulation and Solution of the Master Equation for Multiple-Well Chemical Reactions. *The Journal of Physical Chemistry A.* 2013, **117**(46), pp.12146-12154.

75. Jasper, A.W. “Third-body” collision parameters for hydrocarbons, alcohols, and hydroperoxides and an effective internal rotor approach for estimating them. *International Journal of Chemical Kinetics.* 2020, **52**(6), pp.387-402.

76. Pilling, M.J. and Robertson, S.H. Master Equation Models for Chemical Reactions of Importance in Combustion. *Annual Review of Physical Chemistry.* 2003, **54**(1), pp.245-275.

77. Herbst, E. Tunneling in the C_2H-H_2 reaction at low temperature. *Chemical Physics Letters.* 1994, **222**(3), pp.297-301.

78. Bartis, J.T. and Widom, B. Stochastic models of the interconversion of three or more chemical species. *The Journal of Chemical Physics.* 1974, **60**(9), pp.3474-3482.

Chapter 3

The reaction between the cyano radical (CN) and formaldehyde (CH_2O)

3.1 Introduction

There are still relatively limited studies on the rate coefficients and product branching ratios for gas-phase neutral-neutral reactions at extremely low temperature conditions relevant to the ISM. As suggested in Chapter 1, the limited studies are because typical reactions with barriers following the Arrhenius behaviour are not expected to proceed quickly. However, there are two broad categories of reactions which make it possible to have a significant rate coefficient at very low temperatures.

One category are those for which the entire reaction pathway is submerged relative to the reactants and the rate coefficient can possibly have a negative temperature dependence, where an example is the reaction of the methylidyne radical (CH) with CH_2O (1-3). Experimental measurements at temperatures of 298 – 670 K (1) showed a negative temperature dependence and gave rate coefficient value in the order of 10^{-10} cm^3 $molecule^{-1}$ s^{-1}, and further measurements (2) suggested that below 133 K the rate coefficient can rise to an exceptionally high value of about 10^{-9} cm^3 $molecule^{-1}$ s^{-1} as shown in Figure 3.1. A theoretical study by Nguyen et al. (3) identified three barrierless entrance channels, namely chain addition, cycloaddition and insertion, and the two dominant product sets at low temperature are found to be ketene H_2CCO + H and CH_3 + CO, where the energies of the entire reaction routes can remain lower than that of the reactants as shown in Figure 3.2, that is,

$$\mathrm{CH} + \mathrm{CH_2O} \rightarrow \mathrm{H_2CCO} + \mathrm{H} \qquad \text{R 3.1}$$

$$\mathrm{CH} + \mathrm{CH_2O} \rightarrow \mathrm{CH_3} + \mathrm{CO} \qquad \text{R 3.2}$$

The negative temperature dependence of the rate coefficients has also been suggested from this computational study.

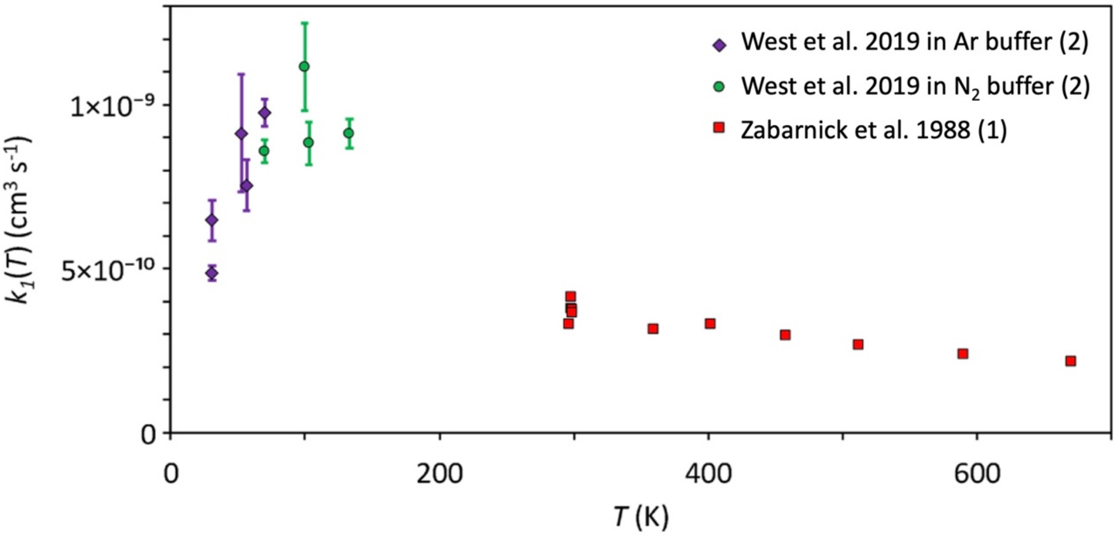

Figure 3.1 Experimental rate coefficients for the CH + CH_2O reaction versus temperature reported in previous literature. Taken from West et al. (2).

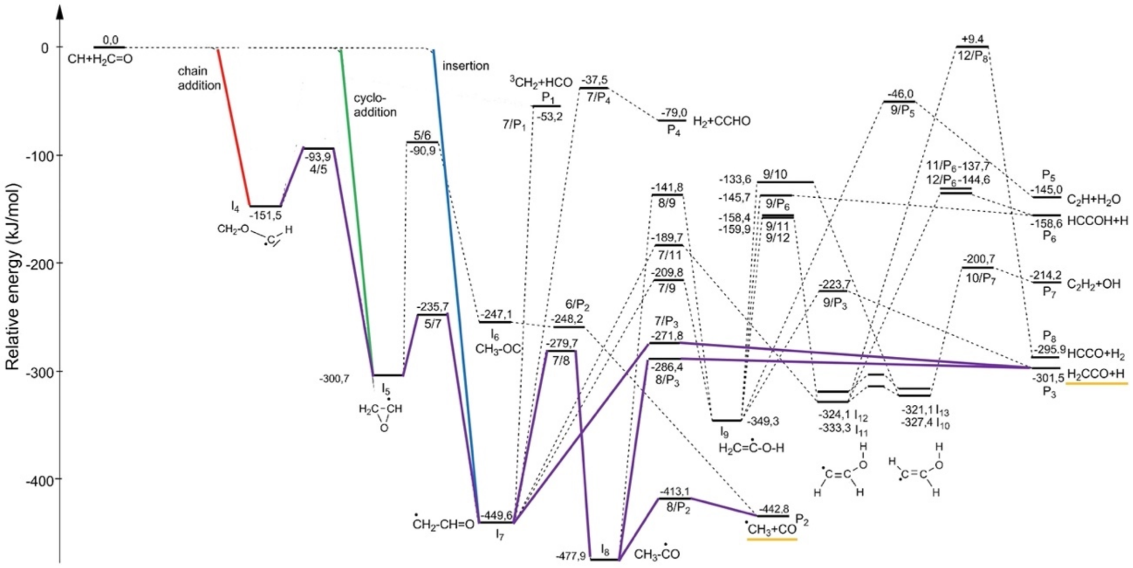

Figure 3.2 Zero-point vibrational energy (ZPVE) corrected potential energy surface in kJ mol^{-1} for the CH + CH_2O reaction at the CCSD(T)/aug-cc-pVTZ//BHandHLYP/aug-cc-pVDZ level. Adapted from Nguyen et al. (3). The three entrance channels, chain addition (red), cycloaddition (green) and insertion (blue) together with the lowest energy pathways (purple) leading to the two dominant product sets, H_2CCO + H and CH_3 + CO (yellow), are highlighted.

Another category are reactions with barriers but the reactants are capable of forming weakly bound complexes in the entrance channels such that the reaction can proceed by tunnelling through the barriers. Examples include the H abstraction reaction of the hydroxyl radical (OH) with a range of volatile organic compounds (VOCs) (4-25), such as methanol (5-12) with the potential energy surface as shown in . While at high temperature, the rate coefficients show a positive temperature dependence, the lengthened lifetime of the pre-reaction complex at low temperature becomes sufficiently long to allow quantum mechanical tunnelling to products to occur, resulting an increase in the rate coefficient with a decrease in temperature and thus an overall V-shaped temperature dependence trend.

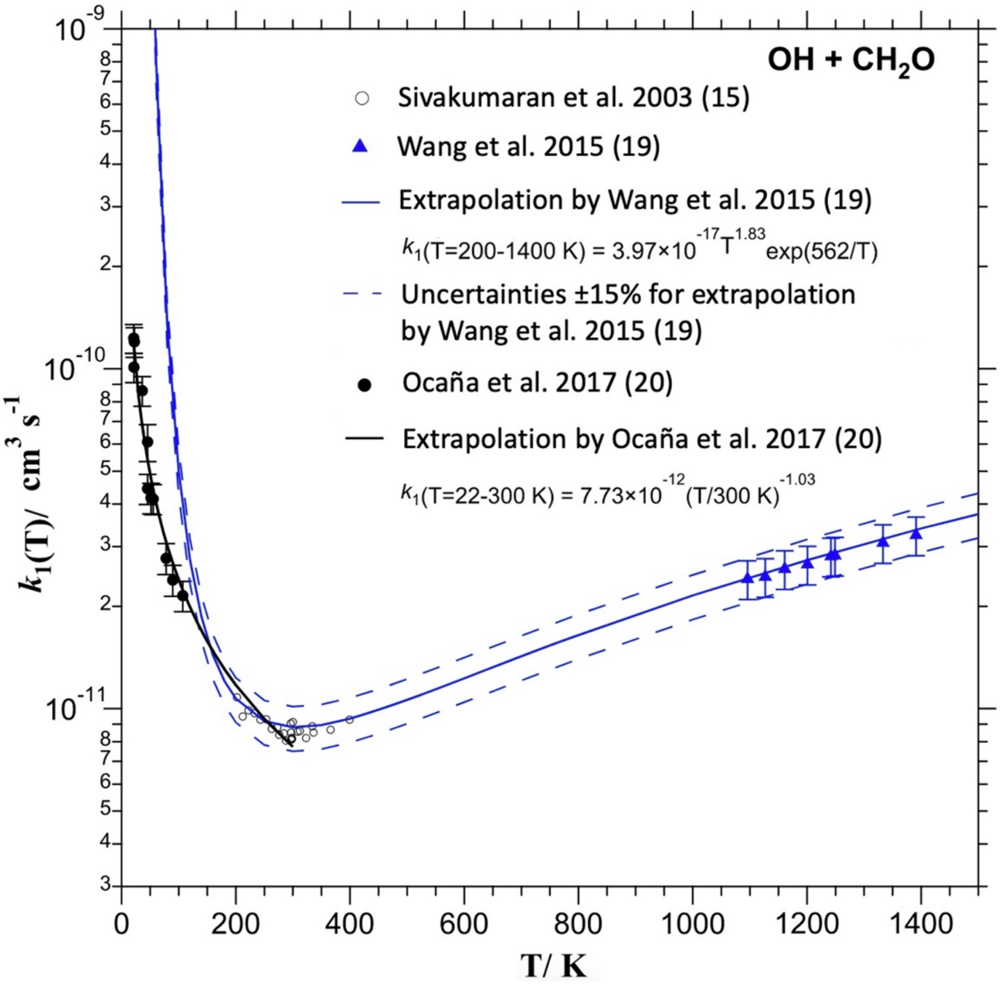

Figure 3.3 Rate coefficients for the OH + CH₂O reaction versus temperature reported in previous literature. Taken from Ocaña et al. (20).

A noteworthy example is the reaction between OH and CH_2O, which has been studied both experimentally and theoretically in previous work (15-21, 26-28). Figure 3.3 shows that the measured rate coefficient for OH + CH_2O demonstrates a V-shaped temperature dependence. The rate coefficient is in the order of 10^{-11} cm^3 $molecule^{-1}$ s^{-1} in the temperature range of 200–1400 K but negative temperature dependence begins to emerge beneath 200 K. While earlier work (19) predicts that the rate coefficient could go up to the order of 10^{-9} cm^3 $molecule^{-1}$ s^{-1} below 50 K, later experimental work (20) finds that the value only rises to about the order of 10^{-10} cm^3 $molecule^{-1}$ s^{-1} and provides an updated expression for extrapolation. From the computational results, a pre-reaction complex is identified after the approach of the two reagents followed by a transition state leading to the products for the H abstraction reaction. However, there are discrepancies across different literature on whether the barrier is positive or submerged. It is suggested (28) that the energies of this saddle point computed with more robust methods tend to give lower values, decreasing the barrier from being slightly positive to slightly submerged as shown in Table 3.1. The latest value reported from Machado et al. (28) obtained at the CCSD(T)/CBS//CCSD/aug-cc-pVDZ level is approximately –5.6 kJ mol^{-1}, with the PES shown in Figure 3.4.

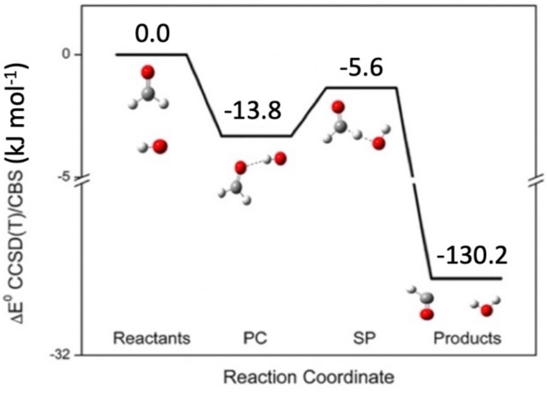

Figure 3.4 Potential energy profile (in kJ mol^{-1}, ZPVE corrected) along the reaction coordinate for the H abstraction reaction of OH + $CH_2O \rightarrow H_2O$ + HCO at the CCSD(T)/CBS//CCSD/aug-cc-pVDZ level of theory. Taken from Machado et al. (28). The reaction starts off with the two reactants OH and CH_2O approaching to form a pre-reaction complex (PC) followed by a saddle point (SP) and eventually generates the products H_2O + HCO.

Table 3.1 Barrier height for the reaction OH + $CH_2O \rightarrow HCO + H_2O$ reported in previous literature calculated at different levels of theory. Adapted from Machado et al. (28).

Level of theory	Energy (kJ mol^{-1})	Reference
QCISD/6-311G(d,p)	7.5	(17)
MP4(SDTQ)/6-311++G(3df,3pd)	6.9	(27)
CCSD(T)/6-311++G(d,p)//CCSD/6-311++G(d,p)	0.9	(18)
CCSD(T)/6-311++G(d,p)	0.5	(27)
CCSD(T)/aug-cc-pVDZ//MP2/aug-cc-pVDZ	–2.9	(16)
CCSD(T)/6-311+G(3df,2p)//CCSD/6-311++G(d,p)	–4.2	(26)
CCSD(T)/CBS//CCSD/aug-cc-pVDZ	–5.6	(28)

In this chapter, the reaction between CN and CH_2O is investigated, in particular the mechanism and the major products at low temperatures. CH_2O is the first discovered interstellar polyatomic organic molecule, with a widespread distribution in different types of galactic and extragalactic objects (29-31). In our solar system, CH_2O is known to have notable abundance in the atmospheres of the Earth (32, 33) and Titan (34, 35), the largest moon of Saturn. For the CN radical, its absorption features could already be identified from spectra from interstellar sources since the 1930s (36, 37). It is believed to exist in interstellar molecular clouds (38-40), as well as in the atmospheres of planets and satellites, for instance, Titan (41-47). The stability arisen from the triple bond between C and N makes the CN radical as well as the set of nitrile compounds possible sinks of atmospheric nitrogen (48). It is also suggested that the reactions involving CN and the subsequent evolution to form various nitrile compounds play an important role in Titan's chemistry (41-47). Consider the reaction between CN and CH_2O where C, N, O and H, which are all elements essential to life, are brought together, a potential type of reaction to occur is H abstraction, that is,

$$\mathrm{CN + CH_2O \rightarrow HCN + HCO} \left(\Delta H^{\ominus}_{r,298\mathrm{K}} = -160\ \mathrm{kJ\ mol^{-1}}\right) \quad \text{R 3.3}$$

$$\mathrm{CN + CH_2O \rightarrow HNC + HCO} \left(\Delta H^{\ominus}_{r,298\mathrm{K}} = -97\ \mathrm{kJ\ mol^{-1}}\right) \quad \text{R 3.4}$$

where the enthalpies are retrieved from the heats of formation given in Ruscic and Bross (49). These possible products, namely HCN, HNC and HCO, have also been detected in the ISM (50-52). It is also proposed that (53) CN + CH_2O can be a primary pathway to the formation of the interstellar molecule formyl cyanide HC(O)CN. Therefore, further research on the CN + CH_2O reaction is likely to provide more insights in the generation of key species in the ISM.

Previous experimental work on the rate coefficients of the CN + CH_2O reaction has been performed respectively by Yu et al. (54) and Chang and Wang (55) using the laser flash photolysis coupled with laser-induced fluorescence technique (LFP-LIF). For Yu et al. (54), measurements were taken in the temperature range of 297–673 K with Ar as the bath gas and the rate coefficients k were fitted by the expression:

$$k(T) = 2.82 \times 10^{-19} \times T^{-2.72} \exp\left(\frac{718\mathrm{K}}{T}\right)\ \mathrm{cm^3\ molecule^{-1}\ s^{-1}} \quad \text{E 3.1}$$

where the main reaction mechanism is suggested to be a simple H abstraction to form HCN + HCO. For Chang and Wang (55), measurements were taken in the temperature range of 294–769 K and the pressure range of 52–201 Torr with He as the bath gas and the rate coefficients k were fitted by the expression:

$$k(T) = (6.7 \pm 1.0) \times 10^{-11} \times \exp\left(\frac{-412 \pm 20\mathrm{K}}{T}\right)\ \mathrm{cm^3\ molecule^{-1}\ s^{-1}} \quad \text{E 3.2}$$

where no pressure dependence was observed. The two expressions for the rate coefficients are plotted in Figure 3.5, where both show a positive temperature dependence over the experimental range.

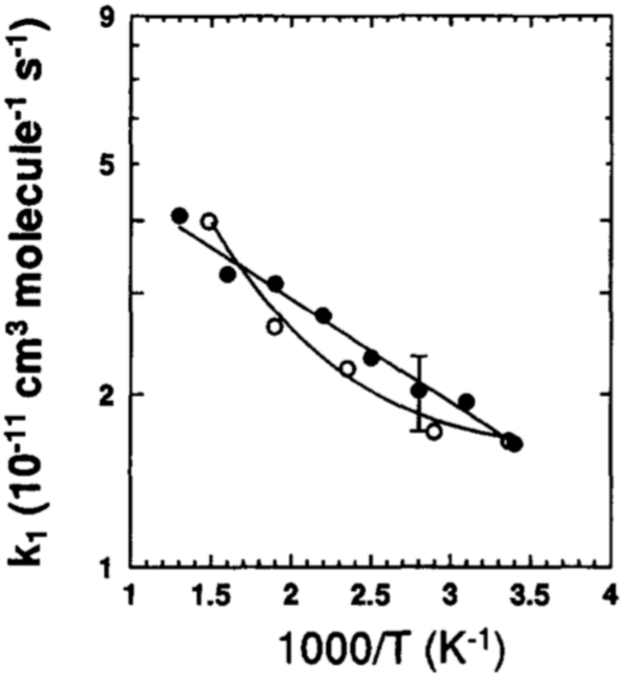

Figure 3.5 Previously published experimentally measured rate coefficients of the reaction CN + CH_2O against the inverse of temperature. Taken from Chang and Wang (55). The open circles are data from Yu et al. (54) while the closed circles are data from Chang and Wang (55).

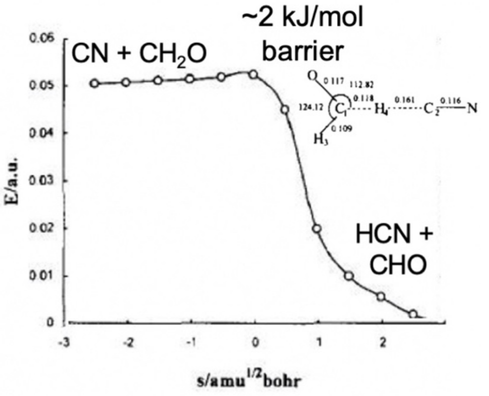

Figure 3.6 Potential energy profile along the reaction coordinate for the direct H abstraction reaction of CN + CH_2O → HCN + HCO at the QCISD/6-31G//UHF/6-31G** level of theory. Adapted from Feng et al. (56). The y-axis is in Hartree, where 1 Hartree = 2625.5 kJ mol^{-1} where the barrier relative to the reactants is ~ 2 kJ mol^{-1}.**

For theoretical work, ab initio calculations were carried out by Feng et al. (56) which focussed on the direct H abstraction channel of CN from CH_2O to form HCN + HCO. Geometry optimisations of the stationary points were performed at the UHF/6-31G** level of theory and the results suggested the involvement of a small barrier, with a geometry change along the linear axis of C - - - H - - - C≡N, relative to the entrance channel as shown in Figure 3.6. Further refinement of the energies at the QCISD/6-31G** and CCSD/6-31G** levels of theory give a barrier height of 2.71 kJ mol^{-1} and 1.26 kJ mol^{-1} respectively. However, it is important to note that the Hartree-Fock method (HF), due to its simplicity, only considers the effect of an average electrostatic field rather than the correlation energy contributed by the interactions among the electrons, and so the results are not expected to be quantitatively correct. Thus, it is worth investigating this reaction by performing ab initio calculations at a higher level of theory which will be described later in this chapter.

More recent calculations have been performed by Tonolo et al. (57) at the CCSD(T)/CBS+CV//B2PLYP/maug-cc-pVTZ-*d*H level and the potential energy surface obtained is shown in Figure 3.7. For the H abstraction route, it is reported to have a pre-reaction complex structure followed by a small submerged barrier that eventually leads to HCN + HCO. The addition pathway has also been explored by Tonolo et al. (57), which would eventually form formyl cyanide HC(O)CN as the product following the removal of a H atom from the N≡C-CH_2O adduct. The formation of the N≡C-CH_2O adduct from the starting reagents, which involves breaking the carbonyl bond in CH_2O and forming a bond between the C of CH_2O and the C of CN, is suggested to be barrierless. However, the rate coefficients calculated from a master equation method based on such a reaction scheme (57) are reported to stay in the order of 10^{-9} cm^3 molecule^{-1} s^{-1} over the temperature range of 50–300 K. In particular, when comparing the calculated room temperature values with previous experiments (54, 55) there is an almost 50 times overestimation by theory.

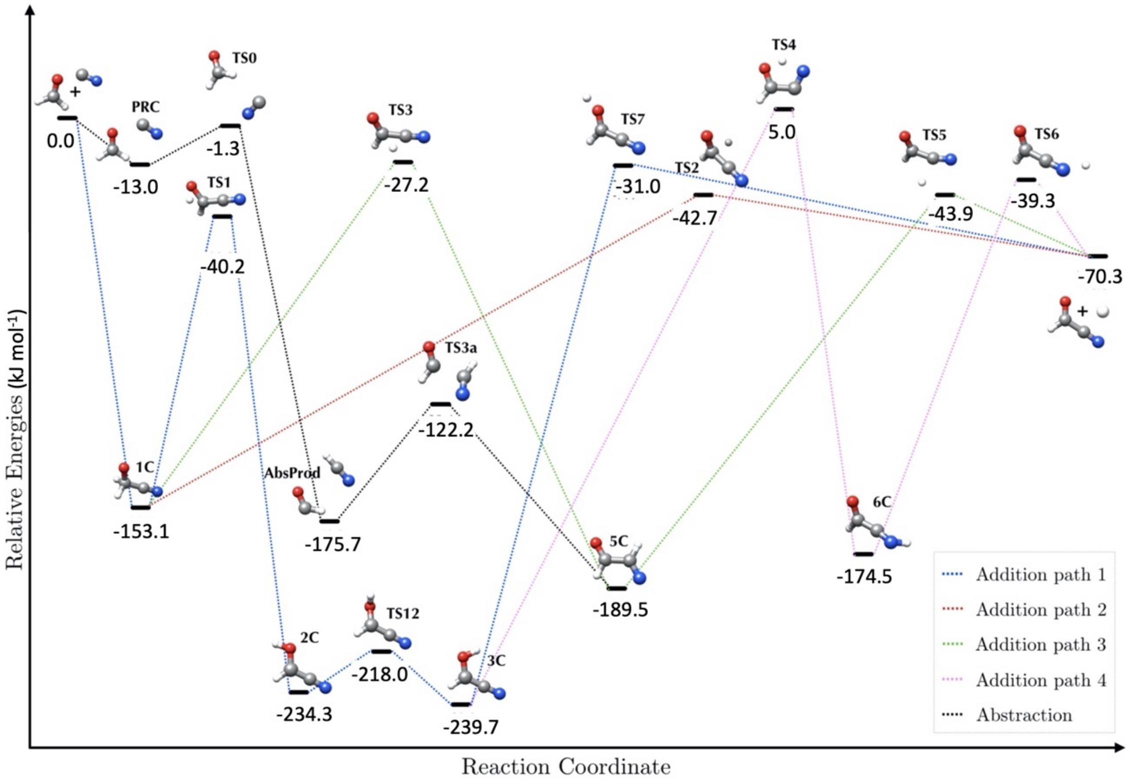

Figure 3.7 Proposed abstraction and addition pathways for the reaction between CN and CH_2O by Tonolo et al. Taken from (57). Energy values (all in kJ mol^{-1}, ZPVE corrected) are obtained at the CCSD(T)/CBS+CV// B2PLYP/maug-cc-pVTZ-*d*H level of theory. PRC denotes the pre-reaction complex while 1C denotes the N≡C-CH_2O adduct.

In this work, an ab initio potential energy surface was calculated for the CN + CH_2O reaction and utilised in the master equation solver to calculate the rate coefficients and product branching ratios. Experiments have been carried out by Dr Niclas West and Mr Edward Rutter (University of Leeds) using the Laval set-up at low temperatures and the results, together with the previous experimental results at high temperatures (54, 55) were used to fit with the calculated results to obtain the set of optimised parameters for extrapolation.

3.2 Computational methods

Theoretical approaches were used in this work to calculate the PES of the CN + CH_2O reaction in order to further explore the reaction mechanisms responsible for the behaviour of the reaction rate coefficients as a function of temperature.

With a more detailed description given in Section 2.1, geometric structures of stationary points (reactants, products, intermediates, and transition states (TSs)) were first optimised at the BHandHLYP/aug-cc-pVDZ level of theory (58-61) and further refined using M06-2X/aug-cc-pVTZ (62). Higher-level single-point energy calculations were performed at the CCSD(T)/aug-cc-pVTZ level (63, 64) to obtain more accurate energies. Vibrational frequency calculations were performed to evaluate zero-point vibrational energies (ZPVE), where TSs were found to have one imaginary vibrational frequency while all positive vibrational frequencies for the other species. The vibrational frequency scaling factors for BHandHLYP/aug-cc-pVDZ and M06-2X/aug-cc-pVTZ are taken to be 0.9589 and 0.956 respectively (65, 66). Intrinsic reaction coordinate (IRC) calculations were carried out for all TSs located during the PES search, unless otherwise specified, to verify that they are indeed saddle points on the minimum energy pathways connecting the respective local minima. In order to further explore the long-range reaction PES as the two reactants approach each other, relaxed scans were performed along the reaction entrance channels at the BHandHLYP/aug-cc-pVDZ and M06-2X/aug-cc-pVTZ levels of theory. All electronic structure calculations were carried out using the Gaussian 09 programme (67).

From the generated PES, statistical rate theory calculations were performed using the MESMER software programme (68), where further details can be found in Section 2.2, in order to obtain the rate coefficients of the system. The stationary points of the ab initio calculations provide the energies, rotational constants, and vibrational constants required by the MESMER input file. The energy wells along the PES are divided into energy grains, where each grain couples the reactant, intermediate, and product species to one another via the microcanonical rate coefficients, $k(E)$. The individual grains can be populated or depopulated by exchange with other grains via collisional energy transfer with the buffer gas. The properties of the bath gases were included in the MESMER input files as listed in Section 2.2. The microcanonical rate coefficients were calculated with either RRKM theory (69) for channels involving a defined transition state or the ILT method (70) for barrierless channels. Collisional energy transfer probabilities were described using the exponential-down model

(71). Corrections for quantum mechanical tunnelling were also included using the Eckart expression (72). The set of coupled differential equations that describe each of the energy grains, known as the energy grained master equation (EGME), was solved by MESMER and the solutions, which were the eigenvalues of the matrix-form EGME, would be the phenomenological rate coefficients. Using the time dependence of the concentration of all species calculated by MESMER, the branching yield of different products can be determined. Apart from performing simulations, given the availability of experimental data for the reaction of CN + CH_2O, the built-in fitting feature of MESMER was used, whereby input parameters, such as the ILT parameters and the energies of the stationary points, can be adjusted to best fit to the experimentally measured rate coefficients.

3.3 Results and discussions

3.3.1 Results from ab initio calculations

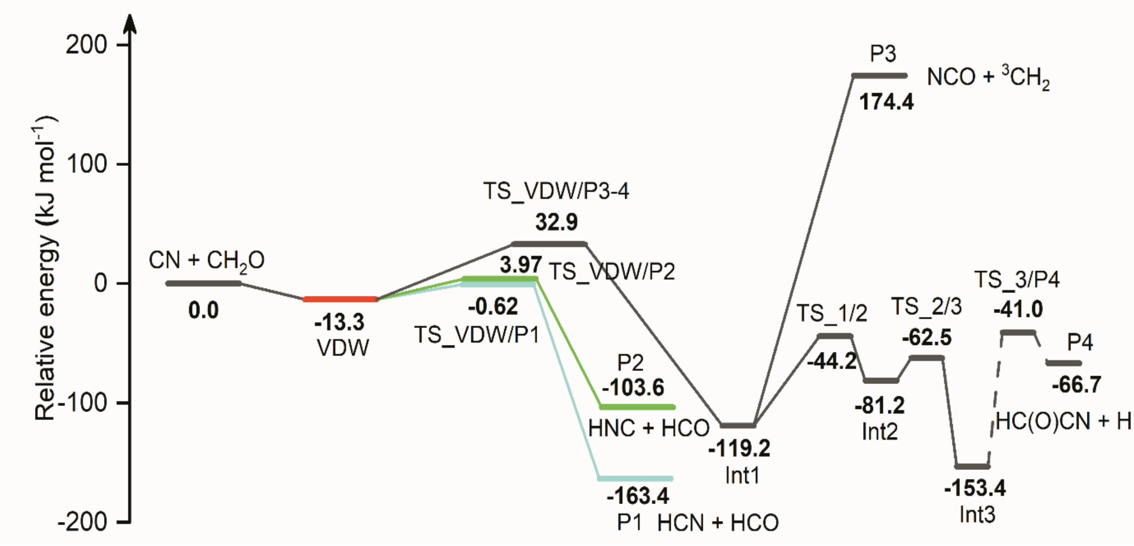

Figure 3.8 PES of the CN + CH_2O reaction obtained at CCSD(T)/aug-cc-pVTZ//M06-2X/aug-cc-pVTZ level of theory. All energy values are in kJ mol^{-1} and with the inclusion of the scaled ZPVE. The red line indicates the only van der Waals complex VDW found in this work. The blue and green paths show the subsequent pathways from VDW leading to HCN + HCO (P1) and HNC + HCO (P2) products, respectively.

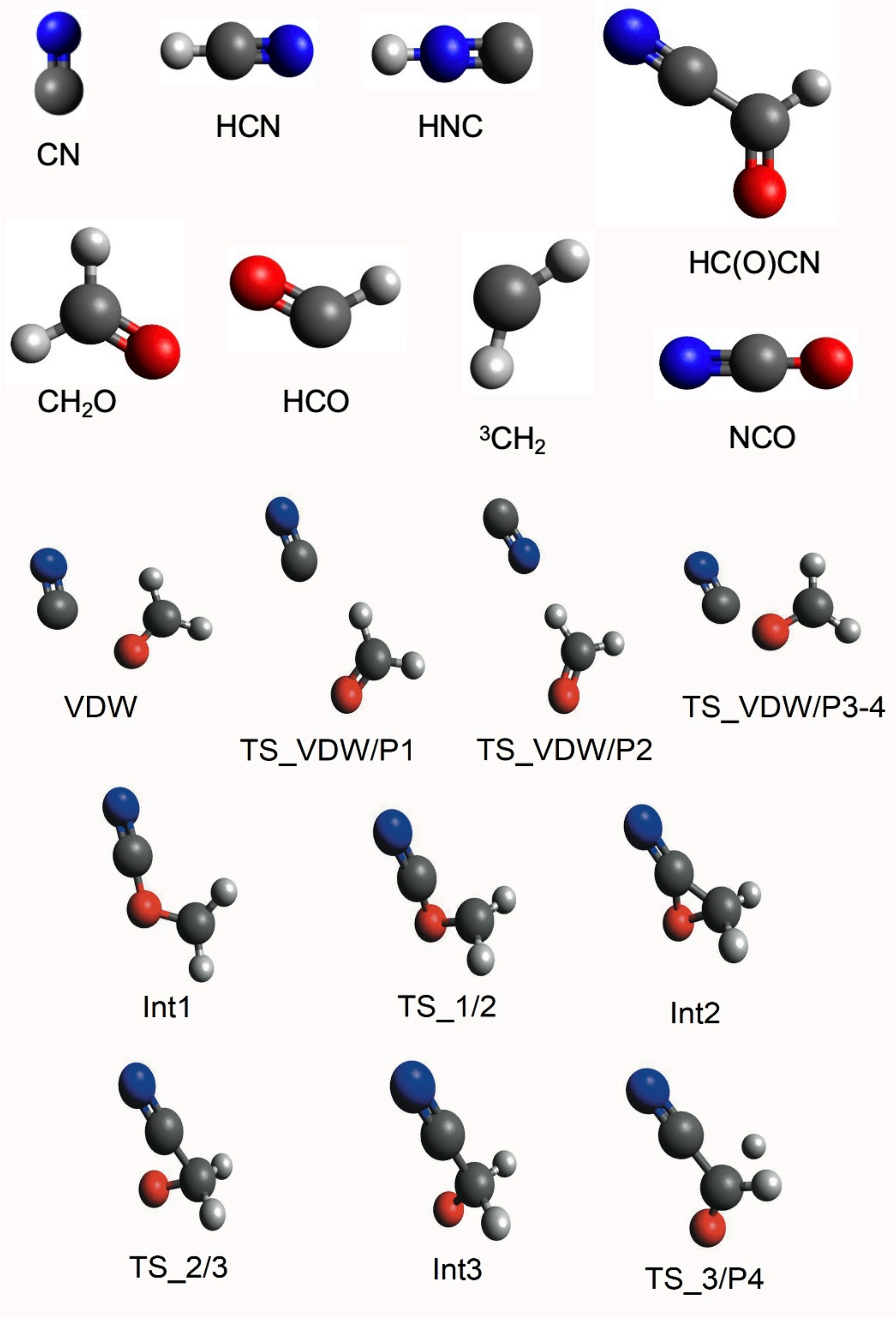

Figure 3.9 Optimised geometries of reactants, products, intermediates and transition states obtained at the M06-2X/aug-cc-pVTZ level of theory for the CN + CH_2O reaction. The labels correspond to those shown in Figure 3.8.

The overall potential energy surface for the CN + CH_2O reaction is shown in Figure 3.8, with energies obtained using CCSD(T)/aug-cc-pVTZ//M06-2X/aug-cc-pVTZ and shown relative to the CN + CH_2O entrance channel.

The geometries of the stationary points, obtained at the M06-2X/aug-cc-pVTZ level of theory, are shown in Figure 3.9. The optimised Cartesian coordinates, vibrational frequencies, and energy values can be found in Appendix B.

A weakly bound van der Waals complex **VDW** (–13.3 kJ mol^{-1}) is identified following the approach of CN to CH_2O. As seen in Figure 3.8, this complex leads to four different product pathways, namely H atom abstraction to form HCN (**P1**), H atom abstraction to form HNC (**P2**), and addition of CN onto the O atom (**P3-4**) eventually forming either NCO + $^3CH_2$ (**P3**) or HC(O)CN + H (**P4**). The formation of HCN + HCO (**P1**, –163.4 kJ mol^{-1}) is accessible through the submerged barrier **TS_VDW/P1** (–0.62 kJ mol^{-1}) while the formation of HNC + HCO (**P2**, –103.6 kJ mol^{-1}) involves a small positive energy barrier relative to the CN + CH_2O entrance channel (**TS_VDW/P2**, 3.97 kJ mol^{-1}). The error of these two calculated barrier heights, even with the higher level of theory used here that that reported by Feng et al. (56), are such that they could both be either positive or submerged barriers if calculated at a different level of theory. At the CCSD(T)/aug-cc-pVTZ level of theory, the error of the energy is estimated to be 3.0–4.5 kJ mol^{-1} (250–450 cm^{-1}) (73). The accuracy of the calculations will be discussed again in Section 3.3.2.1 when discussing fitting experimental data within MESMER to optimise the energies of transition states.

The addition of CN onto the O atom of CH_2O involves surmounting a large barrier **TS_VDW/P3-4** (32.9 kJ mol^{-1}) as shown in Figure 3.8, leading to the formation of the intermediate H_2C–O–CN (**Int1**, –119.2 kJ mol^{-1}). H_2C–O–CN can dissociate to form NCO + $^3CH_2$ (**P3**, 174.4 kJ mol^{-1}) or undergo cyclisation through **TS_1/2** (–44.2 kJ mol^{-1}) to form the cyclic intermediate **Int2** (–81.2 kJ mol^{-1}). By going through **TS_2/3** (–62.5 kJ mol^{-1}), the ring opens to form the intermediate $H_2C(O)CN$ (**Int3**, –153.4 kJ mol^{-1}). Breaking one of the CH bonds gives the products HC(O)CN + H (**P4**, –66.7 kJ mol^{-1}). Although the IRC calculation did not converge successfully for **TS_3/P4** (–41.0 kJ mol^{-1}), judging from the vibrational mode of the imaginary frequency, it is likely that it is the transition state connecting **Int3** and **P4**. A dashed line connecting **TS_3/P4** reflects the incomplete mapping of the IRC along this coordinate.

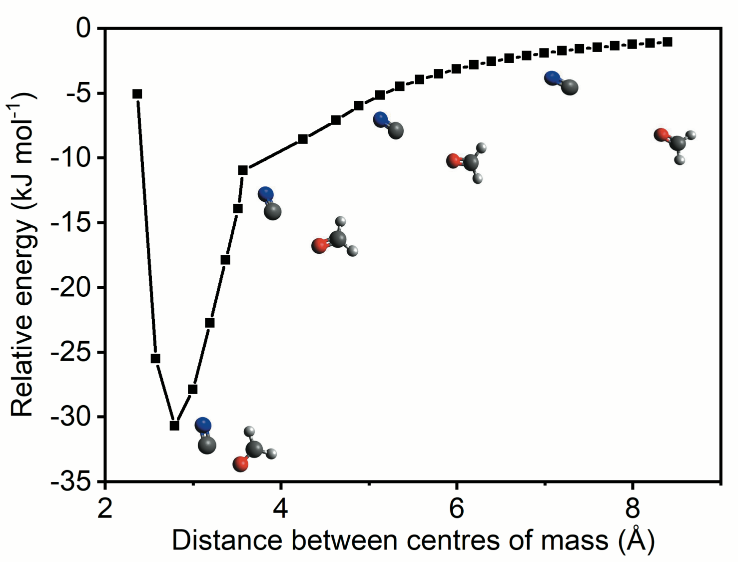

Figure 3.10 Potential energy curve (BHandHLYP/aug-cc-pVDZ, uncorrected for ZPVE) for the approach of CN to the oxygen of CH_2O. The scan coordinate of the relaxed scan is the distance between the carbon atom of the CN moiety and the oxygen atom of CH_2O.

A series of relaxed scans at the BHandHLYP/aug-cc-pVDZ and M06-2X/aug-cc-pVTZ levels of theory were performed in an attempt to map out the approach of the two reactants, CN and CH_2O. Two different reactant approaches were investigated: the CN radical approaching from the oxygen side of CH_2O, and CN approaching from the hydrogen side. For each data point during a scan, the distance between the two reactants was fixed while all other coordinates were allowed to optimise. When CN approaches from the oxygen side of CH_2O, as shown in Figure 3.10, it is favourable for CN to orient the carbon towards CH_2O at the beginning of the approach due to the dipole-dipole attraction. As the carbon side of CN approaches the oxygen side of CH_2O, CN moves to spin towards the geometry of the van der Waals complex and eventually reaches the

VDW potential energy well, where the process is barrierless as suggested from the smooth decrease in the potential energy during the reduction in the separation between the two reagents. There is a slight discontinuity in the relaxed scan shown here, mostly due to issues around the molecule moving between planar and non-planar configurations as the carbon-oxygen distance was scanned to produce Figure 3.10, but no barrier was found when this was investigated further.

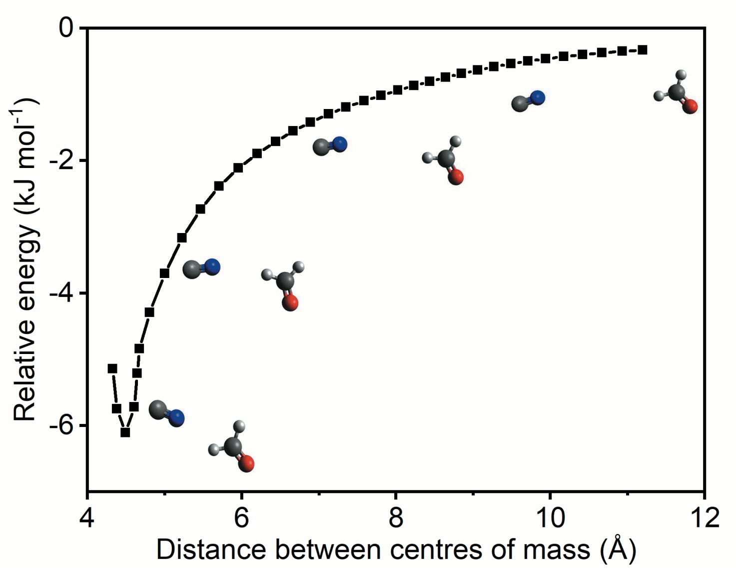

Figure 3.11 Potential energy curve (BHandHLYP/aug-cc-pVDZ, uncorrected for ZPVE) for the approach of CN to the hydrogen of CH_2O. The scan coordinate of the relaxed scan is the distance between the carbon atom of the CN moiety and the hydrogen atom of CH_2O.

In the case where CN approaches from the hydrogen side of CH_2O, as shown in Figure 3.11, it is favourable at first for CN to orient itself such that the nitrogen side points towards CH_2O. The potential energy decreases with decreasing separation between the two moieties until encountering a fairly “flat” region of the potential energy surface, with CN moving to orient itself along the C_2 axis, bisecting the HCH bond angle of CH_2O. Here, with a distance of approximately 3.3 Å between nitrogen the of CN and the carbon of CH_2O, or a centre of mass distance between the moieties of approximately 4.5 Å apart, the overall energy of the system (BHandHLYP/aug-cc-pVDZ, uncorrected for ZPVE) reaches –5 kJ mol^{-1} relative to the entrance channel. When restricting the symmetry in a geometry optimisation procedure, a weakly bound C_{2v} complex can be formed in this way, but it was not significantly stable when allowing the symmetry to relax.

In order to further explore this “flat” region of the PES, a relaxed scan from this point has been done using the O=C - - - N angle as the scanning parameter, as shown in Figure 3.12. While the CN radical rotates around CH_2O, the potential energy first experiences a fairly flat region of the potential and then falls smoothly into the potential energy well corresponding to the van der Waals structure **VDW**. Thus, it is suggested that both ways of approach can eventually lead to the van der Waals structure **VDW**.

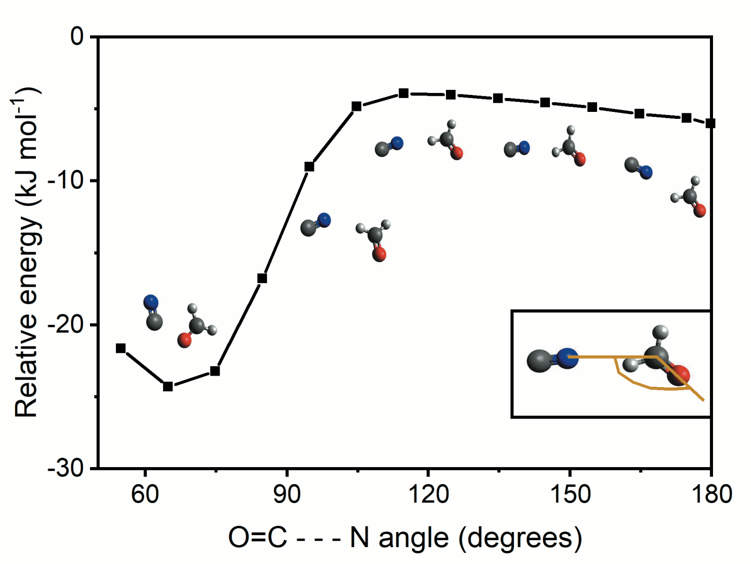

Figure 3.12 Potential energy curve (ZPVE corrected) calculated at the M06-2X/aug-cc-pVTZ level for the rotation of CN around CH_2O for O=C - - - N angle from 55° to 180°. Energy is relative to the sum of the energies (ZPVE corrected) of the two separate reacting species, CN and CH_2O, at the M06-2X/aug-cc-pVTZ level.

The prior theoretical work (56) using the QCISD/6-31G**//UHF/6-31G** and CCSD/6-31G**//UHF/6-31G** levels of theory suggested a direct H abstraction mechanism to form HCN + HCO, which involved overcoming a small positive ~2 kJ mol^{-1} barrier relative to the CN + CH_2O entrance channel as shown in Figure 3.6. The current study and the more recent study by Tonolo et al. (57) have not identified this pathway on the reaction coordinate, perhaps because of the low level of theory used for geometry optimisation (UHF/6-31G**) in the earlier study (56). In the current study, instead of direct abstraction, an indirect channel to form HCN + HCO which involves the van der Waals complex **VDW** and a small submerged barrier **TS_VDW/P1**, is identified. The study by Tonolo et al. (57) also identified the **VDW** structure (–3.1 kcal mol^{-1} or –13.0 kJ mol^{-1} relative to the reactants, including ZPVE, at CCSD(T)/CBS+CV//B2PLYP/maug-cc-pVTZ-*d*H level) on the reaction PES as shown in Figure 3.7 leading to hydrogen abstraction to form HCN + HCO through a submerged barrier (–0.3 kcal mol^{-1} or –1.3 kJ mol^{-1}). This pathway is consistent with the current work, with less than 1 kJ mol^{-1} difference in energy in the complex and barrier. However, this work details for the first time the presence of the HNC pathway from the **VDW** complex.

The work from Tonolo et al. (57) identifies several stationary points along the reaction coordinate not used in the current study. For example, a barrierless addition route is claimed forming a C-C bond directly from the reactants, resulting in a tetrahedral adduct corresponding to the deep potential well (–36.6 kcal mol^{-1} or –153.1 kJ mol^{-1}) labelled as 1C in Figure 3.7. Although in this work this structure is also identified (labelled as **Int3** in Figure 3.8) and it is agreed that this intermediate can be formed, it was unable to connect this structure directly to the reactants. In an attempt to find the TS corresponding to the direct addition of CN carbon to the CH_2O carbon, relaxed scans, like the one shown in Figure 3.13, were performed at the BHandHLYP/aug-cc-pVDZ and M06-2X/aug-cc-pVTZ levels. Starting from the adduct, the C-C distance was increased, without any restriction on other geometric parameters and the symmetry, up to the point where the calculations failed to converged. While the TS was not located, it was still evident that this direct addition involves surmounting a large barrier at least 50 kJ mol^{-1} (CCSD(T)/aug-cc-pVTZ//M06-2X/aug-cc-pVTZ) higher in energy than the reactants. This can be explained by considering the electronegativity of the atoms, where both the CN carbon and the CH_2O carbon are partially positive. Thus, energy is required to bring the two sides with the same electric charge together. It is likely that the overestimated rate coefficients from Tonolo et al. (57) compared to the experimental work are directly related to not identifying a substantial barrier to C-C bond formation in forming the adduct. This will also impact on the relative importance stated for the pathway leading to the formation of formyl cyanide HC(O)CN from this adduct when the barrier is considered.

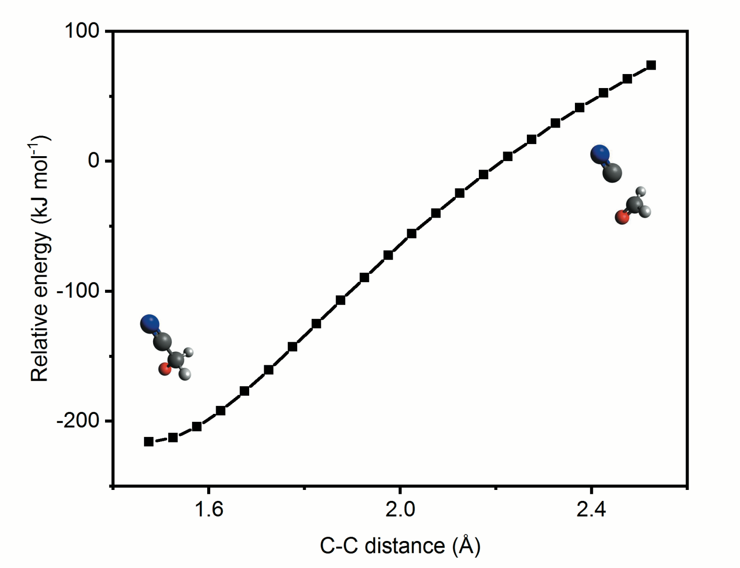

Figure 3.13 Potential energy curve (BHandHLYP/aug-cc-pVDZ, uncorrected for ZPVE) for the relaxed scan of the C-C separation starting from the adduct $H_2C(O)CN$ (Int3).

In comparison with the PES of OH + CH_2O as shown in Figure 3.4, the results from the current work on CN + CH_2O show that both systems share a similar shape of the PES in terms of the energy profile or mechanism for the H abstraction reaction. Following the approach of the two reacting species, a pre-reaction complex is formed followed by a barrier to form products. The difference in energy which determines whether the barrier is positive or submerged relative to the reactants energies is within the uncertainty of most calculation methods, and so whether the TS is submerged or not will depend on the level of theory used.

3.3.2 Results from rate coefficient calculations

The energy values as shown in Figure 3.8, Cartesian coordinates of the stationary points, vibrational frequencies, and rotational constants of the species obtained from the ab initio calculations, which can all be found in Appendix B, were used as the inputs for the master equation solver MESMER in order to calculate the rate coefficients for CN + CH_2O. From simulations over a wide range of temperatures (4–1000 K) and pressures (10^{15}–10^{19} molecule cm^{-3}), it was observed that the reaction channels HCN and HNC accounted for greater than 99.99% of the products, under all conditions. The reaction occurs initially via van der Waals complex (**VDW**) formation followed by transition states **TS_VDW/P1** and **TS_VDW/P2** to form HCN + HCO and HNC + HCO, respectively as shown in Figure 3.8. The HNC channel never accounts for more than 1% yield due to the positive barrier, although uncertainties on the calculated energy barriers (estimated to be 3.0–4.5 kJ mol^{-1} (73)) can potentially result in a reverse situation that may significantly change this HCN/HNC ratio.

No pressure dependence was observed from MESMER calculations between 10^{15}–10^{18} molecule cm^{-3} as shown in Figure 3.14, which was also supported by the Laval experiments near 10^{17} molecule cm^{-3}, while above 10^{19} molecule cm^{-3} and temperature below 50 K pressure dependence was evident. The pressure dependence at high pressure is due to the fact that the **VDW** species was populated. However, considering only the cases when the gas density is below 10^{19} molecule cm^{-3}, the pressure independence implies that the lower energy states of the van der Waals complex is not significantly stabilised, even at the lowest temperatures. Therefore, to a very good approximation, Figure 3.8 can be reduced to just HCN and HNC formation as shown in Figure 3.15 without losing chemical information; reducing the system to just HCN formation would still describe the system to better than 99% of the product yield.

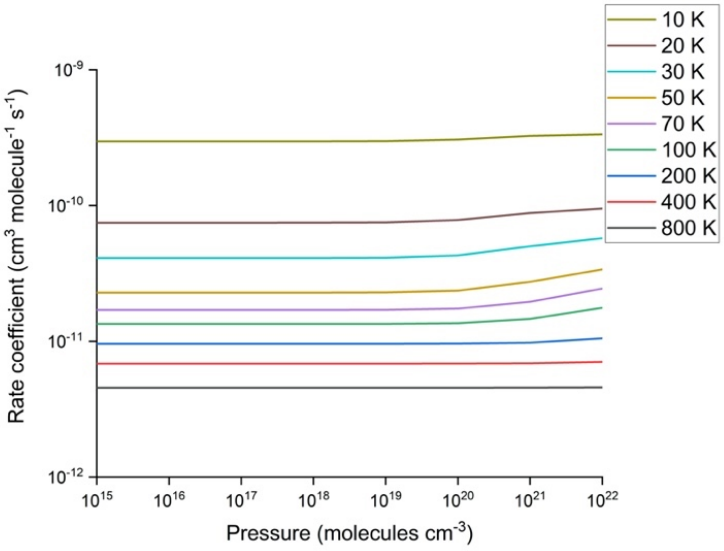

Figure 3.14 Calculated rate coefficients versus pressure at various temperatures which shows the pressure independence for the indirect H abstraction channel over a pressure of 10^{15}–10^{19} molecule cm^{-3}.

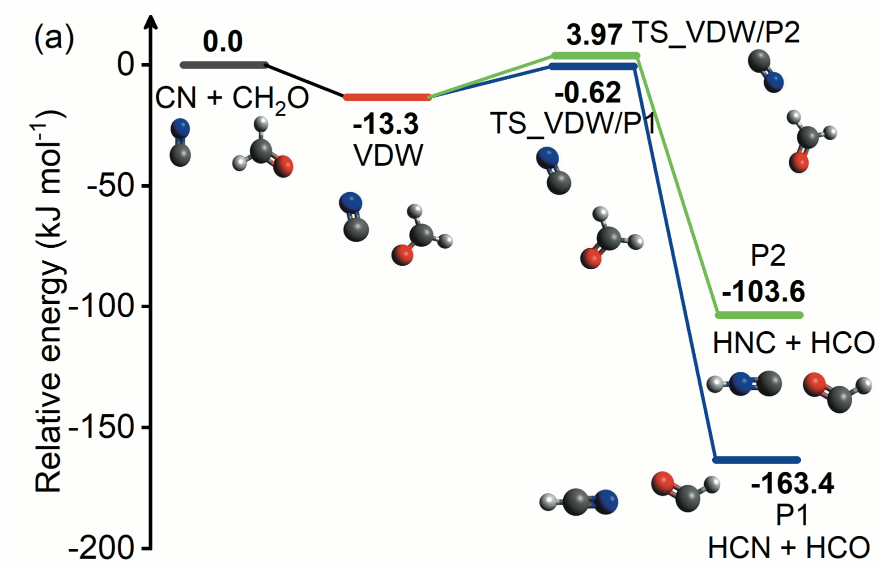

Figure 3.15 A simplified PES used for MESMER fitting scenarios (see Table 3.4) together with molecular structures at key stationary points. Initial van der Waals complex VDW (red) formation is followed by transition states to products, HCN + HCO (P1, blue) and HNC + HCO (P2, green) respectively. See text for details.

3.3.2.1 Data fitting for the optimisation of rate controlling parameters

Table 3.2 Rate coefficients and experimental conditions for kinetic studies of the CN + CH_2O reaction with the Laval set-up by courtesy of Dr Niclas West and Mr Edward Rutter

T **(K)**	**Bath gas**	N_{total} **(10^{16} × molecule cm^{-3})**	***k*** **(10^{-11} × cm^3 $molecule^{-1}$ s^{-1})**
32 ± 2	Ar	3.24 ± 0.24	3.57 ± 0.53
32 ± 2	Ar	3.24 ± 0.24	4.62 ± 0.84
40 ± 4	Ar	8.36 ± 1.19	2.26 ± 2.11
53 ± 4	Ar	7.04 ± 0.74	3.18 ± 1.19
56 ± 6	Ar	7.58 ± 1.11	1.56 ± 1.94
70 ± 11	Ar	11.18 ± 2.54	1.51 ± 0.49
70 ± 2	N_2	2.91 ± 0.20	1.30 ± 0.52
84 ± 3	N_2	7.56 ± 0.63	0.99 ± 0.27
92 ± 6	N_2	4.99 ± 0.74	1.80 ± 0.29
103 ± 10	N_2	6.80 ± 1.57	1.45 ± 0.19

The ILT method as described in Section 2.2 was used to calculate the microcanonical rate coefficients for the barrierless formation of the **VDW** complex from CN + CH_2O, where the ILT parameters were assigned by:

$$k_{\text{ILT,VDW}}^{\infty}(T) = A_{\text{ILT,VDW}}^{\infty}\left(\frac{T}{30\text{K}}\right)^{n_{\text{ILT,VDW}}^{\infty}} \qquad \text{E 3.3}$$

where $A_{\text{ILT,VDW}}^{\infty}$ and $n_{\text{ILT,VDW}}^{\infty}$ are the ILT parameters which describe the rate coefficient for the formation of **VDW** at the high pressure limit. With the availability of experimental data, apart from performing simulations, through data fitting, MESMER can adjust the important rate controlling parameters like the ILT parameters in E 3.3, as well as the transition state energies. During such fitting, MESMER adjusts the parameters in order to minimise χ^2:

$$\chi^2 = \sum_T \frac{\left(k_{\mathrm{expt}}(T) - k_{\mathrm{calc}}(T)\right)^2}{\sigma^2} \qquad \text{E 3.4}$$

where $k_{\mathrm{calc}}(T)$ is the MESMER calculated rate coefficient, and $k_{\mathrm{expt}}(T)$ and σ are the experimental rate coefficients and their associated error. The measure of the goodness of fit can be evaluated by χ^2/N where N is the number of degrees of freedom, which is equal to the number of data points minus the number of fitting parameters. A χ^2/N value close to 1.0 or below represents an acceptable fit as it means the difference between the calculated and experimental rate coefficients is about the same as the experimental uncertainty.

Table 3.3 Rate coefficients of the CN + CH_2O reaction measured at room temperature and above reported in previous literature

T **(K)**	***k*** **(10^{-11} × cm^3 $molecule^{-1}$ s^{-1})**	**Literature**
297	1.66	Yu et al. (54)
345	1.72	
425	2.22	
528	2.62	
673	3.99	
294	1.64	Chang and Wang (55)
323	1.94	
357	2.03	
400	2.32	
455	2.74	
526	3.11	
625	3.23	
769	4.08	

Kinetic experiments on the CN + CH_2O reaction have been carried out by Dr Niclas West and Mr Edward Rutter using the laser flash photolysis coupled with laser-induced fluorescence technique (LFP-LIF) with a uniform supersonic environment of a Laval nozzle expansion to generate and detect the CN radical for rate coefficient measurements. The results are shown in Table 3.2, which cover a temperature range of 32–103 K, together with the uncertainties presented were used for the MESMER fitting exercise, denoted as *Laval* in Table 3.4.

Table 3.4 Fitting scenarios and optimised kinetic parameters from MESMER fitting

Name of fitting scenario	***Laval***	***Laval + Lit 1***	***Laval + Lit 2***
Temperature range (K)	32–103	32–769	32–769
$\boldsymbol{A^{\infty}_{\mathrm{ILT,VDW}}}$ **(10^{-11} × cm^3 $molecule^{-1}$ s^{-1})**	5.29 ± 0.8	2.5 ± 0.8	6.58 ± 0.7
$\boldsymbol{n^{\infty}_{\mathrm{ILT,VDW}}}$	–0.77 ± 0.17	0.016 ± 0.005	–0.10 ± 0.02
TS_VDW/P1 energy (kJ mol^{-1})	–0.62, fixed	–0.62, fixed	4.0 ± 0.9
TS_VDW/P1 imaginary frequency (cm^{-1})	215, fixed	215, fixed	806 ± 24
$\boldsymbol{\chi^2/N}$	1.09	4.24	0.80

$A^{\infty}_{\mathrm{ILT,VDW}}$ and $n^{\infty}_{\mathrm{ILT,VDW}}$ are the ILT parameters defined in E 3.3. **TS_VDW/P1** is as shown in Figure 3.15. χ^2 is defined in E 3.4 while N is the number of degrees of freedom given by the number of data points minus the number of fitting parameters. The reported errors are 1 sigma. See text for further details of the fitting scenarios.

Apart from the low temperature data, the room temperature and above rate coefficients from Yu et al. (54) and Chang and Wang (55) presented in Table 3.3, were also used for fitting, where an error of 0.064 × $k(T)$ was assigned as σ in E 3.4 instead of the reported values in these literature. The uncertainties reported were on average 2.8% for Yu et al. (54), and 1.2% for Chang and Wang (55), which only shed light on the experimental precision and are likely to underestimate the true error rather than reflecting the overall accuracy. The assignment of 0.064 × $k(T)$ error to these high temperature data is necessary to potentially allow χ^2/N close to 1.0 instead of having a large value (> 28). The MESMER fitting scenarios used in this work and the optimised kinetic parameters are summarised in Table 3.4.

Initially, MESMER data fitting was carried out with energies fixed at the ab initio calculated values, as shown in Figure 3.15, with only the ILT parameters in E 3.3 being adjusted. When fitting to just the low temperature Laval nozzle data (black line in Figure 3.16, *Laval* scenario in Table 3.4), an excellent visual fit with the data was obtained. From Table 3.4, it can be seen that the χ^2/N value for *Laval* model is close to 1.0, which indicates the experimental errors in Table 3.2 are realistic.

If MESMER simultaneously tries to fit to the low and high temperature data (blue line in Figure 3.16, *Laval + Lit 1* scenario in Table 3.4), then the fit to the data is much worse, with χ^2/N being above 4. Therefore it is concluded that MESMER calculations based on the ab initio calculated values are not capable of reproducing all the experimental data. Because of the negative ab initio energy value of **TS_VDW/P1** relative to the reactants, the sharp V-shaped temperature dependence of the rate coefficient cannot be reproduced. While perfectly fitting with the low temperature data, if the reaction mechanism proceeds via this submerged TS, the rate coefficient is predicted to keep decreasing with increasing temperature, which is at odds with the high temperature literature data.

One way to account for the variation of rate coefficient across the full range of temperatures is to increase the transition state energy so that it is positive, making it consistent with the high-temperature literature data trends, and to increase the imaginary frequency of the tunnelling coordinate in the transition state simultaneously so that quantum mechanical tunnelling overcomes the effect of the positive barrier, leading to an increase in the rate coefficient at lower temperatures, as is observed experimentally. This leads to the fitting scenario *Laval* + *Lit 2* in Table 3.4 (red line in Figure 3.16), where both the energy and the imaginary frequency of **TS_VDW/P1** are adjusted in the MESMER simulations. The 4.59 kJ mol^{-1} ab initio energy difference between **TS_VDW/P1** and **TS_VDW/P2** is also maintained for this fit. Applying this restriction is reasonable given the similar calculated geometries of the two transition states, but with just the C and N flipped, as shown in Figure 3.9; as well as is practical such that one less parameter is used during fitting. The experimental rate coefficient can then be fitted well across the full range of temperatures, evidenced by a χ^2/N value of 0.80. As shown in Figure 3.16, the MESMER simulation model scenario *Laval* + *Lit 2* provides a much improved fit to the data over *Laval* + *Lit 1*. The optimum adjustments to give the best fit were found to be an increase in the **TS_VDW/P1** energy from –0.62 kJ mol^{-1} to 4.0 kJ mol^{-1} (**TS_VDW/P2** energy from 3.97 kJ mol^{-1} to 8.59 kJ mol^{-1}) and an increase in the **TS_VDW/P1** imaginary frequency from 215 cm^{-1} to 806 cm^{-1}. The transition state energy would need to be increased by ~4.62 kJ mol^{-1} from the ab initio calculated values at the CCSD(T)/aug-cc-pVTZ level of theory, which is reasonable given it is close to the estimated uncertainty of 3.0–4.5 kJ mol^{-1} (73). Similarly, even though the imaginary frequency of **TS_VDW/P1** has been increased significantly, from 215 cm^{-1} to 806 cm^{-1}, the adjusted value of ~800 cm^{-1} is not unreasonable. It is worth noting that the imaginary frequency typically can have a larger uncertainty than the other positive vibrational frequencies, across different levels of theory a deviation of ~1000 cm^{-1} can be possible (74, 75), so an adjustment of an absolute value of ~600 cm^{-1} seems acceptable.

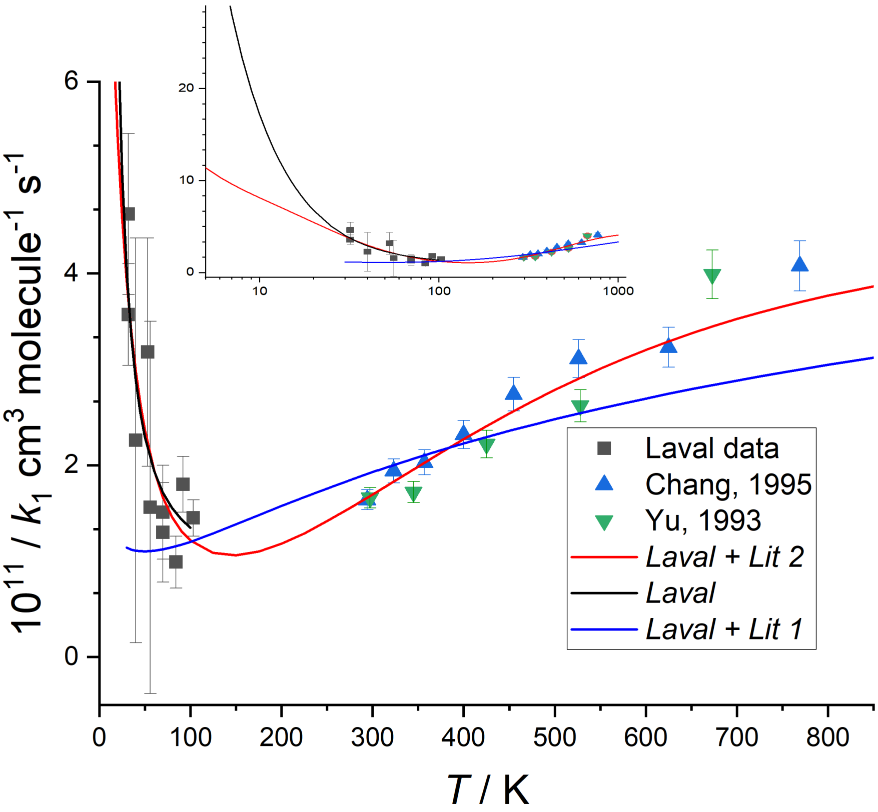

Figure 3.16 Rate coefficients plotted against temperature for results obtained from experiments with the Laval set-up (black squares) and reported from by Yu et al. (54) (green triangles) and Chang and Wang (55) (blue triangles), together with calculations from MESMER with different fitting scenarios listed in Table 3.4 (*Laval* + *Lit 2*: red line; *Laval*: black line; *Laval* + *Lit 1*: blue line). The x-axis is on a logarithmic scale in the inset. The extrapolation of *Laval* and *Laval* + *Lit 2* models only shows a noticeable deviation when the temperature is below 30 K.

From Figure 3.16, it can be seen that the minimum in the rate coefficient occurs at around 150 K, which is the point at which the controlling influences of quantum mechanical tunnelling and the 4.0 kJ mol^{-1} barrier become balanced. Also included in Figure 3.16 is the simulation of the fitting models down to 7 K, where at 10 K the predicted rate coefficient value of the *Laval* model is approximately twice that of the *Laval* + *Lit 2* model. This significant difference emphasises how sensitive the rate coefficient is to the parameters used in the models when extrapolating down to very low temperatures, that is, below 10 K, as both the *Laval* and *Laval* + *Lit 2* models give almost the same quality fits to the measured rate coefficient from the Laval experiments. It also highlights that further work is needed on both high level calculations and experiments at very low temperatures, as well as the kinetic model for this reaction.

3.3.2.2 Product branching and extrapolation from further simulations

The best-fit parameters as shown in Table 3.4 were used as input for MESMER simulations to generate rate coefficient values over a very wide range of temperature from 4–1000 K as tabulated in Appendix B. As the rate coefficients of the CN + CH_2O reaction did not show a pressure dependence, neither experimentally near 10^{17} molecule cm^{-3} nor from MESMER simulations between 10^{15}–10^{18} molecule cm^{-3}, the gas density was set as 10^{13} molecule cm^{-3} (which is within the pressure independent region) for these further MESMER simulations. From 50–1000 K, a 30 cm^{-1} grain size was sufficient to calculate a converged rate coefficient, but it was reduced down to 2 cm^{-1} for the 4–50 K simulations.

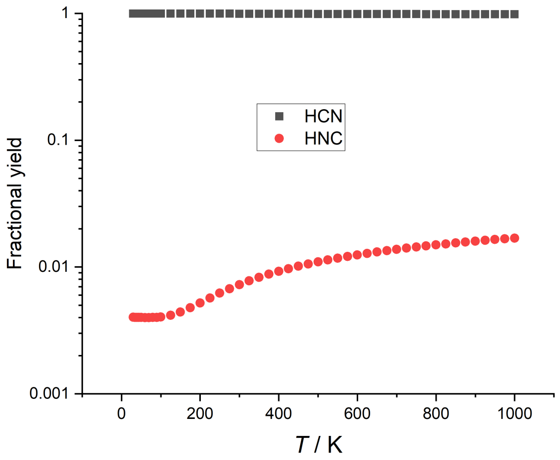

Figure 3.17 Predicted product branching ratios of the CN + CH_2O reaction as a function of temperature using the parameters obtained from the *Laval* + *Lit 2* scenario (black: HCN; red: HNC).

Over the range of 4–1000 K, the MESMER simulations indicate that HCN + HCO are the only significant products formed. The fractional yield of HNC is less than 2% for all temperatures between 4–1000 K due to the higher energy barrier of **TS_VDW/P2** and similar imaginary frequency for tunnelling between **TS_VDW/P1** and **TS_VDW/P2**. The temperature dependence of the fractional yields of products using the parameters from the *Laval* + *Lit 2* scenario is shown in Figure 3.17.

The simulated overall rate coefficients obtained using the parameters from the *Laval* + *Lit 2* scenario are then fitted to the modified Arrhenius expression:

$$k(T) = \alpha \left(\frac{T}{300\mathrm{K}}\right)^{\beta} \exp\left(-\frac{\gamma}{T}\right) \qquad \text{E 3.5}$$

where α, β and γ are the best-fit parameters, which is a usual parameterisation for the astronomical models. Instead of using just one single modified Arrhenius expression covering the full temperature range (4–1000 K), four piecewise expressions are presented in Table 3.5 such that the fits to E 3.5 are within 5% of the MESMER simulation data.

Table 3.5 Best-fitted parameters of the modified Arrhenius expression to the MESMER simulated overall rate coefficient

T range (K)	α (cm^3 molecule^{-1} s^{-1})	β	γ (K)
4–20	(1.18 ± 0.08) × 10^{-11}	–0.58 ± 0.03	0.53 ± 0.24
20–100	(3.72 ± 0.15) × 10^{-12}	–1.09 ± 0.04	5.2 ± 1.8
100–300	(5.99 ± 0.14) × 10^{-11}	2.19 ± 0.04	–313.4 ± 7.7
300–1000	(6.26 ± 0.30) × 10^{-11}	–0.02 ± 0.03	398 ± 16

Comparing across the CN + CH_2O reaction studied in this work, the OH + CH_2O reaction and the CH + CH_2O reaction reported in previous literature, the rate coefficient of all of them show a negative temperature dependence at low temperature. This can be explained by the existence of the submerged entrance channel for all these three reactions. However, in terms of the types of the products formed, H abstraction products dominate for the CN + CH_2O reaction, which is similar to the OH + CH_2O reaction. In contrast, the addition products dominate for the CH + CH2O reaction due to the submerged addition pathway compared with the reactants, but for the case of CN + CH_2O, a substantial barrier exists which makes the addition reaction improbable. In addition to being a radical, CH is a carbene species, so it has different reactivity when compared with CN and OH which are radicals only.

3.4 Conclusion

In this chapter, theoretical investigations on the CN + CH_2O reaction have been carried out by undergoing ab initio calculations and rate-theory calculations in order to explore the overall reaction mechanism that is consistent with the experimentally measured values over a wide range of temperatures. For the PES obtained from ab initio calculations, a van der Waals complex **VDW** with binding energy of 13.3 kJ mol^{-1} has been identified, which then leads to two low energy pathways forming either HNC + HCO via a small positive barrier (3.97 kJ mol^{-1} relative to the reactants) or HCN + HCO via a submerged barrier (–0.62 kJ mol^{-1} relative to the reactants). This calculated PES can explain the negative temperature dependence of the rate coefficients at low temperatures observed in the Laval set-up but it cannot simultaneously fit with the previously reported rate coefficient at room temperature and above (54, 55). By floating the energies of both transition states upwards by ~4.62 kJ mol^{-1} (which is about the uncertainty of the level of theory used) and increasing the imaginary frequency for tunnelling to 806 cm^{-1} in the MESMER calculations, excellent fit to the measured rate coefficients across the full range of temperatures where experimental data are available (32–769 K) is obtained. The postulated mechanism is similar to previous reactions of OH with VOCs which involve the formation of a weakly bound van der Waals complex, whose lifetime is extended at low temperature, followed by quantum mechanical tunnelling through a small barrier to products (4). However, it is still suggested that further higher-level work needs to be done, both theoretically and experimentally, in order to provide a basis for extrapolation to an even lower temperature. No pressure dependence was observed from the calculated results up to a total number density of 10^{18} molecule cm^{-3}.

The product branching results from MESMER calculations indicate that the formation of HCN + HCO dominates, which contributes to >98% of the product yield, while the fractional yield of HNC is no more than 2%. However, the uncertainty in the level of theory used is close to the difference in the calculated energy values of the transition states leading to HCN + HCO and HNC + HCO, which can cause deviation from this predicted HCN/HNC branching ratio. Formation of products from the adduct channel, such as HC(O)CN, at low temperature is unlikely due to the existence of a large barrier (32.9 kJ mol^{-1} relative to the reactants), implying that the CN + CH_2O gas-phase reaction can hardly contribute to the formation of formyl cyanide HC(O)CN in interstellar clouds. By fitting the overall rate coefficient for the CN + CH_2O reaction to the modified Arrhenius expression, four piecewise parameterisations over the temperature range of 4–1000 K are obtained as follows:

$$k(T)\ (\text{in cm}^3\ \text{molecule}^{-1}\ \text{s}^{-1}) =$$

$$(1.18 \pm 0.08) \times 10^{-11} \left(\frac{T}{300\text{K}}\right)^{-0.58\pm0.03} \exp\left(-\frac{0.53\pm0.24\text{K}}{T}\right)\ \text{for } 4-20\text{K} \qquad \text{E 3.6}$$

$$(3.72 \pm 0.15) \times 10^{-12} \left(\frac{T}{300\text{K}}\right)^{-1.09\pm0.04} \exp\left(-\frac{5.2\pm1.8\text{K}}{T}\right)\ \text{for } 20-100\text{K} \qquad \text{E 3.7}$$

$$(5.99 \pm 0.14) \times 10^{-11} \left(\frac{T}{300\text{K}}\right)^{2.19\pm0.04} \exp\left(-\frac{-313.4\pm7.7\text{K}}{T}\right)\ \text{for } 100-300\text{K} \qquad \text{E 3.8}$$

$$(6.26 \pm 0.30) \times 10^{-11} \left(\frac{T}{300\text{K}}\right)^{-0.02\pm0.03} \exp\left(-\frac{398\pm16\text{K}}{T}\right)\ \text{for } 300-1000\text{K} \qquad \text{E 3.9}$$

3.5 References

1. Zabarnick, S., Fleming, J.W. and Lin, M.C. Temperature dependence of CH radical reactions with H_2O and CH_2O. *Symposium (International) on Combustion.* 1988, **21**(1), pp.713-719.

2. West, N.A., Millar, T.J., Van de Sande, M., Rutter, E., Blitz, M.A., Decin, L. and Heard, D.E. Measurements of Low Temperature Rate Coefficients for the Reaction of CH with CH_2O and Application to Dark Cloud and AGB Stellar Wind Models. *The Astrophysical Journal.* 2019, **885**(2), p.134.

3. Nguyen, H.M.T., Nguyen, H.T., Nguyen, T.-N., Van Hoang, H. and Vereecken, L. Theoretical Study on the Reaction of the Methylidyne Radical, CH($X^2\Pi$), with Formaldehyde, CH_2O. *The Journal of Physical Chemistry A.* 2014, **118**(38), pp.8861-8871.

4. Heard, D.E. Rapid Acceleration of Hydrogen Atom Abstraction Reactions of OH at Very Low Temperatures through Weakly Bound Complexes and Tunneling. *Accounts of Chemical Research.* 2018, **51**(11), pp.2620-2627.

5. Xu, S. and Lin, M.C. Theoretical study on the kinetics for OH reactions with CH_3OH and C_2H_5OH. *Proceedings of the Combustion Institute.* 2007, **31**(1), pp.159-166.

6. Shannon, R.J., Blitz, M.A., Goddard, A. and Heard, D.E. Accelerated chemistry in the reaction between the hydroxyl radical and methanol at interstellar temperatures facilitated by tunnelling. *Nature Chemistry.* 2013, **5**(9), pp.745-749.

7. Gómez Martín, J.C., Caravan, R.L., Blitz, M.A., Heard, D.E. and Plane, J.M.C. Low Temperature Kinetics of the CH_3OH + OH Reaction. *The Journal of Physical Chemistry A.* 2014, **118**(15), pp.2693-2701.

8. Antiñolo, M., Agúndez, M., Jiménez, E., Ballesteros, B., Canosa, A., Dib, G.E., Albaladejo, J. and Cernicharo, J. Reactivity of OH and CH_3OH between 22 and 64 K: modeling the gas phase production of CH_3O in Barnard 1b. *The Astrophysical Journal.* 2016, **823**(1), p.25.

9. Roncero, O., Zanchet, A. and Aguado, A. Low temperature reaction dynamics for CH_3OH + OH collisions on a new full dimensional potential energy surface. *Physical Chemistry Chemical Physics.* 2018, **20**(40), pp.25951-25958.

10. Ocaña, A.J., Blázquez, S., Potapov, A., Ballesteros, B., Canosa, A., Antiñolo, M., Vereecken, L., Albaladejo, J. and Jiménez, E. Gas-phase reactivity of CH_3OH toward OH at interstellar temperatures (11.7–177.5 K): experimental and theoretical study. *Physical Chemistry Chemical Physics.* 2019, **21**(13), pp.6942-6957.

11. Nguyen, T.L., Ruscic, B. and Stanton, J.F. A master equation simulation for the •OH + CH_3OH reaction. *The Journal of Chemical Physics.* 2019, **150**(8), p.084105.

12. Naumkin, F., Del Mazo-Sevillano, P., Aguado, A., Suleimanov, Y.V. and Roncero, O. Zero- and high-pressure mechanisms in the complex forming reactions of OH with methanol and formaldehyde at low temperatures. *ACS earth & space chemistry.* 2019, **3**(7), pp.1158-1169.

13. Caravan, R.L., Shannon, R.J., Lewis, T., Blitz, M.A. and Heard, D.E. Measurements of Rate Coefficients for Reactions of OH with Ethanol and Propan-2-ol at Very Low Temperatures. *Journal of Physical Chemistry A.* 2015, **119**(28), pp.7130-7137.

14. Ocaña, A.J., Blázquez, S., Ballesteros, B., Canosa, A., Antiñolo, M., Albaladejo, J. and Jiménez, E. Gas phase kinetics of the OH + CH_3CH_2OH reaction at temperatures of the interstellar medium (T = 21–107 K). *Physical Chemistry Chemical Physics.* 2018, **20**(8), pp.5865-5873.

15. Sivakumaran, V., Hölscher, D., Dillon, T.J. and Crowley, J.N. Reaction between OH and HCHO: temperature dependent rate coefficients (202–399 K) and product pathways (298 K). *Physical Chemistry Chemical Physics.* 2003, **5**(21), pp.4821-4827.

16. D'Anna, B., Bakken, V., Are Beukes, J., Nielsen, C.J., Brudnik, K. and Jodkowski, J.T.Y. Experimental and theoretical studies of gas phase NO_3 and OH radical reactions with formaldehyde, acetaldehyde and their isotopomers. *Physical Chemistry Chemical Physics.* 2003, **5**(9), pp.1790-1805.

17. Li, H.-Y., Pu, M., Ji, Y.-Q., Xu, Z.-F. and Feng, W.-L. Theoretical study on the reaction path and rate constants of the hydrogen atom abstraction reaction of CH_2O with CH_3/OH. *Chemical Physics.* 2004, **307**(1), pp.35 - 43.

18. Vasudevan, V., Davidson, D.F. and Hanson, R.K. Direct measurements of the reaction $OH + CH_2O \rightarrow HCO + H_2O$ at high temperatures. *International Journal of Chemical Kinetics.* 2005, **37**(2), pp.98-109.

19. Wang, S., Davidson, D.F. and Hanson, R.K. High temperature measurements for the rate constants of C_1–C_4 aldehydes with OH in a shock tube. *Proceedings of the Combustion Institute.* 2015, **35**(1), pp.473-480.

20. Ocaña, A.J., Jimenez, E., Ballesteros, B., Canosa, A., Antinolo, M., Albaladejo, J., Agundez, M., Cernicharo, J., Zanchet, A., del Mazo, P., Roncero, O. and Aguado, A. Is the Gas-phase $OH+H_2CO$ Reaction a Source of HCO in Interstellar Cold Dark Clouds? A Kinetic, Dynamic, and Modeling Study. *Astrophysical Journal.* 2017, **850**(1), p.12.

21. Zanchet, A., del Mazo, P., Aguado, A., Roncero, O., Jiménez, E., Canosa, A., Agúndez, M. and Cernicharo, J. Full dimensional potential energy surface and low temperature dynamics of the $H_2CO + OH \rightarrow HCO + H_2O$ reaction. *Physical Chemistry Chemical Physics.* 2018, **20**(8), pp.5415-5426.

22. Shannon, R.J., Taylor, S., Goddard, A., Blitz, M.A. and Heard, D.E. Observation of a large negative temperature dependence for rate coefficients of reactions of OH with oxygenated volatile organic compounds studied at 86-112 K. *Physical Chemistry Chemical Physics.* 2010, **12**(41), pp.13511-13514.

23. Shannon, R.J., Caravan, R.L., Blitz, M.A. and Heard, D.E. A combined experimental and theoretical study of reactions between the hydroxyl radical and oxygenated hydrocarbons relevant to astrochemical environments. *Physical Chemistry Chemical Physics.* 2014, **16**(8), pp.3466-3478.

24. Blázquez, S., González, D., García-Sáez, A., Antiñolo, M., Bergeat, A., Caralp, F., Mereau, R., Canosa, A., Ballesteros, B., Albaladejo, J. and Jiménez, E. Experimental and Theoretical Investigation on the OH + $CH_3C(O)CH_3$ Reaction at Interstellar Temperatures (T = 11.7–64.4 K). *ACS Earth and Space Chemistry.* 2019, **3**(9), pp.1873-1883.

25. Jiménez, E., Antiñolo, M., Ballesteros, B., Canosa, A. and Albaladejo, J. First evidence of the dramatic enhancement of the reactivity of methyl formate ($HC(O)OCH_3$) with OH at temperatures of the interstellar medium: a gas-phase kinetic study between 22 K and 64 K. *Physical Chemistry Chemical Physics.* 2016, **18**(3), pp.2183-2191.

26. Xu, S., Zhu, R.S. and Lin, M.C. Ab initio study of the OH + CH_2O reaction: The effect of the OH··OCH_2 complex on the H-abstraction kinetics. *International Journal of Chemical Kinetics.* 2006, **38**(5), pp.322-326.

27. Zhao, Y., Wang, B., Li, H. and Wang, L. Theoretical studies on the reactions of formaldehyde with OH and OH^-. *Journal of Molecular Structure: THEOCHEM.* 2007, **818**(1), pp.155 - 161.

28. Machado, G.d.S., Martins, E.M., Baptista, L. and Bauerfeldt, G.F. Prediction of Rate Coefficients for the $H_2CO + OH \rightarrow HCO + H_2O$ Reaction at Combustion, Atmospheric and Interstellar Medium Conditions. *The Journal of Physical Chemistry A.* 2020, **124**(11), pp.2309-2317.

29. Snyder, L.E., Buhl, D., Zuckerman, B. and Palmer, P. Microwave Detection of Interstellar Formaldehyde. *Physical Review Letters.* 1969, **22**(13), pp.679-681.

30. Palmer, P., Zuckerman, B., Buhl, D. and Snyder, L.E. Formaldehyde Absorption in Dark Nebulae. *Astrophysical Journal.* 1969, **156**, p.L147.

31. Zuckerman, B., Buhl, D., Palmer, P. and Snyder, L.E. Observations of Interstellar Formaldehyde. *Astrophysical Journal.* 1970, **160**, p.485.

32. Grosjean, E., Williams, E.L. and Grosjean, D. Ambient Levels of Formaldehyde and Acetaldehyde in Atlanta, Georgia. *Air & Waste.* 1993, **43**(4), pp.469-474.

33. Viskari, E.-L., Vartiainen, M. and Pasanen, P. Seasonal and diurnal variation in formaldehyde and acetaldehyde concentrations along a highway in Eastern Finland. *Atmospheric Environment.* 2000, **34**(6), pp.917-923.

34. Krasnopolsky, V.A. A photochemical model of Titan's atmosphere and ionosphere. *Icarus.* 2009, **201**(1), pp.226-256.

35. Nixon, C.A., Achterberg, R.K., Teanby, N.A., Irwin, P.G.J., Flaud, J.-M., Kleiner, I., Dehayem-Kamadjeu, A., Brown, L.R., Sams, R.L., Bézard, B., Coustenis, A., Ansty, T.M., Mamoutkine, A., Vinatier, S., Bjoraker, G.L.,

Jennings, D.E., Romani, P.N. and Flasar, F.M. Upper limits for undetected trace species in the stratosphere of Titan. *Faraday Discussions.* 2010, **147**(0), pp.65-81.

36. Swings, P. and Rosenfeld, L. Considerations Regarding Interstellar Molecules. *Astrophysical Journal.* 1937, **86**, pp.483-486.

37. Agúndez, M. and Wakelam, V. Chemistry of Dark Clouds: Databases, Networks, and Models. *Chemical Reviews.* 2013, **113**(12), pp.8710-8737.

38. Herbst, E. and Klemperer, W. The Formation and Depletion of Molecules in Dense Interstellar Clouds. *Astrophysical Journal.* 1973, **185**, pp.505-534.

39. Viala, Y.P. Chemical equilibrium from diffuse to dense interstellar clouds. I. Galactic molecular clouds. *Astronomy and Astrophysics, Supplement Series.* 1986, **64**, pp.391-437.

40. Bauschlicher, C.W., Jr., Langhoff, S.R. and Taylor, P.R. Theoretical Study of the Dissociation Energy and the Red and Violet Band Systems of CN. *Astrophysical Journal.* 1988, **332**, p.531.

41. Gupta, S., Ochiai, E. and Ponnamperuma, C. Organic synthesis in the atmosphere of Titan. *Nature.* 1981, **293**(5835), pp.725-727.

42. Yung, Y.L., Allen, M. and Pinto, J.P. Photochemistry of the atmosphere of Titan - Comparison between model and observations. *Astrophysical Journal Supplement Series.* 1984, **55**, pp.465-506.

43. Vervack, R.J., Sandel, B.R. and Strobel, D.F. New perspectives on Titan's upper atmosphere from a reanalysis of the Voyager 1 UVS solar occultations. *Icarus.* 2004, **170**(1), pp.91-112.

44. Raulin, F. Exo-Astrobiological Aspects of Europa and Titan: From Observations to Speculations. *Space Science Reviews.* 2005, **116**(1), pp.471-487.

45. Lavvas, P.P., Coustenis, A. and Vardavas, I.M. Coupling photochemistry with haze formation in Titan's atmosphere, Part I: Model description. *Planetary and Space Science.* 2008, **56**(1), pp.27-66.

46. Lavvas, P.P., Coustenis, A. and Vardavas, I.M. Coupling photochemistry with haze formation in Titan's atmosphere, Part II: Results and validation with Cassini/Huygens data. *Planetary and Space Science.* 2008, **56**(1), pp.67-99.

47. Cui, J., Yelle, R.V., Vuitton, V., Waite, J.H., Kasprzak, W.T., Gell, D.A., Niemann, H.B., Müller-Wodarg, I.C.F., Borggren, N., Fletcher, G.G., Patrick, E.L., Raaen, E. and Magee, B.A. Analysis of Titan's neutral upper atmosphere from Cassini Ion Neutral Mass Spectrometer measurements. *Icarus.* 2009, **200**(2), pp.581-615.

48. Gannon, K.L., Glowacki, D.R., Blitz, M.A., Hughes, K.J., Pilling, M.J. and Seakins, P.W. H Atom Yields from the Reactions of CN Radicals with C_2H_2, C_2H_4, C_3H_6, trans-2-C_4H_8, and iso-C_4H_8. *The Journal of Physical Chemistry A.* 2007, **111**(29), pp.6679-6692.

49. Ruscic, B. and Bross, D.H. *Active Thermochemical Tables (ATcT) values based on ver. 1.122g of the Thermochemical Network.* [Online]. 2019. [Accessed 29/09/2022]. Available from: https://atct.anl.gov/Thermochemical%20Data/version%201.122g/index.php

50. Snyder, L.E. and Buhl, D. Observations of Radio Emission from Interstellar Hydrogen Cyanide. *The Astrophysical Journal.* 1971, **163**, p.L47.

51. Harju, J. HCN and HNC Observations Towards Dark Clouds. *Astronomy and Astrophysics.* 1989, **219**, pp.293-302.

52. Snyder, L.E., Hollis, J.M. and Ulich, B.L. Radio detection of the interstellar formyl radical. *The Astrophysical Journal.* 1976, **208**, pp.L91-L94.

53. Remijan, A.J., Hollis, J.M., Lovas, F.J., Stork, W.D., Jewell, P.R. and Meier, D.S. Detection of Interstellar Cyanoformaldehyde (CNCHO). *The Astrophysical Journal.* 2008, **675**(2), pp.L85-L88.

54. Yu, T., Yang, D.L. and Lin, M.C. Kinetics of CN radical reactions with formaldehyde and 1,3,5-trioxane. *International Journal of Chemical Kinetics.* 1993, **25**(12), pp.1053-1064.

55. Chang, Y.-W. and Wang, N.S. Rates of the reactions CN + H_2CO and NCO + H_2CO in the temperature range 294–769 K. *Chemical Physics.* 1995, **200**(3), pp.431-437.

56. Feng, W.L., Wang, Y., Zhang, S.W. and Pang, X.Y. Theoretical investigation of the mechanism and kinetics for HCO + HCN ⇄ HCHO + CN. *Chemical Physics Letters.* 1997, **266**(1-2), pp.43-46.

57. Tonolo, F., Lupi, J., Puzzarini, C. and Barone, V. The Quest for a Plausible Formation Route of Formyl Cyanide in the Interstellar Medium: a State-of-the-art Quantum-chemical and Kinetic Approach. *The Astrophysical Journal.* 2020, **900**(1), p.85.

58. Becke, A.D. A new mixing of Hartree–Fock and local density-functional theories. *The Journal of Chemical Physics.* 1993, **98**(2), pp.1372-1377.

59. Dunning, T.H. Gaussian basis sets for use in correlated molecular calculations. I. The atoms boron through neon and hydrogen. *The Journal of Chemical Physics.* 1989, **90**(2), pp.1007-1023.

60. Kendall, R.A., Dunning, T.H. and Harrison, R.J. Electron affinities of the first-row atoms revisited. Systematic basis sets and wave functions. *The Journal of Chemical Physics.* 1992, **96**(9), pp.6796-6806.

61. Woon, D.E. and Dunning Jr., T.H. Gaussian basis sets for use in correlated molecular calculations. V. Core-valence basis sets for boron through neon. *The Journal of Chemical Physics.* 1995, **103**(11), pp.4572-4585.

62. Zhao, Y. and Truhlar, D.G. The M06 suite of density functionals for main group thermochemistry, thermochemical kinetics, noncovalent interactions, excited states, and transition elements: two new functionals and systematic testing of four M06-class functionals and 12 other functionals. *Theoretical Chemistry Accounts.* 2008, **120**(1), pp.215-241.

63. Pople, J.A., Krishnan, R., Schlegel, H.B. and Binkley, J.S. Electron correlation theories and their application to the study of simple reaction potential surfaces. *International Journal of Quantum Chemistry.* 1978, **14**(5), pp.545-560.

64. Bartlett, R.J. and Purvis, G.D. Many-body perturbation theory, coupled-pair many-electron theory, and the importance of quadruple excitations for the correlation problem. *International Journal of Quantum Chemistry.* 1978, **14**(5), pp.561-581.

65. Laury, M.L., Boesch, S.E., Haken, I., Sinha, P., Wheeler, R.A. and Wilson, A.K. Harmonic vibrational frequencies: Scale factors for pure, hybrid, hybrid meta, and double-hybrid functionals in conjunction with correlation consistent basis sets. *Journal of Computational Chemistry.* 2011, **32**(11), pp.2339-2347.

66. *NIST Computational Chemistry Comparison and Benchmark Database.* [Online]. [Accessed 29/09/2022]. Available from: http://cccbdb.nist.gov/

67. Frisch, M.J., Trucks, G.W., Schlegel, H.B., Scuseria, G.E., Robb, M.A., Cheeseman, J.R., Scalmani, G., Barone, V., Mennucci, B., Petersson, G.A., Nakatsuji, H., Caricato, M., Li, X., Hratchian, H.P., Izmaylov, A.F., Bloino, J., Zheng, G., Sonnenberg, J.L., Hada, M., Ehara, M., Toyota, K., Fukuda, R., Hasegawa, J., Ishida, M., Nakajima, T., Honda, Y., Kitao, O., Nakai, H., Vreven, T., J. A. Montgomery, J., Peralta, J.E., Ogliaro, F., Bearpark, M., Heyd, J.J., Brothers, E., Kudin, K.N., Staroverov, V.N., Keith, T., Kobayashi, R., Normand, J., Raghavachari, K., Rendell, A., Burant, J.C., Iyengar, S.S., Tomasi, J., Cossi, M., Rega, N., Millam, J.M., Klene, M., Knox, J.E., Cross, J.B., Bakken, V., Adamo, C., Jaramillo, J., Gomperts, R., Stratmann, R.E., Yazyev, O., Austin, A.J., Cammi, R., Pomelli, C., Ochterski, J.W., Martin, R.L., Morokuma, K., Zakrzewski, V.G., Voth, G.A., Salvador, P., Dannenberg, J.J., Dapprich, S., Daniels, A.D., Farkas, O., Foresman, J.B., Ortiz, J.V., Cioslowski, J. and Fox, D.J. *Gaussian 09 Revision D.01*. Wallingford CT: Gaussian, Inc. 2013.

68. Glowacki, D.R., Liang, C.-H., Morley, C., Pilling, M.J. and Robertson, S.H. MESMER: An Open-Source Master Equation Solver for Multi-Energy Well Reactions. *The Journal of Physical Chemistry A.* 2012, **116**(38), pp.9545-9560.

69. Marcus, R.A. Unimolecular Dissociations and Free Radical Recombination Reactions. *The Journal of Chemical Physics.* 1952, **20**(3), pp.359-364.

70. Davies, J.W., Green, N.J.B. and Pilling, M.J. The testing of models for unimolecular decomposition via inverse laplace transformation of experimental recombination rate data. *Chemical Physics Letters.* 1986, **126**(3), pp.373 - 379.

71. Troe, J. Theory of thermal unimolecular reactions at low pressures. I. Solutions of the master equation. *The Journal of Chemical Physics.* 1977, **66**(11), pp.4745-4757.

72. Miller, W.H. Tunneling corrections to unimolecular rate constants, with application to formaldehyde. *Journal of the American Chemical Society.* 1979, **101**(23), pp.6810-6814.

73. Czakó, G., Szabó, I. and Telekes, H. On the Choice of the Ab Initio Level of Theory for Potential Energy Surface Developments. *The Journal of Physical Chemistry A.* 2014, **118**(3), pp.646-654.

74. Prager, J., Najm, H.N. and Zádor, J. Uncertainty quantification in the ab initio rate-coefficient calculation for the $CH_3CH(OH)CH_3+OH \rightarrow CH_3C(OH)CH_3+H_2O$ reaction. *Proceedings of the Combustion Institute.* 2013, **34**(1), pp.583-590.

75. Klippenstein, S.J. From theoretical reaction dynamics to chemical modeling of combustion. *Proceedings of the Combustion Institute.* 2017, **36**(1), pp.77-111.

Chapter 4

The reaction between the cyano radical (CN) and methanethiol (CH_3SH) and thioformaldehyde (CH_2S)

4.1 Introduction

Sulphur is the period 3 element in the chalcogen group. It is ubiquitous, existing in living organisms, the geosphere as well as outer space. It exists in two types of amino acids in peptides and proteins, namely methionine ($C_5H_{11}NO_2S$) and cysteine ($C_3H_7NO_2S$), which acts as cellular antioxidants to regulate redox reactions (1). Sulphur can be present with a valence state of +6 to –2, interchanging from the form of sulphate, sulphite, elemental sulphur and sulphide through the metabolisms in animals, plants, fungi and bacteria (2, 3).

Indeed, the sulphur source in the environment can be traced back to have origins in the Earth's crust and mantle, where the release of sulphur, mainly as gases of SO_2 or H_2S, can be via volcanic and hydrothermal activities while, to complete the cycle, the deposition can be as ores in the forms of sulphate or pyrite (FeS_2) (2, 3). The burning of sulphur containing fossil fuel has previously led to an increased contribution of anthropogenically produced sulphur into the atmosphere. This results in adverse issues including acid rain, where SO_2 or H_2S can be oxidised to form sulphuric acid H_2SO_4, visibility reduction and climate change, where the aerosols of sulphur bearing species such as OCS can affect the Earth's albedo by altering the process of cloud generation in the troposphere and the concentration of ozone in the stratosphere (4-7). Hence, there has been research carried out in the field of atmospheric chemistry to understand the reactions involving sulphur bearing species, particularly with the OH radical.

Sulphur bearing species also show their presence in other celestial bodies in our Solar System, where notable examples include the sulphuric acid clouds on Venus (8, 9) and the volcanic ejecta from Io, one of the Jupiter's satellites (10-12). In the interstellar medium, various sulphur bearing species have been observed, including but not limited to H_2S (13, 14), CS (13-18), SO (13, 14, 19, 20), SO_2 (14, 20, 21), OCS (14, 18, 22), HCS (23), CH_2S (14, 17, 18, 24-26), CH_3SH (14, 18, 24, 27, 28) and HC(S)CN (29). It is proposed that there is the sulphur depletion problem, where there is a mismatch between the modelled and the observed sulphur abundance in the dense interstellar medium, suggesting the existence of unknown sulphur reservoirs (30, 31), and thus giving rise to the importance in the study of reactions involving sulphur bearing species in the field of astrochemistry.

Table 4.1 Detected abundance of CH_3SH and CH_2S in selected interstellar objects

Interstellar objects	**CH_3SH (reference)**		**CH_2S (reference)**	
	Column density (cm^{-2})	**Fractional abundance relative to H_2**	**Column density (cm^{-2})**	**Fractional abundance relative to H_2**
Sgr B2	1.5×10^{14} (27)			
TMC-1	$<4 \times 10^{12}$ (24)		2.4×10^{13} (24)	$(1–2) \times 10^{-9}$ (25)
L134N	$<4 \times 10^{12}$ (24)		4×10^{12} (24)	5×10^{-10} (25)
IRAS 16293-2422	5.5×10^{15} (14)	4×10^{-9} (28)	1.5×10^{15} (14)	
IRC +10216			$(0.5–2) \times 10^{13}$ (26)	
MWC 480 disk			$(2.6–5.7) \times 10^{12}$ (17)	
Orion A				$(1–2) \times 10^{-9}$ (25)
NGC7538				$(1–2) \times 10^{-9}$ (25)

In this chapter, methanethiol CH_3SH and thioformaldehyde CH_2S are the two sulphur bearing species of interest. CH_3SH is the simplest thiol species, which has been detected in multiple interstellar objects including Sgr B2 (27), TMC-1 (24), L134N (24) and IRAS 16293-2422 (14, 28). Similarly, CH_2S is the simplest thial species and its presence in the interstellar medium has been observed in different interstellar objects including IRC +10216 (26), IRAS 16293-2422 (14), MWC 480 disk (17), TMC-1 (24, 25), L134N (24, 25), Orion A (25) and NGC7538 (25). The reported abundance from various detections are summarised in Table 4.1.

As mentioned above, for the application of atmospheric chemistry and astrochemistry, there has been research on the kinetics of the gas-phase reactions of the OH radical with sulphur bearing species, and this is the case for CH_3SH. Different experimental measurements on the reaction rate coefficient at room temperature and above (293–313 K) have been carried out using the discharge flow method (32, 33), continuous photolysis coupled with gas chromatography (34), and pulsed laser photolysis coupled with laser-induced fluorescence technique (35). The rate coefficients are found to have values within the range of (2.1–3.8) × 10^{-11} $\mathrm{cm^3\ molecule^{-1}\ s^{-1}}$. With the flash photolysis-resonance fluorescence technique, Atkinson et al. (36) determined that the rate coefficient in the range of 300–423 K follows the expression:

$$k(T) = 8.89 \times 10^{-12} \exp\left(\frac{790 \pm 300\ \mathrm{J\ mol^{-1}}}{RT}\right)\ \mathrm{cm^3\ molecule^{-1}\ s^{-1}} \qquad \text{E 4.1}$$

while Wine et al. (5) obtained the following expression for the range of 244–366 K:

$$k(T) = (1.15 \pm 0.39) \times 10^{-11} \exp\left(\frac{338 \pm 100\ \mathrm{K}}{T}\right)\ \mathrm{cm^3\ molecule^{-1}\ s^{-1}} \qquad \text{E 4.2}$$

where both demonstrated that the rate coefficient shows a negative temperature dependence. These experimental results are summarised in Table 4.2. It is proposed that (5, 37) the reaction between OH and CH_3SH proceeds by forming a weakly bound complex followed by either an addition or a H abstraction.

Table 4.2 Experimental rate coefficients of the OH + CH_3SH reaction reported in previous literature

Experimental method	***T* (K)**	***k* (10^{-11} × cm^3 $molecule^{-1}$ s^{-1})**	**Reference**
Discharge flow	293	2.1 ± 0.2	(33)
	296	2.56 ± 0.44	(32)
Continuous photolysis-gas chromatography	300	3.6 ± 0.4	(34)
	313	3.3 ± 0.4	
Pulsed laser photolysis-laser-induced fluorescence	270	3.6–3.8	(35)
	300	3.3	
Flash photolysis-resonance fluorescence	300	3.39 ± 0.34	(36)
	347	2.73 ± 0.28	
	423	2.30 ± 0.23	
	244	4.83 ± 0.98	(5)
	270	3.84 ± 0.58	
	298	3.37 ± 0.41	
	333	3.22 ± 0.62	
	366	2.97 ± 0.47	

For the results from theoretical calculations, Wilson and Hirst (38) suggested that the H abstraction reaction is exothermic and proceeds via a submerged barrier based on the calculations at the QCISD(T)/6-311G(2d,p)//MP2/6-311G(2d,p) level. However, it is worth noting that H abstraction by OH from CH_3SH can occur at the mercapto site (–SH) or the methyl site (–CH_3). Further calculations at the MCCM-CCSD(T)-CO-2m//MP2/cc-pVDZ (39), CBS-QB3 (40, 41) and CCSD(T)/aug-cc-pV(T,Q)Z//M06-2X/aug-cc-pV(T+d)Z (42) levels suggested that while abstraction from either site begins with the formation of a weakly bound complex, the abstraction from the methyl site involves a positive barrier but a submerged barrier for the mercapto site, making the latter one the dominant product channel. This can be explained by the difference in bond strength of the C–H bond and S–H bond: more energy is required to break the stronger C–H bond. The potential energy surface for the abstraction channels can be found in Figure 4.1. For the addition channel, there have been discrepancies on whether the formation of the adduct $CH_3S(OH)H$ is endothermic (38, 39, 42) or exothermic (40, 41).

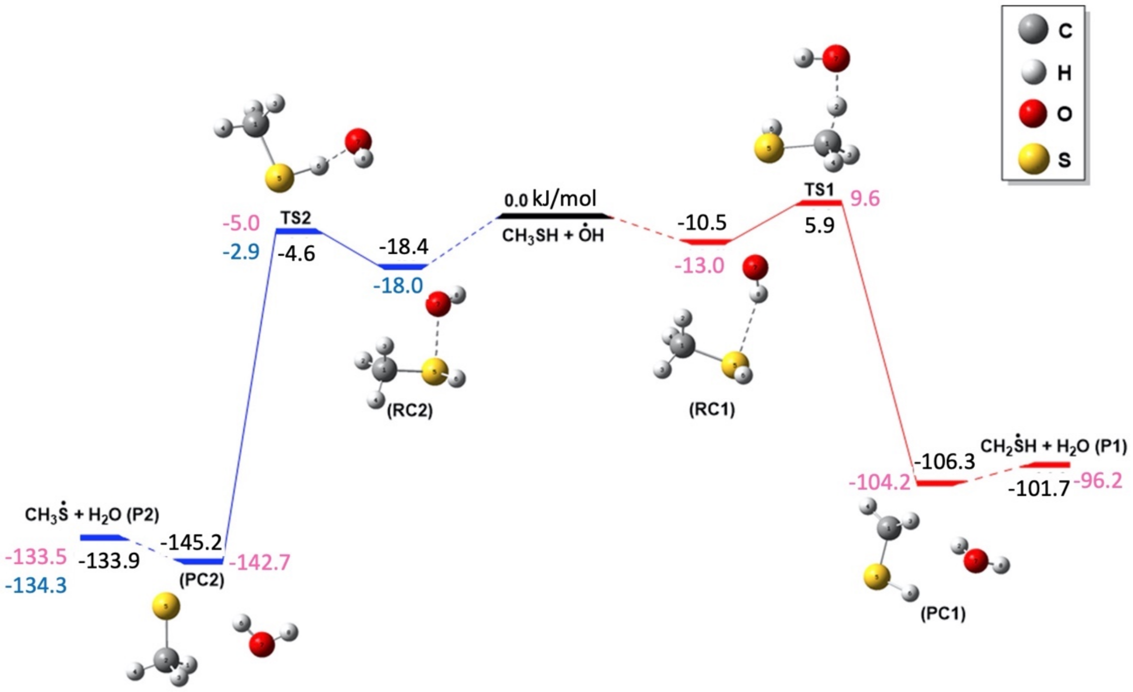

Figure 4.1 Zero-point vibrational energy (ZPVE) corrected potential energy surface in kJ mol^{-1} for the OH + CH_3SH abstraction reaction. Taken from Mai et al. (42). On the right is the H abstraction at the methyl site, which involves a positive barrier TS1 after the formation of the weakly bound complex RC1, while on the left is the H abstraction at the mercapto site, which involves a submerged barrier TS2 after the formation of the weakly bound complex RC2. The energy values in black are obtained from the CCSD(T)/aug-cc-pV(T,Q)Z//M06-2X/aug-cc-pV(T+d)Z level (42), in pink are from the MCCM-CCSD(T)-CO-2m//MP2/cc-pVDZ level (39) and in blue are from the CBS-QB3 level (40).

For the overall rate coefficient of the OH + CH_3SH reaction, Masgrau et al. (39) reported the following expression for the temperature range of 225–1000 K based on the results from variational transition state theory calculations:

$$k(T) = 4.43 \times 10^{-13} \left(\frac{T}{298\ \mathrm{K}}\right)^{1.92} \exp\left(\frac{892\ \mathrm{K}}{T}\right)\ \mathrm{cm^3\ molecule^{-1}\ s^{-1}} \qquad \text{E 4.3}$$

while Mai et al. (42) reported the following expression for the temperature range of 200–2000 K at 760 Torr based on the results from master equation calculations:

$$k(T) = 1.44 \times 10^{-17} T^{1.99} \exp\left(\frac{894\ \mathrm{K}}{T}\right)\ \mathrm{cm^3\ molecule^{-1}\ s^{-1}} \qquad \text{E 4.4}$$

where both show a negative temperature dependence below 500 K but a positive temperature dependence at higher temperatures.

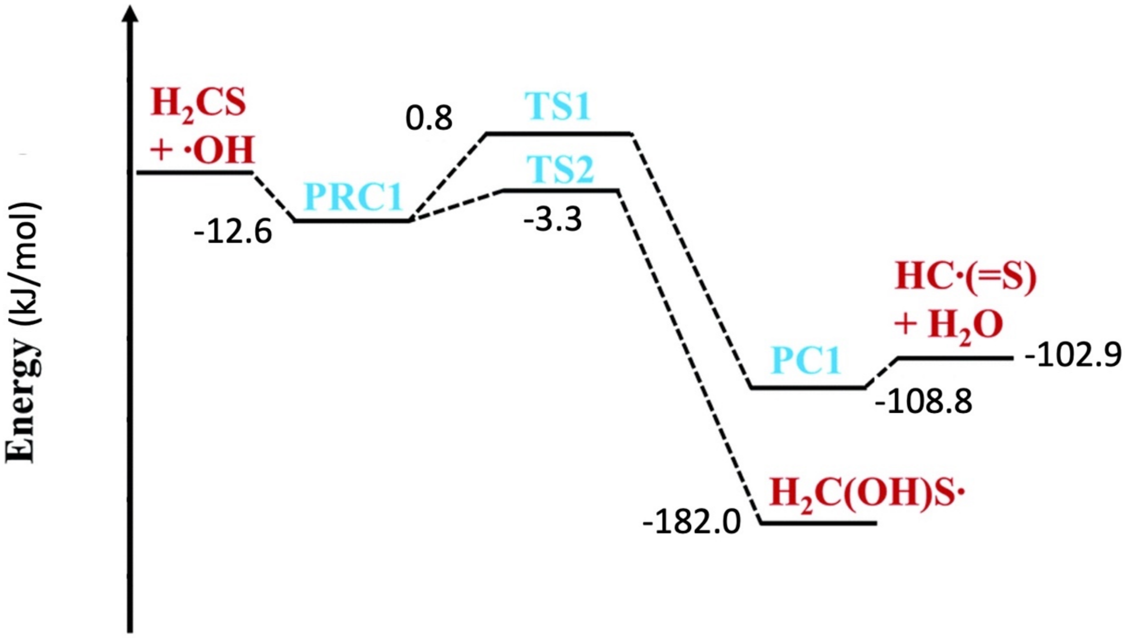

Figure 4.2 ZPVE-corrected potential energy surface in kJ mol^{-1} for the OH + CH_2S reaction at the CCSD(T)/aug-cc-pVTZ//M06-2X/6-311++G(3df,3pd) level obtained by Arathala et al. Taken from (43). Two possible channels are found, namely the H abstraction channel via the positive barrier TS1 and the addition channel to form the adduct $H_2C(OH)S$ via the submerged barrier TS2, after the formation of the pre-reaction complex PRC1.

For the reaction between OH and CH_2S, theoretical calculations carried out by Arathala et al. (43) at the CCSD(T)/aug-cc-pVTZ//M06-2X/6-311++G(3df,3pd) level obtained the potential energy surface shown in Figure 4.2. After the formation of a weakly bound pre-reaction complex (–3.0 kcal mol^{-1} or –12.6 kJ mol^{-1} relative to the reactants), the reaction can proceed by either a H abstraction via a positive barrier (0.2 kcal mol^{-1} or 0.8 kJ mol^{-1}) to form HCS + H_2O or an addition via a submerged barrier (–0.8 kcal mol^{-1} or –3.3 kJ mol^{-1}) to form the adduct $H_2C(OH)S$ (–43.5 kcal mol^{-1} or –182.0 kJ mol^{-1}). Based on these ab initio results, canonical variational transition state theory calculations coupled with the small curvature tunnelling have been performed (43), which give the overall reaction rate coefficient a value of 1.11 × 10^{-11} cm^3 molecule^{-1} s^{-1} at 200 K and 5.90 × 10^{-12} cm^3 molecule^{-1} s^{-1} at 400 K with a negative temperature dependence shown between these two temperatures. The addition channel is found to be more dominant in this temperature range.

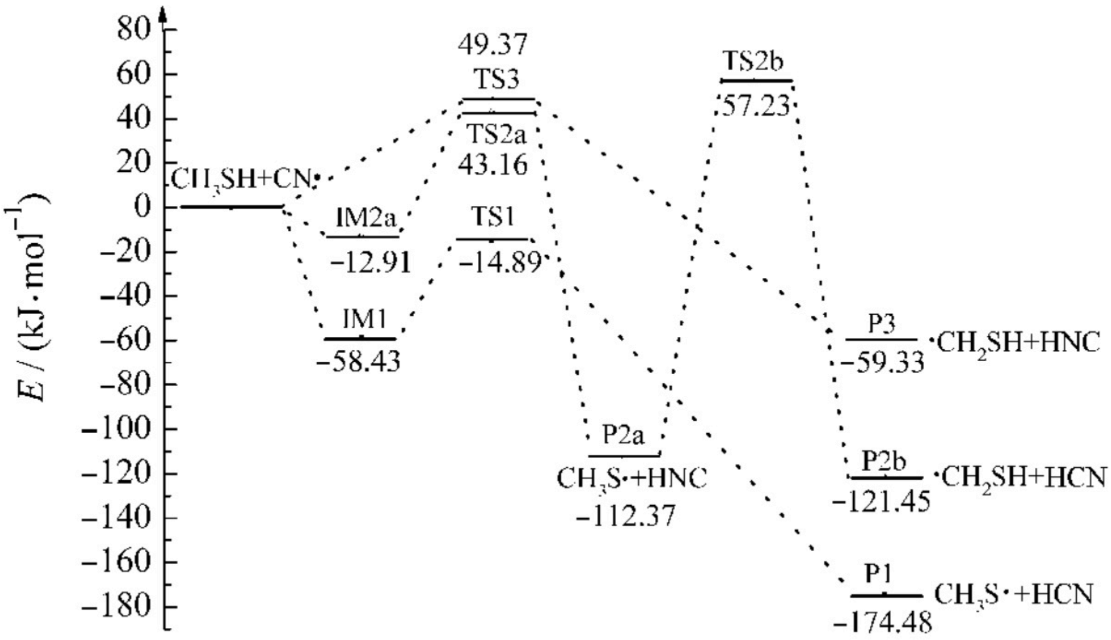

Figure 4.3 ZPVE-corrected potential energy surface in kJ mol^{-1} for the CN + CH_3SH reaction at the CCSD/6-311++G(d,p)//B3LYP/6-311++G(d,p) level obtained by Xu et al. Taken from (45). It is proposed that CH_3S + HCN can be formed via the pre-reaction complex IM1 and the submerged barrier TS1; CH_3S + HNC can be formed via the pre-reaction complex IM2 and the positive barrier TS2a; and CH_2SH + HNC can be formed via the positive barrier TS3. It is reported that CH_2SH + HCN cannot be formed directly from CN + CH_3SH and can only be formed from another reaction between CH_3S and HNC via a positive barrier TS2b.

Considering the title reactions involving the CN radical with sulphur bearing species, previous literature by Decker and Macdonald (44) reported their experimental measurements on the reaction between CN and CH_3SH. Infrared transient absorption spectroscopy was utilised to measure the rate coefficient at 293 K in the pressure range of 0.74–6.6 Torr, which gives a value of $(2.7 \pm 0.3) \times 10^{-10}$ cm^3 $molecule^{-1}$ s^{-1}. HCN and HNC were identified as the products, which were suggested to be potentially formed by a H abstraction from either the mercapto group or the methyl group, while no addition product was found. The product branching fractions for the HCN and HNC channels at 293 K were determined to be 0.81 and 0.19 (±0.08) (44).

Ab initio calculations on the CN + CH_3SH reaction have previously been performed by Xu et al. (45) at the CCSD/6-311++G(d,p)//B3LYP/6-311++G(d,p) level and the potential energy surface obtained is shown in Figure 4.3. Three possible reaction channels are reported where all are overall exothermic. The first one is the formation of CH_3S + HCN via a pre-reaction complex (–58.43 kJ mol^{-1}) followed by a submerged barrier (–14.89 kJ mol^{-1}). The second one is the formation of CH_3S + HNC via a pre-reaction complex (–12.91 kJ mol^{-1}) followed by a positive barrier (43.16 kJ mol^{-1}). The third one is the formation of CH_2SH + HNC via a positive barrier (49.37 kJ mol^{-1}) where no pre-reaction complex has been identified. There is no reported direct route to form CH_2SH + HCN and they can only be attained by a separate reaction between CH_3S and HNC via a simultaneous two-H transfer. Nevertheless, if this potential energy surface could genuinely represent the actual scenario, then at 293 K CH_3S + HCN would be the sole products formed, which contradicts with the 0.81:0.19 HCN/HNC product branching ratio reported from experiments (44) and suggests the necessity to perform a re-calculation at a more advanced level of theory.

For CN + CH_2S, to date there has been no previous literature, either theoretical or experimental, which has reported the research on this reaction. In particular, there has been limited experimental research involving CH_2S because of the short lifetime of its monomer form under terrestrial conditions. While CH_2S has been detected in the ISM, the CH_2S monomer is highly unstable on Earth, with a half-life of about 6 minutes at a pressure of 0.01–0.05 Pa, that is, about 2.4 ×

10^{12}–1.2×10^{13} molecule cm^{-3}, and can readily polymerise into the cyclic trimer form, 1,3,5-trithiane, or decompose to CS and H_2 via photo-oxidation (46-51).

While there is a lack of previous literature focussing on the reactions of CN with sulphur bearing species, there has been research on the reactions of CN with the isovalent oxygen bearing analogues. The reaction between CN and CH_2O has been discussed in Chapter 3 of this thesis, where possible products suggested from the potential energy surface obtained include HCN, HNC, HCO and HC(O)CN. Therefore, it is reasonable to hypothesise that HCN, HNC, HCS and HC(S)CN, where all have been observed in the ISM, are among the list of potential products formed from CN + CH_2S. Indeed, CN + CH_2S is proposed as a candidate reaction leading to the formation of cosmic HC(S)CN (29), thus the significance of the CN + CH_2S reaction should not be underestimated.

Likewise, previous literature have reported the research on the CN + CH_3OH reaction. Sayah et al. (52) made use of the flow tubes coupled with laser-induced fluorescence to determine the rate coefficient of the CN + CH_3OH reaction, which gives a value of $(1.2 \pm 0.2) \times 10^{-10}$ cm^3 molecule^{-1} s^{-1} at 294 K. Later, experiments using the time-resolved infrared diode laser absorption spectroscopy performed by Janssen and Hershberger (53) obtained the following expression for the rate coefficient over a temperature range of 298–421 K:

$$k(T) = (2.16 \pm 0.46) \times 10^{-11} \exp\left(-\frac{214 \pm 76\ \mathrm{K}}{T}\right)\ \mathrm{cm^3\ molecule^{-1}\ s^{-1}} \qquad \text{E 4.5}$$

More recently, kinetic measurements have been extended to cover the lower temperature range. With the pulsed-laser photolysis coupled with laser-induced fluorescence technique, Gupta et al. (54) measured the rate coefficient in the temperature range of 16.7–296 K attained from a Laval nozzle setup, and the results can be represented by the following expression:

$$k(T) = 1.26 \times 10^{-11} \left(\frac{T}{300\ \mathrm{K}}\right)^{-0.7} \exp\left(-\frac{5.4\ \mathrm{K}}{T}\right)\ \mathrm{cm^3\ molecule^{-1}\ s^{-1}} \qquad \text{E 4.6}$$

where H abstraction is suggested to be the dominant reaction.

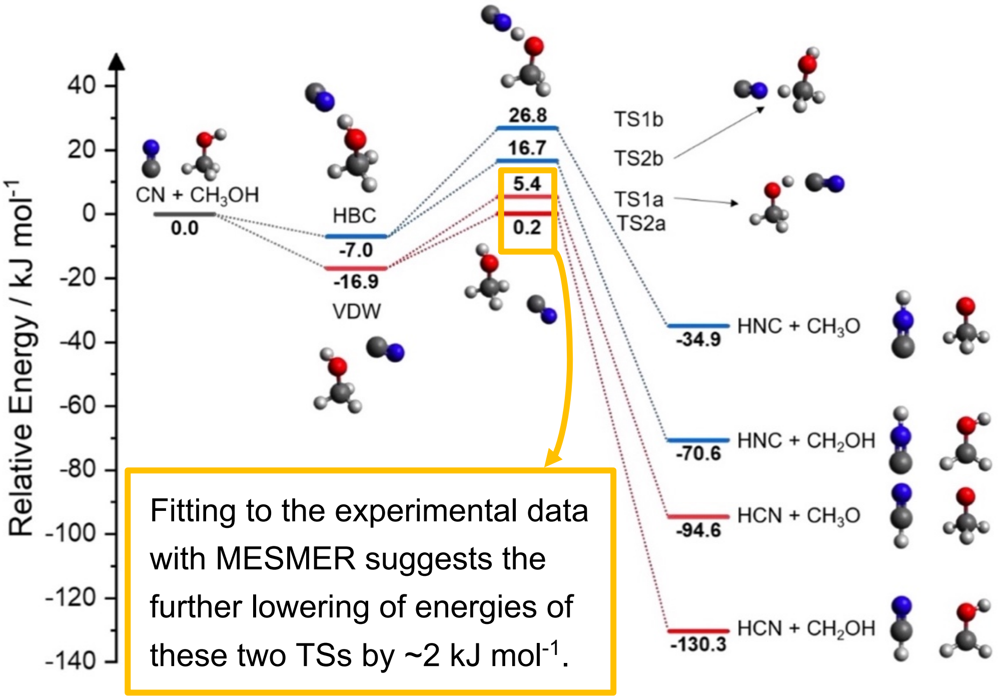

Figure 4.4 ZPVE-corrected potential energy surface in kJ mol^{-1} for the CN + CH_3OH reaction at the CCSD(T)/aug-cc-pVTZ//M06-2X/aug-cc-pVTZ level obtained by Lucas. Adapted from (55). Four possible product channels are identified, from the lowest energy to the highest energy: HCN + CH_2OH, HCN + CH_3O, HNC + CH_2OH, HNC + CH_3O, where all involve the formation of a pre-reaction complex followed by surmounting a barrier. MESMER fitting to the experimental data suggest the further lowering of the energies of the transition states respectively leading to HCN + CH_2OH (TS2a) and HCN + CH_3O (TS1a) by ~2 kJ mol^{-1}, which will make the former one change from being positive to submerged.

Theoretical calculations carried out by Mr Daniel Lucas (University of Leeds) (55) at the CCSD(T)/aug-cc-pVTZ//M06-2X/aug-cc-pVTZ level give the potential energy surface presented in Figure 4.4. Two pre-reaction complexes have been identified, the more stable one is with the CN carbon end closer to CH_3OH (VDW, –16.9 kJ mol^{-1}) which subsequently forms HCN as the product via either transition state TS2a or TS1a, while the other one is with the CN nitrogen end closer to CH_3OH (HBC, –7.0 kJ mol^{-1}) which subsequently forms HNC as the product via either transition state TS2b or TS1b. It is important to note that the optimised structures of TS2a and TS2b may not be the genuine transition states on the reaction pathways but just approximations as suggested by Lucas (55) due to the failure for the intrinsic reaction calculations (IRC) to converge contributed from the small magnitude of the imaginary frequency values (–167 cm^{-1} and –362 cm^{-1} respectively) and the relatively flat shape of the PES in the nearby regions. Hydrogen atom abstraction can occur at the methyl site via TS2a or TS2b to generate CH_2OH or the hydroxyl site via TS1a or TS1b to generate CH_3O, with the former one being more stable.

The results from ab initio calculations indicated that all the transition states have positive energies relative to the starting reagents. However, MESMER fittings have been done with reference to the low temperature experimental data (54) by floating the transition state energies and in order to be in line with the temperature dependence observed in experiments, the fitting results suggested the lowering of the energies of transition states TS2a and TS1a by ~2 kJ mol^{-1} (55). (The details about data fitting with MESMER can be found in Section 2.2 and another example is presented in Chapter 3.) Although this value is within the computational error, such a change will make the transition state with the lowest energy (TS2a, originally 0.2 kJ mol^{-1} relative to the reactants), which is the one leading to HCN + CH_2OH, become submerged. HCN + CH_2OH are found to be the major products, up to 90% below 100 K, given that the pathway to their formation is of the lowest energy. These research work on CN + CH_3OH have provided valuable results to be compared with the CN + CH_3SH reaction.

In this chapter, the reactions between the CN radical with CH_3SH and with CH_2S are explored using theoretical approaches. The potential energy surfaces of these two reactions are obtained using ab initio methods, which are then utilised for the rate coefficient calculations. The results can help to fill out the research gap for these reactions, help evaluate the astrophysical significance of the reactions, as well as act as comparisons with the reactions involving the oxygen bearing isovalent analogues.

4.2 Computational methods

Ab initio calculations were carried out to explore the potential energy surfaces of the CN + CH_3SH and CN + CH_2S reactions respectively with the use of the Gaussian 09 programme (56), where a more detailed description of the procedures can be found in Section 2.1. Geometric structures of stationary points (reactants, products, intermediates including adducts and van der Waals complexes, and transition states (TSs)) were first optimised at the BHandHLYP/aug-cc-pVDZ level of theory (57-60) and further refined at the M06-2X/aug-cc-pVTZ level (61). For all the DFT calculations, the option of the ultrafine integration grids in Gaussian was applied. Using the same level of theory as the geometry optimisation steps, vibrational frequency calculations were carried out to obtain the zero-point vibrational energies (ZPVE) as well as characterise the stationary points, where the TSs were found to have only one imaginary vibrational frequency while the reactants, products and intermediates have all frequencies being positive. Scaling factors were used to correct the ZPVE obtained, which are taken to be 0.9589 for BHandHLYP/aug-cc-pVDZ (62) and 0.956 for M06-2X/aug-cc-pVTZ (63) respectively. For all the TSs located, unless otherwise specified, IRC calculations were performed to verify that they are the saddle points connecting to the respective local minima on the PES. Based on the optimised structures, calculations at the CCSD(T)/aug-cc-pVTZ level (64, 65) were carried out to refine the single-point energies of all the species and obtain the dipole moment values of the reactants.

Statistical rate theory calculations were performed with the use of the master equation solver programme MESMER (66) based on the ab initio results, where further details can be found in Section 2.2. For the calculations of the density of states, the rigid rotor-harmonic oscillator approximation was applied for all modes of all the species involved. For reactions involving a defined transition state, the microcanonical rate coefficients $k(E)$ were calculated using the RRKM theory (67). For the barrierless entrance channels, the ILT method (68) was applied with the microcanonical rate coefficients given by the following expression in terms of the ILT parameters:

$$k_{\mathrm{ILT}}^{\infty}(T) = A_{\mathrm{ILT}}^{\infty}\left(\frac{T}{298\mathrm{K}}\right)^{n_{\mathrm{ILT}}^{\infty}} \qquad \text{E 4.7}$$

where for the case of CN + CH_3SH, there exists, although limited, experimental data from previous literature (44) to allow the fitting of ILT parameters to be done in a similar way as reported in Chapter 3 for CN + CH_2O but for the case of CN + CH_2S, no experimental data are available. Therefore, classical capture theory using the model reported by Stoecklin et al. (69) was utilised to determine the collision limit, which $k_{\mathrm{ILT}}^{\infty}(T)$ was assigned to be. Based on the classical capture theory, the predicted collision rate coefficient $k_{\mathrm{coll}}(T)$ is given by (69-72):

$$k_{\mathrm{coll}}(T) = 1.353\pi\left(\frac{2C_6}{k_{\mathrm{B}}T}\right)^{\frac{1}{3}}\left(\frac{8k_{\mathrm{B}}T}{\pi\mu}\right)^{\frac{1}{2}} \qquad \text{E 4.8}$$

where k_{B} is the Boltzmann constant and $\mu = \frac{m_1 m_2}{m_1+m_2}$ is the reduced mass of the two colliding reagents 1 and 2. C_6 is the sum of the coefficients contributed from different attractive forces: dipole-dipole C_6^{D-D}, dipole-induced dipole C_6^{D-iD} and dispersion C_6^{Disp} forces, that is:

$$C_6 = C_6^{D-D} + C_6^{D-iD} + C_6^{Disp} \qquad \text{E 4.9}$$

where C_6^{D-D} is given by:

$$C_6^{D-D} = \frac{2}{3}\left(\frac{\mu_1^2\mu_2^2}{k_{\mathrm{B}}T(4\pi\varepsilon_0)^2}\right) \qquad \text{E 4.10}$$

with μ_1 and μ_2 being the dipole moments of the colliding reagents 1 and 2 and ε_0 being the permittivity of free space, C_6^{D-iD} is given by:

$$C_6^{D-iD} = \frac{\mu_1^2\alpha_2+\mu_2^2\alpha_1}{4\pi\varepsilon_0} \qquad \text{E 4.11}$$

with α_1 and α_2 being the polarisabilities of the colliding reagents 1 and 2, and C_6^{Disp} is given by:

$$C_6^{Disp} = \frac{3}{2}\alpha_1\alpha_2\left(\frac{I_1 I_2}{I_1+I_2}\right) \qquad \text{E 4.12}$$

with I_1 and I_2 being the ionisation energies of the colliding reagents 1 and 2. It can be shown that the contributions from the dipole-dipole forces on k_{coll} follow the relationship of $T^{-1/6}$, while from the dipole-induced dipole and dispersion forces follow $T^{1/6}$. At low temperature, the contributions from the dipole-dipole forces dominate and so for simplicity, C_6 is approximated to only consist of C_6^{D-D} and then $k_{\mathrm{coll}}(T)$ becomes:

$$k_{\mathrm{coll}}(T) = 1.353\pi \left(\frac{2\left(\frac{2}{3}\left(\frac{\mu_1^2\mu_2^2}{k_{\mathrm{B}}T(4\pi\varepsilon_0)^2}\right)\right)}{k_{\mathrm{B}}T} \right)^{\frac{1}{3}} \left(\frac{8k_{\mathrm{B}}T}{\pi\mu}\right)^{\frac{1}{2}} \quad \text{E 4.13}$$

$$= 1.353\pi \left(\frac{\mu_1^2\mu_2^2}{12k_{\mathrm{B}}^2\pi^2\varepsilon_0^2}\right)^{\frac{1}{3}} \left(\frac{8k_{\mathrm{B}}}{\pi\mu}\right)^{\frac{1}{2}} T^{-\frac{1}{6}}$$

Comparing with E 1.7, the ILT temperature dependence index $n_{\mathrm{ILT}}^{\infty}$ was then set as $-\frac{1}{6}$ while the pre-exponential factor $A_{\mathrm{ILT}}^{\infty}$ for each entrance channel was computed from the dipole moments of the two reactants using E 1.13 divided by the number of available entrance channels assuming that it is equally likely to enter each entrance channel. For the population and depopulation of energy grains via collisional energy transfer with the bath gas, the probabilities were described using the exponential-down model (73), where the properties of the bath gas can be found in Section 2.2. The calculations were performed with a grain size of 100 cm^{-1} using Ar as the bath gas.

4.3 Results and discussions

4.3.1 Results from ab initio calculations and discussions

4.3.1.1 CN + CH_3SH

Possible reaction channels for the CN + CH_3SH reaction include the H abstraction from the mercapto group, where the related PES obtained is shown in Figure 4.5, and the H abstraction from the methyl group, where the related PES obtained is shown in Figure 4.6. No addition channel has been found for this reaction. The zero-point corrected energies relative to the reactants calculated at the CCSD(T)/aug-cc-pVTZ//M06-2X/aug-cc-pVTZ level of theory are also shown in Figure 4.5 and Figure 4.6.

The optimised geometries of the stationary points shown in Figure 4.5 and Figure 4.6 at the M06-2X/aug-cc-pVTZ level are shown in Figure 4.7. The optimised Cartesian coordinates, vibrational frequencies, rotational constants and energy values are provided in Appendix C.

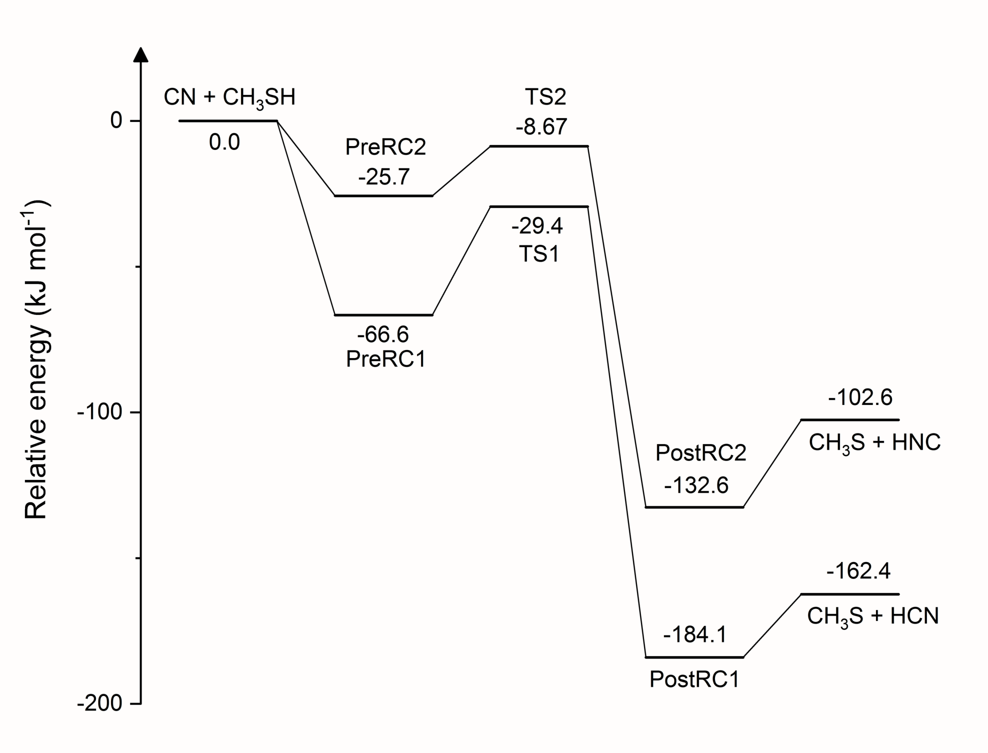

Figure 4.5 PES of the H abstraction from the mercapto group for the CN + CH_3SH reaction obtained at the CCSD(T)/aug-cc-pVTZ//M06-2X/aug-cc-pVTZ level of theory. All energy values are in kJ mol^{-1} and are corrected with scaled ZPVE.

For the abstraction reaction to occur at the mercapto site as shown in Figure 4.5, following the approach of CN to CH_3SH, two different pre-reaction van der Waals complexes **PreRC1** (–66.6 kJ mol^{-1}) and **PreRC2** (–25.7 kJ mol^{-1}) are identified, which can be formed without encountering any barriers. Comparing with the PES obtained from previous literature (45) at the CCSD/6-311++G(d,p)//B3LYP/6-311++G(d,p) level, **PreRC1** and **PreRC2** are indeed of the similar structures as the pre-reaction complexes IM1 (–58.43 kJ mol^{-1}) and IM2a (–12.91 kJ mol^{-1}) respectively as shown in Figure 4.3. For **PreRC1**, the CN radical carbon is closer to the mercapto group of CH_3SH while for **PreRC2**, the CN radical nitrogen is closer to the mercapto group. **PreRC1** allows the reaction to proceed by a H abstraction using the CN carbon from the mercapto group, which involves a submerged barrier **TS1** (–29.4 kJ mol^{-1}) relative the reactants and leads to the post-reaction complex **PostRC1** (–184.1 kJ mol^{-1}). The dissociation of the post-reaction complex **PostRC1** forms the products CH_3S + HCN (–162.4 kJ mol^{-1}). On the other hand, **PreRC2** allows the reaction to proceed by a H abstraction using the CN nitrogen from the mercapto group, which involves a submerged barrier **TS2** (–8.67 kJ mol^{-1}) relative the reactants and leads to the post-reaction complex **PostRC2** (–132.6 kJ mol^{-1}). The dissociation of the post-reaction complex **PostRC2** forms the products CH_3S + HNC (–102.6 kJ mol^{-1}).

For the abstraction reaction to occur at the methyl site as shown in Figure 4.6, two transition states **TS3** and **TS4** were identified. From the IRC calculations on the forward reaction direction, **TS3** is found to lead to the post-reaction complex **PostRC3** (–139.8 kJ mol^{-1}) of which its dissociation generates the products CH_2SH + HCN (–132.2 kJ mol^{-1}), while **TS4** is found to lead to the post-reaction complex **PostRC4** (–87.6 kJ mol^{-1}) of which its dissociation generates the products CH_2SH + HNC (–72.4 kJ mol^{-1}). Nonetheless, for the IRC calculations on the reverse reaction direction from these two transition states, the general movement observed is the gradual separation of the two reacting species but the calculations fail to converge to stable structures that can be classified as local minima on the PES. No pre-reaction complex structure has been identified with the CN radical closer to the methyl end rather than the mercapto end of CH_3SH at the M06-2X/aug-cc-pVTZ level. Therefore, based on the results obtained it is difficult to assign for sure whether the pathways leading to these two transition states originate from the two separating reactants directly or from the aforementioned pre-reaction complexes **PreRC1** and **PreRC2**. Another uncertainty is whether these two transition states are submerged or not. At the M06-2X/aug-cc-pVTZ level, **TS4** is a positive barrier with a relative energy of 7.69 kJ mol^{-1} while **TS3** is submerged with a relative energy of –5.99 kJ mol^{-1}. However, after the refinement at CCSD(T)/aug-cc-pVTZ level, **TS4** becomes submerged with a relative energy of –6.86 kJ mol^{-1} while **TS3** becomes a huge barrier with a relative energy of 128.6 kJ mol^{-1}. These uncertainties are represented by the dotted lines in the PES shown in Figure 4.6. The large uncertainties imply issues in the calculations performed during the structure optimisation of these two TSs, potentially due to the choice of the basis set. The aug-cc-pVTZ basis set used in the current work is possibly insufficient in describing the d-orbitals of sulphur. Therefore, further calculations using a larger basis set with extra d-orbitals, for instance aug-cc-pV(T+d)Z, are needed in order to understand the H abstraction reaction at the methyl site.

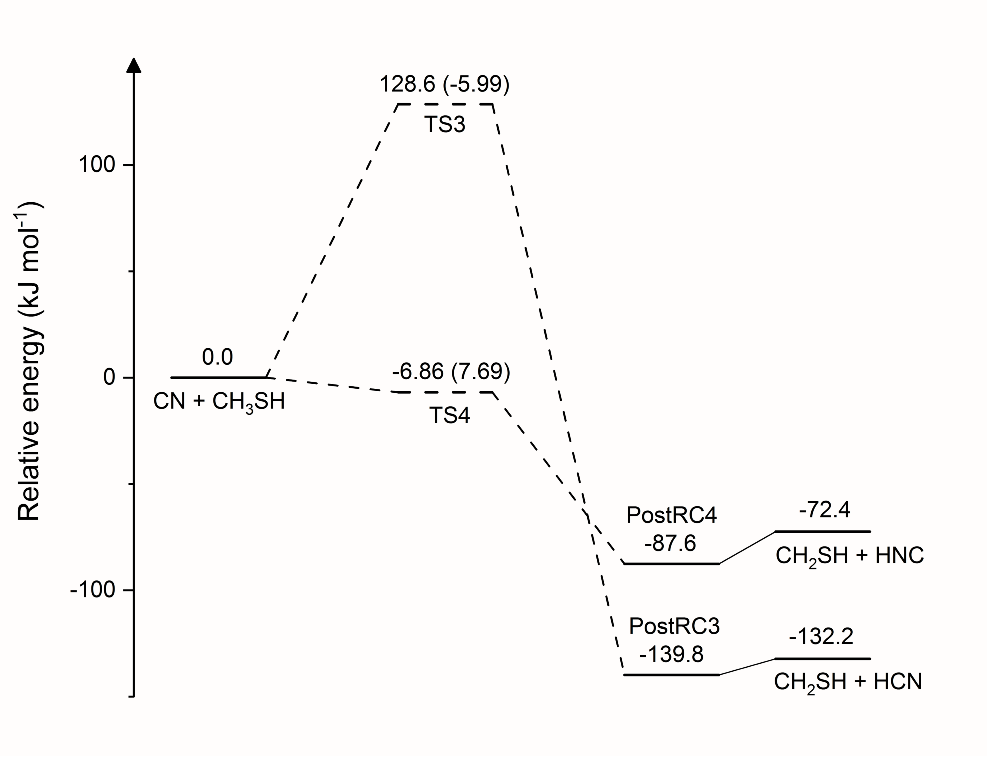

Figure 4.6 PES of the H abstraction from the methyl group for the CN + CH3SH reaction. For all the species, the relative energies obtained at the CCSD(T)/aug-cc-pVTZ//M06-2X/aug-cc-pVTZ level are presented. For the two transition states, the relative energies obtained at the M06-2X/aug-cc-pVTZ level are also presented within the parentheses. All energy values are in kJ mol^{-1} and are corrected with scaled ZPVE. The dotted lines indicate large uncertainties in the transition states, which highlights the issues in the current calculations and will require further work.

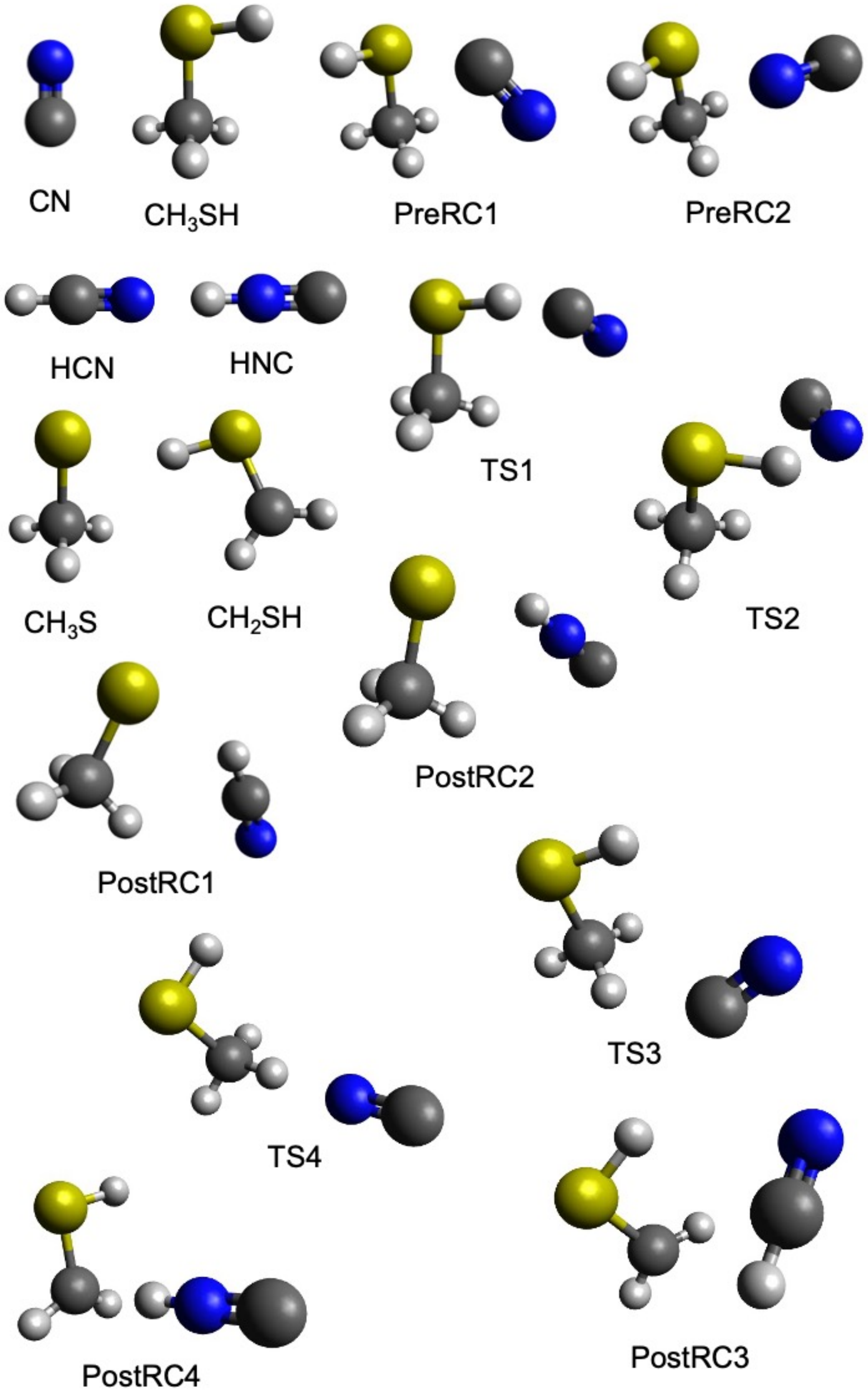

Figure 4.7 Optimised geometries of reactants, products, intermediates and transition states obtained at the M06-2X/aug-cc-pVTZ level of theory for the CN + CH_3SH reaction. The labels correspond to those shown in Figure 4.5 and Figure 4.6.

Four possible combinations of product sets (CH_3S + HCN, CH_3S + HNC, CH_2SH + HCN and CH_2SH + HNC) from the exothermic H abstraction reaction are identified in this work for the CN + CH_3SH reaction, which are in line with the suggestions from previous work on the same reaction (44, 45) as well as similar to the reaction between CN with the isovalent analogue CH_3OH (54, 55). For CN + CH_3OH, the previous theoretical work (55) also suggested the difficulty in pinpointing the exact location of the transition states for the H abstraction from the methyl group. Similar issues have been observed here for CN + CH_3SH, indicated by the large uncertainty on the relative energies (whether they are submerged or not) of **TS3** and **TS4** and the failure to converge for the IRC calculations in the reverse reaction direction. However, instead of having the pathway for the H abstraction at the methyl site with lower energy like that in the CN + CH_3OH reaction, previous theoretical work on the CN + CH_3SH reaction (45) as well as the findings from the OH + CH_3SH reaction (39, 42) show that the pathway for the H abstraction at the methyl site are of higher energy than that at the mercapto site. In this work on the CN + CH_3SH reaction, the same abstraction channel at the mercapto site is identified while the results of the abstraction channel at the methyl site are of high uncertainties. Comparing the abstraction channel at the mercapto site with the previous theoretical work by Xu et al. (45), one noticeable difference is the transition state leading to CH_3S + HNC (**TS2** in this work), which is now found to be submerged at the CCSD(T)/aug-cc-pVTZ/M06-2X/aug-cc-pVTZ level.

4.3.1.2 CN + CH_2S

Possible reaction channels for the CN + CH_2S reaction include the addition reaction, where the related PES obtained is shown in Figure 4.8, and the H abstraction reaction, where the related PES obtained is shown in Figure 4.9, with the zero-point corrected energies relative to the reactants calculated at the CCSD(T)/aug-cc-pVTZ//M06-2X/aug-cc-pVTZ level of theory presented alongside.

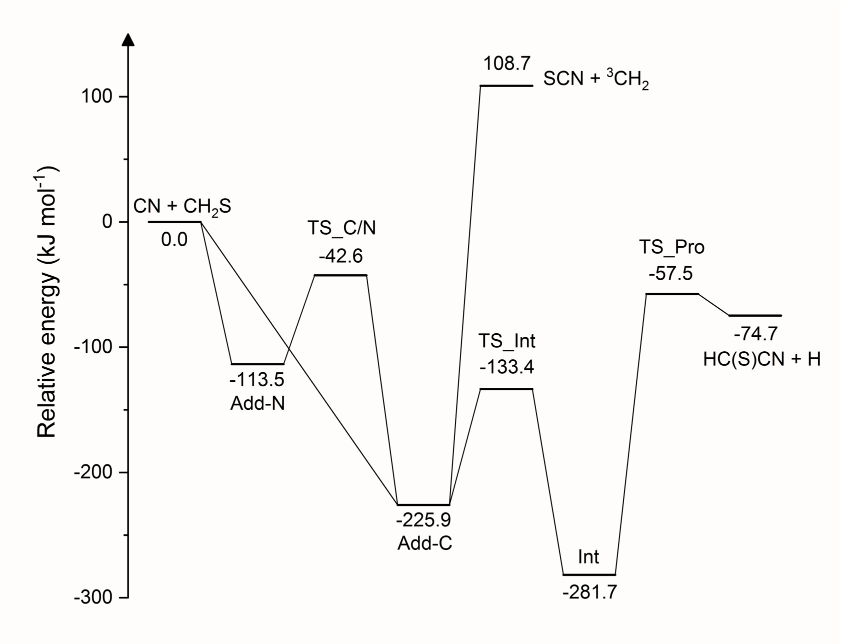

Figure 4.8 PES of the addition channel for the CN + CH₂S reaction obtained at the CCSD(T)/aug-cc-pVTZ level of theory. All energy values are in kJ mol^{-1} and are corrected with scaled ZPVE.

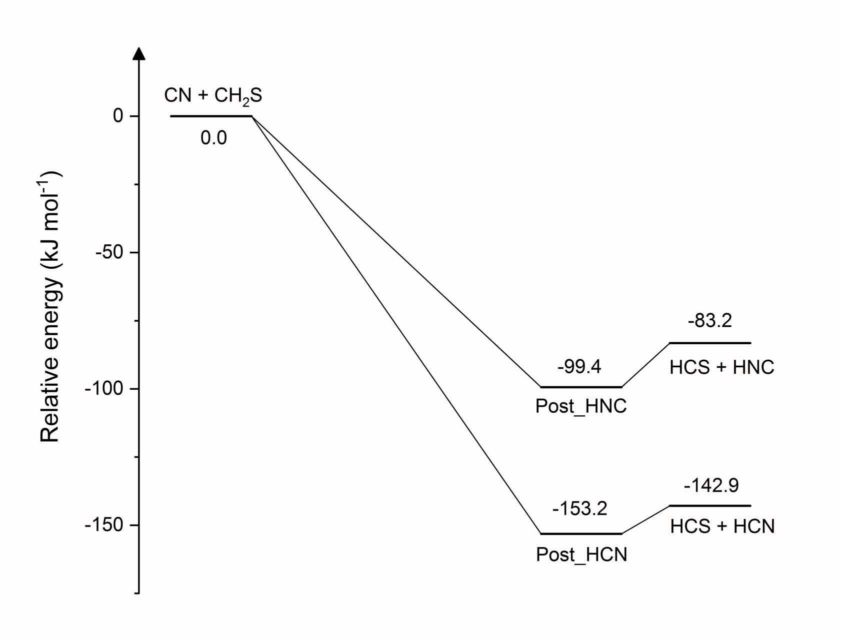

Figure 4.9 PES of the H abstraction channel for the CN + CH₂S reaction obtained at the CCSD(T)/aug-cc-pVTZ level of theory. All energy values are in kJ mol^{-1} and are corrected with scaled ZPVE.

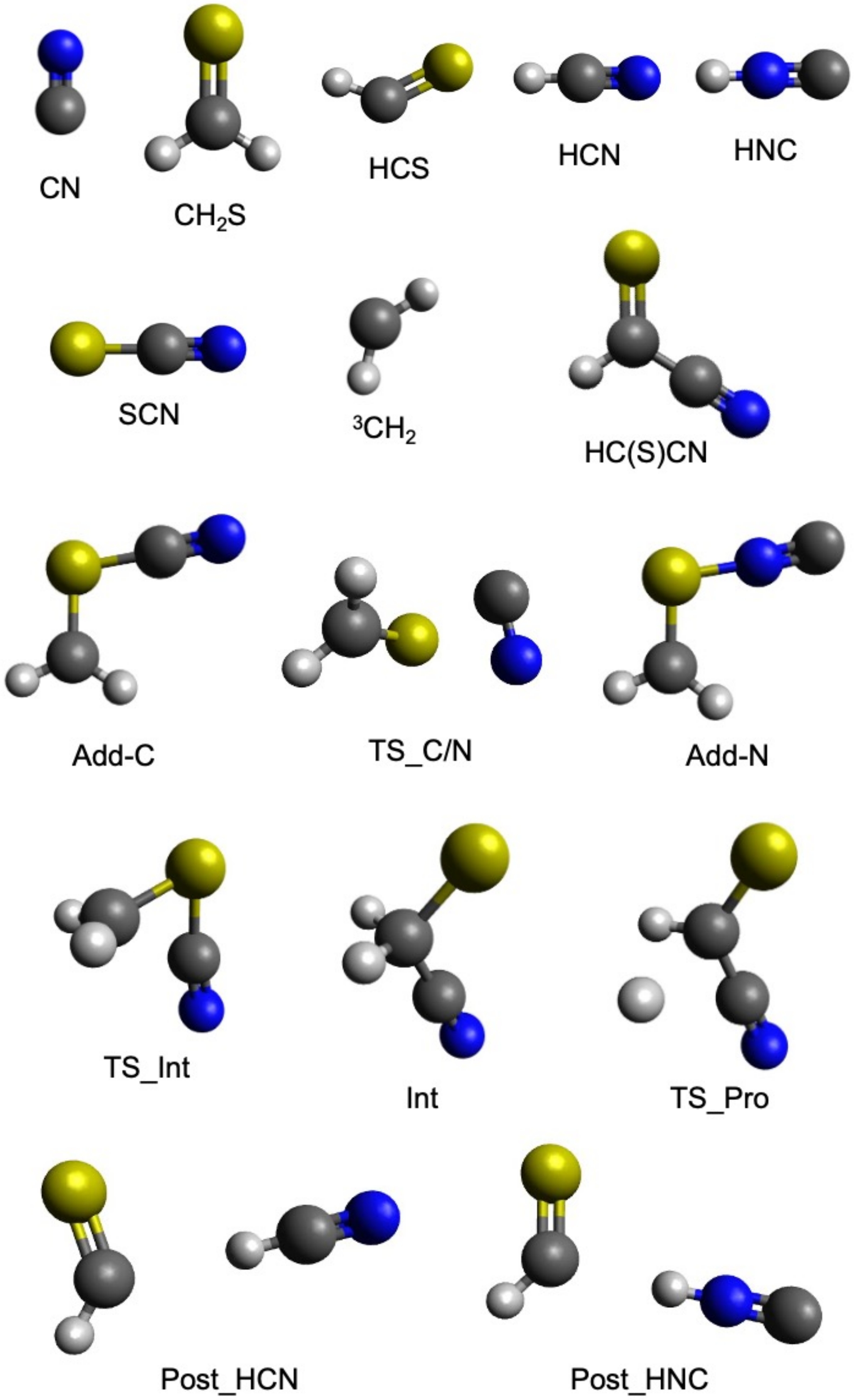

Figure 4.10 Optimised geometries of reactants, products, intermediates and transition states obtained at the M06-2X/aug-cc-pVTZ level of theory for the CN + CH_2S reaction. The labels correspond to those shown in Figure 4.8 and Figure 4.9.

The optimised geometries of the stationary points shown in Figure 4.8 and Figure 4.9 at the M06-2X/aug-cc-pVTZ level are shown in Figure 4.10. The optimised Cartesian coordinates, vibrational frequencies, rotational constants and energy values are provided in Appendix C.

For the addition reaction shown in Figure 4.8, two entrance channels have been identified. The CN radical can either use the carbon end adding to the sulphur of CH_2S to form the adduct $H_2C–S–CN$ (**Add-C**, –225.9 kJ mol^{-1}) or use the nitrogen end to form the adduct $H_2C–S–NC$ (**Add-N**, –113.5 kJ mol^{-1}). Both additions can be attained directly following the approach of the two separated reactants without any pre-reaction complex or barrier being located. These two adducts can be interconverted via the submerged barrier **TS_C/N** (–42.6 kJ mol^{-1}). **Add-C** can either dissociate to form SCN + $^3CH_2$ (108.7 kJ mol^{-1}) or undergo an isomerisation to form the intermediate $H_2C(S)CN$ (**Int**, –281.7 kJ mol^{-1}). The isomerisation from **Add-C** to **Int** involves a submerged barrier **TS_Int** (–133.4 kJ mol^{-1}) and the CN radical originally bonded to the sulphur of CH_2S shifts to the carbon of CH_2S. The cleavage of one of the CH bonds in **Int** gives the products HC(S)CN + H (–74.7 kJ mol^{-1}) after the surmounting the submerged barrier **TS_Pro** (–57.5 kJ mol^{-1}).

For the abstraction reaction shown in Figure 4.9, again no pre-reaction complex or barrier has been identified. H abstraction can occur directly either using the CN carbon to form the post-reaction complex **Post_HCN** (–153.2 kJ mol^{-1}), which subsequently gives the products HCS + HCN (–142.9 kJ mol^{-1}) after dissociation, or using the CN nitrogen to form the post-reaction complex **Post_HNC** (–99.4 kJ mol^{-1}), which subsequently gives the products HCS + HNC (–83.2 kJ mol^{-1}) after dissociation.

The PES for the CN + CH_2S reaction shows significant differences compared with that for the CN + CH_2O reaction as reported in Chapter 3 in this thesis. No pre-reaction complex has been identified for CN + CH_2S as the valence electrons of sulphur are further away from the nucleus than those of oxygen, which destabilises the potential energy surface. Instead of forming a van der

Waals complex, an adduct is formed directly. There is no longer a big barrier for the addition channel following the approach of the CN radical, which is similar to the entirely submerged addition pathway for the OH + CH_2S reaction (43), because sulphur can make use of the vacant d orbitals to accommodate the extra bond. For the isomerisation from $H_2C–S–CN$ to $H_2C(S)CN$, it can be achieved in a single step rather than involving a cyclisation step to form three-membered (C–O–C) ring like the case of the CN + CH_2O reaction due to the bigger size of the sulphur atom. The current results provide an entirely submerged pathway from CN + CH_2S to the formation of cyano thioformaldehyde HC(S)CN, which contrasts with the addition pathway from CN + CH_2O to the formation of formyl cyanide HC(O)CN presented in Chapter 3.

4.3.2 Results from rate coefficient calculations and discussions

4.3.2.1 CN + CH_3SH

Rate coefficient calculations have been carried out with the MESMER programme using the ab initio results including the energy values obtained at the CCSD(T)/aug-cc-pVTZ//M06-2/aug-cc-pVTZ level, vibrational frequencies and rotational constants for the CN + CH_3SH reaction. As suggested earlier, this work shows that H abstraction at the mercapto site can proceed via entirely submerged pathways while at the methyl site high uncertainties exist. However, according to the previous work by Xu et al. (45), the pathways for the H abstraction at the mercapto site are deemed to be more stable. With reference to the results of the CN + CH_3OH reaction (55) where the lowest energy pathway dominates the generation of products, here only the pathways leading to the abstraction at the mercapto site, that is, only the PES presented in Figure 4.5, were considered in the MESMER calculations by assuming that all the H abstractions happen at the mercapto moiety. The MESMER calculations are then unaffected by the aforementioned uncertainties regarding the transition states corresponding to the abstraction from the methyl moiety (shown in Figure 4.6) as they are left out.

Table 4.3 Parameters used to calculated $A_{\mathrm{ILT}}^{\infty}$ for the reaction between CN and CH_3SH

Dipole moment (Debye)		$k_{\mathrm{coll}}(T)$ (cm^3 molecule^{-1} s^{-1})	No. of entrance channels	$A_{\mathrm{ILT}}^{\infty}$ (cm^3 molecule^{-1} s^{-1})
CN	CH_3SH			
2.2154	1.6774	$5.76 \times 10^{-10}\ T^{-1/6}$	2	2.88×10^{-10}

For the purpose of an initial simulation for the CN + CH_3SH reaction system, the estimation for the input ILT parameters regarding the initial barrierless complex formation steps was performed based on the dipole moment of the reactants obtained at the CCSD(T)/aug-cc-pVTZ//M06-2X/aug-cc-pVTZ level as shown in Table 4.3. $k_{\mathrm{coll}}(T)$ was then found to be $5.76 \times 10^{-10}\ T^{-1/6}$ cm^3 molecule^{-1} s^{-1} using E 1.13 attained from the classical capture theory and given that only two entrance channels (abstraction to form CH_3S + HCN and abstraction to form CH_3S + HNC) are considered, $A_{\mathrm{ILT}}^{\infty}$ for each channel was then set as 2.88×10^{-10} cm^3 molecule^{-1} s^{-1}.

From the initial simulation, the calculated rate coefficient, given as the bimolecular removal rate coefficient of the CN radical, was obtained based on the aforementioned settings at the same experimental conditions (293 K, 0.74–6.6 Torr) as reported by Decker and Macdonald (44), with a value of 2.63×10^{-10} cm^3 molecule^{-1} s^{-1}. The corresponding HCN/HNC ratio was calculated to be 0.96:0.04. The rate coefficient value matches with that obtained in experiments (2.7×10^{-10} cm^3 molecule^{-1} s^{-1}), but the predicted HCN fractional yield is considerably greater than observed (HCN/HNC ratio = 0.81:0.19).

With the availability of experimental data, Marquardt least-square data fitting was performed with MESMER, where further details can be found in Section 2.2 and a previous example is the CN + CH_2O reaction in Chapter 3. Based on the experimental rate coefficient and HCN/HCN ratio, the ILT exponential $A_{\mathrm{ILT}}^{\infty}$ and the transition state energies are the rate controlling parameters to be optimised. The $A_{\mathrm{ILT}}^{\infty}$ for the two channels were set to be the same based on the assumption that it is equally likely to enter each entrance channel and the calculated difference in energy between **TS1** and **TS2** was maintained with the assumption that they suffer similar error as they were obtained at the same level of theory. The returned best-fit $A_{\mathrm{ILT}}^{\infty}$ is found to be 2.22 × 10^{-10} cm^3 $\mathrm{molecule}^{-1}$ s^{-1}, which is not far from the initial guess from classical capture theory (2.88 × 10^{-10} cm^3 $\mathrm{molecule}^{-1}$ s^{-1}) as shown in Table 4.3. The returned best-fit energies for the transition states **TS1** and **TS2** suggest a further reduction of 7.9 kJ mol^{-1} from those obtained at the CCSD(T)/aug-cc-pVTZ//M06-2X/aug-cc-pVTZ level, changing to –37.3 kJ mol^{-1} and –16.6 kJ mol^{-1} respectively. These transition state energies indicate that the ab initio results obtained in this work (–29.4 kJ mol^{-1} and –8.67 kJ mol^{-1}) are more reasonable than the previous work (45) at the CCSD/6-311++G(d,p)//B3LYP/6-311++G(d,p) level (–14.89 kJ mol^{-1} and 43.16 kJ mol^{-1}).

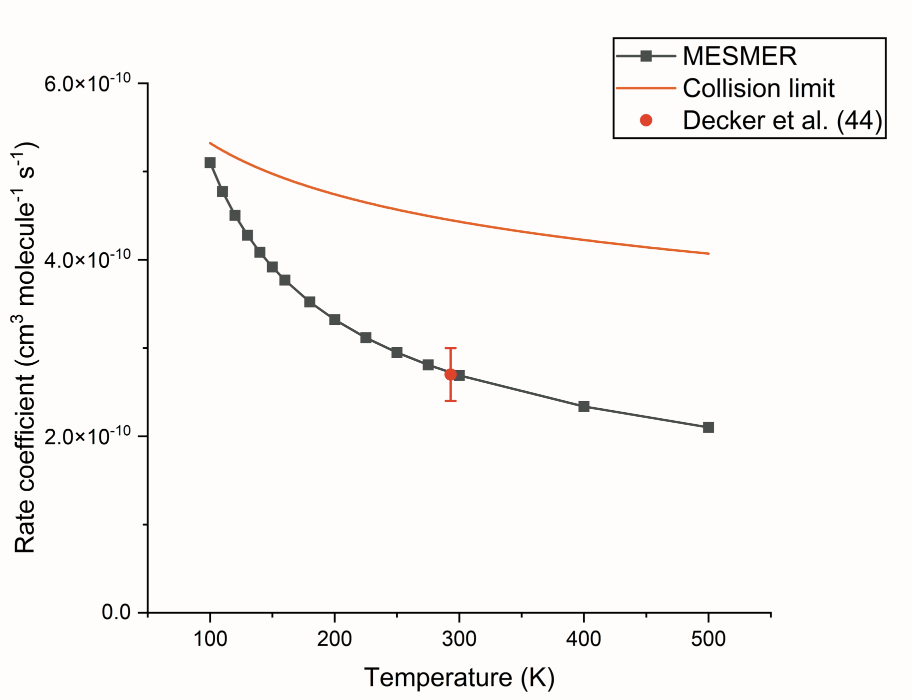

Figure 4.11 Rate coefficient for the CN + CH_3SH reaction versus temperature in the range of T = 100–500 K. The black line is the results from MESMER calculations where no pressure dependence is observed in the total density range of 10^{13}–10^{21} molecule cm^{-3}. The red data point is from the experimental result reported by Decker and Macdonald (44). The orange line plotted alongside is the collision limit set by the ILT input parameters.

The best-fit $A^{\infty}_{\mathrm{ILT}}$ and transition state energies were then used as input for MESMER simulations to generate rate coefficient values over a temperature range of 100–500 K and a total density range of 10^{13}–10^{21} molecule cm^{-3}, where the results are plotted in Figure 4.11. No pressure dependence was observed in this total density range while a negative temperature dependence of the rate coefficients can be seen. Below 100 K, the reaction rate coefficient can be considered as approaching the collision limit. In the temperature range of 100–500 K, a modified Arrhenius expression was used to fit the rate coefficients, which was found to be:

$$k(T) = 2.14 \times 10^{-10}\left(\frac{T}{298\ \mathrm{K}}\right)^{-0.714} e^{7.24\times10^{-4}T}\ \mathrm{cm^3\ molecule^{-1}\ s^{-1}} \qquad \text{E 4.14}$$

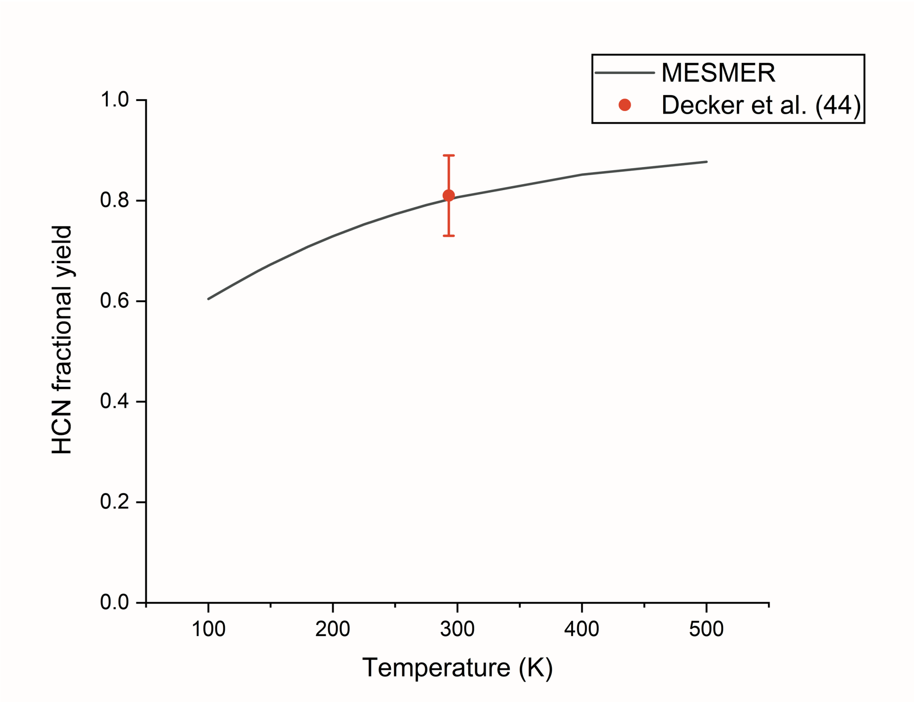

Figure 4.12 HCN fractional yield of the CN + CH_3SH reaction as a function of temperature. The black line is the results from MESMER calculations where no pressure dependence is observed in the total density range of 10^{13}–10^{21} molecule cm^{-3}. The red data point is from the experimental result reported by Decker and Macdonald (44).

The corresponding fractional yield of HCN is presented in Figure 4.12, where again no pressure dependence is observed in the range of 10^{13}–10^{21} molecule cm^{-3}. All of the reactants eventually form either HCN or HNC. In the temperature range of 100–500 K, HCN is the dominant species rather than HNC. However, as the temperature decreases from 500 K to 100 K, the fractional yield of HCN gradually decreases from 88% to 61%.

4.3.2.2 CN + CH_2S

Similarly, for the CN + CH_2S reaction, with all the addition and abstraction channels being considered, the ab initio results including the energy values, vibrational frequencies and rotational constants are used to perform rate coefficient calculations with the MESMER programme. The dipole moment of the reactants obtained at the CCSD(T)/aug-cc-pVTZ//M06-2X/aug-cc-pVTZ level are shown in Table 4.4 and the calculated $k_{\mathrm{coll}}(T)$ using E 1.13 was found to be $6.82 \times 10^{-10}\ T^{-1/6}$ cm^3 molecule^{-1} s^{-1}. As there are four entrance channels, namely addiction to form **Add-C**, addition to form **Add-N**, abstraction to form HCN and abstraction to form HNC, the $A_{\mathrm{ILT}}^{\infty}$ for each channel is estimated to be 1.71×10^{-10} cm^3 molecule^{-1} s^{-1}, which is then used as the input for MESMER calculations.

Table 4.4 Parameters used to calculated $A_{\mathrm{ILT}}^{\infty}$ for the reaction between CN and CH_2S

Dipole moment (Debye)		$k_{\mathrm{coll}}(T)$ (cm^3 molecule^{-1} s^{-1})	No. of entrance channels	$A_{\mathrm{ILT}}^{\infty}$ (cm^3 molecule^{-1} s^{-1})
CN	CH_2S			
2.2154	2.1363	$6.82 \times 10^{-10}\ T^{-1/6}$	4	1.71×10^{-10}

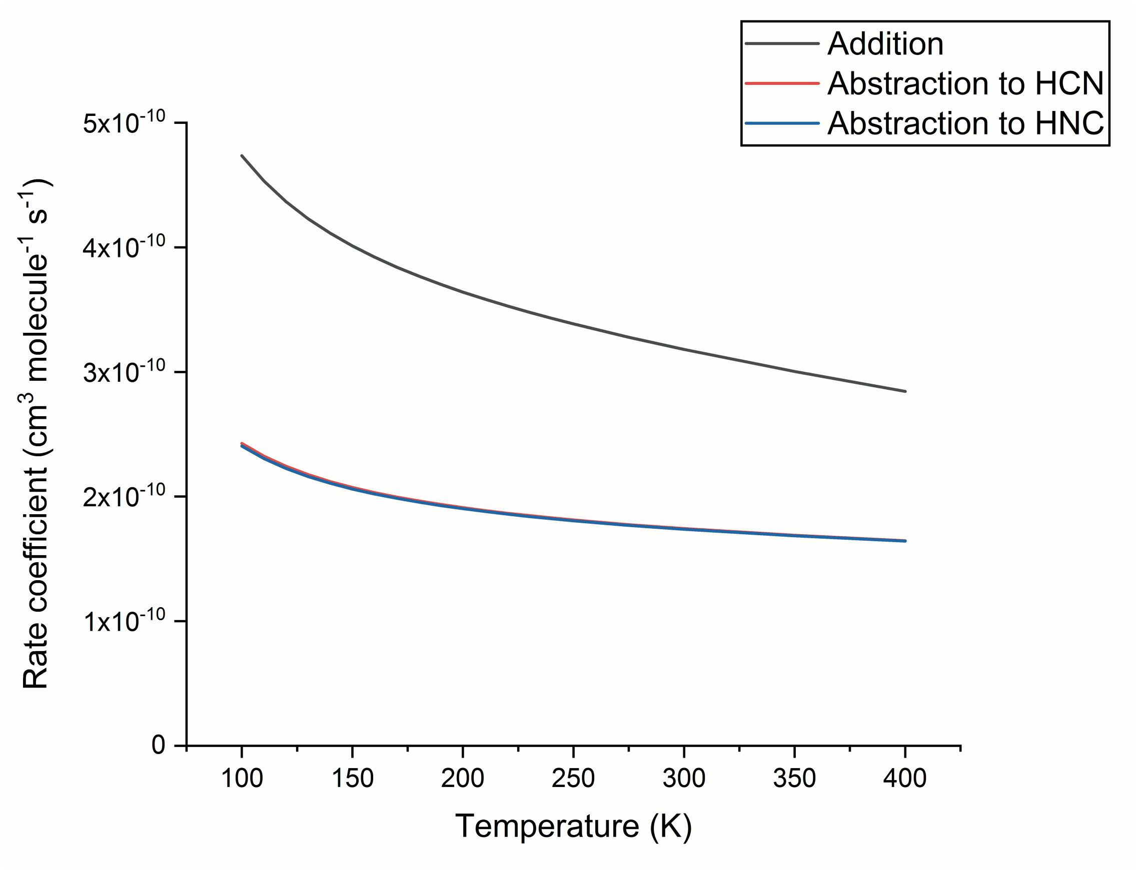

Figure 4.13 Calculated rate coefficients for all the addition and abstraction channels of the CN + CH_2S reaction versus temperature in the range of 100–400 K. The two lines corresponding to the two abstraction channels overlap. No pressure dependence is observed in the total density range of 10^{13}–10^{17} molecule cm^{-3}.

MESMER simulations have been carried out to calculate the rate coefficient values over a temperature range of 100–400 K and a total density range of 10^{13}–10^{17} molecule cm^{-3}. The calculations are not extended to even lower temperature because the deep well problem is encountered, which means the energy well on the PES is so deep that the rate coefficient for the reacting species to get out of the well is too small to be captured by the precision of MESMER. There is limited physical significance to extend the calculations to even higher total density because the reaction rate can easily reach the collision limit given the deep wells at the entrance channels as well as the reaction can readily end as a stabilisation into the potential wells at higher total density, in particular the oligomerisation of CH_2S as suggested from the short lifetime of the monomer form of CH_2S previously. For the addition channels, in the total density range of 10^{13}–10^{17} molecule cm^{-3}, no pressure dependence is observed. **Add-N** is found to be isomerising into **Add-C** anyway, and eventually all lead to the formation of products HC(S)CN + H. Therefore, these two entrance channels can be effectively combined together and be considered as leading to **Add-C** directly, which in the end produces HC(S)CN + H. The rate coefficient as a function of temperature for the combined together addition channel, together with the abstraction channels to form HCS + HCN and HCS + HNC, is shown in Figure 4.13. The rate coefficients are found to be pressure independent for all the channels.

Indeed, the rate coefficients for all the channels under the conditions covered in the graphs are at the collision limit. The ratio of the rate coefficients between the addition channel (combining both the addition to **Add-C** and **Add-N**), the H abstraction channel to HCN and the H abstraction channel to HNC is about 2:1:1, which is actually arisen from the assumption of equal $A_{\mathrm{ILT}}^{\infty}$ for all the channels.

For both CN + CH_3SH and CN + CH_2S reactions, a negative temperature dependence is observed. While the graphs end at 100 K, the reaction rate coefficients tend to the collision limit and under ISM conditions where the temperature is below 100 K, these reactions are fast. For CN + CH_3SH, H abstraction can occur at the mercapto site to give either HCN or HNC. For CN + CH_2S, apart from the abstraction channels forming either HCN or HNC, HC(S)CN in particular can be readily formed via the addition of CN to CH_2S, which supports the speculation from previous literature (29) and is the opposite of the CN + CH_2O reaction reported in Chapter 3, where the generation of HC(O)CN is insignificant due to the big barrier in the addition channel.

The rate coefficients reach the collision limit beneath 100 K for CN + CH_3SH and at least 400 K for CN + CH_2S. The rate coefficients and the branching ratios of each channel are then mainly controlled by how the approach of the two species occurs leading towards the respective entrance channels. Therefore, further investigation regarding the collisions between the two reactants, together with the use of the variational transition state theory will be needed in order to answer the questions such as the actual rate coefficients and branching ratios between the addition and abstraction channels for CN + CH_2S.

4.4 Conclusion

In this chapter, theoretical approaches consisting of ab initio calculations followed by rate coefficient calculations have been carried out for the CN + CH_3SH and the CN + CH_2S reactions. Potential energy surfaces have been obtained for both reactions. For CN + CH_3SH, there are four possible combinations of H abstraction products: CH_3S + HCN, CH_3S + HNC, CH_2SH + HCN and CH_2SH + HNC, which are all exothermic. Following the approach of the reactants, two pre-reaction complexes (**PreRC1**: –66.6 kJ mol^{-1}, **PreRC2**: –25.7 kJ mol^{-1}) are located, which subsequently lead to either CH_3S + HCN or CH_3S + HNC via the respective submerged barriers (**TS1**: –29.4 kJ mol^{-1}, **TS2**: –8.67 kJ mol^{-1}). For the transition states corresponding to the abstraction at the methyl group, it is dubious on whether they are submerged or connected to any pre-reaction complex. This suggests potential issues regarding the choice of basis set in this work and further calculations should be done using a larger basis set with extra d orbitals for the sulphur species. For CN + CH_2S, the reactions can proceed by H abstraction to form HCN or HNC or addition to form adducts **Add-C** (–225.9 kJ mol^{-1}) or **Add-N** (–113.5 kJ mol^{-1}), where both adducts eventually can form products HC(S)CN + H. No pre-reaction van der Waals complex has been identified. The energy of the entire reaction pathway for all the channels lies below that of the sum of the two reactants, in particular for the addition channel leading to HC(S)CN, which displays a huge difference with CN + CH_2O where surmounting a positive barrier is required for forming the addition product HC(O)CN.

Rate coefficient calculations were then performed with the MESMER programme down to 100 K. For CN + CH_3SH, previous experimental work (44) allows the optimisation of the rate controlling input parameters to be done. From the data fitting, the adjustment on the energies of the transition states **TS1** and

TS2 is suggested to be –7.9 kJ mol^{-1} with a best-fit $A^{\infty}_{\mathrm{ILT}}$ of 2.22 × 10^{-10} cm^3 molecule^{-1} s^{-1} assuming that the abstraction only occurs at the mercapto moiety. Using the optimised parameters, the resulted rate coefficients show no pressure dependence within the range of 10^{13}–10^{21} molecule cm^{-3} but a negative temperature dependence. In the range of 100–500 K, the rate coefficient can be represented by a modified Arrhenius expression:

$$k(T) = 2.14 \times 10^{-10}\left(\frac{T}{298\ \mathrm{K}}\right)^{-0.714} e^{7.24\times10^{-4}T}\ \mathrm{cm^3\ molecule^{-1}\ s^{-1}} \qquad \text{E 4.15}$$

Below 100 K, the reaction can be considered as reaching the collision limit. For the product branching yield, the HCN/HNC ratio changes from 0.88:0.12 at 500 K to 0.61:0.39 at 100 K. For CN + CH_2S, no experimental data are available due to the short lifetime of CH_2S under terrestrial conditions. From the MESMER simulations, the results suggest that the rate coefficients are pressure independent in the range of 10^{13}–10^{17} molecule cm^{-3} and all of the reactants can be converted into the final products for all the channels. The rate coefficients for all the channels demonstrate a negative temperature dependence and are at the collision limit beneath 400 K. These results imply that CN + CH_3SH and CN + CH_2S can be possible reaction routes in the ISM for the removal of CN, CH_3SH and CH_2S and the formation of HCN, HNC, CH_3S, HCS and HC(S)CN. Nonetheless, further studies are required regarding the approach of the reactants in order to provide a better picture of the collision limit of the entrance channels. Astrochemical modelling is also needed to test the impact of these reactions on the abundances of sulphur containing species.

4.5 References

1. Kim, G., Weiss, S.J. and Levine, R.L. Methionine oxidation and reduction in proteins. *Biochimica et Biophysica Acta (BBA) - General Subjects.* 2014, **1840**(2), pp.901-905.

2. Krouse, H.R. and Grinenko, V.A. *Stable isotopes : natural and anthropogenic sulphur in the environment.* Chichester: Published on behalf of the Scientific Committee on Problems of the Environment SCOPE of the International Council of Scientific Unions ICSU in

collaboration with the United Nations Environment Programme by Wiley, 1991.

3. Fike, D.A., Bradley, A.S. and Rose, C.V. Rethinking the Ancient Sulfur Cycle. *Annual Review of Earth and Planetary Sciences.* 2015, **43**(1), pp.593-622.

4. Graedel, T.E. The homogeneous chemistry of atmospheric sulfur. *Reviews of Geophysics.* 1977, **15**(4), pp.421-428.

5. Wine, P.H., Kreutter, N.M., Gump, C.A. and Ravishankara, A.R. Kinetics of hydroxyl radical reactions with the atmospheric sulfur compounds hydrogen sulfide, methanethiol, ethanethiol, and dimethyl disulfide. *The Journal of Physical Chemistry.* 1981, **85**(18), pp.2660-2665.

6. Wine, P.H., Thompson, R.J. and Semmes, D.H. Kinetics of OH reactions with aliphatic thiols. *International Journal of Chemical Kinetics.* 1984, **16**(12), pp.1623-1636.

7. Tyndall, G.S. and Ravishankara, A.R. Atmospheric oxidation of reduced sulfur species. *International Journal of Chemical Kinetics.* 1991, **23**(6), pp.483-527.

8. Toon, O.B., Turco, R.P. and Pollack, J.B. The ultraviolet absorber on Venus: Amorphous sulfur. *Icarus.* 1982, **51**(2), pp.358-373.

9. Marcq, E., Bertaux, J.-L., Montmessin, F. and Belyaev, D. Variations of sulphur dioxide at the cloud top of Venus's dynamic atmosphere. *Nature Geoscience.* 2013, **6**(1), pp.25-28.

10. Spencer, J.R. and Schneider, N.M. Io on the eve of the Galileo mission. *Annual Review of Earth and Planetary Sciences.* 1996, **24**(1), pp.125-190.

11. Zolotov, M.Y. and Fegley, B. Volcanic Production of Sulfur Monoxide (SO) on Io. *Icarus.* 1998, **132**(2), pp.431-434.

12. Russell, C.T. and Kivelson, M.G. Evidence for sulfur dioxide, sulfur monoxide, and hydrogen sulfide in the Io exosphere. *Journal of Geophysical Research: Planets.* 2001, **106**(E12), pp.33267-33272.

13. Neufeld, D.A., Godard, B., Gerin, M., Pineau des Forêts, G., Bernier, C., Falgarone, E., Graf, U.U., Güsten, R., Herbst, E., Lesaffre, P., Schilke, P., Sonnentrucker, P. and Wiesemeyer, H. Sulphur-bearing molecules in diffuse molecular clouds: new results from SOFIA/GREAT and the IRAM 30 m telescope. *Astronomy & Astrophysics.* 2015, **577**.

14. Drozdovskaya, M.N., van Dishoeck, E.F., Jørgensen, J.K., Calmonte, U., van der Wiel, M.H.D., Coutens, A., Calcutt, H., Müller, H.S.P., Bjerkeli, P., Persson, M.V., Wampfler, S.F. and Altwegg, K. The ALMA-PILS survey: the sulphur connection between protostars and comets: IRAS 16293–2422 B and 67P/Churyumov–Gerasimenko. *Monthly Notices of the Royal Astronomical Society.* 2018, **476**(4), pp.4949-4964.

15. Lada, E.A., Bally, J. and Stark, A.A. An Unbiased Survey for Dense Cores in the Lynds 1630 Molecular Cloud. *The Astrophysical Journal.* 1991, **368**, p.432.

16. Plume, R., Jaffe, D.T., Evans Ii, N.J., Martin-Pintado, J. and Gomez-Gonzalez, J. Dense Gas and Star Formation: Characteristics of Cloud Cores Associated with Water Masers. *The Astrophysical Journal.* 1997, **476**(2), pp.730-749.

17. Le Gal, R., Öberg, K.I., Loomis, R.A., Pegues, J. and Bergner, J.B. Sulfur Chemistry in Protoplanetary Disks: CS and H_2CS. *The Astrophysical Journal.* 2019, **876**(1), p.72.

18. el Akel, M., Kristensen, L.E., Le Gal, R., van der Walt, S.J., Pitts, R.L. and Dulieu, F. Unlocking the sulphur chemistry in intermediate-mass protostars of Cygnus X. *Astronomy & Astrophysics.* 2022, **659**.

19. Sakai, N., Sakai, T., Hirota, T., Watanabe, Y., Ceccarelli, C., Kahane, C., Bottinelli, S., Caux, E., Demyk, K., Vastel, C., Coutens, A., Taquet, V., Ohashi, N., Takakuwa, S., Yen, H.-W., Aikawa, Y. and Yamamoto, S. Change in the chemical composition of infalling gas forming a disk around a protostar. *Nature.* 2014, **507**(7490), pp.78-80.

20. Podio, L., Codella, C., Gueth, F., Cabrit, S., Bachiller, R., Gusdorf, A., Lee, C.F., Lefloch, B., Leurini, S., Nisini, B. and Tafalla, M. The jet and the disk of the HH 212 low-mass protostar imaged by ALMA: SO and SO_2 emission. *Astronomy & Astrophysics.* 2015, **581**.

21. Boogert, A.C.A., Schutte, W.A., Helmich, F.P., Tielens, A.G.G.M. and Wooden, D.H. Infrared observations and laboratory simulations of interstellar CH_4 and SO_2. *Astronomy and Astrophysics.* 1997, **317**, pp.929-941.

22. Palumbo, M.E., Geballe, T.R. and Tielens, A.G.G.M. Solid Carbonyl Sulfide (OCS) in Dense Molecular Clouds. *The Astrophysical Journal.* 1997, **479**(2), pp.839-844.

23. Agúndez, M., Marcelino, N., Cernicharo, J. and Tafalla, M. Detection of interstellar HCS and its metastable isomer HSC: new pieces in the puzzle of sulfur chemistry. *Astronomy & Astrophysics.* 2018, **611**.

24. Irvine, W.M., Friberg, P., Kaifu, N., Kawaguchi, K., Kitamura, Y., Matthews, H.E., Minh, Y., Saito, S., Ukita, N. and Yamamoto, S. Observations of Some Oxygen-containing and Sulfur-containing Organic Molecules in Cold Dark Clouds. *The Astrophysical Journal.* 1989, **342**, p.871.

25. Minh, Y.C., Irvine, W.M. and Brewer, M.K. H_2CS abundances and ortho-to-para ratios in interstellar clouds. *Astronomy and Astrophysics.* 1991, **244**, p.181.

26. Agúndez, M., Fonfría, J.P., Cernicharo, J., Pardo, J.R. and Guélin, M. Detection of circumstellar CH_2CHCN, CH_2CN, CH_3CCH, and H_2CS. *Astronomy & Astrophysics.* 2008, **479**(2), pp.493-501.

27. Linke, R.A., Frerking, M.A. and Thaddeus, P. Interstellar methyl mercaptan. *The Astrophysical Journal.* 1979, **234**, pp.L139-L142.

28. Majumdar, L., Gratier, P., Vidal, T., Wakelam, V., Loison, J.C., Hickson, K.M. and Caux, E. Detection of CH_3SH in protostar IRAS 16293-2422. *Monthly Notices of the Royal Astronomical Society.* 2016, **458**, pp.1859-1865.

29. Cernicharo, J., Cabezas, C., Endo, Y., Agúndez, M., Tercero, B., Pardo, J.R., Marcelino, N. and de Vicente, P. The sulphur saga in TMC-1: Discovery of HCSCN and HCSCCH. *Astronomy & Astrophysics.* 2021, **650**.

30. Ruffle, D.P., Hartquist, T.W., Caselli, P. and Williams, D.A. The sulphur depletion problem. *Monthly Notices of the Royal Astronomical Society.* 1999, **306**(3), pp.691-695.

31. Vidal, T.H.G., Loison, J.-C., Jaziri, A.Y., Ruaud, M., Gratier, P. and Wakelam, V. On the reservoir of sulphur in dark clouds: chemistry and elemental abundance reconciled. *Monthly Notices of the Royal Astronomical Society.* 2017, **469**(1), pp.435-447.

32. Lee, J.H. and Tang, I.N. Absolute rate constants for the hydroxyl radical reactions with CH_3SH and C_2H_5SH at room temperature. *The Journal of Chemical Physics.* 1983, **78**(11), pp.6646-6649.

33. Mac Leod, H., Jourdain, J.L., Poulet, G. and Le Bras, G. Kinetic study of reactions of some organic sulfur compounds with OH radicals. *Atmospheric Environment (1967).* 1984, **18**(12), pp.2621-2626.

34. Barnes, I., Bastian, V., Becker, K.H., Fink, E.H. and Nelsen, W. Oxidation of sulphur compounds in the atmosphere: I. Rate constants of OH radical reactions with sulphur dioxide, hydrogen sulphide, aliphatic thiols and thiophenol. *Journal of Atmospheric Chemistry.* 1986, **4**(4), pp.445-466.

35. Hynes, A.J. and Wine, P.H. Kinetics of the hydroxyl radical + methyl mercaptan reaction under atmospheric conditions. *The Journal of Physical Chemistry.* 1987, **91**(13), pp.3672-3676.

36. Atkinson, R., Perry, R.A. and Pitts, J.N. Rate constants for the reaction of the OH radical with CH_3SH and CH_3NH_2 over the temperature range 299–426 °K. *The Journal of Chemical Physics.* 1977, **66**(4), pp.1578-1581.

37. Hatakeyama, S. and Akimoto, H. Reactions of hydroxyl radicals with methanethiol, dimethyl sulfide, and dimethyl disulfide in air. *The Journal of Physical Chemistry.* 1983, **87**(13), pp.2387-2395.

38. Wilson, C. and Hirst, D.M. Theoretical ab initio study of the reaction of CH_3SH with OH radical. *Journal of the Chemical Society, Faraday Transactions.* 1995, **91**(21), pp.3783-3785.

39. Masgrau, L., González-Lafont, À. and Lluch, J.M. Variational Transition-State Theory Rate Constant Calculations of the OH + CH_3SH Reaction and Several Isotopic Variants. *The Journal of Physical Chemistry A.* 2003, **107**(22), pp.4490-4496.

40. Tahan, A. and Shiroudi, A. Oxidation reaction mechanism and kinetics between OH radicals and alkyl-substituted aliphatic thiols: H-abstraction pathways. *Progress in Reaction Kinetics and Mechanism.* 2019, **45**, p.1468678319886129.

41. Tahan, A. and Shiroudi, A. Oxidation reaction mechanism and kinetics between OH radicals and alkyl-substituted aliphatic thiols: OH-addition pathways. *Progress in Reaction Kinetics and Mechanism.* 2019, **44**(2), pp.157-174.

42. Mai, T.V.T., Nguyen, H.T. and Huynh, L.K. Kinetics of hydrogen abstraction from CH_3SH by OH radicals: An ab initio RRKM-based master equation study. *Atmospheric Environment.* 2020, **242**, p.117833.

43. Arathala, P., Katz, M. and Musah, R.A. Reaction mechanism, energetics, and kinetics of the water-assisted thioformaldehyde + $^{\bullet}OH$ reaction and the fate of its product radical under tropospheric conditions. *Physical Chemistry Chemical Physics.* 2020, **22**(18), pp.10027-10042.

44. Decker, B.K. and Macdonald, R.G. Channeling of Products in the Hot Atom Reaction $H + (CN)_2 \rightarrow HCN/HNC + CN$ and in the Reaction of CN with CH_3SH. *The Journal of Physical Chemistry A.* 2001, **105**(28), pp.6817-6825.

45. Xu, B.E., Li, X.Y., Zeng, Y.L., Meng, L.P., Zhang, P. and Liu, Z.R. Reaction mechanisms and topological studies of electronic density on the reaction of CH_3SH with CN· radical. *Acta Physico-Chimica Sinica.* 2008, **24**(7), pp.1245-1251.

46. Mayer, R., Morgenstern, J. and Fabian, J. Aliphatic Thioketones. *Angewandte Chemie International Edition in English.* 1964, **3**(4), pp.277-286.

47. Johnson, D.R., Powell, F.X. and Kirchhoff, W.H. Microwave spectrum, ground state structure, and dipole moment of thioformaldehyde. *Journal of Molecular Spectroscopy.* 1971, **39**(1), pp.136-145.

48. Tachibana, A., Okazaki, I., Koizumi, M., Hori, K. and Yamabe, T. Stability of the reaction coordinate in the unimolecular reaction of thioformaldehyde. *Journal of the American Chemical Society.* 1985, **107**(5), pp.1190-1196.

49. Usov, V.A., Timokhina, L.V. and Voronkov, M.G. The synthesis and properties of thioaldehydes. *Russian Chemical Reviews.* 1990, **59**(4), pp.378-395.

50. Krantz, K.E., Senning, A. and Shim, I. An ab initio study of the mechanisms of the di- and tri-merization of thiocarbonyl compounds resulting in cyclic oligomers. *Journal of Molecular Structure: THEOCHEM.* 2010, **944**(1), pp.83-88.

51. Van Dornshuld, E., Holy, C.M. and Tschumper, G.S. Homogeneous and Heterogeneous Noncovalent Dimers of Formaldehyde and Thioformaldehyde: Structures, Energetics, and Vibrational Frequencies. *The Journal of Physical Chemistry A.* 2014, **118**(18), pp.3376-3385.

52. Sayah, N., Li, X., Caballero, J.F. and Jackson, W.M. Laser induced fluorescence studies of CN reactions with alkanes, alkenes and substituted aliphatic species. *Journal of Photochemistry and Photobiology A: Chemistry.* 1988, **45**(2), pp.177-194.

53. Janssen, E. and Hershberger, J.F. Reaction kinetics of the CN radical with primary alcohols. *Chemical Physics Letters.* 2015, **625**, pp.26-29.

54. Gupta, D., Cheikh Sid Ely, S., Cooke, I.R., Guillaume, T., Abdelkader Khedaoui, O., Hearne, T.S., Hays, B.M. and Sims, I.R. Low Temperature Kinetics of the Reaction Between Methanol and the CN Radical. *The Journal of Physical Chemistry A.* 2019, **123**(46), pp.9995-10003.

55. Lucas, D. *Extreme Chemistry around Stars and Planets - Unravelling the Kinetics of Astrochemical Reactions at Very Low Temperatures.* University of Leeds, 2021.

56. Frisch, M.J., Trucks, G.W., Schlegel, H.B., Scuseria, G.E., Robb, M.A., Cheeseman, J.R., Scalmani, G., Barone, V., Mennucci, B., Petersson, G.A., Nakatsuji, H., Caricato, M., Li, X., Hratchian, H.P., Izmaylov, A.F., Bloino, J., Zheng, G., Sonnenberg, J.L., Hada, M., Ehara, M., Toyota, K., Fukuda, R., Hasegawa, J., Ishida, M., Nakajima, T., Honda, Y., Kitao, O., Nakai, H., Vreven, T., J. A. Montgomery, J., Peralta, J.E., Ogliaro, F., Bearpark, M., Heyd, J.J., Brothers, E., Kudin, K.N., Staroverov, V.N., Keith, T., Kobayashi, R., Normand, J., Raghavachari, K., Rendell, A., Burant, J.C., Iyengar, S.S., Tomasi, J., Cossi, M., Rega, N., Millam, J.M., Klene, M., Knox, J.E., Cross, J.B., Bakken, V., Adamo, C., Jaramillo, J., Gomperts, R., Stratmann, R.E., Yazyev, O., Austin, A.J., Cammi, R., Pomelli, C., Ochterski, J.W., Martin, R.L., Morokuma, K., Zakrzewski, V.G., Voth, G.A., Salvador, P., Dannenberg, J.J., Dapprich, S., Daniels, A.D., Farkas, O., Foresman, J.B., Ortiz, J.V., Cioslowski, J. and Fox, D.J. *Gaussian 09 Revision D.01*. Wallingford CT: Gaussian, Inc. 2013.

57. Becke, A.D. A new mixing of Hartree–Fock and local density-functional theories. *The Journal of Chemical Physics.* 1993, **98**(2), pp.1372-1377.

58. Dunning, T.H. Gaussian basis sets for use in correlated molecular calculations. I. The atoms boron through neon and hydrogen. *The Journal of Chemical Physics.* 1989, **90**(2), pp.1007-1023.

59. Kendall, R.A., Dunning, T.H. and Harrison, R.J. Electron affinities of the first-row atoms revisited. Systematic basis sets and wave functions. *The Journal of Chemical Physics.* 1992, **96**(9), pp.6796-6806.

60. Woon, D.E. and Dunning Jr., T.H. Gaussian basis sets for use in correlated molecular calculations. V. Core-valence basis sets for boron through neon. *The Journal of Chemical Physics.* 1995, **103**(11), pp.4572-4585.

61. Zhao, Y. and Truhlar, D.G. The M06 suite of density functionals for main group thermochemistry, thermochemical kinetics, noncovalent interactions, excited states, and transition elements: two new functionals and systematic testing of four M06-class functionals and 12 other functionals. *Theoretical Chemistry Accounts.* 2008, **120**(1), pp.215-241.

62. Laury, M.L., Boesch, S.E., Haken, I., Sinha, P., Wheeler, R.A. and Wilson, A.K. Harmonic vibrational frequencies: Scale factors for pure,

hybrid, hybrid meta, and double-hybrid functionals in conjunction with correlation consistent basis sets. *Journal of Computational Chemistry.* 2011, **32**(11), pp.2339-2347.

63. *NIST Computational Chemistry Comparison and Benchmark Database.* [Online]. [Accessed 29/09/2022]. Available from: http://cccbdb.nist.gov/

64. Pople, J.A., Krishnan, R., Schlegel, H.B. and Binkley, J.S. Electron correlation theories and their application to the study of simple reaction potential surfaces. *International Journal of Quantum Chemistry.* 1978, **14**(5), pp.545-560.

65. Bartlett, R.J. and Purvis, G.D. Many-body perturbation theory, coupled-pair many-electron theory, and the importance of quadruple excitations for the correlation problem. *International Journal of Quantum Chemistry.* 1978, **14**(5), pp.561-581.

66. Glowacki, D.R., Liang, C.-H., Morley, C., Pilling, M.J. and Robertson, S.H. MESMER: An Open-Source Master Equation Solver for Multi-Energy Well Reactions. *The Journal of Physical Chemistry A.* 2012, **116**(38), pp.9545-9560.

67. Marcus, R.A. Unimolecular Dissociations and Free Radical Recombination Reactions. *The Journal of Chemical Physics.* 1952, **20**(3), pp.359-364.

68. Davies, J.W., Green, N.J.B. and Pilling, M.J. The testing of models for unimolecular decomposition via inverse laplace transformation of experimental recombination rate data. *Chemical Physics Letters.* 1986, **126**(3), pp.373 - 379.

69. Stoecklin, T., Dateo, C.E. and Clary, D.C. Rate constant calculations on fast diatom–diatom reactions. *Journal of the Chemical Society, Faraday Transactions.* 1991, **87**(11), pp.1667-1679.

70. Hirschfelder, J.O., Curtiss, C.F. and Bird, R.B. *Molecular theory of gases and liquids.* New York: Wiley, 1954.

71. Smith, I.W.M. *Kinetics and dynamics of elementary gas reactions.* London: Butterworths, 1980.

72. West, N.A., Millar, T.J., Van de Sande, M., Rutter, E., Blitz, M.A., Decin, L. and Heard, D.E. Measurements of Low Temperature Rate Coefficients for the Reaction of CH with CH_2O and Application to Dark Cloud and AGB Stellar Wind Models. *The Astrophysical Journal.* 2019, **885**(2), p.134.

73. Troe, J. Theory of thermal unimolecular reactions at low pressures. I. Solutions of the master equation. *The Journal of Chemical Physics.* 1977, **66**(11), pp.4745-4757.

Chapter 5

The reaction between the amidogen radical (NH_2) and acetaldehyde (CH_3CHO)

5.1 Introduction

The peptide bond, which joins amino acids to form proteins, can be seen as a combination of an amino -NH_2 group with a carbonyl C=O group (NH-C=O). In living cells, when the messenger ribonucleic acid (mRNA) gets a copy of the genetic sequence read by the ribosome, the transfer ribonucleic acid (tRNA) will bring in the suitable amino acids and at the ribosome, peptide bonds are formed to link the amino acids into peptides. A protein is then synthesised by building longer-chain peptides and wrapping them in a certain way. On the other hand, species with the peptide bond are capable to synthesise nucleobases (adenine (A), cytosine (C), guanine (G), thymine (T), uracil (U)), which can then lead to the production of ribonucleic acid (RNA) and deoxyribonucleic acid (DNA) (1, 2). Thus, the peptide bond is of high significance to life. Among the molecular species observed in the interstellar medium, the ones that contain the peptide bond include formamide NH_2CHO (3-7), acetamide $NH_2C(O)CH_3$ (7, 8), N-methylformamide CH_3NHCHO (9), urea $(NH_2)_2CO$ (10) and propionamide $NH_2C(O)C_2H_5$ (11). From an astrochemical point of view, it is important to understand their formation pathways as they are precursors of larger species which can go on to generate more complex species to provide the ingredients for life (1, 2).

For the formation of formamide, there have been attempts in models to make it from gas-grain reactions at low temperatures relevant to astrochemical environments. Successful examples include electron bombardment on ice mixtures with carbon monoxide CO and ammonia NH_3 (12), and ultraviolet irradiation on ice mixtures with methane CH_4 and isocyanic acid HNCO (13). The reaction responsible for the production of formamide in these cases was identified to be the combination of an amidogen radical NH_2 with a formyl radical HCO (12, 13). On the other hand, the bombardment of HNCO ice with H atoms was performed and no noticeable quantity of formamide was generated (14), which suggested that it is improbable for the hydrogenation reaction of

HNCO on grain surfaces to be a reliable source of formamide in the interstellar medium.

For gas-phase reactions, previous literature has reported theoretical work on reactions of different combinations of amino species with carbonyl species. For instance, the neutral-neutral reaction between ammonia NH_3 and formaldehyde CH_2O was studied by Ali (15) where, as shown in Figure 5.1, a 130.5 kJ mol^{-1} barrier relative to the reactants is encountered after the pre-reaction complex before the formation of a strongly bound adduct. For the ion-neutral reaction between the protonated ammonia $[NH_4]^+$ and CH_2O, as shown in Figure 5.2, the protonated formamide can only be formed by overcoming barriers with energy of at least 215 kJ mol^{-1} above that of the reactants as suggested from the calculations by Redondo et al. (16). Darla and Sitha (17) investigated the reaction between ammonia and carbon monoxide and their results are summarised in Figure 5.3. For the neutral-neutral addition to form formamide, the transition state has an energy of 293.3 kJ mol^{-1} relative to the reactants; and for the ion-neutral reaction between ammonia cation $[NH_3]^+$ and CO the corresponding barrier is lowered to 105.4 kJ mol^{-1}. However, these barriers are too high to allow the formation of formamide to be significant at cryogenic temperatures (< 120 K). Alternatively, the barrier becomes submerged and the energy of the entire reaction path lies below that of the reactants only for the reaction between NH_3 and $[CO]^+$ because of the high ionisation energy required to make $[CO]^+$ from CO.

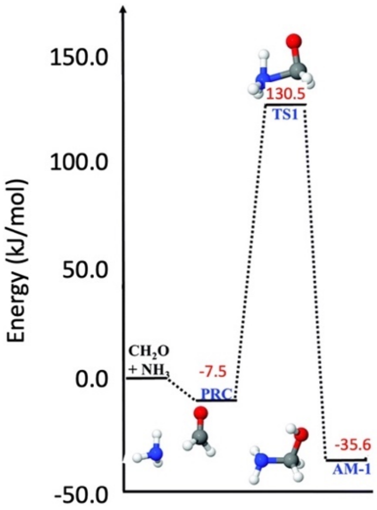

Figure 5.1 Zero-point vibrational energy (ZPVE) corrected potential energy surface in kJ mol^{-1} for the CH$_2$O + NH$_3$ reaction at the CCSD(T)/6-311++G(3df,3pd)//M06-2X/6-311++G(3df,3pd) level obtained by Ali. Adapted from (15).

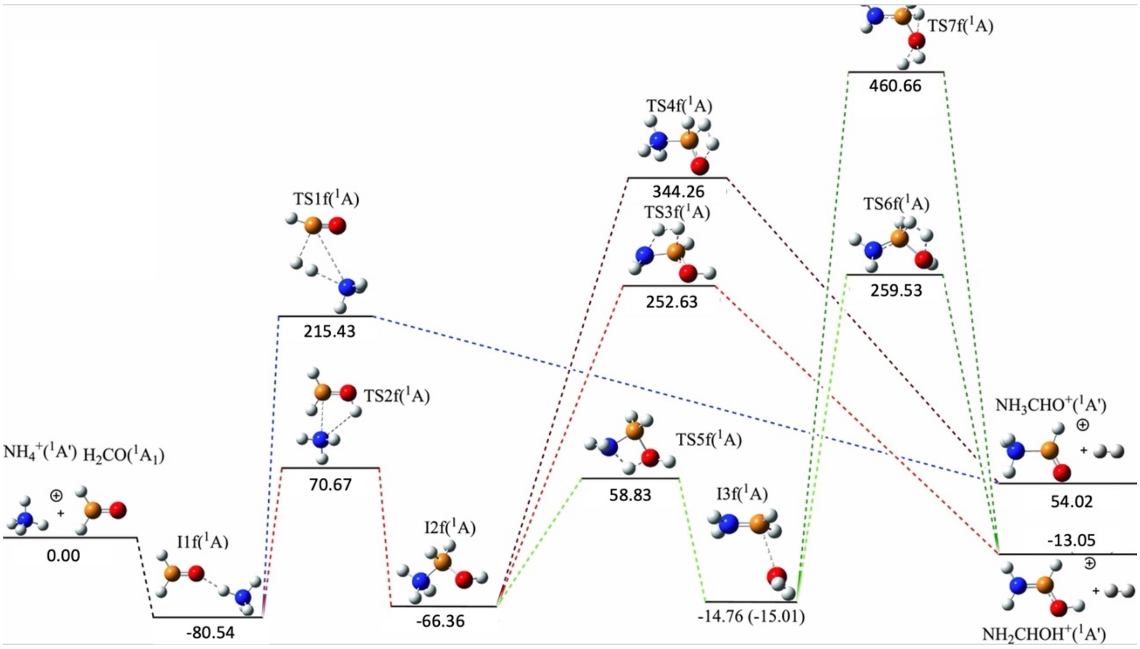

Figure 5.2 ZPVE-corrected potential energy surface in kJ mol^{-1} for the CH$_2$O + [NH$_4$]$^+$ reaction at the CCSD(T)/aug-cc-pVTZ//MP2/aug-cc-pVTZ level obtained by Redondo et al. Adapted from (16).

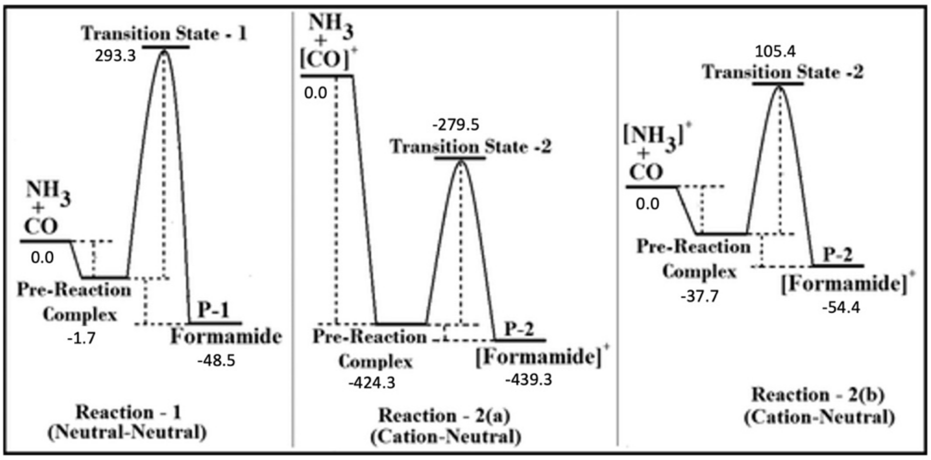

Figure 5.3 Energies (kJ mol^{-1}) obtained at the ωB97xD/aug-cc-pVTZ level by Darla and Sitha for different reaction pathways leading to formamide formation: left: NH_3 + CO; central: NH_3 + $[CO]^+$; right: $[NH_3]^+$ + CO. Adapted from (17).

Focusing on gas-phase neutral-neutral reactions, the combination of amidogen radical NH_2 with CH_2O has been suggested as a potential candidate to generate formamide under low temperature conditions (18-20). NH_2 radical plays an important role in the chemistry of planetary atmospheres (21-23) and it has also been detected in interstellar clouds (24), with an observed column density of 5 × 10^{15} cm^{-2}, that is, a fractional abundance of about (1–3) × 10^{-8} relative to H_2 in the Sgr B2 molecular cloud. The reaction pathway for the formation of the formamide from NH_2 and CH_2O initially proposed by the Barone group in 2015 (18) is shown in Figure 5.4, where the first step involves the formation of a C–N bond resulting in a more stable $H_2N–CH_2O$ adduct relative to the reactants, followed by the cleavage of C–H bond to form formamide over a transition state of energy about the same as the reactants. The calculated rate coefficient k based on such a reaction scheme as a function of temperature in the range of 10–300 K is reported to be (18):

$$k(T) = 2.6 \times 10^{-12} \times \left(\frac{T}{300\mathrm{K}}\right)^{-2.1} \exp\left(\frac{-26.9\mathrm{K}}{T}\right)\ \mathrm{cm^3\ molecule^{-1}\ s^{-1}} \qquad \text{E 5.1}$$

The rate coefficient for formamide formation would then increase almost monotonically with lower temperature in the range of 10–300 K and in particular, the value at 10 K would be 2.23 × 10^{-10} cm^3 molecule^{-1} s^{-1} while at 300 K it would still be as large as 2.38 × 10^{-12} cm^3 molecule^{-1} s^{-1} as shown in Figure 5.5.

Nonetheless, a closer look into the first step suggests that along the approach of NH_2 to attack the carbon atom of CH_2O, there exists a van der Waals complex followed by a transition state before reaching the intermediate adduct $H_2N–CH_2O$ as presented in Figure 5.6. With respect to the reactants, the relative electronic energy of this transition state at the CCSD(T)/CBS+CV level is reported to be 3.6 kJ mol^{-1} and with the inclusion of zero-point energy correction at the B2PLYP-D3/m-aug-cc-pVTZ level this value increases to 18.9 kJ mol^{-1} (19). A re-evaluation of the rate coefficient by Song and Kästner in 2016 (25) where consideration of this barrier, together with ZPVE, is included gives a value in the order of 10^{-22}–10^{-21} cm^3 molecule^{-1} s^{-1}. However, the Barone group in 2017 (20) still suggested that this reaction is feasible to form a significant portion of formamide in low temperature by omitting this barrier and the pre-reaction complex on the path of approach, and the reasons given are that: 1) their electronic energies can drop further by “extrapolating to the full configuration interaction limit”; and 2) their ZPVE correction “is not warranted” and “is realistic to be neglected” as following the approach of the two reagents the ZPVE will take into account of the new modes, including “a very loose stretching mode” and “two loose bending modes”, of which “the frequencies would tend to be grossly overestimated”.

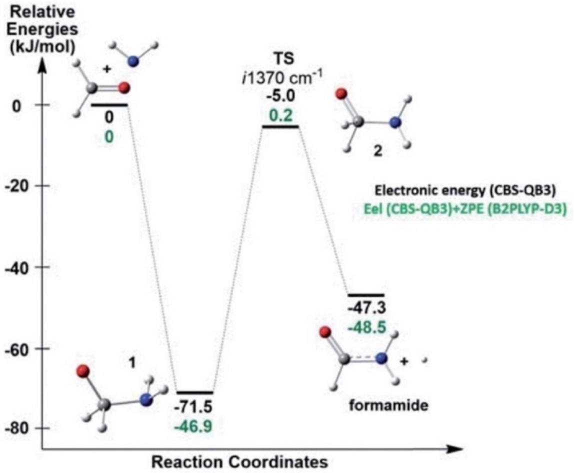

Figure 5.4 Proposed formamide formation pathway for the reaction between NH_2 and CH_2O by Barone et al. Taken from (18). Energy values in black are the electronic energies obtained at CBS-QB3 while in green are with the inclusion of B2PLYP-D3/m-aug-cc-pVTZ ZPVE corrections. Structure labelled as 1 is the $H_2N–CH_2O$ adduct.

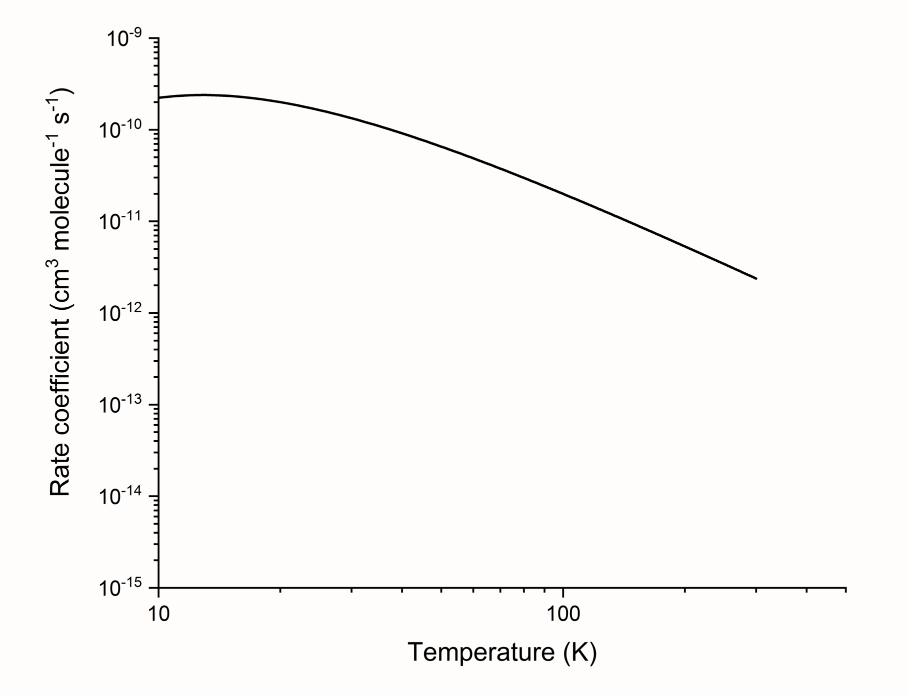

Figure 5.5 Predicted rate coefficient of the reaction of NH_2 + CH_2O versus temperature by Barone et al. based on the potential energy surface shown in Figure 5.4. Adapted from (18).

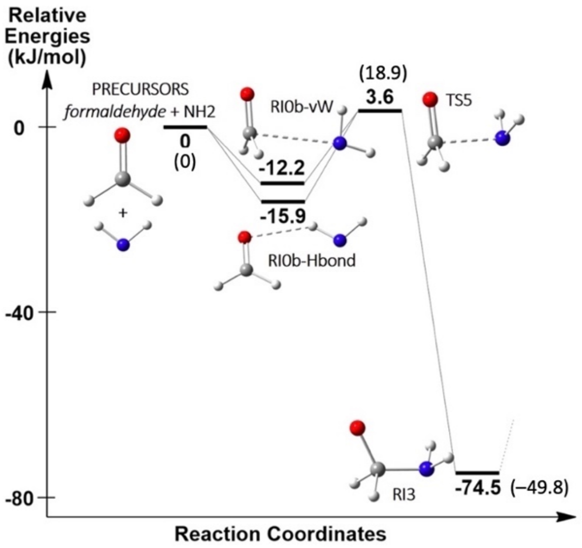

Figure 5.6 Proposed pathway for the approach of NH_2 + CH_2O to form the adduct by Vazart et al. Adapted from (19). Energy values in bold are the electronic energies obtained at CCSD(T)/CBS+CV while in parentheses are with the inclusion of B2PLYP-D3/m-aug-cc-pVTZ ZPVE corrections.

Table 5.1 Proposed H abstraction pathway for the NH_2 + CH_2O reaction and ZPVE corrected relative energies (kJ mol^{-1}) obtained at various levels by Li and Lü. Adapted from (26).

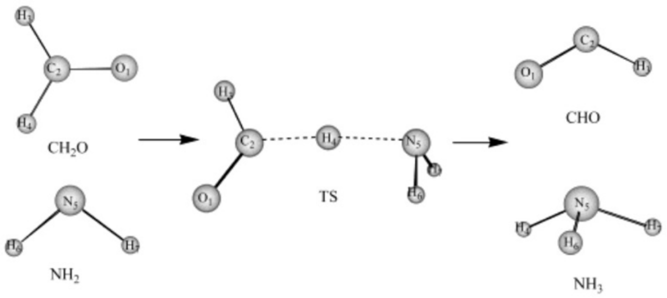		
Levels of theory	**ZPVE corrected relative energies (kJ mol^{-1}) of**	
	Transition state	**Products**
UMP2/6-311+G(d,p)	44.02	–88.62
CCSD(T)//6-311+G(3df,2p) //UMP2/6-311+G(d,p)	29.41	–75.94
G2//UMP2/6-311+G(d,p)	24.64	–77.57

Apart from undergoing an addition reaction, it is worth noting that the NH_2 radical is also capable of performing a hydrogen abstraction reaction to give NH_3, that is,

$$\mathrm{NH_2 + CH_2O \rightarrow NH_3 + HCO}\ \left(\Delta H^{\ominus}_{r,298\mathrm{K}} = -81\ \mathrm{kJ\ mol^{-1}}\right) \tag{R 5.1}$$

where the enthalpies are retrieved from the heats of formation given in Ruscic and Bross (27). A previous study by Li and Lü (26) focused on this hydrogen abstraction channel to form NH_3 + CHO from the reaction between NH_2 and CH_2O and the results are summarised in Table 5.1. As NH_2 approaches CH_2O, the reaction proceeds by going over a barrier and eventually forming the abstraction products. The ZPVE corrected energy of the barrier calculated at the UMP2/6-311+G(d,p), CCSD(T)//6-311+G(3df,2p)//UMP2/6-311+G(d,p) and G2//UMP2/6-311+G(d,p) levels are 44.02, 29.41 and 24.64 kJ mol^{-1} with respect to the reactants respectively, while for the NH_3 + CHO products the values are reported to be –88.62, –75.94 and –77.57 kJ mol^{-1} relative to the reactants. This H abstraction channel is found to be more exothermic than the addition channel.

The calculated abstraction rate coefficient from canonical variational transition state theory with small-curvature tunnelling correction decreases from the order of 10^{-11} to the order of 10^{-19} cm^3 molecule^{-1} s^{-1} for the temperature range of 2500 K to 250 K.

A very recent study within this group (28) reported experimental measurements of the NH_2 + CH_2O reaction down to 34 K using the Laval nozzle apparatus with the rate coefficient suggested to be $<6 \times 10^{-12}$ cm^3 molecule^{-1} s^{-1}. A 18.4 kJ mol^{-1} barrier is also identified at the CCSD(T)/aug-cc-pVTZ//M06-2X/aug-cc-pVTZ level for the formation of formamide from the calculations reported in the same study (28).

The next largest molecule after formamide in the amide homologous series being observed in the interstellar medium is acetamide and some suggestions of its formation mechanism are proposed, which are mainly ion-neutral reactions such as the combination of formamide with protonated methane $[CH_5]^+$ or methyl cation $[CH_3]^+$ or the combination of $[NH_4]^+$ with acetaldehyde CH_3CHO (7). For gas-grain reactions, Ligterink et al. (13) successfully generated acetamide from ice mixtures containing CH_4 and HNCO at 20 K with far-UV irradiation, and it is proposed that the formation mechanism first involves the combination of an amidogen radical NH_2 with carbon monoxide CO to give a NH_2CO radical followed by the reaction with a methyl radical CH_3. However, limited research has been done for neutral-neutral gas-phase reactions at low temperatures. With reference to the aforementioned reaction between NH_2 and CH_2O, it is sensible to investigate in the possibility of acetamide formation from the reaction between NH_2 and CH_3CHO, the next largest aldehyde after formaldehyde where its detection in the cold dust clouds has been previously reported (29), with an observed column density of 6×10^{12} cm^{-2} in the cold dust clouds TMC-1 and L134N.

A previous study by Hack et al. (30) reported kinetic measurements on the gas-phase reaction of NH_2 and CH_3CHO using the laser flash photolysis coupled with laser-induced fluorescence technique (LFP-LIF) over a temperature range of 297–543 K, where the rate coefficient, which shows a positive temperature dependence, can be represented by the following expression:

$$k(T) = 3.49 \times 10^{-13} \exp\left(-\frac{10.4 \pm 2\ \mathrm{kJ\ mol^{-1}}}{RT}\right)\ \mathrm{cm^3\ molecule^{-1}\ s^{-1}} \qquad \text{E 5.2}$$

The measurements were taken by the detection of the loss of NH_2 radical and no measurement was made of the branching ratio of the products. Nonetheless, it is still suggested that the H abstraction to form NH_3 is the main channel for this reaction system. It is also reported that this reaction can be comparable in terms of the rate coefficient with the reactions of NH_2 with other hydrocarbons such as toluene and 2,2-dimethylpropane, where all involve the cleavage of a C-H bond and the capture of the H atom by NH_2 (30).

In this chapter, the reaction mechanism between NH_2 and CH_3CHO is investigated with the exploration of a detailed potential energy surface followed by rate coefficient calculations. Fractional product branching yields obtained will give insights in the competition between the addition and H abstraction channels. In particular, H abstraction from CH_3CHO can possibly happen at both the carbonyl and methyl group sites and so the product branching ratios will provide the details of the more favourable abstraction route. Experiments have been carried out by Dr Kevin Douglas (University of Leeds) on the NH_2 + CH_3CHO reaction using the Laval set-up and some preliminary results will also be shown here to compare with the theoretical results.

5.2 Computational methods

In order to explore the potential energy surface of the NH_2 + CH_3CHO reaction, electronic structure calculations were carried out using the Gaussian 09 programme (31). Geometric structures of stationary points involved (reactants, products, intermediates including adducts and van der Waals complexes, and transition states (TSs)) were initially optimised at the BHandHLYP/aug-cc-pVDZ level of theory (32-35) and further refined at M06-2X/aug-cc-pVTZ level (36). A more detailed description of the levels of theory can be found in Section 2.1. The option of the ultrafine integration grids in Gaussian was chosen for all the DFT calculations. Vibrational frequency calculations were performed at the same level of theory as the geometry optimisation steps to characterise the stationary points and evaluate the zero-point vibrational energies (ZPVE). For TSs, they were found to have only one imaginary vibrational frequency while for the reactants, products and intermediates, all of the vibrational frequency values were positive. ZPVE obtained from the harmonic frequencies were then corrected with a scaling factor of 0.9589 for BHandHLYP/aug-cc-pVDZ (37) and 0.956 for M06-2X/aug-cc-pVTZ (38) respectively. Intrinsic reaction coordinate (IRC) calculations were performed for all the TSs identified to verify their linkage with the respective local minima on the PES. More accurate single-point energy values were obtained at the CCSD(T)/aug-cc-pVTZ level (39, 40) upon the optimised structures.

Based on the ab initio results, statistical rate calculations were performed using the master equation solver programme MESMER (41). Further details on MESMER and its underlying principles can be found in Section 2.2. The rigid rotor-harmonic oscillator approximation was applied for all modes of all the species involved in the reaction in the calculations of density of states. The microcanonical rate coefficients for the reactive steps involving a defined transition state were calculated with the RRKM theory (42). For the H abstraction steps, the corrections for quantum mechanical tunnelling were activated using the one dimensional Eckart model (43). For barrierless reactions, which refer to the approaching steps of the reactants forming the pre-reaction complexes that will be shown in the results section, the ILT method (44) was used. The ILT pre-exponential factor A^{∞} for each entrance channel was set as 3×10^{-10} cm^3 $molecule^{-1}$ s^{-1} and the temperature dependence index n^{∞} as 0, which is suggested to be a reasonable estimate of the upper capture limit for neutral-neutral reactions (45, 46), although in reality the capture limit varies with the long-range interactions between the two species and can be temperature dependent. To describe the collisional energy transfer probabilities, the exponential-down model was used (47) as described in Section 2.2. With Ar as the bath gas, simulations were carried out for total density in the range of 10^{13}–10^{23} molecule cm^{-3}, which is in attempt to cover the Laval conditions, as well as all the way from the low pressure limit to the high pressure limit as predicted from the Lindemann-Hinshelwood mechanism. Simulations were performed in the temperature range 25–400 K, where a grain size of 30 cm^{-1} was used for all of the conditions.

5.3 Results and discussions

5.3.1 Results from ab initio calculations

The full potential energy surface for the NH_2 + CH_3CHO reaction obtained is shown in Figure 5.7, where the energies shown are zero-point corrected energies relative to the reactants calculated at the CCSD(T)/aug-cc-pVTZ//M06-2X/aug-cc-pVTZ level of theory.

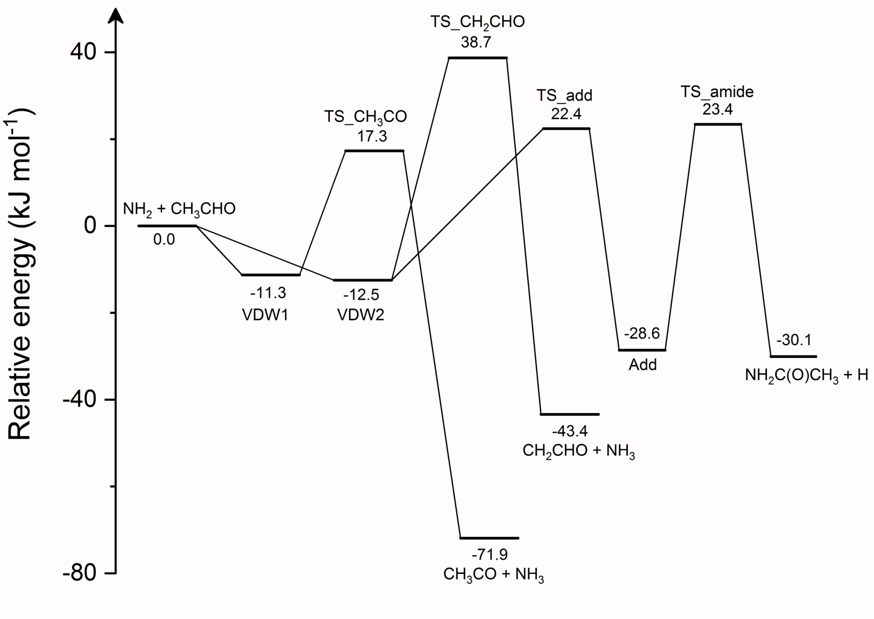

Figure 5.7 PES of the NH_2 + CH_3CHO reaction obtained at CCSD(T)/aug-cc-pVTZ//M06-2X/aug-cc-pVTZ level of theory. All energy values are in kJ mol^{-1} and are corrected with scaled ZPVE.

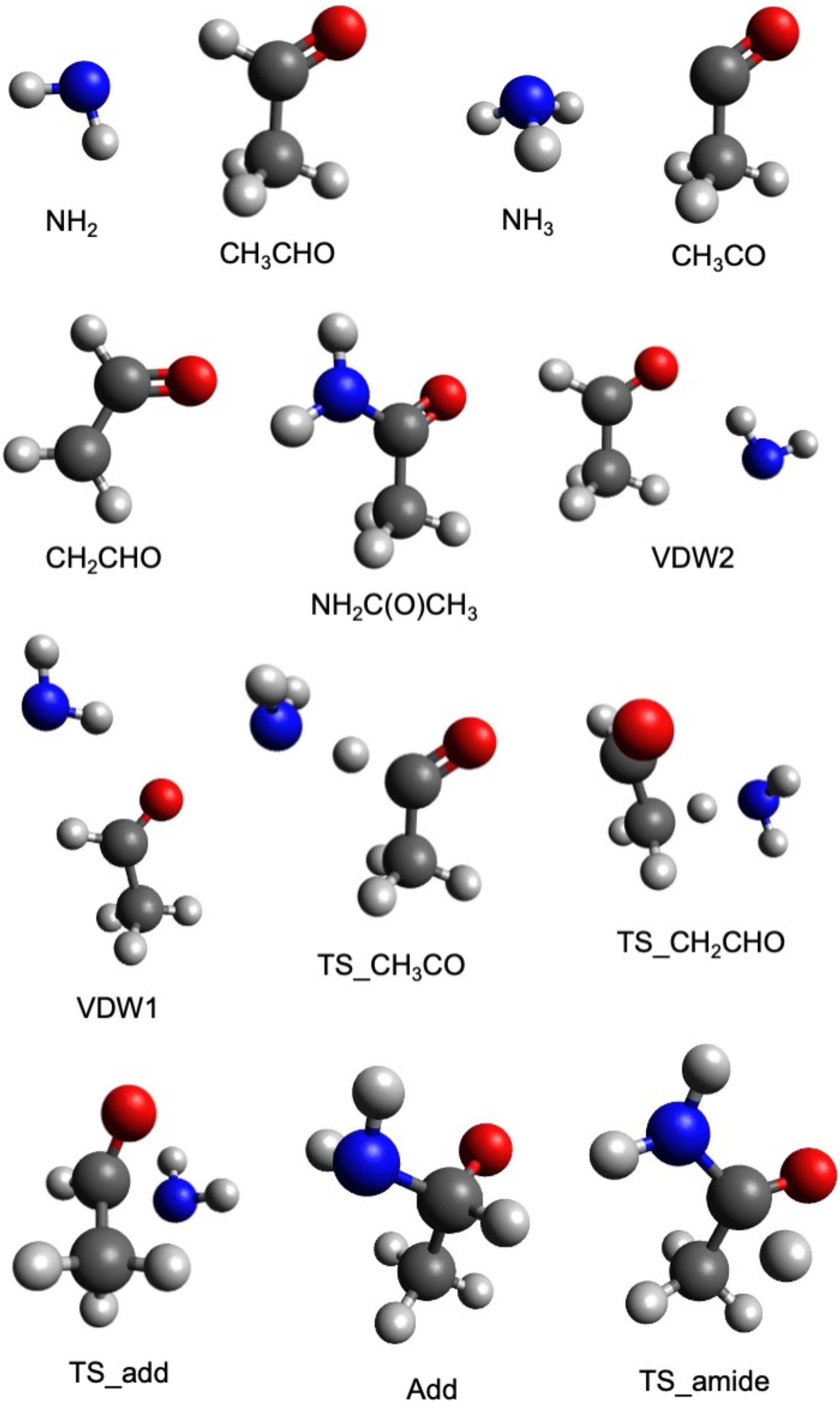

NH_2 CH_3CHO NH_3 CH_3CO

CH_2CHO $NH_2C(O)CH_3$ VDW2

VDW1 TS_CH_3CO TS_CH_2CHO

TS_add Add TS_amide

Figure 5.8 Optimised geometries of reactants, products, intermediates and transition states obtained at the M06-2X/aug-cc-pVTZ level of theory for the NH_2 + CH_3CHO reaction. The labels correspond to those shown in Figure 5.7.

The optimised geometries of the stationary points at the M06-2X/aug-cc-pVTZ level are shown in Figure 5.8. The optimised Cartesian coordinates, vibrational frequencies, rotational constants and energy values can be found in Appendix D.

Following the approach of NH_2 to CH_3CHO, two different weakly bound van der Waals complexes **VDW1** (–11.3 kJ mol^{-1}) and **VDW2** (–12.5 kJ mol^{-1}) are identified, which can be formed without encountering any barriers. For **VDW1**, the NH_2 radical is closer to the carbonyl end and further from the methyl end of CH_3CHO. For **VDW2**, NH_2 is by the side of CH_3CHO at a similar distance to the methyl group and to the carbonyl group but furthest from the carbonyl H. **VDW1** allows the reaction to proceed by undergoing H atom abstraction from the carbonyl moiety, which involves a positive barrier **TS_CH$_3$CO** (17.3 kJ mol^{-1}) and eventually leads to the products CH_3CO + NH_3 (–71.9 kJ mol^{-1}). On the other hand, **VDW2** can lead to two different product pathways. One pathway is H atom abstraction reaction from the methyl moiety where a higher barrier **TS_CH$_2$CHO** (38.7 kJ mol^{-1}) is involved before reaching the products CH_2CHO + NH_3 (–43.4 kJ mol^{-1}). Another channel is the addition reaction of NH_2 onto the carbonyl C atom of CH_3CHO via a barrier **TS_add** (22.4 kJ mol^{-1}), forming a peptide bond to give the adduct **Add** (–28.6 kJ mol^{-1}). By surmounting another barrier **TS_amide** (23.4 kJ mol^{-1}), the cleavage of the C–H bond at the carbonyl group of this intermediate adduct gives the combination of an acetamide and a hydrogen atom $NH_2C(O)CH_3$ + H (–30.1 kJ mol^{-1}) as the products.

In comparison with the reaction between NH_2 and CH_2O, for the abstraction processes, the similarity with the results shown here for NH_2 + CH_3CHO is the presence of a positive barrier. However, contrasting with the previous study by Li and Lü (26) on NH_2 + CH_2O where no pre-reaction complex structure optimised at the UMP2/6-311+G(d,p) level was reported, van der Waals complexes have been identified, which is similar to the CN + CH_2O reaction reported in Chapter 3, and reported here for NH_2 + CH_3CHO. Nonetheless, recent recalculations of the potential energy surface of NH_2 + CH_2O by Douglas et al. (28) also suggest that pre-reaction complex structures can be obtained and optimised at the M06-2X/aug-cc-pVTZ level, and the shape of the energy profiles of the abstraction pathways for the two reactions are in line with each other. For the addition channel that leads to amide formation, the shape of the PES is also comparable to the complete addition pathway for NH_2 + CH_2O reported before (18-20, 28). For NH_2 + CH_3CHO, both the barriers after the pre-reaction complex corresponding to the peptide bond formation and the C–H bond dissociation are not submerged, with energy values relative to the reactants slightly higher than those for the NH_2 + CH_2O reaction reported by the Barone group (18-20). These features of pre-reaction complexes and positive barriers found on the PES are not omitted during the rate coefficient calculations in this work.

5.3.2 Results from rate coefficient calculations

5.3.2.1 Rate coefficients

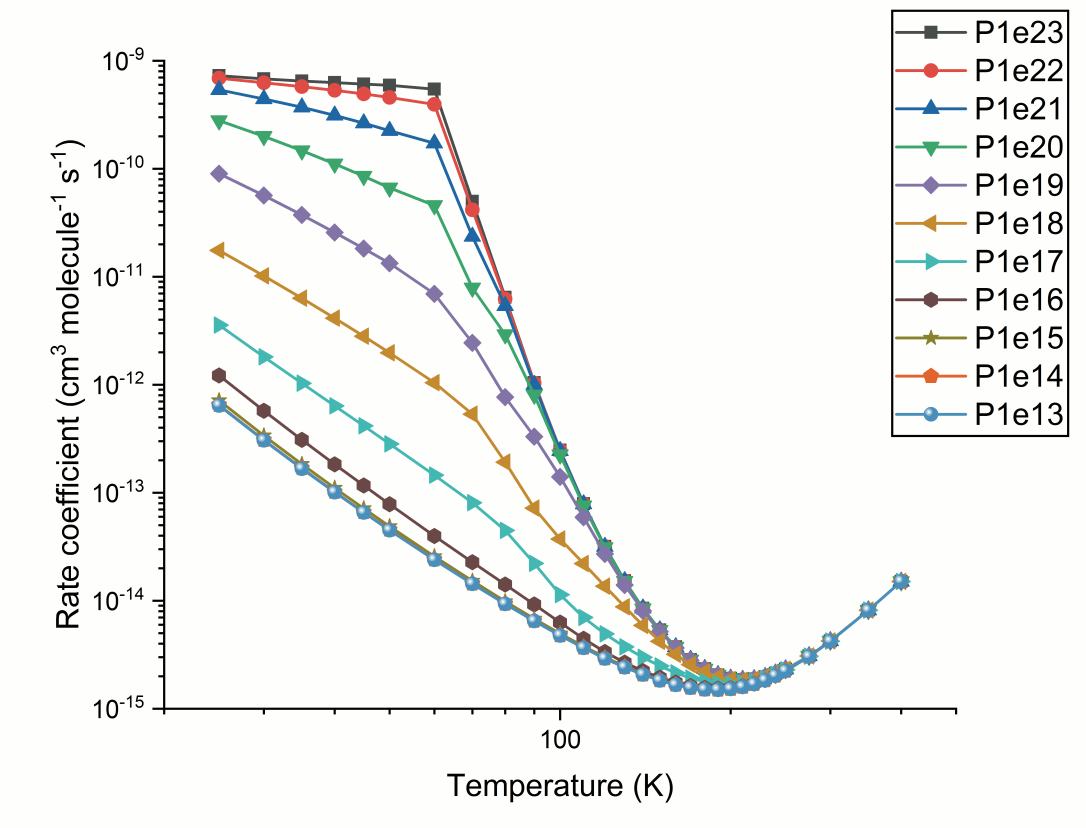

Figure 5.9 Calculated rate coefficients for the NH_2 + CH_3CHO reaction versus temperature in the range *T* = 25–400 K at various pressures. The legend denotes the number densities from 10^{13}–10^{23} molecule cm^{-3}.

Rate coefficient calculations on the NH_2 + CH_3CHO reaction with the MESMER programme have been performed using the energy values calculated at the CCSD(T)/aug-cc-pVTZ//M06-2X/aug-cc-pVTZ level, vibrational frequencies and rotational constants obtained from ab initio calculations. The calculated bimolecular rate coefficients for the removal rate of the NH_2 radical, where more details of the calculations method are described in Section 2.2, are obtained as the eigenvalues of the master equations solved. The rate coefficients are plotted as a function of temperature in Figure 5.9, whilst as a function of pressure for selected temperatures in Figure 5.10.

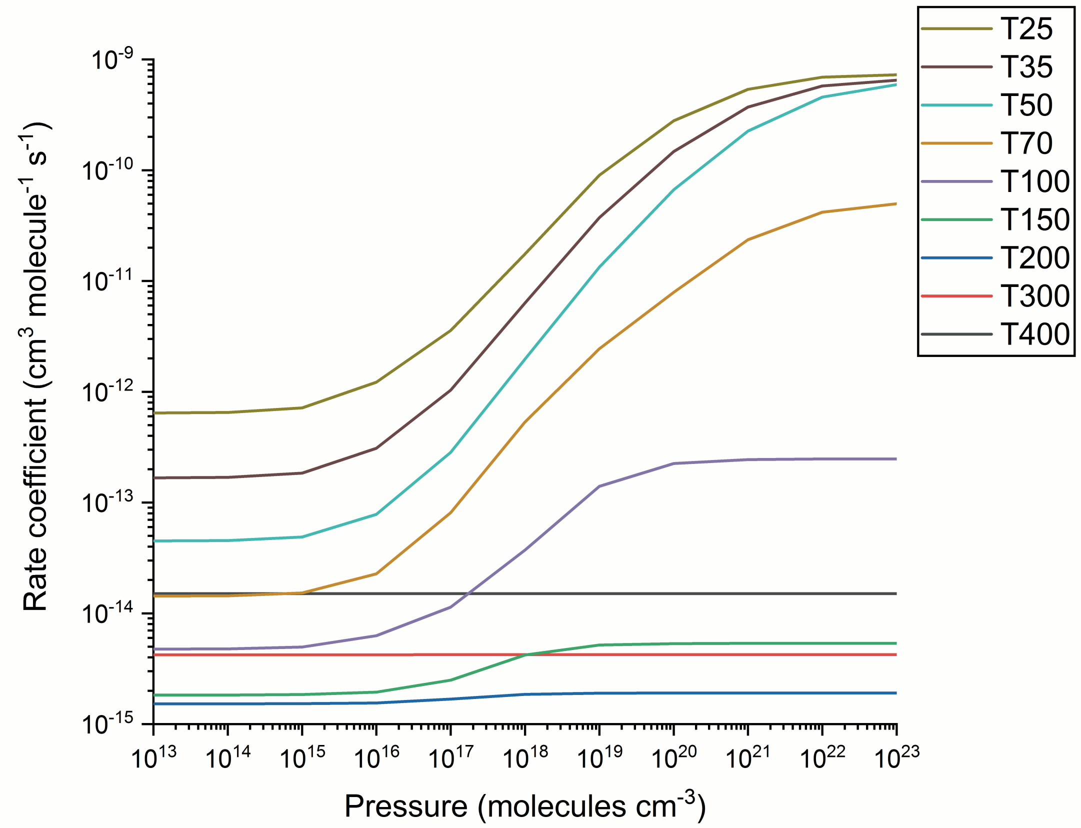

Figure 5.10 Calculated rate coefficients for the NH_2 + CH_3CHO reaction versus pressure in the range of $P = 10^{13}$–10^{23} molecule cm^{-3} at various temperatures. The legend denotes the temperatures from 25 K to 400 K.

In the temperature range of 25–400 K, the calculated rate coefficients when plotted against temperature show a V-shaped trend as shown in Figure 5.9. For all pressures, at room temperature and above, the rate coefficients are in the order of 10^{-14} cm^3 molecule^{-1} s^{-1} and steadily decreases to the order of 10^{-15} cm^3

molecule^{-1} s^{-1} as temperature decreases down to ~200 K as shown in Figure 5.9. As the temperature drops further, the rate coefficients instead display a negative temperature dependence. The extent of the increment in rate coefficients at low temperatures diverges for different pressures. When the pressure reaches 10^{15} molecule cm^{-3} and below, the rate coefficients are pressure independent indicated from the coincidence of the curves in Figure 5.9 and the flat portions of the curves in Figure 5.10, which can be considered as at the low pressure limit in the context of the Lindemann-Hinshelwood mechanism, and gradually increase to the order of 10^{-12} cm^3 molecule^{-1} s^{-1} at 25 K. At higher pressure, the rate coefficients increase more quickly with lowering temperature to a larger value, resulting in some crossings of the curves in Figure 5.10. However, when the total pressure is above 10^{21} molecule cm^{-3}, which corresponds to a pressure of about 40 atm (being relevant to a combustion engine), after the initial rapid increase in rate coefficient, which exceeds 10^{-10} cm^3 molecule^{-1} s^{-1} at 60 K, as the temperature further decreases the rate coefficients reach a plateau. This upper bound and the resulting kink in the curves shown in Figure 5.9 is actually rooted from the summation of the high pressure collision limit of the two approaching channels set by the ILT pre-exponential factor *A*.

Based on the above results, a plausible explanation for the reaction mechanism is as follows. At high temperature, the reaction proceeds directly by surmounting the barriers shown in Figure 5.7, resulting in the positive temperature dependence of the rate coefficients. Following the identification of the pre-reaction complexes as presented in Figure 5.7, at low temperature, the pre-reaction complexes allow the reagents to come close to each other and the reaction can instead proceed indirectly by quantum mechanical tunnelling or trap in the potential wells at high pressure conditions. The switch in mechanism leads to the temperature and pressure dependence as shown in Figure 5.9 and Figure 5.10. These different outcomes will be presented later as a product branching ratio.

Table 5.2 Preliminary rate coefficients and experimental conditions for kinetic studies of the NH_2 + CH_3CHO reaction by courtesy of Dr Kevin Douglas

T / K	P / 10^{16} molecule cm^{-3}	k / 10^{-11} cm^3 molecule^{-1} s^{-1}
45.0	6.22	3.17 ± 0.09
45.0	11.22	4.22 ± 0.23
45.0	16.52	8.46 ± 0.37
45.0	28.20	9.60 ± 0.76
45.2	6.24	4.89 ± 0.11
45.2	11.24	9.95 ± 0.91
45.2	15.94	11.62 ± 0.69
51.3	10.02	1.56 ± 0.09
51.3	10.02	1.76 ± 0.10
51.3	17.95	3.21 ± 0.24
51.3	23.52	3.72 ± 0.36
52.0	7.44	0.67 ± 0.04
52.0	10.10	2.30 ± 0.12
52.0	14.00	3.13 ± 0.18
55.3	8.82	3.70 ± 0.21
55.3	14.98	6.28 ± 0.59
55.3	20.48	9.69 ± 0.61
62.1	6.83	0.80 ± 0.14
62.1	13.48	0.73 ± 0.14
62.1	18.61	1.61 ± 0.22
83.3	4.19	0.72 ± 0.10
83.3	7.40	0.57 ± 0.22
83.3	12.95	2.57 ± 0.31
83.3	17.68	1.43 ± 0.42
88.7	5.28	0.17 ± 0.05
88.7	9.12	0.92 ± 0.18
88.7	12.70	1.14 ± 0.18
101.1	7.55	0.42 ± 0.04
101.1	12.66	0.21 ± 0.03
101.1	17.66	0.21 ± 0.08

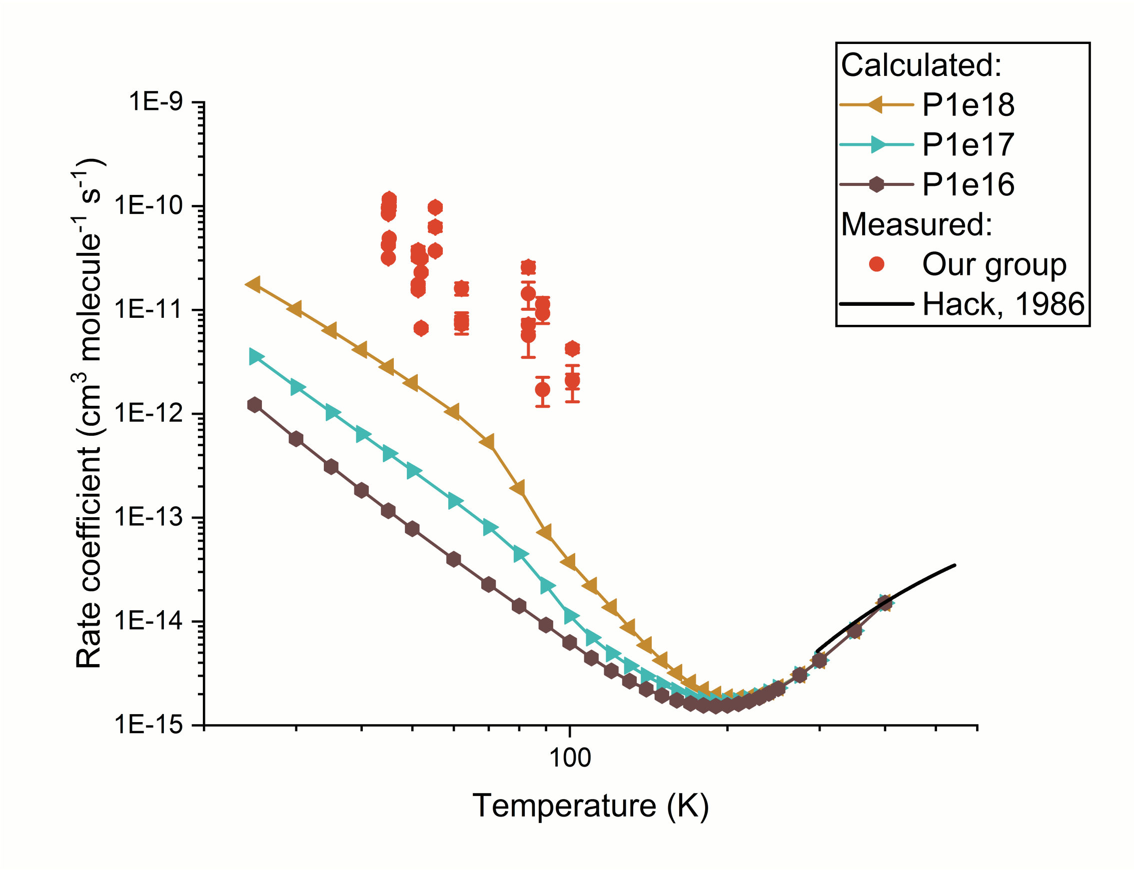

Figure 5.11 Rate coefficients plotted against temperature for results obtained from experiments with the Laval set-up (red circles) and reported from Hack et al. (30) (black line), together with calculations from MESMER for different total number density conditions (dark brown: 10^{16} molecule cm^{-3}; cyan: 10^{17} molecule cm^{-3}; gold: 10^{18} molecule cm^{-3}).

Kinetics experiments on the NH_2 + CH_3CHO reaction have been recently carried out by Dr Kevin Douglas in the temperature range of 45–101.1 K using the laser flash photolysis coupled with laser-induced fluorescence technique (LFP-LIF) with a uniform supersonic environment of a Laval nozzle expansion to generate and detect the NH_2 radical for rate coefficient measurements. Some preliminary results on the temperature dependence of the rate coefficients are shown in Table 5.2. Experiments were performed within the pressure range of $4 \times 10^{16} – 3 \times 10^{17}$ molecule cm^{-3}. As shown in Figure 5.11, the measured rate coefficients show a negative temperature dependence, increasing from the order of 10^{-12} cm^3 molecule^{-1} s^{-1} at 101.1 K to the order of 10^{-10} cm^3 molecule^{-1} s^{-1} at 45 K. Together with the previously reported results at room temperature and above (30), the experimental data are plotted alongside with calculated values obtained for comparable pressure range in Figure 5.11.

At room temperature or above, the calculated rate coefficients match very well with the experimental data in terms of the order of magnitude, about 10^{-14} cm^3 molecule^{-1} s^{-1}, as well as the positive temperature dependence trend and the pressure independence. On the other hand, in the low temperature regime, the calculated rate coefficients successfully capture the negative temperature dependence trend. In general, the V-shaped temperature dependence trend of the experimental rate coefficients is evidence to support the aforementioned proposal of the reaction mechanism: overcoming the barrier directly at high temperature and proceeding indirectly via the pre-reaction complexes followed by tunnelling at low temperature. However, in the low temperature regime, the measured values are about 1–2 orders of magnitude larger than the calculated ones. Potential ways to reduce the discrepancy are the inclusion of hindered rotor potentials, applying an increment of the collisional energy transferred parameters which are still inadequately understood at low temperatures, or further refining the energies of the pre-reaction complexes and the imaginary frequencies of the transition states.

Although it is not the same reaction, these findings can also provide insights into previous literature of the similar reaction system NH_2 + CH_2O. The study by Li and Lü (26) on the H abstraction of NH_2 + CH_2O only provides details of the barrier but has not shed light on any potential pre-reaction complex structures. Based solely on the positive temperature dependence trend arisen from the barrier, an extrapolation from a rate coefficient in the order of 10^{-19} cm^3 molecule^{-1} s^{-1} at 250 K to lower temperatures can lead to the oversight of a change in the temperature dependence trend and the underestimation of the reaction rate under ISM conditions. On the other hand, for the study by the Barone group (18-20), by ignoring the barrier, the reported formamide formation rate coefficient from NH_2 + CH_2O easily exceeds 10^{-12} cm^3 molecule^{-1} s^{-1} even at room temperature as shown in Figure 5.5. Should the barrier be omitted in the NH_2 + CH_3CHO reaction, the calculated rate coefficients would then not be able to reproduce the values as small as the order of 10^{-14} cm^3 molecule^{-1} s^{-1}

and the positive temperature dependence reported in experiments at room temperature and above. This suggests that the pre-reaction complexes together with the following positive barriers cannot be intentionally neglected during the calculations of the rate coefficients and the complete pathway similar to that in Figure 5.7 has to be considered.

5.3.2.2 Tunnelling and product branching ratios

In order to study the effect of quantum mechanical tunnelling in the NH_2 + CH_3CHO reaction, MESMER simulations have also been performed without the Eckart tunnelling corrections for comparison and to further explore the importance of tunnelling. Time dependent species profiles with a concentration of 10^{14} molecule cm^{-3} of the excess reactant CH_3CHO under selected conditions for both with and without the inclusion of tunnelling corrections are shown in Figure 5.12 and Figure 5.13. In these plots, the progress of the reaction can be followed from the removal of reactants, the formation and removal of intermediates and the formation of products. Considering T = 100 K as shown in Figure 5.12, the significant loss of NH_2 radical happens at a much later time without tunnelling, which would mean a much slower reaction rate in contrast to the experimental observations. In terms of the resulting products, while with tunnelling some CH_2CHO can be formed, without tunnelling essentially CH_3CO + NH_3 is the only product channel, which is mainly contributed by the higher barrier of **TS_CH_2CHO** than **TS_CH_3CO**. Comparing the scenarios between different total densities, 10^{15} molecule cm^{-3} and 10^{19} molecule cm^{-3} in this case shown in Figure 5.12, no pressure dependence is observed for the rate coefficients without tunnelling, but the different timescale of the disappearance of NH_2 radical when tunnelling is included implies the opposite, thus the contribution of the indirect pathway to product formation is required given there is no observable fraction of stabilised VDW complexes at T = 100 K shown from the species profiles.

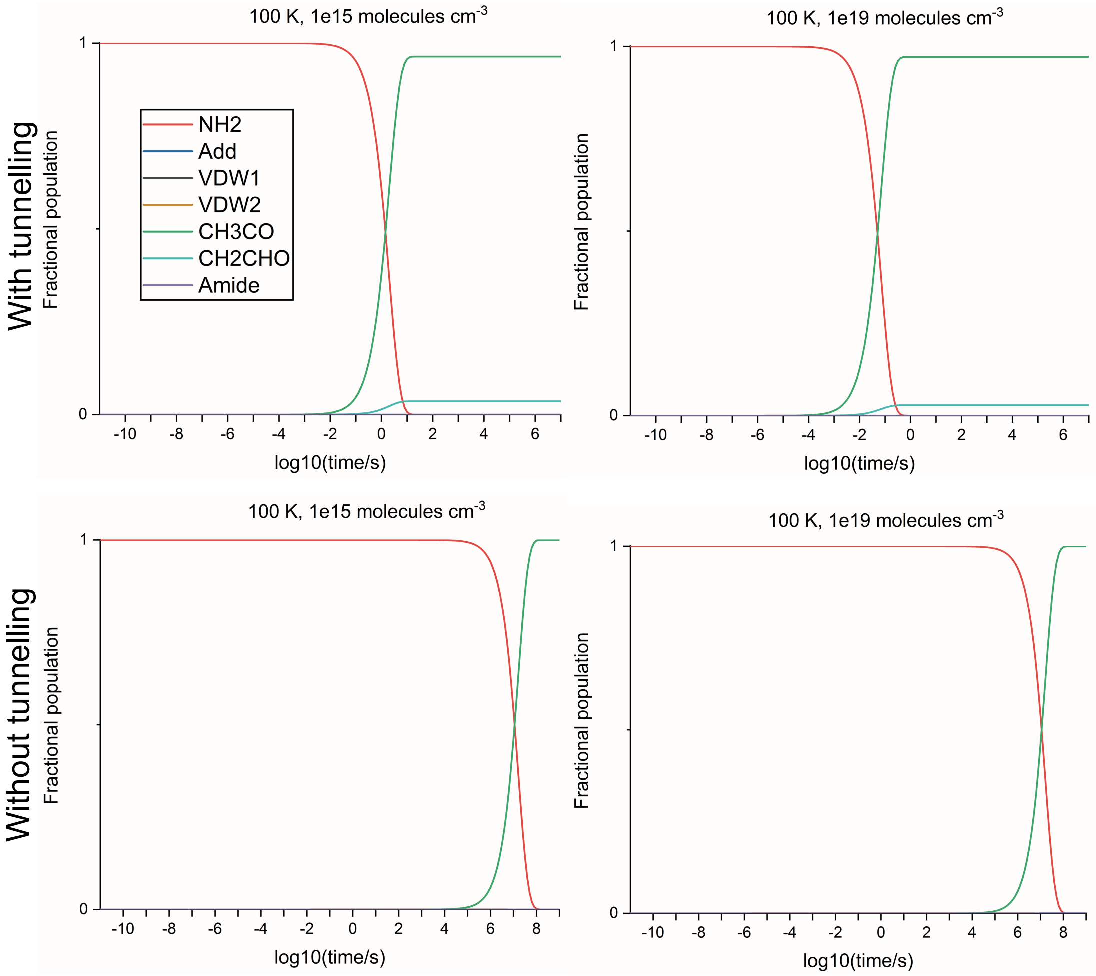

Figure 5.12 Fractional population of various relevant species of the NH_2 + CH_3CHO reaction system (red: the limiting reactant NH_2 radical; blue: the adduct Add; black: pre-reaction complex VDW1; yellow: pre-reaction complex VDW2; green: product set CH_3CO + NH_3; cyan: product set CH_2CHO + NH_3; purple: product set $NH_2C(O)CH_3$ amide + H) using a concentration of 10^{14} molecule cm^{-3} of the excess reactant CH_3CHO against time with (top) and without (bottom) tunnelling corrections at 100 K with a total density of 10^{15} molecule cm^{-3} (left) and 10^{19} molecule cm^{-3} (right) respectively.

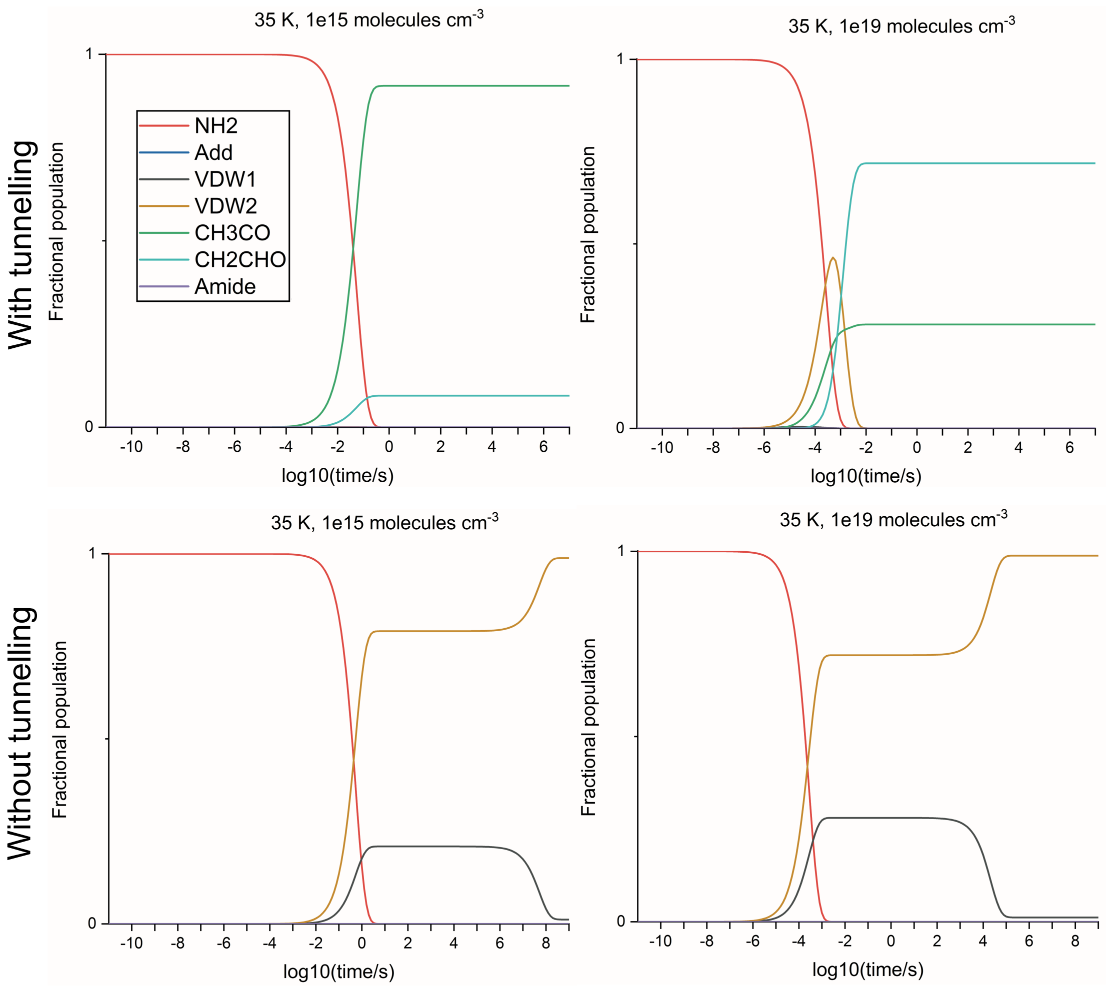

Figure 5.13 Fractional population of various relevant species of the NH_2 + CH_3CHO reaction system (red: the limiting reactant NH_2 radical; blue: the adduct Add; black: pre-reaction complex VDW1; yellow: pre-reaction complex VDW2; green: product set $CH_3CO + NH_3$; cyan: product set $CH_2CHO + NH_3$; purple: product set $NH_2C(O)CH_3$ amide + H) using a concentration of 10^{14} molecule cm^{-3} of the excess reactant CH_3CHO against time with (top) and without (bottom) tunnelling corrections at 35 K with a total density of 10^{15} molecule cm^{-3} (left) and 10^{19} molecule cm^{-3} (right) respectively.

The bimolecular product formation rate coefficient without tunnelling against temperature is shown in Figure 5.14, which only includes the direct channel as there is no tunnelling for the indirect channel to proceed. Although it is not the same as the bimolecular NH_2 removal rate coefficient for the full temperature range where the latter one also includes the complex formation, at 100 K the two are comparable as there is no noticeable complex stabilisation as shown from the species profiles in Figure 5.12. There is no pressure dependence for the direct product formation channel, which matches the aforementioned observations in the NH_2 radical removal from the species profiles for the scenarios without tunnelling in Figure 5.12. The product formation rate coefficient at 100 K shown in Figure 5.14, which represents the scenario without tunnelling, is in the order of 10^{-21} cm^3 $molecule^{-1}$ s^{-1} while the NH_2 removal rate coefficient at 100 K shown in Figure 5.9, where tunnelling is included, is in the order of 10^{-14} cm^3 $molecule^{-1}$ s^{-1} and above. Solely the stabilisation of the complexes, which is shown to be not noticeable, cannot explain this large difference and thus there exists production formation pathway other than the direct channel, which can be provided by tunnelling to remove the reactants and complexes through the indirect channel.

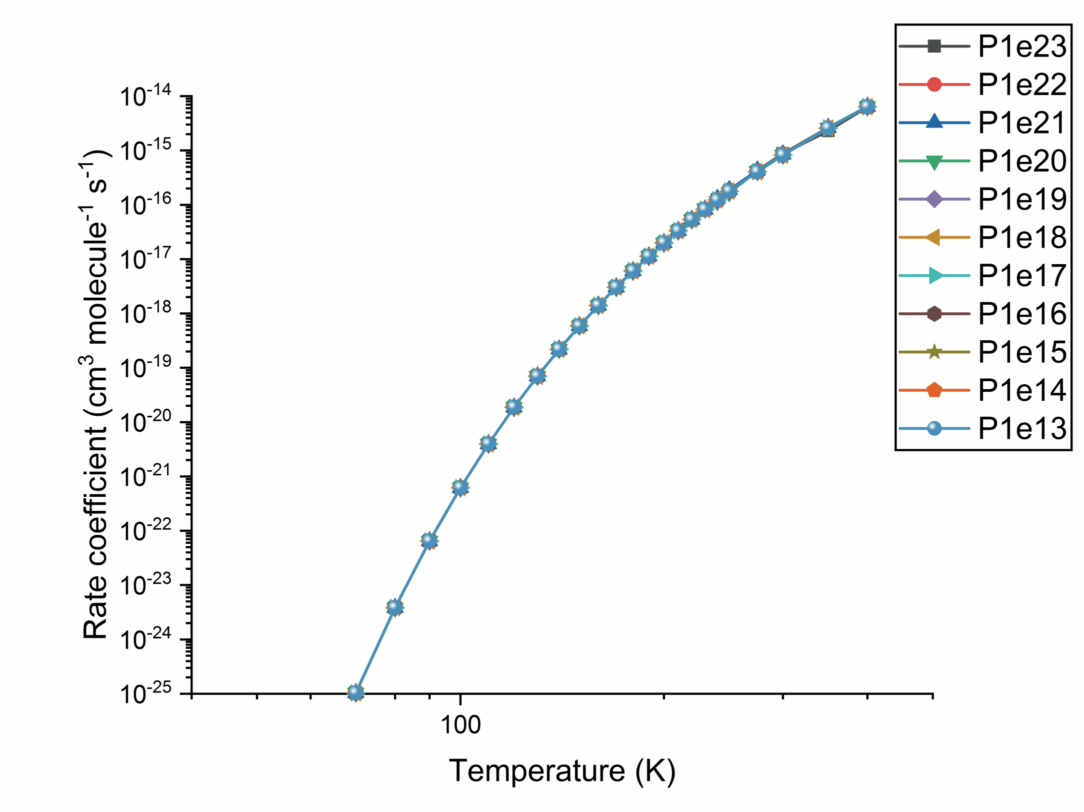

Figure 5.14 Bimolecular product formation rate coefficient for the direct channel of the NH_2 + CH_3CHO reaction without the inclusion of quantum mechanical tunnelling against temperature. There is no pressure dependence as all the lines coincide with each other.

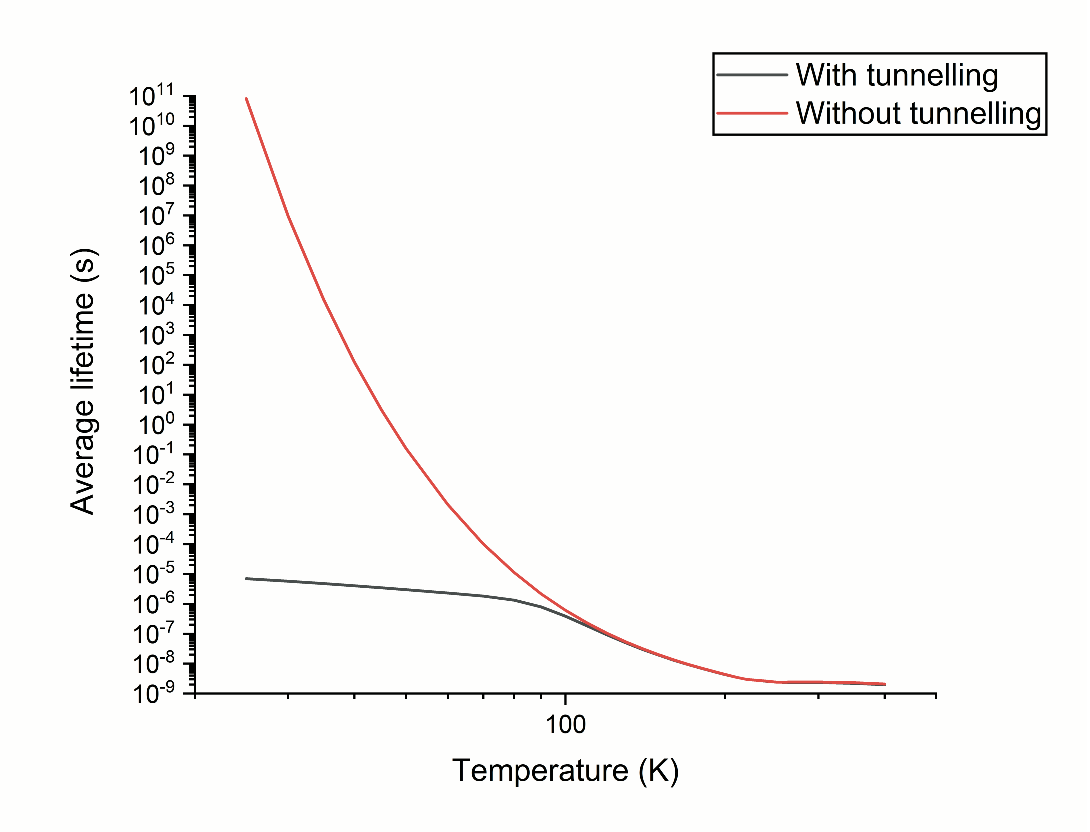

Figure 5.15 Average lifetime of the pre-reaction complexes with (black) and without (red) tunnelling against temperature with a total pressure of 10^{19} molecule cm^{-3} and an excess reactant CH_3CHO concentration of 10^{14} molecule cm^{-3} in the temperature range of 25–400 K.

Considering the species profiles at *T* = 35 K in Figure 5.13, without tunnelling, the reaction system will just stabilise in the potential wells of the two pre-reaction complexes **VDW1** and **VDW2**. On the other hand, with tunnelling, the reaction system can proceed to the products, in particular at high pressure, where after the brief emergence of a significant fraction of pre-reaction complexes the reaction system eventually goes to completion to generate the H abstraction products. The average lifetime of the pre-reaction complexes when the total pressure is at 10^{19} molecule cm^{-3} and the excess reactant CH_3CHO concentration is at 10^{14} molecule cm^{-3}, computed from the reciprocal of the sum of the pseudo-first order loss rate coefficients of **VDW1** and **VDW2**, is plotted against temperature in Figure 5.15, which clearly shows the increase of the lifetime of the pre-reaction complexes at low temperature. In particular, there is a rapid increase for the curve corresponding the case when there is no tunnelling, which solely shows the temperature effect. When tunnelling is considered, however, the rapid increase in the lifetime at low temperature disappears, as tunnelling helps remove the complexes to form products. These results suggest the pivotal role of quantum mechanical tunnelling in the promotion of the reaction rates and the determination of the branching ratios of different products.

Based on the time dependent species profiles with the inclusion of the tunnelling corrections for H abstraction, branching ratios of the product yield can be obtained. Figure 5.16 shows the yields of the product sets CH_3CO + NH_3, CH_2CHO + NH_3 and $NH_2C(O)CH_3$ + H respectively as a function of temperature and pressure. The temperature-dependent fraction yield at a fixed density of 10^{16} molecule cm^{-3} is shown in Figure 5.17 while the pressure-dependent fractional yields at various selected temperatures are shown in Figure 5.18. At high temperature, almost all of the reactants will undergo H abstraction from the carbonyl group to form CH_3CO + NH_3. As the temperature decreases, it can be split into three different pressure scenarios. At low pressure, CH_3CO + NH_3 remains as the dominant product set. However, as the pressure increases, the yield for CH_3CO + NH_3 drops initially. For instance at P = 10^{16} molecule cm^{-3} as shown in Figure 5.17, the percentage yield for CH_3CO + NH_3 is > 99% when the temperature is above 200 K but it decreases to ~ 60% at T = 25 K. For the contour map shown in Figure 5.16, the minimum yield for CH_3CO + NH_3 of 23.6% is obtained for T = 60 K, P = 10^{18} molecule cm^{-3}, indicating that it becomes the minor product instead. As the pressure further increases to the high-pressure limit, the yield for CH_3CO + NH_3 increases again, and at very low temperature it increases back to about 50%. The yield for CH_2CHO + NH_3 is basically complementary of that for CH_3CO + NH_3 and adding up this two constitutes all the products formed at low temperature. The yield for acetamide has a positive temperature dependence but it only contributes < 0.1% of the products when the temperature is below 400 K.

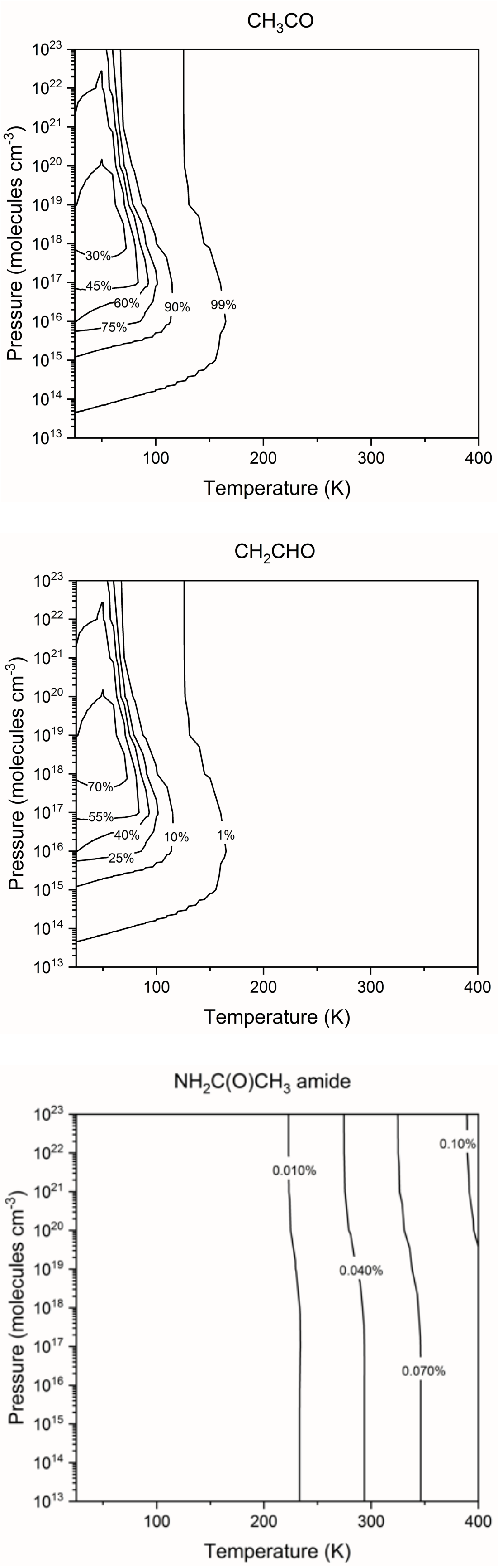

Figure 5.16 Percentage yields of different products of the NH_2 + CH_3CHO reaction as a function of temperature and pressure.

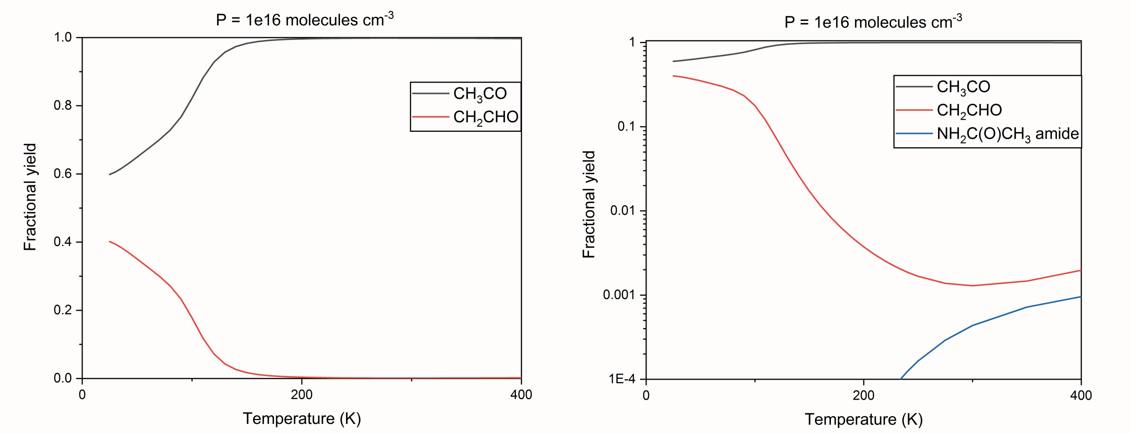

Figure 5.17 Fractional yields of different products of the NH_2 + CH_3CHO reaction as a function of temperature at $P = 10^{16}$ molecule cm^{-3}. On the left, the y-axis is on a linear scale and the yield of $NH_2C(O)CH_3$ amide is too small to be visible on the graph. On the right, the y-axis is on a logarithmic scale.

Such product distribution trends can be explained as follows. Kinetically the barrier for the H abstraction from the carbonyl group **TS_CH_3CO** is the lowest and thermodynamically CH_3CO + NH_3 is the most stable product set, and these make CH_3CO + NH_3 the dominant products at high temperature, as well as at low temperature when the pressure is low for complex stabilisation. Nonetheless, at low temperature, due to the availability of the indirect route via the pre-reaction complex followed by tunnelling, product yields by H abstraction from the methyl group become noticeable. In particular, as shown in Figure 5.7, the pre-reaction complex leading to CH_2CHO + NH_3, **VDW2**, is slightly more stable than that leading to CH_3CO + NH_3, **VDW1**. Thus, as the pressure increases to intermediate pressure, **VDW2** comes out first as shown in the time profile in Figure 5.13 as going into the potential well of **VDW2** is more preferred than that of **VDW1**. The lengthened lifetime of **VDW2** allows the chance of tunnelling to increase, together with a higher transmission probability to form CH_2CHO from **VDW2** than that to form CH_3CO from **VDW1**, resulting an increase in the yield through this channel. However, as the pressure increases even further, apart from stabilising in the potential well of **VDW2**, the potential well of **VDW1** also becomes populated. The similar argument applies, and with a longer lifetime for the pre-reaction complex and a higher probability of tunnelling, as a result, the yield for $CH_3CO + NH_3$ rises again. Basically at the high pressure limit, at low temperature the reactants stabilise in the two potential wells of the pre-reaction complexes first before the reaction further proceeds as re-dissociation is essentially zero, and the complexation step is the rate-limiting step. For acetamide, the yield remains low because of the presence of the positive barrier in the addition channel.

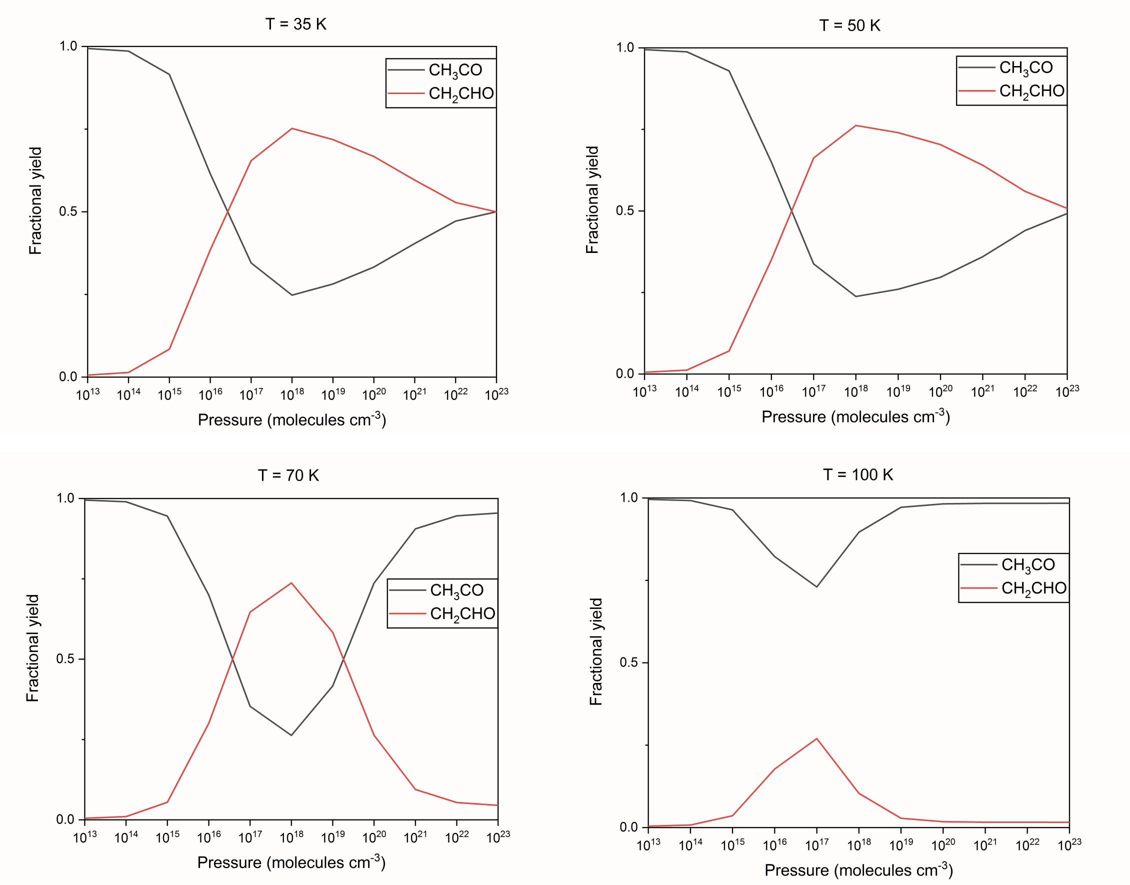

Figure 5.18 Fractional yields of different products of the $NH_2 + CH_3CHO$ reaction as a function of pressure at *T* = 35 K, 50 K, 70 K and 100 K respectively. The yield of $NH_2C(O)CH_3$ amide is too small to be visible on the graphs.

For the application to the ISM environment, the low pressure results should be considered, which means the rate coefficients are pressure independent and essentially $CH_3CO + NH_3$ are the only products. For the Laval experiments, they are carried out in the intermediate pressure regime. The measured rate coefficients will then be pressure dependent and products of H abstraction from either the carbonyl group or the methyl group can be formed.

A previously reported example of a change in the branching ratio of the product yield due to tunnelling at low temperature is the OH + CH_3OH reaction (48, 49) as shown in Chapter 1. H abstraction can occur at either the methyl site to form CH_2OH + H_2O or the hydroxyl site to form CH_3O + H_2O. Both channels involve positive barriers, where the transition state leading to CH_2OH is ~4 kJ mol^{-1} relative to the reactants and the one leading to CH_3O is even higher by ~10 kJ mol^{-1} (48-50). At room temperature, CH_2OH is the dominant product with a yield of ~64% but with the availability of forming a ~–20 kJ mol^{-1} pre-reaction complex, at low temperature tunnelling starts to play a significant role, where the yield for CH_3O becomes ~99% at 70 K (48). Apart from the barrier height, the tunnelling probability depends on the barrier width, which is related to the imaginary frequency, and a much larger imaginary frequency value for the transition state to CH_3O (2958 cm^{-1}) compared with that to CH_2OH (1420 cm^{-1}) is suggested to be the reason to favour a significant yield of CH_3O at low temperature through tunnelling (48). Considering the NH_2 + CH_3CHO reaction in this work, the unscaled imaginary frequency values obtained at M06-2X/aug-cc-pVTZ level for **TS_CH$_2$CHO** and **TS_CH$_3$CO** are 1763.61 cm^{-1} and 1200.89 cm^{-1} respectively. A larger imaginary frequency value for **TS_CH$_2$CHO** can therefore lead to a higher transmission probability, resulting in the increased yield of CH_2CHO at low temperature, despite the fact that the branching ratio at low temperature is not so extreme as that for OH + CH_3OH due to a smaller difference in the imaginary frequency values between **TS_CH$_2$CHO** and **TS_CH$_3$CO** and a noticeably higher barrier height of **TS_CH$_2$CHO**.

5.3.2.3 Troe fitting

Overall, the rate coefficient *k* of NH_2 + CH_3CHO depends on both the temperature and pressure. In order to provide an expression for modelling purposes, the rate coefficients obtained from MESMER are fitted with a Troe formalism (51-54). The Troe expression can be written as:

$$k'(T,[\mathrm{M}]) = \frac{k_0[\mathrm{M}]k_\infty}{k_\infty + k_0[\mathrm{M}]}F \qquad \text{E 5.3}$$

The fraction $\frac{k_0[\mathrm{M}]k_\infty}{k_\infty + k_0[\mathrm{M}]}$ in E 5.3 is actually the Lindemann expression with $k_0[\mathrm{M}]$ being the low pressure limit and k_∞ being the high pressure limit. The details of the Lindemann theory can be found in Chapter 1. Considering a plot of rate coefficient against pressure similar to that in Figure 5.10, at high pressure, the rate coefficient for a given temperature is pressure independent as it reaches the high pressure limit k_∞, while at low pressure the reaction rate coefficient increases with $[\mathrm{M}]$, with the slope given by k_0. In between these two extremes the plot shows curvature, known as the fall-off region. In order to better fit these curved plots than is possible via the simple Lindemann expression, a broadening factor F is introduced in the Troe expression. In this work, k_0 and k_∞ are fitted respectively as modified Arrhenius expressions as follows:

$$k_0 = A_{\mathrm{low}}\left(\frac{T}{298}\right)^{n_{\mathrm{low}}} e^{-\frac{E_{\mathrm{low}}}{RT}} \qquad \text{E 5.4}$$

$$k_\infty = A_{\mathrm{high}}\left(\frac{T}{298}\right)^{n_{\mathrm{high}}} e^{-\frac{E_{\mathrm{high}}}{RT}} \qquad \text{E 5.5}$$

The broadening factor *F* is represented by:

$$\log F = \frac{\log F_{\mathrm{cent}}}{1 + \left(\frac{\log \frac{k_0[\mathrm{M}]}{k_\infty}}{N}\right)^2} \qquad \text{E 5.6}$$

where the centre broadening factor F_{cent} and the width parameter N are fitted respectively by the following:

$$F_{\mathrm{cent}} = e^{-\frac{T}{F_{\mathrm{cent},T}}} \qquad \text{E 5.7}$$

$$N = p - 1.27\log F_{\mathrm{cent}} \qquad \text{E 5.8}$$

Typically a Troe expression with the above parameters is already capable of fitting quite well the reaction rate coefficients, such as the addition reaction of OH to isoprene $CH_2{=}C(CH_3){-}CH{=}CH_2$ (55) or the decomposition of alkyl hydroperoxy radical QOOH into a cyclic ether and OH (56). However, this is not case for the NH_2 + CH_3CHO reaction. Considering the fraction $\frac{k_0[\mathrm{M}]k_\infty}{k_\infty + k_0[\mathrm{M}]}$ in E 5.3, when the total pressure is approaching zero, the rate coefficient should keep decreasing down to zero, but this contradicts with the results shown in Figure 5.10. With quantum mechanical tunnelling, the rate coefficients for NH_2 + CH_3CHO reach a plateau instead of zero when the pressure further decreases. To cater for the contribution from tunnelling in the reaction rate coefficient, k_{tunnel} is introduced and is given by:

$$k_{\mathrm{tunnel}} = A_{\mathrm{tunnel}} \left(\frac{T}{298}\right)^{n_{\mathrm{tunnel}}} e^{-E_{\mathrm{tunnel}}T} \qquad \text{E 5.9}$$

The Troe expression used to fit the rate coefficients then becomes:

$$k(T, [\mathrm{M}]) = \frac{k_0[\mathrm{M}]k_\infty}{k_\infty + k_0[\mathrm{M}]} F + k_{\mathrm{tunnel}} \qquad \text{E 5.10}$$

where the fitted parameters include A_{low}, n_{low}, E_{low}, A_{high}, n_{high}, E_{high}, $F_{\mathrm{cent},T}$, p, A_{tunnel}, n_{tunnel} and E_{tunnel}, which has previously been successfully used to fit to for instance the H abstraction reaction of OH from acetone $(CH_3)_2CO$ (57). All of the data points for the conditions *T* = 25–400 K, *P* = 10^{13}–10^{23} molecule cm^{-3} obtained from MESMER calculations are used for fitting and by assigning a 10% error to all the data points as the weighting, the set of optimised parameters are presented in Table 5.3 with a reduced χ^2 value of 5.88. The Troe fits together with the MESMER calculated rate coefficients against pressure at selected temperatures are shown in Figure 5.19.

The set of optimised parameters presented in Table 5.3 are recommended for modelling with E 1.10. However, it is important to note that the ISM is sparsely populated, that is, the number density is extremely low, and so under such conditions the zero-pressure limit can be taken as the reaction rate coefficient, of which the Troe expression is reduced to only containing the k_{tunnel} term, that is to say:

$$k = 6.57 \times 10^{-19} \left(\frac{T}{298}\right)^{-5.40} e^{0.029T}\ \mathrm{cm}^3\ \mathrm{molecule}^{-1}\ \mathrm{s}^{-1} \qquad \text{E 5.11}$$

Table 5.3 The set of optimised Troe fit parameters for the MESMER calculated rate coefficients for the NH_2 + CH_3CHO reaction

A_{low} / cm^6 molecule^{-2} s^{-1}	2.54 × 10^{-28}
n_{low}	1.21
E_{low} / J mol^{-1}	–374
A_{high} / cm^3 molecule^{-1} s^{-1}	4.21 × 10^{-12}
n_{high}	–6.73
E_{high} / J mol^{-1}	2057
$F_{\mathrm{cent},T}$ / K	30.1
p	43.3
A_{tunnel} / cm^3 molecule^{-1} s^{-1}	6.57 × 10^{-19}
n_{tunnel}	–5.40
E_{tunnel} / K^{-1}	–0.029

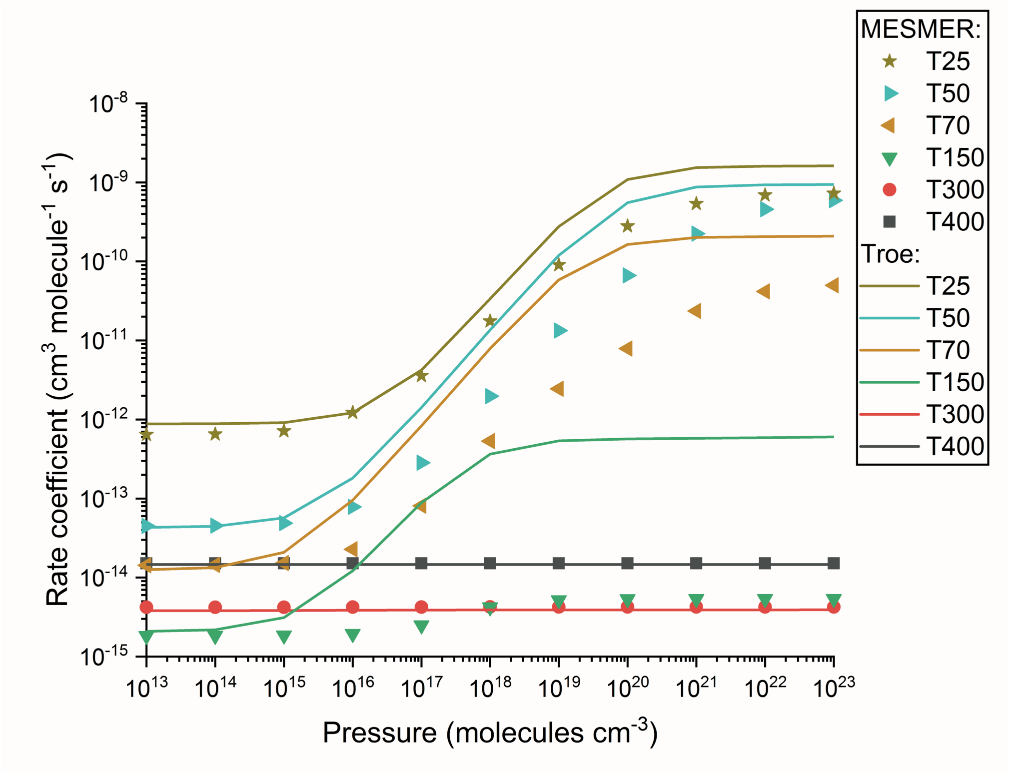

Figure 5.19 The Troe fits to the MESMER calculated rate coefficients for the NH_2 + CH_3CHO reaction at various temperatures. The markers are the MESMER calculated rate coefficients while the lines of the same colour are the Troe fits. The legend denotes the temperatures from 25 K to 400 K.

5.4 Conclusion

To conclude, in this chapter, the NH_2 + CH_3CHO reaction is studied theoretically by performing ab initio calculations followed by rate coefficient calculations. A detailed potential energy surface is obtained from the ab initio results, where three product channels are found, namely H abstraction at the carbonyl site to form CH_3CO + NH_3, H abstraction at the methyl site to form CH_2CHO + NH_3 and addition to form a C–N bond that eventually gives $NH_2C(O)CH_3$ + H. All three channels involve positive barriers but pre-reaction complex structures have also been found. By considering the full PES, for the conditions T = 25–400 K, P = 10^{13}–10^{23} molecule cm^{-3}, rate coefficients are obtained which match the experimental results in terms of the trend of the temperature dependence. The calculated rate coefficient values are in line with the measured values at room temperature or above while smaller by 1–2 orders of magnitude at cryogenic temperatures. At high temperature the rate coefficient is pressure independent and has a positive temperature dependence while at low temperature the rate coefficient is pressure dependent and has a negative temperature dependence. While at high temperature the reaction proceeds directly, this switch in the temperature dependence can be explained by an indirect reaction mechanism involving the formation of pre-reaction complexes followed by quantum mechanical tunnelling which becomes important at low temperature. The importance of tunnelling in changing the reaction rate coefficient and product branching ratio is demonstrated and the pre-reaction complexes and positive barriers have to be taken into account when rationalising the reaction mechanism.

The product branching ratio is pressure and temperature dependent, with CH_3CO + NH_3 being the major products under most conditions. At low temperature, as the pressure increases, the yield for CH_2CHO + NH_3 becomes comparable. However, under the ISM conditions with an extremely low particle density, essentially the reaction will proceed by abstracting a hydrogen at the carbonyl site to form CH_3CO. The yield of acetamide formation via addition is tiny, and so NH_2 + CH_3CHO is unlikely to be the gas-phase reaction that can substantially generate acetamide in the ISM, which means the research on other alternative reactions will be needed to explain its formation in the ISM. The overall reaction rate as a function of temperature and pressure is fitted with a Troe expression in the form of $k(T,[\mathrm{M}]) = \frac{k_0[\mathrm{M}]k_\infty}{k_\infty + k_0[\mathrm{M}]}F + k_{\mathrm{tunnel}}$, where in the sparsely populated ISM this can be reduced to $k(T) = k_{\mathrm{tunnel}} = 6.57 \times 10^{-19}\left(\frac{T}{298}\right)^{-5.40} e^{0.029T}\ \mathrm{cm^3\ molecule^{-1}\ s^{-1}}$. This provides a new expression for astrochemical modelling, as this neutral-neutral reaction was previously unexplored under low temperature conditions.

5.5 References

1. Saladino, R., Crestini, C., Pino, S., Costanzo, G. and Di Mauro, E. Formamide and the origin of life. *Physics of Life Reviews.* 2012, **9**(1), pp.84-104.

2. Saladino, R., Botta, G., Pino, S., Costanzo, G. and Di Mauro, E. Genetics first or metabolism first? The formamide clue. *Chemical Society Reviews.* 2012, **41**(16), pp.5526-5565.

3. Rubin, R.H., Swenson, G.W., Jr., Benson, R.C., Tigelaar, H.L. and Flygare, W.H. Microwave Detection of Interstellar Formamide. *The Astrophysical Journal.* 1971, **169**, p.L39.

4. Adande, G.R., Woolf, N.J. and Ziurys, L.M. Observations of Interstellar Formamide: Availability of a Prebiotic Precursor in the Galactic Habitable Zone. *Astrobiology.* 2013, **13**(5), pp.439-453.

5. López-Sepulcre, A., Jaber, A.A., Mendoza, E., Lefloch, B., Ceccarelli, C., Vastel, C., Bachiller, R., Cernicharo, J., Codella, C., Kahane, C., Kama, M. and Tafalla, M. Shedding light on the formation of the pre-biotic molecule formamide with ASAI. *Monthly Notices of the Royal Astronomical Society.* 2015, **449**(3), pp.2438-2458.

6. Corby, J.F., Jones, P.A., Cunningham, M.R., Menten, K.M., Belloche, A., Schwab, F.R., Walsh, A.J., Balnozan, E., Bronfman, L., Lo, N. and Remijan, A.J. An ATCA survey of Sagittarius B2 at 7 mm: chemical

complexity meets broad-band interferometry. *Monthly Notices of the Royal Astronomical Society.* 2015, **452**(4), pp.3969-3993.

7. Halfen, D.T., Ilyushin, V. and Ziurys, L.M. Formation of peptide bonds in space: a comprehensive study of formamide and acetamide in Sgr B2(N). *The Astrophysical Journal.* 2011, **743**(1), p.60.

8. Hollis, J.M., Lovas, F.J., Remijan, A.J., Jewell, P.R., Ilyushin, V.V. and Kleiner, I. Detection of Acetamide (CH_3CONH_2): The Largest Interstellar Molecule with a Peptide Bond. *The Astrophysical Journal.* 2006, **643**(1), pp.L25-L28.

9. Belloche, A., Meshcheryakov, A.A., Garrod, R.T., Ilyushin, V.V., Alekseev, E.A., Motiyenko, R.A., Margulès, L., Müller, H.S.P. and Menten, K.M. Rotational spectroscopy, tentative interstellar detection, and chemical modeling of N-methylformamide. *Astronomy & Astrophysics.* 2017, **601**.

10. Belloche, A., Garrod, R.T., Müller, H.S.P., Menten, K.M., Medvedev, I., Thomas, J. and Kisiel, Z. Re-exploring Molecular Complexity with ALMA (ReMoCA): interstellar detection of urea. *Astronomy & Astrophysics.* 2019, **628**.

11. Li, J., Wang, J., Lu, X., Ilyushin, V., Motiyenko, R.A., Gou, Q., Alekseev, E.A., Quan, D., Margulès, L., Gao, F., Lovas, F.J., Wu, Y., Bergin, E., Li, S., Shen, Z., Du, F., Li, M., Zheng, S. and Zheng, X. Propionamide ($C_2H_5CONH_2$): The Largest Peptide-like Molecule in Space. *The Astrophysical Journal.* 2021, **919**(1), p.4.

12. Jones, B.M., Bennett, C.J. and Kaiser, R.I. Mechanistical studies on the production of formamide (H_2NCHO) within interstellar ice analogs. *The Astrophysical Journal.* 2011, **734**(2), p.78.

13. Ligterink, N.F.W., Terwisscha van Scheltinga, J., Taquet, V., Jørgensen, J.K., Cazaux, S., van Dishoeck, E.F. and Linnartz, H. The formation of peptide-like molecules on interstellar dust grains. *Monthly Notices of the Royal Astronomical Society.* 2018, **480**(3), pp.3628-3643.

14. Noble, J.A., Theule, P., Congiu, E., Dulieu, F., Bonnin, M., Bassas, A., Duvernay, F., Danger, G. and Chiavassa, T. Hydrogenation at low

temperatures does not always lead to saturation: the case of HNCO. *Astronomy & Astrophysics.* 2015, **576**.

15. Ali, M.A. Theoretical study on the gas phase reaction of $CH_2O + NH_3$: the formation of $CH_2O \cdots NH_3$, NH_2CH_2OH, or $CH_2NH + H_2O$. *Physical Chemistry Chemical Physics.* 2019, **21**(35), pp.19242-19251.

16. Redondo, P., Barrientos, C. and Largo, A. Peptide bond formation through gas-phase reactions in the interstellar medium: formamide and acetamide as prototypes. *The Astrophysical Journal.* 2014, **793**(1), p.32.

17. Darla, N. and Sitha, S. Reaction between NH_3 ($\check{X}^1A_1$) and CO ($X^1\Sigma^+$): A Computational Insight into the Reaction Mechanism of Formamide (H_2N–CHO) Formation. *The Journal of Physical Chemistry A.* 2019, **123**(41), pp.8921-8931.

18. Barone, V., Latouche, C., Skouteris, D., Vazart, F., Balucani, N., Ceccarelli, C. and Lefloch, B. Gas-phase formation of the prebiotic molecule formamide: insights from new quantum computations. *Monthly Notices of the Royal Astronomical Society: Letters.* 2015, **453**(1), pp.L31-L35.

19. Vazart, F., Calderini, D., Puzzarini, C., Skouteris, D. and Barone, V. State-of-the-Art Thermochemical and Kinetic Computations for Astrochemical Complex Organic Molecules: Formamide Formation in Cold Interstellar Clouds as a Case Study. *Journal of Chemical Theory and Computation.* 2016, **12**(11), pp.5385-5397.

20. Skouteris, D., Vazart, F., Ceccarelli, C., Balucani, N., Puzzarini, C. and Barone, V. New quantum chemical computations of formamide deuteration support gas-phase formation of this prebiotic molecule. *Monthly Notices of the Royal Astronomical Society: Letters.* 2017, **468**(1), pp.L1-L5.

21. Strobel, D.F. Photochemistry of the Reducing Atmospheres of Jupiter, Saturn and Titan. *International Reviews in Physical Chemistry.* 1983, **3**(2), pp.145-176.

22. Yung, Y.L., Allen, M. and Pinto, J.P. Photochemistry of the atmosphere of Titan - Comparison between model and observations. *Astrophysical Journal Supplement Series.* 1984, **55**, pp.465-506.

23. Loison, J.C., Hébrard, E., Dobrijevic, M., Hickson, K.M., Caralp, F., Hue, V., Gronoff, G., Venot, O. and Bénilan, Y. The neutral photochemistry of nitriles, amines and imines in the atmosphere of Titan. *Icarus.* 2015, **247**, pp.218-247.

24. van Dishoeck, E.F., Jansen, D.J., Schilke, P. and Phillips, T.G. Detection of the Interstellar NH_2 Radical. *The Astrophysical Journal.* 1993, **416**, p.L83.

25. Song, L. and Kästner, J. Formation of the prebiotic molecule NH_2CHO on astronomical amorphous solid water surfaces: accurate tunneling rate calculations. *Physical Chemistry Chemical Physics.* 2016, **18**(42), pp.29278-29285.

26. Li, Q.S. and Lü, R.H. Direction Dynamics Study of the Hydrogen Abstraction Reaction $CH_2O + NH_2 \rightarrow CHO + NH_3$. *The Journal of Physical Chemistry A.* 2002, **106**(41), pp.9446-9450.

27. Ruscic, B. and Bross, D.H. *Active Thermochemical Tables (ATcT) values based on ver. 1.122g of the Thermochemical Network.* [Online]. 2019. [Accessed 29/09/2022]. Available from: https://atct.anl.gov/Thermochemical%20Data/version%201.122g/index.php

28. Douglas, K.M., Lucas, D.I., Walsh, C., West, N.A., Blitz, M.A. and Heard, D.E. The Gas-phase Reaction of NH_2 with Formaldehyde (CH_2O) is not a Source of Formamide (NH_2CHO) in Interstellar Environments. *The Astrophysical Journal Letters.* 2022, **937**(1), p.L16.

29. Matthews, H.E., Friberg, P. and Irvine, W.M. The detection of acetaldehyde in cold dust clouds. *The Astrophysical Journal.* 1985, **290**, pp.609-614.

30. Hack, W., Kurzke, H., Rouveirolles, P. and Wagner, H.G. Hydrogen Abstraction Reactions by $NH_2(\tilde{X}^2B_1)$-Radicals from Hydrocarbons in the

Gas Phase. *Berichte der Bunsengesellschaft für physikalische Chemie.* 1986, **90**(12), pp.1210-1219.

31. Frisch, M.J., Trucks, G.W., Schlegel, H.B., Scuseria, G.E., Robb, M.A., Cheeseman, J.R., Scalmani, G., Barone, V., Mennucci, B., Petersson, G.A., Nakatsuji, H., Caricato, M., Li, X., Hratchian, H.P., Izmaylov, A.F., Bloino, J., Zheng, G., Sonnenberg, J.L., Hada, M., Ehara, M., Toyota, K., Fukuda, R., Hasegawa, J., Ishida, M., Nakajima, T., Honda, Y., Kitao, O., Nakai, H., Vreven, T., J. A. Montgomery, J., Peralta, J.E., Ogliaro, F., Bearpark, M., Heyd, J.J., Brothers, E., Kudin, K.N., Staroverov, V.N., Keith, T., Kobayashi, R., Normand, J., Raghavachari, K., Rendell, A., Burant, J.C., Iyengar, S.S., Tomasi, J., Cossi, M., Rega, N., Millam, J.M., Klene, M., Knox, J.E., Cross, J.B., Bakken, V., Adamo, C., Jaramillo, J., Gomperts, R., Stratmann, R.E., Yazyev, O., Austin, A.J., Cammi, R., Pomelli, C., Ochterski, J.W., Martin, R.L., Morokuma, K., Zakrzewski, V.G., Voth, G.A., Salvador, P., Dannenberg, J.J., Dapprich, S., Daniels, A.D., Farkas, O., Foresman, J.B., Ortiz, J.V., Cioslowski, J. and Fox, D.J. *Gaussian 09 Revision D.01*. Wallingford CT: Gaussian, Inc. 2013.

32. Becke, A.D. A new mixing of Hartree–Fock and local density-functional theories. *The Journal of Chemical Physics.* 1993, **98**(2), pp.1372-1377.

33. Dunning, T.H. Gaussian basis sets for use in correlated molecular calculations. I. The atoms boron through neon and hydrogen. *The Journal of Chemical Physics.* 1989, **90**(2), pp.1007-1023.

34. Kendall, R.A., Dunning, T.H. and Harrison, R.J. Electron affinities of the first-row atoms revisited. Systematic basis sets and wave functions. *The Journal of Chemical Physics.* 1992, **96**(9), pp.6796-6806.

35. Woon, D.E. and Dunning Jr., T.H. Gaussian basis sets for use in correlated molecular calculations. V. Core-valence basis sets for boron through neon. *The Journal of Chemical Physics.* 1995, **103**(11), pp.4572-4585.

36. Zhao, Y. and Truhlar, D.G. The M06 suite of density functionals for main group thermochemistry, thermochemical kinetics, noncovalent interactions, excited states, and transition elements: two new functionals and systematic testing of four M06-class functionals and 12 other functionals. *Theoretical Chemistry Accounts.* 2008, **120**(1), pp.215-241.

37. Laury, M.L., Boesch, S.E., Haken, I., Sinha, P., Wheeler, R.A. and Wilson, A.K. Harmonic vibrational frequencies: Scale factors for pure, hybrid, hybrid meta, and double-hybrid functionals in conjunction with correlation consistent basis sets. *Journal of Computational Chemistry.* 2011, **32**(11), pp.2339-2347.

38. *NIST Computational Chemistry Comparison and Benchmark Database.* [Online]. [Accessed 29/09/2022]. Available from: http://cccbdb.nist.gov/

39. Pople, J.A., Krishnan, R., Schlegel, H.B. and Binkley, J.S. Electron correlation theories and their application to the study of simple reaction potential surfaces. *International Journal of Quantum Chemistry.* 1978, **14**(5), pp.545-560.

40. Bartlett, R.J. and Purvis, G.D. Many-body perturbation theory, coupled-pair many-electron theory, and the importance of quadruple excitations for the correlation problem. *International Journal of Quantum Chemistry.* 1978, **14**(5), pp.561-581.

41. Glowacki, D.R., Liang, C.-H., Morley, C., Pilling, M.J. and Robertson, S.H. MESMER: An Open-Source Master Equation Solver for Multi-Energy Well Reactions. *The Journal of Physical Chemistry A.* 2012, **116**(38), pp.9545-9560.

42. Marcus, R.A. Unimolecular Dissociations and Free Radical Recombination Reactions. *The Journal of Chemical Physics.* 1952, **20**(3), pp.359-364.

43. Miller, W.H. Tunneling corrections to unimolecular rate constants, with application to formaldehyde. *Journal of the American Chemical Society.* 1979, **101**(23), pp.6810-6814.

44. Davies, J.W., Green, N.J.B. and Pilling, M.J. The testing of models for unimolecular decomposition via inverse laplace transformation of experimental recombination rate data. *Chemical Physics Letters.* 1986, **126**(3), pp.373 - 379.

45. Herbst, E. Tunneling in the C_2H-H_2 reaction at low temperature. *Chemical Physics Letters.* 1994, **222**(3), pp.297-301.

46. Shannon, R.J. *Experimental and computational studies of hydroxyl radical kinetics at very low temperatures*. Dissertation/Thesis thesis, University of Leeds, 2012.

47. Troe, J. Theory of thermal unimolecular reactions at low pressures. I. Solutions of the master equation. *The Journal of Chemical Physics.* 1977, **66**(11), pp.4745-4757.

48. Shannon, R.J., Blitz, M.A., Goddard, A. and Heard, D.E. Accelerated chemistry in the reaction between the hydroxyl radical and methanol at interstellar temperatures facilitated by tunnelling. *Nature Chemistry.* 2013, **5**(9), pp.745-749.

49. Ocaña, A.J., Blázquez, S., Potapov, A., Ballesteros, B., Canosa, A., Antiñolo, M., Vereecken, L., Albaladejo, J. and Jiménez, E. Gas-phase reactivity of CH_3OH toward OH at interstellar temperatures (11.7–177.5 K): experimental and theoretical study. *Physical Chemistry Chemical Physics.* 2019, **21**(13), pp.6942-6957.

50. Xu, S. and Lin, M.C. Theoretical study on the kinetics for OH reactions with CH_3OH and C_2H_5OH. *Proceedings of the Combustion Institute.* 2007, **31**(1), pp.159-166.

51. Troe, J. Predictive possibilities of unimolecular rate theory. *The Journal of Physical Chemistry.* 1979, **83**(1), pp.114-126.

52. Gilbert, R.G., Luther, K. and Troe, J. Theory of Thermal Unimolecular Reactions in the Fall-off Range. II. Weak Collision Rate Constants. *Berichte der Bunsengesellschaft für physikalische Chemie.* 1983, **87**(2), pp.169-177.

53. Troe, J. and Ushakov, V.G. Representation of “Broad” Falloff Curves for Dissociation and Recombination Reactions. *Zeitschrift für Physikalische Chemie.* 2014, **228**(1), pp.1-10.

54. Holbrook, K.A., Pilling, M.J., Robertson, S.H. and Robinson, P.J. *Unimolecular reactions.* Second edition. ed. Chichester: Wiley, 1996.

55. Medeiros, D.J., Blitz, M.A., James, L., Speak, T.H. and Seakins, P.W. Kinetics of the Reaction of OH with Isoprene over a Wide Range of

Temperature and Pressure Including Direct Observation of Equilibrium with the OH Adducts. *The Journal of Physical Chemistry A.* 2018, **122**(37), pp.7239-7255.

56. Whelan, C.A., Blitz, M.A., Shannon, R., Onel, L., Lockhart, J.P., Seakins, P.W. and Stone, D. Temperature and Pressure Dependent Kinetics of QOOH Decomposition and Reaction with O_2: Experimental and Theoretical Investigations of QOOH Radicals Derived from Cl + $(CH_3)_3COOH$. *The Journal of Physical Chemistry A.* 2019, **123**(47), pp.10254-10262.

57. Shannon, R.J., Caravan, R.L., Blitz, M.A. and Heard, D.E. A combined experimental and theoretical study of reactions between the hydroxyl radical and oxygenated hydrocarbons relevant to astrochemical environments. *Physical Chemistry Chemical Physics.* 2014, **16**(8), pp.3466-3478.

Chapter 6

Theoretical calculations of dimerisation reactions in the context of Laval nozzle experiments

6.1 Introduction

Dimerisation refers to the conversion of two monomers to form a dimer (1). The formation of an equivalent dimer, assuming it is non-reversible, can be represented as

$$2\mathrm{A} \rightarrow \mathrm{A}_2 \qquad \text{R 6.1}$$

and the removal rate of the monomer A and the formation rate of the dimer A_2 can be related by:

$$-\frac{d[\mathrm{A}]}{dt} = 2\frac{d[\mathrm{A}_2]}{dt} \qquad \text{E 6.1}$$

The bimolecular rate coefficient of the loss of monomers k_{loss} is defined by:

$$\frac{d[\mathrm{A}]}{dt} = -k_{\mathrm{loss}}[\mathrm{A}]^2 \qquad \text{E 6.2}$$

and integration of E 1.2 gives the following:

$$\frac{1}{[\mathrm{A}]} = \frac{1}{[\mathrm{A}]_0} + k_{\mathrm{loss}}t \qquad \text{E 6.3}$$

where $[\mathrm{A}]_0$ refers to the initial monomer concentration.

While the number densities of different regions in the interstellar medium span from 10^{-3} – 10^{6} molecule cm^{-3} (2-4), where the chance for the gaseous organic molecules encountering an identical entity within the lifetime of the species to form a dimer is very limited, the motivation for this chapter is to understand the experimental observations potentially arising from dimerisation in the kinetics experiment performed using the Laval nozzle setup.

The study of dimer formation is a broad research area with numerous examples, a notable one is the NO_2/N_2O_4 system

$$2\mathrm{NO}_2(\mathrm{g}) \rightleftharpoons \mathrm{N}_2\mathrm{O}_4(\mathrm{g}) \qquad \text{R 6.2}$$

The equilibrium is attained when the forward reaction rate is equal to the reverse reaction rate, with the equilibrium constant K defined as:

$$K = \frac{k_{\mathrm{forward}}}{k_{\mathrm{reverse}}} = \frac{[\mathrm{N_2O_4}]_{\mathrm{eqm}}}{[\mathrm{NO_2}]_{\mathrm{eqm}}{}^2} = \frac{q_{\mathrm{N_2O_4}}}{q_{\mathrm{NO_2}}{}^2} e^{(-\Delta E/RT)} \qquad \text{E 6.4}$$

where $q_{\mathrm{N_2O_4}}$ and $q_{\mathrm{NO_2}}$ are the partition functions of the respective species. At a given time t, one can determine the direction of the reaction by considering the reaction quotient Q, where:

$$Q = \frac{[\mathrm{N_2O_4}]_t}{[\mathrm{NO_2}]_t{}^2} \qquad \text{E 6.5}$$

When $Q < K$, the reaction proceeds from left to right and vice versa when $Q > K$. $Q = K$ when the reaction reaches equilibrium. As the NO_2 gas has a distinct reddish brown colour while the N_2O_4 gas is colourless, experiments can be carried out by using the colour intensity of the gas mixture as an indicator of the shift of the equilibrium at different conditions, for instance with a UV-vis spectrophotometer (5). The values of K, both measured and calculated in previous studies (5-10), increase, that is, the formation of N_2O_4 is favoured at decreasing temperature. This change can be explained by Le Chatelier's principle which states that when a dynamic equilibrium is subjected to a change in conditions, the position of equilibrium will shift to counteract the change to re-establish the equilibrium. The overall dimerisation reaction of NO_2 is found to be exothermic with $\Delta H_{298\mathrm{K}}$ found to be –57.3 – –55.1 kJ mol^{-1} (6, 11), where calculations at B3LYP and CASSCF levels demonstrate that there is no barrier (12, 13). The existence of the unpaired electron makes NO_2 monomers readily to form N–N bonds to give the symmetric form of N_2O_4 (14). As N_2O_4 is held by N–N covalent bond, it is classified as a covalent dimer.

Another example of a covalent bonded dimer is dioxetane, which can be considered as the combination of two formaldehyde (CH_2O) monomers. However, this dimerisation is endothermic as it involves the cleavage of the C=O π bond in both of the monomers to form a four-membered ring. The electronic energy of 1,2-dioxetane, where its structure is shown in Figure 6.1, is reported to be 251 – 309 kJ mol^{-1} higher than that of two CH_2O monomers and it requires an extra 75 – 92 kJ mol^{-1} to overcome the reaction barrier (15-17).

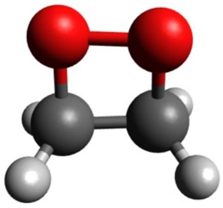

Figure 6.1 Structure of 1,2-dioxetane ($C_2O_2H_4$).

Apart from covalent bonds, dimers can also be formed and held together by intermolecular forces, which are known as non-covalent dimers. The simplest case is the coming together of inert gas atoms, for instance, two argon (Ar) atoms capable to form an argon dimer because of the presence of London dispersion forces. Information of the potential well of the approach of the two Ar atoms, which in turn gives insight into the equilibrium distance and binding energy, has been explored experimentally by scattering or spectroscopic techniques (18-24). For the results from ab initio calculations, the binding energy of the argon dimer is found to be 1.11 – 1.19 kJ mol^{-1}, which reflects the weak nature of the dispersion forces, with an equilibrium internuclear distance of 3.75 – 3.77 Å (25-27).

Non-covalent dimers with deeper potential wells are possible when polar molecules are involved as the two monomers can be bound to each other by electrostatic forces between opposite dipoles. Stronger interaction between the two monomers can also be found when the formation of H bond is available. Notable examples include HF and H_2O, where the computed zero-point corrected dissociation energies of $(HF)_2$ and $(H_2O)_2$ are reported to be 12.4 – 12.8 kJ mol^{-1} (28, 29) and 13.2 – 14.9 kJ mol^{-1} (30, 31) respectively. A range of spectroscopic experiments (32-57) have been performed to investigate in the properties of $(HF)_2$ and $(H_2O)_2$ in order to provide insight into the structure and the electronic potential of the dimers. One of the common methods to provide a source of the dimer in these experiments is through supersonic jet expansion via a nozzle to generate low temperature conditions for the weakly bound dimers to exist. Research effort has also been extended to heterodimers, such as H_2O - - - HF (58-64), or with the involvement of the buffer gas like Ar - - - HF

(65-78) and Ar - - - H_2O (79-94) where dipole-induced dipole forces are in effect to hold them together, or the aggregation to higher order oligomers or clusters (95-99). In particular, uniform supersonic flows are used to generate the clusters for the studies of the nucleation process during phase transitions (100), and by coupling with mass spectrometry (101-106), X-ray or neutron scattering (107-113) and Fourier-transform infrared spectroscopy (106-108, 114-121), properties of the condensed particles like the size, the composition and the structure can be known.

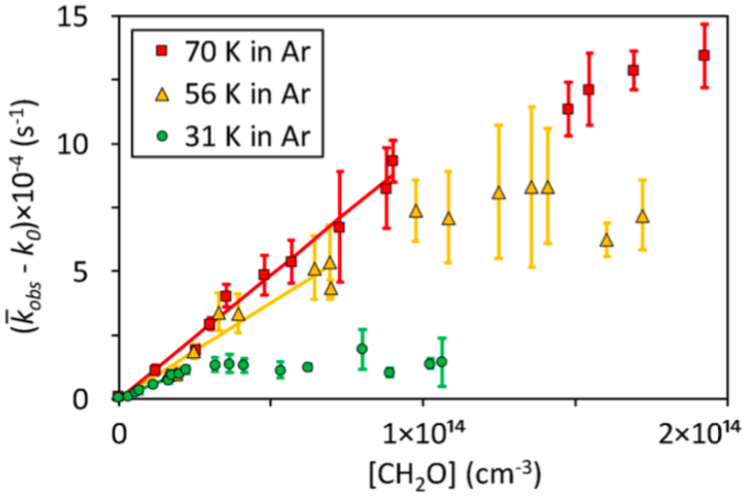

Figure 6.2 Rate of loss of CH radical against the concentration of CH_2O at different temperatures: red: 70 K; yellow: 56 K; green: 31 K, for an overall density of [Ar] = 10^{16}–10^{17} molecule cm^{-3}. The straight lines are the linear least-square fits to the data, where the data points obtained at higher concentrations of CH_2O are observed to be lying below this linear trend, which is thought to be due to the dimerisation of CH_2O. Taken from West et al. (122).

In contrast to nucleation experiments where the clusters are intended to be made (100), suitable conditions need to be chosen in order for any dimerisation not to have an impact during kinetic measurements. Typically for the radical-neutral reactions, as mentioned in Chapter 1, the radicals in the gas flow are generated by laser flash photolysis (LFP) and then the concentrations of the radicals are measured as a function of time following reaction initiation with the laser induced fluorescence technique (LIF) to monitor their rate of loss. Repeating the experiments with different concentrations of excess reactants and plotting the observed rates of loss versus the concentration of the excess reagent generate the bimolecular plots. Two examples are presented here in Figure 6.2 and Figure 6.3, which correspond to the CH + CH_2O reaction (122) and OH + $CH_3C(O)CH_3$ reaction (123, 124) respectively.

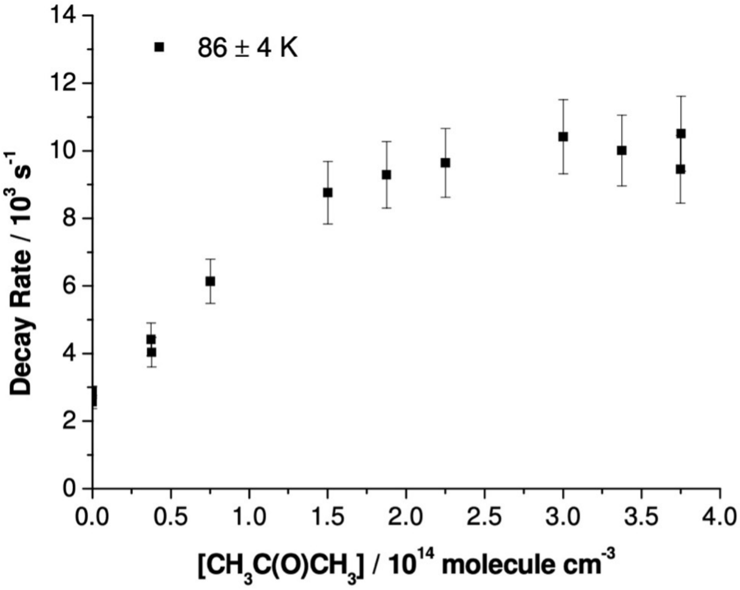

Figure 6.3 Rate of loss of OH radicals as a function of the concentration of $CH_3C(O)CH_3$ at 86 ± 4 K using *tu*-BuOOH as the precursor and N_2 as the bath gas with [M] = 4 × 10^{16} molecule cm^{-3}. Negative curvature is observed in the bimolecular plot at higher concentrations. Taken from Taylor (123).

The slope of the linear portion of the plots, mainly the part with lower concentration of excess reactants, was taken to be the measured bimolecular rate coefficient. However, deviation from the linear trend in the bimolecular plots was observed when the concentration of the excess reactants further increased and it is essential not to consider this portion in the reported experimental bimolecular rate coefficient. A plausible explanation for the negative curvature shown is that with a high concentration of excess reactant monomers, dimers or even higher order oligomers of the excess reactants were formed and their rate coefficients with the radicals were smaller than those in monomer form. This competing reaction is undesirable when the reaction of interest is that between the radical and the monomer form of the excess reactant. Thus, it is important to understand the dimerisation reaction and its effect on the measurement of rate coefficients in the Laval setup, with the work being done in this Chapter aiming to determine via computation the structure and energetics of the dimers. The kinetics of the dimerisation reaction will also be determined, particularly the reaction which takes places in the section along the gas flow, where dimers or higher oligomers can potentially be formed, reducing the proportion of monomers left in the Laval experiment. The analysis will cover the region within and out of the nozzle, where the latter is in the uniform flow region.

The effect of the dimerisation of methanol (CH_3OH) in the Laval experiment on the radical-methanol reaction has been discussed in the previous literature in the context of determining the rate coefficient for OH + CH_3OH reaction (125-129). The non-covalent dimer of methanol as shown in Figure 6.4 has a reported binding energy of ~18 kJ mol^{-1} (128, 130). Together with the temperature and density profiles within a 52 K nozzle used in the experiment (126), MESMER calculations were done to obtain the dimerisation rates, which were used to estimate the upper limit of the fraction of dimers formed all the way from the expansion region within the nozzle to the stable flow region outside of the nozzle during the Laval experiment. For an experiment with 0.5% of the total concentration as the initial concentration of CH_3OH, which is towards the higher end of concentrations used in experiments, and nitrogen N_2 as the bath gas, it was reported (128) that theoretically at least 92.8 ± 4.2% of methanol should remain in the monomer form at the exit of the 52 K nozzle, and if continuing into the stable flow region, for a 56 K experiment with $[\text{methanol}]_0 = 2.2 \times 10^{14}$ molecule cm^{-3}, 82.2 ± 9.4% remain as monomers when the Laval reaction window was taken to be 300 μs, which can be considered as the maximum time for the flow to reach the end of the reaction distance and the measurements to be taken.

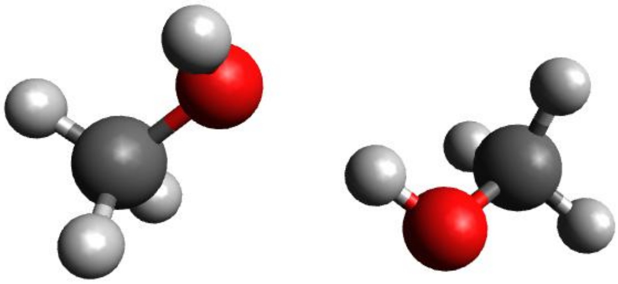

Figure 6.4 Structure of the methanol non-covalent dimer.

Similar calculations have been done for formaldehyde CH_2O, acetaldehyde CH_3CHO, acetone $CH_3C(O)CH_3$ and ammonia NH_3, which are polar molecules which have been used by our group in the Laval nozzle setup that can potentially form non-covalent dimers, and the results are reported in this chapter. For CH_2O, while earlier literature (131) suggested that three stable non-covalent dimer structures (with C_s, C_{2h} and C_{2v} symmetry) were found with C_{2h} being the most stable, later literature (132-135) suggested that only C_s and C_{2h} are stable with C_s being the more stable structure. For the structure of the CH_3CHO dimer, six minima were obtained in the earlier studies (136, 137) while a more recent work (138) at more advanced level of theory reported eight minima. Two minima were obtained for the $CH_3C(O)CH_3$ dimer in the previous study (139). For the structures of the NH_3 dimer, two stable forms have been reported respectively (140-146). In this chapter, the calculation methods will first be presented, which include ab initio and master equation calculations. For the results section, it will begin with the geometric structures and energy values of the dimers obtained from ab initio calculations. Calculations related to anharmonicity and hindered rotors will also be discussed. Dimerisation rate coefficients from MESMER calculations based on different models will be presented. The fraction of dimers formed in the nozzle region and in the stable flow region will be estimated, which will be used to compare with the experimental data our group recently obtained.

6.2 Computational methods

Ab initio and master equation calculations have been carried out for the dimerisation reactions of CH_2O, CH_3CHO, $CH_3C(O)CH_3$ and NH_3. Geometric structures of the monomers and non-covalent dimers of CH_2O, CH_3CHO, $CH_3C(O)CH_3$ and NH_3 were optimised at the BHandHLYP/aug-cc-pVDZ level of theory (147-150) using the Gaussian 09 programme (151). Harmonic frequency calculations were performed at the same level of theory on the optimised structures to verify that they are the minimum points and obtain the ZPVE and the ro-vibrational parameters needed for MESMER calculations. Higher level single-point energy calculations were done for more accurate binding energy values. For the case of CH_2O, CH_3CHO and NH_3, these were done at the CCSD(T)/aug-cc-pVTZ level (152, 153) while for $CH_3C(O)CH_3$, these were done at the CCSD(T)/jul-cc-pVTZ level (154) due to the limitations of calculation time granted from the available computational resources.

In an attempt to investigate the effect of anharmonicity and hindered rotors on the density of states (DOS) in the MESMER calculations on the dimerisation rate, anharmonic frequency calculations and hindered rotor calculations were also performed at the BHandHLYP/aug-cc-pVDZ level. There are six types of molecular vibrational motions: symmetric stretching, asymmetric stretching, in-plane rocking, in-plane scissoring, out-of-plane wagging and out-of-plane twisting (155). The number of vibrational modes for non-linear molecules is given by $3N – 6$ where N is the number of atoms. Thus, compared with two monomers that are at infinite distance apart, the dimer has six additional vibrational modes, apart from those that can be assigned to vibrational motions that are already present within the individual monomers, which only arise due to the interactions between the two monomers. Typically, these six additional modes are of lower frequencies due to the weak nature of the intermolecular forces and hence small force constants. The hindered rotors particularly concerned here in this chapter refer to the twisting about the newly arisen internal rotation mode due to the formation of the non-covalent dimer. Although intrinsically for the monomers containing a methyl $–CH_3$ group the rotation of the $–CH_3$ group can also be described as a hindered rotor, it exists in both the monomer and the dimer, so there is a cancellation of errors even if this is assigned as a harmonic vibration. Relaxed scans for a full 360° rotation about the dihedral angles that can assemble the most of the twisting were carried out to obtain the hindered rotor potentials.

Results from the ab initio calculations were then used to set up the master equations in the MESMER programme (156) to determine the rate coefficients of dimerisation. For simplicity, only one dimer structure, which corresponds to the most stable non-covalent one, was included in the MESMER calculations for each species in the beginning of the calculations. Different models were used for the calculations of the ro-vibrational DOS: harmonic, anharmonic, with or without hindered rotors. For the cases using harmonic frequencies, the scaling factor for the BHandHLYP/aug-cc-pVDZ level included in the input file was taken to be 0.9589 (157). For the hindered rotors, the potentials obtained from ab initio calculations were included in the input file while at the same time replacing the corresponding vibrational modes. Information about the vibrational frequencies can be included in the MESMER input files in two ways: a list of vibrational frequency values or the Hessian matrix. For the former one where the hindered rotor potential is included, the replacement has to be done by manually removing the frequency value of the vibrational mode corresponding to the hindered rotor from the list of vibrational frequencies in the input file; while for the latter one, the MESMER programme will automatically project it out from the Hessian matrix from the hindered rotor potential provided. The latter method was chosen when the hindered rotor potentials were included in the input file as it is difficult to pinpoint the twisting to the contribution solely from one vibrational mode.

As the formation of non-covalent dimers can be considered as a single-step barrierless reaction, the reactive probability was treated with the ILT method (158) discussed in Section 2.2.1.3. The ILT pre-exponential A^{∞} was set as $3 \times 10^{-10}\ \mathrm{molecule}^{-1}\ \mathrm{s}^{-1}$, which is the high pressure limiting collision rate coefficient, while the modified Arrhenius factor n^{∞}, which corresponds to the temperature dependence, and the activation energy E_a^{∞} were both set as 0. The exponential-down model (159) discussed in Section 2.2.1.5 was used to treat the collisional energy transferred. A grain size of 30 cm^{-1} was used for all the conditions.

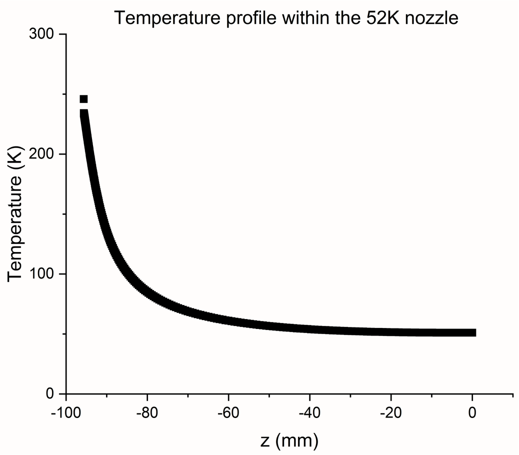

Figure 6.5 Temperature profile within the 52 K nozzle used by Antiñolo et al. (126). Distance *z* is set as 0 for the exit of the nozzle. The leftmost data point corresponds to the sonic point.

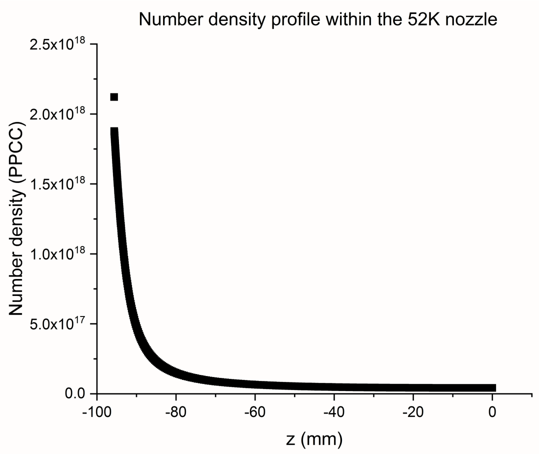

Figure 6.6 Total number density profile in molecule cm^{-3} within the 52 K nozzle used by Antiñolo et al. (126). Distance *z* is set as 0 for the exit of the nozzle. The leftmost data point corresponds to the sonic point.

For the calculations performed in this work on the dimerisation under the context of the actual Laval experiments, the Laval expansion and uniform flow was divided into two parts: the convergent-divergent region within the nozzle and the stable flow region out of the nozzle. Inside the nozzle, before the establishment of a stable flow, the temperature, pressure and flow velocity are all changing and they depend on the cross-sectional area of the nozzle along the flow axis (160, 161). While such data for the nozzles used by our group are not yet available, Dr Robin Shannon (University of Leeds) kindly shared the calculations done by Dr Andre Canosa (University of Rennes 1) on the temperature and number density profiles from the sonic point (Mach number = 1) to the nozzle exit within a 52 K nozzle used by Antiñolo et al. (126). Figure 6.5 and Figure 6.6 respectively show the temperature and number density profiles within the 52 K nozzle. Figure 6.7 provides a schematic of the Laval nozzle environment for ease of visualisation. For the convention used in this chapter, the exit of the nozzle is set to be at distance $z = 0$; $z < 0$ is for the region within the nozzle while $z > 0$ is the stable flow region. For the 52 K nozzle, the sonic point, where the Mach number is equal to 1, was found to be located at $z = -95.6$ mm. The temperature and number density profiles consisted of 248 data points and they were all used as the temperature-pressure pairs in the MESMER input to calculate the dimerisation rate coefficient at each point. The convergent region of the Laval nozzle was ignored because of the lack of previously calculated values and a shorter distance compared with the divergent region and the stable flow region. For the stable flow region, the conditions were taken to be constant and the same as that at the exit of the nozzle, which corresponds to a temperature of 51 K, a number density of 4.16×10^{16} molecule cm^{-3} and a Mach number of 4.891 in this case.

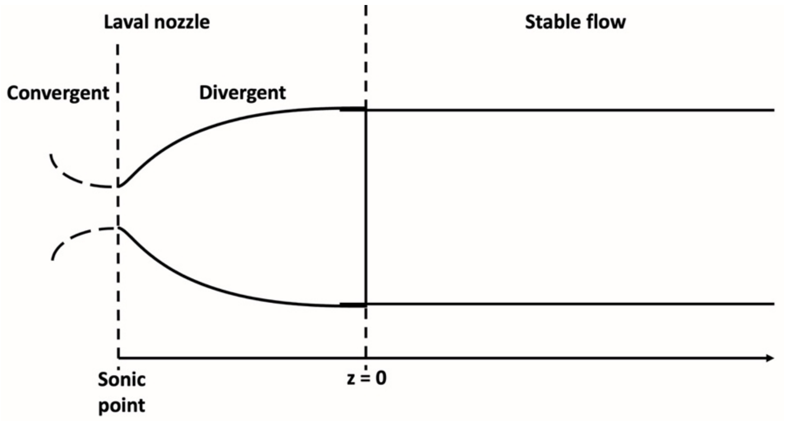

Figure 6.7 A schematic of the Laval nozzle setup to explain the convention used in this chapter. The exit of the nozzle is set to be at distance *z* = 0. Within the nozzle, *z* < 0; out in the stable flow region, *z* > 0. As there are only data up to the sonic point for the temperature and number density profiles, the convergent region of the Laval nozzle is ignored in this chapter.

The pseudo 1st-order rate coefficients of the loss of monomers were obtained from MESMER as a function of time. Dividing them by the concentration of the monomers gave the bimolecular rate coefficients of the loss of monomers k_{loss} for every temperature-pressure pair. It is defined that at every point:

$$[\mathrm{monomer}]_0 = [\mathrm{monomer}] + 2[\mathrm{dimer}] \qquad \text{E 6.6}$$

and so:

$$k_{\mathrm{loss}} = 2k_{\mathrm{dimer}} \qquad \text{E 6.7}$$

where k_{dimer} is the 2nd-order rate coefficient for dimer formation. Considering E 1.3 and E 1.7, the new fraction of monomer f_{monomer} can be defined by (128):

$$\begin{aligned} f_{\mathrm{monomer}} = \frac{[\mathrm{monomer}]}{[\mathrm{monomer}]_0} &= \frac{1}{[\mathrm{monomer}]_0\left(\frac{1}{[\mathrm{monomer}]_0} + k_{\mathrm{loss}}t\right)} \\ &= \frac{1}{1 + k_{\mathrm{loss}}[\mathrm{monomer}]_0 t} \\ &= \frac{1}{1 + 2k_{\mathrm{dimer}}[\mathrm{monomer}]_0 t} \end{aligned} \qquad \text{E 6.8}$$

The fraction of dimer f_{dimer} is given by:

$$f_{\mathrm{dimer}} = 0.5(1 - f_{\mathrm{monomer}}) \text{ or } f_{\mathrm{mononmer}} = 1 - 2f_{\mathrm{dimer}} \qquad \text{E 6.9}$$

and so $f_{\mathrm{dimer}} = 0.5$ corresponds to the complete conversion of monomers into dimers. For a small time interval from t to $t + \Delta t$, one can define:

$$\Delta f_{\mathrm{dimer}} = 0.5\left(1 - \frac{1}{1 + 2k_{\mathrm{dimer}}(t)[\mathrm{monomer}]_0(t)\Delta t}\right) \qquad \text{E 6.10}$$

For the region within the nozzle, Δt can be taken as the time for the gas flow to travel from one to the subsequent point among the 248 data points in the temperature and number density profiles. For the stable flow region, Δt was chosen as the time for the flow to travel every 1 mm. The fraction of dimer f_{dimer} at a particular point can be obtained from an integration of df_{dimer}, that is:

$$f_{\mathrm{dimer}} = \int df_{\mathrm{dimer}}\, dt \qquad \text{E 6.11}$$

The continuously changing conditions within the nozzle imply the necessity of an integration, but there are only 248 discrete data points of conditions within the nozzle available. Conversion to continuous variables by interpolation across the discrete points can be a possible way to tackle the problem. On the other hand, by the best approximation, f_{dimer} can also be computed as a summation, that is:

$$f_{\mathrm{dimer}} \approx \sum \Delta f_{\mathrm{dimer}}\,\Delta t \qquad \text{E 6.12}$$

and this is valid if Δt is sufficiently small. Δt here in this case under the aforementioned settings is less than or in the order of 10^{-6} s. The actual concentration of monomer at a given point $[\mathrm{monomer}]_0(t)$ can be found by multiplying the concentration of monomer when there is no dimerisation with f_{monomer}. It is important to note that for the calculation method presented here, it is assumed that the time for the stabilised dimers, which refer to those that have lost energy via collisions and fallen into the bottom of the potential well, to dissociate back to monomers is longer than that to travel to the next point down the flow. That is to say, the stabilised dimers remain as dimer form when travelling down the flow. Thus, the calculation will give an estimation of the lower limit of f_{monomer} and in particular an underprediction of f_{monomer} at high temperature (128). In order to generate plots that can be compared with experimental measurements taken by Dr Kevin Douglas and Dr Mark Blitz (both of the University of Leeds), the fractions of monomer were computed for different initial concentrations of monomers.

The 52 K nozzle data provided from Dr Robin Shannon were obtained from experiments using N_2 as the bath gas. When the calculations of f_{monomer} are extended to the cases using other bath gases for example Ar or He, apart from changing the bath gas in the MESMER input file which changes the collisional energy transferred and in turn the calculated k_{loss}, the speed of the gas flow v, which determines Δt, also needs to be scaled. The scaling can be done by the Graham's law of diffusion (162):

$$\frac{v_{\mathrm{gas}}}{v_{\mathrm{N_2}}} = \sqrt{\frac{m_{\mathrm{N_2}}}{m_{\mathrm{gas}}}} \qquad \text{E 6.13}$$

where m denotes the molar mass.

Although the exact temperature and number density profiles are only available for the 52 K nozzle, some scaling was made to approximate the profiles for other nozzles used in our group in order to have a better understanding of potential dimer formation in our experimental setup. Table 6.1 reports the properties of the Laval nozzles used by our group.

Table 6.1 Properties of the nozzles used in the Laval experiments in our group provided by Dr Kevin Douglas

Name	**Bath gas**	**Nozzle length *L* (mm)**	**Final Mach number**	**Final temperature (K)**	**Final density (molecule cm^{-3})**
M2.25	N_2	30	3.02	106	6.7×10^{16}
M2.75	N_2	35	3.36	91	4.93×10^{16}
M3.3	N_2	40	3.54	85	7.49×10^{16}
M4	He	100	4.75	35	4.66×10^{16}

Some approximations are applied in order to do the scaling with reference to the 52 K nozzle. The isentropic cores of the nozzles in our group are assumed to be of the similar shape as the 52 K nozzle as such the gas flow is expanded and diluted in the same fashion. The full nozzle lengths shown in Table 6.1 are taken to be the distances between the sonic point and the exit of the nozzle, that is, assuming there was no convergent region for the nozzles and the sonic point were at $z = -L$, as the latter cannot be obtained easily just by a measurement with a ruler. Information for the Mach number $M(z)$ at a given distance z within the 52 K nozzle is available for each of the 248 data points and basically the parameters being scaled for the nozzles in our group are the distance z' and the Mach number M', with the formulae:

$$\frac{z'}{-L} = \frac{z_{\mathrm{52K\,nozzle}}}{-95.6} \qquad \text{E 6.14}$$

$$\frac{M'(z')-1}{M'(0)-1}=\frac{M(z_{52\mathrm{K\ nozzle}})-1}{4.891-1} \qquad \text{E 6.15}$$

each $(z, M(z))$ pair of the 248 data points of the 52 K nozzle is mapped to $(z', M'(z'))$ for our nozzles. The distance between the sonic point and the exit of the 52 K nozzle is 95.6 mm and the Mach number at the exit of the 52 K nozzle $M(0)$ is 4.891. Information for L and $M'(0)$ can be found in Table 6.1. By mapping with these formulae, one can check that *M'* = 1 at *z'* = –*L* and *M'* is equal to the final Mach number at *z'* = 0. The temperature and number density profiles can then be computed by the following formulae that describe the properties of the isentropic core of the Laval nozzle (160, 161):

$$\frac{T_{\mathrm{res}}}{T(z')}=1+\frac{\gamma-1}{2}\left(M'(z')\right)^2 \qquad \text{E 6.16}$$

$$\frac{n_{\mathrm{res}}}{n(z')}=\left(\frac{T_{\mathrm{res}}}{T(z')}\right)^{\frac{1}{\gamma-1}} \qquad \text{E 6.17}$$

By first inputting *z'* = 0, the reservoir temperature T_{res} and number density n_{res} for a particular nozzle can be found, and then the values obtained can be used to compute $T(z')$ and $n(z')$ for all the $(z', M'(z'))$ pairs. γ is the ratio of heat capacities $\frac{C_p}{C_v}$, which is equal to $\frac{5}{3}$ for monoatomic gas like Ar or He and $\frac{7}{5}$ for diatomic gas like N_2. After obtaining an estimation of the temperature and number density profiles for the nozzles of our group, f_{monomer} calculations similar to that carried out for the 52 K nozzle were performed.

6.3 Results and discussions

6.3.1 Results from ab initio calculations

The geometries of the stationary points, obtained at the BHandHLYP/aug-cc-pVDZ level of theory, for the monomers and non-covalent dimers are shown in Figure 6.8. The optimised Cartesian coordinates can be found in Appendix E.

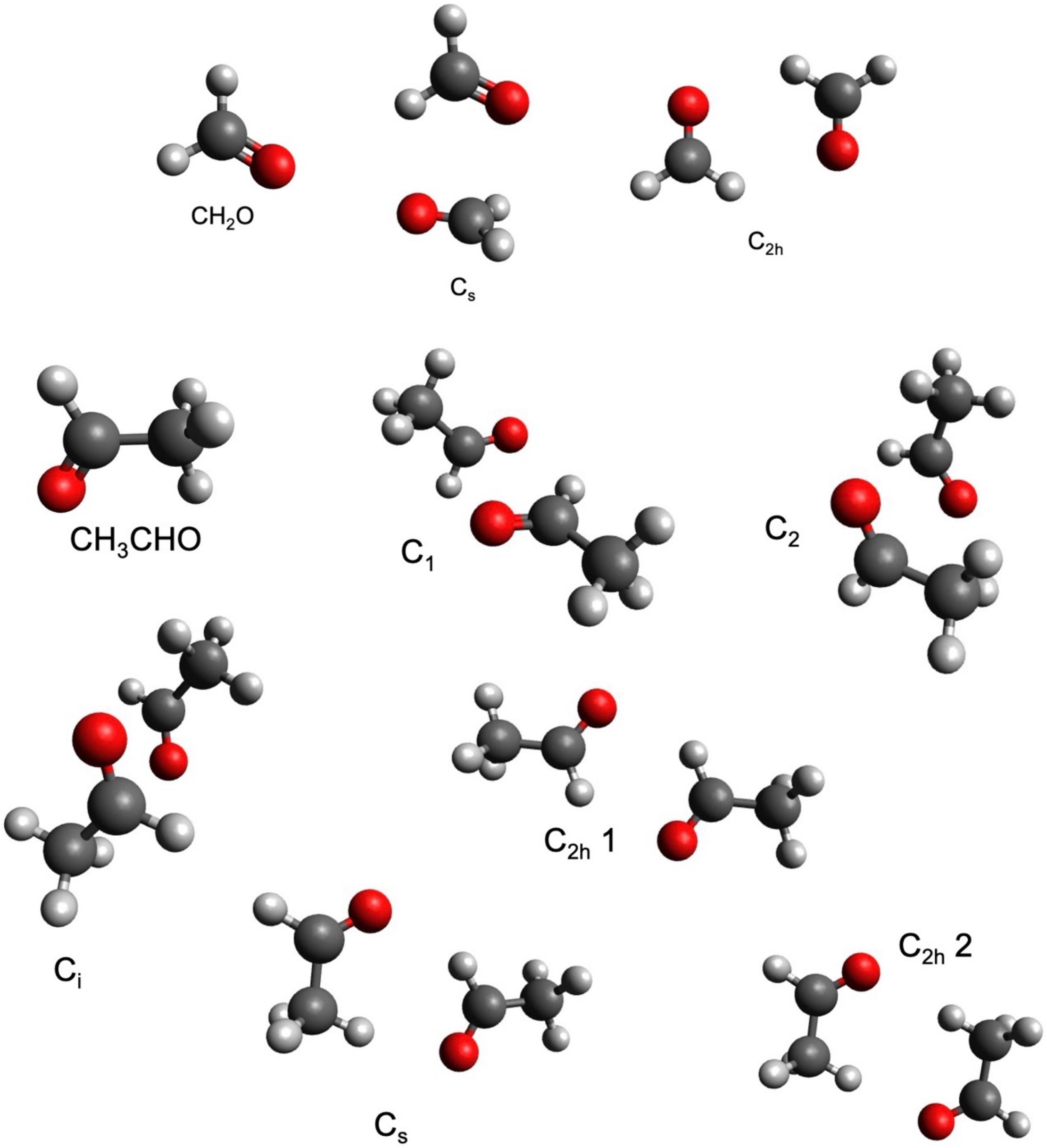

Figure 6.8 Optimised geometries of monomers and non-covalent dimers of CH_2O, CH_3CHO, $CH_3C(O)CH_3$ and NH_3 obtained at the BHandHLYP/aug-cc-pVDZ level of theory. The Cartesian coordinates of the geometries can be found in the tables in Appendix E.

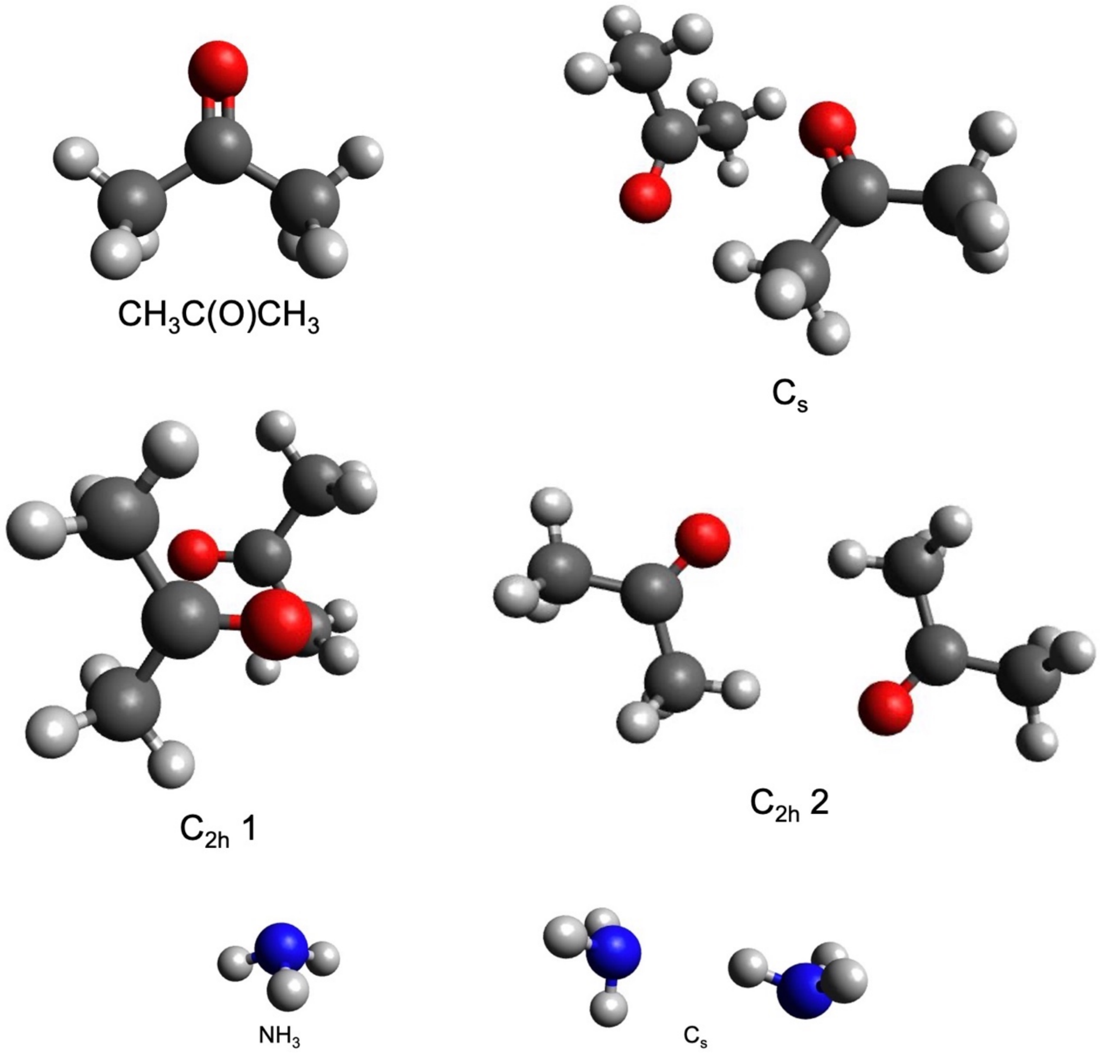

Figure 6.8 (continued)

For CH_2O, two stable dimer structures, one with C_s and the other with C_{2h} geometries, were identified. The scaled ZPVE corrected energy values relative to the monomer obtained at the CCSD(T)/aug-cc-pVTZ//BHandHLYP/aug-cc-pVDZ level were found to be –13.49 kJ mol^{-1} and –12.00 kJ mol^{-1} respectively. The C_s structure was found to be more stable, which is consistent with the more recent theoretical results (132-135), as shown in Table 6.2. In particular, the energy difference from the benchmark study (132) is less than 0.3 kJ mol^{-1}, which suggests that the calculation methods used in this work can provide a good level of accuracy.

Table 6.2 ZPVE corrected relative energies (kJ mol^{-1}) of different structures of the CH_2O dimer

Method	C_s	C_{2h}
This work 1	–13.49	–12.00
This work 2	–10.59	–10.03
Ref. (131)	–8.20	–8.49
Ref. (132)	–13.26	–12.05
Ref. (133)	–12.26	–11.72
Ref. (134)	–13.10	–12.50
Ref. (135)	–15.75	–13.13

This work 1: CCSD(T)/aug-cc-pVTZ//BHandHLYP/aug-cc-pVDZ
This work 2: BHandHLYP/aug-cc-pVDZ
Ref. (131): MP2/6-31++G**
Ref. (132): CCSD(T)/CBS
Ref. (133): CCSD(T)-F12/haTZ
Ref. (134): CCSD(T)/aug-cc-pVTZ//MP2/aug-cc-pVTZ
Ref. (135): CCSD/6-311++G(3df,3pd)//B3LYP/6-311++G(3df,3pd)

For CH_3CHO, six minimum points were found for the non-covalent dimers at the BHandHLYP/aug-cc-pVDZ level of theory, which have symmetries C_1, C_2, C_i, C_s, C_{2h} and C_{2h} respectively. The scaled ZPVE corrected relative energy values at the CCSD(T)/aug-cc-pVTZ//BHandHLYP/aug-cc-pVDZ level were found to be –18.39 kJ mol^{-1}, –18.70 kJ mol^{-1}, –18.39 kJ mol^{-1}, –14.61 kJ mol^{-1}, –14.20 kJ mol^{-1} and –13.37 kJ mol^{-1} respectively. In general, the more non-planar structures (C_1, C_2 and C_i) were found to be more stable than the more planar ones (C_s, C_{2h} and C_{2h}), which agrees with previous literature (136-138). However, previous literature suggested that the C_1 structure is more stable than the C_2 structure. While the energy values obtained at the CCSD(T)/aug-cc-pVTZ//BHandHLYP/aug-cc-pVDZ level indicate otherwise, the values at the BHandHLYP/aug-cc-pVDZ level are consistent with previous literature, as shown in Table 6.3. It is also worth noting that such energy difference is < 1 kJ mol^{-1}, which is within the level of uncertainty. For the most recent work by Neeman et al. (138), two extra stable structures were optimised at the more advanced M06-2X-D3/aug-cc-pVTZ level of theory, with one having C_i symmetry with relative energy of –9.08 kJ mol^{-1} and the other having C_s symmetry with relative energy of –7.57 kJ mol^{-1} respectively. These two dimer structures have higher energies than the other six stable structures and unfortunately in this work, they were not identified as stable CH_3CHO dimer structures at the BHandHLYP/aug-cc-pVDZ level of theory.

Table 6.3 ZPVE corrected relative energies (kJ mol^{-1}) of different structures of the CH_3CHO dimer

Method	C_1	C_2	C_i	C_s	C_{2h} 1	C_{2h} 2
This work 1	–18.39	–18.70	–18.39	–14.61	–14.20	–13.37
This work 2	–13.47	–12.49	–12.22	–11.68	–11.47	–10.49
Ref. (136)	–15.27	–15.10	–14.94	–12.30	–12.01	–10.96
Ref. (137)	–16.40	–15.90	–14.76	–11.91	–11.18	–11.16
Ref. (138)	–18.03	–17.28	–17.45	–11.72	–12.05	–10.59

This work 1: CCSD(T)/aug-cc-pVTZ//BHandHLYP/aug-cc-pVDZ
This work 2: BHandHLYP/aug-cc-pVDZ
Ref. (136): MP2/6-31+G*
Ref. (137): M06/6-31++G**
Ref. (138): CCSD(T)/aug-cc-pVTZ//M06-2X-D3/aug-cc-pVTZ

For $CH_3C(O)CH_3$, three minimum structures were found for the dimers at the BHandHLYP/aug-cc-pVDZ level. Apart from the two structures with C_{2h} geometry as mentioned in previous literature (139), a C_s structure, which was classified as a transition state at the MP2/6-31+G* level of theory, was also found to be a stable point. In terms of the trend of the binding energy, as shown in Table 6.4, the C_{2h} structure with the two planes of the carbonyl group stacking on top of each other is the most stable while the other C_{2h} structure, which has the two planes of carbonyl group side by side, is the least stable, with the C_s structure somewhere in between. The ZPVE corrected binding energies at CCSD(T)/jul-cc-pVTZ//BHandHLYP/aug-cc-pVDZ for the two C_{2h} structures and C_s structure were found to be –26.16 kJ mol^{-1}, –12.41 kJ mol^{-1} and –19.73 kJ mol^{-1} respectively.

Table 6.4 ZPVE corrected relative energies (kJ mol^{-1}) of different structures of the $CH_3C(O)CH_3$ dimer

Method	**C_s**	**C_{2h} 1**	**C_{2h} 2**
This work 1	–19.73	–26.16	–12.41
This work 2	–13.82	–16.30	–10.03
Ref. (139)	–15.69	–20.29	–9.71
This work 1: CCSD(T)/jul-cc-pVTZ//BHandHLYP/aug-cc-pVDZ This work 2: BHandHLYP/aug-cc-pVDZ Ref. (139): MP2/6-31+G*			

For NH_3, the results from an initial literature (140) provided two possible non-covalent dimer structures, C_s and C_{2h} respectively, and suggested that whether the particular structure is the optimised equilibrium, or which particular structure is more stable, depends on the level of theory used. As more studies have been done, in general, the C_s structure is considered to be the most stable equilibrium structure (141-143, 145, 146). However, as listed in Table 6.5, the energy difference between the C_s and C_{2h} structures at the same level of theory is less than 1 kJ mol^{-1}, which is within the computational error, and so it is suggested that (144) these two structures can be considered as degenerate. This actually makes sense due to the proximity of the two geometric structures and the floppy nature of the non-covalent dimer. In this work, when the optimisation calculations were done at the BHandHLYP/aug-cc-pVDZ level, only the C_s structure was suggested to be a stable structure. The ZPVE corrected binding energy at CCSD(T)/aug-cc-pVTZ//BHandHLYP/aug-cc-pVDZ was found to be 7.52 kJ mol^{-1}. Both the ZPVE corrected and uncorrected energies are reported in Table 6.5 because many of the previous literature only reported the values uncorrected for ZPVE, and by comparison, the results from this work match with previously reported values.

Table 6.5 Relative energies (kJ mol^{-1}) of different structures of the NH_3 dimer

Method	**C_s**	**C_{2h}**
ZPVE corrected		
This work 1	–7.52	
This work 2	–6.67	
Ref. (142)	–10.88	–10.59
Ref. (143) 1	–7.98	
Ref. (143) 2	–9.89	
Uncorrected for ZPVE		
This work 1	–13.62	
This work 2	–12.76	
Ref. (140)	–11.52	–11.39
Ref. (141)	–13.20	
Ref. (142)	–16.86	–16.02
Ref. (143) 1	–13.83	
Ref. (143) 2	–15.63	
Ref. (145)	–13.18	
Ref. (146)	–13.63	–13.53

This work 1: CCSD(T)/aug-cc-pVTZ//BHandHLYP/aug-cc-pVDZ
This work 2: BHandHLYP/aug-cc-pVDZ
Ref. (140): MP2/6-311+G(3d,2p), Ref. (141): MP2/CBS
Ref. (142): MP2/6-311++G(d,p), Ref. (143) 1: MP2/aug-cc-pVTZ
Ref. (143) 2: B3LYP/aug-cc-pVTZ, Ref. (145): CCSD(T)/CBS
Ref. (146): Frozen-core UCCSD(T)-F12a/aug-cc-pVTZ

Table 6.6 Rotational constants and vibrational frequencies of the species included in the MESMER calculations obtained at the BHandHLYP/aug-cc-pVDZ level of theory

Species	Rotational constants (GHz)	Harmonic vibrational frequencies (cm^{-1}) [Anharmonic]
CH_2O monomer	284.94442 39.54571 34.72626	1253.49 1293.41 1567.47 1893.75 3013.16 3091.70 [1231.11 1273.79 1534.87 1868.93 2860.89 2922.58]
CH_2O dimer C_s structure	18.92418 3.76374 3.20960	93.38 110.56 142.56 198.67 200.88 254.20 1243.21 1271.66 1293.03 1303.83 1567.03 1568.57 1871.58 1883.80 3034.00 3037.76 3118.87 3125.91 [73.74 83.44 100.72 130.82 150.59 155.50 1224.33 1239.03 1272.19 1278.73 1535.43 1537.74 1850.25 1859.49 2874.82 2879.71 2943.77 2949.68]
CH_3CHO monomer	57.53259 10.27456 9.21161	168.26 522.03 798.92 927.64 1167.18 1174.73 1413.72 1463.72 1483.38 1494.26 1896.26 3011.09 3115.80 3181.08 3239.69
CH_3CHO dimer C_1 structure	7.26735 1.43007 1.27115	39.94 72.93 80.62 92.52 108.83 125.43 172.96 191.04 524.78 529.31 805.22 814.14 931.11 933.03 1169.48 1171.16 1172.38 1189.37 1411.25 1415.97 1466.72 1476.27 1486.00 1487.07 1495.85 1498.09 1872.58 1886.38 3042.83 3064.24 3116.20 3119.13 3181.07 3191.79 3237.15 3239.40
$CH_3C(O)CH_3$ monomer	10.31073 8.58419 4.97078	21.64 146.60 390.82 508.14 551.16 827.41 903.78 923.98 1113.67 1148.14 1286.35 1421.57 1437.18 1483.86 1490.50 1494.51 1515.39 1877.18 3117.12 3124.05 3181.22 3189.14 3243.57 3244.68
$CH_3C(O)CH_3$ dimer C_{2h} 1 structure	2.66699 1.18975 1.10554	23.44 49.39 53.00 55.65 59.54 71.00 85.66 88.59 152.99 154.54 395.94 397.00 506.70 513.76 551.12 553.09 831.87 832.16 903.32 905.11 935.16 935.61 1118.64 1119.16 1151.59 1153.28 1288.23 1294.59 1420.80 1421.99 1439.03 1439.88 1486.14 1488.91 1492.93 1497.71 1499.04 1500.15 1516.86 1521.96 1854.22 1866.95 3120.24 3120.37 3126.64 3127.25 3189.79 3189.89 3197.28 3198.02 3239.24 3239.83 3240.95 3241.27
NH_3 monomer	302.33802 302.33769 189.84799	1043.84 1693.33 1693.34 3587.47 3720.08 3720.10
NH_3 dimer C_s structure	120.20348 5.17083 5.11319	43.67 101.05 115.79 142.34 253.86 389.90 1075.88 1085.91 1687.65 1694.53 1698.31 1719.31 3554.00 3585.52 3684.29 3714.52 3714.95 3718.00

Only one dimer for each species was included in the MESMER simulations for the time being for simplicity. For NH_3, as the BHandHLYP/aug-cc-pVDZ level only gives one optimised stable non-covalent dimer structure (C_s), this selection process is trivial. For CH_2O, the C_s structure was chosen as it is the more stable non-covalent dimer. For $CH_3C(O)CH_3$, the C_{2h} dimer with lower energy was chosen following similar reasoning. For CH_3CHO, at the CCSD(T)/aug-cc-pVTZ//BHandHLYP/aug-cc-pVDZ level, the C_2 structure has the lowest energy value but its difference with the second-lowest, namely the C_1 structure, is just 0.31 kJ mol^{-1}, which is within the theoretical error. Also, as shown in Table 6.3, the C_1 structure has a lower energy value at other levels of theory. Therefore, in this occasion, the C_1 structure was used for MESMER calculations. Indeed, the difference between having a potential well of –18.39 kJ mol^{-1} and –18.70 kJ mol^{-1} is deemed to be too small to have a significant effect in the calculated rate coefficient. The rotational constants and vibrational frequencies of the species used in the MESMER calculations are reported in Table 6.6, while in Appendix E for the other species.

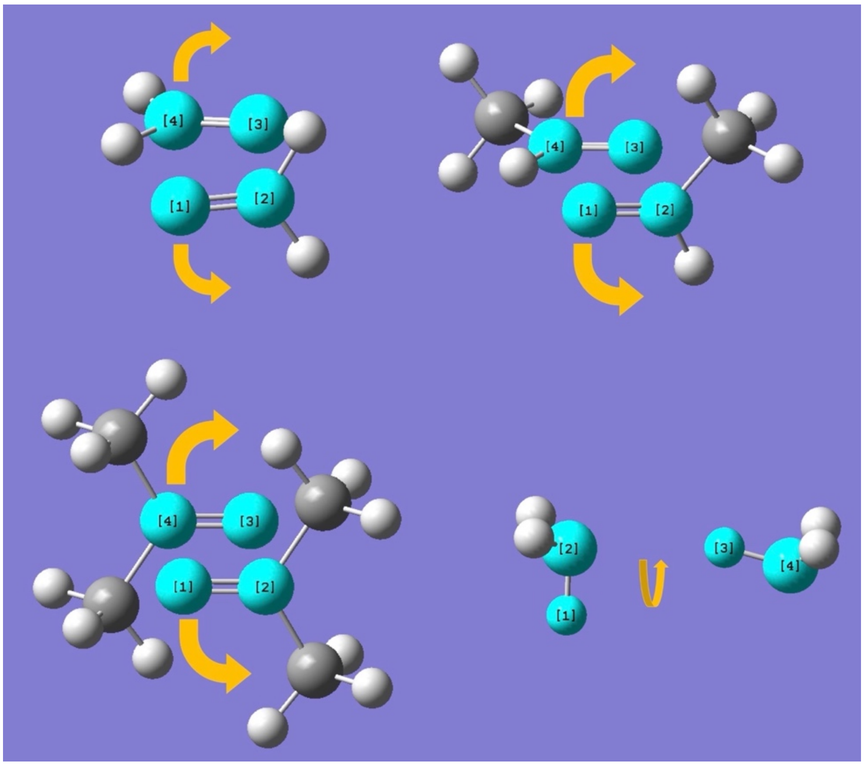

Figure 6.9 Internal rotations taken to be hindered rotor potentials during MESMER calculations for (top left) CH_2O C_s dimer, (top right) CH_3CHO C_1 dimer, (bottom left) $CH_3C(O)CH_3$ C_{2h} 1 dimer and (bottom right) NH_3 C_s dimer respectively. Relaxed scans were performed for rotation about the dihedral angle 1234 formed by the cyan atoms and the yellow arrows indicate how the rotation was done about the dihedral angle 1234.

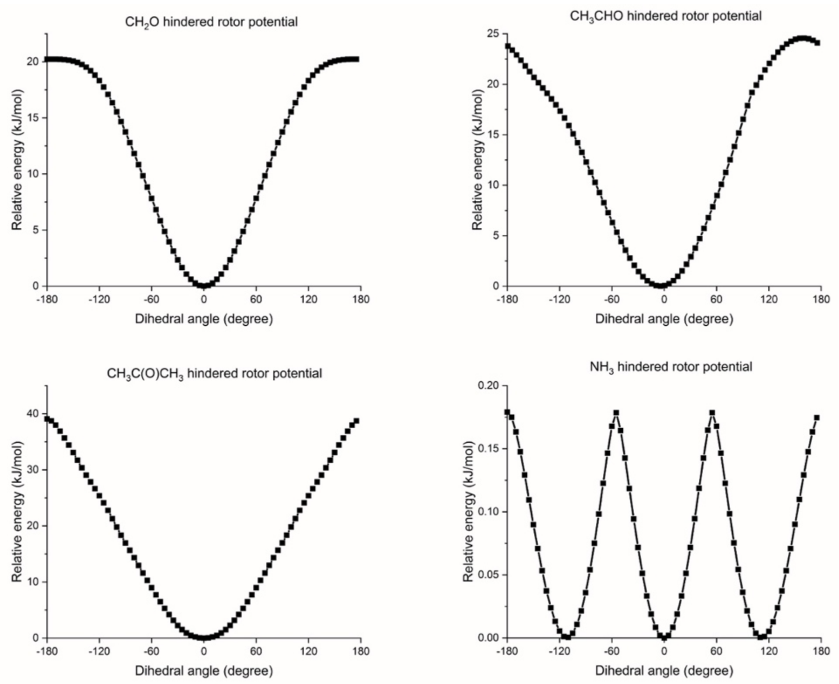

Figure 6.10 Hindered rotor potentials obtained from the relaxed scans of the dihedral angles shown in Figure 6.9 for (top left) CH_2O C_s dimer, (top right) CH_3CHO C_1 dimer, (bottom left) $CH_3C(O)CH_3$ C_{2h} 1 dimer and (bottom right) NH_3 C_s dimer respectively at the BHandHLYP/aug-cc-pVDZ level of theory. The original optimised equilibrium dimer structures were set at a relative energy = 0 kJ/mol.

As mentioned in the previous section, in order to describe the low frequency mode corresponding to the internal rotation between the two monomers for a better calculation of the density of states (DOS), relaxed scans with Gaussian for a 360° hindered rotor potential were performed. For the species containing the carbonyl C=O groups, it was found that the hindered rotation corresponds to the twisting of the two monomers about an axis between them such that the plane originally formed by the two C=O going out of plane as indicated in Figure 6.9. To the best approximation, it was assigned as a rotation about the O=C - - - O=C dihedral angle and the potentials obtained from the relaxed scans are shown in Figure 6.10. For NH_3 dimer, the hindered rotation was found to be along the N - - - H hydrogen bond, and so a relaxed scan about the H-N - - - H-N was performed as shown in Figure 6.9 and the results are presented in Figure 6.10. There is significant difference between these two hindered rotors in terms of the energy: while it is facile for the rotation along the N - - - H hydrogen bond in NH_3 dimer to occur, the out-of-plane twisting of the two C=O in the carbonyl C=O group bearing species requires energy comparable to the binding energy.

6.3.2 Rate coefficient calculations

Results obtained from the ab initio calculations reported in Section 6.3.1 were used as inputs for the MESMER calculations. As mentioned above, only one of the dimer structures was chosen for each species to be put into the MESMER calculations. The potential energy surfaces actually used are shown in Figure 6.11, which are all single-step barrierless reactions.

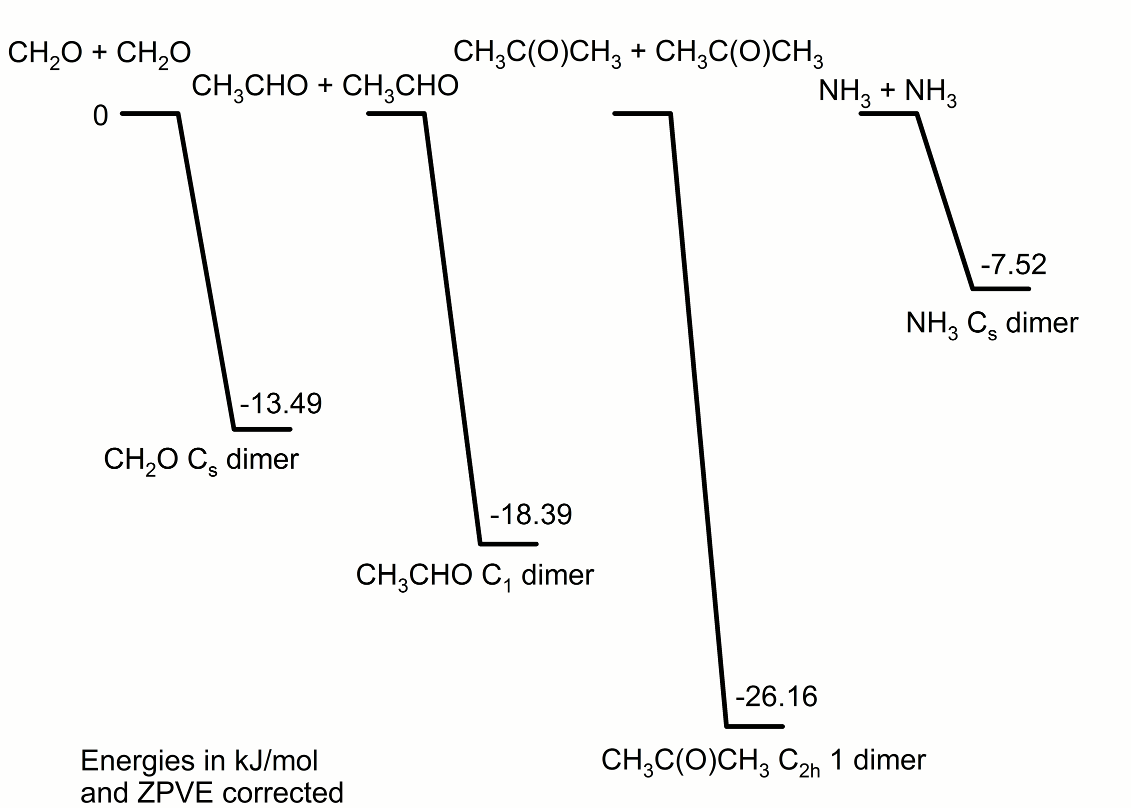

Figure 6.11 Potential energy surfaces used in MESMER for the dimerisation reactions of (from left to right) CH_2O, CH_3CHO, $CH_3C(O)CH_3$ and NH_3 respectively.

The rate coefficients for the loss of monomer k_{loss} due to dimerisation were computed for CH_2O, CH_3CHO, $CH_3C(O)CH_3$ and NH_3 in the temperature range 25–250 K, with a total density of 10^{17} molecule cm^{-3}, which is close to the highest total density near the exit of the Laval nozzle during the experiments performed by our group. The results are shown from Figure 6.12 to Figure 6.15. The general trend for k_{loss} is that it has a negative temperature dependence because the dimerisation is a single-step barrierless association reaction and at low temperature stabilisation into the potential well is favoured. Calculations have been done for cases using Ar and He as the bath gas and the corresponding collisional transferred energies described by the delta E down, $\langle \Delta E \rangle_{down}$ model were given as $\langle \Delta E \rangle_{down,\mathrm{Ar}} = 200\left(\frac{T}{298\ \mathrm{K}}\right)^{0.5}\ \mathrm{cm}^{-1}$ and $\langle \Delta E \rangle_{down,\mathrm{He}} = 100\left(\frac{T}{298\ \mathrm{K}}\right)^{1.0}\ \mathrm{cm}^{-1}$. As shown from the plots, k_{loss} are smaller by slightly more than an order of magnitude when He is used as the bath gas instead of Ar while keeping the other factors constant. This is explained by a smaller $\langle \Delta E \rangle_{down}$ for the weaker collider He, which makes the collisional stabilisation into the dimer potential well less efficient.

Different models to calculate the rovibronic DOS have been used and the results have been included in the plots from Figure 6.12 to Figure 6.15. The models applied include using the harmonic Hessian matrix from the ab initio calculations alongside the scaling factor for BHandHLYP/aug-cc-pVDZ (0.9589) (157) without the hindered rotor potential, which is named “Harmonic hessian” in the plots, and with the hindered rotor potential, which is named “Harmonic hessian + 1 dihedral”. For CH_2O, the “Anharmonic” model has also been used, which used the anharmonic frequency values from the ab initio results as the input instead. The combination of the anharmonic frequencies with the hindered rotor potential, which can be considered as a more complete description of the species, was not used as MESMER does not support the input setting of an anharmonic Hessian together with the hindered rotor and it would be difficult to assign the hindered rotor potential solely to one particular anharmonic vibrational mode and replace it from the list of anharmonic frequency values.

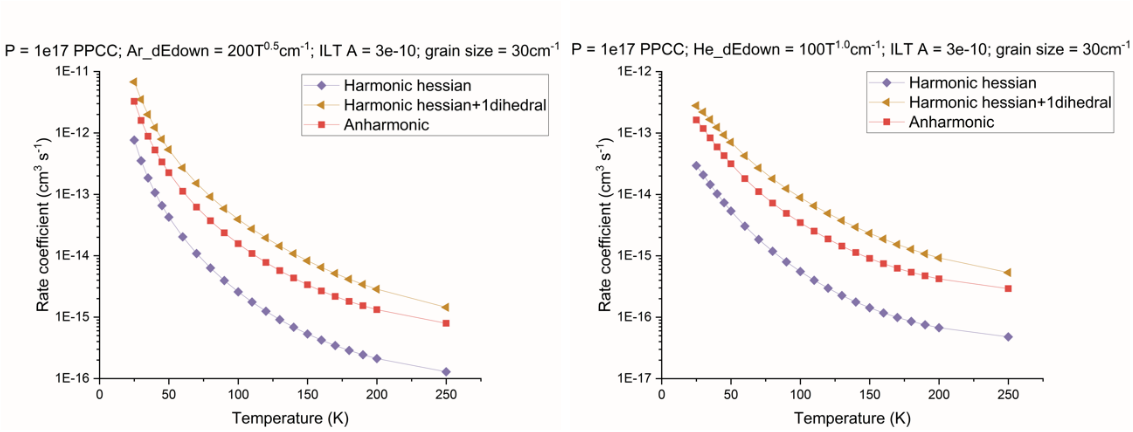

Figure 6.12 Calculated k_{loss} for the dimerisation reaction of CH_2O versus temperature in the range of T = 25–250 K with a total density of 10^{17} molecule cm^{-3}. Ar is used as the bath gas on the left while He is used as the bath gas on the right. Purple line (Harmonic hessian) is for the case when the DOS are calculated from the harmonic Hessian together with the scaling factor without the inclusion of the hindered rotor potential. Gold line (Harmonic hessian + 1 dihedral) is for the case when the DOS are calculated from the harmonic Hessian together with the scaling factor with the inclusion of the hindered rotor potential. Red line (Anharmonic) is for the case when the DOS are calculated from the anharmonic frequencies.

Comparing the “Harmonic hessian” and “Anharmonic” models for CH_2O, k_{loss} increases by about 5 times when the “Anharmonic” model was used. This can be explained by an increase in the total number of states available for the dimer. Considering the frequency values listed in Table 6.6, the six lowest unscaled harmonic frequency values arising from the formation of the dimer for the CH_2O C_s dimer are 93.38 cm^{-1}, 110.56 cm^{-1}, 142.56 cm^{-1}, 198.67 cm^{-1}, 200.88 cm^{-1} and 254.20 cm^{-1}, and multiplying the scaling factor yields 89.54 cm^{-1}, 106.02 cm^{-1}, 136.70 cm^{-1}, 190.50 cm^{-1}, 192.62 cm^{-1} and 243.75 cm^{-1}, which are all greater than the calculated anharmonic values (73.74 cm^{-1}, 83.44 cm^{-1}, 100.72 cm^{-1}, 130.82 cm^{-1}, 150.59 cm^{-1} and 155.50 cm^{-1}). This discrepancy is due to the fact that the scaling factors are derived for molecular vibrations instead of the low-frequency modes in dimer association and the scaled harmonic frequencies turn out to be still greater than the anharmonic ones. The results show that the calculation of DOS is sensitive to the low frequency values and having smaller values for these vibrational frequencies give a larger DOS and thus a larger k_{loss}. For other species, the anharmonic frequencies were not used for MESMER calculations because for some of the structures some negative values emerged, which raise concerns over the accuracy of the anharmonic frequency values obtained. Therefore, only the calculations with the "Harmonic hessian" and "Harmonic hessian + 1 dihedral" for different species will be discussed in the following.

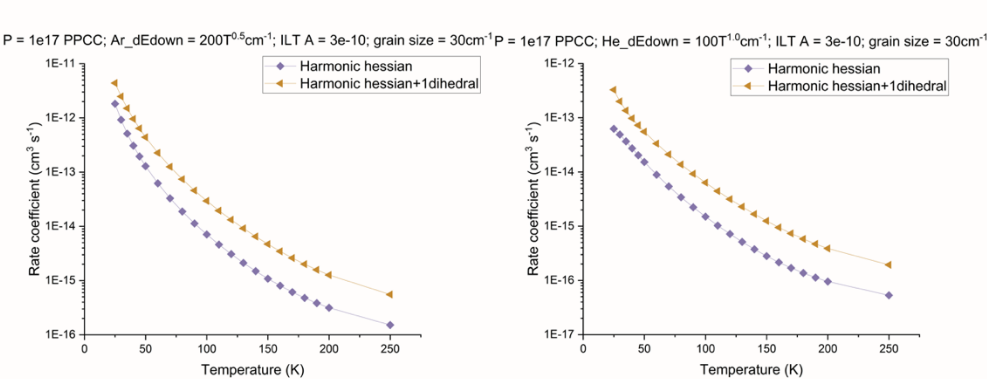

Figure 6.13 Calculated k_{loss} for the dimerisation reaction of CH_3CHO versus temperature in the range of T = 25–250 K with a total density of 10^{17} molecule cm^{-3}. Ar is used as the bath gas on the left while He is used as the bath gas on the right. Purple line (Harmonic hessian) is for the case when the DOS are calculated from the harmonic Hessian together with the scaling factor without the inclusion of the hindered rotor potential. Gold line (Harmonic hessian + 1 dihedral) is for the case when the DOS are calculated from the harmonic Hessian together with the scaling factor with the inclusion of the hindered rotor potential.

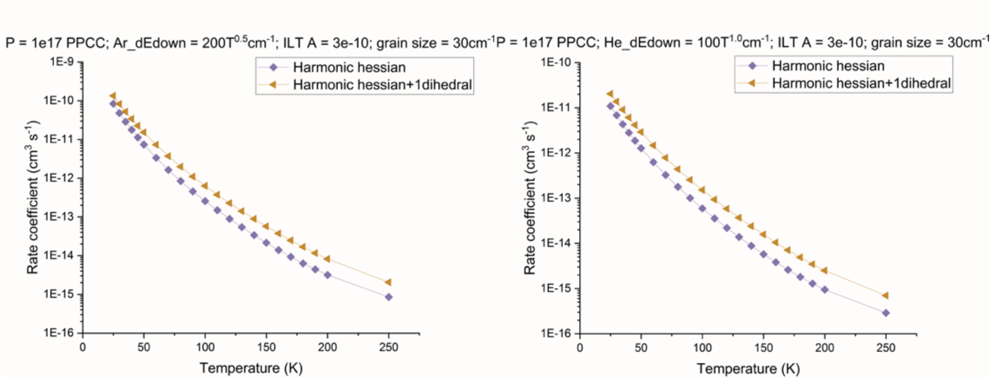

Figure 6.14 Calculated k_{loss} for the dimerisation reaction of CH_3COCH_3 versus temperature in the range of T = 25–250 K with a total density of 10^{17} molecule cm^{-3}. Ar is used as the bath gas on the left while He is used as the bath gas on the right. Purple line (Harmonic hessian) is for the case when the DOS are calculated from the harmonic Hessian together with the scaling factor without the inclusion of the hindered rotor potential. Gold line (Harmonic hessian + 1 dihedral) is for the case when the DOS are calculated from the harmonic Hessian together with the scaling factor with the inclusion of the hindered rotor potential.

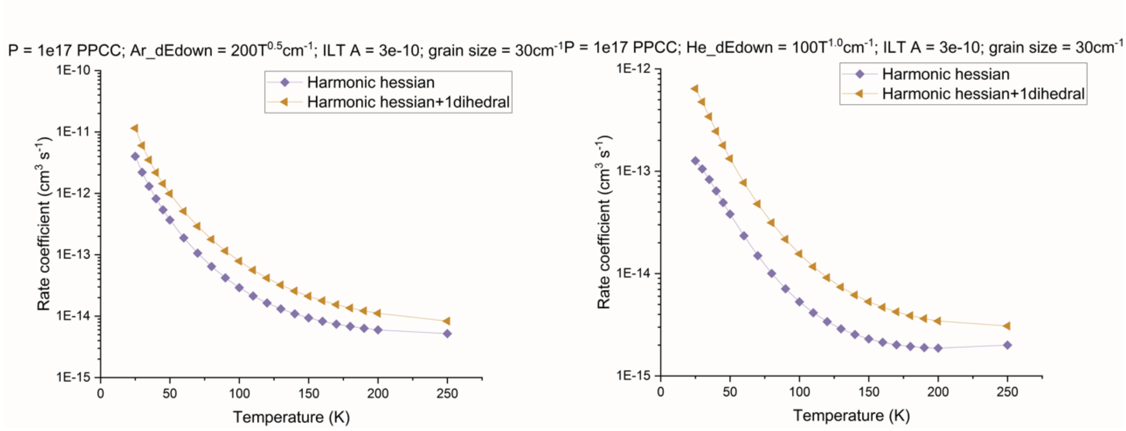

Figure 6.15 Calculated k_{loss} for the dimerisation reaction of NH_3 versus temperature in the range of T = 25–250 K with a total density of 10^{17} molecule cm^{-3}. Ar is used as the bath gas on the left while He is used as the bath gas on the right. Purple line (Harmonic hessian) is for the case when the DOS are calculated from the harmonic Hessian together with the scaling factor without the inclusion of the hindered rotor potential. Gold line (Harmonic hessian + 1 dihedral) is for the case when the DOS are calculated from the harmonic Hessian together with the scaling factor with the inclusion of the hindered rotor potential.

Comparing between the k_{loss} obtained from the “Harmonic hessian” and “Harmonic hessian + 1 dihedral” models, the inclusion of the hindered rotor potential promotes k_{loss} for all the species but the degree of change varies. At 25 K with a total density of 10^{-17} molecule cm^{-3}, for CH_2O, the k_{loss} rises from 7.65×10^{-13} to 6.77×10^{-12} cm^3 molecule^{-1} s^{-1}; for CH_3CHO, it is from 1.82×10^{-12} to 4.39×10^{-12} cm^3 molecule^{-1} s^{-1}; for $CH_3C(O)CH_3$, it is from 8.36×10^{-11} to 1.34×10^{-10} cm^3 molecule^{-1} s^{-1}; and for NH_3, it is from 4.02×10^{-12} to 1.15×10^{-11} cm^3 molecule^{-1} s^{-1}. The difference in the increment can be explained by the ratio of the DOS of the dimer calculated from the “Harmonic hessian + 1 dihedral” model to that from the “Harmonic hessian” model. The plots of the DOS against the grain energy, which are based on the output from the MESMER calculations, can be found in Figure 6.16. While the DOS obtained from both models are of about the same order of magnitude for other species, there is an obvious diverging trend for CH_2O, with the DOS higher by almost an order of magnitude with the inclusion of the hindered rotor potential. Therefore, the increment in k_{loss} is slightly more than an order of magnitude for CH_2O, higher than the 1.5–4 times for the other species, when the hindered rotor potential is used in the calculations.

Considering the trend of the calculated k_{loss} across different species, at low temperature, $CH_3C(O)CH_3$ has the largest calculated k_{loss} followed by NH_3. CH_2O has a slightly smaller k_{loss} than CH_3CHO when the “Harmonic hessian” model is considered but this is reversed when the hindered rotor potential is included. The results show that k_{loss} depends on both the dimerisation energy and the DOS. The $CH_3C(O)CH_3$ dimer has the deepest potential well among the species, which explains the largest k_{loss}. Based on the relative energy of the dimer structure, CH_3CHO should have a greater k_{loss} than CH_2O. However, as shown in Figure 6.16, CH_2O has a higher ratio of the dimer DOS to the monomer DOS than CH_3CHO, which makes k_{loss} of CH_2O become comparable with that of CH_3CHO, and the introduction of the hindered rotor potential helps boost the CH_2O dimer DOS to a larger extent, further increasing k_{loss} as mentioned above to a level even higher than that of CH_3CHO. The effect of the promotion of k_{loss} by the DOS can also be seen for NH_3. Although the NH_3

dimer has the shallowest potential well among these four species, it has a remarkably high k_{loss}, which is higher than that for both CH_2O and CH_3CHO and even higher than for $CH_3C(O)CH_3$ at higher temperature. This is due to the exceptionally large dimer DOS to monomer DOS ratio, about 10^2–10^4 as shown in Figure 6.16. This large ratio is contributed from those small frequency values of the new vibrational modes, in particular the smallest one (43.67 cm^{-1}, although such values can be of high uncertainties), emerging from the formation of the dimers when compared with the frequency values of the vibrational modes that originally were present in the monomer (H-N-H bending and N-H stretching) as listed in Table 6.6.

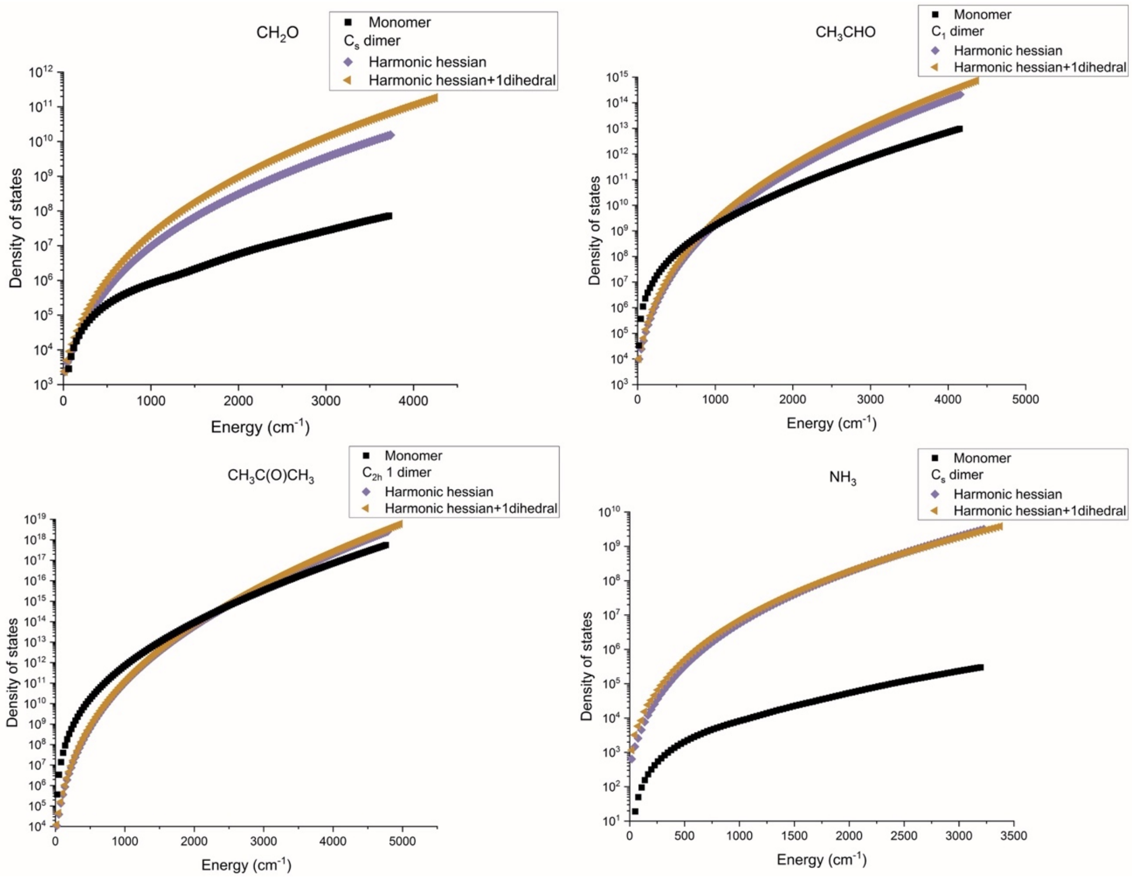

Figure 6.16 Plots of grain rovibronic DOS of both the monomers (black) and the dimers of (top left) CH_2O, (top right) CH_3CHO, (bottom left) $CH_3C(O)CH_3$ and (bottom right) NH_3 against the grain energy. Purple points are for the case when the "Harmonic hessian" model was used for the calculation of DOS while gold points are for the case when the "Harmonic hessian + 1 dihedral" model was used.

6.3.3 Dimerisation under the context of the Laval nozzle experiments

MESMER calculations were then performed using the conditions of the Laval experiments. Using the temperature and number density profiles of the 52 K nozzle shown in Figure 6.5 and Figure 6.6 respectively, with Ar as the bath gas, values of k_{loss} along the gas flow within the nozzle were computed and plotted in Figure 6.17. As the molecules travel along the flow, two competing factors are in effect, a decreasing temperature which favours the dimer formation but a decreasing total number density due to the expansion which makes the association reaction less probable to occur. It was found that in general k_{loss} is higher near the exit of the nozzle compared to that near the sonic point. For CH_2O, from the sonic point to the nozzle exit, k_{loss} increases from 2.02×10^{-15} to 1.38×10^{-14} cm^3 molecule^{-1} s^{-1} and from 2.26×10^{-14} to 1.79×10^{-13} cm^3 molecule^{-1} s^{-1} for the “Harmonic hessian” and “Harmonic hessian + 1 dihedral” model respectively. For CH_3CHO, k_{loss} increases from 2.36×10^{-15} to 3.81×10^{-14} cm^3 molecule^{-1} s^{-1} for the “Harmonic hessian” model and from 8.66×10^{-15} to 1.35×10^{-13} cm^3 molecule^{-1} s^{-1} for the “Harmonic hessian + 1 dihedral” model. For $CH_3C(O)CH_3$, k_{loss} increases from 1.28×10^{-14} to 2.79×10^{-12} cm^3 molecule^{-1} s^{-1} for the “Harmonic hessian” model and from 3.02×10^{-14} to 6.19×10^{-12} cm^3 molecule^{-1} s^{-1} when the hindered rotor potential is included. The curve for NH_3 is slightly different, for the “Harmonic hessian” model, k_{loss} initially decreases from 8.24×10^{-14} cm^3 molecule^{-1} s^{-1} down to 4.34×10^{-14} cm^3 molecule^{-1} s^{-1} before rising to 1.18×10^{-13} cm^3 molecule^{-1} s^{-1} and for the “Harmonic hessian + 1 dihedral” model drops from 1.30×10^{-13} cm^3 molecule^{-1} s^{-1} to 9.63×10^{-14} cm^3 molecule^{-1} s^{-1} before rising to 3.72×10^{-13} cm^3 molecule^{-1} s^{-1}. The trend of k_{loss} comparing across different monomer species is the same as described in the previous section.

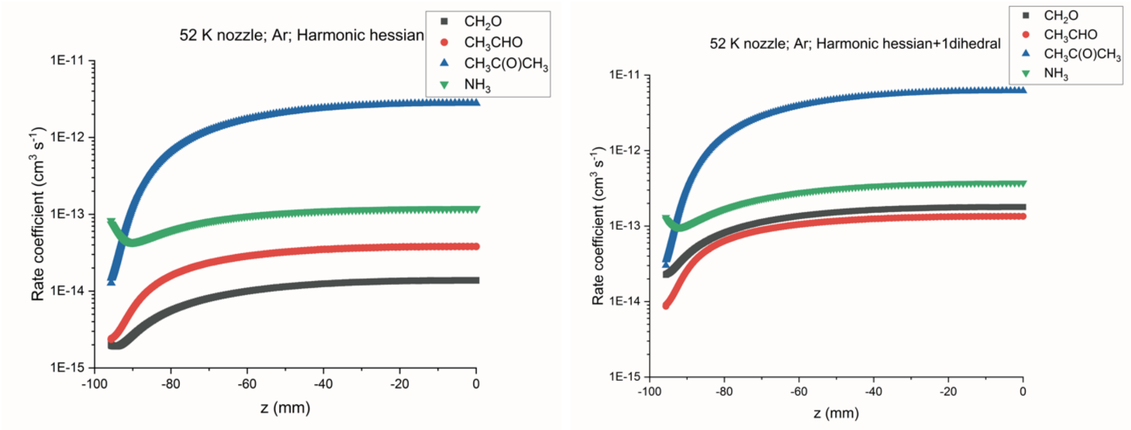

Figure 6.17 Calculated k_{loss} for the monomers of (black) CH_2O, (red) CH_3CHO, (blue) $CH_3C(O)CH_3$ and (green) NH_3 within the 52 K nozzle from the sonic point to the exit of the nozzle using Ar as the bath gas. "Harmonic hessian" model was used on the left while "Harmonic hessian + 1 dihedral" model was used on the right.

Based on the k_{loss} obtained, the fraction of dimers f_{dimer} and monomers f_{monomer} present were computed as a function of distance for different concentrations of monomers used. The calculations extended from within the nozzle down to the stable flow region by assuming the conditions in the stable flow region are constant and the same as those right at the nozzle exit. Apart from showing the plots of f_{monomer} along the gas flow, plots of f_{monomer} in the stable flow region at *z* = 100 mm are presented as typically this is where the kinetic measurements are taken and beyond that the jet may start to break up. Multiplying the values of f_{monomer} at *z* = 100 mm with the concentration of monomers if there is no dimerisation gives the actual concentration of monomers, which can be compared with the experimental results provided by Dr Kevin Douglas and Dr Mark Blitz obtained from the fluorescence signals from the monomers, which are measurements of the actual concentration of monomers.

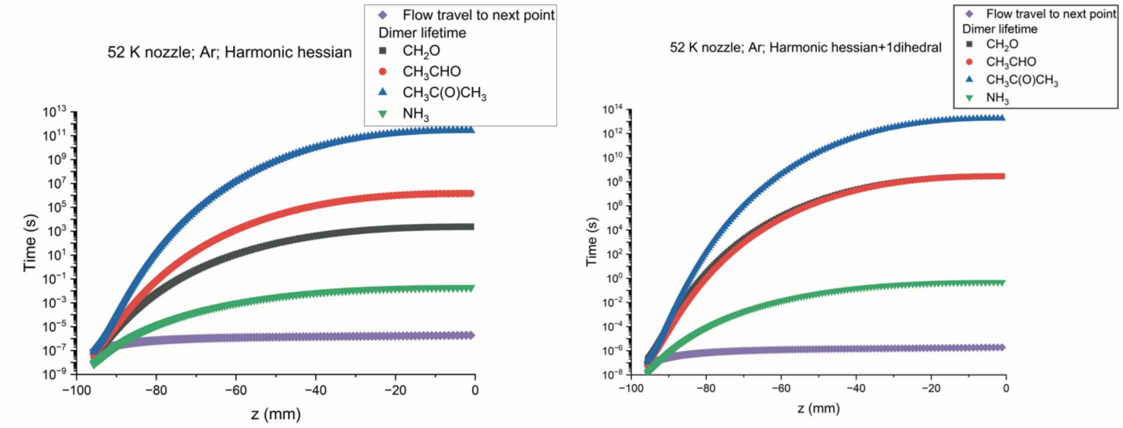

Figure 6.18 Lifetime of the stabilised dimers of (black) CH_2O, (red) CH_3CHO, (blue) $CH_3C(O)CH_3$ and (green) NH_3 within the 52 K nozzle from the sonic point to the exit of the nozzle using Ar as the bath gas and a monomer concentration of 2×10^{14} molecule cm^{-3} at the exit of the nozzle if there is no dimerisation. Plotted together is the travelling time of the gas flow from one data point to the subsequent data point (purple). “Harmonic hessian” model was used on the left while “Harmonic hessian + 1 dihedral” model was used on the right.

As mentioned before, it is assumed here that the lifetime of the stabilised dimers is longer than the time for them to travel down the gas flow. Figure 6.18 shows the lifetime of the stabilised dimers with the 52 K nozzle, together with the travelling time of the gas flow from one data point to the subsequent one. It can be seen that for CH_2O, CH_3CHO, and $CH_3C(O)CH_3$, the lifetime of the stabilised dimers is longer than the time to travel from one data point to the subsequent one at each data point. However, the lifetime is approximately the same order of magnitude as the travelling time in the earlier portion, about the first 5 mm when using the “Harmonic hessian” model while about the first 2 mm when using the “Harmonic hessian + 1 dihedral” model, of the 52 K nozzle. For NH_3, the lifetime of the stabilised dimer is actually shorter than the travelling time to the subsequent data point in the 52 K nozzle for the first 6 mm when using the “Harmonic hessian” model while the first 4 mm when using the “Harmonic hessian + 1 dihedral” model. Therefore, for the following calculations, it is expected that there is a larger overestimation in f_{dimer} for NH_3.

For CH_2O, with Ar as the bath gas, f_{monomer} along the gas flow for different $[\mathrm{monomer}]$ used are shown in Figure 6.19. f_{monomer} decreases slowly and steadily all the way when low $[\mathrm{monomer}]$ is used and the drop is slightly faster within the nozzle for higher $[\mathrm{monomer}]$. For the maximum $[\mathrm{monomer}]$ used in experiments performed by our group, this value is typically no bigger than 10^{15} molecule cm^{-3} at the nozzle exit, and usually considerably lower than this. Closest to this value will be the yellow-green points in Figure 6.19 corresponding to a $[\mathrm{monomer}]$ of 9.8×10^{14} molecule cm^{-3} at the nozzle exit without dimerisation, and the results show that theoretically ~99.7% and ~99.4% of CH_2O should remain in the monomer form at the nozzle exit and at z = 150 mm respectively for the "Harmonic hessian" model. These two values change to ~96.1% and ~92.2% when the hindered rotor potential is included. This result suggests that there is a similar share of the contributions of dimers formed within the nozzle and out of the nozzle as the dimer formation rate at a particular point depends on both the k_{loss}, which is larger in the stable flow than the beginning of the nozzle, and the monomer concentration, which is diluting during the expansion, at that point. Considering the deviation from the scenario when there is no dimerisation at all, at z = 100 mm, for the "Harmonic hessian" model, the curvature only occurs beyond a $[\mathrm{monomer}]$ of 2×10^{15} molecule cm^{-3}, while for the "Harmonic hessian + 1 dihedral" model, it starts to occur at about 6×10^{14} molecule cm^{-3} as shown in the left panel of Figure 6.20. Experimental data have been obtained at 40 K using He and Ar as the bath gas and are plotted in the right panel of Figure 6.20. Curvature starts to be observed when $[\mathrm{monomer}]$ is beyond 2×10^{14} molecule cm^{-3} for He and 5×10^{13} molecule cm^{-3} for Ar. Although the conditions, such as the temperature and the nozzle used, between the experiments and the calculations are different, it still shows that the curvature begins to occur at a much lower $[\mathrm{monomer}]$ during experiments than predicted from the MESMER calculations.

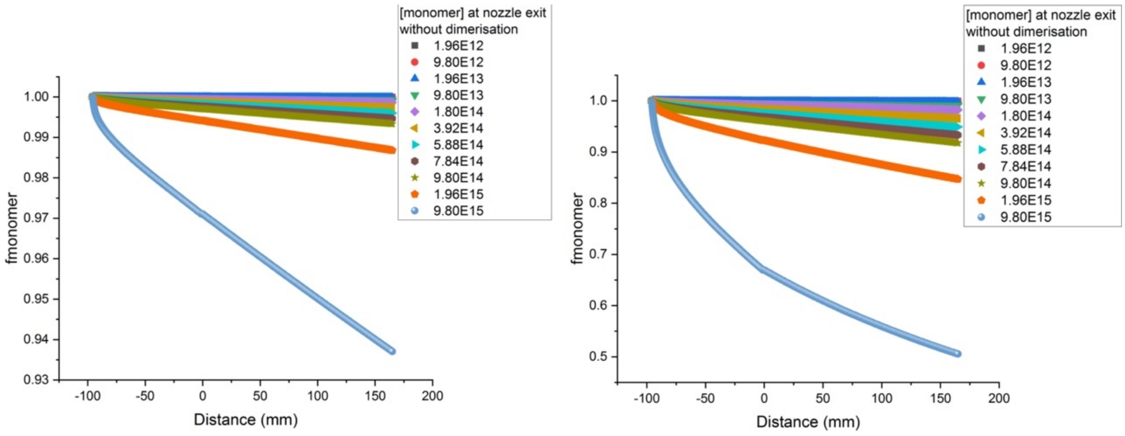

Figure 6.19 Calculated $f_{monomer}$ of CH_2O at different distances along the gas flow with different monomer concentrations using the “Harmonic hessian” model (left) and “Harmonic hessian + 1 dihedral” model (right) respectively using Ar as the bath gas. The values in the legend correspond to the supposed monomer concentration in molecule cm^{-3} at the exit of the 52 K nozzle and in the stable flow ($z \geq 0$) if there is no dimerisation.

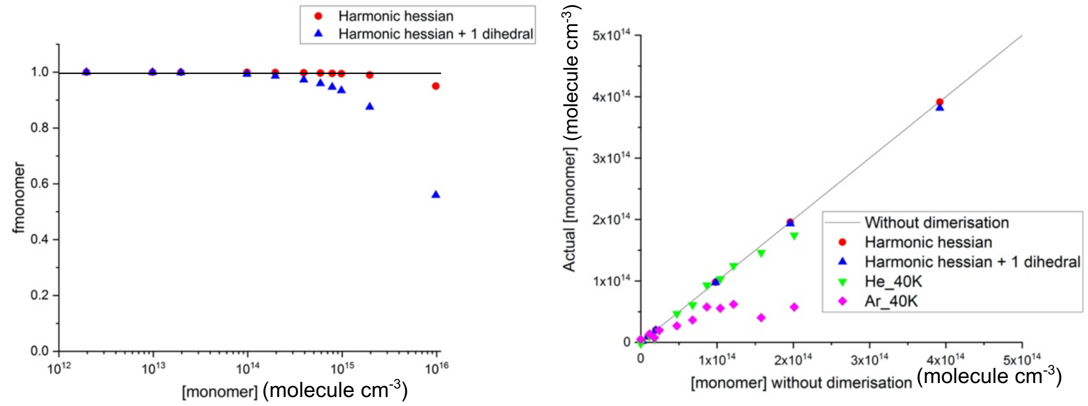

Figure 6.20 (left) Calculated $f_{monomer}$ of CH_2O at z = 100 mm using the “Harmonic hessian” model (red) and “Harmonic hessian + 1 dihedral” model (blue) plotted against the [monomer] if there is no dimerisation. Curvature can be seen as a deviation from the $f_{monomer}$ = 1 level, the latter represents the scenario if there is no dimerisation. (right) Actual [monomer] present at z = 100 mm plotted against the [monomer] if there is no dimerisation. In addition to the calculated results, experimental data obtained at 40 K with He (green) and Ar (pink) as the bath gas are included as a comparison. Curvature can be seen as a deviation from the black line, which represents the scenario if there is no dimerisation.

For CH_3CHO, the calculated f_{monomer} along the gas flow for different $[\mathrm{monomer}]$ is plotted in Figure 6.21 and show a similar trend as that of CH_2O. Considering a $[\mathrm{monomer}]$ of 9.8 × 10^{14} molecule cm^{-3} at the nozzle exit without dimerisation, for the "Harmonic hessian" model theoretically ~99.3% and ~98.2% of CH_3CHO should remain in the monomer form at the nozzle exit and at z = 150 mm respectively. The inclusion of the hindered rotor potential changes these two values to ~97.2% and ~94.2%. Again there is a similar contribution of the formation of dimers from the region within the nozzle and out of the nozzle. At z = 100 mm, the emergence of an observable curvature in the f_{monomer} is predicted to be at $[\mathrm{monomer}]$ = 2 × 10^{15} molecule cm^{-3} and 8 × 10^{14} molecule cm^{-3} using the "Harmonic hessian" model and "Harmonic hessian + 1 dihedral" model respectively as shown in Figure 6.22. Experimental data are available at 25 K with Ar as the bath gas, and the curvature in the actual $[\mathrm{monomer}]$ begins to occur at $[\mathrm{monomer}]$ = 1 × 10^{15} molecule cm^{-3} but it decreases faster than the calculated values as the $[\mathrm{monomer}]$ used increases. However, the discrepancy between the experimental measurements and the calculated values predicted from the models is smaller than that in the case for CH_2O.

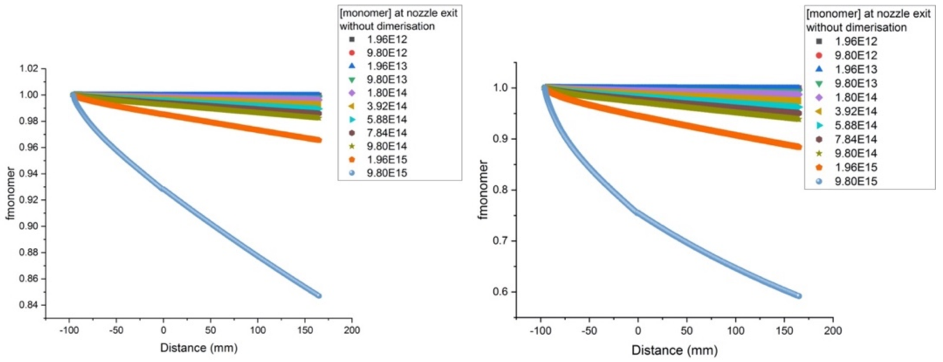

Figure 6.21 Calculated f_{monomer} of CH_3CHO at different distances along the gas flow with different monomer concentrations using the "Harmonic hessian" model (left) and "Harmonic hessian + 1 dihedral" model (right) respectively using Ar as the bath gas. The values in the legend correspond to the supposed monomer concentration in molecule cm^{-3} at the exit of the 52 K nozzle and in the stable flow ($z \geq 0$) if there is no dimerisation.

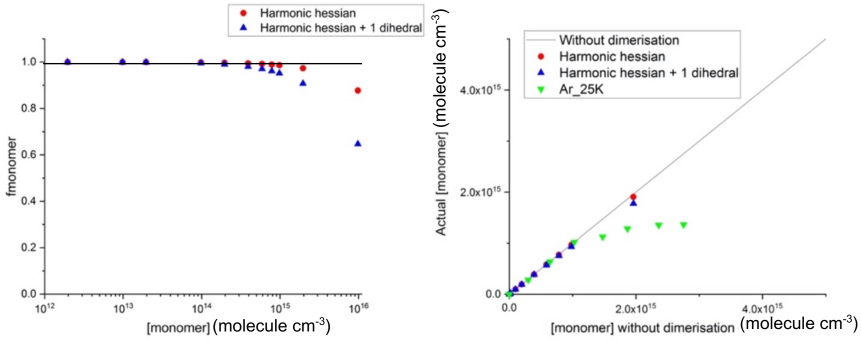

Figure 6.22 (left) Calculated f_{monomer} of CH_3CHO at z = 100 mm using the "Harmonic hessian" model (red) and "Harmonic hessian + 1 dihedral" model (blue) plotted against the [monomer] if there is no dimerisation. Curvature can be seen as a deviation from the f_{monomer} = 1 level, which represents the scenario if there is no dimerisation. (right) Actual [monomer] present at z = 100 mm plotted against the [monomer] if there is no dimerisation. In addition to the calculated results, experimental data obtained at 25 K with Ar (green) as the bath gas are included as a comparison. Curvature can be seen as a deviation from the black line, which represents the scenario if there is no dimerisation.

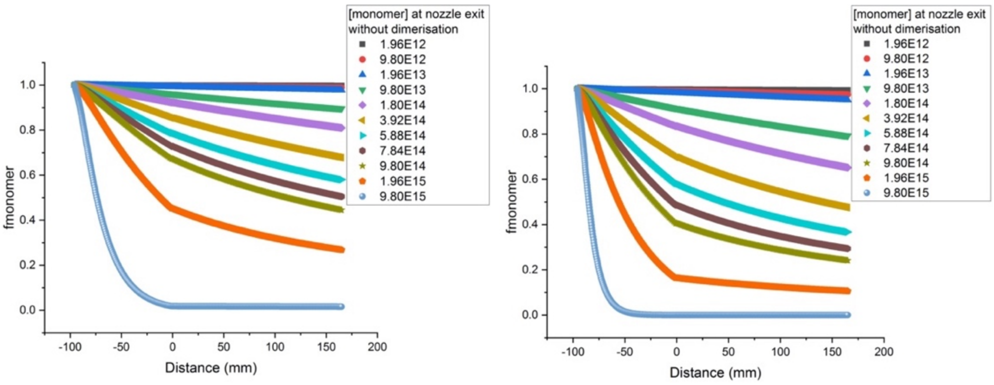

Figure 6.23 Calculated f_{monomer} of $CH_3C(O)CH_3$ at different distances along the gas flow with different monomer concentrations using the "Harmonic hessian" model (left) and "Harmonic hessian + 1 dihedral" model (right) respectively using Ar as the bath gas. The values in the legend correspond to the supposed monomer concentration in molecule cm^{-3} at the exit of the 52 K nozzle and in the stable flow ($z \geq 0$) if there is no dimerisation.

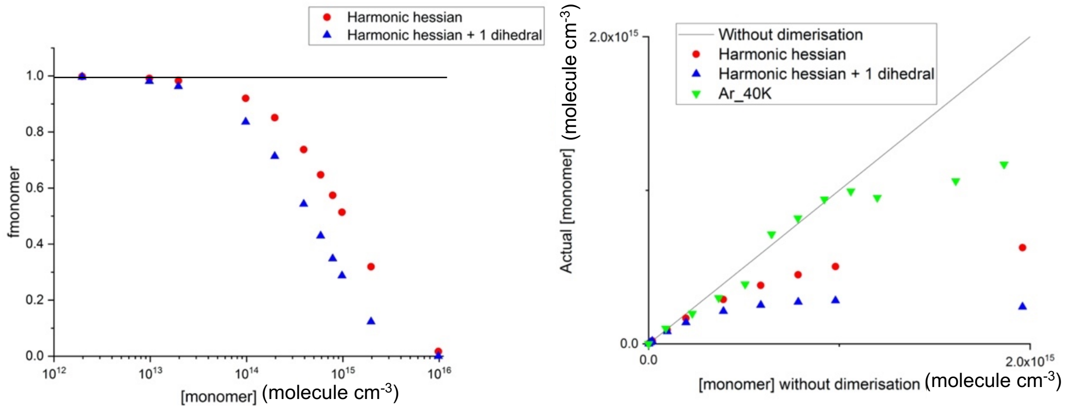

Figure 6.24 (left) Calculated *f*$_{\mathrm{monomer}}$ of $CH_3C(O)CH_3$ at *z* = 100 mm using the "Harmonic hessian" model (red) and "Harmonic hessian + 1 dihedral" model (blue) plotted against the [monomer] if there is no dimerisation. Curvature can be seen as a deviation from the *f*$_{\mathrm{monomer}}$ = 1 level, which represents the scenario if there is no dimerisation. (right) Actual [monomer] present at *z* = 100 mm plotted against the [monomer] if there is no dimerisation. In addition to the calculated results, experimental data obtained at 40 K with Ar (green) as the bath gas are included as a comparison. Curvature can be seen as a deviation from the black line, which represents the scenario if there is no dimerisation.

For $CH_3C(O)CH_3$, because of having a larger value of k_{loss}, there is a greater drop in f_{monomer} within the nozzle before the gas flow reaches the stable flow region, indicating that there is a bigger share of dimers which are formed within the nozzle. Considering a $[\mathrm{monomer}]$ of 9.8×10^{14} molecule cm^{-3} at the nozzle exit without dimerisation, as shown in Figure 6.23, it is predicted that only ~67.3% and ~46.0% of $CH_3C(O)CH_3$ remain in the monomer form at the nozzle exit and at *z* = 150 mm respectively with the "Harmonic hessian" model and the values drop even lower to ~40.6% and ~25.1% with the "Harmonic hessian + 1 dihedral" model. All of the monomers are depleted within the nozzle before being able to come out if a $[\mathrm{monomer}]$ of 9.8×10^{15} molecule cm^{-3} is attempted to be used. Thus, the concentration of $CH_3C(O)CH_3$ used in previous kinetics experiments by our group (123), typically no more than 1–4 × 10^{14} molecule cm^{-3} at the nozzle exit, was much less than that for other species. At *z* = 100 mm, f_{monomer} starts to curve over at $[\mathrm{monomer}]$ = 1×10^{14} molecule cm^{-3} and 2

× 10^{13} molecule cm^{-3} using the "Harmonic hessian" model and "Harmonic hessian + 1 dihedral" model respectively as shown in Figure 6.24. Experiments were performed at 40 K with Ar as the bath gas and the curvature in the actual $[\mathrm{monomer}]$ emerges beyond 1 × 10^{15} molecule cm^{-3} $[\mathrm{monomer}]$, which in contrast to the other monomers (CH_2O and CH_3CHO) is at a higher concentration than for the predicted values.

For NH_3, as near the sonic point the value of k_{loss} is comparable to that in the stable flow, f_{monomer} show an initial dip first before continuing for a more gradual decrease as shown in Figure 6.25. Therefore, it is expected that there is a higher proportion of dimers formed within the nozzle. Considering a $[\mathrm{monomer}]$ of 9.8 × 10^{14} molecule cm^{-3} at the nozzle exit without dimerisation, f_{monomer} are found to be ~96.0% and ~93.4% at the nozzle exit and at z = 150 mm respectively with the "Harmonic hessian" model and ~90.6% and ~83.6% when the hindered rotor potential is included. At z = 100 mm, f_{monomer} starts to curve over at $[\mathrm{monomer}]$ = 6 × 10^{14} molecule cm^{-3} and 4 × 10^{14} molecule cm^{-3} using the "Harmonic hessian" model and "Harmonic hessian + 1 dihedral" model respectively as shown in Figure 6.26. Experimental data have been obtained at 40 K using Ar as the bath gas and curvature in $[\mathrm{monomer}]$ starts to be observed when it is beyond 2 × 10^{14} molecule cm^{-3}. In spite of the difference between the experimental and the calculated values for NH_3, the discrepancy is smaller than that for CH_2O.

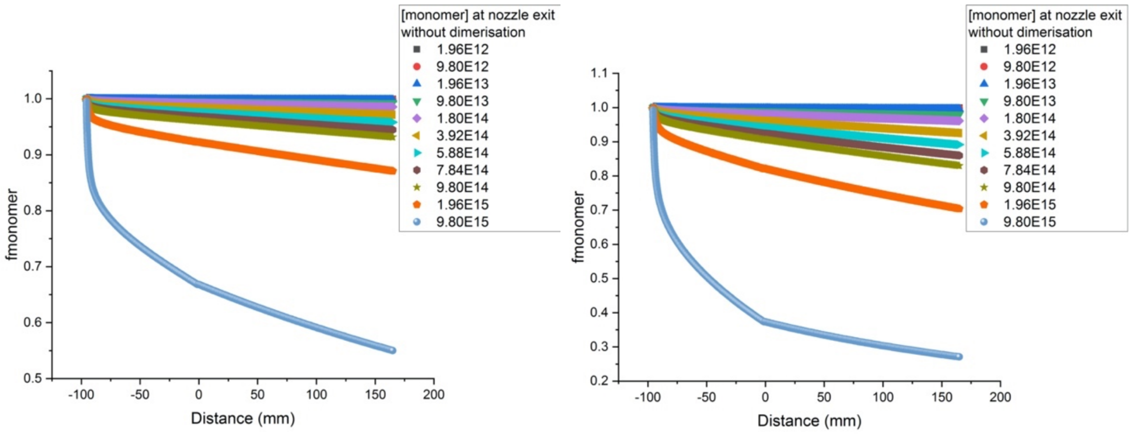

Figure 6.25 Calculated $f_{monomer}$ of NH_3 at different distances along the gas flow with different monomer concentrations using the "Harmonic hessian" model (left) and "Harmonic hessian + 1 dihedral" model (right) respectively using Ar as the bath gas. The values in the legend correspond to the supposed monomer concentration in molecule cm^{-3} at the exit of the 52 K nozzle and in the stable flow ($z \geq 0$) if there is no dimerisation.

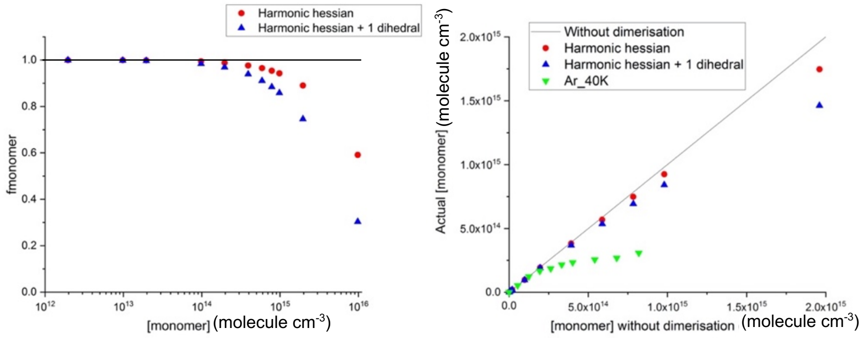

Figure 6.26 (left) Calculated $f_{monomer}$ of NH_3 at z = 100 mm using the "Harmonic hessian" model (red) and "Harmonic hessian + 1 dihedral" model (blue) plotted against the [monomer] if there is no dimerisation. Curvature can be seen as a deviation from the $f_{monomer}$ = 1 level, which represents the scenario if there is no dimerisation. (right) Actual [monomer] present at z = 100 mm plotted against the [monomer] if there is no dimerisation. In addition to the calculated results, experimental data obtained at 40 K with Ar (green) as the bath gas are included as a comparison. Curvature can be seen as a deviation from the black line, which represents the scenario if there is no dimerisation.

The properties of the nozzles used by our group (M2.25 N_2 106K, M2.75 N_2 91K, M3.3 N_2 85K, M4 He 35K) as listed in Table 6.1 were then scaled with respect to those of the 52 K nozzle. The scaled temperature, number density, Mach number and flow speed profiles within the four nozzles can be found in the upper panels of Figure 6.27, Figure 6.29, Figure 6.31 and Figure 6.33. The calculated k_{loss} based on these scaled parameters for the respective nozzles are plotted in the lower panels of these figures. Consider the 106 K, 91 K and 85 K nozzles, given using the same DOS calculation model, k_{loss} for all the species increases slightly when switching to a nozzle with lower temperature. This is because the dimerisation reaction is favoured at a lower temperature. However, when switching to the 35 K nozzle, k_{loss} for the 35 K nozzle do not emerge to be higher than those for the 106 K, 91 K and 85 K nozzles because of the use of a different bath gas. He, with $\langle \Delta E \rangle_{down,\mathrm{He}} = 100 \left(\frac{T}{298\ \mathrm{K}}\right)^{1.0}\ \mathrm{cm}^{-1}$, is a weaker collider compared with N_2, with $\langle \Delta E \rangle_{down,\mathrm{N_2}} = 250 \left(\frac{T}{298\ \mathrm{K}}\right)^{0.25}\ \mathrm{cm}^{-1}$.

Comparing the k_{loss} profiles within all these four nozzles with that of the 52 K nozzle using Ar bath gas, the values are higher for the 52 K nozzle. A lower temperature is the main factor for the 52 K nozzle to have larger k_{loss} than the 106 K, 91 K and 85 K nozzles while having a stronger collider as the bath gas is the main factor to have larger k_{loss} than the 35 K nozzle. Calculated f_{monomer} for different species at *z* = 100 mm in the stable flow region out of these nozzles are plotted in Figure 6.28, Figure 6.30, Figure 6.32 and Figure 6.34. The curvature for all the species happens at a higher $[\mathrm{monomer}]$ for these four nozzles used by our group than the 52 K Ar nozzle. The reasons include a larger k_{loss} as mentioned above, a smaller flow speed v due to the choice of the bath gas (Ar) and a longer nozzle distance L, which lead to a bigger Δt.

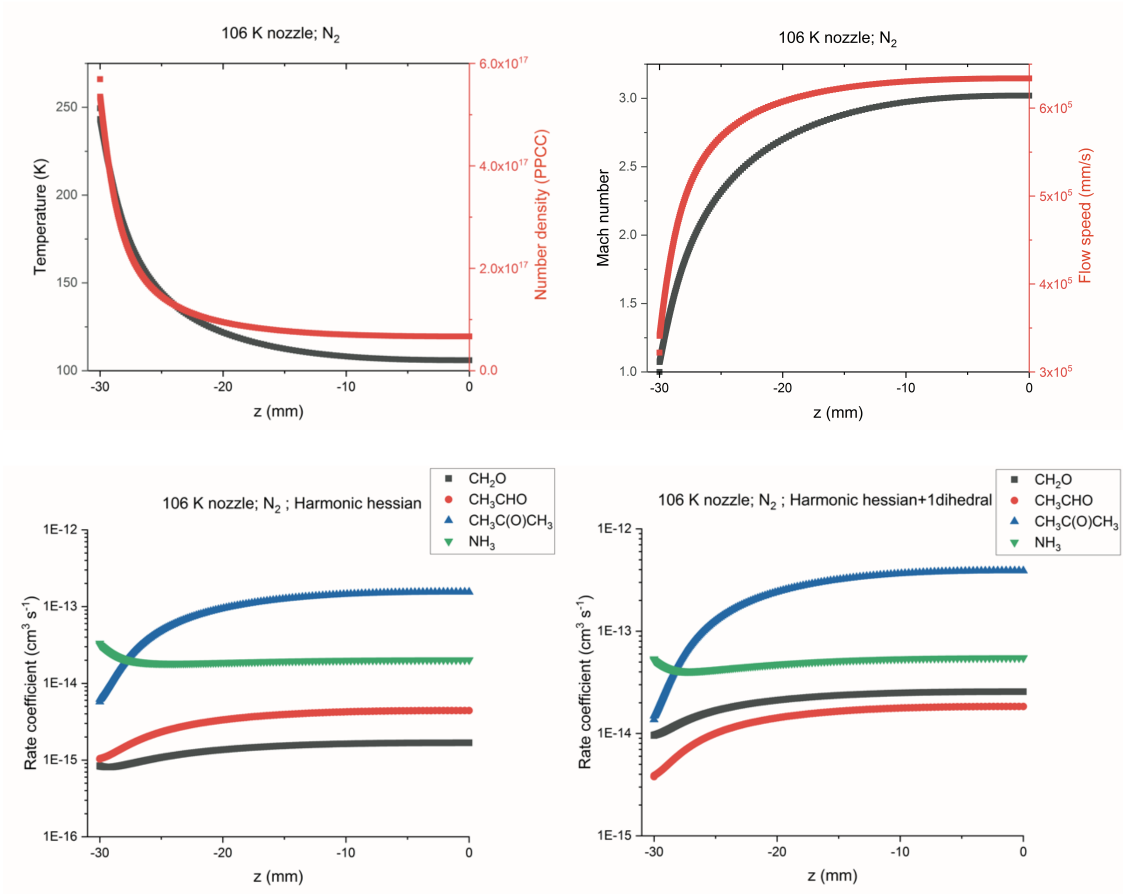

Figure 6.27 (Upper left) Temperature and number density profile within the M2.25 N_2 106 K nozzle from the sonic point to the nozzle exit. (Upper right) Mach number and flow speed profile within the M2.25 N_2 106 K nozzle from the sonic point to the nozzle exit. (Lower) Calculated k_{loss} for the monomers of (black) CH_2O, (red) CH_3CHO, (blue) $CH_3C(O)CH_3$ and (green) NH_3 within the M2.25 N_2 106 K nozzle from the sonic point to nozzle exit. "Harmonic hessian" model was used on the left while "Harmonic hessian + 1 dihedral" model was used on the right.

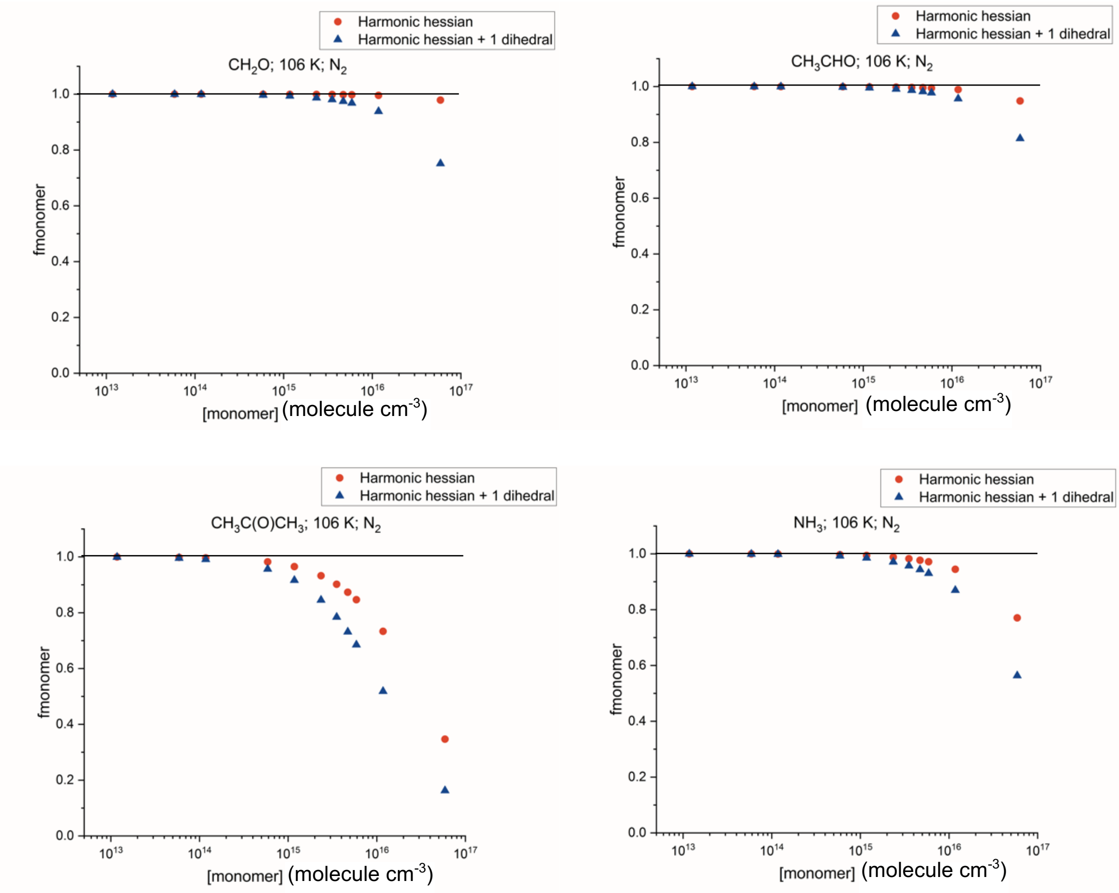

Figure 6.28 Calculated $f_{monomer}$ of (upper left) CH$_2$O, (upper right) CH$_3$CHO, (lower left) CH$_3$C(O)CH$_3$ and (lower right) NH$_3$ at z = 100 mm out of the M2.25 N$_2$ 106 K nozzle using the "Harmonic hessian" model (red) and "Harmonic hessian + 1 dihedral" model (blue) plotted against the [monomer] if there is no dimerisation. Curvature can be seen as a deviation from the $f_{monomer}$ = 1 level (black line), which represents the scenario if there is no dimerisation.

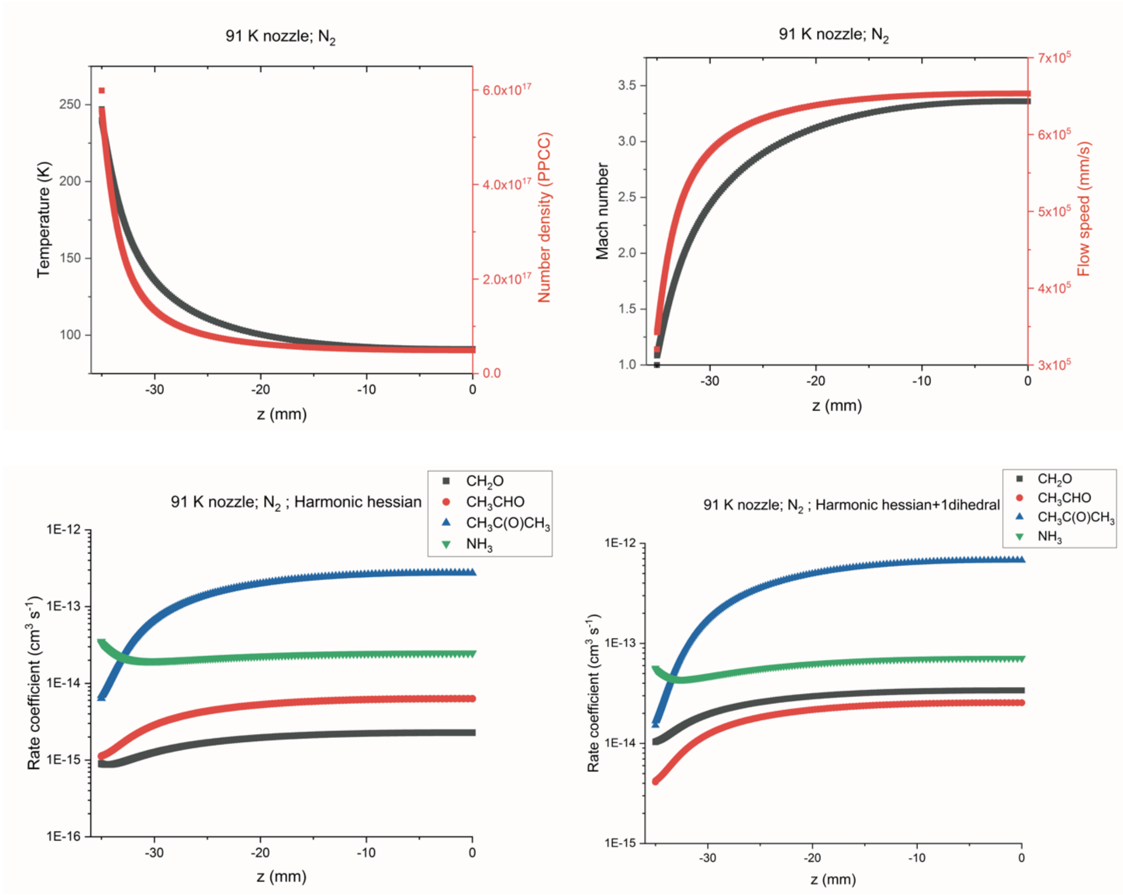

Figure 6.29 (Upper left) Temperature and number density profile within the M2.75 N_2 91 K nozzle from the sonic point to the nozzle exit. (Upper right) Mach number and flow speed profile within the M2.75 N_2 91 K nozzle from the sonic point to the nozzle exit. (Lower) Calculated k_{loss} for the monomers of (black) CH_2O, (red) CH_3CHO, (blue) $CH_3C(O)CH_3$ and (green) NH_3 within the M2.75 N_2 91 K nozzle from the sonic point to nozzle exit. "Harmonic hessian" model was used on the left while "Harmonic hessian + 1 dihedral" model was used on the right.

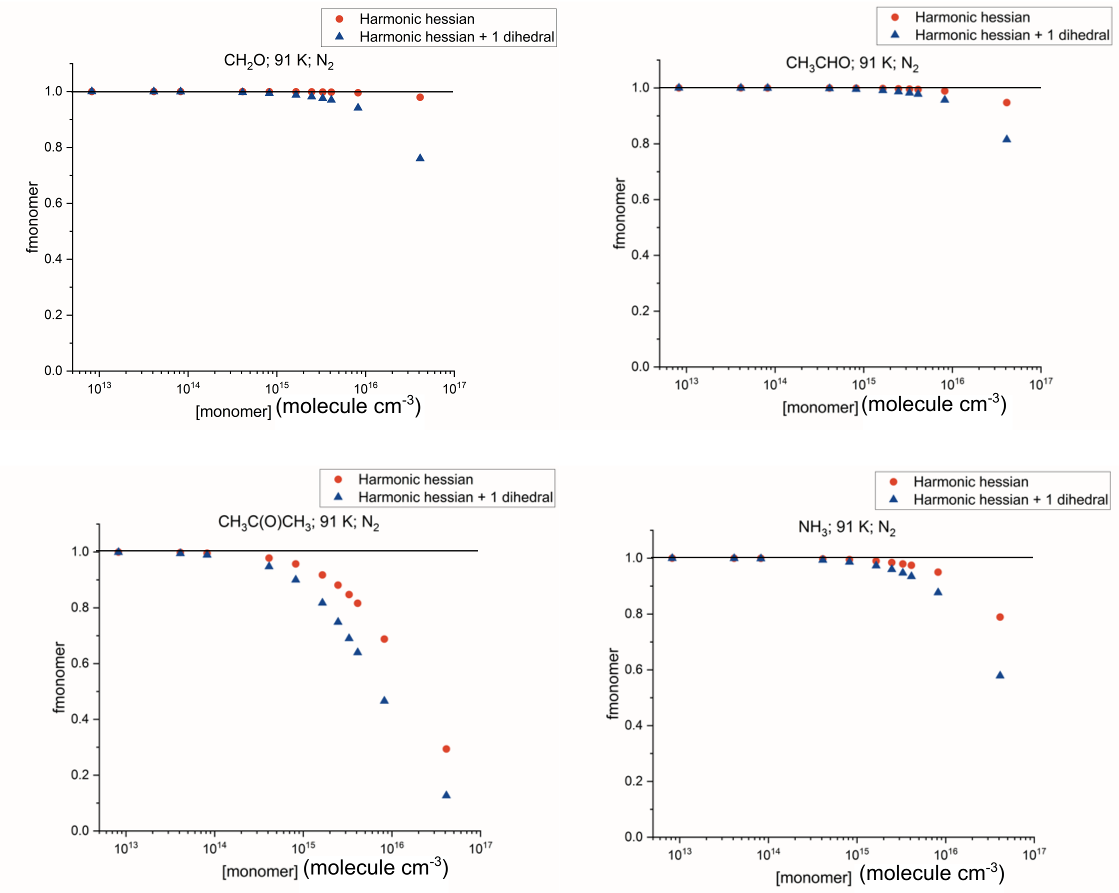

Figure 6.30 Calculated $f_{monomer}$ of (upper left) CH_2O, (upper right) CH_3CHO, (lower left) $CH_3C(O)CH_3$ and (lower right) NH_3 at z = 100 mm out of the M2.75 N_2 91 K nozzle using the "Harmonic hessian" model (red) and "Harmonic hessian + 1 dihedral" model (blue) plotted against the [monomer] if there is no dimerisation. Curvature can be seen as a deviation from the $f_{monomer}$ = 1 level (black line), which represents the scenario if there is no dimerisation.

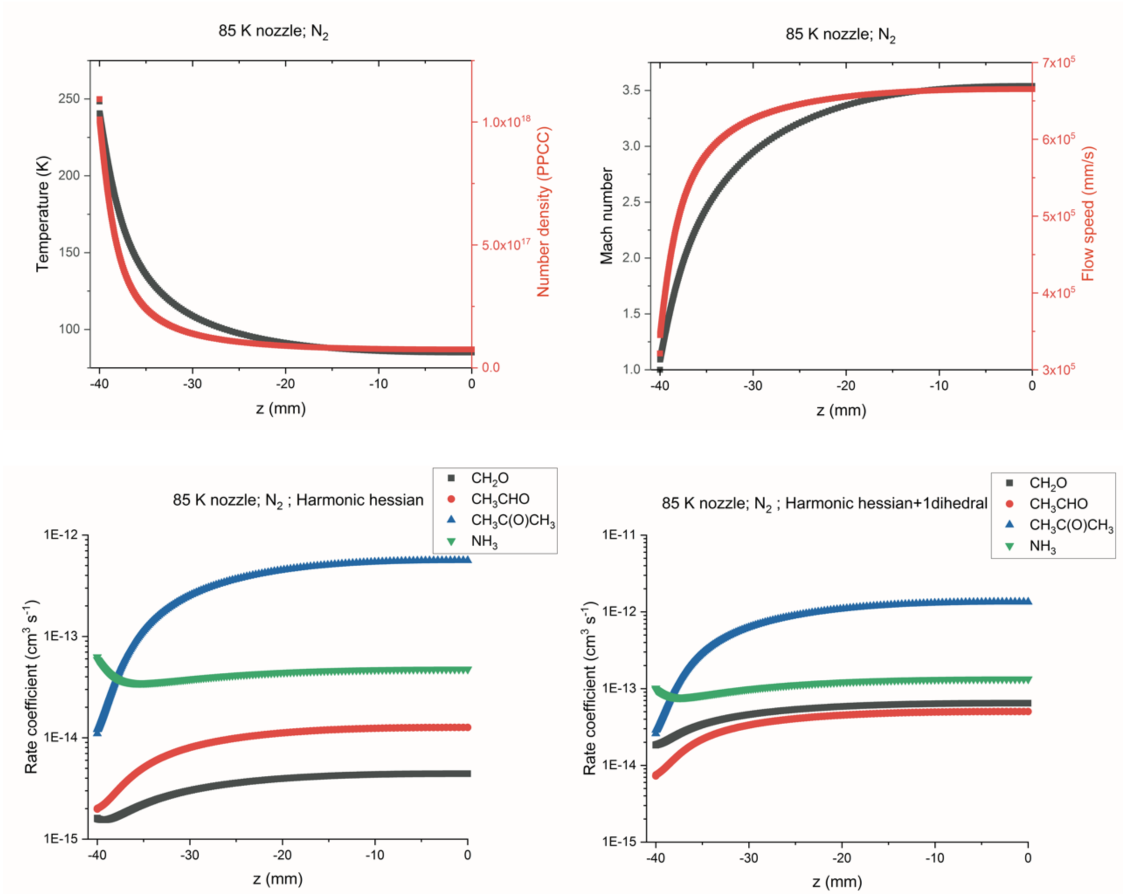

Figure 6.31 (Upper left) Temperature and number density profile within the M3.3 N_2 85 K nozzle from the sonic point to the nozzle exit. (Upper right) Mach number and flow speed profile within the M3.3 N_2 85 K nozzle from the sonic point to the nozzle exit. (Lower) Calculated k_{loss} for the monomers of (black) CH_2O, (red) CH_3CHO, (blue) $CH_3C(O)CH_3$ and (green) NH_3 within the M3.3 N_2 85 K nozzle from the sonic point to nozzle exit. “Harmonic hessian” model was used on the left while “Harmonic hessian + 1 dihedral” model was used on the right.

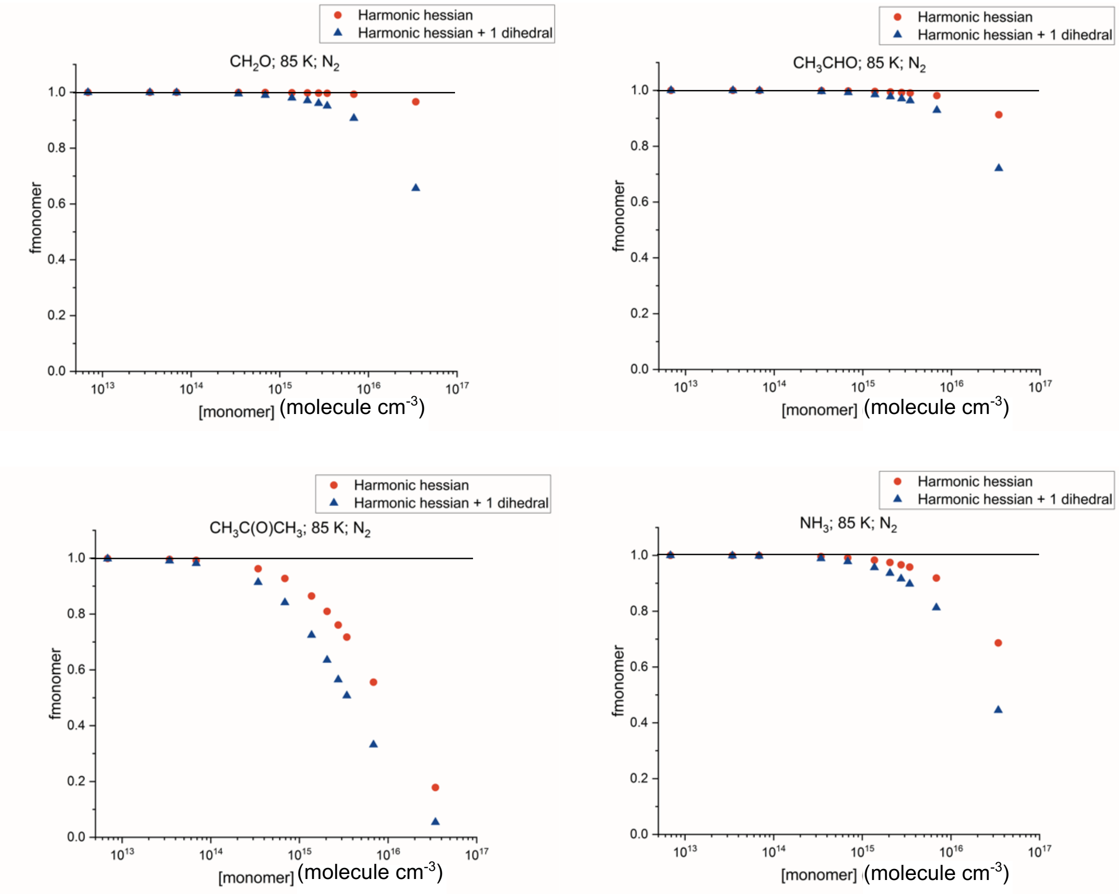

Figure 6.32 Calculated f_{monomer} of (upper left) CH_2O, (upper right) CH_3CHO, (lower left) $CH_3C(O)CH_3$ and (lower right) NH_3 at z = 100 mm out of the M3.3 N_2 85 K nozzle using the “Harmonic hessian” model (red) and “Harmonic hessian + 1 dihedral” model (blue) plotted against the [monomer] if there is no dimerisation. Curvature can be seen as a deviation from the f_{monomer} = 1 level (black line), which represents the scenario if there is no dimerisation.

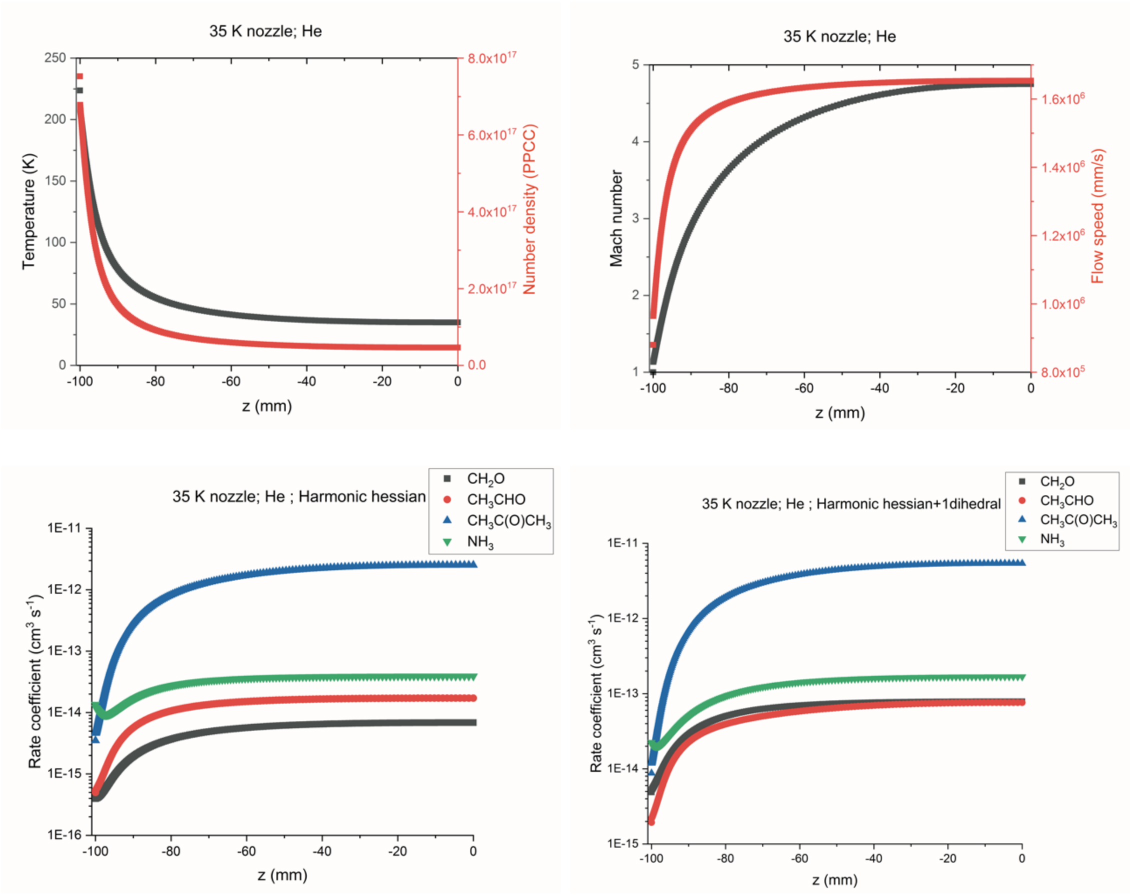

Figure 6.33 (Upper left) Temperature and number density profile within the M4 He 35 K nozzle from the sonic point to the nozzle exit. (Upper right) Mach number and flow speed profile within the M4 He 35 K nozzle from the sonic point to the nozzle exit. (Lower) Calculated k_{loss} for the monomers of (black) CH_2O, (red) CH_3CHO, (blue) $CH_3C(O)CH_3$ and (green) NH_3 within the M4 He 35 K nozzle from the sonic point to nozzle exit. "Harmonic hessian" model was used on the left while "Harmonic hessian + 1 dihedral" model was used on the right.

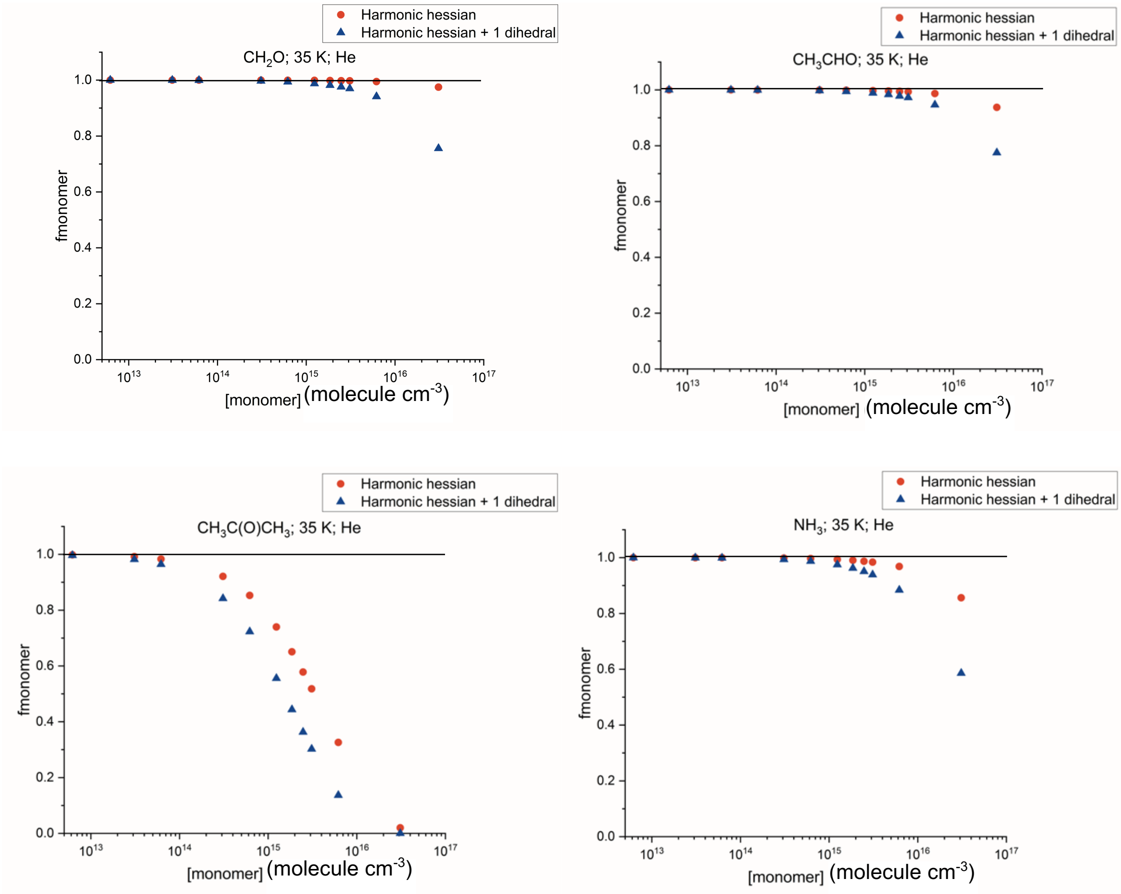

Figure 6.34 Calculated *f*$_{\mathbf{monomer}}$ of (upper left) CH_2O, (upper right) CH_3CHO, (lower left) $CH_3C(O)CH_3$ and (lower right) NH_3 at *z* = 100 mm out of the M4 He 35 K nozzle using the "Harmonic hessian" model (red) and "Harmonic hessian + 1 dihedral" model (blue) plotted against the [monomer] if there is no dimerisation. Curvature can be seen as a deviation from the *f*$_{\mathbf{monomer}}$ = 1 level (black line), which represents the scenario if there is no dimerisation.

6.3.4 Discussion

In this work, the rate coefficients of dimerisation are computed using statistical rate theory approach based on the computational chemistry results. While predictions for CH_2O, CH_3CHO, $CH_3C(O)CH_3$ and NH_3 have been made, some limitations in the approach are identified. First, the calculations based on the DOS are sensitive to the low vibrational frequency values, particularly those that only arise from the approach of the two monomers. These values are subject to large relative errors due to the floppy nature of the dimer structure arising from the weak intermolecular interactions. In addition, anharmonic oscillators, together with the full hindered rotor potentials, can give a better description of the molecular species than the simple harmonic oscillator model. However, due to the constraints of the software programmes used, calculations with the anharmonic model cannot be done. The relaxed scans of the dihedral angle also may not be exactly the same as the movement of the corresponding internal rotation which also contributes to the errors.

Despite the above limitations, the calculations performed by this work using the “Harmonic hessian + 1 dihedral” model give a better starting point for estimation of the dimerisation reaction under the conditions relevant to the Laval experiments. The agreement between the calculations and the experiments for the concentration of monomer at which a loss of monomer is first observed is closer for CH_3CHO, $CH_3C(O)CH_3$ and NH_3. However, CH_2O stands out as the odd one, with a much lower proportion remaining in the monomer form in experiments compared to that predicted from calculations. In order to provide a rough idea of the inconsistency, f_{monomer} were computed again for the 52 K Ar nozzle data but with k_{loss} artificially increased 10 times and then 100 times the original values. Figure 6.35 shows the corresponding calculated actual $[\text{monomer}]$ against different $[\text{monomer}]$ used in comparison with the experimental results. Considering the “Harmonic hessian + 1 dihedral” model for the 52 K Ar nozzle, the curvature of the data points matches with the experimental data at 40 K in He when a 10-fold increase in k_{loss} is used and with those in Ar when a 100-fold k_{loss} is used. This suggests that some factors are not fully understood and included in the current model in explaining the dimerisation of CH_2O. Similar multiplication to the calculated k_{loss} has also been done for other dimers to find the factor required to best fit the experimental data. It was found that this factor is ~50 for CH_2O, ~7 for CH_3CHO, ~0.1 for $CH_3C(O)CH_3$, and ~1 for NH_3.

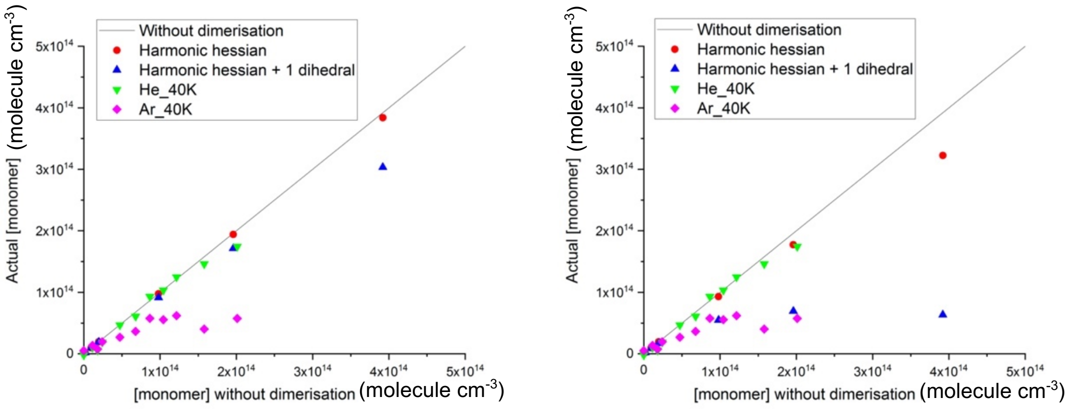

Figure 6.35 Actual [monomer] present at *z* = 100 mm using the "Harmonic hessian" model (red) and "Harmonic hessian + 1 dihedral" model (blue) with 10 times (left) and 100 times (right) the original k_{loss} plotted against the [monomer] if there is no dimerisation. Apart from the calculated results, experimental data obtained at 40 K with He (green) and Ar (pink) as the bath gas are included as comparison. Curvature can be seen as a deviation from the *y* = *x* black line, which represents the scenario if there is no dimerisation.

Some analysis has been performed on several different factors in their effect to increase the calculated k_{loss} so as to close the gap between the predicted and the experimental values. The first factor is the existence of multiple stable dimer structures. In particular, CH_3CHO dimer has the most number of different stable conformers, with six identified in this work (and eight identified at a more advanced level according to the recent study (138)), where the energy difference between the three lowest-energy conformers (C_1, C_2, C_i) is ~1 kJ mol^{-1}. Figure 6.36 shows the k_{loss} of CH_3CHO when multiple conformers are considered. Instead of only including a single channel (with ILT pre-exponential A^{∞} set as $3 \times 10^{-10}\ \mathrm{molecule}^{-1}\ \mathrm{s}^{-1}$) forming the C_1 dimer, calculations including three channels (each with ILT pre-exponential A^{∞} set as $1 \times 10^{-10}\ \mathrm{molecule}^{-1}\ \mathrm{s}^{-1}$) forming the three lowest-energy conformers (C_1, C_2, C_i) respectively and six channels (each with ILT pre-exponential A^{∞} set as $5 \times 10^{-11}\ \mathrm{molecule}^{-1}\ \mathrm{s}^{-1}$) forming all the conformers identified in this work have been done. The adjustment made to the ILT pre-exponential, that is, dividing the original value of $3 \times 10^{-10}\ \mathrm{molecule}^{-1}\ \mathrm{s}^{-1}$ by the number of available entrance channels, is based on the assumption that it is equally likely to enter each entrance channel. With the inclusion of three, instead of one, lowest-energy conformers, the k_{loss} is increased by a factor of 3–4, which can be explained by the increment of the DOS available. However, the increment in the k_{loss} by the further inclusion of the other higher-energy conformers is less significant. Nevertheless, the consideration of multiple conformers has already noticeable closed down the aforementioned gap of a factor of ~7.

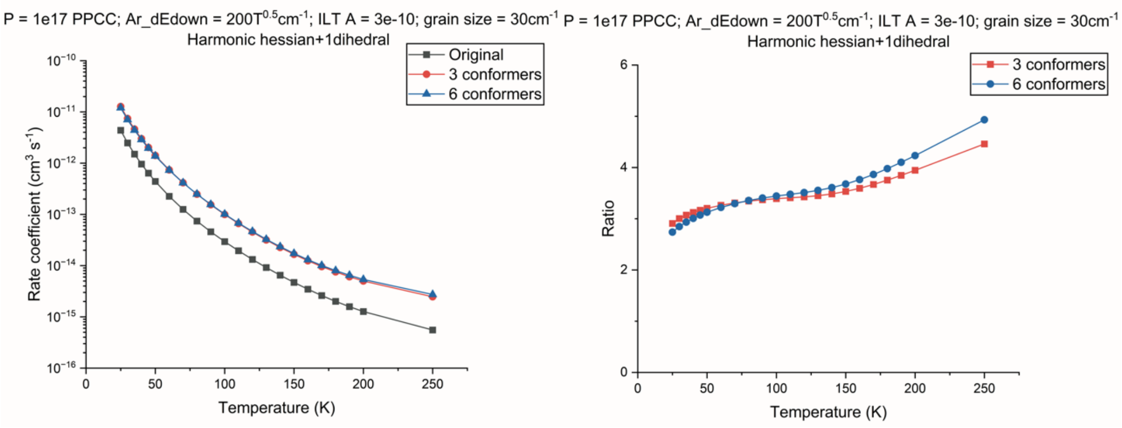

Figure 6.36 (Left) Calculated k_{loss} for the dimerisation reaction of CH_3CHO versus temperature in the range of T = 25–250 K with a total density of 10^{17} molecule cm^{-3} in Ar bath gas using the "Harmonic hessian + 1 dihedral" model when different number of dimer conformers are included in the MESMER calculations. Original: C_1 only; 3 conformers: the three lowest-energy conformers (C_1, C_2, C_i); 6 conformers: all the six conformers identified in this work (C_1, C_2, C_i, C_s, C_{2h} 1, C_{2h} 2). (Right) Ratio of k_{loss} using multiple number of conformers versus using only one conformer in the original model.

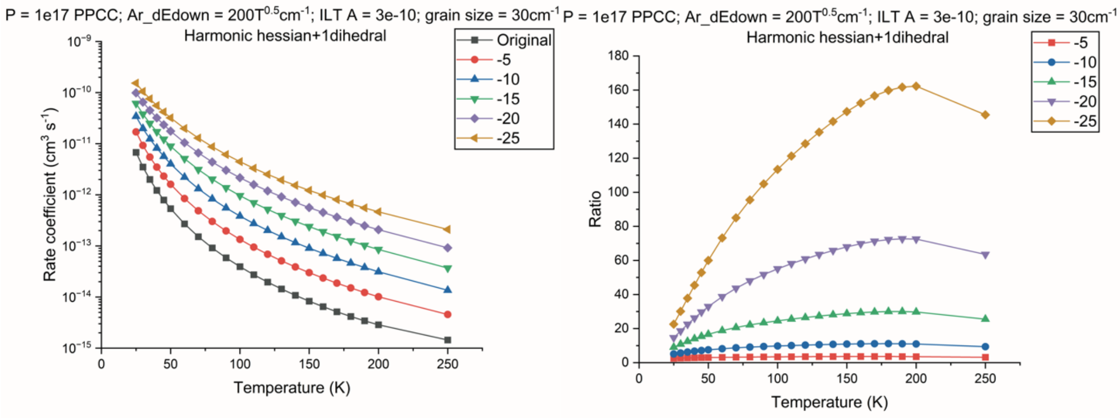

Figure 6.37 (Left) Calculated k_{loss} for the dimerisation reaction of CH_2O versus temperature in the range of T = 25–250 K with a total density of 10^{17} molecule cm^{-3} in Ar bath gas using the “Harmonic hessian + 1 dihedral” model when the relative energy of the dimer is artificially lowered. The legend denotes the amount of energy lowered in kJ mol^{-1}. (Right) Ratio of k_{loss} using the artificially lowered dimer energy value versus using the original energy value.

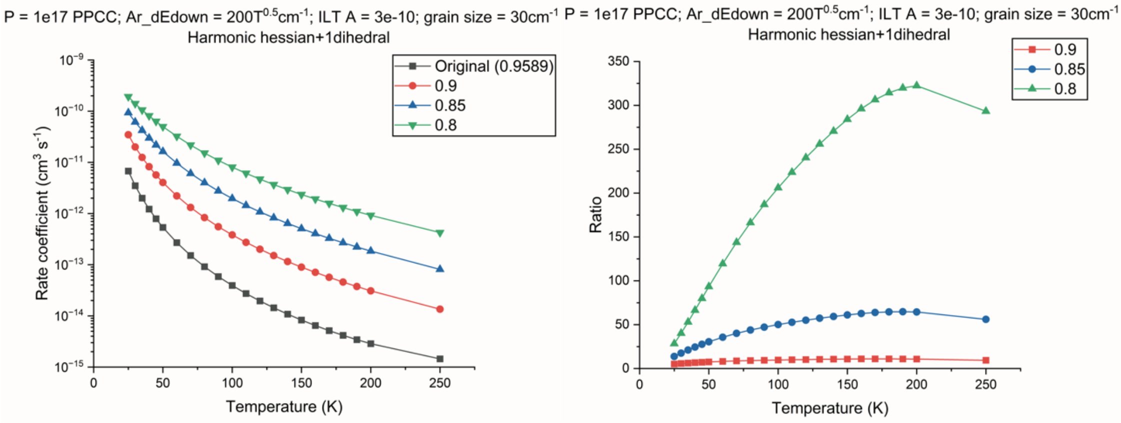

Figure 6.38 (Left) Calculated k_{loss} for the dimerisation reaction of CH_2O versus temperature in the range of T = 25–250 K with a total density of 10^{17} molecule cm^{-3} in Ar bath gas using the “Harmonic hessian + 1 dihedral” model when the frequency values of the dimer are artificially lowered by using a different scaling factor. The legend denotes the scaling factor used. (Right) Ratio of k_{loss} using the artificially lowered dimer frequency values versus using the original frequency values.

For CH_2O dimer, the gap between the calculated and the experimental k_{loss} is about a factor of 50, which can hardly be explained by the inclusion of the higher-energy C_{2h} conformer apart from the C_s conformer. Sensitivity analysis has been carried out in order to quantify this gap in terms of a change in the relative energy and vibrational frequencies. Figure 6.37 is obtained by artificially lowering the relative energy of the CH_2O dimer and it shows that a change of about –20 kJ mol^{-1} is required in order to increase the calculated k_{loss} by about a factor of 50. On the other hand, Figure 6.38 is obtained by using a different scaling factor (0.9, 0.85 and 0.8 which correspond to a change of –6.1%, –11.4% and –16.6% to all of the original scaled frequency values respectively) instead of the original value of 0.9589. The calculated k_{loss} can be increased by a factor of 50 by using a scaling factor with value slightly smaller than 0.85.

A possible factor that can potentially explain the difference between the experimental observations with the current model is the poor description of the DOS of the dimers. As demonstrated above, the k_{loss} can be increased by the inclusion of multiple stable conformers of dimers, as well as the lowering of frequency values. In particular, the low frequency values can have larger uncertainties and anharmonicity is neglected here.

Another factor that can possibly increase the loss of monomer significantly is by changing the collisional energy transfer value assigned. As demonstrated in this chapter, the fraction of dimer formed when He is used as the bath gas is smaller than that when Ar is used instead given the same conditions. This is due to a smaller assigned $\langle \Delta E \rangle_{down}$ value to the collision between He and the dimers. As suggested in Section 2.2, these values can have considerable uncertainties, particularly at low temperature, although the ordering between different bath gases is in general correct. More understandings in these collision energy transfer processes will be required.

One of the other possible factors that can contribute to an increasing loss of the monomer is the existence of the chaperone effect. The chaperone molecule is the third body particle that helps stabilise product formation through complexation. Some previously reported examples include the H_2 molecule in the ionic association of COH^+ + CO to form $(CO)_2H^+$ (163), the Ar molecule in the combination reaction of O + O_2 to form O_3 (164) and S + S_2 to form S_3 (165), and the water vapour H_2O in the self-reaction of hydroperoxy radical HO_2 and methylperoxy radical CH_3O_2 (166). For the CH_2O dimerisation reaction experiment in our Laval setup, in the gas flow it contains CH_2O and the buffer gas, either He, N_2 or Ar. Therefore, when considering the dimerisation of CH_2O, possible chaperone molecules in the system can be the buffer gas and other CH_2O molecules present. Thus, further studies on the third body reactions will be needed.

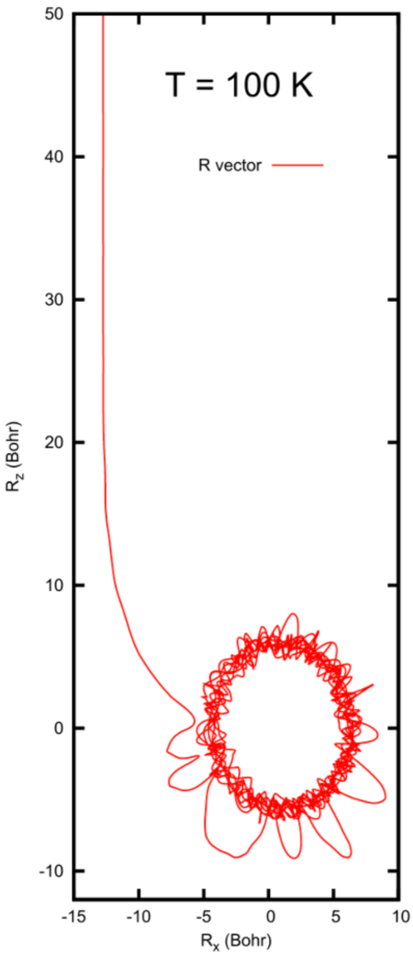

Figure 6.39 Evolution of the R vector defined as the vector between the centres-of-mass of the two reactants for the OH + CH_2O reaction. It can be seen that the two species are in "roaming state", that is, they are trapped to rotate about each other. Taken from (167).

Another possible factor can be that the statistical approach does not capture certain effects like the quantum roaming. A recent study (167) investigated in the quantum dynamics of the OH + CH_2O and the OH + CH_3OH reaction using the ring polymer molecular dynamics method. By studying the trajectories of the approach of the two species, for example the one shown in Figure 6.39, it was demonstrated that the long-range dipole-dipole interaction can effectively lead to the capture, or the trapping of the two species to rotate about each other. The phenomenon becomes more dominant at low temperature and the trapping due to the quantum effects results in a longer lifetime of the non-covalent complex structure. Given that CH_2O has a strong dipole moment, if this type of "roaming state" turns out to be prevalent in the CH_2O gas flow, then the CH_2O will have more time to stay close to each other rather than individually as monomers, although more investigations are needed.

6.4 Conclusion

In this chapter, the dimerisation reaction of four species that have been used as the excess reagent by our group in the Laval experiments, namely CH_2O, CH_3CHO, $CH_3C(O)CH_3$ and NH_3, have been studied. Ab initio calculations have been carried out to obtain the optimised geometric structures, relative energies and ro-vibrational properties of the non-covalent dimers of these species. Two stable structures for CH_2O dimer, six for CH_3CHO, three for $CH_3C(O)CH_3$, and one for NH_3 have been optimised. Considering the most stable geometry obtained, $CH_3C(O)CH_3$ dimer has the lowest energy, followed by CH_3CHO dimer and then CH_2O dimer. The most (potentially second-most for CH_3CHO) stable non-covalent dimers for each species, namely CH_2O C_s dimer (–13.49 kJ mol^{-1}), CH_3CHO C_1 dimer (–18.39 kJ mol^{-1}), $CH_3C(O)CH_3$ C_{2h} 1 dimer (–26.16 kJ mol^{-1}) and NH_3 C_s dimer (–7.52 kJ mol^{-1}), were selected for rate coefficient calculation and dimerisation for each species was treated as a single-step barrierless reactive process. Two models were used respectively for the calculations, both with the scaled harmonic Hessian matrices, one with the hindered rotor potentials and the other without. It was found that the dimerisation rate coefficients depend on the potential well depths, as well as the densities of states which are sensitive to low vibrational frequency values emerged from the formation of dimers. At low temperature, $CH_3C(O)CH_3$ has the largest k_{loss} followed by NH_3. Without the inclusion of the hindered rotor potential, CH_2O has the smallest k_{loss} but this changes to CH_3CHO when the hindered rotors are considered.

The goal for these calculations in the end is to help better understand the loss of the monomer species when high concentrations of monomers are used in the Laval nozzle experiment. Rate coefficient calculations have been done under the context of the Laval nozzle setup. k_{loss} are found to be dependent on the temperature and total number density profiles, which are related to the parameters of the isentropic core of the nozzles, as well as the buffer gas used. As the signals collected from the experiments are measurements of the actual $[\mathrm{monomer}]$, f_{monomer} were computed for comparison, which, apart from depending on k_{loss}, involve the time for interaction t, computed from the flow speed and the nozzle length, and the concentration of monomers used. For CH_2O and CH_3CHO, the dimer fraction formed within the nozzle is predicted to be similar to that in the stable flow region and for $CH_3C(O)CH_3$ and NH_3, it is predicted to have more contribution from the dimerisation within the nozzle. With the inclusion of the hindered rotor potentials, for the 52 K Ar nozzle, at 100 mm out of the nozzle exit, the loss of monomers due to dimerisation is estimated to be observable when the supposed concentration of the monomers used at the nozzle exit is above 6×10^{14} molecule cm^{-3} for CH_2O, 8×10^{14} molecule cm^{-3} for CH_3CHO, 2×10^{13} molecule cm^{-3} for $CH_3C(O)CH_3$ and 4×10^{14} molecule cm^{-3} for NH_3. It is an underprediction for $CH_3C(O)CH_3$ while an overprediction for CH_3CHO and NH_3 when compared with experimental data, but the discrepancies are fairly acceptable, with the best fit k_{loss} a factor of ~0.1, ~7 and ~1 of the calculated k_{loss} for $CH_3C(O)CH_3$, CH_3CHO and NH_3 respectively. In particular, the k_{loss} for CH_3CHO can be increased by about a factor of 3–4 when multiple conformers are considered. For CH_2O, it is a significant overprediction as the experimental results suggest that a substantial loss of CH_2O monomers already occurs when a lower concentration of CH_2O is used. In order to match the experimental observations, the calculated k_{loss} for CH_2O has to be about 2 order of magnitude larger. Therefore, some possible directions to improve on the current model include investigations in a better description of the DOS of the dimers and the related re-dissociation rates, the magnitude of the energy transfer at low temperature, the chaperone effect which involves the third-body particle, and quantum effect which may not be well captured by the statistical approach.

6.5 References

1. IUPAC. *Compendium of Chemical Terminology, 2nd ed. (the "Gold Book").* [Online]. 1997. [Accessed].

2. Tielens, A.G.G.M. *The physics and chemistry of the interstellar medium.* Repr. with corr. ed. Cambridge; New York: Cambridge University Press, 2006.

3. Kwok, S. *Physics and chemistry of the interstellar medium.* University Science Books, 2007.

4. Vallance, C. *Astrochemistry: from the Big Bang to the present day.* London: World Scientific Publishing, 2017.

5. Vosper, A.J. Dissociation of dinitrogen tetroxide in the gas phase. *Journal of the Chemical Society A: Inorganic, Physical, Theoretical.* 1970, (0), pp.625-627.

6. Giauque, W.F. and Kemp, J.D. The Entropies of Nitrogen Tetroxide and Nitrogen Dioxide. The Heat Capacity from 15°K to the Boiling Point. The Heat of Vaporization and Vapor Pressure. The Equilibria N_2O_4=$2NO_2$=$2NO+O_2$. *The Journal of Chemical Physics.* 1938, **6**(1), pp.40-52.

7. Stull, D.R., Prophet, H., United, S. and National Bureau of, S. JANAF thermochemical tables. 1971.

8. Chao, J., Wilhoit, R.C. and Zwolinski, B.J. Gas phase chemical equilibrium in dinitrogen trioxide and dinitrogen tetroxide. *Thermochimica Acta.* 1974, **10**(4), pp.359-371.

9. Roscoe, H.K. and Hind, A.K. The equilibrium constant of NO_2 with N_2O_4 and the temperature dependence of the visible spectrum of NO_2: A critical review and the implications for measurements of NO_2 in the polar stratosphere. *Journal of Atmospheric Chemistry.* 1993, **16**(3), pp.257-276.

10. Harwood, M.H. and Jones, R.L. Temperature dependent ultraviolet-visible absorption cross sections of N_2O and N_2O_4: Low-temperature measurements of the equilibrium constant for $2NO_2 \rightleftharpoons N_2O_4$. *Journal of Geophysical Research: Atmospheres.* 1994, **99**(D11), pp.22955-22964.

11. Guttman, A. and Penner, S.S. Experimental Determination of the Heat of Dissociation of $N_2O_4 \rightarrow 2NO_2$ from the Temperature Dependence of Absolute Infrared Intensities. *The Journal of Chemical Physics.* 1962, **36**(1), pp.98-99.

12. McKee, M.L. Ab Initio Study of the N_2O_4 Potential Energy Surface. Computational Evidence for a New N_2O_4 Isomer. *Journal of the American Chemical Society.* 1995, **117**(5), pp.1629-1637.

13. Luo, G. and Chen, X. Ground-State Intermolecular Proton Transfer of N_2O_4 and H_2O: An Important Source of Atmospheric Hydroxyl Radical? *The Journal of Physical Chemistry Letters.* 2012, **3**(9), pp.1147-1153.

14. Serre, J. On the electronic structures of NO_2 and its plane dimer N_2O_4. *Molecular Physics.* 1961, **4**(3), pp.269-270.

15. Tanaka, C. and Tanaka, J. Ab Initio Molecular Orbital Studies on the Chemiluminescence of 1,2-Dioxetanes. *The Journal of Physical Chemistry A.* 2000, **104**(10), pp.2078-2090.

16. West, A.C., Schmidt, M.W., Gordon, M.S. and Ruedenberg, K. A Comprehensive Analysis in Terms of Molecule-Intrinsic Quasi-Atomic Orbitals. IV. Bond Breaking and Bond Forming along the Dissociative Reaction Path of Dioxetane. *The Journal of Physical Chemistry A.* 2015, **119**(41), pp.10376-10389.

17. Vacher, M., Brakestad, A., Karlsson, H.O., Fdez. Galván, I. and Lindh, R. Dynamical Insights into the Decomposition of 1,2-Dioxetane. *Journal of Chemical Theory and Computation.* 2017, **13**(6), pp.2448-2457.

18. Parson, J.M., Siska, P.E. and Lee, Y.T. Intermolecular Potentials from Crossed-Beam Differential Elastic Scattering Measurements. IV. Ar+Ar. *The Journal of Chemical Physics.* 1972, **56**(4), pp.1511-1516.

19. Tanaka, Y. and Yoshino, K. Absorption Spectrum of the Argon Molecule in the Vacuum-uv Region. *The Journal of Chemical Physics.* 1970, **53**(5), pp.2012-2030.

20. Colbourn, E.A. and Douglas, A.E. The spectrum and ground state potential curve of Ar_2. *The Journal of Chemical Physics.* 1976, **65**(5), pp.1741-1745.

21. Herman, P.R., LaRocque, P.E. and Stoicheff, B.P. Vacuum ultraviolet laser spectroscopy. V. Rovibronic spectra of Ar_2 and constants of the ground and excited states. *The Journal of Chemical Physics.* 1988, **89**(8), pp.4535-4549.

22. Wu, J., Vredenborg, A., Ulrich, B., Schmidt, L.P.H., Meckel, M., Voss, S., Sann, H., Kim, H., Jahnke, T. and Dörner, R. Nonadiabatic alignment of van der Waals--force-bound argon dimers by femtosecond laser pulses. *Physical Review A.* 2011, **83**(6), p.061403.

23. Veltheim, A.v., Borchers, B., Steinmeyer, G. and Rottke, H. Imaging the impulsive alignment of noble-gas dimers via Coulomb explosion. *Physical Review A.* 2014, **89**(2), p.023432.

24. Mizuse, K., Sato, U., Tobata, Y. and Ohshima, Y. Rotational spectroscopy of the argon dimer by time-resolved Coulomb explosion imaging of rotational wave packets. *Physical Chemistry Chemical Physics.* 2022, **24**(18), pp.11014-11022.

25. Patkowski, K., Murdachaew, G., Fou, C.-M. and Szalewicz *, K. Accurate ab initio potential for argon dimer including highly repulsive region. *Molecular Physics.* 2005, **103**(15-16), pp.2031-2045.

26. Jäger, B., Hellmann, R., Bich, E. and Vogel, E. Ab initio pair potential energy curve for the argon atom pair and thermophysical properties of the dilute argon gas. I. Argon–argon interatomic potential and rovibrational spectra. *Molecular Physics.* 2009, **107**(20), pp.2181-2188.

27. Hilal, R., Hassan, W.M.I., Elroby, S.A.K. and Aziz, S.G. Theoretical Investigation of the Dispersion Interaction in Argon Dimer and Trimer. *Procedia Computer Science.* 2013, **18**, pp.826-834.

28. Huang, J., Yang, D., Zhou, Y. and Xie, D. A new full-dimensional ab initio intermolecular potential energy surface and vibrational states for $(HF)_2$ and $(DF)_2$. *The Journal of Chemical Physics.* 2019, **150**(15), p.154302.

29. Ovsyannikov, R.I., Makhnev, V.Y., Zobov, N.F., Koput, J., Tennyson, J. and Polyansky, O.L. Highly accurate HF dimer ab initio potential energy surface. *The Journal of Chemical Physics.* 2022, **156**(16), p.164305.

30. Shank, A., Wang, Y., Kaledin, A., Braams, B.J. and Bowman, J.M. Accurate ab initio and “hybrid” potential energy surfaces, intramolecular vibrational energies, and classical ir spectrum of the water dimer. *The Journal of Chemical Physics.* 2009, **130**(14), p.144314.

31. Czakó, G., Wang, Y. and Bowman, J.M. Communication: Quasiclassical trajectory calculations of correlated product-state distributions for the dissociation of $(H_2O)_2$ and $(D_2O)_2$. *The Journal of Chemical Physics.* 2011, **135**(15), p.151102.

32. Dyke, T.R., Howard, B.J. and Klemperer, W. Radiofrequency and Microwave Spectrum of the Hydrogen Fluoride Dimer; a Nonrigid Molecule. *The Journal of Chemical Physics.* 1972, **56**(5), pp.2442-2454.

33. Howard, B.J., Dyke, T.R. and Klemperer, W. The molecular beam spectrum and the structure of the hydrogen fluoride dimer. *The Journal of Chemical Physics.* 1984, **81**(12), pp.5417-5425.

34. Gutowsky, H.S., Chuang, C., Keen, J.D., Klots, T.D. and Emilsson, T. Microwave rotational spectra, hyperfine interactions, and structure of the hydrogen fluoride dimers. *The Journal of Chemical Physics.* 1985, **83**(5), pp.2070-2077.

35. Belov, S.P., Karyakin, E.N., Kozin, I.N., Krupnov, A.F., Polyansky, O.L., Tretyakov, M.Y., Zobov, N.F., Suenram, R.D. and Lafferty, W.J. Tunneling-rotation spectrum of the hydrogen fluoride dimer. *Journal of Molecular Spectroscopy.* 1990, **141**(2), pp.204-222.

36. Dyke, T.R. and Muenter, J.S. Microwave spectrum and structure of hydrogen bonded water dimer. *The Journal of Chemical Physics.* 1974, **60**(7), pp.2929-2930.

37. Dyke, T.R., Mack, K.M. and Muenter, J.S. The structure of water dimer from molecular beam electric resonance spectroscopy. *The Journal of Chemical Physics.* 1977, **66**(2), pp.498-510.

38. Coudert, L.H., Lovas, F.J., Suenram, R.D. and Hougen, J.T. New measurements of microwave transitions in the water dimer. *The Journal of Chemical Physics.* 1987, **87**(11), pp.6290-6299.

39. Odutola, J.A., Hu, T.A., Prinslow, D., O'dell, S.E. and Dyke, T.R. Water dimer tunneling states with K=0. *The Journal of Chemical Physics.* 1988, **88**(9), pp.5352-5361.

40. Fraser, G.T., Suenram, R.D. and Coudert, L.H. Microwave electric-resonance optothermal spectroscopy of $(H_2O)_2$. *The Journal of Chemical Physics.* 1989, **90**(11), pp.6077-6085.

41. Zwart, E., ter Meulen, J.J., Leo Meerts, W. and Coudert, L.H. The submillimeter rotation tunneling spectrum of the water dimer. *Journal of Molecular Spectroscopy.* 1991, **147**(1), pp.27-39.

42. Coudert, L.H., Caminati, W., Schnell, M. and Grabow, J.U. Hyperfine coupling and large amplitude motions interaction in the water dimer. *Journal of Molecular Spectroscopy.* 2007, **242**(2), pp.118-128.

43. Tretyakov, M.Y., Serov, E.A., Koshelev, M.A., Parshin, V.V. and Krupnov, A.F. Water Dimer Rotationally Resolved Millimeter-Wave Spectrum Observation at Room Temperature. *Physical Review Letters.* 2013, **110**(9), p.093001.

44. Pine, A.S. and Lafferty, W.J. Rotational structure and vibrational predissociation in the HF stretching bands of the HF dimer. *The Journal of Chemical Physics.* 1983, **78**(5), pp.2154-2162.

45. DeLeon, R.L. and Muenter, J.S. Vibrational predissociation in the hydrogen fluoride dimer. *The Journal of Chemical Physics.* 1984, **80**(12), pp.6092-6094.

46. Suhm, M.A., Farrell, J.T., McIlroy, A. and Nesbitt, D.J. High resolution 1.3 µm overtone spectroscopy of HF dimer in a slit jet: $K_a=0\leftarrow0$ and $K_a=1\leftarrow0$ subbands of $v_{acc}=2\leftarrow0$. *The Journal of Chemical Physics.* 1992, **97**(8), pp.5341-5354.

47. Bohac, E.J. and Miller, R.E. The trans-bending and F–F stretching vibrations of HF dimer in vHF=1: The influence of intermolecular vibrational excitation on the predissociation dynamics. *The Journal of Chemical Physics.* 1993, **99**(3), pp.1537-1544.

48. Chang, H.C. and Klemperer, W. State-specific vibrational predissociation and interconversion tunneling quenching at $3v_1$ and $3v_2$ of $(HF)_2$. *The Journal of Chemical Physics.* 1993, **98**(12), pp.9266-9278.

49. Laush, C., Lisy, J.M., Huisken, F. and Kulcke, A. The experimental determination of vibrational transition moments for HF dimer. *The Journal of Chemical Physics.* 1993, **98**(7), pp.5982-5984.

50. Laush, C. and Lisy, J.M. Saturation predissociation spectroscopy: Vibrational transition moments of HF dimer. *The Journal of Chemical Physics.* 1994, **101**(9), pp.7480-7487.

51. He, Y., Müller, H.B., Quack, M. and Suhm, M.A. High Resolution FTIR and Diode Laser Supersonic Jet Spectroscopy of the $N = 2$ HF Stretching Polyad in $(HF)_2$ and (HFDF): Hydrogen Bond Switching and Predissociation Dynamics. *Zeitschrift für Physikalische Chemie.* 2007, **221**(11-12), pp.1581-1645.

52. Page, R.H., Frey, J.G., Shen, Y.R. and Lee, Y.T. Infrared predissociation spectra of water dimer in a supersonic molecular beam. *Chemical Physics Letters.* 1984, **106**(5), pp.373-376.

53. Huang, Z.S. and Miller, R.E. High-resolution near-infrared spectroscopy of water dimer. *The Journal of Chemical Physics.* 1989, **91**(11), pp.6613-6631.

54. Vigasin, A.A., Jin, Y. and Ikawa, S. On the water dimer contribution to the OH stretching absorption band profile in pressurized water vapour. *Molecular Physics.* 2008, **106**(9-10), pp.1155-1159.

55. Kuyanov-Prozument, K., Choi, M.Y. and Vilesov, A.F. Spectrum and infrared intensities of OH-stretching bands of water dimers. *The Journal of Chemical Physics.* 2010, **132**(1), p.014304.

56. Kvaran, Á., Sigurbjörnsson, Ó.F. and Wang, H. REMPI-TOF studies of the HF dimer. *Journal of Molecular Structure.* 2006, **790**(1), pp.27-30.

57. Rocher-Casterline, B.E., Ch'ng, L.C., Mollner, A.K. and Reisler, H. Communication: Determination of the bond dissociation energy (D_0) of the water dimer, $(H_2O)_2$, by velocity map imaging. *The Journal of Chemical Physics.* 2011, **134**(21), p.211101.

58. Bevan, J.W., Kisiel, Z., Legon, A.C., Millen, D.J., Rogers, S.C. and Sheppard, N. Spectroscopic investigations of hydrogen bonding interactions in the gas phase. IV. The heterodimer H_2O • • • HF: the observation and analysis of its microwave rotational spectrum and the determination of its molecular geometry and electric dipole moment. *Proceedings of the Royal Society of London. A. Mathematical and Physical Sciences.* 1980, **372**(1750), pp.441-451.

59. Legon, A.C. and Willoughby, L.C. D-nuclear quadrupole and H(D),^{19}F nuclear-spin—nuclear-spin hyperfine coupling constants from rotational spectra of H_2O…DF and H_2O…HF. *Chemical Physics Letters.* 1982, **92**(4), pp.333-338.

60. Kisiel, Z., Legon, A.C. and Millen, D.J. Stark effects in the rotational spectrum of the dimer H_2O···HF and the variation of the electric dipole moment with excitation of the low-frequency, hydrogen-bond modes. *The Journal of Chemical Physics.* 1983, **78**(6), pp.2910-2914.

61. Andrews, L. and Johnson, G.L. FTIR spectra of water–hydrogen fluoride complexes in solid argon. Evidence for inversion doubling in the HF librational modes of H_2O– –HF. *The Journal of Chemical Physics.* 1983, **79**(8), pp.3670-3677.

62. Cazzoli, G., Favero, P.G., Lister, D.G., Legon, A.C., Millen, D.J. and Kisiel, Z. The rotational spectrum of the hydrogen-bonded heterodimer H_2O…HF in the frequency range 40–80 GHz. *Chemical Physics Letters.* 1985, **117**(6), pp.543-549.

63. Legon, A.C., Millen, D.J. and North, H.M. Experimental determination of the dissociation energies D_0 and D_e of H_2O…HF. *Chemical Physics Letters.* 1987, **135**(3), pp.303-306.

64. Bulychev, V.P., Gromova, E.I. and Tokhadze, K.G. Experimental and theoretical study of the v(HF) absorption band structure in the H_2O…HF complex. *Optics and Spectroscopy.* 2004, **96**(5), pp.774-788.

65. Dixon, T.A., Joyner, C.H., Baiocchi, F.A. and Klemperer, W. The rotational and hyperfine spectrum of Ar–HF. *The Journal of Chemical Physics.* 1981, **74**(12), pp.6539-6543.

66. Lovejoy, C.M., Schuder, M.D. and Nesbitt, D.J. Sub-doppler infrared absorption spectroscopy of Ar-HF [(1000) ← (0000)] in a linear supersonic jet. *Chemical Physics Letters.* 1986, **127**(4), pp.374-376.

67. Dvorak, M.A., Reeve, S.W., Burns, W.A., Grushow, A. and Leopold, K.R. Observation of three intermolecular vibrational states of Ar–HF. *Chemical Physics Letters.* 1991, **185**(3), pp.399-402.

68. Stockman, P.A. and Blake, G.A. Improved ground state rotational constants for the argon–hydrogen fluoride dimer. *The Journal of Chemical Physics.* 1993, **98**(5), pp.4307-4308.

69. Chang, H.C., Tao, F.M., Klemperer, W., Healey, C. and Hutson, J.M. The Ar–HF intermolecular potential: Overtone spectroscopy and ab initio calculations. *The Journal of Chemical Physics.* 1993, **99**(12), pp.9337-9349.

70. Chang, H.C. and Klemperer, W. Observation of ArHF(3000) and its combination modes by laser-induced fluorescence. *The Journal of Chemical Physics.* 1993, **98**(4), pp.2497-2506.

71. Pine, A.S. Line shape asymmetries in Ar-broadened HF(v=1–0) in the Dicke-narrowing regime. *The Journal of Chemical Physics.* 1994, **101**(5), pp.3444-3452.

72. Block, P.A. and Miller, R.E. Infrared-infrared double resonance spectroscopy of Ar-HF. Intermolecular state dependence of the dipole

moment and vibrational predissociation in vHF = 2. *Chemical Physics Letters.* 1994, **226**(3), pp.317-324.

73. Chang, H.-C., Tao, F.-M., Tsang, S.N. and Klmpcrer, W. Dependence of the Interaction Potentials of Ar-HF and N_2-HF on HF Bond Length. *Journal of the Chinese Chemical Society.* 1995, **42**(2), pp.141-148.

74. van Duijn, E.J., Nokhai, R.N. and Hermans, L.J.F. Experimental investigation of the rotational- and vibrational-state dependence of the HF–Rg interactions. *The Journal of Chemical Physics.* 1996, **105**(15), pp.6375-6384.

75. Chapman, W.B., Weida, M.J. and Nesbitt, D.J. Scattering dynamics in HF+He, Ne, and Ar: State-to-state cross sections, Dopplerimetry, and alignment measurement via direct infrared laser absorption in crossed supersonic jets. *The Journal of Chemical Physics.* 1997, **106**(6), pp.2248-2264.

76. Chuang, C.-C., Higgins, K.J., Fu, H.C. and Klemperer, W. Weak bond stretching for three orientations of Ar–HF at vHF=3. *The Journal of Chemical Physics.* 2000, **112**(16), pp.7022-7031.

77. Chuang, C.-C. and Klemperer, W. The dependence of intermolecular interactions upon valence coordinate excitation: The vHF=4 levels of ArHF. *The Journal of Chemical Physics.* 2000, **113**(10), pp.4116-4123.

78. Nauta, K. and Miller, R.E. Vibrational relaxation of Ne, Ar, Kr–HF (v=1) binary complexes in helium nanodroplets. *The Journal of Chemical Physics.* 2001, **115**(10), pp.4508-4514.

79. Cohen, R.C., Busarow, K.L., Laughlin, K.B., Blake, G.A., Havenith, M., Lee, Y.T. and Saykally, R.J. Tunable far infrared laser spectroscopy of van der Waals bonds: Vibration–rotation–tunneling spectra of Ar–H_2O. *The Journal of Chemical Physics.* 1988, **89**(8), pp.4494-4504.

80. Fraser, G.T., Lovas, F.J., Suenram, R.D. and Matsumura, K. Microwave spectrum of Ar–H_2O: Dipole moment, isotopic studies, and ^{17}O quadrupole coupling constants. *Journal of Molecular Spectroscopy.* 1990, **144**(1), pp.97-112.

81. Cohen, R.C., Busarow, K.L., Lee, Y.T. and Saykally, R.J. Tunable far infrared laser spectroscopy of van der Waals bonds: The intermolecular stretching vibration and effective radial potentials for Ar–H_2O. *The Journal of Chemical Physics.* 1990, **92**(1), pp.169-177.

82. Lascola, R. and Nesbitt, D.J. Slit-jet near-infrared spectroscopy and internal rotor dynamics of the ArH_2O van der Waals complex: An angular potential-energy surface for internal H_2O rotation. *The Journal of Chemical Physics.* 1991, **95**(11), pp.7917-7932.

83. Cohen, R.C. and Saykally, R.J. Multidimensional intermolecular dynamics from tunable far-infrared laser spectroscopy: Angular-radial coupling in the intermolecular potential of argon–H_2O. *The Journal of Chemical Physics.* 1991, **95**(11), pp.7891-7906.

84. Nesbitt, D.J. and Lascola, R. Vibration, rotation, and parity specific predissociation dynamics in asymmetric OH stretch excited ArH_2O: A half collision study of resonant V–V energy transfer in a weakly bound complex. *The Journal of Chemical Physics.* 1992, **97**(11), pp.8096-8110.

85. Germann, T.C. and Gutowsky, H.S. Nuclear hyperfine interactions and dynamic state of H_2O in Ar–H_2O. *The Journal of Chemical Physics.* 1993, **98**(7), pp.5235-5238.

86. Plusquellic, D.F., Votava, O. and Nesbitt, D.J. Photodissociation dynamics in quantum state-selected clusters: A test of the one-atom cage effect in Ar–H_2O. *The Journal of Chemical Physics.* 1994, **101**(7), pp.6356-6358.

87. Weida, M.J. and Nesbitt, D.J. High resolution mid-infrared spectroscopy of ArH_2O: The v_2 bend region of H_2O. *The Journal of Chemical Physics.* 1997, **106**(8), pp.3078-3089.

88. Chapman, W.B., Kulcke, A., Blackmon, B.W. and Nesbitt, D.J. Rotationally inelastic scattering of jet cooled H_2O with Ar: State-to-state cross sections and rotational alignment effects. *The Journal of Chemical Physics.* 1999, **110**(17), pp.8543-8554.

89. Votava, O., Plusquellic, D.F., Myers, T.L. and Nesbitt, D.J. Bond-breaking in quantum state selected clusters: Inelastic and nonadiabatic

intracluster collision dynamics in Ar–H_2O→Ar+H(^2S)+OH($^2\Pi_{1/2,3/2}^{\pm}$;N). *The Journal of Chemical Physics.* 2000, **112**(17), pp.7449-7460.

90. Nizkorodov, S.A., Ziemkiewicz, M., Nesbitt, D.J. and Knight, A.E.W. Overtone spectroscopy of H_2O clusters in the vOH=2 manifold: Infrared-ultraviolet vibrationally mediated dissociation studies. *The Journal of Chemical Physics.* 2005, **122**(19), p.194316.

91. Kuma, S., Slipchenko, M.N., Momose, T. and Vilesov, A.F. Infrared Spectra and Intensities of Ar−H_2O and O_2−H_2O Complexes in the Range of the v_3 Band of H_2O. *The Journal of Physical Chemistry A.* 2010, **114**(34), pp.9022-9027.

92. Liu, X. and Xu, Y. New rovibrational bands of the Ar–H_2O complex at the v_2 bend region of H_2O. *Journal of Molecular Spectroscopy.* 2014, **301**, pp.1-8.

93. Vanfleteren, T., Földes, T. and Herman, M. Analysis of a perpendicular band in Ar–H_2O with origin close to the v_1+v_3, R(0) line in H_2O. *Chemical Physics Letters.* 2015, **627**, pp.36-38.

94. Zou, L. and Widicus Weaver, S.L. Direct measurement of additional Ar–H_2O vibration–rotation-tunneling bands in the millimeter–submillimeter range. *Journal of Molecular Spectroscopy.* 2016, **324**, pp.12-19.

95. Andrews, L., Davis, S.R. and Hunt, R.D. Far infrared spectra of $(HF)_2$ and $(HF)_3$ in solid argon. *Molecular Physics.* 1992, **77**(5), pp.993-1003.

96. Coker, D.F., Miller, R.E. and Watts, R.O. The infrared predissociation spectra of water clusters. *The Journal of Chemical Physics.* 1985, **82**(8), pp.3554-3562.

97. Page, R.H., Vernon, M.F., Shen, Y.R. and Lee, Y.T. Infrared vibrational predissociation spectra of large water clusters. *Chemical Physics Letters.* 1987, **141**(1), pp.1-6.

98. Häber, T., Schmitt, U. and A. Suhm, M. FTIR-spectroscopy of molecular clusters in pulsed supersonic slit-jet expansions. *Physical Chemistry Chemical Physics.* 1999, **1**(24), pp.5573-5582.

99. Bačić, Z. and Miller, R.E. Molecular Clusters: Structure and Dynamics of Weakly Bound Systems. *The Journal of Physical Chemistry.* 1996, **100**(31), pp.12945-12959.

100. Rowe, B.R., Canosa, A. and Heard, D.E. *Uniform supersonic flows in chemical physics : chemistry close to absolute zero studied using the CRESU method.* New Jersey: World Scientific, 2022.

101. Sabbah, H., Biennier, L., Klippenstein, S.J., Sims, I.R. and Rowe, B.R. Exploring the Role of PAHs in the Formation of Soot: Pyrene Dimerization. *The Journal of Physical Chemistry Letters.* 2010, **1**(19), pp.2962-2967.

102. Bourgalais, J., Roussel, V., Capron, M., Benidar, A., Jasper, A.W., Klippenstein, S.J., Biennier, L. and Le Picard, S.D. Low Temperature Kinetics of the First Steps of Water Cluster Formation. *Physical Review Letters.* 2016, **116**(11), p.113401.

103. Ferreiro, J.J., Chakrabarty, S., Schläppi, B. and Signorell, R. Observation of propane cluster size distributions during nucleation and growth in a Laval expansion. *The Journal of Chemical Physics.* 2016, **145**(21), p.211907.

104. Chakrabarty, S., Ferreiro, J.J., Lippe, M. and Signorell, R. Toluene Cluster Formation in Laval Expansions: Nucleation and Growth. *The Journal of Physical Chemistry A.* 2017, **121**(20), pp.3991-4001.

105. Lippe, M., Chakrabarty, S., Ferreiro, J.J., Tanaka, K.K. and Signorell, R. Water nucleation at extreme supersaturation. *The Journal of Chemical Physics.* 2018, **149**(24), p.244303.

106. Lippe, M., Szczepaniak, U., Hou, G.-L., Chakrabarty, S., Ferreiro, J.J., Chasovskikh, E. and Signorell, R. Infrared Spectroscopy and Mass Spectrometry of CO_2 Clusters during Nucleation and Growth. *The Journal of Physical Chemistry A.* 2019, **123**(12), pp.2426-2437.

107. Modak, V.P., Amaya, A.J. and Wyslouzil, B.E. Freezing of supercooled n-decane nanodroplets: from surface driven to frustrated crystallization. *Physical Chemistry Chemical Physics.* 2017, **19**(44), pp.30181-30194.

108. Amaya, A.J. and Wyslouzil, B.E. Ice nucleation rates near ~225 K. *The Journal of Chemical Physics.* 2018, **148**(8), p.084501.

109. Pathak, H., Obeidat, A., Wilemski, G. and Wyslouzil, B. The structure of D_2O-nonane nanodroplets. *The Journal of Chemical Physics.* 2014, **140**(22), p.224318.

110. Amaya, A.J., Pathak, H., Modak, V.P., Laksmono, H., Loh, N.D., Sellberg, J.A., Sierra, R.G., McQueen, T.A., Hayes, M.J., Williams, G.J., Messerschmidt, M., Boutet, S., Bogan, M.J., Nilsson, A., Stan, C.A. and Wyslouzil, B.E. How Cubic Can Ice Be? *The Journal of Physical Chemistry Letters.* 2017, **8**(14), pp.3216-3222.

111. Wyslouzil, B.E., Cheung, J.L., Wilemski, G. and Strey, R. Small Angle Neutron Scattering from Nanodroplet Aerosols. *Physical Review Letters.* 1997, **79**(3), pp.431-434.

112. Wyslouzil, B.E., Wilemski, G., Strey, R., Heath, C.H. and Dieregsweiler, U. Experimental evidence for internal structure in aqueous–organic nanodroplets. *Physical Chemistry Chemical Physics.* 2006, **8**(1), pp.54-57.

113. Wyslouzil, B.E., Wilemski, G., Strey, R., Seifert, S. and Winans, R.E. Small angle X-ray scattering measurements probe water nanodroplet evolution under highly non-equilibrium conditions. *Physical Chemistry Chemical Physics.* 2007, **9**(39), pp.5353-5358.

114. Bonnamy, A., Georges, R., Benidar, A., Boissoles, J., Canosa, A. and Rowe, B.R. Infrared spectroscopy of $(CO_2)_N$ nanoparticles ($30<N<14500$) flowing in a uniform supersonic expansion. *The Journal of Chemical Physics.* 2003, **118**(8), pp.3612-3621.

115. Bonnamy, A., Georges, R., Hugo, E. and Signorell, R. IR signature of $(CO_2)_N$ clusters: size, shape and structural effects. *Physical Chemistry Chemical Physics.* 2005, **7**(5), pp.963-969.

116. Laksmono, H., Tanimura, S., Allen, H.C., Wilemski, G., Zahniser, M.S., Shorter, J.H., Nelson, D.D., McManus, J.B. and Wyslouzil, B.E. Monomer, clusters, liquid: an integrated spectroscopic study of methanol

condensation. *Physical Chemistry Chemical Physics.* 2011, **13**(13), pp.5855-5871.

117. Modak, V.P., Pathak, H., Thayer, M., Singer, S.J. and Wyslouzil, B.E. Experimental evidence for surface freezing in supercooled n-alkane nanodroplets. *Physical Chemistry Chemical Physics.* 2013, **15**(18), pp.6783-6795.

118. Bhabhe, A., Pathak, H. and Wyslouzil, B.E. Freezing of Heavy Water (D_2O) Nanodroplets. *The Journal of Physical Chemistry A.* 2013, **117**(26), pp.5472-5482.

119. Pathak, H., Wölk, J., Strey, R. and Wyslouzil, B.E. Co-condensation of nonane and D_2O in a supersonic nozzle. *The Journal of Chemical Physics.* 2014, **140**(3), p.034304.

120. Park, Y. and Wyslouzil, B.E. CO_2 condensation onto alkanes: unconventional cases of heterogeneous nucleation. *Physical Chemistry Chemical Physics.* 2019, **21**(16), pp.8295-8313.

121. Dingilian, K.K., Halonen, R., Tikkanen, V., Reischl, B., Vehkamäki, H. and Wyslouzil, B.E. Homogeneous nucleation of carbon dioxide in supersonic nozzles I: experiments and classical theories. *Physical Chemistry Chemical Physics.* 2020, **22**(34), pp.19282-19298.

122. West, N.A., Millar, T.J., Van de Sande, M., Rutter, E., Blitz, M.A., Decin, L. and Heard, D.E. Measurements of Low Temperature Rate Coefficients for the Reaction of CH with CH_2O and Application to Dark Cloud and AGB Stellar Wind Models. *The Astrophysical Journal.* 2019, **885**(2), p.134.

123. Taylor, S.E. *Reaction kinetics at very low temperatures measured using a pulsed Laval nozzle system*. Dissertation/Thesis thesis, University of Leeds, 2007.

124. Shannon, R.J., Taylor, S., Goddard, A., Blitz, M.A. and Heard, D.E. Observation of a large negative temperature dependence for rate coefficients of reactions of OH with oxygenated volatile organic compounds studied at 86-112 K. *Physical Chemistry Chemical Physics.* 2010, **12**(41), pp.13511-13514.

125. Shannon, R.J., Blitz, M.A., Goddard, A. and Heard, D.E. Accelerated chemistry in the reaction between the hydroxyl radical and methanol at interstellar temperatures facilitated by tunnelling. *Nature Chemistry.* 2013, **5**(9), pp.745-749.

126. Antiñolo, M., Agúndez, M., Jiménez, E., Ballesteros, B., Canosa, A., Dib, G.E., Albaladejo, J. and Cernicharo, J. Reactivity of OH and CH_3OH between 22 and 64 K: modeling the gas phase production of CH_3O in Barnard 1b. *The Astrophysical Journal.* 2016, **823**(1), p.25.

127. Siebrand, W., Smedarchina, Z., Martínez-Núñez, E. and Fernández-Ramos, A. Methanol dimer formation drastically enhances hydrogen abstraction from methanol by OH at low temperature. *Physical Chemistry Chemical Physics.* 2016, **18**(32), pp.22712-22718.

128. Shannon, R.J., Gómez Martín, J.C., Caravan, R.L., Blitz, M.A., Plane, J.M.C., Heard, D.E., Antiñolo, M., Agúndez, M., Jiménez, E., Ballesteros, B., Canosa, A., El Dib, G., Albaladejo, J. and Cernicharo, J. Comment on “Methanol dimer formation drastically enhances hydrogen abstraction from methanol by OH at low temperature” by W. Siebrand, Z. Smedarchina, E. Martínez-Núñez and A. Fernández-Ramos, Phys. Chem. Chem. Phys., 2016, 18, 22712. *Physical Chemistry Chemical Physics.* 2018, **20**(12), pp.8349-8354.

129. Siebrand, W., Smedarchina, Z., Ferro-Costas, D., Martínez-Núñez, E. and Fernández-Ramos, A. Reply to the ‘Comment on “Methanol dimer formation drastically enhances hydrogen abstraction from methanol by OH at low temperature”’ by D. Heard, R. Shannon, J. Gomez Martin, R. Caravan, M. Blitz, J. Plane, M. Antiñolo, M. Agundez, E. Jimenez, B. Ballesteros, A. Canosa, G. El Dib, J. Albaladejo and J. Cernicharo, Phys. Chem. Chem. Phys., 2018, 20, DOI: 10.1039/C7CP04561A. *Physical Chemistry Chemical Physics.* 2018, **20**(12), pp.8355-8357.

130. Heger, M., Suhm, M.A. and Mata, R.A. Communication: Towards the binding energy and vibrational red shift of the simplest organic hydrogen bond: Harmonic constraints for methanol dimer. *The Journal of Chemical Physics.* 2014, **141**(10), p.101105.

131. Ford, T.A. and Glasser, L. Ab initio calculations of the structural, energetic and vibrational properties of some hydrogen bonded and van

der Waals dimers Part 3. The formaldehyde dimer. *Journal of Molecular Structure: THEOCHEM.* 1997, **398-399**, pp.381-394.

132. Dolgonos, G.A. Which isomeric form of formaldehyde dimer is the most stable – a high-level coupled-cluster study. *Chemical Physics Letters.* 2013, **585**, pp.37-41.

133. Van Dornshuld, E., Holy, C.M. and Tschumper, G.S. Homogeneous and Heterogeneous Noncovalent Dimers of Formaldehyde and Thioformaldehyde: Structures, Energetics, and Vibrational Frequencies. *The Journal of Physical Chemistry A.* 2014, **118**(18), pp.3376-3385.

134. Karpfen, A. On the potential energy surfaces of dimers formed between trans-glyoxal, trans-acrolein and formaldehyde. *Computational and Theoretical Chemistry.* 2015, **1061**, pp.60-71.

135. Mirdoraghi, S., Piri, F. and Vahedpour, M. A computational study on multiple formaldehyde complexes and their possible chemical reactions as well as the catalytic effect in the gas phase. *SN Applied Sciences.* 2020, **2**(4), p.623.

136. Hermida-Ramón, J.M. and Ríos, M.A. Ab initio molecular orbital analysis of acetaldehyde dimers.: Thermodynamic properties. *Chemical Physics Letters.* 1998, **290**(4), pp.431-436.

137. Stefanov, B.I., Topalian, Z., Granqvist, C.G. and Österlund, L. Acetaldehyde adsorption and condensation on anatase TiO_2: Influence of acetaldehyde dimerization. *Journal of Molecular Catalysis A: Chemical.* 2014, **381**, pp.77-88.

138. Neeman, E.M., González, D., Blázquez, S., Ballesteros, B., Canosa, A., Antiñolo, M., Vereecken, L., Albaladejo, J. and Jiménez, E. The impact of water vapor on the OH reactivity toward CH_3CHO at ultra-low temperatures (21.7–135.0 K): Experiments and theory. *The Journal of Chemical Physics.* 2021, **155**(3), p.034306.

139. Hermida-Ramón, J.M. and Ríos, M.A. The Energy of Interaction between Two Acetone Molecules: A Potential Function Constructed from ab Initio Data. *The Journal of Physical Chemistry A.* 1998, **102**(15), pp.2594-2602.

140. Tao, F.M. and Klemperer, W. Ab initio search for the equilibrium structure of the ammonia dimer. *The Journal of Chemical Physics.* 1993, **99**(8), pp.5976-5982.

141. Lee, J.S. and Park, S.Y. Ab initio study of $(NH_3)_2$: Accurate structure and energetics. *The Journal of Chemical Physics.* 1999, **112**(1), pp.230-237.

142. Kulkarni, S.A. and Pathak, R.K. Ab initio investigations on neutral clusters of ammonia: $(NH_3)_n$ (n=2–6). *Chemical Physics Letters.* 2001, **336**(3), pp.278-283.

143. Altmann, J.A., Govender, M.G. and Ford, T.A. Ab initio and DFT calculations of some weakly bound dimers and complexes. I. The dimers of ammonia and phosphine. *Molecular Physics.* 2005, **103**(6-8), pp.949-961.

144. Malloum, A., Fifen, J.J., Dhaouadi, Z., Engo, S.G.N. and Jaidane, N.-E. Structures and relative stabilities of ammonia clusters at different temperatures: DFT vs. ab initio. *Physical Chemistry Chemical Physics.* 2015, **17**(43), pp.29226-29242.

145. Malloum, A. and Conradie, J. Accurate binding energies of ammonia clusters and benchmarking of hybrid DFT functionals. *Computational and Theoretical Chemistry.* 2021, **1200**, p.113236.

146. Yang, S., Zhang, Z. and Zhang, D.H. A full-dimensional ab initio potential energy and dipole moment surfaces for $(NH_3)_2$. *The Journal of Chemical Physics.* 2021, **155**(16), p.164306.

147. Becke, A.D. A new mixing of Hartree–Fock and local density-functional theories. *The Journal of Chemical Physics.* 1993, **98**(2), pp.1372-1377.

148. Dunning, T.H. Gaussian basis sets for use in correlated molecular calculations. I. The atoms boron through neon and hydrogen. *The Journal of Chemical Physics.* 1989, **90**(2), pp.1007-1023.

149. Kendall, R.A., Dunning, T.H. and Harrison, R.J. Electron affinities of the first-row atoms revisited. Systematic basis sets and wave functions. *The Journal of Chemical Physics.* 1992, **96**(9), pp.6796-6806.

150. Woon, D.E. and Dunning Jr., T.H. Gaussian basis sets for use in correlated molecular calculations. V. Core-valence basis sets for boron through neon. *The Journal of Chemical Physics.* 1995, **103**(11), pp.4572-4585.

151. Frisch, M.J., Trucks, G.W., Schlegel, H.B., Scuseria, G.E., Robb, M.A., Cheeseman, J.R., Scalmani, G., Barone, V., Mennucci, B., Petersson, G.A., Nakatsuji, H., Caricato, M., Li, X., Hratchian, H.P., Izmaylov, A.F., Bloino, J., Zheng, G., Sonnenberg, J.L., Hada, M., Ehara, M., Toyota, K., Fukuda, R., Hasegawa, J., Ishida, M., Nakajima, T., Honda, Y., Kitao, O., Nakai, H., Vreven, T., J. A. Montgomery, J., Peralta, J.E., Ogliaro, F., Bearpark, M., Heyd, J.J., Brothers, E., Kudin, K.N., Staroverov, V.N., Keith, T., Kobayashi, R., Normand, J., Raghavachari, K., Rendell, A., Burant, J.C., Iyengar, S.S., Tomasi, J., Cossi, M., Rega, N., Millam, J.M., Klene, M., Knox, J.E., Cross, J.B., Bakken, V., Adamo, C., Jaramillo, J., Gomperts, R., Stratmann, R.E., Yazyev, O., Austin, A.J., Cammi, R., Pomelli, C., Ochterski, J.W., Martin, R.L., Morokuma, K., Zakrzewski, V.G., Voth, G.A., Salvador, P., Dannenberg, J.J., Dapprich, S., Daniels, A.D., Farkas, O., Foresman, J.B., Ortiz, J.V., Cioslowski, J. and Fox, D.J. *Gaussian 09 Revision D.01*. Wallingford CT: Gaussian, Inc. 2013.

152. Pople, J.A., Krishnan, R., Schlegel, H.B. and Binkley, J.S. Electron correlation theories and their application to the study of simple reaction potential surfaces. *International Journal of Quantum Chemistry.* 1978, **14**(5), pp.545-560.

153. Bartlett, R.J. and Purvis, G.D. Many-body perturbation theory, coupled-pair many-electron theory, and the importance of quadruple excitations for the correlation problem. *International Journal of Quantum Chemistry.* 1978, **14**(5), pp.561-581.

154. Papajak, E., Zheng, J., Xu, X., Leverentz, H.R. and Truhlar, D.G. Perspectives on Basis Sets Beautiful: Seasonal Plantings of Diffuse Basis Functions. *Journal of Chemical Theory and Computation.* 2011, **7**(10), pp.3027-3034.

155. Skoog, D.A., Holler, F.J. and Crouch, S.R. *Principles of instrumental analysis.* Sixth edition. ed. Australia: Thomson Brooks/Cole, 2007.

156. Glowacki, D.R., Liang, C.-H., Morley, C., Pilling, M.J. and Robertson, S.H. MESMER: An Open-Source Master Equation Solver for Multi-Energy Well Reactions. *The Journal of Physical Chemistry A.* 2012, **116**(38), pp.9545-9560.

157. Laury, M.L., Boesch, S.E., Haken, I., Sinha, P., Wheeler, R.A. and Wilson, A.K. Harmonic vibrational frequencies: Scale factors for pure, hybrid, hybrid meta, and double-hybrid functionals in conjunction with correlation consistent basis sets. *Journal of Computational Chemistry.* 2011, **32**(11), pp.2339-2347.

158. Davies, J.W., Green, N.J.B. and Pilling, M.J. The testing of models for unimolecular decomposition via inverse laplace transformation of experimental recombination rate data. *Chemical Physics Letters.* 1986, **126**(3), pp.373 - 379.

159. Troe, J. Theory of thermal unimolecular reactions at low pressures. I. Solutions of the master equation. *The Journal of Chemical Physics.* 1977, **66**(11), pp.4745-4757.

160. Atkinson, D.B. and Smith, M.A. Design and characterization of pulsed uniform supersonic expansions for chemical applications. *Review of Scientific Instruments.* 1995, **66**(9), pp.4434-4446.

161. Potapov, A., Canosa, A., Jimenez, E. and Rowe, B. Uniform Supersonic Chemical Reactors: 30 Years of Astrochemical History and Future Challenges. *Angewandte Chemie-International Edition.* 2017, **56**(30), pp.8618-8640.

162. Graham, T. and Smith, R.A. *Chemical and physical researches.* Edinburgh: printed by Constable, 1876.

163. Blades, A.T. and Kebarle, P. Chaperone participation in three body ion association reactions. The systems $COH^{+}+CO=(CO)_2H^{+}$ and $N_2H^{+}+N_2=(N_2)_2H^{+}$. *The Journal of Chemical Physics.* 1983, **78**(2), pp.783-789.

164. Ivanov, M.V. and Schinke, R. Recombination of ozone via the chaperon mechanism. *The Journal of Chemical Physics.* 2006, **124**(10), p.104303.

165. Du, S., Germann, T.C., Francisco, J.S., Peterson, K.A., Yu, H.-G. and Lyons, J.R. The kinetics study of the $S + S_2 \rightarrow S_3$ reaction by the chaperone mechanism. *The Journal of Chemical Physics.* 2011, **134**(15), p.154508.

166. English, A.M., Hansen, J.C., Szente, J.J. and Maricq, M.M. The Effects of Water Vapor on the CH_3O_2 Self-Reaction and Reaction with HO_2. *The Journal of Physical Chemistry A.* 2008, **112**(39), pp.9220-9228.

167. del Mazo-Sevillano, P., Aguado, A., Jiménez, E., Suleimanov, Y.V. and Roncero, O. Quantum Roaming in the Complex-Forming Mechanism of the Reactions of OH with Formaldehyde and Methanol at Low Temperature and Zero Pressure: A Ring Polymer Molecular Dynamics Approach. *The Journal of Physical Chemistry Letters.* 2019, **10**(8), pp.1900-1907.

Chapter 7

Conclusion and future work

In this thesis, theoretical approaches have been used in the investigations of various gas-phase neutral-neutral reaction systems, including the calculations for the potential energy surfaces as well as the rate coefficients. Optimised geometric parameters, relative energies, vibrational frequencies and rotational constants of the relevant species in the reaction systems are obtained. The potential energy surfaces are constructed for the subsequent master equation calculations, which generate the rate coefficients and the product branching yields. The temperature and pressure dependence or independence of the reaction rate coefficients indicated from the results obtained give information regarding the reaction mechanisms. Systems with different types of reaction pathways are investigated, including entirely submerged pathways directly to the products as well as pathways involving the formation of a weakly bound van der Waals complex before encountering a barrier.

Chapter 3 considers the CN + CH_2O reaction, where a pre-reaction complex has been identified. The subsequent addition pathway is blocked by a noticeable barrier, while the H abstraction pathway, with a lower energy barrier, is more favourable, making HCN + HCO the dominant products. Simulations using the ab initio results fit well with the Laval experimental data, but fitting with experimental data over a temperature range of 32–796 K shows that the best-fit scenario requires the barrier height for H abstraction to be slightly positive rather than slightly submerged, coupled with an increment in the imaginary frequency, where the change in the barrier height (~4.62 kJ mol^{-1}) is about the uncertainty of the level of theory used. The rate coefficient shows a V-shaped temperature dependence trend, while no pressure dependence is observed below a total number density of 10^{18} molecule cm^{-3}. While simulations from using the ab initio results and the best-fit parameters both match well within the temperature range where Laval data are available, they are different by almost a factor of 2 when extrapolated to 10 K, which indicates a potential danger in extrapolating to conditions outside the temperature range where experimental data are available, which highlights that further work is needed on both high level calculations and experiments at very low temperatures.

CN + CH_2S and CN + CH_3SH reactions are discussed in Chapter 4. Pathways to the products with energies below that of the reactants are identified for both reactions, indicating that they can proceed quickly at low temperature. Although rate coefficient calculations have only be done down to 100 K, the results are approaching the collision limit, indicating that they are very probable to proceed in the ISM below 100 K. H abstraction is energetically more favourable at the mercapto site for the CN + CH_3SH reaction. Apart from H abstraction, addition reaction is also possible for CN + CH_2S, which shows a big contrast with CN + CH_2O. However, further research is needed in order to understand their approach for the determination of the exact product branching ratio. Also, further calculations with an expanded basis set which includes extra d orbitals are recommended to prevent the issues of having high uncertainties in the calculated energy values encountered in this work.

The NH_2 + CH_3CHO reaction was discussed in Chapter 5, and similar to CN + CH_2O, a pre-reaction complex was identified. Addition to form acetamide at low temperature is unlikely due to the barrier, while tunnelling allows the H abstraction products to be formed, with the overall rate coefficients showing the V-shaped temperature dependence. Under most conditions, H abstraction at the carbonyl site dominates, however at low temperature and high pressure, abstraction at the methyl site is also probable. Both the rate coefficients and the product branching ratios demonstrate a pressure dependence, but this is only relevant to the conditions typically carried out in the Laval nozzle experiments. In the ISM, the dominant species will still be CH_3CHO + NH_3 due to the extremely low number density.

Chapter 6 considers the dimerisation reactions of CH_2O, CH_3CHO, $CH_3C(O)CH_3$ and NH_3 with an attempt to explain the observations in the Laval nozzle experiments where there is a loss of monomers apart from reacting with the radicals. The ab initio results show that, for the most stable conformer structure, $CH_3C(O)CH_3$ dimer has the lowest energy, followed by CH_3CHO dimer and then CH_2O dimer. Subsequent simulations on the dimerisation reaction in the Laval nozzle give predicted fractions of dimers similar to what being observed for CH_3CHO, $CH_3C(O)CH_3$ and NH_3, with the inclusion of multiple conformers identified as an improvement in the calculation model for CH_3CHO. Nonetheless, the calculated fraction of dimer for CH_2O is far from enough to explain the curvature in the bimolecular plots, which requires further investigations to figure out the reasons behind. Studies to provide a better description of the density of states and a more accurate collision energy transfer value at low temperature will also help for these low temperature kinetics studies.

From the astrochemical perspective, this work has provided updated expressions of the H abstraction rate coefficient of the CN + CH_2O and NH_2 + CH_3CHO reactions to be used for modelling. However, the addition channel to amide formation is found to be unlikely which means further explorations on the alternatives other than these two gas-phase reactions are needed to explain the amide formation in the ISM. Nevertheless, this work demonstrates that the addition of CN to CH_2S is facile and can be a possible reaction route of sulphur-bearing species in the ISM to be looked into. From the experimental perspective, this work has demonstrated the use of theoretical approaches in predicting the fraction of dimers in the Laval nozzle set-up to give a guidance on the maximum monomer concentration to be used for kinetic experiments. On the other hand, future experimental work should be carried out to provide more data for comparison with the predicted values from calculations. In particular, lower temperature data for the reactions like CN + CH_2O will be helpful in the determinations of the best-fit parameters for extrapolation. From the electronic calculation perspective, this work has provided the PES of CN + CH_2O, CN + CH_3SH, CN + CH_2S, NH_2 + CH_3CHO and the dimerisation reaction of CH_2O, CH_3CHO, $CH_3C(O)CH_3$ and NH_3. Calculations at the more advanced level of theory on these reactions are still recommended, for instance for the CN + CH_2O reaction where the relative energy of the barrier is within the calculation error, or for the sulphur-bearing species where extra d orbitals are needed in the basis set, or for the dimerisation reaction where the dimerisation rate coefficient is sensitive to the low frequency values and the number of conformers. From the kinetic theory perspective, while statistical rate theory has been applied throughout this work, more accurate descriptions of the density of states, magnitude of collisional energy transfer and the approaching of the reacting species are worth investigating. Calculations involving the variational transition state theory or quantum effect that may not be captured by the statistical theory should also be considered in the future.

Appendix A

Supplementary information for the theoretical background and computational methods

Further details for Gaussian calculations

An input text file for the Gaussian programme is saved as .com format. Depending on the keyword included in the route section of the input file, various properties of the system being investigated can be computed, including but not limited to, single-point energy, vibrational frequencies and optimised geometry for both minimum and transition state structures. Adapted from Foresman and Frisch (1), different essential components in the input file are explained in the following:

% Link 0 Commands	Specifies file location and computational resources needed
# Route Section	Specifies job type, method and basis sets
Title Section	For naming or job description purpose
Molecule Specification	Specifies the structure of the molecule

The output text file is in .log format and a checkpoint .chk file can also be created by specifying in the Link 0 Commands section. Both the Gaussian input and output files can be viewed visually with the graphical interface GaussView.

Further details for MESMER calculations

The MESMER input file is in .xml format, which can be edited with a text editor and displayed visually in Firefox, which acts as the graphical user interface (2). The input file consists of several essential sections as follows:

Header	
Molecule list	Specifies the species relevant to the system together with their properties
Reaction list	Specifies the reactive elementary steps involved
Conditions	Specifies the physical conditions and the precision to be run
Model parameters	Specifies the parameters relevant to the energy grains
Control	Specifies the content of the output file
Footer	

First, there is the molecule list section to specify the properties of species present in the system under consideration, including the reactants, the products, the intermediates, the transition states and the bath gases. Results obtained from the Gaussian calculations are included in this section, which can be readily retrieved from Gaussian .log output file and converted to chemical markup language (cml) format using OpenBabel software. Gaussian results can give information regarding the geometric parameters (the symmetry number and the Cartesian coordinates), the energy values, the vibrational frequencies, the scaling factor and the rotational constants. Information of the hindered rotor potential can also be included in this molecule list section. Other properties required include the molecular weight and the spin multiplicity, as well as the

Lennard-Jones ε and σ parameters for the bath gases and the collisional transferred energy $\langle \Delta E \rangle_{down}$ for the intermediates with different bath gases.

The next section is the reaction list which includes all the individual elementary steps of the reaction system. The roles of each species involved in the reaction are specified (deficient reactant, excess reactant, transition state, sink or modelled molecules). Calculation using the RRKM theory is selected for a reactive step with a well-defined barrier, where the option of including the corrections for quantum mechanical tunnelling is available. For a reactive step without a well-defined barrier, the ILT method is selected to calculate the microcanonical rate coefficients.

In the conditions section of the MESMER input file, the physical conditions are specified such as the pressure, the temperature, and the bath gas used. The precision is also specified here, where in the MESMER programme three levels of precision are available. They are, from the lowest to the highest precision, ‘double’, ‘double-double’ and ‘quad-double’, which correspond to approximately 16 digits, 31 digits and 62 digits respectively (3). For data fitting purpose, the experimentally measured rate coefficients k_{expt} and uncertainties σk_{expt} alongside the corresponding experimental conditions are included in this section.

The model parameters section deals with the details regarding the energy grains, for example the grain size and the upper limit of the energy range spanned by the grains.

Lastly, the control section determines the content to be displayed in the output file. Items that can be displayed include the conversion rate coefficients between different species, eigenvalues, density of states and the species profile. The displayed energy offset value and the maximum time evolution of the species profile can also be set in this section. The fitting function of

MESMER can be requested in this section by providing information regarding the number of fitting iterations or the tolerance for the fitting.

Upon the completion of every MESMER calculation, three output files are generated, namely a .log file, a .test file and a .xml file. The .log file lists the operations done during the calculations and any runtime error encountered, so it can act as a tracker of the calculation progress. The .test file contains the output requested in the control section of the input file, arranged in tabular form, in particular values of the properties used during the calculations such as the density of states. The new .xml file contains the input .xml file as well as important results obtained such as the microcanonical rate coefficients and the species profile, where such format allows the viewing of the output file through graphical user interfaces, for example, displaying the species-time profile as a plot of fractional population against time.

References

1. Foresman, J.B. and Frisch, Æ. *Exploring Chemistry with Electronic Structure Methods.* 3rd ed. USA: Gaussian, 2015.

2. Glowacki, D.R., Liang, C.-H., Morley, C., Pilling, M.J. and Robertson, S.H. MESMER: An Open-Source Master Equation Solver for Multi-Energy Well Reactions. *The Journal of Physical Chemistry A.* 2012, **116**(38), pp.9545-9560.

3. Hida, Y., Li, X.S. and Bailey, D.H. *Library for Double-Double and Quad-Double Arithmetic.* [Online]. [Accessed 27/02/2023]. Available from: https://www.davidhbailey.com/dhbsoftware/

Appendix B

Supplementary information for the reaction between the cyano radical (CN) and formaldehyde (CH_2O)

Table B1 Energies (Hartree) of the stationary points indicated in Figure 3.8

Molecule	BHandHLYP/aug-cc-pVDZ	CCSD(T)/aug-cc-pVTZ//BHandHLYP/aug-cc-pVDZ	M06-2X/aug-cc-pVTZ	CCSD(T)/aug-cc-pVTZ//M06-2X/aug-cc-pVTZ
CN	–92.6664471287	–92.570361289	–92.7109177045	–92.569940822
CH_2O	–114.454045365	–114.34248213	–114.498972536	–114.34256827
HCO	–113.808282507	–113.69205366	–113.849422185	–113.69211894
HCN	–93.3790556343	–93.280586134	–93.4240033474	–93.280464138
HNC	–93.3594694496	–93.257196852	–93.4034421705	–93.257105778
NCO	–167.937803563	–167.76167372	–168.001757582	–167.76182601
$^3CH_2$	–39.1344871171	–39.080082343	–39.1458950805	–39.080080114
HC(O)CN	–206.647867188	–206.43312185	–206.737485619	–206.43315497
H	–0.49807845526	–0.4998211760	–0.49820646135	–0.4998211760
VDW	–207.132179226	–206.92006960	–207.221791874	–206.92007837
TS_VDW/P1	–207.120946339	–206.91346038	–207.210896230	–206.91241474

TS_VDW/P2	–207.116552769	–206.90715307	–207.206033093	–206.90988176
TS_VDW/P3-4	–207.114313148	–206.90158148	–207.206393549	–206.90180253
Int1	–207.182819014	–206.96199619	–207.271625866	–206.96219122
TS_1/2	–207.149948879	–206.93246933	–207.241603107	–206.93246368
Int2	–207.171060223	–206.94904180	–207.258174359	–206.94900109
TS_2/3	–207.159894959	–206.94051055	–207.246790812	–206.94037893
Int3	–207.202787376	–206.97558554	–207.281454928	–206.97550823
TS_3/P4	–207.140727011	–206.92519810	–207.228517443	–206.92466699

Table B2 Zero-point energies (ZPVE) (Hartree) of the stationary points indicated in Figure 3.8

Molecule	Unscaled BHandHLYP/aug-cc-pVDZ	Scaled BHandHLYP/aug-cc-pVDZ (scaling factor: 0.9589)	Unscaled M06-2X/aug-cc-pVTZ	Scaled M06-2X/aug-cc-pVTZ (scaling factor: 0.956)
CN	0.005120	0.004910	0.005108	0.004883
CH_2O	0.027595	0.026461	0.027038	0.025848
HCO	0.013500	0.012945	0.013274	0.012690
HCN	0.016876	0.016182	0.016612	0.015881
HNC	0.016059	0.015399	0.015985	0.015282
NCO	0.010383	0.009956	0.010285	0.009832

$^3CH_2$	0.017655	0.016929	0.017475	0.016706
HC(O)CN	0.027624	0.026489	0.027002	0.025814
H	0	0	0	0
VDW	0.035518	0.034058	0.034778	0.033248
TS_VDW/P1	0.032986	0.031630	0.031802	0.030403
TS_VDW/P2	0.030044	0.028809	0.030978	0.029615
TS_VDW/P3-4	0.034419	0.033004	0.034061	0.032562
Int1	0.037169	0.035641	0.036643	0.035031
TS_1/2	0.036018	0.034538	0.035395	0.033838
Int2	0.038832	0.037236	0.037962	0.036292
TS_2/3	0.036990	0.035470	0.036382	0.034781
Int3	0.037752	0.036200	0.036944	0.035318
TS_3/P4	0.028990	0.027799	0.028548	0.027292

Table B3 Relative energies of the stationary points indicated in Figure 3.8.

Molecule	Energy (CCSD(T)/aug-cc-pVTZ//M06-2X/aug-cc-pVTZ) + ZPVE (Scaled M06-2X/aug-cc-pVTZ frequencies) (Hartree)	Relative energy (Hartree)	Relative energy (kJ/mol)
CN	–92.565057574		

CH_2O	–114.316719942		
CN + CH_2O	–206.881777516	0	0
HCO	–113.679428996		
HCN	–93.264583066		
P1: HCO + HCN	–206.944012062	–0.062234546	–163.4
HNC	–93.241824118		
P2: HCO + HNC	–206.921253114	–0.039475598	–103.6
NCO	–167.75199355		
$^3CH_2$	–39.063374014		
P3: NCO + $^3CH_2$	–206.815367564	0.066409952	174.4
HC(O)CN	–206.407341058		
H	–0.4998211760		
P4: HC(O)CN + H	–206.907162234	–0.025384718	–66.7
VDW	–206.886830602	–0.005053086	–13.3
TS_VDW/P1	–206.882012028	–0.000234512	–0.62
TS_VDW/P2	–206.880266792	0.001510724	3.97
TS_VDW/P3-4	–206.869240214	0.012537302	32.9
Int1	–206.927160512	–0.045382996	–119.2

TS_1/2	–206.898626060	–0.016848544	–44.2
Int2	–206.912709418	–0.030931902	–81.2
TS_2/3	–206.905597738	–0.023820222	–62.5
Int3	–206.940189766	–0.058412250	–153.4
TS_3/P4	–206.897375102	–0.015597586	–41.0

Table B4 Optimised (BHandHLYP/aug-cc-pVDZ) Cartesian coordinates of the stationary points indicated in Figure 3.8.

Molecule	Atom	x	y	z
CN	C	0.0000000000	0.0000000000	0.0000070329
	N	0.0000000000	0.0000000000	1.1576529671
CH_2O	C	–0.0006269948	0.0000000000	–0.0004261838
	H	0.0000480566	0.0000000000	1.1029486987
	H	0.9868903289	0.0000000000	–0.4926113577
	O	–1.0163210369	0.0000000000	–0.6286262781
HCO	C	–1.1472608710	0.5108400621	–0.0693120621
	H	–2.1447035514	0.1497120150	0.2918159850
	O	–0.1159875776	0.1253359229	0.3161920771

HCN	C	–0.5012343391	0.2744630000	0.0000000000
	H	–1.5682846496	0.2744630000	0.0000000000
	N	0.6425389887	0.2744630000	0.0060188531
HNC	C	–0.6724460247	0.0859950800	2.1606269968
	H	–2.8299501604	0.0859950800	–0.0003623584
	N	–1.8358884249	0.0859950800	0.0025813953
NCO	C	–0.8286716441	0.3937950000	0.0935497776
	O	0.3372382922	0.3937950000	0.0900557182
	N	–2.0494519481	0.3937950000	0.0972090743
$^3CH_2$	C	–1.1518343493	0.8803618846	0.0000000000
	H	–0.5776428291	–0.0345635056	0.0000000000
	H	–2.2058255616	1.1167651410	0.0000000000
HC(O)CN	C	–4.4927412614	1.4312470592	1.6834996406
	H	–5.1162507065	2.3340601295	1.7150244670
	O	–3.3020663641	1.4587260846	1.6844629141
	C	–5.2500533317	0.1725471803	1.6395447126
	N	–5.8899343362	–0.7787584536	1.6063292656

VDW	C	0.1877328202	0.2711591310	–0.0330258805
	H	–0.2638490932	–0.6575597712	–0.4004401128
	H	0.9018087043	0.2168579409	0.7989691294
	O	–0.0830754105	1.3368653015	–0.5208162508
	C	–1.5175299875	0.9610130588	–2.1121827767
	N	–2.0220890333	0.0092783390	–2.5370281086
TS_VDW/P1	C	0.1359454235	0.2711243165	–0.2392824058
	H	1.2211917712	0.3136928104	–0.0177114384
	H	–0.3706552739	1.2435061946	–0.3585458806
	O	–0.4434274181	–0.7655423221	–0.3413919637
	C	3.2764185131	–0.9057404902	0.4234054596
	N	4.3024639841	–0.4095275092	0.6258532290
TS_VDW/P2	C	0.2661916136	–0.0236503220	0.6255598564
	H	1.3309111832	–0.1206752452	1.0254334191
	H	0.1859451594	–0.0084199370	–0.4785156740
	O	–0.6741770760	0.0541778703	1.3389681349
	C	3.5873140848	–0.3322721305	2.5342800458

	N	2.9672800350	–0.2691802355	1.5413972179
TS_VDW/P3-4	C	0.0920364602	0.2338898231	–0.0041991112
	H	–0.4428112964	–0.7137798210	0.0318507450
	H	1.0701180432	0.3407789529	0.4618604688
	O	–0.3772697775	1.2024634090	–0.6290982936
	C	–1.1261006683	0.8310588287	–2.1016021509
	N	–2.0129747613	0.2432038074	–2.5633356582
Int1	C	–0.0000008938	–0.0000061102	–0.0000014823
	H	–0.0000031530	–0.0000040487	1.0759509496
	H	0.8778810616	0.0000048253	–0.6268846190
	O	–1.1520814144	0.5622824272	–0.5224902562
	C	–1.2155804539	0.7114641955	–1.7979934490
	N	–1.3072451023	0.8637902144	–2.9331206285
TS_1/2	C	0.0931909504	0.1465526740	–0.3064537607
	H	0.0207105412	–0.8404824956	0.1250322672
	H	0.9592219679	0.7814679011	–0.1944497331
	O	–1.1432935063	0.8327859824	–0.4548828491

	C	–0.9337927174	0.4676094052	–1.6933915468
	N	–1.0194901257	0.2888840830	–2.8524941576
Int2	C	–2.1024967554	0.8015706954	0.0702475238
	H	–1.9179351684	–0.2654446290	0.0738140035
	H	–1.9248247908	1.3420588008	–0.8511123852
	O	–1.6552179011	1.4965763103	1.2748225196
	C	–2.9829519448	1.3708393455	1.0661845959
	N	–4.0687154396	1.6558544769	1.5696247425
TS_2/3	C	–2.0660532269	0.8323085785	0.1233983868
	H	–1.9313875963	–0.2470491519	0.0864227857
	H	–1.9382059875	1.3436290052	–0.8288204941
	O	–1.5294087403	1.4802575468	1.2455242471
	C	–3.1175694576	1.3213088099	0.9811071968
	N	–4.0695169913	1.6709992116	1.5959508777
Int3	C	2.1011728269	0.2673227771	–0.0263689090
	H	2.4306421008	–0.7781140666	–0.0879827475
	H	2.4306859917	0.7365453773	–0.9626032918

	O	2.7543879051	0.8656889591	1.0099136322
	C	0.6292312494	0.3168629311	0.0593544211
	N	–0.5154950739	0.3435340221	0.1054898949
TS_3/P4	C	2.0719329264	0.6454968366	0.0344230737
	H	2.4614827055	–1.1957132990	–0.1714942902
	H	2.4745770964	0.7109166164	–0.9835082782
	O	2.7181586587	0.9227998774	1.0152793237
	C	0.6202410070	0.4128591593	0.0998715841
	N	–0.5157683940	0.2554818094	0.1032315870

Table B5 Optimised (M06-2X/aug-cc-pVTZ) Cartesian coordinates of the stationary points indicated in Figure 3.8.

Molecule	Atom	x	y	z
CN	C	0.0000000000	0.0000000000	0.0026490599
	N	0.0000000000	0.0000000000	1.1550109401
CH_2O	C	0.0001485802	0.0000000000	0.0000495740
	H	–0.0001405588	0.0000000000	1.1031921816
	H	0.9870338276	0.0000000000	–0.4928861636

	O	–1.0170514952	0.0000000000	–0.6290707129
HCO	C	–1.1478502975	0.5141164213	–0.0725884213
	H	–2.1413115962	0.1481177562	0.2934102438
	O	–0.1187901063	0.1236538225	0.3178741775
HCN	C	–0.5009704719	0.2744629999	0.0000000001
	H	–1.5672104034	0.2744630000	0.0000000000
	N	0.6412008754	0.2744630000	0.0000000000
HNC	C	0.0000000000	0.0000000000	2.1606269968
	H	0.0000000000	0.0000000000	0.0009053833
	N	0.0000000000	0.0000000000	0.9990676199
NCO	C	–0.8286470860	0.3937947400	0.0740993138
	O	0.3388251903	0.3937947400	0.0714754171
	N	–2.0512108442	0.3937947400	0.0768467291
$^{3}CH_{2}$	C	–1.1506440635	0.8820149934	0.0000000000
	H	–0.5835642543	–0.0316382648	0.0000000000
	H	–2.2010944222	1.1121867914	0.0000000000
HC(O)CN	C	0.0032967422	–0.0000002047	1.1906161951

	H	0.9209549067	0.0000004152	1.7928472351
	O	–0.0015665304	0.0000004720	–0.0017081873
	C	–1.2430500638	–0.0000019747	1.9813255879
	N	–2.1822720597	–0.0000033753	2.6374370909
VDW	C	–0.0802996529	0.1415542821	0.0886125371
	H	0.3496471560	–0.0961093270	1.0703091894
	H	0.5472902933	0.0377236402	–0.8054473223
	O	–1.2243327195	0.5096266809	0.0078247294
	C	–1.5449835579	0.8356580995	–2.1280613547
	N	–0.8443245190	0.7091606244	–3.0377607789
TS_VDW/P1	C	0.1716529423	0.2587231536	–0.2325318080
	H	1.2616271691	0.3753610457	–0.0227715791
	H	–0.3944269679	1.1975579239	–0.3527164016
	O	–0.3334755327	–0.8157694274	–0.3181451437
	C	3.1448813234	–0.6399711328	0.3875280146
	N	4.2716790658	–0.6283885630	0.6309639178
TS_VDW/P2	C	0.2113600000	–0.0187690000	0.6031100000

	H	1.2133530000	–0.1107640000	1.1232550000
	H	0.2482040000	–0.0123130000	–0.5040380000
	O	–0.8088380000	0.0649370000	1.2039010000
	C	3.9161060000	–0.3597260000	2.3440750000
	N	2.8832790000	–0.2633860000	1.8168200000
TS_VDW/P3-4	C	–0.0116283756	0.1813465161	0.0270360337
	H	0.0291975418	–0.2980508345	1.0030401411
	H	0.7985096458	0.0656845292	–0.6909816016
	O	–1.0343488706	0.8203321919	–0.2769992306
	C	–1.5011454612	0.6329863407	–1.8962339024
	N	–1.0775884803	0.7353152567	–2.9703854402
Int1	C	–0.0064939441	–0.0139702952	–0.0015974672
	H	0.0122374291	0.0112781460	1.0722481941
	H	0.8678708603	0.0047991567	–0.6309435748
	O	–1.1606985987	0.5580962510	–0.5156613165
	C	–1.2162074000	0.7120354299	–1.7963994727
	N	–1.2937106462	0.8653759968	–2.9321701796

TS_1/2	C	0.0879953265	0.1494321889	–0.3052931015
	H	0.0190707113	–0.8428251218	0.1105866138
	H	0.9574269136	0.7794121972	–0.2078289364
	O	–1.1499014895	0.8385652739	–0.4422518661
	C	–0.9371549787	0.4710474619	–1.6882849988
	N	–1.0008893731	0.2811855500	–2.8435674912
Int2	C	–2.0934364379	0.8028707424	0.0724275401
	H	–1.9211421562	–0.2651836430	0.0754841440
	H	–1.9280438389	1.3433442997	–0.8500462091
	O	–1.6509548511	1.4932901570	1.2691054179
	C	–2.9875027967	1.3727799976	1.0695708324
	N	–4.0710619193	1.6543524462	1.5670412748
TS_2/3	C	–2.0565893803	0.8355409283	0.1285849616
	H	–1.9384682443	–0.2456553068	0.0885760969
	H	–1.9428643134	1.3478379113	–0.8249170764
	O	–1.5124574751	1.4758666455	1.2429259904
	C	–3.1327740514	1.3178461229	0.9749756185

	N	–4.0689885354	1.6700166987	1.5934374090
Int3	C	2.1019519703	0.2689745078	–0.0233970520
	H	2.4311880099	–0.7772828818	–0.0910711717
	H	2.4311601750	0.7334860708	–0.9633416719
	O	2.7550285184	0.8665912714	1.0113692084
	C	0.6273189309	0.3161569553	0.0582102287
	N	–0.5160226045	0.3439140766	0.1060334586
TS_3/P4	C	2.0900040565	0.6431041278	0.0376043407
	H	2.3885960779	–1.1549710693	–0.1743549441
	H	2.4921201804	0.7060797797	–0.9829747076
	O	2.7284378186	0.9373352605	1.0186570996
	C	0.6320234888	0.3973763644	0.0971419418
	N	–0.5005576222	0.2229175369	0.1017302696

Table B6 Unscaled harmonic vibrational frequencies (cm^{-1}) of the stationary points indicated in Figure 3.8 (BHandHLYP/aug-cc-pVDZ).

Molecule	Wavenumber (cm^{-1})

CN	2247.3106
CH_2O	1253.4937 1293.4062 1567.4704 1893.7491 3013.1585 3091.7026
HCO	1127.8469 2018.0359 2780.0316
HCN	781.9379 781.9379 2295.8436 3548.1368
HNC	469.8860 469.8873 2190.8722 3918.4467
NCO	541.0596 623.8794 1349.4921 2043.3909
$^3CH_2$	1091.4693 3204.6888 3453.4607
HC(O)CN	244.3149 313.7408 647.4999 964.6374 1045.5923 1444.7613 1882.3985 2457.8298 3124.8194
VDW	112.5553 114.5264 274.7901 299.5249 322.1122 1271.1946 1282.3253 1544.0397 1844.3247 2254.3442 3080.8598 3189.8143
TS_VDW/P1	–139.2544 27.2536 37.2742 55.8459 116.4252 1249.7897 1275.1838 1558.0157 1895.5680 2250.0120 2941.3277 3072.5828
TS_VDW/P2	–539.1909 38.0694 65.5620 151.7302 294.6677 1208.5307 1250.1347 1414.3783 1556.2042 1960.5812 2239.6025 3008.2362
TS_VDW/P3-4	–936.1640 98.5446 158.9751 449.6762 494.2486 1071.7107 1250.8951 1360.1802 1567.5274 2218.5304 3149.2681 3288.8040
Int1	216.8530 252.1633 502.3936 537.7094 646.8613 985.8456 1204.3661 1302.3194 1491.2028 2482.6848 3258.2562 3434.5003

TS_1/2	–855.2504 365.7461 432.8525 622.8138 844.4755 1013.2573 1135.0087 1162.7004 1495.0897 2102.5012 3235.7245 3399.7794
Int2	444.5194 445.2710 760.6977 942.9260 1019.6413 1120.4699 1133.0812 1223.1826 1529.6402 1876.0723 3217.8224 3332.1531
TS_2/3	–781.9591 377.3786 393.3708 882.3567 1040.3693 1147.6051 1169.5877 1282.5490 1541.5014 1989.0210 3161.6952 3251.2184
Int3	238.0977 347.7046 608.5778 650.3364 939.2090 1117.4834 1200.9026 1378.6666 1423.2928 2474.3670 3080.2164 3112.5181
TS_3/P4	–836.2741 242.6908 283.8152 407.6675 451.0981 644.5861 958.4904 1020.5629 1423.6047 1712.7181 2458.5362 3121.2336

Table B7 Unscaled harmonic vibrational frequencies (cm^{-1}) of the stationary points indicated in Figure 3.8 (M06-2X/aug-cc-pVTZ).

Molecule	Wavenumber (cm^{-1})
CN	2241.9799
CH_2O	1216.3324 1275.0095 1540.7191 1869.4302 2948.5832 3018.3473
HCO	1103.4473 1993.0627 2729.8956
HCN	785.3481 785.3481 2254.5540 3466.4178
HNC	528.7255 528.7255 2147.7615 3811.6074

NCO	533.0140 614.6710 1326.9732 2039.9448
$^3CH_2$	1096.3069 3177.8218 3396.7268
HC(O)CN	235.3323 310.0780 630.6469 932.1926 1016.9040 1415.0844 1853.2170 2407.2828 3051.7761
VDW	116.7742 129.4838 262.3213 301.7164 306.4708 1229.0710 1264.4117 1513.7341 1821.9598 2212.0823 3004.5679 3103.2415
TS_VDW/P1	–214.6595 23.3018 35.5117 50.7396 91.0436 1196.6207 1227.9601 1509.2793 1876.0265 2226.6387 2725.6977 2996.8099
TS_VDW/P2	–222.6725 48.6415 67.4455 134.4869 266.0340 1209.1278 1212.2454 1479.9321 1841.4504 2080.0746 2325.2605 2932.8990
TS_VDW/P3-4	–850.0448 114.6174 180.3015 455.8172 522.2467 1064.1180 1230.1891 1379.3882 1546.5007 2177.9188 3075.0931 3204.8833
Int1	229.7909 247.1081 526.2839 557.0405 641.1308 975.9125 1189.5383 1281.1086 1469.3312 2432.9556 3187.0090 3347.4220
TS_1/2	–781.1002 372.5848 426.2327 606.2279 809.4990 992.8945 1131.9599 1142.4768 1465.7413 2100.9242 3166.7193 3321.3474
Int2	428.9031 437.4089 778.5354 899.1928 986.8137 1110.9110 1125.4648 1186.6388 1498.4004 1814.2092 3145.0780 3251.9897
TS_2/3	–661.6184 364.7564 387.8360 866.2833 1012.5754 1134.0929 1168.9878 1254.5642 1511.9142 2015.1175 3085.8493 3167.9682

Int3	232.3747 341.2933 598.7539 669.1942 913.7207 1093.4184 1182.8619 1344.0640 1391.4860 2424.4943 3000.6790 3024.2660
TS_3/P4	–927.9940 234.7680 284.0235 429.7689 469.1457 627.3944 922.0683 1015.6697 1393.0411 1721.4685 2403.7170 3029.8942

Table B8 Rotational constants (GHz) of the stationary points indicated in Figure 3.8 (BHandHLYP/aug-cc-pVDZ).

Molecule	Rotational constants (GHz)
CN	58.356032
CH_2O	284.94442 39.54571 34.72626
HCO	735.99076 45.40460 42.76627
HCN	45.114810
HNC	45.854396
NCO	11.876083
$^3CH_2$	1696.16249 252.20695 219.55999
HC(O)CN	69.20026 5.05119 4.70756
VDW	30.74881 4.38635 3.83875
TS_VDW/P1	39.06318 2.08177 1.97645
TS_VDW/P2	39.86240 2.62094 2.45925

TS_VDW/P3-4	38.78166 5.05054 4.57598
Int1	52.55168 5.55680 5.03272
TS_1/2	29.12886 7.41526 6.17356
Int2	26.72865 8.25964 6.59524
TS_2/3	26.91551 7.68428 6.22771
Int3	41.55366 4.93283 4.53128
TS_3/P4	42.80559 4.87796 4.60759

Table B9 Rotational constants (GHz) of the stationary points indicated in Figure 3.8 (M06-2X/aug-cc-pVTZ).

Molecule	Rotational constants (GHz)
CN	58.892432
CH_2O	284.75755 39.45537 34.65382
HCO	720.91067 45.43688 42.74292
HCN	45.232416
HNC	45.932654
NCO	11.842920
$^3CH_2$	1671.48960 255.53548 221.64989
HC(O)CN	68.47755 5.04092 4.69528

VDW	29.57540 4.52700 3.92605
TS_VDW/P1	44.25913 2.22853 2.12172
TS_VDW/P2	63.66131 2.27792 2.19922
TS_VDW/P3-4	36.12996 5.25240 4.68349
Int1	51.43216 5.57054 5.03485
TS_1/2	28.66960 7.46924 6.18979
Int2	26.99825 8.20895 6.57940
TS_2/3	26.95494 7.61005 6.18138
Int3	41.58770 4.92674 4.52590
TS_3/P4	43.54483 4.86961 4.59540

Table B10 Rate coefficients (cm^3 molecule^{-1} s^{-1}) versus temperature using the Laval and Laval + Lit 2 scenarios.

T (K)	*k* from Laval + Lit 2	*k* from Laval
4	1.299E-10	6.339E-10
5	1.138E-10	4.534E-10
6	9.735E-11	3.662E-10
7	9.524E-11	2.852E-10

8	9.187E-11	2.321E-10
9	8.799E-11	1.949E-10
10	8.398E-11	1.676E-10
11	8.003E-11	1.467E-10
12	7.625E-11	1.303E-10
13	7.268E-11	1.171E-10
14	6.934E-11	1.063E-10
15	6.622E-11	9.718E-11
16	6.332E-11	8.950E-11
17	6.062E-11	8.291E-11
18	5.811E-11	7.720E-11
19	5.578E-11	7.221E-11
20	5.360E-11	6.781E-11
25	4.468E-11	5.187E-11
30	3.816E-11	4.192E-11
35	3.321E-11	3.512E-11
40	2.934E-11	3.020E-11

45	2.625E-11	2.647E-11
50	2.372E-11	2.355E-11
60	1.985E-11	1.927E-11
70	1.702E-11	1.630E-11
80	1.488E-11	1.411E-11
90	1.298E-11	
100	1.185E-11	
125	1.073E-11	
150	1.071E-11	
175	1.119E-11	
200	1.198E-11	
225	1.298E-11	
250	1.413E-11	
275	1.542E-11	
300	1.682E-11	
325	1.833E-11	
350	1.999E-11	

375	2.154E-11	
400	2.300E-11	
425	2.437E-11	
450	2.565E-11	
475	2.685E-11	
500	2.798E-11	
525	2.904E-11	
550	3.004E-11	
575	3.098E-11	
600	3.187E-11	
625	3.270E-11	
650	3.350E-11	
675	3.425E-11	
700	3.496E-11	
725	3.563E-11	
750	3.627E-11	
775	3.688E-11	

800	3.746E-11	
825	3.801E-11	
850	3.854E-11	
875	3.904E-11	
900	3.952E-11	
925	3.998E-11	
950	4.042E-11	
975	4.084E-11	
1000	4.124E-11	

Appendix C

Supplementary information for the reaction between the cyano radical (CN) and methanethiol (CH_3SH) and thioformaldehyde

Table C1 Energies (Hartree) of the stationary points indicated in Figure 4.5 and Figure 4.6

Molecule	BHandHLYP/aug-cc-pVDZ	CCSD(T)/aug-cc-pVTZ//BHandHLYP/aug-cc-pVDZ	M06-2X/aug-cc-pVTZ	CCSD(T)/aug-cc-pVTZ//M06-2X/aug-cc-pVTZ
CN	-92.66644713	-92.57036129	-92.71091770	-92.56994082
CH_3SH	-438.6747938	-438.1776139	-438.6902035	-438.1775829
HCN	-93.37905563	-93.28058613	-93.42400335	-93.28046414
HNC	-93.35946945	-93.25719685	-93.40344217	-93.25710578
CH_3S	-438.0391223	-437.5336126	-438.0482863	-437.5335405
CH_2SH	-438.0183918	-437.5144272	-438.0284766	-437.5143885
PreRC1	-531.3737018	-530.7752709	-531.4357556	-530.7752903
TS1	-531.3556248	-530.7580885	-531.4174103	-530.7581615
PostRC1	-531.4234369	-530.8200448	-531.4779743	-530.8199941
PreRC2	-531.3619766	-530.7590067	-531.4211046	-530.7592370

TS2	-531.3510143	-530.7491051	-531.4096632	-530.7492702
PostRC2	-531.4073265	-530.8002623	-531.4606518	-530.8002774
TS3	-531.3414326	-530.7505673	-531.4026866	-530.6978398
PostRC3	-531.4016815	-530.8000150	-531.4578045	-530.7994714
TS4	-531.3354879	-530.7474974	-531.3966352	-530.7485786
PostRC4	-531.3839035	-530.7794633	-531.4391417	-530.7794004

Table C2 Energies (Hartree) of the stationary points indicated in Figure 4.8 and Figure 4.9

Molecule	BHandHLYP/aug-cc-pVDZ	CCSD(T)/aug-cc-pVTZ//BHandHLYP/aug-cc-pVDZ	M06-2X/aug-cc-pVTZ	CCSD(T)/aug-cc-pVTZ//M06-2X/aug-cc-pVTZ
CN	-92.66644713	-92.57036129	-92.71091770	-92.56994082
CH_2S	-437.4400260	-436.9416095	-437.4552684	-436.9414085
HCN	-93.37905563	-93.28058613	-93.42400335	-93.28046414
HNC	-93.35946945	-93.25719685	-93.40344217	-93.25710578
HCS	-436.7871099	-436.2839745	-436.7989216	-436.2837906
SCN	-490.9470208	-490.3859343	-490.9838581	-490.3856980
$^3CH_2$	-39.13448712	-39.08008234	-39.14589508	-39.08008011
HC(S)CN	-529.6368485	-529.0353010	-529.6976763	-529.0350459

H	-0.498078455	-0.499821176	-0.498206461	-0.499821176
Add-C	-530.2038800	-529.5994682	-530.2632006	-529.5993870
TS_C/N	-530.1313838	-529.5292489	-530.1955719	-529.5287126
Add-N	-530.1618359	-529.5563698	-530.2239167	-529.5562816
TS_Int	-530.1674067	-529.5649018	-530.2301352	-529.5646360
Int	-530.2338168	-529.6243601	-530.2877887	-529.6242251
TS_Pro	-530.1335237	-529.5303806	-530.1919877	-529.5295852
Post_HCN	-530.1701001	-529.5698149	-530.2278315	-529.5695863
Post_HNC	-530.1529609	-529.5491351	-530.2097531	-529.5489163

Table C3 Zero-point energies (ZPVE) (Hartree) of the stationary points indicated in Figure 4.5 and Figure 4.6

Molecule	Unscaled BHandHLYP/aug-cc-pVDZ	Scaled BHandHLYP/aug-cc-pVDZ (scaling factor: 0.9589)	Unscaled M06-2X/aug-cc-pVTZ	Scaled M06-2X/aug-cc-pVTZ (scaling factor: 0.956)
CN	0.005120	0.004909568	0.005108	0.004883248
CH_3SH	0.047095	0.045159396	0.046448	0.044404288
HCN	0.016876	0.016182396	0.016612	0.015881072
HNC	0.016059	0.015398975	0.015985	0.015281660
CH_3S	0.036448	0.034949987	0.039790	0.038039240

CH_2SH	0.032126	0.030805621	0.031783	0.030384548
PreRC1	0.054919	0.052661829	0.054058	0.051679448
TS1	0.052026	0.049887731	0.050977	0.048734012
PostRC1	0.055124	0.052858404	0.054035	0.051657460
PreRC2	0.054460	0.052221694	0.053553	0.051196668
TS2	0.051312	0.049203077	0.049930	0.047733080
PostRC2	0.054935	0.052677172	0.053906	0.051534136
TS3	0.052542	0.050382524	0.050807	0.048571492
PostRC3	0.050398	0.048326642	0.050198	0.047989288
TS4	0.049840	0.047791576	0.049927	0.047730212
PostRC4	0.050940	0.048846366	0.050013	0.047812428

Table C4 Zero-point energies (ZPVE) (Hartree) of the stationary points indicated in Figure 4.8 and Figure 4.9

Molecule	Unscaled BHandHLYP/aug-cc-pVDZ	Scaled BHandHLYP/aug-cc-pVDZ (scaling factor: 0.9589)	Unscaled M06-2X/aug-cc-pVTZ	Scaled M06-2X/aug-cc-pVTZ (scaling factor: 0.956)
CN	0.005120	0.004909568	0.005108	0.004883248
CH_2S	0.025584	0.024532498	0.024986	0.023886616
HCN	0.016876	0.016182396	0.016612	0.015881072

HNC	0.016059	0.015398975	0.015985	0.015281660
HCS	0.012146	0.011646799	0.011879	0.011356324
SCN	0.008238	0.007899418	0.008244	0.007881264
$^3CH_2$	0.017655	0.016929380	0.017475	0.016706100
HC(S)CN	0.025528	0.024478799	0.024951	0.023853156
H	0	0	0	0
Add-C	0.032914	0.031561235	0.032163	0.030747828
TS_C/N	0.031625	0.030325213	0.031285	0.029908460
Add-N	0.032331	0.031002196	0.031864	0.030461984
TS_Int	0.033384	0.032011918	0.032682	0.031243992
Int	0.036705	0.035196425	0.035927	0.034346212
TS_Pro	0.026399	0.025314001	0.026277	0.025120812
Post_HCN	0.030531	0.029276176	0.029959	0.028640804
Post_HNC	0.030499	0.029245491	0.029806	0.028494536

Table C5 Relative energies of the stationary points indicated in Figure 4.5 and Figure 4.6

Molecule	Energy (CCSD(T)/aug-cc-pVTZ//M06-2X/aug-cc-pVTZ) + ZPVE (Scaled M06-2X/aug-cc-pVTZ frequencies) (Hartree)	Relative energy (Hartree)	Relative energy (kJ/mol)

CN	-92.56505757		
CH_3SH	-438.1331787		
CN + CH_3SH	-530.6982362	0	0
HCN	-93.26458307		
HNC	-93.24182412		
CH_3S	-437.4955012		
CH_2SH	-437.4840039		
HCN + CH_3S	-530.7600843	-0.061848080	-162.4
HNC + CH_3S	-530.7373254	-0.039089132	-102.6
HCN + CH_2SH	-530.7485870	-0.050350772	-132.2
HNC + CH_2SH	-530.7258281	-0.027591824	-72.4
PreRC1	-530.7236109	-0.025374626	-66.6
TS1	-530.7094275	-0.011191242	-29.4
PostRC1	-530.7683367	-0.070100424	-184.0
PreRC2	-530.7080404	-0.009804136	-25.7
TS2	-530.7015371	-0.003300894	-8.67
PostRC2	-530.7487432	-0.050506988	-132.6
TS3	-530.6492683	0.048967878	128.6

PostRC3	-530.7514821	-0.053245836	-139.8
TS4	-530.7008483	-0.002612122	-6.86
PostRC4	-530.7315880	-0.033351776	-87.6

Table C6 Relative energies of the stationary points indicated in Figure 4.8 and Figure 4.9

Molecule	Energy (CCSD(T)/aug-cc-pVTZ//M06-2X/aug-cc-pVTZ) + ZPVE (Scaled M06-2X/aug-cc-pVTZ frequencies) (Hartree)	Relative energy (Hartree)	Relative energy (kJ/mol)
CN	-92.56505757		
CH_2S	-436.9175219		
CN + CH_2S	-529.4825795	0	0
HCN	-93.26458307		
HNC	-93.24182412		
HCS	-436.2724342		
HCN + HCS	-529.5370173	-0.054437814	-142.9
HNC + HCS	-529.5142583	-0.031678866	-83.2
SCN	-490.3778167		
$^3CH_2$	-39.06337401		
SCN + $^3CH_2$	-529.4411907	0.041388758	108.7

HC(S)CN	-529.01119270		
H	-0.499821176		
HC(S)CN + H	-529.5110139	-0.028434412	-74.7
Add-C	-529.5686392	-0.086059734	-225.9
TS_C/N	-529.4988042	-0.016224682	-42.6
Add-N	-529.5258196	-0.043240138	-113.5
TS_Int	-529.5333920	-0.050812500	-133.4
Int	-529.5898789	-0.107299430	-281.7
TS_Pro	-529.5044644	-0.021884940	-57.5
Post_HCN	-529.5409455	-0.058366038	-153.2
Post_HNC	-529.5204218	-0.037842326	-99.4

Table C7 Optimised (BHandHLYP/aug-cc-pVDZ) Cartesian coordinates of the stationary points indicated in Figure 4.5 and Figure 4.6

Molecule	Atom, (x, y, z) coordinates
CN	C 0.00000000 0.00000000 0.00000700 N 0.00000000 0.00000000 1.15765300
CH_3SH	C -0.00490300 0.03082100 0.01012700 H 0.35669800 -0.99603900 0.00863900

	H	0.36663800	0.53522700	-0.87909500
	H	-1.09258400	0.02009300	0.01459600
	S	0.65170000	0.80007100	1.52561000
	H	0.11430200	2.01949200	1.35002800
HCN	C	-0.50123400	0.27446300	0.00000000
	H	-1.56828500	0.27446300	0.00000000
	N	0.64253900	0.27446300	0.00000000
HNC	N	-1.83588800	0.08599500	0.00258100
	H	-2.82995000	0.08599500	-0.00036200
	C	-0.67244600	0.08599500	0.00601900
CH_3S	C	-0.01131500	-0.01478900	0.01635400
	H	0.36505200	-1.03587600	-0.01974500
	H	0.36512500	0.51940300	-0.86090800
	H	-1.09953800	0.00100000	-0.01687900
	S	0.61421200	0.86495500	1.45876100
CH_2SH	C	0.28242400	0.03134100	0.03988500
	H	0.35602100	-1.04361200	-0.00936300
	H	0.13554800	0.62929200	-0.84446300
	S	0.41357500	0.75392000	1.60625100
	H	0.27491200	2.03871100	1.23802100
PreRC1	C	-0.16233000	0.02059400	0.00376500
	H	0.86988300	-0.11522000	-0.30940000
	H	-0.80698100	-0.77437700	-0.35775400
	H	-0.22042600	0.07463200	1.08808000
	S	-0.77071900	1.62052100	-0.60883600
	H	-0.73628200	1.35193200	-1.92528900

	C	-2.98723300	0.86330000	-0.64252600
	N	-3.58728900	-0.04278300	-0.23744700
TS1	C	0.00476400	0.04401800	0.12894600
	H	0.70246400	-0.33672400	-0.61294900
	H	-0.85105100	-0.61892900	0.22991500
	H	0.49583200	0.15154600	1.09318900
	S	-0.57834200	1.69560600	-0.35335400
	H	-1.38060500	1.30609900	-1.42821600
	C	-2.93886300	0.72991800	-1.05513500
	N	-3.85557600	0.02706500	-0.99180300
PostRC1	C	0.43692700	0.05071400	0.32418500
	H	0.81474600	-0.47413100	-0.55793500
	H	-0.41084600	-0.51055400	0.71435000
	H	1.23523200	0.11281400	1.06059300
	S	-0.06799800	1.68949100	-0.23093300
	H	-2.49303500	1.09968100	-1.11787300
	C	-3.44998400	0.72127100	-1.42752900
	N	-4.46641900	0.30931500	-1.75426600
PreRC2	C	0.19744200	-0.00486200	0.08822900
	H	-0.30710100	0.55470600	-0.69638700
	H	-0.50449600	-0.46554100	0.77591300
	H	0.84303800	-0.76313700	-0.34801200
	S	1.28139700	1.10711100	1.02068000
	H	0.33148600	1.84843900	1.61457000
	N	1.03333700	-0.21442400	2.88137600
	C	2.02901800	-0.64040900	3.36258200

TS2	C	0.25330500	-0.05681000	-0.00219100
	H	-0.56389700	0.51864000	-0.43411100
	H	-0.12034900	-0.72956500	0.76587000
	H	0.77617300	-0.61728900	-0.77233200
	S	1.43502700	1.07783100	0.76861300
	H	0.71413600	1.31983700	1.96449000
	N	0.81035100	0.39590000	3.21820700
	C	1.59937500	-0.48666100	3.19040400
PostRC2	C	-0.84328100	-0.49183900	-1.76395900
	H	-1.87947500	-0.23867500	-1.52424400
	H	-0.60924400	-1.43526500	-1.27138600
	H	-0.73464400	-0.57870900	-2.84225800
	S	0.18760000	0.83112000	-1.10290900
	H	0.02455800	0.19703600	1.18241600
	N	-0.10292600	-0.16069500	2.11703200
	C	-0.25243100	-0.57656300	3.19208800
TS3	C	-0.02815100	0.03294000	0.03970100
	H	-0.11655200	-0.08186300	1.11843900
	H	1.03060400	0.12491400	-0.21149600
	H	-0.45350900	-0.84109800	-0.44736200
	S	-0.93598400	1.54453300	-0.39916800
	H	-0.74212700	1.48012600	-1.72811000
	N	1.62860000	0.12647400	-3.49953100
	C	2.17718700	-0.09888400	-2.50534400
PostRC3	C	-0.66418200	-0.80388500	1.58331800
	H	0.10326100	-0.91005600	2.33389400
	H	1.22540400	-0.11919500	-0.93898600
	H	-1.43366900	-1.54710900	1.45264700

	S	-0.73087600	0.71307000	0.74710600
	H	-1.79101100	0.45628200	-0.03834200
	N	2.79318400	-0.92225900	-2.28396400
	C	1.98459300	-0.50793600	-1.58854800
TS4	C	-1.68078000	-0.73687000	0.05129400
	H	-1.06407600	-0.47671200	-0.86355100
	H	-0.98255800	-0.93555500	0.86131500
	H	-2.31106200	0.11852800	0.28370400
	S	-2.73896800	-2.12798500	-0.30030900
	H	-1.79531300	-3.08668000	-0.28267000
	N	-0.04571700	0.12191000	-2.09285300
	C	0.02182800	1.08088700	-2.76851700
PostRC4	C	-0.29241000	0.09473000	1.37643900
	H	0.80253800	0.80110600	-0.47349800
	H	0.56840500	-0.10396100	1.99788200
	H	-0.87166600	0.99468100	1.52839600
	S	-1.12013800	-1.20270600	0.58737400
	H	-0.15462600	-2.13366300	0.68350000
	N	1.35534700	1.14739800	-1.23645000
	C	2.00034800	1.55376800	-2.11372700

Table C8 Optimised (BHandHLYP/aug-cc-pVDZ) Cartesian coordinates of the stationary points indicated in Figure 4.8 and Figure 4.9

Molecule	Atom, (x, y, z) coordinates			
CN	C	0.00000000	0.00000000	0.00000700

	N	0.00000000	0.00000000	1.15765300
CH_2S	C	-0.00490300	0.03082100	0.01012700
	H	0.35669800	-0.99603900	0.00863900
	H	0.36663800	0.53522700	-0.87909500
	H	-1.09258400	0.02009300	0.01459600
	S	0.65170000	0.80007100	1.52561000
	H	0.11430200	2.01949200	1.35002800
HCN	C	-0.50123400	0.27446300	0.00000000
	H	-1.56828500	0.27446300	0.00000000
	N	0.64253900	0.27446300	0.00000000
HNC	N	-1.83588800	0.08599500	0.00258100
	H	-2.82995000	0.08599500	-0.00036200
	C	-0.67244600	0.08599500	0.00601900
HCS	C	-1.29177200	0.51177700	-0.07024900
	H	-2.27339700	0.17675900	0.26476900
	S	0.15721700	0.09735200	0.34417600
SCN	C	0.36940500	0.46827800	0.00000000
	S	2.00816600	0.46827800	0.00000000
	N	-0.79943900	0.46827800	0.00000000
$^3CH_2$	C	-1.15183400	0.88036200	0.00000000
	H	-0.57764300	-0.03456400	0.00000000
	H	-2.20582600	1.11676500	0.00000000
HC(S)CN	C	0.94762600	0.76630000	0.03531500
	H	0.74885400	-0.30000700	-0.04607100
	S	0.99620700	1.51687400	1.46143400

	C	1.15825500	1.43054400	-1.21503600
	N	1.32326200	1.93751900	-2.23328300
Add-C	C	-0.59095600	-0.14056000	0.11483100
	H	-0.12150900	-0.72191400	-0.66113500
	H	-1.33373600	-0.53745400	0.78880700
	S	-0.18232600	1.52751400	0.35481700
	C	0.97994400	1.75829100	-0.86482600
	N	1.77094500	1.96140000	-1.67541600
TS_C/N	C	0.03417800	0.20909500	0.05646200
	H	0.89945700	0.69240400	-0.37521600
	H	0.14589700	-0.55022500	0.81884000
	S	-1.50513400	0.57531700	-0.45754800
	C	-1.16360100	1.21370000	-2.32571600
	N	-1.59993900	0.12354100	-2.54956300
Add-N	C	-0.54122900	-0.15086600	0.14641600
	H	-0.23571200	-0.72823600	-0.71240200
	H	-1.20394700	-0.53929600	0.90584600
	S	-0.32642100	1.55286000	0.17192200
	C	1.85730100	1.98241900	-1.58916500
	N	0.97237200	1.73039500	-0.86554000
TS_Int	C	-0.34182700	0.03070200	-0.03051600
	H	0.22203300	-0.88872000	-0.07183800
	H	-1.36695700	0.08745400	-0.36349000
	S	0.29461700	1.36601300	0.97133100
	C	0.67437500	1.49057900	-0.68081600
	N	1.04012100	1.76124900	-1.76759300

Int	C	0.59524900	0.75122400	-0.02808500
	H	0.93452300	-0.28657300	-0.02375200
	H	-0.49628500	0.72518900	-0.02375700
	S	1.14135000	1.52350200	1.51488800
	C	1.06425900	1.41448400	-1.23952500
	N	1.42817200	1.92912300	-2.19741100
TS_Pro	C	0.45911000	1.21790300	0.06579800
	H	1.09474200	-0.96068800	-0.14359600
	H	-0.49749000	0.70588700	0.00556900
	S	1.10430700	1.66405400	1.49215100
	C	1.03500200	1.57143100	-1.19687000
	N	1.47159700	1.85836300	-2.22069400
Post_HCN	C	-1.89346400	0.19333700	-0.02195800
	H	-0.30215100	-1.71756400	0.00504100
	H	-2.97822400	0.10462100	-0.07346100
	S	-0.94062400	1.42776300	0.05089500
	C	0.35220100	-2.56662800	0.01470700
	N	1.04664100	-3.47580400	0.02477400
Post_HNC	C	-1.73775100	0.09975000	0.00000000
	H	-0.37359300	-1.63235100	0.00000000
	H	-2.81060300	-0.09132600	0.00000000
	S	-0.90966700	1.42155400	0.00000000
	N	0.21862100	-2.44419600	0.00000000
	C	0.89737100	-3.38770600	0.00000000

Table C9 Optimised (M06-2X/aug-cc-pVTZ) Cartesian coordinates of the stationary points indicated in Figure 4.5 and Figure 4.6

Molecule	Atom, (x, y, z) coordinates			
CN	C	0.00000000	0.00000000	0.00264900
	N	0.00000000	0.00000000	1.15501100
CH$_3$SH	C	-0.00448100	0.03326900	0.01236400
	H	0.35670200	-0.99162800	0.01022500
	H	0.36682800	0.53862800	-0.87390500
	H	-1.09012700	0.02355100	0.01733900
	S	0.65051000	0.79711200	1.52436600
	H	0.11242000	2.00873300	1.33951300
HCN	C	-0.50097000	0.27446300	0.00000000
	H	-1.56721000	0.27446300	0.00000000
	N	0.64120100	0.27446300	0.00000000
HNC	N	-1.83368000	0.08599500	0.00241700
	H	-2.83293500	0.08599500	-0.00534200
	C	-0.67166900	0.08599500	0.01116200
CH$_3$S	C	-0.01137400	-0.01487100	0.01843700
	H	0.36471500	-1.03390700	-0.01952600
	H	0.36540500	0.51968200	-0.85685200
	H	-1.09757500	0.00134400	-0.01653300
	S	0.61236700	0.86244500	1.45205700
CH$_2$SH	C	0.25295300	0.03423000	0.04805800
	H	0.35013900	-1.03584000	-0.00627600
	H	0.16186500	0.63237800	-0.84049300
	S	0.44452000	0.75262000	1.59691700
	H	0.25300200	2.02626400	1.23212300

PreRC1	C	-0.19388900	0.03069000	-0.00202900
	H	0.85436100	-0.09992500	-0.25231400
	H	-0.81688800	-0.76091900	-0.40379100
	H	-0.32218400	0.07881100	1.07536300
	S	-0.77028700	1.62405900	-0.63607000
	H	-0.74301700	1.33063700	-1.94274800
	C	-2.94870800	0.86343700	-0.64490500
	N	-3.46076800	-0.06819200	-0.18291200
TS1	C	-0.03417700	0.05943400	0.12048500
	H	0.71922900	-0.31225500	-0.56718100
	H	-0.89743300	-0.60075500	0.14018800
	H	0.37512800	0.15021400	1.12172600
	S	-0.57740900	1.70886200	-0.38397700
	H	-1.37090500	1.30328500	-1.46875200
	C	-2.87534600	0.71199500	-1.08461000
	N	-3.74046600	-0.02218100	-0.86728600
PostRC1	C	0.18674700	0.04486700	0.00456200
	H	1.12648100	-0.39821300	-0.31595700
	H	-0.65819400	-0.45194000	-0.46708900
	H	0.10809700	-0.08479900	1.08662800
	S	0.19107500	1.81221200	-0.29624200
	H	-2.34867200	1.46324100	-0.87628200
	C	-3.11013000	0.71657000	-1.00027500
	N	-3.89678300	-0.10334100	-1.12475100
PreRC2	C	0.23277500	-0.01062400	0.15275400
	H	-0.25816400	0.45419700	-0.69758400
	H	-0.47775700	-0.43459500	0.85359100
	H	0.92251000	-0.78056000	-0.18034200

	S	1.23733100	1.21405800	1.01413600
	H	0.24248100	1.91450800	1.57330600
	N	1.12356900	-0.02721600	2.88976200
	C	1.88137600	-0.90788600	3.09332800
TS2	C	0.26452500	-0.05495800	0.01925100
	H	-0.54714700	0.51320100	-0.42929500
	H	-0.11717100	-0.70427200	0.80309500
	H	0.78564300	-0.63840600	-0.73216200
	S	1.43866600	1.08515800	0.77081500
	H	0.71319900	1.29680100	1.99712000
	N	0.78804000	0.39484600	3.20278700
	C	1.57836600	-0.47048700	3.06733900
PostRC2	C	-0.90681900	-0.41739500	-1.52811900
	H	-1.67149400	-0.32892300	-2.29508200
	H	-1.29683600	-0.90065600	-0.63531300
	H	-0.09469800	-1.03105200	-1.92595800
	S	-0.19061300	1.18416300	-1.15684300
	H	0.08645100	0.36965400	1.06066100
	N	-0.00279700	-0.28119500	1.83167800
	C	-0.12029900	-1.04911600	2.69492700
TS3	C	0.02004200	0.02788100	-0.03665000
	H	-0.00442800	-0.07340600	1.04546300
	H	1.07953600	0.09194400	-0.34320000
	H	-0.42994100	-0.84417000	-0.49968300
	S	-0.85191000	1.54420300	-0.45854200
	H	-0.76914900	1.40322300	-1.78921100
	N	1.60622700	0.19207600	-3.31840900

	C	1.90969200	-0.05461100	-2.23263900
PostRC3	C	-0.47570600	-0.74950000	1.31152600
	H	-0.38860400	-0.87843200	2.37743500
	H	2.13155200	-0.37120800	-0.17266100
	H	-0.58698500	-1.60287500	0.66432800
	S	-0.92549200	0.81929400	0.76997900
	H	-0.95595300	0.54983100	-0.54279800
	N	1.06257100	-0.81939900	-2.05418300
	C	1.62532100	-0.58879900	-1.08650000
TS4	C	-1.74356300	-0.72334100	0.13089900
	H	-1.17137300	-0.30549800	-0.75411400
	H	-1.02316200	-0.94273900	0.91380300
	H	-2.45343300	0.03230200	0.45504500
	S	-2.65736900	-2.15893300	-0.37034900
	H	-1.62400300	-3.01011700	-0.43462800
	N	-0.24308300	0.36677900	-2.04342800
	C	0.31933900	0.69906700	-3.00881500
PostRC4	C	-0.37148300	0.14076000	1.42667200
	H	0.67678300	0.92254000	-0.40494800
	H	0.51134000	-0.01557900	2.02491900
	H	-1.02877300	0.96596800	1.65020800
	S	-1.08024500	-1.16245400	0.56081900
	H	-0.02053500	-1.98268900	0.56665000
	N	1.25184200	1.21634000	-1.18025900
	C	1.92204700	1.55529000	-2.06584300

Table C10 Optimised (M06-2X/aug-cc-pVTZ) Cartesian coordinates of the stationary points indicated in Figure 4.8 and Figure 4.9

Molecule	Atom, (x, y, z) coordinates			
CN	C	0.00000000	0.00000000	0.00264900
	N	0.00000000	0.00000000	1.15501100
CH_2S	C	-0.00490300	0.03082100	0.01012700
	H	0.35669800	-0.99603900	0.00863900
	H	0.36663800	0.53522700	-0.87909500
	H	-1.09258400	0.02009300	0.01459600
	S	0.65170000	0.80007100	1.52561000
	H	0.11430200	2.01949200	1.35002800
HCN	C	-0.50097000	0.27446300	0.00000000
	H	-1.56721000	0.27446300	0.00000000
	N	0.64120100	0.27446300	0.00000000
HNC	N	-1.83368000	0.08599500	0.00241700
	H	-2.83293500	0.08599500	-0.00534200
	C	-0.67166900	0.08599500	0.01116200
HCS	C	-1.28922800	0.50982000	-0.06829200
	H	-2.26986500	0.17689300	0.26463500
	S	0.15114100	0.09917500	0.34235300
SCN	C	0.36616700	0.46827800	0.00000000
	S	2.00917900	0.46827800	0.00000000
	N	-0.79721400	0.46827800	0.00000000
$^3CH_2$	C	-1.15064400	0.88201500	0.00000000
	H	-0.58356400	-0.03163800	0.00000000

	H	-2.20109400	1.11218700	0.00000000
HC(S)CN	C	0.94682000	0.76340100	0.03756300
	H	0.74788200	-0.30162000	-0.04445000
	S	0.99721000	1.51965900	1.45299900
	C	1.15799900	1.42769100	-1.21540600
	N	1.32429300	1.94209900	-2.22834700
Add-C	C	0.02636200	0.09527600	0.11473500
	H	0.17745800	-0.07323100	1.16675400
	H	0.82288500	0.07010200	-0.60658600
	S	-1.56096800	0.58795300	-0.33615100
	N	-1.28140500	0.84865900	-3.15610200
	C	-1.37347400	0.73507400	-2.01539200
TS_C/N	C	0.02671200	0.21074200	0.04580600
	H	0.89259500	0.68605900	-0.38915500
	H	0.13672500	-0.53444000	0.81967200
	S	-1.49495200	0.55782400	-0.47565600
	C	-1.15703300	1.21520900	-2.30276600
	N	-1.59318900	0.12843900	-2.53064300
Add-N	C	-0.60892200	-0.11580000	0.07057400
	H	0.00501600	-0.79705300	-0.49452200
	H	-1.44839700	-0.44793900	0.65889600
	S	-0.04905600	1.45253200	0.43004700
	C	1.68048800	2.01269000	-1.73802300
	N	0.94323600	1.74284800	-0.86989400
TS_Int	C	-0.34085800	0.03464300	-0.02221100
	H	0.22915600	-0.87754300	-0.08296100

	H	-1.35710600	0.09724500	-0.37436500
	S	0.29170500	1.36223800	0.97526800
	C	0.67302500	1.49107200	-0.67338900
	N	1.02644000	1.73962200	-1.76526300
Int	C	0.59493300	0.75079400	-0.02745100
	H	0.93296200	-0.28660100	-0.02128400
	H	-0.49579300	0.72369500	-0.02149100
	S	1.14146300	1.52356800	1.50478700
	C	1.06352900	1.41335200	-1.23950000
	N	1.43017400	1.93214300	-2.19270200
TS_Pro	C	0.46366400	1.18121800	0.08368800
	H	1.08290100	-0.79900800	-0.20175000
	H	-0.50140200	0.68595000	0.02227600
	S	1.10018700	1.65686700	1.49513900
	C	1.03992700	1.52515100	-1.18792000
	N	1.48199100	1.80677100	-2.20907500
Post_HCN	C	-1.91147200	0.15799700	-0.02302900
	H	-0.38587900	-1.73410800	0.00117500
	H	-2.99786900	0.16342400	-0.07335700
	S	-0.85010100	1.28683200	0.05137700
	C	0.33290800	-2.52931300	0.01477000
	N	1.09679200	-3.37910700	0.02906300
Post_HNC	C	-1.77608900	0.08164400	0.00000000
	H	-0.42999900	-1.65472700	0.00000000
	H	-2.85923400	-0.01805100	0.00000000
	S	-0.82882900	1.30843700	0.00000000
	N	0.21854700	-2.42903200	0.00000000

	C 0.95998400 -3.32254600 0.00000000

Table C11 Unscaled harmonic vibrational frequencies (cm^{-1}) of the stationary points indicated in Figure 4.5 and Figure 4.6 (BHandHLYP/aug-cc-pVDZ).

Molecule	Wavenumber (cm^{-1})
CN	2247.3106
CH_3SH	237.0518 734.0747 814.7963 993.6447 1122.9959 1381.5186 1493.3406 1505.0557 2766.4196 3143.1512 3239.3349 3240.7851
HCN	781.9379 781.9379 2295.8436 3548.1368
HNC	469.8860 469.8873 2190.8722 3918.4467
CH_3S	602.9114 739.7860 886.5508 1357.1314 1401.7373 1489.0719 3110.6217 3193.9866 3216.9981
CH_2SH	102.7104 336.7388 804.6505 862.2522 1099.8219 1448.6088 2773.2896 3266.7402 3407.0051
PreRC1	50.4857 93.9631 128.5076 189.8011 361.8762 548.6498 721.8724 810.0644 994.2531 1123.7005 1379.2399 1484.4999 1490.5167 2260.3273 2773.4234 3155.5808 3261.6646 3278.2490
TS1	-1004.4476 56.2669 82.2890 99.2969 189.8729 267.2085 723.8979 850.1892 975.5137 1109.8504 1372.6768 1486.5908 1489.8011 2163.7511 2303.2314 3149.5434 3257.5241 3259.0511

PostRC1	25.7018 45.4299 98.9365 104.0987 131.0095 735.9611 827.4458 861.7858 878.1341 944.8321 1358.9378 1440.0019 1489.0109 2280.6647 3112.1845 3197.0069 3233.6091 3431.7818
PreRC2	28.9034 126.0873 142.0048 194.9657 314.3610 531.7066 729.4045 814.8532 985.3111 1123.6425 1373.4974 1482.2961 1491.3381 2094.4218 2780.9925 3153.2319 3257.9418 3280.0916
TS2	-908.8376 92.0640 106.3590 155.6181 170.7102 295.1439 727.1855 880.1649 952.5675 1115.1654 1365.1104 1481.3318 1483.1190 1972.5338 2068.6591 3143.5761 3247.4235 3266.6368
PostRC2	34.8788 39.6668 124.4368 130.3401 148.5760 659.8072 731.9040 737.6990 855.5650 981.6838 1359.5334 1453.3461 1485.3705 2189.6958 3114.7444 3196.4352 3240.6113 3629.4059
TS3	-73.2400 27.8314 43.0726 62.5402 90.1416 270.0725 738.6418 814.9228 987.2000 1120.9408 1376.5129 1484.7886 1490.3479 2247.4471 2765.0900 3099.1168 3201.2053 3243.3208
PostRC3	27.4302 70.8010 84.3524 99.7650 142.9066 231.0568 383.2338 803.9314 832.6760 843.9405 856.8156 1099.6368 1448.7918 2285.7970 2769.4530 3264.7126 3407.0233 3470.0021
TS4	-362.5388 18.3079 76.6510 13.7393 197.7406 367.1665 767.0185 834.3408 977.2757 1127.0819 1265.9374 1411.1364 1436.8043 1826.8725 2257.1160 2763.0605 3178.2133 3258.7849

PostRC4	48.8867 96.3398 117.1049 118.9921 179.6944 379.9702 573.1190 638.7541 672.8660 812.2087 866.6557 1108.4902 1446.8508 2192.6737 2768.1258 3240.8466 3375.6521 3723.0320

Table C12 Unscaled harmonic vibrational frequencies (cm^{-1}) of the stationary points indicated in Figure 4.8 and Figure 4.9 (BHandHLYP/aug-cc-pVDZ).

Molecule	Wavenumber (cm^{-1})
CN	2247.3106
CH_2S	1031.0744 1084.3513 1135.2027 1535.5456 3173.1339 3270.6952
HCN	781.9379 781.9379 2295.8436 3548.1368
HNC	469.8860 469.8873 2190.8722 3918.4467
HCS	866.3277 1252.4571 3212.6025
SCN	361.4529 435.8574 762.2326 2056.7257
$^3CH_2$	1091.4693 3204.6888 3453.4607
HC(S)CN	213.3245 367.1022 554.6028 885.9735 942.3495 1173.8541 1402.3255 2436.6572 3229.3066
Add-C	87.6047 191.3849 272.4321 396.2560 482.0046 704.5585 826.8362 975.7683 1431.5514 2391.3337 3266.6833 3421.0696
TS_C/N	-261.5996 189.3369 276.4110 356.8675 488.8630 705.3381 868.1383 964.4256 1451.8039 1975.9715 3234.2486 3370.1899

Add-N	154.8710 211.4217 259.9733 373.4462 399.5171 694.6453 832.2137 959.9699 1422.1625 2232.7785 3251.0732 3399.7874
TS_Int	-712.3607 324.7078 385.9529 598.6151 693.0688 746.2756 819.0662 975.3491 1444.4145 2025.2206 3243.0982 3397.9024
Int	194.8605 362.2770 513.6432 609.7204 747.1248 981.0664 1193.4520 1283.2277 1439.3434 2470.3418 3140.2266 3176.2622
TS_Pro	-476.0664 204.9336 232.0165 260.7244 408.0493 550.8215 861.9906 921.2953 1114.7898 1368.7153 2426.9504 3237.5462
Post_HCN	32.9888 91.5767 96.3924 105.5198 295.0903 830.8643 842.5711 871.1183 1258.6807 2286.1087 3218.5997 3471.8989
Post_HNC	44.6519 117.3892 121.8619 142.7644 341.9394 671.2122 706.1166 872.0527 1263.1387 2191.7144 3217.7845 3697.0782

Table C13 Unscaled harmonic vibrational frequencies (cm^{-1}) of the stationary points indicated in Figure 4.5 and Figure 4.6 (M06-2X/aug-cc-pVTZ).

Molecule	Wavenumber (cm^{-1})
CN	2241.9799
CH_3SH	276.1450 727.8781 800.3452 976.3162 1096.9937 1358.2969 1481.7894 1494.1411 2731.7300 3089.7897 3176.8876 3178.1156
HCN	785.3481 785.3481 2254.5540 3466.4178

HNC	528.7255 528.7255 2147.7615 3811.6074
CH_3S	736.1921 869.0177 1270.0579 1334.3274 1479.0390 2269.1693 3054.0431 3129.5144 3324.2744
CH_2SH	156.2286 363.6929 796.6508 855.4842 1082.2700 1411.3125 2742.8478 3207.3958 3335.1369
PreRC1	45.7063 94.5459 139.5086 207.4888 374.9778 538.9140 724.1106 794.0481 979.2229 1098.3097 1358.0273 1468.1934 1473.0383 2211.2927 2727.1031 3096.0629 3193.2585 3204.8128
TS1	-1065.7990 61.2649 86.6347 103.5372 205.2532 287.2561 723.0377 838.6082 958.5006 1080.6484 1349.6990 1474.1582 1475.6690 2008.7789 2262.0153 3088.5083 3181.5490 3191.0911
PostRC1	31.6115 53.3244 70.8783 122.0011 138.0170 729.9868 782.9699 834.1089 853.7626 931.6929 1339.8241 1419.5162 1477.7403 2240.8850 3051.9304 3126.4950 3155.0025 3358.9668
PreRC2	31.6950 106.9400 132.2274 205.3692 328.3653 520.2156 726.8325 803.4692 970.0540 1099.1433 1352.7795 1464.5703 1473.0765 2072.4515 2734.1418 3092.4120 3188.5847 3204.5807
TS2	-1007.6074 84.7333 119.8280 166.3369 185.8603 270.5782 730.2862 865.6207 933.9361 1078.1254 1344.1795 1465.6463 1468.9892 1717.9837 2037.0148 3081.5105 3171.8761 3194.1637

PostRC2	42.9043 60.1549 99.1727 141.9083 151.6004 642.8462 720.4161 734.8973 868.0336 939.1187 1340.0724 1427.2894 1474.4735 2143.5202 3051.0691 3128.4519 3163.4360 3532.8006
TS3	-405.1131 42.0472 68.0518 105.9414 157.0478 314.9413 727.6255 772.5311 948.1032 1077.4149 1336.9913 1359.9768 1460.6411 2183.7077 2711.9363 2729.7534 3121.2006 3183.7841
PostRC3	41.5701 61.6721 92.7720 136.5436 207.9072 371.6441 470.8781 778.0517 791.9936 795.6359 855.4201 1080.2469 1410.9651 2248.5689 2722.7055 3191.6136 3316.8557 3459.4631
TS4	-224.9975 42.4279 64.5879 118.8002 196.8764 366.1995 765.4157 824.1578 957.4963 1106.4409 1313.7032 1411.6377 1424.0451 2036.5966 2255.7649 2726.5655 3115.4319 3189.3583
PostRC4	45.0062 81.7067 110.4223 137.3512 198.3182 389.5286 563.0790 651.8421 679.4600 791.6606 858.6316 1076.6125 1415.0301 2145.5640 2722.0211 3180.2697 3303.3007 3603.3707

Table C14 Unscaled harmonic vibrational frequencies (cm^{-1}) of the stationary points indicated in Figure 4.8 and Figure 4.9 (M06-2X/aug-cc-pVTZ).

Molecule	Wavenumber (cm^{-1})
CN	2241.9799
CH_2S	1007.2367 1043.0690 1126.6462 1503.7697 3101.0270 3185.8806

HCN	785.3481 785.3481 2254.5540 3466.4178
HNC	528.7255 528.7255 2147.7615 3811.6074
HCS	825.6847 1246.2622 3142.4357
SCN	359.4858 427.8734 738.8191 2092.5346
$^3CH_2$	1096.3069 3177.8218 3396.7268
HC(S)CN	204.9736 359.3566 545.6008 859.7987 921.1702 1154.9073 1368.5547 2388.2483 3149.6072
Add-C	93.8207 188.3706 212.7811 392.5506 483.4363 693.5238 819.9928 949.6358 1393.3599 2342.0736 3203.6513 3344.8994
TS_C/N	-264.7013 202.1944 287.0667 392.4361 525.5126 693.2465 877.3070 938.1144 1414.3137 1951.7609 3163.8509 3286.8969
Add-N	163.9322 222.8079 277.9545 382.2349 411.7359 693.4937 823.3423 937.2006 1386.1807 2179.7793 3186.6629 3321.4594
TS_Int	-679.3926 324.9819 383.5202 559.4563 670.0781 718.5772 810.1638 946.8822 1407.5408 2029.9427 3175.8677 3318.8434
Int	188.4885 357.0182 510.6746 575.1578 740.3073 960.4375 1170.8492 1249.4111 1417.6517 2421.3253 3075.7517 3103.2191
TS_Pro	-863.0167 201.7114 268.6527 318.7518 429.8183 541.5828 872.7980 906.4294 1114.1936 1341.4610 2391.6939 3147.1151
Post_HCN	30.1921 77.4377 104.8783 119.3701 286.7646 822.9675 837.8733 840.2206 1252.9268 2244.4903 3147.4217 3385.8050

Post_HNC	42.6518 94.8527 125.8100 150.2525 327.4496 676.8381 691.5384 841.2318 1259.9340 2146.2525 3147.8013 3578.6057

Table C15 Rotational constants (GHz) of the stationary points indicated in Figure 4.5 and Figure 4.6 (BHandHLYP/aug-cc-pVDZ).

Molecule	Rotational constants (GHz)
CN	58.35603
CH_3SH	103.17369 12.86765 12.33982
HCN	45.11481
HNC	45.85440
CH_3S	158.89255 13.35244 13.32965
CH_2SH	144.47407 15.39886 13.91566
PreRC1	11.31000 3.49058 2.76531
TS1	12.44536 2.67164 2.24944
PostRC1	13.88799 1.47236 1.34227
PreRC2	12.63873 3.55576 3.01275
TS2	11.44143 3.44334 2.99057
PostRC2	13.82261 1.78625 1.59746
TS3	11.78749 1.90230 1.68569

PostRC3	13.95991 1.47766 1.36067
TS4	20.37964 1.71718 1.64667
PostRC4	16.02449 1.66288 1.53831

Table C16 Rotational constants (GHz) of the stationary points indicated in Figure 4.8 and Figure 4.9 (BHandHLYP/aug-cc-pVDZ).

Molecule	Rotational constants (GHz)
CN	58.35603
CH_2S	293.70849 17.78609 16.77052
HCN	45.11481
HNC	45.85440
HCS	917.48128 20.33844 19.89736
SCN	6.11802
$^3CH_2$	1696.16249 252.20695 219.55999
HC(S)CN	43.82859 3.20056 2.98275
Add-C	19.15151 4.23209 3.46615
TS_C/N	16.43500 5.06952 4.53685
Add-N	20.14868 4.49387 3.68496
TS_Int	14.36892 5.53971 4.11515

Int	26.88285 3.11925 2.84362
TS_Pro	27.49394 3.11587 2.92430
Post_HCN	23.70911 1.41065 1.33143
Post_HNC	27.18686 1.59230 1.50420

Table C17 Rotational constants (GHz) of the stationary points indicated in Figure 4.5 and Figure 4.6 (M06-2X/aug-cc-pVTZ).

Molecule	Rotational constants (GHz)
CN	58.89243
CH_3SH	103.57405 12.95597 12.42341
HCN	45.23242
HNC	45.93265
CH_3S	159.45992 13.47592 13.45230
CH_2SH	145.25017 15.60797 14.10055
PreRC1	11.21933 3.72129 2.90214
TS1	12.17883 2.85156 2.37330
PostRC1	13.01160 1.85657 1.64130
PreRC2	11.67277 3.82356 3.15990
TS2	11.37438 3.62199 3.12610

PostRC2	12.94457 2.03696 1.77936
TS3	12.34071 2.27821 1.97763
PostRC3	11.92463 2.34568 2.11652
TS4	18.28591 1.74291 1.62383
PostRC4	15.32738 1.74948 1.60435

Table C18 Rotational constants (GHz) of the stationary points indicated in Figure 4.8 and Figure 4.9 (M06-2X/aug-cc-pVTZ).

Molecule	Rotational constants (GHz)
CN	58.89243
CH_2S	295.08548 17.92432 16.89790
HCN	45.23242
HNC	45.93265
HCS	927.29532 20.58265 20.13571
SCN	6.11781
$^3CH_2$	1671.48960 255.53548 221.64989
HC(S)CN	43.33167 3.22242 2.99937
Add-C	19.12653 4.28612 3.50192
TS_C/N	16.89874 5.19915 4.66348

Add-N	20.12310 4.56431 3.73339
TS_Int	14.54295 5.56456 4.14270
Int	26.81433 3.14305 2.86246
TS_Pro	28.82429 3.13907 2.94172
Post_HCN	21.78902 1.53274 1.43200
Post_HNC	24.19565 1.69424 1.58336

Appendix D

Supplementary information for the reaction between the amidogen radical (NH_2) and acetaldehyde (CH_3CHO)

Table D1 Energies (Hartree) of the stationary points indicated in Figure 5.7

Molecule	BHandHLYP/aug-cc-pVDZ	CCSD(T)/aug-cc-pVTZ//BHandHLYP/aug-cc-pVDZ	M06-2X/aug-cc-pVTZ	CCSD(T)/aug-cc-pVTZ//M06-2X/aug-cc-pVTZ
NH_2	–55.8589791011	–55.799797984	–55.8719284624	–55.799829483
CH_3CHO	–153.760053914	–153.59802683	–153.820793847	–153.59813079
NH_3	–56.5305370620	–56.480457169	–56.5529642916	–56.480527651
CH_3CO	–153.114033439	–152.94735907	–153.171232213	–152.94744810
CH_2CHO	–153.107965838	–152.93606211	–153.161746096	–152.93609487
$NH_2C(O)CH_3$	–209.126692943	–208.90810119	–209.211556650	–208.90827582
H	–0.49807845526	–0.4998211760	–0.49820646135	–0.4998211760
VDW1	–209.625359646	–209.40446664	–209.699497606	–209.40457579
TS_CH_3CO	–209.607124568	–209.39052990	–209.686797217	–209.39039278
VDW2	–209.625469279	–209.40468654	–209.699531572	–209.40481646
TS_CH_2CHO	–209.599480111	–209.38222816	–209.678957880	–209.38250358

TS_Add	–209.612370780	–209.39440597	–209.690114263	–209.39453032
Add	–209.641961674	–209.41761370	–209.717699613	–209.41754241
TS_amide	–209.608701096	–209.39076622	–209.692287914	–209.39057191

Table D2 Zero-point energies (ZPVE) (Hartree) of the stationary points indicated in Figure 5.7

Molecule	Unscaled BHandHLYP/aug-cc-pVDZ	Scaled BHandHLYP/aug-cc-pVDZ (scaling factor: 0.9589)	Unscaled M06-2X/aug-cc-pVTZ	Scaled M06-2X/aug-cc-pVTZ (scaling factor: 0.956)
NH_2	0.019651	0.018843343	0.019207	0.018361892
CH_3CHO	0.057086	0.054739765	0.055972	0.053509232
NH_3	0.035216	0.033768622	0.034461	0.032944716
CH_3CO	0.044360	0.042536804	0.043467	0.041554452
CH_2CHO	0.043819	0.042018039	0.042959	0.041068804
$NH_2C(O)CH_3$	0.075492	0.072389278	0.073785	0.070538460
H	0	0	0	0
VDW1	0.079401	0.076137618	0.077596	0.074181776
TS_CH_3CO	0.075903	0.072783386	0.074159	0.070896004
VDW2	0.079439	0.076174057	0.077370	0.073965720
TS_CH_2CHO	0.076063	0.072936810	0.074416	0.071141696

TS_Add	0.082360	0.078975004	0.080528	0.076984768
Add	0.087071	0.083492381	0.084276	0.080567856
TS_amide	0.078584	0.075354197	0.076767	0.073389252

Table D3 Relative energies of the stationary points indicated in Figure 5.7.

Molecule	Energy (CCSD(T)/aug-cc-pVTZ//M06-2X/aug-cc-pVTZ) + ZPVE (Scaled M06-2X/aug-cc-pVTZ frequencies) (Hartree)	Relative energy (Hartree)	Relative energy (kJ/mol)
NH_2	–55.781467591		
CH_3CHO	–153.544621558		
NH_2 + CH_3CHO	–209.326089149	0	0
NH_3	–56.447582935		
CH_3CO	–152.905893648		
NH_3 + CH_3CO	–209.353476583	–0.027387434	–71.9
CH_2CHO	–152.895026066		
NH_3 + CH_2CHO	–209.342609001	–0.016519852	–43.4
$NH_2C(O)CH_3$	–208.837737360		
H	–0.4998211760		
$NH_2C(O)CH_3$ + H	–209.337558536	–0.011469387	–30.1

VDW1	–209.330394014	–0.004304865	–11.3
TS_CH_3CO	–209.319496776	0.006592373	17.3
VDW2	–209.330850740	–0.004761591	–12.5
TS_CH_2CHO	–209.311361884	0.014727265	38.7
TS_Add	–209.317545552	0.008543597	22.4
Add	–209.336974554	–0.010885405	–28.6
TS_amide	–209.317182658	0.008906491	23.4

Table D4 Optimised (BHandHLYP/aug-cc-pVDZ) Cartesian coordinates of the stationary points indicated in Figure 5.7.

Molecule	Atom, (x, y, z) coordinates
NH_2	N -0.32903600 -0.74345900 0.02569500
	H 0.03575500 -1.69694400 -0.01953300
	H 0.03577200 -0.30589200 -0.82265800
CH_3CHO	C -0.40610500 0.55132900 0.02466600
	H -0.37094400 -0.52271200 0.22594100
	H 0.26496300 0.73826700 -0.81797000
	H -1.42032700 0.85466900 -0.22673300
	C 0.08725700 1.29539200 1.22399700

	H	1.11570600	1.04649700	1.54968300
	O	-0.54830600	2.11372200	1.82549400
NH_3	N	-0.03910700	0.12702000	0.00000200
	H	0.33096400	-0.81130700	-0.00000100
	H	0.33098200	0.59617900	0.81261100
	H	0.33097200	0.59617900	-0.81261200
CH_3CO	C	-1.13580300	0.24273400	-0.03370800
	H	-0.80890700	-0.77617300	0.17490600
	H	-0.75153600	0.51553400	-1.01679800
	H	-2.22561000	0.31010700	-0.01314000
	C	-0.52164800	1.15743300	0.98734700
	O	-1.04697700	1.88044200	1.74592900
CH_2CHO	C	-1.88872000	0.70846300	0.03333700
	H	-1.89165100	1.31121700	-0.86538800
	H	-2.31298100	-0.28672800	0.01272200
	C	-1.32704200	1.23731800	1.22311200
	H	-1.34093000	0.59711600	2.11801100
	O	-0.83734100	2.36137900	1.28328400

$NH_2C(O)CH_3$	C	1.41675700	0.81445900	-1.05068600
	H	1.67022600	-0.08958800	-0.49630000
	H	1.81959400	1.68670000	-0.54263300
	H	1.87326000	0.75179700	-2.04046000
	C	-0.07065600	0.99339700	-1.21513400
	O	-0.58739600	2.08328400	-1.31023300
	N	-0.79776200	-0.15200900	-1.27717900
	H	-0.37903800	-1.05524100	-1.20407800
	H	-1.78426400	-0.08213400	-1.43113300
VDW1	C	-0.43676100	0.67908700	0.08956400
	H	-0.51665100	-0.41035200	0.04580800
	H	0.19879100	0.98270000	-0.74653700
	H	-1.42088600	1.13405200	0.00085800
	C	0.21814800	1.07223900	1.37215100
	H	1.22529800	0.65839000	1.55376700
	O	-0.28219700	1.79535300	2.19190800
	N	2.23003800	1.50323300	3.94636900
	H	2.43305600	1.91673700	4.85652800

	H	1.29600100	1.84871700	3.71066000
TS_CH$_3$CO	C	-0.13138500	0.63037900	0.40952100
	H	0.14226300	-0.39542900	0.66444600
	H	0.66788700	1.02775500	-0.21883100
	H	-1.08500300	0.65444200	-0.11561700
	C	-0.19995600	1.43994000	1.66850700
	H	0.90290900	1.44535400	2.29214400
	O	-1.13546200	2.03940400	2.08073900
	N	2.06084700	1.44208700	3.01585800
	H	1.87013400	0.64627800	3.62338500
	H	1.85260600	2.24994500	3.60092500
VDW2	C	-0.55151600	0.36117900	0.14902100
	H	-1.04731000	1.20957700	-0.33062900
	H	-1.31989800	-0.39945900	0.31234300
	H	0.23827600	-0.02794000	-0.48992100
	C	-0.01493100	0.79876000	1.47157500
	H	-0.75923700	1.20778000	2.17954400
	O	1.13861100	0.73494400	1.80100800

	N	2.83211400	-0.48995000	-0.54637500
	H	3.83996200	-0.63417900	-0.47979200
	H	2.56962100	-0.08494300	0.35590300
TS_CH_2CHO	C	-0.09297600	0.37061400	0.23633000
	H	1.10798100	-0.01140800	-0.04785100
	H	-0.42797900	0.75631900	-0.72395200
	H	-0.62667400	-0.50839100	0.58438500
	C	0.11586600	1.39135300	1.27598300
	H	0.39654000	2.39771000	0.91869400
	O	0.03153400	1.17141300	2.45742000
	N	2.23475600	-0.62240700	-0.25891800
	H	1.92160500	-1.40846200	-0.82560100
	H	2.39166200	-1.02215000	0.66485700
TS_Add	C	-1.80224000	0.75772400	-0.04612100
	H	-1.53746200	-0.29752400	-0.00551700
	H	-1.49805100	1.15630800	-1.01748700
	H	-2.87938000	0.88404100	0.05501400
	C	-1.07767400	1.53317900	1.01587800

	H	-0.00927800	1.29718200	1.11638900
	N	-1.57030100	0.55576900	2.64787100
	H	-1.08806900	1.06961400	3.38279700
	H	-2.55014700	0.80878200	2.76715300
	O	-1.50042900	2.61709400	1.44417900
Add	C	-1.80490400	0.73413400	0.03139200
	H	-1.50103300	-0.30735500	-0.07870400
	H	-1.53045300	1.27942900	-0.87198100
	H	-2.88915800	0.78286500	0.14653800
	C	-1.12399000	1.34390900	1.23440900
	H	-0.03692100	1.23758000	1.16276700
	N	-1.54743800	0.71153400	2.46334200
	H	-1.06678000	1.09855100	3.26038800
	H	-2.54101200	0.82521700	2.60140500
	O	-1.47134300	2.67630500	1.41060200
TS_amide	C	-1.91538500	0.80400400	0.06277000
	H	-1.77178800	-0.27430000	0.13052300
	H	-1.40491900	1.18954900	-0.81508600

	H	-2.98444600	1.00661500	-0.02761800
	C	-1.41267400	1.52608300	1.29508700
	H	0.13644300	1.09802100	1.10854500
	N	-1.79421800	0.95397100	2.49274900
	H	-1.43793500	1.40498000	3.31492000
	H	-1.85505000	-0.04444200	2.54279900
	O	-1.07306100	2.71768900	1.25547000

Table D5 Optimised (M06-2X/aug-cc-pVTZ) Cartesian coordinates of the stationary points indicated in Figure 5.7.

Molecule	Atom, (x, y, z) coordinates			
NH_2	N	-0.32996800	-0.74279100	0.02683100
	H	0.03622300	-1.69829700	-0.01951600
	H	0.03623600	-0.30520600	-0.82381200
CH_3CHO	C	-0.38354600	0.55805300	0.00919700
	H	0.27434600	-0.29351400	-0.17297800
	H	-0.39390600	1.21803100	-0.85356500
	H	-1.38166800	0.15521600	0.18998100
	C	0.08280500	1.29322600	1.22909700

	H	0.12602700	0.69534800	2.15979200
	O	0.39818600	2.45080400	1.24355300
NH_3	N	-0.04248000	0.12703500	0.00000200
	H	0.33209300	-0.81320500	-0.00000100
	H	0.33210500	0.59712000	0.81427900
	H	0.33209300	0.59712000	-0.81428000
CH_3CO	C	-1.13580300	0.24273400	-0.03370800
	H	-0.80890700	-0.77617300	0.17490600
	H	-0.75153600	0.51553400	-1.01679800
	H	-2.22561000	0.31010700	-0.01314000
	C	-0.52164800	1.15743300	0.98734700
	O	-1.04697700	1.88044200	1.74592900
CH_2CHO	C	-1.89060400	0.70618900	0.03088800
	H	-1.89387000	1.31134800	-0.86350600
	H	-2.31185700	-0.28748200	0.00961400
	C	-1.32467300	1.24089300	1.22566200
	H	-1.33843900	0.59529300	2.11771200
	O	-0.83922300	2.36252300	1.28470600

$NH_2C(O)CH_3$	C	1.41838600	0.81428300	-1.04838300
	H	1.66843500	-0.08890200	-0.49484200
	H	1.82153100	1.68567300	-0.54202200
	H	1.87126800	0.75126800	-2.03802900
	C	-0.07235000	0.99748400	-1.21388000
	O	-0.58894700	2.08841700	-1.31078200
	N	-0.79811800	-0.15357800	-1.27370500
	H	-0.37160000	-1.05831300	-1.20988500
	H	-1.78788300	-0.08566700	-1.43630600
VDW1	C	-0.41613300	0.67822400	0.10560600
	H	-0.48282500	-0.41065600	0.07253100
	H	0.23359700	0.97978200	-0.71785400
	H	-1.40138100	1.12119200	-0.00806600
	C	0.20636000	1.09378400	1.40127200
	H	1.21482300	0.69562700	1.61218100
	O	-0.32636400	1.82066300	2.20037300
	N	2.19704700	1.47886500	3.87363800
	H	2.46077800	1.86522500	4.78361600

	H	1.25893600	1.85745000	3.69777800
TS_CH_3CO	C	-0.11739000	0.67200100	0.38692600
	H	0.19495000	-0.35803800	0.56073300
	H	0.68105900	1.15351900	-0.17821300
	H	-1.05658800	0.70719800	-0.15900800
	C	-0.24616300	1.36201500	1.71312900
	H	0.80188400	1.33006700	2.33604000
	O	-1.21617100	1.88879100	2.15237100
	N	2.07080300	1.26995100	3.04615800
	H	1.69561000	0.88195500	3.91705000
	H	2.13684400	2.27269600	3.24589100
VDW2	C	-0.52218400	0.35513300	0.14572000
	H	-1.01590300	1.19734500	-0.34309400
	H	-1.28577200	-0.41030900	0.29749800
	H	0.28200600	-0.02807000	-0.47708600
	C	-0.01053000	0.80058500	1.47853600
	H	-0.76894500	1.20496600	2.17462400
	O	1.14069200	0.74603300	1.82498900

	N	2.77683500	-0.47848500	-0.54456800
	H	3.78645500	-0.64041100	-0.50217400
	H	2.54303800	-0.07101800	0.36823200
TS_CH_2CHO	C	-0.10764000	0.39719200	0.16087900
	H	1.04571200	0.01668300	-0.16813400
	H	-0.48761600	0.85240800	-0.74888200
	H	-0.64083000	-0.49407300	0.47447100
	C	0.16493200	1.33488700	1.26895700
	H	0.34951300	2.38639500	0.98475000
	O	0.23991700	0.99606700	2.42380200
	N	2.21837600	-0.64106900	-0.26452700
	H	1.88221800	-1.55288100	-0.58631700
	H	2.38773300	-0.78101800	0.73634600
TS_Add	C	-1.80603000	0.75863600	-0.04080000
	H	-1.52573700	-0.29139200	-0.01488600
	H	-1.53796400	1.17130500	-1.01511800
	H	-2.87977600	0.87060300	0.09638300
	C	-1.06541200	1.54118300	1.01027500

	H	0.00443400	1.30057800	1.10627700
	N	-1.56125400	0.54299600	2.64666400
	H	-1.10027500	1.08119100	3.38452900
	H	-2.55068500	0.79042300	2.73744900
	O	-1.49033300	2.61664500	1.44938200
Add	C	-1.81890300	0.75782800	0.04773300
	H	-1.56658700	-0.29900000	0.01401600
	H	-1.49383600	1.25149900	-0.86348500
	H	-2.89905200	0.86474300	0.14473000
	C	-1.13401200	1.37620000	1.27400800
	H	-0.04681800	1.29015800	1.14542500
	N	-1.50395200	0.65896200	2.47039400
	H	-1.08806300	1.09169400	3.28533600
	H	-2.50985500	0.67694000	2.59485400
	O	-1.45195500	2.71314500	1.24714500
TS_amide	C	-1.92047200	0.81043400	0.06117600
	H	-1.77713400	-0.26631000	0.13042300
	H	-1.41220300	1.19755200	-0.81615100

	H	-2.98777000	1.01907800	-0.02035700
	C	-1.40811200	1.53588500	1.29617200
	H	0.07874000	1.08467200	1.09404700
	N	-1.77076300	0.93796900	2.49622400
	H	-1.41522200	1.39321900	3.32225900
	H	-1.79815700	-0.06691200	2.53393900
	O	-1.10194000	2.73657900	1.26242300

Table D6 Unscaled harmonic vibrational frequencies (cm^{-1}) of the stationary points indicated in Figure 5.7 (BHandHLYP/aug-cc-pVDZ).

Molecule	Wavenumber (cm^{-1})
NH_2	1562.3111 3484.3004 3579.3958
CH_3CHO	168.2578 522.0315 798.9242 927.6380 1167.1782 1174.7331 1413.7219 1463.7198 1483.3808 1494.2641 1896.2627 3011.0857 3115.8032 3181.0775 3239.6917
NH_3	1043.8405 1693.3273 1693.3350 3587.4683 3720.0774 3720.1032
CH_3CO	116.5343 481.6027 904.7953 978.4791 1082.5310 1386.7412 1477.3675 1478.0669 2014.3938 3115.4497 3215.9617 3219.7761
CH_2CHO	474.1450 518.4068 804.5854 1011.0953 1013.1129 1196.1698 1430.9626 1515.3866 1576.8099 3086.3072 3241.8424 3365.5242

$NH_2C(O)CH_3$	42.8004 203.4613 436.1535 538.0495 569.0810 673.5025 885.8370 1016.4394 1084.4356 1158.6111 1384.6429 1448.3971 1497.3111 1515.9774 1681.4966 1843.6590 3132.8450 3204.3066 3247.0427 3713.9070 3858.9885
VDW1	63.4740 72.8051 142.3611 164.3188 190.0444 288.8085 321.6679 529.2707 811.0845 932.1787 1170.9450 1186.3458 1415.8587 1474.9163 1485.5456 1495.1525 1581.4307 1879.5806 3055.5910 3116.4287 3181.4216 3240.4171 3473.5705 3579.8448
TS_CH_3CO	–1850.6679 49.5382 109.2023 118.6554 239.5590 381.9279 588.0539 654.8794 790.4939 948.4066 974.0471 1149.4469 1293.9652 1405.1884 1459.4133 1481.3829 1491.2609 1568.2372 1941.8720 3123.2268 3201.4265
VDW2	75.3664 88.9259 136.8906 161.4470 188.7746 289.8010 341.7989 534.9120 804.4276 930.4510 1180.2612 1181.2359 1418.6714 1467.7298 1488.6092 1499.9824 1579.8524 1884.1157 3025.9068 3113.2153 3177.3073 3244.3104 3475.2702 3580.5385
TS_CH_2CHO	–2013.4913 62.8348 99.3324 176.6653 411.5991 525.8080 533.8599 702.5348 878.5845 948.4680 1010.6177 1134.4280 1175.6767 1309.4302 1434.9849 1450.8371 1489.4462 1573.8747 1827.5338 3039.9803 3184.0491 3284.4844 3518.5563 3614.1184
TS_Add	–475.2806 196.4869 225.7981 280.1899 398.3618 514.0174 715.9603 815.6773 910.4042 979.5641 1108.7952 1170.3148 1411.1484 1434.5204 1492.5629 1501.0066 1584.3345 1631.7521 3079.7744 3124.5595 3201.6477 3235.7204 3520.7788 3618.3292
Add	235.5689 341.3458 366.3362 403.7121 524.5315 844.7607 894.7502 949.5714 1041.9000 1124.7920 1207.7822 1287.5286 1384.4895 1429.8402 1473.2358 1506.7133 1516.2783 1697.9910 3116.2678 3124.8318 3206.5523 3213.8160 3615.8711 3711.0653

TS_amide	–1183.9284 197.6172 396.9177 456.6549 505.9138 533.3263 616.1236 652.7528 713.9536 892.7061 1018.7042 1086.2524 1171.5184 1365.7974 1440.3566 1500.0675 1510.8677 1649.0294 1696.6625 3133.0659 3206.5427 3252.7111 3685.1503 3811.8970

Table D7 Unscaled harmonic vibrational frequencies (cm^{-1}) of the stationary points indicated in Figure 5.7 (M06-2X/aug-cc-pVTZ).

Molecule	Wavenumber (cm^{-1})
NH_2	1531.5886 3405.6604 3493.6840
CH_3CHO	163.0217 513.5663 779.0266 900.9351 1138.1867 1146.0322 1381.6376 1430.3317 1466.0849 1475.7589 1865.7796 2944.0370 3061.8928 3124.6679 3177.7397
NH_3	1031.9317 1659.0495 1659.6365 3508.5788 3633.1568 3634.3644
CH_3CO	97.5784 468.9292 866.6931 955.3696 1049.5196 1353.0407 1459.2567 1461.8530 1985.8134 3062.1509 3158.2204 3161.5624
CH_2CHO	455.4787 509.7045 758.0600 981.9680 990.3857 1169.9461 1409.2589 1481.2105 1629.1315 3004.7145 3176.0083 3290.8471
$NH_2C(O)CH_3$	31.7408 192.0489 430.6848 523.1225 558.1449 656.4375 862.9309 989.8007 1059.5074 1124.8236 1349.0716 1410.1745 1475.4682 1494.4322 1619.8078 1815.1507 3079.2226 3148.1184 3185.2431 3620.2650 3761.8716

VDW1	55.6568 99.1263 112.9618 154.8242 155.7337 285.3817 293.7395 521.7478 788.9190 907.1814 1141.2044 1155.9669 1382.0418 1447.6286 1464.8835 1473.8642 1540.5115 1846.6502 2987.4797 3063.3513 3125.4053 3180.0175 3389.7937 3486.8190
TS_CH$_3$CO	–1200.8949 51.5501 82.6841 101.3744 209.8910 422.1135 612.8750 615.7110 800.4342 919.1571 932.2367 1131.7470 1249.9571 1367.7572 1397.0826 1460.4349 1464.5411 1535.3418 1909.5105 3068.4341 3139.6207 3176.9727 3407.0030 3495.5199
VDW2	38.9721 66.4894 104.6598 145.9590 157.3993 286.0806 301.3625 527.0971 778.9759 905.1303 1149.6458 1151.9267 1386.6857 1434.5115 1467.6241 1480.0896 1540.7119 1852.8525 2954.3881 3058.4084 3120.6282 3174.8979 3390.0869 3486.7586
TS_CH$_2$CHO	–1763.6131 48.7993 96.5360 162.8539 378.8652 511.9414 599.6075 676.8147 864.3537 928.8687 967.2125 1115.0167 1144.6584 1324.2884 1391.7473 1419.9615 1459.3245 1543.0341 1813.1255 2965.6825 3124.2843 3214.9062 3411.4196 3501.3848
TS_Add	–441.3410 202.1770 209.0855 274.3182 392.1498 505.7420 683.0005 793.6056 885.7569 953.9560 1095.9959 1140.5138 1380.5501 1402.2874 1469.9607 1479.6699 1544.8232 1627.5916 2993.7140 3068.9930 3142.4992 3174.3743 3416.8154 3510.0638
Add	215.2174 249.4492 362.2812 418.5156 495.8771 843.4580 874.0290 896.9706 984.9806 1036.7524 1151.8491 1243.0039 1249.3068 1383.8119 1392.1951 1484.9125 1495.6467 1655.0698 3007.3603 3079.0880 3158.6738 3181.6867 3523.4833 3609.1511
TS_amide	–1138.4853 200.8816 387.5029 445.8028 496.0434 522.4663 593.1430 647.6512 695.5432 870.1973 988.1287 1062.8554 1138.5968 1316.7719 1395.3313 1474.4090 1486.0081 1610.6980 1652.7921 3075.2056 3148.5428 3186.5426 3589.4411 3712.3672

Table D8 Rotational constants (GHz) of the stationary points indicated in Figure 5.7 (BHandHLYP/aug-cc-pVDZ).

Molecule	Rotational constants (GHz)
NH_2	718.40325 388.71937 252.23697
CH_3CHO	57.53259 10.27456 9.21161
NH_3	302.33802 302.33769 189.84799
CH_3CO	85.93271 10.04165 9.51871
CH_2CHO	67.45633 11.58912 9.89000
$NH_2C(O)CH_3$	10.98923 9.37061 5.22180
VDW1	21.67963 2.60649 2.36049
TS_CH_3CO	9.85842 4.22055 3.04919
VDW2	10.39363 3.57711 2.70539
TS_CH_2CHO	14.78695 3.38101 3.00616
TS_Add	9.90600 7.03590 4.71836
Add	10.44193 8.27545 5.32766
TS_amide	10.08034 8.78889 5.15439

Table D9 Rotational constants (GHz) of the stationary points indicated in Figure 5.7 (M06-2X/aug-cc-pVTZ).

Molecule	Rotational constants (GHz)

NH_2	712.93038 387.58406 251.08298
CH_3CHO	57.34273 10.25604 9.19039
NH_3	299.87944 299.86305 189.07759
CH_3CO	84.85115 10.05365 9.51476
CH_2CHO	67.51344 11.54901 9.86199
$NH_2C(O)CH_3$	10.92316 9.35601 5.20205
VDW1	20.28384 2.72350 2.43694
TS_CH_3CO	9.77287 4.13050 3.00151
VDW2	10.27356 3.69276 2.76228
TS_CH_2CHO	13.03348 3.73154 3.17434
TS_Add	9.82481 7.05492 4.71539
Add	9.85698 8.53711 5.21715
TS_amide	10.03827 8.77972 5.13009

Appendix E

Supplementary information for the theoretical calculations of dimerisation reactions in the context of Laval nozzle experiments

Table E1 Energies (Hartree) of the stationary points indicated in Figure 6.8

Molecule	Single point energy at CCSD(T)/aug-cc-pVTZ//BHandHLYP/aug-cc-pVDZ	Single point energy at BHandHLYP/aug-cc-pVDZ	Unscaled ZPVE at BHandHLYP/aug-cc-pVDZ
CH_2O	–114.34248213	–114.454045365	0.027595
$(CH_2O)_2$ C_s	–228.69249081	–228.914515232	0.057682
$(CH_2O)_2$ C_{2h}	–228.69129565	–228.913672476	0.057026
Molecule	Single point energy at CCSD(T)/aug-cc-pVTZ//BHandHLYP/aug-cc-pVDZ	Single point energy at BHandHLYP/aug-cc-pVDZ	Unscaled ZPVE at BHandHLYP/aug-cc-pVDZ
CH_3CHO	–153.59802683	–153.760053914	0.057086
$(CH_3CHO)_2$ C_1	–307.20458006	–307.526760497	0.115759
$(CH_3CHO)_2$ C_2	–307.20410117	–307.525791173	0.115136
$(CH_3CHO)_2$ C_i	–307.20403493	–307.525738388	0.115190
$(CH_3CHO)_2$ C_s	–307.20301712	–307.525955135	0.115629

$(CH_3CHO)_2$ C_{2h} 1	–307.20272656	–307.525741239	0.115491
$(CH_3CHO)_2$ C_{2h} 2	–307.20246323	–307.525419817	0.115545
Molecule	Single point energy at CCSD(T)/jul-cc-pVTZ//BHandHLYP/aug-cc-pVDZ	Single point energy at BHandHLYP/aug-cc-pVDZ	Unscaled ZPVE at BHandHLYP/aug-cc-pVDZ
$CH_3C(O)CH_3$	–192.84931130	–193.062352642	0.085754
$(CH_3C(O)CH_3)_2$ C_s	–385.70735327	–386.131186618	0.172777
$(CH_3C(O)CH_3)_2$ C_{2h} 1	–385.70983901	–386.132168433	0.172816
$(CH_3C(O)CH_3)_2$ C_{2h} 2	–385.70464310	–386.129817676	0.172857
Molecule	Single point energy at CCSD(T)/aug-cc-pVTZ//BHandHLYP/aug-cc-pVDZ	Single point energy at BHandHLYP/aug-cc-pVDZ	Unscaled ZPVE at BHandHLYP/aug-cc-pVDZ
NH_3	–56.480457169	–56.5305370620	0.035216
$(NH_3)_2$ C_s	–112.96610227	–113.065935248	0.072855

Table E2 Optimised (BHandHLYP/aug-cc-pVDZ) Cartesian coordinates of the stationary points indicated in Figure 6.8.

Molecule	Atom, (x, y, z) coordinates			
CH_2O	C	-0.00062699	0.00000000	-0.00042618
	H	0.00004806	0.00000000	1.10294870
	H	0.98689033	0.00000000	-0.49261136

	O	-1.01632104	0.00000000	-0.62862628
$(CH_2O)_2$ C_s	H	-0.24104900	0.03917500	-0.12356500
	O	0.06687100	0.01261800	2.31044700
	C	0.63532200	0.01931300	-0.78965300
	H	0.44784900	0.03284200	-1.87510100
	O	1.75019600	-0.01566300	-0.35324600
	C	1.26409500	-0.02031800	2.33760300
	H	1.87061500	0.89805700	2.36406000
	H	1.81946000	-0.97074700	2.35323100
$(CH_2O)_2$ C_{2h}	H	-0.16194400	0.05504300	-0.19044000
	O	0.13607300	0.04241100	2.28191200
	C	0.59854600	0.01692800	-0.98381900
	H	0.24562400	0.03672000	-2.02872300
	O	1.76738500	-0.04379600	-0.72645400
	C	1.30479000	-0.01810200	2.53977200
	H	2.06561700	-0.05578000	1.74671900
	H	1.65726700	-0.03813100	3.58482300
CH_3CHO	C	-0.40610500	0.55132900	0.02466600

	H	-0.37094400	-0.52271200	0.22594100
	H	0.26496300	0.73826700	-0.81797000
	H	-1.42032700	0.85466900	-0.22673300
	C	0.08725700	1.29539200	1.22399700
	H	1.11570600	1.04649700	1.54968300
	O	-0.54830600	2.11372200	1.82549400
$(CH_3CHO)_2$ C_1	C	2.14388600	1.26618800	2.56668700
	H	2.69120600	1.12480900	3.50246900
	H	2.87929800	1.32470900	1.76231500
	H	1.55474200	2.17996000	2.61214700
	C	1.26655200	0.08190600	2.32817700
	H	1.78837800	-0.88872800	2.26556900
	O	0.07052300	0.12929500	2.22211100
	C	0.31620600	-0.04164700	-2.36373400
	H	-0.26696000	-0.94284200	-2.57074800
	H	-0.32602600	0.81044000	-2.60169700
	H	1.21331100	-0.02227600	-2.97870000
	C	0.66163200	-0.00433100	-0.91129500

	H	-0.18535600	-0.02245300	-0.20454100
	O	1.78530600	0.04367100	-0.48663600
$(CH_3CHO)_2$ C_2	C	2.39681200	0.96422700	2.56655700
	H	2.72569500	0.78775100	3.59326600
	H	3.09729500	0.45027000	1.90298800
	H	2.38814200	2.02938000	2.34508000
	C	1.04555100	0.36831400	2.35951000
	H	0.94453500	-0.69382800	2.64825800
	O	0.10259300	0.95353700	1.89980600
	C	0.75725100	1.34027300	-1.40217800
	H	0.32211100	1.31617800	-2.40392400
	H	0.00345500	1.75061500	-0.72499400
	H	1.64917000	1.96311900	-1.38706600
	C	1.07132400	-0.04701700	-0.95420600
	H	0.23852400	-0.77023400	-1.02576300
	O	2.13443500	-0.40260100	-0.52254300
$(CH_3CHO)_2$ C_i	C	2.23510500	1.25951700	2.48313500
	H	2.79535400	1.22065200	3.42007500

	H	2.95894000	1.26816500	1.66413000
	H	1.62393700	2.15812700	2.43751400
	C	1.39228200	0.03640700	2.34992800
	H	1.92024500	-0.92482400	2.49210500
	O	0.21886900	0.03773700	2.09381300
	C	-0.33192000	-0.11988500	-1.18730000
	H	-1.03042000	0.15808700	-1.98038500
	H	-0.92311000	-0.42202900	-0.31965100
	H	0.30511500	-0.94008800	-1.51190000
	C	0.48642900	1.06744400	-0.80473000
	H	-0.08796700	1.96582900	-0.51464800
	O	1.68699700	1.09518500	-0.78979200
$(CH_3CHO)_2$ C_s	C	-0.54673600	0.09061600	-0.02124400
	H	-1.35797200	-0.60517100	-0.25342800
	H	-0.98345900	1.09321400	-0.03531900
	H	-0.12676800	-0.12789800	0.95913500
	C	0.48757300	0.00018700	-1.09318500
	H	0.13317200	0.21026200	-2.12005800

	O	1.64222900	-0.27755600	-0.91361700
	C	3.55396100	-1.22647100	3.18861100
	H	3.95875200	-2.17434900	2.82392100
	H	4.33399300	-0.47450300	3.04225000
	H	3.29878100	-1.30561000	4.24330300
	C	2.35592800	-0.85748500	2.37482200
	H	2.51320800	-0.75263800	1.28842700
	O	1.26086600	-0.67533100	2.83841300
$(CH_3CHO)_2$ C_{2h} 1	C	-0.67698900	0.22744600	-1.74654700
	H	-1.44605000	-0.54913000	-1.71866900
	H	-1.16424400	1.16355000	-1.46089300
	H	-0.25926900	0.30941500	-2.74779700
	C	0.38729300	-0.09780500	-0.74903400
	H	0.06277000	-0.20226500	0.29965500
	O	1.54754600	-0.24643500	-1.02975800
	C	3.35596900	-1.17765900	3.18389000
	H	3.84322400	-2.11376200	2.89823500
	H	4.12502900	-0.40108200	3.15601100

	H	2.93824900	-1.25962700	4.18514000
	C	2.29168600	-0.85240800	2.18637700
	H	2.61620800	-0.74794800	1.13768900
	O	1.13143200	-0.70377800	2.46710200
$(CH_3CHO)_2$ C_{2h} 2	C	-1.34541600	0.21003600	0.97940800
	H	-2.11038500	-0.56762800	1.05804600
	H	-1.82571000	1.14891800	1.26913200
	H	-0.51006500	-0.00988800	1.64118800
	C	-0.90532400	0.31195600	-0.44294400
	H	-1.70313100	0.53450500	-1.17693900
	O	0.22436900	0.17158000	-0.82481500
	C	2.98919100	-0.53761200	1.20726100
	H	3.75416100	0.24005200	1.12862800
	H	3.46948600	-1.47649300	0.91753600
	H	2.15384200	-0.31768600	0.54548000
	C	2.54909800	-0.63953600	2.62961300
	H	3.34690300	-0.86208900	3.36360800
	O	1.41940400	-0.49916000	3.01148200

$CH_3C(O)CH_3$	C	-1.40614000	0.23161100	-0.03568200
	H	-0.49033900	-0.13328400	-0.50676800
	H	-1.91284300	0.92522700	-0.70172900
	H	-2.04038100	-0.63922700	0.14619000
	C	-1.07955700	0.91401600	1.26677000
	C	-0.37597500	0.08646900	2.31025100
	H	-0.19210200	0.68599300	3.19807600
	H	-0.98337300	-0.78394900	2.56948600
	H	0.56985000	-0.29080300	1.91430300
	O	-1.36719000	2.06600900	1.46434600
$(CH_3C(O)CH_3)_2$ C_s	C	2.25976200	1.26129800	2.57843700
	H	3.06831400	1.30043200	3.31179400
	H	2.71284400	1.25826400	1.58581900
	H	1.61600800	2.13002500	2.69132600
	C	1.46024500	0.00027300	2.75510600
	C	2.21234300	-1.29644900	2.64066800
	H	3.06256700	-1.30659200	3.32587700
	H	2.60328100	-1.38329600	1.62545500

	H	1.55083300	-2.13198500	2.85556600
	O	0.27321800	0.02742900	2.96977000
	C	0.40095100	0.16803100	-2.50234100
	H	-0.20396400	-0.60510000	-2.98052600
	H	-0.06479700	1.12806600	-2.73866600
	H	1.41449300	0.14862600	-2.89422600
	C	0.41681600	-0.02423600	-1.00945800
	C	-0.91376700	-0.17389100	-0.32626600
	H	-1.36997600	-1.11682200	-0.63934400
	H	-1.59150700	0.62365600	-0.63749800
	H	-0.79282000	-0.16686200	0.75356200
	O	1.45512200	-0.05724900	-0.39501600
$(CH_3C(O)CH_3)_2$ C_{2h} 1	C	2.22321900	1.08469200	2.49911100
	H	2.61552900	1.01233200	3.51510300
	H	2.97877300	0.67769600	1.82366800
	H	2.02718400	2.12386400	2.24749100
	C	0.96721000	0.27139100	2.35716800
	C	1.04324400	-1.17041800	2.77500300

	H	1.41898000	-1.25470500	3.79637700
	H	1.74883900	-1.68614100	2.12015800
	H	0.06350200	-1.63498800	2.69831100
	O	-0.04549900	0.74555400	1.90131300
	C	0.96206700	1.27851700	-1.34358500
	H	0.58632900	1.36280400	-2.36495800
	H	0.25647400	1.79424000	-0.68873800
	H	1.94181000	1.74308700	-1.26689500
	C	1.03810300	-0.16329200	-0.92575000
	C	-0.21790500	-0.97659300	-1.06769300
	H	-0.61021500	-0.90423500	-2.08368500
	H	-0.97346100	-0.56959600	-0.39225100
	H	-0.02187100	-2.01576500	-0.81607000
	O	2.05081200	-0.63745400	-0.46989400
$(CH_3C(O)CH_3)_2$ C_{2h} 2	C	-1.34441300	0.09219400	0.95122300
	H	-2.04509100	-0.74616200	0.99124000
	H	-1.88297400	0.96911000	1.31755100
	H	-0.48736100	-0.11604900	1.58690900

	C	-0.91621900	0.30688200	-0.47362300
	C	-1.97945100	0.74008500	-1.44869300
	H	-2.83162200	0.05816100	-1.41016500
	H	-2.35030500	1.72923500	-1.16873500
	H	-1.57210100	0.77429100	-2.45579700
	O	0.22437600	0.14089900	-0.82949200
	C	2.95049700	-0.64829000	1.20702700
	H	3.35147300	-1.62995900	0.94069500
	H	3.75242100	0.07427100	1.03953200
	H	2.09718600	-0.41712900	0.57423800
	C	2.55650300	-0.65569000	2.65766300
	C	3.66296900	-0.82665400	3.66532700
	H	4.25659200	-1.71310300	3.43182200
	H	4.33829500	0.03109200	3.61498200
	H	3.24807900	-0.90661100	4.66674500
	O	1.40888000	-0.53237900	3.00824500
NH_3	N	-0.03910700	0.12702000	0.00000200
	H	0.33096400	-0.81130700	-0.00000100

	H	0.33098200	0.59617900	0.81261100
	H	0.33097200	0.59617900	-0.81261200
$(NH_3)_2$ C_s	N	1.56915900	0.00000000	-0.02036900
	H	1.56919200	-0.00000100	0.98853600
	H	2.08759000	-0.81189200	-0.31897200
	H	2.08759000	0.81189200	-0.31897100
	N	-1.70810500	0.00000000	0.09956000
	H	-0.72160300	0.00000000	-0.12918500
	H	-2.12331400	-0.81057700	-0.33386900
	H	-2.12331300	0.81057900	-0.33386700

Table E3 Unscaled harmonic vibrational frequencies (cm^{-1}) of the stationary points indicated in Figure 6.8 (BHandHLYP/aug-cc-pVDZ).

Molecule	Wavenumber (cm^{-1})
CH_2O	Harmonic: 1253.49 1293.41 1567.47 1893.75 3013.16 3091.70 Anharmonic: 1231.11 1273.79 1534.87 1868.93 2860.89 2922.58
$(CH_2O)_2$ C_s	Harmonic: 93.38 110.56 142.56 198.67 200.88 254.20 1243.21 1271.66 1293.03 1303.83 1567.03 1568.57 1871.58 1883.80 3034.00 3037.76 3118.87 3125.91

	Anharmonic: 73.74 83.44 100.72 130.82 150.59 155.50 1224.33 1239.03 1272.19 1278.73 1535.43 1537.74 1850.25 1859.49 2874.82 2879.71 2943.77 2949.68
$(CH_2O)_2$ C_{2h}	Harmonic: 72.41 75.98 118.70 129.25 130.73 141.08 1275.27 1276.17 1306.07 1306.10 1568.26 1569.43 1867.24 1883.32 3023.92 3026.16 3129.73 3131.92 Anharmonic: 67.84 71.21 72.27 77.13 113.37 126.50 1240.74 1240.99 1279.35 1280.64 1538.21 1538.25 1846.65 1859.66 2864.01 2864.31 2874.40 2875.95
CH_3CHO	168.26 522.03 798.92 927.64 1167.18 1174.73 1413.72 1463.72 1483.38 1494.26 1896.26 3011.09 3115.80 3181.08 3239.69
$(CH_3CHO)_2$ C_1	39.94 72.93 80.62 92.52 108.83 125.43 172.96 191.04 524.78 529.31 805.22 814.14 931.11 933.03 1169.48 1171.16 1172.38 1189.37 1411.25 1415.97 1466.72 1476.27 1486.00 1487.07 1495.85 1498.09 1872.58 1886.38 3042.83 3064.24 3116.20 3119.13 3181.07 3191.79 3237.15 3239.40
$(CH_3CHO)_2$ C_2	18.60 35.00 54.46 76.55 85.01 87.62 163.87 172.98 524.16 525.81 797.95 799.72 934.74 934.83 1170.88 1172.35 1176.94 1178.22 1412.91 1413.83 1465.71 1466.88 1483.96 1484.94 1495.15 1497.84 1878.81 1888.29 3027.72 3028.53 3116.99 3117.25 3187.33 3187.80 3237.37 3237.74
$(CH_3CHO)_2$ C_i	29.12 35.53 61.80 79.19 81.58 91.90 159.51 174.13 524.27 526.35 797.69 801.57 932.86 935.37 1170.58 1172.89 1176.07 1177.78 1413.17 1416.18 1465.27 1466.87 1480.25 1485.79 1495.52 1497.20 1880.17 1889.02 3022.74 3029.57 3118.40 3118.95 3188.58 3189.58 3237.48 3239.68
$(CH_3CHO)_2$ C_s	37.92 67.30 67.55 88.38 97.26 98.26 172.62 188.57 525.71 535.59 804.74 816.90 929.54 931.55 1167.45 1182.07 1182.47 1197.12 1415.47 1420.07 1467.03

	1480.55 1490.84 1494.79 1496.23 1503.63 1870.35 1888.36 3015.23 3074.37 3107.06 3115.06 3172.65 3179.67 3235.85 3237.17
$(CH_3CHO)_2$ C_{2h} 1	28.73 60.64 62.16 69.91 70.72 91.35 170.00 175.16 523.97 525.95 811.25 813.21 927.27 931.08 1165.85 1168.83 1192.28 1192.83 1414.81 1415.06 1478.65 1479.41 1488.82 1489.68 1495.63 1495.65 1864.60 1882.94 3070.24 3072.66 3115.08 3115.15 3179.88 3179.92 3237.59 3237.64
$(CH_3CHO)_2$ C_{2h} 2	37.12 63.43 71.35 91.28 94.68 101.12 188.70 195.64 531.44 533.39 803.01 806.05 931.23 931.39 1178.50 1181.94 1182.77 1182.84 1419.14 1420.73 1466.71 1468.34 1490.05 1493.91 1503.52 1506.95 1881.61 1891.62 3010.60 3011.98 3108.26 3108.87 3172.29 3172.41 3242.69 3242.73
$CH_3C(O)CH_3$	21.64 146.60 390.82 508.14 551.16 827.41 903.78 923.98 1113.67 1148.14 1286.35 1421.57 1437.18 1483.86 1490.50 1494.51 1515.39 1877.18 3117.12 3124.05 3181.22 3189.14 3243.57 3244.68
$(CH_3C(O)CH_3)_2$ C_s	13.58 27.24 53.97 59.24 77.11 81.18 85.12 87.52 147.88 152.28 394.82 398.35 507.68 511.32 551.57 554.25 829.86 832.01 905.23 907.65 931.13 933.40 1118.49 1118.74 1151.23 1151.31 1289.87 1294.41 1418.31 1426.25 1437.80 1441.66 1486.81 1487.67 1492.52 1496.08 1499.34 1499.84 1518.76 1519.98 1859.72 1869.34 3114.83 3120.64 3122.93 3127.16 3179.40 3188.52 3192.34 3199.35 3239.47 3241.09 3243.12 3250.94
$(CH_3C(O)CH_3)_2$ C_{2h} 1	23.44 49.39 53.00 55.65 59.54 71.00 85.66 88.59 152.99 154.54 395.94 397.00 506.70 513.76 551.12 553.09 831.87 832.16 903.32 905.11 935.16 935.61 1118.64 1119.16 1151.59 1153.28 1288.23 1294.59 1420.80 1421.99 1439.03 1439.88 1486.14 1488.91 1492.93 1497.71 1499.04 1500.15 1516.86 1521.96 1854.22

	1866.95 3120.24 3120.37 3126.64 3127.25 3189.79 3189.89 3197.28 3198.02 3239.24 3239.83 3240.95 3241.27
$(CH_3C(O)CH_3)_2$ C_{2h} 2	13.24 22.95 33.89 64.29 73.95 82.08 89.09 97.55 166.29 173.99 397.90 400.31 512.94 514.27 555.79 555.99 829.72 830.94 906.09 907.38 931.76 931.91 1118.31 1118.95 1151.39 1151.96 1292.26 1296.15 1425.40 1426.50 1442.02 1442.38 1487.22 1488.29 1494.79 1496.12 1500.00 1503.30 1521.52 1524.30 1861.87 1871.30 3111.33 3111.64 3121.52 3121.81 3175.67 3175.82 3187.01 3187.11 3242.19 3242.24 3246.04 3246.62
NH_3	1043.84 1693.33 1693.34 3587.47 3720.08 3720.10
$(NH_3)_2$ C_s	43.67 101.05 115.79 142.34 253.86 389.90 1075.88 1085.91 1687.65 1694.53 1698.31 1719.31 3554.00 3585.52 3684.29 3714.52 3714.95 3718.00

Table E4 Rotational constants (GHz) of the stationary points indicated in Figure 6.8 (BHandHLYP/aug-cc-pVDZ).

Molecule	Rotational constants (GHz)
CH_2O	284.94442 39.54571 34.72626
$(CH_2O)_2$ C_s	18.92418 3.76374 3.20960
$(CH_2O)_2$ C_{2h}	19.82679 3.02387 2.62371
CH_3CHO	57.53259 10.27456 9.21161
$(CH_3CHO)_2$ C_1	7.26735 1.43007 1.27115
$(CH_3CHO)_2$ C_2	4.93951 1.83320 1.59053

$(CH_3CHO)_2$ C_i	5.19440 1.86715 1.48487
$(CH_3CHO)_2$ C_s	6.35617 1.27809 1.07819
$(CH_3CHO)_2$ C_{2h} 1	9.67610 1.06723 0.97270
$(CH_3CHO)_2$ C_{2h} 2	5.12685 1.43945 1.13959
$CH_3C(O)CH_3$	10.31073 8.58419 4.97078
$(CH_3C(O)CH_3)_2$ C_s	3.24117 0.88143 0.82620
$(CH_3C(O)CH_3)_2$ C_{2h} 1	2.66699 1.18975 1.10554
$(CH_3C(O)CH_3)_2$ C_{2h} 2	4.80880 0.62856 0.56480
NH_3	302.33802 302.33769 189.84799
$(NH_3)_2$ C_s	120.20348 5.17083 5.11319